

RIKEN Accelerator Progress Report

1996

vol. **30**

理化学研究所
The Institute of Physical and Chemical Research (RIKEN)

RIKEN Accelerator Progress Report 1996
January-December

vol. 30

理化学研究所
The Institute of Physical and Chemical Research (RIKEN)
Wako-shi, Saitama, 351-01 JAPAN

Editors

A. Goto	T. Ichihara
T. Kambara	T. Kobayashi
Y. Kobayashi	T. Okada
I. Shimamura	M. Takami
S. Yamaji	F. Yatagai

All rights reserved. This report or any part thereof may not be reproduced in any form (including photostatic or microfilm form) without written permission from the publisher.

All reports are written on authors' responsibility and thus the editors are not liable for the contents of the report.

CONTENTS

	Page
I. PREFACE	1
II. OPERATION OF ACCELERATORS	
RRC and AVF Cyclotron Operations	3
RILAC Operation	5
The Tandem Operation	7
III. RESEARCH ACTIVITIES	
1. Nuclear Physics	
Distribution of the Gamow-Teller Strength in ^{11}Li	9
Stochastic Variational Method with Non-Central Potentials	10
Occupation Probability of Harmonic-Oscillator Quanta for Microscopic Cluster-Model Wave Functions	11
Reaction Cross Sections and Radii of $A = 17$ and $A = 20$ Isobars	12
New $SU(3)$ Symmetry in Superdeformation, Hyperdeformation, and Highly-Deformed Shape	13
Origin of $\Delta I = 2$ Staggering in Superdeformed States	14
Role of the x_0 Factor of Skyrme Force in the Interaction Radius of Extremely Neutron-Rich Nucleus	15
A Modified Second Order Glauber Model Calculation of the Interaction Cross Sections of Extremely Neutron Rich Nuclei	16
Electric Dipole Transitions in Neutron Capture and Coulomb Dissociation Processes	17
Quantum Monte Carlo Diagonalization Method for Nuclear Many Body Problem	18
Spreading of Gamow-Teller Resonance in ^{90}Nb and ^{208}Bi	19
Two-Dimensional GCM Calculation of TAR States	20
Variation of Transport Coefficients for Average Fission Dynamics with Temperature and Shape	21
The Continuity Equation of the Nuclear Four-Current	22
Unstable Nuclei and the Equation of State of Asymmetric Nuclear Matter	23
Effect of Relativistic Equation of State on Vortex Pinning to the Nuclei in Neutron Star Crusts	24
Baryon Properties Based on the Chiral Quark Soliton Model	25
QCD Corrections to the Structure Function g_2	26
Next-to-Leading-Order Q^2 Evolution Program for Spin-Dependent Structure Functions	27
Q^2 -Evolution of the Chiral-Odd Twist-3 Parton Distributions $h_L(x, Q^2)$ and $e(x, Q^2)$ in the Large N_c Limit	28

Q^2 -Evolution of Chiral-Odd Twist-3 Structure Function and Fragmentation Function: $e(x, Q^2)$ and $\hat{e}(z, Q^2)$	29
Quark Helicity Distributions Using QCD Sum Rule Approach	30
Quark Helicity in Proton by Semi-Inclusive Asymmetries of Kaons	31
Test of Δg in Spin Correlations between Target Protons and Produced Λ_c^+ at COMPASS Experiment	32
RHIC Spin Project	33
Spin Physics with PHENIX Detector System at RHIC	34
Study of Polarized Parton Distribution Functions in the Nucleon	35
R&D of Iarocci Tube for RHIC Spin Project	36
Measurement of Neutrons from Muon Catalyzed dt Fusion Reaction at RIKEN-RAL Muon Facility	37
Muon Transfer in Excited States of Muonic Hydrogen Atoms Observed with X-ray Measurement	38
Measurement of X-rays from α -Sticking in Muon Catalyzed dt Fusion Reaction at RIKEN-RAL Muon Facility	39
Experimental Study of CSB Force in N-d Scatterings at 12 MeV	40
Cross Sections of αxn Channels in the $^{40}\text{Ar} + ^{209}\text{Bi}$ Reaction	41
High-Spin States in ^{146}Eu	42
Study of High-Lying States in ^{147}Eu	43
High Spin Isomer Beam Line	44
Measurement of Deuteron Spin-Flip Probability in the $^{12}\text{C}(\vec{d}, \vec{d}')$ Reaction at $E_d = 270$ MeV	45
Measurement of Polarization Correlation Coefficient for the $^3\text{He}(d, p)^4\text{He}$ Reaction	46
Spin-Flip Dipole State of ^{90}Y Studied by the $^{90}\text{Zr}(d, ^2\text{He})$ Reaction at $E_d = 270$ MeV	47
Production Cross Sections of Projectile-like Fragments in the $^{48}\text{Ca} + ^{64}\text{Ni}$ and $^{48}\text{Ca} + ^{181}\text{Ta}$ Reactions at 70A MeV	48
New Neutron-Rich Isotopes ^{38}Mg , ^{40}Al , and ^{41}Al Produced by Fragmentation of a 70A MeV ^{48}Ca Beam	49
Isomer Production in Fragmentation Reactions Induced by a 70A MeV ^{48}Ca Beam	50
Angular Distribution of the ^8B Dissociation and E2 Components	51
Charge Exchange Reactions of Neutron-Rich Nuclei	52
Quasifree Nucleon-Knockout Reactions from ^6He and ^{11}Li	53
Reaction Cross Sections Measured for ^8B to Obtain Its Density Distribution	54
Momentum Distribution of ^7Be Produced through ^8B Fragmentation	55

Electromagnetic Dissociation of ^8B at 2A GeV	56
Nuclear Radii of Na and Mg Isotopes	57
Beta Decay of ^{11}Li	58
β -Delayed Neutron Decay of Spin Polarized ^{17}B	59
Measurement of β -decay Branching Ratio of ^{17}Ne into the First Excited State of ^{17}F	60
Magnetic Moments of ^{17}N and ^{17}B	61
Quadrupole Moment of ^{23}Mg	62
Asymmetry Parameter of ^{23}Mg Beta Decay	63
Development of Polarized ^{129}Xe Solid for Polarizing Unstable Nuclei	64
Production of a Low Energy ^{12}B Beam and Observation of its Nuclear Polarization	65
2. Atomic and Solid-State Physics	
Inelastic Processes in Collisions of H^+ Ions with C, N, and O Atoms below 1 keV	67
Electron Capture Rates in Collisions of H^+ Ions with Si Atoms: Capture by the ground and excited state	68
Charge Transfer in Collisions H^+ Ions with Ground State Mg Atom at Low keV Collision Energies	69
Triple-Center Expansion Study of Ionization Processes	70
Elastic and Inelastic Processes in $\text{H}^+ + \text{C}_2\text{H}_2$ Collisions below 1.5 keV Regime	71
Double Electron Detachment from Negative Hydrogen Ions under High Energy, Highly Charged Ion Impact	72
Theoretical Study for Absorption and Emission Spectra of Alkali Atom and Liquid-He Composite System	73
Photodetachment Cross-Sections of the Positronium Negative Ion	74
Recoil-Ion Momentum Spectroscopy of 0.25 MeV/nucleon Ar-He Collisions	75
Recoil-Ion Momentum Analyses of Single-Electron Capture of He by $\text{B}^{4+,5+}$ at 0.5–1 MeV/nucleon	76
Beam Foil Spectra of Highly Charged Argon Ion in Visible Region	77
Beam Foil Spectra of Highly Charged Neon Ion in Visible Region	78
Intercombination Line Oscillator Strengths for High-Z Mg- and Al-like Ions	79
Lifetimes for the Be- and B-like Fe Intercombination Lines	80
Oscillator Strengths for Resonance Transitions in Na-like Kr	81
Wavelengths for Al- and Si-like Intercombination Lines	82
Charge Transfer Cross Sections of Low-Energy Highly Charged Ions with N_2	83
Diode-Laser Spectroscopy of Atomic Beams	84
Laser Spectroscopy of AgHe_2 Exciplex in Liquid Helium	85

Temperature Dependence of Al-LVV Auger Electron Spectra (I)	86
Temperature Dependence of Al-LVV Auger Electron Spectra (II)	87
Mössbauer Spectroscopy using ^{57}Mn Beam from RIPS	88
Hyperfine Interactions of ^{61}Ni in Distorted Spinel Chromites	89
Magnetic Properties of $\text{YSr}_2\text{Cu}_{3-x}\text{Fe}_x\text{O}_{7+\delta}$ and Effects of Hot Isostatic Pressing	90
^{57}Fe Mössbauer Spectroscopy of $\text{Cu}_{1-x}\text{Fe}_x\text{GeO}_3$	91
^{61}Ni Mössbauer Spectroscopy of LiNiO_2 and NaNiO_2	92
Effect of 4s Electrons on the Electronic State of Ni^{3+} Ions in LiNiO_2 and NaNiO_2	93
Channeling Study on H in Nb-Mo Alloys	94
μ^+ SR Study of Polaron Motion in Polyaniline	95
Magnetic State of $\text{TlBa}_2\text{Y}_{1-x}\text{Ca}_x\text{CuO}_y$ Studied by μ^+ SR	96
Evidence for Muonium Passivation in n-Doped Ge	97
μ SR Study on the Two-Leg Ladder Compound, $\text{La}_{1-x}\text{Sr}_x\text{CuO}_{2.5}$	98
Bose-Glass Transition of the Heavy-Ion Irradiated $\text{La}_{1.85}\text{Sr}_{0.15}\text{CuO}_4$ Single Crystal	99
Heavy-Ion Irradiation Effects on the Super-Conducting Material, $\text{La}_{1.85}\text{Sr}_{0.15}\text{CuO}_4$...	100
Studies of Columnar Defects in $\text{Bi}_2\text{Sr}_2\text{CaCu}_2\text{O}_x$ by TEM and STS	101
An Evaluation of Single Event Upset on Memories	102

3. Radiochemistry and Nuclear Chemistry

In-Beam Mössbauer Study on Jump Processes of Self-Interstitial in Pure Iron after $^{56}\text{Fe}(d, p)^{57}\text{Fe}$ Reaction	103
In-Beam Mössbauer Spectroscopy on ^{57}Fe in Solid Ar and Solid Xe after Coulomb-Excitation and Recoil-Implantation	104
Simultaneous Determination of Biobehavior of Sc, Mn, Fe, Co, Zn, Se, Rb, Y, and Zr in Mice Bred under Different O_2 Gas Percentage Circumstance	105
Uptake Behavior of Multitracers in LEC Rats before Jaundice Development (II)	106
<i>In vivo</i> Behavior of Various Elements in Hepatopathic Animals (I) Metabolic study of trace elements in acute alcoholic mice	107
<i>In vivo</i> Behavior of Various Elements in Hepatopathic Animals (II) Metabolic study of trace elements in liver-cancer bearing rat	108
Accumulation of Inorganic Elements in the ddY Mice Implanted with Ehrlich Sarcoma	109
Metabolic Study of Trace Elements in Se-deficient Rats	110
Metabolic Study on Ca-deficient Rats Using a Multitracer	111
<i>In vitro</i> Binding Assay of the Trace Elements in Bovine Serum Proteins	112
Binding Activity of Various Metallic Elements to Blood Components	113

Beneficial Effect of Rare Earth Elements on the Growth of <i>Dryopteris erythrosora</i>	114
Influence of Aluminum on the Uptake of Various Cations from a Solution into Carrots	115
Translocation and Re-distribution of Radionuclides from the Leaf Surface in Plants	116
Studies on Some Parameters that May Influence the Uptake of Radioisotopes by Plants from the Soil	117
Uptake Rate of Trace Elements by Soybean Plant	118
Multitracer Studies on the Extraction of Noble Metals with N,N-Dialkyl Aliphatic Amides from Nitric Acid Solutions	119
Separation of a Multitracer from the Gold Target Irradiated with High-Energy Heavy Ions by Means of a Supported Liquid Membrane	120
Multitracer Study for the Effect of Humate Formation on the Adsorption Behavior of Metal Ions on Kaolinite and Silica Gel	121
Model Study of Acid Rain Effect on Adsorption of Trace Elements on Soils (I)	122
Model Study of Acid Rain Effect on Adsorption of Trace Elements on Soils (II)	123
Linear Momentum Transfer in the Heavy-Ion Reactions at Intermediate Energies	124
Preparation of Positron Emitter Sources for Slow Positron Generation by the Bombardment of a Liquid or Gas Target	125
Measurement of Spin Polarization of Positron Beam	126
4. Radiation Chemistry and Radiation Biology	
An Effective Mutation Method for Plants Using Heavy-Ion Beams	127
Physical Characteristics of Irradiation Field for Proton Radiotherapy	128
Decay Enhancement of Self-Trapped Excitons at High Excitation-Density and Low Temperature in an Ion-Irradiated BaF ₂ Single Crystal	129
Effects of Ne Ion Beams on Survival of <i>Arabidopsis thaliana</i>	130
Response of Radio-Sensitive Mutant Cell Line against Heavy-Ion Beams	131
LET Dependence of Interphase Cell Death Induction for CHO Cells Exposed to Accelerated Heavy-Ions	132
Analysis of the Mutations in Human <i>HPRT</i> Gene Induced by Heavy-ion Irradiations (III)	133
Mutation of Human Cancer Cell-Line Caused by Heavy-Ions and X-Rays	134
5. Instrumentation	
A Rotating Target System for High-Intensity Heavy Ion Beams	135
Windowless Gas Target for High-Spin Isomer Beam Production	136
Ge Telescope for γ -Ray Doppler Correction	137
Development of a Polarized ³ He Target System	139
Performance Study of a Phoswich Detector in the Mixed Field of Neutrons and Charged Particles	141

Proton-Knockout (p,2p) Reactions from ^{12}C with Normal and Inverse Kinematics	142
Development of a MUSIC (MULTi-Sampling Ionization Chamber)-type Detector for Identification of Low Energy Nuclear Reactions	143
Toroidal Spectrometer for Measurement of Emitted Electron Spectra Arising from Collisions between Highly Charged Ions and Neutral Atoms	145
Mounting of a CCD Detector on the Rowland Circle of a Grazing-Incidence Spectrometer for Use in Beam-Foil Spectroscopy	146
Proton Beam Test of Cosmic Ray Telescope for the First Brazilian Scientific Satellite	147
Development of a Liquid Argon Ionization Chamber with Excellent Energy Resolution for High Energy Heavy Ions	148
Collinear Laser Spectroscopy of Li-like ^{11}B Beam	149
Development of an On-Line Laser Ion Source	150
Completion of Tritium Gas Handling System for Muon Catalyzed Fusion Experiment at RIKEN-RAL Muon Facility	151
Compact CAMAC Data Acquisition System with ACC K3976 and PC-Linux	152
Evaluation of UNIX DAQ System (UNIDAQ) on VME	154
Computing Environment around the Accelerator Research Facility	155
Fabrication of the Muon Magnet for the RHIC Spin Project	156
6. Material Analysis	
Development of an In-Air High-Resolution PIXE System	159
Positron/Positronium Annihilation in Nanocrystalline Si	161
Development of a TOF-ERDA System for Wide Mass Range	162
7. Miscellaneous	
Strong X-Ray Emission due to a Charge-Up Effect	163
Residual Radioactivity Produced by 2.9 MeV/nucleon α -Particles	164
IV. NUCLEAR DATA	
Status Report of the Nuclear Data Group	165
V. DEVELOPMENT OF ACCELERATOR FACILITIES	
Production of ^{48}Ca Ions in 10 GHz ECRIS	167
Present Status of RIKEN 14.5 GHz Caprice	168
RIKEN Duoplasmatron Ion Source: The performance characterization and background physics	169
Recent Progress in ECRIS Physics Study: Radial distribution of negative potential, hot ring, and instability	171
Beam Optics Study of Superconducting Solenoid Focusing in RI Beam Production Beamline	173
A Liquid He-Free Solenoid for RI Beam Production	175

Study of Spin Dynamics for RHIC Spin Project	176
Optimization Method Using 2D Analysis in Helical Dipole Magnets for RHIC	178
High Current Design of Superconducting Helical Dipole Magnets for RHIC Spin Project	180
Field Analysis of a Helical Dipole Magnet	182
Analytical Field Calculation of Helical Coils for RHIC Spin Project	183
Observation of Slow Transient Effect of Magnetic Field Gradient in RIKEN Ring Cyclotron Magnet	185
Commissioning Run of a New Injector System for RILAC	186
Development of RIKEN 18 GHz ECRIS	188
Performance Tests of a Variable-Frequency RFQ Linac for RILAC	189
Beam Matching Section in the New Injector for RILAC	191
Maximum Beam Current in a Low-Energy Transport Line	193
Progress of RIKEN RI Beam Factory Project	195
The Superconducting Ring Cyclotrons for RIKEN RI Beam Factory	196
Design Study of Sector Magnets for RIKEN Superconducting Ring Cyclotron (I)	197
Design Study of Sector Magnets for RIKEN Superconducting Ring Cyclotron (II)	199
Design of a Model Sector Magnet for RIKEN Superconducting Ring Cyclotron	201
Design Study of Injection System for RIKEN Superconducting Ring Cyclotron (I) ...	203
Design Study of Injection System for RIKEN Superconducting Ring Cyclotron (II) ...	205
Design Study of Injection System for RIKEN Superconducting Ring Cyclotron (III) Analysis of the injected beam trajectories	207
Optimization of Trim Coils in a Superconducting Ring Cyclotron	209
Design Study of the Accumulator Cooler Ring for MUSES	211
Design Study of Electron Cooling for ACR in MUSES	213
Design of the Booster Synchrotron for MUSES	215
Design of the Double Storage Rings for MUSES	217
Expected Luminosity at MUSES	219
One-Dimensional Compensation Scheme for Beam-Beam Effects	221
Hamiltonian Treatment of Nonlinear Beam-Beam Resonances	223
Beam-Beam Instability due to Noise in Opposing Beam Size	225
Beam Emittance Growth in Storage Ring due to the Ground Noise	227
Simulation of Beam Bunching by Electron Cooling for DSR in MUSES	229
An RF System for the Electron Beam at DSR	231
An Undulator for Elliptically Polarized X-ray Beam Line at DSR	233

Calculations of Radiation Shield for RIKEN RI Beam Factory	235
VI. RADIATION MONITORING	
Leakage Radiation Measurements in the Ring Cyclotron Facility	237
Dose Rates due to Residual Activities in the Ring Cyclotron Facility	239
VII. LIST OF PUBLICATIONS	241
VIII. LIST OF PREPRINTS	249
IX. PAPERS PRESENTED AT MEETINGS	251
X. LIST OF SYMPOSIA	263
XI. LIST OF SEMINARS	264
XII. LIST OF PERSONNEL	267
AUTHOR INDEX	

I. PREFACE

This issue reports the research activities of the RIKEN Accelerator Research Facility (RARF) during the calendar year of 1996. The research programs have been coordinated in the framework of the project entitled by Multidisciplinary Researches on Heavy Ion Science. The project involves a variety of fields such as; nuclear physics, atomic physics, nuclear chemistry, radiation biology, condensed matter physics in terms of accelerator or radiation, basic studies on energy production, basic studies on accelerator cancer therapy, material characterization, application to space science, accelerator physics and engineering, laser technology, and computational technology. The whole project involved 12 laboratories in RIKEN and more than 400 researchers including outside users.

Major research activities of RARF are based on a heavy-ion accelerator complex consisting of the $K = 540$ RIKEN Ring Cyclotron (RRC) and its subordinate accelerators, i.e., the energy-variable heavy ion linear accelerator (RILAC) and the $K = 70$ Azimuthally Variable Field (AVF) cyclotron, which has altogether delivered a beam time (on the target) of more than 8000 hours through the year. Besides, the RARF carries out two international collaboration programs based on oversea accelerator facilities; one is the muon science collaboration with the Rutherford-Appleton Laboratory (RAL) and another is the spin physics program in collaboration with the Brookhaven National Laboratory (BNL).

The year of 1996 should be marked as the 10th anniversary since the completion of RRC. A memorial symposium was performed in November-96 and a booklet summarizing the 10-years' achievement was issued. Taking this opportunity a brief summary is given below of the characteristic features and important achievement in our research programs spanned for the 10 years followed by the perspectives for the future.

The three accelerators currently available provide heavy ion beams in a broad range of elements with energies covering from a few A MeV to 135A MeV. They have been used in different configurations. Studies on nuclear physics primarily utilized the RRC to exploit the high-energy beams, while studies on other domains often utilized the RILAC and AVF in their stand-alone mode of operation. Nuclear physics composes nearly half of the whole activities, while the other disciplines combined compose another half.

In the domain of nuclear physics the primary emphasis has been placed on the studies of unstable nuclei by exploiting powerful capabilities of radioactive beams. Uniquely, three different types of radioactive beams, namely; projectile-fragment (PF) radioactive beam;

spin-polarized radioactive beam; and high-spin isomer beam, have been developed to facilitate broad types of experiments. Major subjects pursued are: 1) exotic nuclear structure and new dynamics of extremely neutron-rich nuclei (such as with neutron halo or skin), 2) nuclear astrophysics involving unstable-nucleus reactions, 3) synthesis of new unstable isotopes far from the valley of stability, 4) extensive measurement of nuclear moments, and 5) challenge to high spin physics by means of isomer beams. A variety of experimental methods have been cultivated, and many new findings have been revealed. These studies constitute an important portion of the frontier of radioactive-beam experiments, which is a world-widely emerging field in the contemporary nuclear physics.

Studies on nuclear physics have been also performed utilizing the primary beams, where the RRC's characteristic beam energies around 100A MeV was most appreciated to pursue spectroscopy with direct reactions. In particular, a polarized ion source of deuterons has been developed, and spin-isospin responses of different modes were studied by means of $(d, ^2\text{He})$ and $(d, d(0^+))$ reactions. Similarly, heavy-ion exchange reactions have been proved to be a useful means for investigation of spin-isospin response.

The RARF has offered a rich capability for atomic physics research with beams of an extremely wide range of highly charged ions as provided by the combination of the ECR ion source, RILAC, and RRC. Spectroscopy of multiply-excited atomic states and study on collision dynamics of highly charged ions have been extensively pursued in various aspects. As for recent developments, a high precision recoil-ion momentum spectroscopy has been developed to open up a new possibility of final-substate-resolved differential analysis of high-energy reactions. An extensive program of beam-foil spectroscopy for highly-charged heavy ions is in progress. Irradiation effect of energetic heavy ions on materials is another subject of current interest, and physics of columnar defects is studied in relation to pinning phenomena of high- T_c superconductors.

The research of nuclear chemistry and condensed-matter physics has involved two main domains: One is the microscopic analysis or characterization of condensed matter using accelerated beams and radioactive sources, and another is the application of radio isotopes as a tracer. In the first category, the condensed matter study by means of channeling effect has been a unique program consistently pursued. Studies of Moessbauer spectroscopy and of perturbed angular correlations have also been promoted with a current emphasis on in-beam Moessbauer methods with ^{57}Fe

and ^{57}Mn sources. In the latter category, a remarkable development has been accomplished on a novel methodology of multi-tracer. The method utilizes a useful feature of high-energy reactions which allows easy production of mixed sources of different radioactive elements to trace the circulation of a variety of elements in the same time. Application of the multi-tracer method is now developing over the broad fields of bio-inorganic chemistry, dietetics, toxicology, pharmacology, environmental issues, and medical fields in general.

Irradiation effects of high-energy heavy-ion beams are studied in several aspects. The most important has been the research on radiation biology. Effects of high LET are studied for biological samples. Basic studies for the heavy-ion-beam cancer therapy were conducted in collaboration with National Institute of Radiological Science to offer basis for practical medical operation. As a remarkable recent finding, a striking mutagenic effect has been observed on the embryo of a tobacco plant shot by heavy ions. This presents a new possibility in the mutation research featuring an efficient and well-controlled method in terms of heavy-ion irradiation. Another important research concerns the space technology. High-energy heavy ions from RRC served as a good simulator of cosmic rays in space. In particular, studies of radiation effect on electronic devices are made in collaboration with National Space Development Agency of Japan.

Naturally, the whole research activities and the qualities of outcomes have strongly depended on capabilities of the accelerator facilities. Continuous efforts of upgrading the capabilities have been pursued. Most recently, a set of a 18 GHz ECR ion source and a frequency-variable RFQ linac has been completed and replaced the upstream end of RILAC system, which drastically improved beam intensities of the accelerator. Besides, beam of ^{48}Ca has been initiated and acceleration of other rare isotopes including uranium is in preparation. Also, emittance of the PF beam has been improved significantly by installing a super-conducting solenoid along the beam line.

The accelerators at the RARF focus on heavy ions by emphasizing the aspect of intermediate-energy and

intense beams. Beyond this capability the RARF tries to coordinate international research programs for utilizing oversea facilities. Two such programs are on-going. The muon science program at RAL is based on the muon beam facility constructed at the site of the proton synchrotron (ISIS). The operation has started since 1995 to carry out versatile research programs using powerful pulsed muon beams. Problems of the muon-catalyzed fusion have been studied among others. Another international project is on relativistic-energy spin physics which is to be carried out at BNL by facilitating spin-polarized proton beams at RHIC. The program aims at investigation of quark-gluon spin structure functions and related properties of nucleons. The project was initiated in 1995 and construction of apparatuses is in progress.

To conclude shortly, we believe, the RARF has been successful in promoting productive activities over a variety of research fields, which have contributed considerably to open up and advance new frontiers of heavy-ion science. In particular we are proud of our contribution to the development of the science to use radioactive ion beams (RIB). With this belief we have proposed a new project so called RIKEN Radioactive Ion Beam Factory, which will promote global development of the next generation RIB science. After two years of R & D research, construction of a superconducting cyclotron system with K-number around 1600 has been approved this year to start in FY 1997. The new accelerator system will serve as an energy booster for the existing RRC to achieve sufficiently high energy beams of heavier elements, and thereby to produce PF radioactive beams over an extended range of unstable nuclei. The RARF has been determined further to strengthen the international collaboration programs. In this context, installation of a new RIKEN research branch called RIKEN BNL Research Center has been approved to start in FY 1997 to intensively promote the program on spin physics and RHIC physics. With the approval of these new projects we can foresee enhanced development of our activities and thus an enlarged contribution to the world enterprise of heavy ion science in coming years.

M. Ishihara

Director

RIKEN Accelerator Research Facility

II. OPERATION OF ACCELERATORS

RRC and AVF Cyclotron Operations

M. Kase, A. Goto, T. Kageyama, I. Yokoyama, M. Nagase, S. Kohara, T. Nakagawa, N. Inabe,
K. Ikegami, O. Kamigaito, J. Fujita, H. Isshiki,* H. Akagi,* R. Ichikawa,* N. Tsukiori,*
R. Abe,* K. Takahashi,* T. Maie,* T. Homma,* and Y. Yano

It has passed 10 years since the first beam of 21 MeV/u ^{40}Ar was extracted from the RIKEN Ring Cyclotron (RRC) successfully. Figure 1 shows the statistics of the RRC operation during these 10 years. A total of the operation time is gradually increasing after the RIKEN Accelerator Research Facility (RARF) was fully completed in 1990 and recently reaching to 6500 hrs in a year, which is a practical upper limit if holidays

and maintenance times are taken into account.

All the beams accelerated in these ten years are listed in Table 1, together with their acceleration conditions and beam intensities. There appear more than 90 kinds of combinations of ion and energy. Their masses as well as their energies cover almost fully the available regions with the two injectors, AVF cyclotron and RILAC.

Table 1. RRC Beams (1987–1996).

ION	q	Energy (MeV/u)	RF (MHz)	Injector	Intensity (pnA)
p	1	150–210	34–39	AVF	1000
H ₂	1	70–135	25–33	AVF	1000
d	1	70–134	25–33	AVF	300
pol. d	1	134	33	AVF	280
α	2	100/135	29/33	AVF	50
¹¹ B	2	15	24	RILAC	190
	5	70	25	AVF	200
¹² C	5	42	35	RILAC	40
	6	70–135	25–33	AVF	500
¹³ C	6	42	35	RILAC	10
	6	70–100	25–29	AVF	160
¹⁴ N	4/6	21–42	25–35	RILAC	100
	7	70–135	25–33	AVF	230
¹⁵ N	5	11–42	20–35	RILAC	20
	7	70–115	25–31	AVF	30
¹⁶ O	8	80–135	26–33	AVF	300
¹⁸ O	7	42	35	RILAC	70
	8	70–100	25–29	AVF	380
²⁰ Ne	9	37	33	RILAC	17
	10	135	33	AVF	70
²² Ne	8	21	28	RILAC	5
	9/10	70–110	25–30	AVF	150
²⁴ Mg	12	100	29	AVF	50
²⁷ Al	13	100	29	AVF	5
²⁸ Si	14	135	33	AVF	6
³⁶ Ar	5	7.5	19	RILAC	1000
⁴⁰ Ar	5	7.5	19	RILAC	500
	11–15	9–40	19–34	RILAC	140–13
	16/17	80/95	26/28	AVF	10/30
⁴⁰ Ca	14	26	28	RILAC	0.7
⁴⁸ Ca	18	70	25	AVF	4
⁴⁸ Ti	7	7.6	19	RILAC	18
⁵⁰ Ti	20	80	26	AVF	8
⁵⁶ Fe	24	90	28	AVF	2
⁵⁸ Ni	9	10	20	RILAC	30
	25	95	28	AVF	4
⁵⁹ Co	24	80	26	AVF	4
⁶⁴ Zn	20	21	25	RILAC	0.5
⁶⁵ Cu	8/18	7/17	18/25	RILAC	3/0.5
⁸⁴ Kr	13–15	11–36	20–33	RILAC	6–0.8
¹³⁰ Te	22	7.5	19	RILAC	5
¹³⁹ Xe	22	7.5	19	RILAC	5
¹³² Xe	21	7	18	RILAC	3
¹³⁶ Xe	21–31	7.5–26	19–28	RILAC	2–10
¹⁴⁰ Ce	22	7	18	RILAC	2
¹⁶⁶ Er	32	16	22	RILAC	2
¹⁷⁰ Er	24	7	18	RILAC	1.5
¹⁸¹ Ta	37	21	25	RILAC	0.1

* Sumijyu Accelerator Service, Ltd.

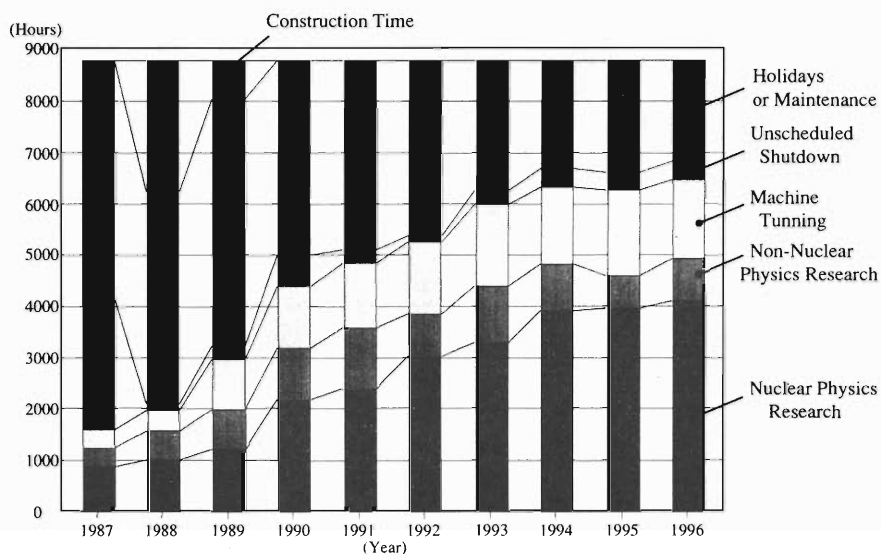


Fig. 1. Statistics of RRC operation from 1987 to 1996.

In 1996, a total of the beam service time was 5000 hrs. Most of the beam time (85%) was devoted to nuclear physics experiments and the rest (15%) to experiments in the other fields, such as medical science, radio-chemistry, health physics, material science, biology, and atomic physics. The number of users for biologic researches is increasing in recent years.

The AVF-RRC operation was performed for 150 days (80%) and the RILAC-RRC operation for 38.5 days (20%). The stand-alone use of the AVF cyclotron was limited in this year, partly because the RILAC had been shutdown since July 1996 due to the installation of its new pre-injector. A total of the AVF stand alone amounted 500 hrs, being half of that in 1995.

As shown in Fig. 1, a total of the unscheduled shutdowns, which occurred frequently for a few years just after the competition, minimized in 1992, and after that increased a little bit and in recent years reached a constant around 300 hrs. There were a variety of reasons for them until 1992, including serious vacuum leaks of cooling water into a vacuum chamber of RRC. On the other hand, in these four years, most of the troubles have been concentrating on parts of the AVF cyclotron (i.e. deflector, magnetic channel, and rf cavity).

In June of this year, a serious vacuum leak occurred inside a plasma chamber of the 10 GHz ECR ion source. It was found that the coolant inside a cooling jacket of the sextupole magnet leaked into the chamber through a small hole on the surface of the jacket, which had been produced probably due to some kind of spark. In a course of its repair, some sets of the sextupole magnet bars, which had been composed of many small magnet-blocks (SmCo), were partly broken into pieces. After a temporary repair, due to the

imperfection of the sextupole magnet, the obtainable beam intensity decreased down to half of the full performance in case of heavy ions. The sextupole magnet was replaced with a new one in December 1996.

In May, a beam of ^{48}Ca was successfully produced with the 10 GHz ECR ion source. The same method was used as that for ^{50}Ti tried in 1995 in order to save the quantity of enriched material. A beam of 70 MeV/u ^{48}Ca was accelerated with the intensity of 4 pA for ten days. As a result, new isotopes of ^{38}Mg , ^{40}Al , and ^{41}Al were found using the RIPS under the international collaboration with JINR (Dubna).

After the installation of a new pre-injector system of RILAC (an 18 GHz ECR ion source and a variable frequency RFQ linac), a beam test, in the RILAC-RRC operation, began in December 1996. A beam of 7.6 MeV/u ^{36}Ar has been already upgraded as for the intensity on target up to 1 pA, reaching the present official limit. It is the first-step improvement of the accelerators in aim of the new project, the RI beam factory.

In this winter, a new focusing element (a superconducting solenoid, 6.8 Tm) will be installed in just front of a production target of RIPS in place of the beam swinger. With the new device, a beam size on the target will be expected to be as small as 0.4 mm in a diameter, being 25% of the present value. In advance of its installation, in the last summer, a table of the swinger system, which consists of two sets of dipole magnets, was replaced with a movable one on three floor rails. When the new solenoid is used, the swinger system will move away from the beam line of the RIPS, and give the space to the solenoid. The switch between the new solenoid and the beam swinger will be easily done.

RILAC Operation

E. Ikezawa, M. Hemmi, T. Chiba, S. Kohara, T. Aihara,* T. Ohki,* H. Hasebe,*
H. Yamauchi,* and Y. Miyazawa

RILAC has been in a steady operation, and has supplied various kinds of ion beams for the experiments. Table 1 gives the statistics of operation from January through July 5, 1996. Table 2 summarizes the number of days allotted to individual research groups. The percentage of the beam time used by RIKEN Ring Cyclotron (RRC) was about 34% of the total; the ions of $^{11}\text{B}^{2+}$, $^{14}\text{N}^{3+}$, $^{40}\text{Ar}^{5+}$, $^{48}\text{Ti}^{7+}$, $^{58}\text{Ni}^{8+}$, $^{84}\text{Kr}^{11+}$, and $^{136}\text{Xe}^{15+}$ from RILAC were injected to RRC. Table 3 gives the statistics of ions used in this year. Total 19 kinds of ion beams were used for the experiments and beam acceleration tests. The percentage of the beam time to use metallic ions amounted to about 38% of the total. Among them, a $^{103}\text{Rh}^{16+}$ beam at the acceleration frequency of 35 MHz is new.

Table 3. List of ions used in this year.

Ion	Mass	Charge state	Days
He	4	1, 2	10
B	11	1, 2, 3	22
C	12	4	8
N	14	3	2
Ne	20	3	3
Ar	40	5, 6, 8	21
Ti	48	7	4
Fe	56	11	6
Ni	58	8	2
Kr	84	11, 13	8
Y	89	14	2
Rh	103	16	4
Xe	136	15	13

Table 1. Statistics of the RILAC operation from Jan. 1 through July 5, 1996.

	Days	%
Beam time	105	56.1
Frequency change	7	3.7
Overhaul and improvement	7	3.7
Periodic inspection and repair	13	7.0
Machine trouble	0	0.0
Scheduled shut down	55	29.4
Total	187	100

Table 2. Beam time allocated for individual research groups.

	Days	%
Atomic physics	37	35.2
Nuclear physics	14	13.3
Nuclear chemistry	4	3.8
Radiation chemistry	12	11.4
Accelerator research	2	1.9
Beam transportation to RRC	36	34.3
Total	105	100

We had following machine troubles: (1) In the resonator No. 6, the thin copper sheets (each had 10 cm wide, 7 cm long, and 0.3 mm thick) used for electric contact were melted due to the too-high rf currents with parasitic oscillation. This trouble rarely occurred at the acceleration frequency of 32 MHz or above and at the acceleration voltage of 200 kV or above. (2) A sliding transformer was worn out in the filament power supply dedicated for the final vacuum tube (No. 1); replaced by a new one. (3) A high voltage power supply for the final vacuum tubes had troubles; overhauled in this summer. (4) The computer system controlling RILAC had troubles; the CPU card, memory cards, and the DC power supplies were replaced by spare parts.

For the 8 GHz ECR ion source we have tested to produce metallic ions employing so-called MIVOC-method (metal ions from volatile compounds).¹⁾ We obtained the unstable beam currents of 500 enA for Ni^{6+} and 350 enA for Ru^{10+} from volatile compounds such as $\text{Ni}(\text{C}_5\text{H}_5)_2$ and $\text{Ru}(\text{C}_5\text{H}_5)_2$. Also, we obtained 7 μA of the Fe^{6+} beam by use of the $\text{Fe}(\text{C}_5\text{H}_5)_2$ volatile compound.

The RILAC operation was temporarily discontinued by July 5, and an installation work of a new pre-injector system consisting of a variable frequency RFQ linac and a 18 GHz ECR ion source for the RIKEN RI beam factory project started in July 8. The existing beam transport line between the 450 kV Cockcroft-Walton injector (equipped with 8 GHz ECR ion source) and the rf resonator No. 1 was modified, and the new pre-injector was installed in parallel to the existing injector. Figure 1 shows the layout of the new pre-injector system for RILAC together with the

* Sumijyu Accelerator Service, Ltd.

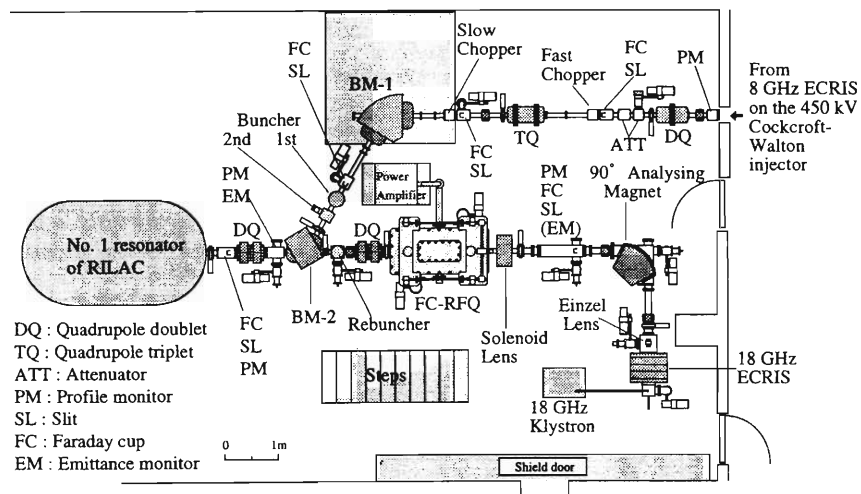


Fig. 1. Layout of the new pre-injector system for RILAC together with the beam transport line from the existing injector.

beam transport line from the existing injector. The details of the new pre-injector system are reported in this issue.²⁻⁴⁾ The beam acceleration tests used the existing injector which started in the middle of October. The beam service for user will be reopened in the middle of January 1997. A beam acceleration test with the new pre-injector system was started in this November for the gaseous ions.

References

- 1) J. Arje et al.: 12th Int. Workshop on ECR Ion Sources, RIKEN, p. 136 (1995).
- 2) A. Goto et al.: RIKEN Accel. Prog. Rep. **30**, 186 (1997).
- 3) O. Kamigaito et al.: RIKEN Accel. Prog. Rep. **30**, 189 (1997).
- 4) T. Nakagawa et al.: RIKEN Accel. Prog. Rep. **30**, 188 (1997).

The Tandem Operation

E. Yagi, K. Ogiwara, and T. Urai

The tandem accelerator was operated for 96 days except for the machine inspection, beam test, and so on during the period from Nov. 1, 1995 to Oct. 31, 1996. The construction of beam lines for the PIXE, RBS, and channeling experiments was completed. Here, PIXE and RBS stand for Particle-Induced X-ray Emission and Rutherford Backscattering Spectroscopy, respectively.

Experimental studies on the following subjects are made in progress.

(1) Rutherford Backscattering Spectroscopy (RBS)

(a) Behavior of Xe atoms implanted into iron (Muon Science Lab).

(b) RBS analysis of the polystyrene surfaces modified by ion implantation (Surface Characterization Center).

(c) Characterization of the oxide films grown on SrTiO₃ (Surface Chemistry Lab).

(d) RBS study of multilayer films, welded steel, and oxides (Linear Accelerator Lab).

(2) Nuclear Reaction Analysis (NRA)

(a) Lattice location of hydrogen in niobium alloys by a channelling method (Muon Science Lab).

(3) Particle-Induced X-ray Emission (PIXE)

(a) Application of PIXE to the biomedical and material sciences: Trace element analysis using energy-dispersive X-ray spectrometry, and chemical state analysis using wave-dispersive X-ray spectrometry (Inorganic Chemical Physics Lab).

(b) Development of an X-ray detector (Cyclotron Lab).

(c) Development of an in-air high-resolution PIXE system for chemical state analysis (Inorganic Chemical Physics Lab).

(d) Channeling analysis of dopants in II-VI compound semiconductors (Muon Science Lab).

III. RESEARCH ACTIVITIES

1. Nuclear Physics

Distribution of the Gamow-Teller Strength in ^{11}Li

T. Suzuki and T. Otsuka

[Neutron halo, GT β decay]

The distribution of the Gamow-Teller (GT) strength in ^{11}Li is investigated. We study: 1) where we can find GT strengths of the transitions $^{11}\text{Li} (3/2_{g.s.}^-) \rightarrow ^{11}\text{Be} (1/2^-, 3/2^-, 5/2^-)$ and 2) quenching effects due to the Δ -h contribution. Connection with GT sum rule and effects of the halo structure of ^{11}Li on the strength are discussed. The shell gap between p-shell and sd-shell is found to modify the structure of the distribution of strengths.

We, first, give the result of reinvestigation of the structure of two-neutron halo in $^{11}\text{Li}^1$ obtained from the recent two new measurements at RIKEN²⁾ and ISOLDE,³⁾ which indicates more retardation of the transition $^{11}\text{Li} \rightarrow ^{11}\text{Be} (1/2^-, 0.32 \text{ MeV})$ than before: $\log ft = 5.67 \pm 0.04^2)$ and $5.73 \pm 0.03^3)$ respectively. We change the probability of $\nu p_{1/2}^2$ configuration, $P(p_{1/2}^2)$, by lowering the single-particle energy of $1s_{1/2}$ orbit and study the variation of the calculated $\log ft$ values. We find that $P(p_{1/2}^2)$ for the two recent measurements is around 50% (45% \sim 55%).

The GT sum rule⁴⁾ suggests $S_{\beta^-} - S_{\beta^+} = 3(N - Z) = 15$, where $S_{\beta^\pm} = \sum_f | \langle f | \sigma_{\pm} | i \rangle |^2$. Within the p-shell, $S_{\beta^-} = 15$ and $S_{\beta^+} = 0$. When the two $p_{1/2}$ neutrons are excited into the $1s_{1/2}$ shell with probability $1 - \alpha$, then $S_{\beta^-} = 15\alpha + 49/3(1 - \alpha)$ and $S_{\beta^+} = 4/3(1 - \alpha)$. The sum rule remains valid. The halo reduces the overlaps: $\langle \pi p | \nu p_{1/2} \rangle = 0.85$ and $\langle \pi 1s_{1/2} | \nu 1s_{1/2} \rangle = 0.625$. When these halo effects are taken into account, $S_{\beta^-}(\text{halo}) = 13.705\alpha + 12.677(1 - \alpha)$ and $S_{\beta^+}(\text{halo}) = 0.963(1 - \alpha)$. For $\alpha = 50\%$, $S_{\beta^-}(\text{halo}) = 13.191$ and $S_{\beta^+}(\text{halo}) = 0.482$. The sum rule is not satisfied any more in the p-sd shell model space. For neutron-rich nuclei, we can expect to observe in experiment mostly the S_{β^-} .

We show in Fig. 1 calculated results of the GT strength S_{β^-} for $^{11}\text{Li} (3/2_{g.s.}^-) \rightarrow ^{11}\text{Be} (1/2^-, 3/2^-, 5/2^-)$ obtained in the p-sd shell model configuration space with Millener-Kurath interaction [PSDMK2⁵⁾]. Here, the single-particle energy of $1s_{1/2}$ orbit is lowered to increase the probability of the admixture of $p^5(sd)^2$ configurations to $P(p_{1/2}^2) = 55\%$. The S_{β^-} summed up to the IAS state in ^{11}Be is 10.58 (11.41) for the case with (without) the Δ_{33} contributions. Quenching of the strength by 0.83 due to the coupling to the Δ -h configuration is seen. The effect of the halo is to reduce the summed strength by 0.81. The strengths from $0p \rightarrow 0p$ and $sd \rightarrow sd$ contributions are mixed, resulting in the remaining of the strengths at higher energy. Without the change of single-particle energies of the sd-shell, the structure of the strength is much simpler and there is little mixing between the two contribu-

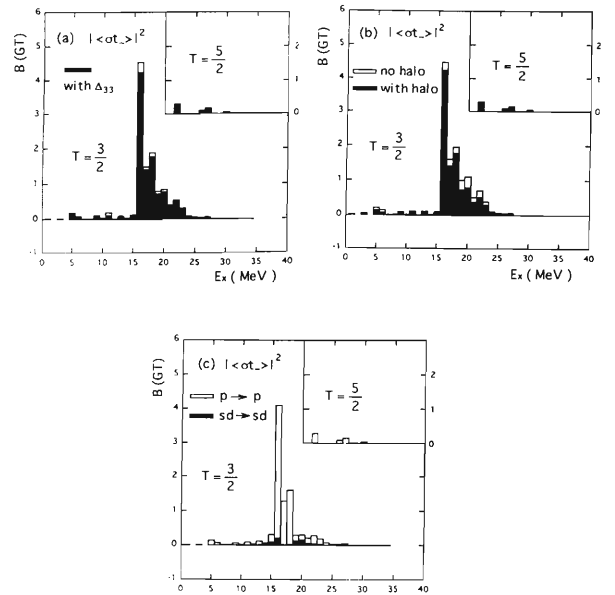


Fig. 1. (a) Calculated GT strength S_{β^-} for $^{11}\text{Li} (3/2_{g.s.}^-) \rightarrow ^{11}\text{Be} (1/2^-, 3/2^-, 5/2^-)$ as a function of the excitation energy (E_x) of ^{11}Be . The sum of the strength within $E_x = N - 0.5 \sim N + 0.5$ MeV ($N = \text{integer}$) is plotted. Black (White) histograms are obtained with (without) the Δ_{33} contributions. Here, the single-particle energy of $1s_{1/2}$ -shell is lowered to increase the probability of the admixture of $p^5(sd)^2$ configurations: $P(p^7) = 55\%$ (b) Effects of the halo on S_{β^-} . The black histograms obtained with the halo is same as in Fig. 1a. The white ones are obtained without the halo effects. (c) Same as in Fig. 1a for separate contributions from $0p \rightarrow 0p$, and $1s \rightarrow 1s$ and $0d \rightarrow 0d$ transitions.

tions. There is little contribution from the $sd \rightarrow sd$ transitions below $E_x = E_{\text{IAS}}$. The narrowing of the shell-gap between the p- and sd-shells, thus, leads to a spreading of the GT distribution.

In summary, we conclude that about 2/3 of the sum rule value can be observed below $E_x = E_{\text{IAS}}$. There is a preliminary report^{2,3)} describing that a substantial GT strength was found around $E_x = 18.5$ MeV.

References

- 1) T. Suzuki and T. Otsuka: Phys. Rev. C **50**, R555 (1994).
- 2) N. Aoi: preprint (RIKEN-AF-NP-240,241).
- 3) M. J. G. Borge et al.: submitted to Phys. Rev. C.
- 4) K. Ikeda, S. Fujii, and J. I. Fujita: Phys. Lett. **3**, 271 (1963).
- 5) W.-T. Chou, E. K. Warburton, and B. A. Brown: Phys. Rev. C **47**, 163 (1993).

Stochastic Variational Method with Non-Central Potentials

Y. Ohbayasi,* K. Varga, and Y. Suzuki

[Few-body systems, Stochastic variational method, Realistic potentials]

In a recent paper¹⁾ we have shown that the stochastic variational method (SVM) with correlated Gaussian basis provides an accurate solution for various few-body systems. Applications of the SVM were, however, limited to central interactions so far. The real challenge in nuclear few-body problems is the solution with a realistic nucleon-nucleon interaction including spin-orbit, tensor, etc. The application of SVM for realistic interactions is, therefore, a stringent test of the usefulness of the method.

We applied SVM calculations to the ^3H and ^4He nuclei with the interactions V6 ($1, \sigma \cdot \sigma, \tau \cdot \tau, \sigma \cdot \sigma \tau \cdot \tau, S, S\tau \cdot \tau$) and V8 ($1, \sigma \cdot \sigma, \tau \cdot \tau, \sigma \cdot \sigma \tau \cdot \tau, S, S\tau \cdot \tau, L \cdot S, L \cdot S\tau \cdot \tau$). For the triton, we used all partial wave channels with $(l_1, l_2)L$, ($l_1 + l_2 \leq 4$), and $L = 0, 1, 2$. For the alpha particle, all partial waves $((l_1, l_2)l_{12}, l_3)L$ satisfying $l_1 + l_2 + l_3 \leq 4$, $|l_1 - l_2| \geq l_{12} \leq l_1 + l_2$, and $L = 0, 1, 2$ have been tried. There are 3 spin and 2 isospin channels for the triton, and 6 spin and 2 isospin channels for the alpha particle.

Basis setup for the SVM can be briefly described as follows: Let us assume that the dimension of the basis is $K - 1$.

(1) Generate \mathcal{N} random candidates to find the K th basis function.

(1a) Pick up a spin, isospin, and partial wave channel randomly.

(1b) Select the nonlinear parameters randomly from a "physically" important interval.

(2) Calculate the ground state energy on the K basis states.

(3) Select the basis state which gave the lowest energy among the randomly generated trial functions, and add it to the basis.

(4) Increase the dimension to $K + 1$.

Table 1 shows the results for triton and alpha with the Reid V8 potential.²⁾ We obtain the energy of triton(alpha) within 100(400) basis. Results given by Green Function Monte Carlo (GFMC) and that by Faddeev Method (FY) are compared. The low dimen-

Table 1. Energies (in MeV) and radii (in fm) of the triton and alpha by different methods with Reid V8 potential. The probability P_L is given in %.

		SVM	GFMC ³⁾	FY ³⁾
RV8 triton	$\langle T \rangle$	52.2	54.0(0.20)	52.2
	$\langle V \rangle$	-59.8	-62.0(0.20)	-59.8
	$\langle V_{LS} \rangle$	1.0		
	$\langle r^2 \rangle^{\frac{1}{2}}$	1.75	1.68(0.07)	1.76
	P_S	90.3		
	P_P	0.1		
	P_D	9.7		
	E	-7.59	-7.54(0.10)	-7.59
RV8 alpha	$\langle T \rangle$	111.7	109.2(0.20)	
	$\langle V_6 \rangle$	-138.3	-137.5(0.20)	
	$\langle V_{LS} \rangle$	2.1	2.45(0.23)	
	$\langle V_{coul} \rangle$		0.71(0.02)	
	$\langle r^2 \rangle^{\frac{1}{2}}$	1.51	1.53(0.02)	
	P_S	84.1		
	P_P	0.4		
	P_D	15.5	15.5(0.20)	
	E	-24.49	-24.55(0.13)	

sion of the bases required to solve the $A = 3-4$ problems confirms that it is possible to treat heavier nuclei with realistic forces by the SVM.

In summary, we have presented a stochastic variational solution for the triton and alpha particles with realistic nuclear forces. The fact that the results are in good agreement with those of the best calculations in the literature encourages the applications of the method to the other cases, such as $A = 6$ and 7 nuclei.

References

- 1) K. Varga and Y. Suzuki: Phys. Rev. C **52**, 2885 (1995).
- 2) R. B. Wiringa and V. R. Pandharipande: Nucl. Phys. A **317**, 1 (1979).
- 3) J. Carlson: Phys. Rev. C **38**, 1879 (1988).

* Graduate School of Science and Technology, Niigata University

Occupation Probability of Harmonic-Oscillator Quanta for Microscopic Cluster-Model Wave Functions

Y. Suzuki, K. Arai,* Y. Ogawa, and K. Varga

[Microscopic cluster model]

The microscopic cluster model (MCM) is a many-nucleon theory which provides a unified picture of bound-state properties of nuclei and nuclear reactions.¹⁾ Though the MCM is capable of describing a variety of structures, its application has been limited mostly to two- or three-cluster systems. The stochastic variational method,²⁾ on the other hand, enabled one to treat systems containing more than three clusters, thereby giving a detailed description of light nuclei including halo nuclei.³⁾

The utility, understanding, and appreciation of MCM would considerably increase, if its wave function and model space are easily related to the other nuclear models and calculations. The MCM has a relationship with the widely used nuclear shell model. However, it is hard to analyse a general MCM wave function in terms of shell-model configurations. We show that it is easy to calculate the fraction of various HO excitations contained in the MCM wave function. The present paper introduces a useful and efficient way to compare MCM wave functions with shell model wave functions, and opens a possibility of comparing different MCM wave functions as well.

The occupation probability P_Q of a definite number of total HO quanta Q for the A -nucleon system is obtained by calculating the expectation value of the operator \mathcal{O} given by

$$\mathcal{O} = \frac{1}{2\pi} \int_0^{2\pi} d\theta \exp\left(i\theta \left(\sum_{i=1}^A P_i [H_{\text{HO}}(i) - \frac{3}{2}] - Q \right)\right).$$

Here, $H_{\text{HO}}(i)$ is the 3-dimensional HO Hamiltonian divided by $\hbar\omega = \frac{2\hbar^2}{m}\gamma$ and P_i projects out either protons or neutrons. It is set by the unit operator when one calculates the number of total quanta occupied by both protons and neutrons. Computational method of the expectation value of the operator \mathcal{O} can be found in Ref. 4.

Table 1 lists the P_Q values in percentage for nucleon. The wave functions used were obtained in our recent MCM calculations using the Minnesota potential. γ , one input-parameter of HO, is set to be 0.17 fm⁻² ($\hbar\omega = 14.4$ MeV); which is a standard value used in a shell-model calculation for p -shell nuclei. The P_Q values are given as a function of $Q_{\text{exc}} = Q - Q_{\text{min}}$, where Q_{min} is the minimum number of HO quanta for

the lowest Pauli-allowed configuration. The lowest $0\hbar\omega$ component is around 50–60% for most cases. Admixtures of the higher components than $Q_{\text{exc}} = 4$ are significant in the ground states of ⁶Li and ⁹Be, and also in the ground state of ⁶He corresponding to its extended halo structure. The probability distribution spreads out to a very large number of HO quanta in ⁸Be and the 0_2^+ state of ¹²C, well-known cluster states. It is noted that no component is dominant in the 0_2^+ state of ¹²C. Of course, it would be possible to maximize the probability with lower Q by choosing an appropriate value of γ . However, the probability distribution would then spread to higher HO quanta in the ground state of ¹²C.

Table 1. Occupation probability of the number of harmonic-oscillator quanta for microscopic multicuster-model wave functions. The probabilities are given in %. Asterisk indicates the probability of less than 1%.

Nuclei	Q_{exc}						$\langle Q_{\text{exc}} \rangle$
	0	2	4	6	8	10	
⁶ He(0^+)	60	14	12	5	3	2	2.2
⁶ Li(1^+)	62	16	10	5	3	2	1.9
⁷ Li($3/2^-$)	63	20	9	4	2	*	1.4
⁸ Li(2^+)	61	18	11	4	2	1	1.7
⁸ Be(0^+)	36	18	12	7	5	4	7.6
⁹ Li($3/2^-$)	66	17	11	4	2	*	1.3
⁹ Be($3/2^-$)	54	21	12	5	3	2	2.1
¹² C(0_1^+)	54	30	11	3	*	*	1.4
¹² C(0_2^+)	*	11	12	12	10	8	16.1

We have presented a new and simple method of calculating the occupation probability of the number of harmonic-oscillator quanta. The analysis is found to be useful for comparing various wave functions by quantifying the amount of excitations across the major shell.

References

- 1) K. Wildermuth and Y. C. Tang: in *A Unified Theory of Nucleus*, (Vieweg, Braunschweig, 1977); K. Langanke: *Adv. Nucl. Phys.* **21**, 85 (1994).
- 2) K. Varga et al.: *Nucl. Phys. A* **371**, 447 (1994).
- 3) Y. Suzuki et al.: *Nucl. Phys. A* **588**, 15c (1995).
- 4) Y. Suzuki et al.: *Phys. Rev. C* **54**, 2073 (1996).

* Graduate School of Science and Technology, Niigata University

Reaction Cross Sections and Radii of $A = 17$ and $A = 20$ Isobars

H. Kitagawa, N. Tajima, and H. Sagawa

[Glauber model, Hartree-Fock]

Measurements of the reaction cross sections of $A = 17$ isobars (^{17}Ne , ^{17}F , ^{17}N , ^{17}B) at LBL (incident energy at around 700 MeV/nucleon) revealed an anomaly in ^{17}Ne and ^{17}B ;¹⁾ the measured cross sections of the two nuclei on carbon targets are substantially larger than those of the other isobars. As far as the separation energies are concerned, ^{17}Ne is similar to ^{11}Li . It might be interesting to study whether ^{17}Ne has characteristic features of “proton halo” in the reaction cross sections since the small separation energy is responsible to induce the halo phenomena together with the low centrifugal barrier. Recently, the reaction cross sections of $A = 20$ isobars are reported showing a large enhancement of the reaction cross sections of ^{20}Mg and ^{20}Ne .²⁾ These data provide the information of deformation and “skin” in $A = 20$ isobars. It is interesting how the deformation and skin are predicted by Hartree-Fock (HF) calculations and how it compares with the empirical information.

Data of mirror nuclei provide an opportunity to discuss the isospin symmetry which plays an important role in nuclear physics. It is interesting to see whether the isospin symmetry is preserved or violated in the reaction cross sections of mirror nuclei, because of the small separation energies and Coulomb interaction.

We use the Glauber model taking into account the effects of Coulomb interaction and Pauli blocking. We study the reactions of ^{17}Ne , ^{17}F , ^{17}O , and ^{17}N nuclei with three targets ^9Be , ^{12}C , and ^{27}Al . For $A = 20$ isobars, the reaction cross sections of 9 isobars which are stable for HF calculations are calculated on carbon target.

We calculate the densities of $A = 17$ and 20 isobars using spherical and deformed HF approximation with Skyrme interactions. In the spherical calculations for ^{17}B , ^{17}C , ^{17}N , and ^{17}Ne , we take into account the effect of small separation energies on radii by adjusting the central part of the potential in order to reproduce the empirical separation energies. The deformed HF calculations are performed on a Cartesian mesh which can describe low-density tails correctly.

Although the calculated cross sections are somewhat overshooting the experimental ones of $A = 17$ nuclei, the isospin dependence is obtained in a reasonable way by the calculations with $1d_{5/2}$ valence configuration in the cases of Be and Al targets. On the other hand, the experimental data show a substantial increase of the cross sections of ^{17}Ne on C targets in comparison with those of ^{17}F and ^{17}N . This tendency is consistent

with the calculated results which include the proton halo effect of $2s_{1/2}$ configuration. These comparisons suggest that the evidence of proton halo in ^{17}Ne is still not conclusive.

We performed the deformed HF calculations of $A = 17$ nuclei and found large prolate deformations in ^{17}C , ^{17}B , and ^{17}Na around $\delta = 0.3$, while the deformation of ^{17}N and ^{17}O are somewhat smaller than the former ones. The effect of deformation on the reaction cross sections is only a few percent at most and much smaller than the halo effect.

The densities of $A = 20$ isobars were also calculated by the spherical and deformed HF models and compared with experimental data. The calculated deformations of $A = 20$ isobars are larger than those of $A = 17$ isobars. We found that the calculated results in Fig. 1 show a similar irregular pattern of the empirical mass radii as a function of the z -component of the isospin, T_z while the missing correlations in the HF approximation might further enhance this irregularity.

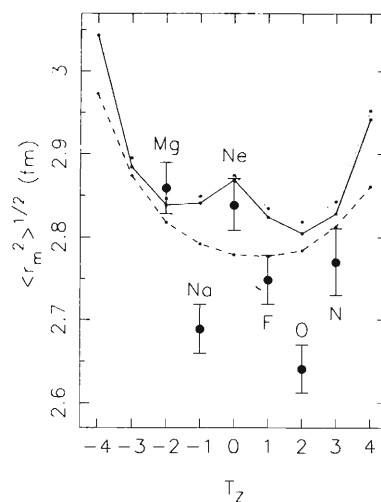


Fig. 1. The rms mass radii of $A = 20$ isobars. The dashed and solid lines are by the spherical and deformed HF calculations with SGII force, respectively; while the dotted lines correspond to the deformed HF results with SIII interaction. The experimental values are taken from Ref. 2.

References

- 1) A. Ozawa et al.: Phys. Lett. B **334**, 18 (1994).
- 2) L. Chulkov et al.: GSI preprint (November, 1995).

New SU(3) Symmetry in Superdeformation, Hyperdeformation, and Highly-Deformed Shape

K. Sugawara-Tanabe and A. Arima

[SU(3) symmetry, Superdeformation, Hyperdeformation]

We have previously shown that the $L - S$ coupling scheme is restored around the superdeformation, instead of the $j - j$ coupling scheme, because of the large quadrupole field.¹⁾ Thus, we can extend our discussion using an axi-symmetrically deformed harmonic oscillator Hamiltonian without the residual \mathbf{I}_s and \mathbf{I}^2 interactions. For the case of superdeformation (sd), we construct new boson operators d and d^\dagger as a biproduct of the harmonic oscillator bosons, c_i and c_i^\dagger . Because of the degeneracy of the vacuum of d , we have two kinds of bosons:

$$d = \frac{1}{\sqrt{2 + 2c_z^\dagger c_z}} c_z c_z, \quad d = \frac{1}{\sqrt{4 + 2c_z^\dagger c_z}} c_z c_z. \quad (1)$$

We obtain the new set of group operators, \tilde{Q} and $\tilde{\ell}$. In contrast to Elliott's case²⁾ where $\pm 2\hbar\omega_0$ excitations are excluded, our group operators exclude $\pm 2\hbar\omega_{sd}$ excitations. Now we extend our formalism to the many-body problem. Let us put n_{total} particles into the superdeformed oscillator shell from 0 to $N_{sd}(= 2n_\perp + n_z)$, and we assume that n particles out of n_{total} are in the final N_{sd} shell. The eigenstate of the n_{total} particle system is denoted by $|\Psi\rangle\rangle$. The particles which occupy the shells up to $N_{sd} - 1$ do not contribute to the expectation value of $\langle\langle \Psi | \tilde{Q}_0 | \Psi \rangle\rangle$ nor of $\langle\langle \Psi | \tilde{L}_z | \Psi \rangle\rangle$. Thus, only the n particles in the outer-most shell, N_{sd} , contribute to these expectation values. In the representation of (λ, μ) developed by Elliott, the expectation value of the many-body Casimir operator becomes

$$\langle\langle \Psi | \mathbf{C} | \Psi \rangle\rangle = 2[\lambda^2 + \lambda\mu + \mu^2 + 3(\lambda + \mu)]. \quad (2)$$

Similar to the case of sd, we can construct new boson operators which form SU(3) group at hyperdeformation (hd), where parity is not mixed in the N_{sh} as $N_{sh} = 3n_\perp + n_z$. In this case we obtain three kinds of solutions which satisfy the boson commutation relation, $[g, g^\dagger] = 1$. Here, the SU(3) is not doublet but triplet. We can obtain 8 generators for hd in the same way as obtained for sd, i.e., we replace d^\dagger and d by g^\dagger and g , respectively. The Casimir operator is similarly obtained by replacing \hat{n}_d by $\hat{n}_g = g^\dagger g$. For the case of superdeformation at $A \sim 130$ or for highly-deformed shape, where ω_\perp / ω_z is given by 3/2, different parity levels are mixed in the $N_{sh}(= 3n_\perp + 2n_z)$, corresponding to odd n_z . We introduce two kinds of bosons, i.e., d bosons for \perp -axis and g boson for z -axis. Bosons for $x - y$ plane, d and d^\dagger are defined in the same equation as in (1), but with c_\pm^\dagger and c_\pm . The other bosons for z -axis are defined by g and g^\dagger . Now, the SU(3) here is double in n_d and triple in n_g . The sixfold degeneracy is for $N_{sh} = 6m, 6m + 2, 6m + 3, 6m + 4, 6m + 5, \text{ and } 6m + 7$. The 8 generators for 3/2 deformation is given by the same equation as given for sd, but d^\dagger and d are replaced by g^\dagger and g , and c_\pm^\dagger and c_\pm are replaced by d_\pm^\dagger and d_\pm .

References

- 1) K. Sugawara-Tanabe and A. Arima: Phys. Lett. B **317**, 1 (1993); K. Sugawara-Tanabe, A. Arima, and N. Yoshida: Phys. Rev. C **51**, 1809 (1995); Phys. Rev. C **53**, 195 (1996).
- 2) J. P. Elliott: Proc. Roy. Soc. A **245**, 128 and 562 (1958).

Origin of $\Delta I = 2$ Staggering in Superdeformed States

K. Tanabe and K. Sugawara-Tanabe

[$C_{m/n}$ symmetry, $\Delta I=2$ staggering, Superdeformation]

Recent observations of the $\Delta I = 2$ staggerings in several superdeformed bands have shed a light on the internal nuclear structure. We propose a dynamical mechanism, in which the staggering originates from the symmetry of the intrinsic wave function which describes nucleons moving in the field induced by the precession of the angular frequency vector $\vec{\omega}(t)$ around the 1-axis in the body-fixed frame (B). The vector $\vec{\omega}(t)$ is decomposed into a component with the constant rotational frequency ω_0 pointing in the direction of the rotation axis 1, and a component $\Delta\vec{\omega}(t)$ which corresponds to the precessional motion caused by the small asymmetry. An important remark is that $\Delta\vec{\omega}(t)$ oscillates with the precessional angular frequency ω_p which is related to ω_0 by

$$\frac{\omega_0}{\omega_p} = \frac{\tau_p}{\tau_0} = \lambda \pmod{1}. \quad (1)$$

Thus, especially when these two periods are *commensurable* so that the ratio is expressed as $\lambda = m/n (< 1)$ in terms of two irreducible positive integers m and n , the nuclear system comes back to its original position and direction after the time-duration $n\tau_p$.

We start from the generic microscopic Hamiltonian H defined in the laboratory frame (L). We assume a rotational motion with the rotational frequency of $\vec{\omega}(t)$. Next, we transform the laboratory frame to the body-fixed frame (B) by employing unitary operators. Then, the corresponding Schrödinger equation at the frame (B) becomes,

$$i \frac{\partial}{\partial t} |\Psi(t)\rangle_B = [H_B - \bar{\omega}_0 I_1 - \Delta\vec{\omega}(t)\vec{I}] |\Psi(t)\rangle_B. \quad (2)$$

An important remark here is that Eq. (2) has the periodicity of τ_p and is invariant under the transformation of $\hat{T} = \exp(i\nu\tau_p \frac{\partial}{\partial t})$ (ν : integer). Manifestly invariant solution describing the doubly periodic system can be constructed by summing up a finite series of interfering terms with different hysteresies. Now, we identify the state $|\Psi(0)\rangle_L$ with $|IM\alpha\rangle_L$, and $|\Psi(0)\rangle_B$ with $|IM\alpha\rangle_B$, where α corresponds to $I_3 = K$ for the case of axially symmetric deformation (uniform rotation). Hence, the stationary wave function of the $C_{m/n}$ -type, $\Psi_{IM\alpha}^{m/n}(q, \Omega)$, is constructed from this periodic solution, which reduces to the axially symmetric solution in the limit $\Delta\vec{\omega}(t) \rightarrow 0$. Expectation value of the asymmetric part of the rotor Hamiltonian with respect to $\Psi_{IM\alpha}^{1/4}(q, \Omega)$ reproduces the experimental data quite well. Similar numerical analysis was performed also for the $C_{1/3}$ -type symmetry, and the result predicts the $\Delta I = 6$ trifurcation as a new possibility. From the relationship of Eq. (1), we can show that there exists a domain of allowance for the stability of the state of $C_{m/n}$ -type against the change of the ratio ω_0/ω_p in such a way that $|\delta(\omega_0/\omega_p)| < 1/n^2$. The $E2$ transition rate calculated from the wave function of Eq. (2) yields the $B(E2)$ value which deviates from the ordinary result for the axially symmetric rotor only in the second order of energy shift.

Role of the x_0 Factor of Skyrme Force in the Interaction Radius of Extremely Neutron-Rich Nucleus

H. Sato

[Nuclear interaction radii]

We study the isotone dependence of the interaction cross sections and interaction radii of the p shell nuclei at neutron magic numbers $N=6$ and $N=8$ scattering off on a carbon target. We have used the Glauber model including terms up to the second order of nucleon-nucleon profile function which was evaluated with the nuclear density distributions given by the density dependent Hartree Fock type variational calculation with shell corrections.¹⁾ First, we study an interaction radius dependence on the force parameters t_0 , t_1 , t_2 , t_3 , x_0 , and W_0 of Skyrme (SK) forces. And we find that an increase of the x_0 factor can reproduce the experimental trend of the isotone dependence on the interaction radius. Also we find that, if a parabolic type of isotonic dependence on the interaction radii ($R_I = aZ^2 + bZ + c$) is assumed, the coefficients of

the parabolic curve obtained are a smooth linear function of the x_0 factor employed in each force parameter set. Then, by readjusting the force parameters so as to reproduce the single neutron energy of the $1p_{1/2}$ state of ^{11}Li (0.15 MeV), we obtained the values of -1128.75 MeVfm^3 , 330 MeVfm^5 , -120 MeVfm^5 , 16400 MeVfm^6 , 0.618 , and 125 MeVfm^5 , respectively for the t_0 , t_1 , t_2 , t_3 , x_0 , and W_0 of the SKIII force.²⁾ With this parameter set, we calculate the interaction cross sections, and summarize them in Table 1 with those by SKIII force. We find that the second order Glauber model calculation of the interaction cross section can reproduce the experimental feature of the isotone dependent interaction cross sections, and can reproduce about a half of the difference between theoretical and experimental values observed in the original

Table 1. The interaction cross sections for scattering of the p shell nuclei of $N=6$ and 8 on a carbon target at 0.79 GeV/nucleon calculated with the SKIII and modified SKIII forces.

Nucleus	σ_{int} (SKIII) mb	σ_{int} (Modified SKIII) mb		σ_{exp} mb
	2nd order	1st order	2nd order	
^8He	793	914	825	817 ± 6
^9Li	781	857	790	796 ± 6
^{10}Be	796	866	801	825 ± 10
^{11}Li	926	1088	978	1056 ± 14
^{12}Be	899	993	916	927 ± 18
^{13}B	903	985	914	883 ± 14

Glauber model calculation of ^{11}Li . We also find that the first order Glauber model calculation now gives a larger interaction cross section of ^{11}Li than the experimental one due to loosely bound neutrons in the $1p_{1/2}$ state.

References

- 1) H. Sato and Y. Okuhara: Phys. Rev. C **34**, 2171 (1986).
- 2) M. Beiner, H. Flocard, N. Van Giai, and P. Quentin: Nucl. Phys. A **238**, 29 (1975).

A Modified Second Order Glauber Model Calculation of the Interaction Cross Sections of Extremely Neutron Rich Nuclei

H. Sato

[Nuclear interaction radii]

Some extremely neutron-rich nuclei, like ^{11}Li , have a halo type neutron distribution due to the existence of extremely loosely bound neutrons.¹⁾ To study the effect of extremely loosely bound neutrons in the interaction cross section, we re-investigate the second order Glauber model calculation.

The optical phase-shift function is given by the evaluation of the powers of the nucleon-nucleon (NN) profile function Γ .²⁾ While the loosely bound neutrons do not affect the optical phase-shift function due to the first order NN profile function, they may cause an overestimation in the second order Glauber model calculation through the second order NN profile function:

$$2 \sum_{\beta > \alpha}^A \sum_{b > a}^B \Gamma_{\alpha a} \Gamma_{\beta b} + \sum_{\alpha}^A \sum_{b > a}^B \Gamma_{\alpha a} \Gamma_{\alpha b} + \sum_{\beta > \alpha}^A \sum_a^B \Gamma_{\alpha a} \Gamma_{\beta a}.$$

Here, $\Gamma_{\alpha\alpha}$ are the NN profile functions between nu-

cleons α and a , respectively, in the projectile and target. For example, in the second term of the above expression, the nucleons in the projectile are assumed to bear double collisions with nucleons in the target. However, extremely loosely bound nucleons may be easily kicked out from the projectile by the first collision against the target nucleons. Therefore, the contribution from the loosely bound nucleon should be taken out from the sum of the second term in the above expression. With such a modification of the second order Glauber model we evaluate the interaction cross sections for the scattering of ^6He and ^{11}Li on a carbon target at 0.79 GeV/nucleon, and compare the results with ordinary second order Glauber model calculations in Table 1. Here we have employed the Skyrme (SK) III and modified SKIII³⁾ forces. We find that the modified second order Glauber model calculation reproduces the experimental interaction cross sections of ^6He and ^{11}Li

Table 1. The interaction cross sections for the nucleus-carbon scattering at 0.79 GeV/nucleon calculated with the second and modified second order Glauber model.

Nucleus	Separation energy (MeV)	σ_{int} (SKIII) mb		σ_{int} (Modified SKIII) mb		σ_{exp} mb
		2nd	Modified 2nd	2nd	Modified 2nd	
^6He	0.97 (2n)	675	731	683	742	722 ± 6
^{11}Li	0.247 (2n)	926	972	978	1046	1056 ± 14

very nicely, particularly with the modified SKIII force. From these analyses, we can conclude that, as far as the interaction cross sections are concerned, the ground states of ^6He and ^{11}Li can be expressed by a Slater determinant of a simple configuration of the $1s_{1/2}$, $1p_{3/2}$, and $1p_{1/2}$ states (no $2s_{1d}$ shell).

References

- 1) I. Tanihata: to be published in J. Phys. G: Nucl. Part. Phys. as a Topical Review.
- 2) V. France and G. Varma: Phys. Rev. C **15**, 1375 (1977); Phys. Rev. C **18**, 349 (1978).
- 3) H. Sato: the previous paper.

Electric Dipole Transitions in Neutron Capture and Coulomb Dissociation Processes

A. Mengoni, T. Otsuka, T. Nakamura, and M. Ishihara

[Neutron capture, Coulomb break-up, Neutron-rich nuclei, Neutron halo]

Electric dipole (E1) radiation emitted (or absorbed) by light neutron-rich nuclei carries important information on the structure of the nuclear states involved in the gamma decay transition. For example, a neutron capture process in which E1 radiation is emitted in the transition from a given state Ψ_c , describing the incident neutron in the continuum, to a bound state Φ_b is essentially determined by the matrix elements

$$Q_{b \leftarrow c}^{(E1)} = \langle \Psi_c | \hat{T}^{E1} | \Psi_b \rangle.$$

If a reliable description of the two-body continuum is available,¹⁾ the matrix elements $Q_{b \leftarrow c}^{(E1)}$ may be used to track down the structure of the bound state Φ_b . The matrix elements $Q_{b \leftarrow c}^{(E1)}$ may be obtained from the neutron capture, (n, γ) , as well as Coulomb dissociation experiments. In the latter case, the E1 strength distribution following the dissociation of neutron-rich radioactive nuclei can be measured and the result be used to derive information on exotic structures such as halo and skin states of nuclei far from the beta stability line.

We have recently developed a technique in which the $B(E1)$ strength distribution of a Coulomb break-up experiment can be used to derive the structure of halo states.²⁾ In fact, the strength distribution is related to the E1 matrix elements by

$$\frac{dB(E1)}{dE_x} = \frac{k^2}{\pi^2 \hbar v} \bar{e}^2 \frac{2J_c + 1}{2J_b + 1} |Q_{b \leftarrow c}^{(E1)}|^2.$$

Here E_x is the excitation energy (defined as the sum of the neutron-residual nucleus relative energy plus the neutron binding energy), k is the wave number of the neutron relative motion in the continuum (and v its velocity), \bar{e} the E1 effective charge, J_b the total angular momentum of the bound state, and J_c the spin of the residual nucleus in the continuum. Under suitable assumptions concerning the description of the relative motion of the neutron in the continuum, it can be shown that the radial part of the bound state wave function is related to the radial part of the E1 matrix elements, $\mathcal{I}_{01}(k)$, by the Fourier-Bessel integral:

$$\mathcal{I}_{01}(k) = 2i\sqrt{3\pi} \int_0^\infty u_0(r) r^2 j_1(kr) dr.$$

Here, the subscripts 0 and 1 refer to the $l = 0$ and 1 components of the neutron-core relative motion. By a suitable inversion of the last equation it is possible to obtain the radial component of loosely bound s -orbits (halo states).

An example of the reconstruction of the radial part of a halo-state wave function (for the ^{11}Be ground state) is shown in the Fig. 1. The $B(E1)$ strength distribution used to derive $u_0(r)$ is what was measured in RIKEN.³⁾ Further developments and results obtainable by the use of this technique can be expected because new data from planned Coulomb dissociation experiments will be available in the near future.

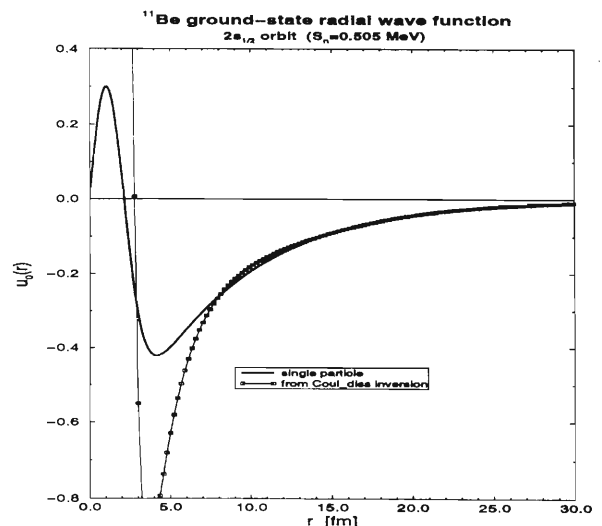


Fig. 1. Reconstruction of the radial wave function of the ground-state of ^{11}Be . The single particle wave function calculated from a Woods-Saxon potential is also shown for comparison.

References

- 1) A. Mengoni, T. Otsuka, and M. Ishihara: Phys. Rev. **52**, R2334 (1995).
- 2) A. Mengoni, T. Otsuka, T. Nakamura, and M. Ishihara: Proc. Int. Symp. Capture Gamma-ray Spectroscopy, Budapest, 1996-10, edited by G. Molnar (Springer-Verlag) in press.
- 3) T. Nakamura et al.: Phys. Lett. B **331**, 296 (1994).

Quantum Monte Carlo Diagonalization Method for Nuclear Many Body Problem

T. Otsuka, T. Mizusaki, and M. Honma

[Monte Carlo method, Nuclear structure]

The nuclear shell model has been successful in the description of various aspects of nuclear structure, partly because the model is based on a minimum number of natural assumptions. Although the direct diagonalization of the Hamiltonian matrix in the full valence-nucleon Hilbert space is desired, the dimension of such a space is too large in many cases, thereby preventing us from performing the full calculations.

Recently, active developments have been made in the stochastic approaches to overcome this difficulty. For an instance, the Shell Model Monte Carlo (SMMC)¹⁾ method has been developed by the Caltech group, which was successful in clarifying the zero temperature and thermal properties of the ground state for huge systems. However, its application also suffers from the so-called *minus-sign* problem. Furthermore, the structure of excited states can be seen only through the response functions. For spectroscopic investigations of the nuclear structure physics, it is a crucial step to remove or relax such restrictions. Thus we proposed a new stochastic approach for solving the nuclear shell model, whose formulation is shown in Ref. 2. By this method, we can study the spectroscopic properties based on the nuclear shell model. The feasibility of this method was well-tested by comparing the exact sd or pf shell calculations with realistic forces.²⁾ As this method is based on the Quantum Monte Carlo method and Diagonalization method, we refer it as the Quantum Monte Carlo Diagonalization (QMCD) method.²⁾

Here, we report a recent application of this method on ⁶⁴Ge, which is considered to show the γ -soft nature. If we take the pf shell as its model space, its shell model dimension is over two billion. In Fig. 1, calculated low-lying spectra by the QMCD method are compared with experimental data. It is remarkable that the calculated levels show a rather good agreement with experimental ones without any adjustment. The γ -soft nature is evident also in the calculation. The calculated ratio of the excitation energies of 2_2^+ to 2_1^+ is 1.9 and that of 4_1^+ to 2_1^+ is 2.6. Experimentally, these ratios are 1.75 and 2.27, respectively. The relative magnitudes of $B(E2)$ values are shown in Fig. 1. With $e_p = 1.33e$ and $e_n = 0.64e$, $B(E2; 2_1^+ \rightarrow 0_1^+) = 5 \times 10^2$

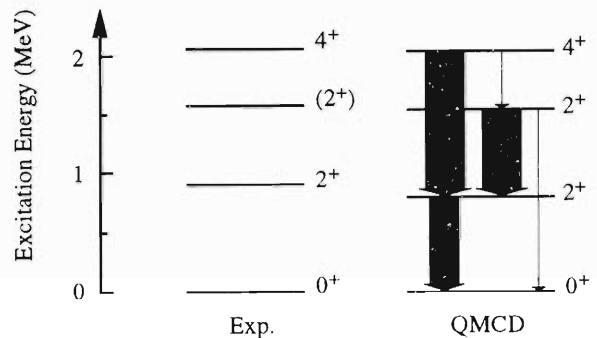


Fig. 1. Experimental and calculated energy levels of ⁶⁴Ge. The arrows designate E2 transitions with $B(E2)$ values indicated by their widths.

($e^2\text{fm}^4$) is obtained, which corresponds to $\beta_2 \sim 0.28$. The $B(E2)$ values of the $4_1^+ \rightarrow 2_1^+$ and $2_2^+ \rightarrow 2_1^+$ transitions are about 1.3 times larger than that of $B(E2; 2_1^+ \rightarrow 0_1^+)$, suggesting γ -softness. We obtain $B(E2; 2_2^+ \rightarrow 0_1^+)/B(E2; 2_2^+ \rightarrow 2_1^+) \sim 2 \times 10^{-3}$, which is quite small similarly to the experimental value, suggesting $\gamma \sim 30^\circ$ in triaxial deformation models. Calculated quadrupole moments appear to be small (typically, $|Q| < 10 \text{ efm}^2$), consistently with γ -softness. Thus, the present QMCD method can radically widen the scope of the shell model calculation.

References

- 1) C. W. Johnson, S. E. Koonin, G. H. Lang, and W. E. Ormand: Phys. Rev. Lett. **69**, 3157 (1992); W. E. Ormand, D. J. Dean, C. W. Johnson, G. H. Lang, and S. E. Koonin: Phys. Rev. C **49**, 1422 (1994); S. E. Koonin, D. J. Dean, and K. Langanke: to be published in Phys. Repts. (1996).
- 2) M. Honma, T. Mizusaki, and T. Otsuka: Phys. Rev. Lett. **75**, 1284 (1995); T. Mizusaki, M. Honma, and T. Otsuka: Phys. Rev. C **53**, 2786 (1996); M. Honma, T. Mizusaki, and T. Otsuka: Phys. Rev. Lett. **77**, 3315 (1996); T. Otsuka, M. Honma, and T. Mizusaki: Proc. Workshop on Contemporary Nuclear Shell Model, 1996-4, Drexel Univ., U.S.A., to be published in Lecture Notes in Physics (Springer-Verlag).

Spreading of Gamow-Teller Resonance in ^{90}Nb and ^{208}Bi

N. Dinh Dang, A. Arima, T. Suzuki, and S. Yamaji

[Gamow-Teller resonance, $2p2h$ configuration mixing]

The giant Gamow-Teller resonance (GTR) was predicted in 1963¹⁾ to explain the hindrance of allowed unfavored β decays. It was experimentally observed first in 1975 in the $^{90}\text{Zr}(p, n)$ reaction.²⁾ A measure of the total observed transition strength for the GTR is provided by the model-independent Ikeda sum rule,¹⁾ which should be nearly exhausted by the transition strength summed over all GT states in the daughter ($Z + 1, N - 1$) nucleus. However, during the last 20 years experimental systematics over a wide range of the periodic table found only around 60% of this sum rule value. The $\Delta(1232)$ isobar-hole admixtures in the nuclear wave function³⁾ were first proposed as a mechanism for the GTR quenching. Theoretical studies have shown that this effect seems to be small.⁴⁻⁶⁾ The $2p2h$ -configuration mixing must be taken into account. If this mechanism plays an important role, the missing GT strength should be spread over the physical background below and beyond the GTR.^{6,7)} Several models, including Ref. 8, have been proposed to calculate the spreading of GTR due to a mixing with $2p2h$ configurations. Even though all of them recover the Ikeda sum rule in the energy interval below 50 ~ 60 MeV, the amount of strength in the GTR region as well as the shape of the strength function varies noticeably depending on models. Recently, high-resolution measurements of GTR in the $^{208}\text{Pb}(^3\text{He}, t)^{208}\text{Bi}$ reaction⁹⁾ and in the $^{90}\text{Zr}(p, n)^{90}\text{Nb}$ reaction¹⁰⁾ were carried out in RCNP (Osaka). In particular, the authors of Ref. 10 were able to extract, for the first time, the $L = 0$ cross section in the continuum, resulting in a long tail of GTR extending up to around 60 MeV, which seems to recover the missing part of the GTR strength. These new experimental results^{9,10)} have motivated the present work.

We propose an approach to the damping of GTR, where the GTR is generated by proton particle - neutron hole phonons ($p_\pi - h_\nu$ phonons) within the renormalized random phase approximation (RPA). The renormalization is due to the ground-state correlations beyond RPA. The second-order configuration mixing beyond RPA was realized by constructing two-phonon configurations, in which one of two intermediate phonon states was a $p_\pi - h_\nu$ phonon. The numerical calculations were performed in the parent nuclei ^{90}Zr and ^{208}Pb making use of the nucleon-nucleon effective $M3Y$ interaction¹¹⁾ and of the single-particle wave functions obtained in the standard harmonic oscillator potential. The single-particle energies around the Fermi surface were substituted with the empirical values or those given by a Woods-Saxon potential.

Results obtained have provided a reasonable account for recent experimental findings of the spreading and quenching of GTR in these nuclei (Fig. 1). An extension of the present approach to highly-excited (hot) nuclei was also performed. We found that the GTR is stable against increasing temperature up to ~ 6 MeV.

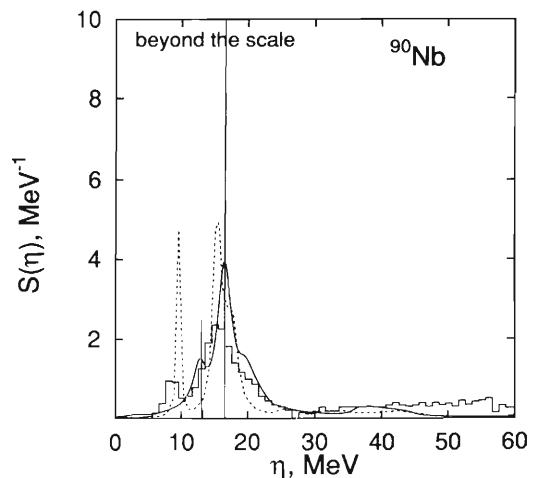


Fig. 1. Strength function of GTR in ^{90}Nb . Energies are measured with respect to the ground state of ^{90}Zr . The experimental distribution from Ref. 10 is shown by the histogram. Impulses show the RPA results. Dotted and solid curves refer to the results of Ref. 8 and our results, respectively.

References

- 1) K. Ikeda, S. Fujii, and J. I. Fujita: Phys. Rev. Lett. **3**, 271 (1963).
- 2) R. R. Doering et al.: Phys. Rev. Lett. **35**, 1961 (1975).
- 3) M. Rho: Nucl. Phys. A **231**, 493 (1974); E. Oset and M. Rho: Phys. Rev. Lett. **42**, 47 (1979).
- 4) K. Shimizu, M. Ichimura, and A. Arima: Nucl. Phys. A **226**, 282 (1974); A. Arima and H. Hyuga: in *Meson in nuclei* (North-Holland, Amsterdam, 1979), p. 683.
- 5) L. S. Towner and F. C. Khanna: Phys. Rev. Lett. **42**, 51 (1979).
- 6) F. Osterfeld: Rev. Mod. Phys. **64**, 491 (1992).
- 7) C. Gaarde et al.: Nucl. Phys. A **369**, 258 (1981).
- 8) S. Drożdż et al.: Phys. Lett. B **166**, 18 (1986).
- 9) H. Akimune et al.: Phys. Rev. C **52**, 604 (1995).
- 10) T. Wakasa et al.: Proc. Int. Symp. on Non-Nucl. Degrees of Freedom detected in Nucleus, Osaka, 1996-9, to be published.
- 11) G. F. Bertsch and I. Hamamoto: Phys. Rev. C **26**, 1323 (1982).

Two-Dimensional GCM Calculation of TAR States

T. Horibata, M. Oi, and N. Onishi

[Tilted rotation, Generator coordinate method, Signature splitting]

We have been carrying out a systematic calculation based on a self-consistent three-dimensional cranked HFB method in $A \sim 180$ region and have found a solution which represents a Tilted Axis Rotating (TAR) state using an appropriately chosen set of force parameters.^{1,2)} This fact means that the intrinsic states become more stable through mixing of the *odd* angular momentum members in the wave functions.

Taking notice of this feature we tried to explain the experimental fact that the energies of *odd* angular momentum members are very low; these states were considered to be the same members of the yrast band. A three-band mixing analysis with *g*-band, *t*-band and *s*-band gives, however, a different interpretation for an observed signature splitting and also for the yrast band structure. That is, the yrast is mainly composed of the *s*-band, and the signature splitting *t*-band (odd and even) locates just above the yrast.³⁾

Previously, we tried to describe the signature splitting in terms of the Generator Coordinate Method (GCM),⁴⁾ in which the north-latitude along the prime meridian is employed as a generator coordinate. The method is quite general and an interesting approach in describing the excited band as well as the yrast band where the quantum tunneling between two wells located symmetrically with respect to an equator is expected.

Since the one-dimensional GCM calculation could not give any stable plateau against the increase of number of states in the *s*-band, we extended the calculation into the two-dimensional(2D) space. We took 837 points of grid in the plane for the numerical integration. In the one-dimensional(1D) case only 31 points were considered. The norm kernel is first diagonalized. In this step we found the existence of negative solutions whose absolute values are not negligibly small. We will discuss the characteristic feature of these solutions in a separate report. The discretized hamiltonian matrices are diagonalized by utilizing only the positive eigenvalues of the norm kernel to obtain energy eigenvalues.

The energy eigenvalues of the five lowest states for $J = 16\hbar$ (*s*-band) are depicted in Fig. 1 as a function of the number of states employed. We found a stable plateau in the result in contrast with the previous (1D) case. The employed number of states in the calculation are, however, restricted only to less than 200 solutions for the diagonalization of the norm kernel. Many solutions which give very small eigen values in the diagonalization of the norm kernel are left behind

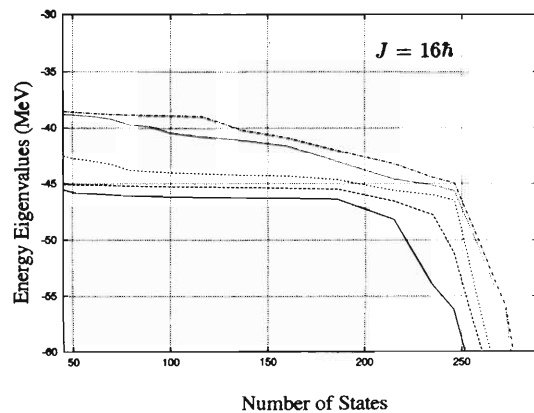


Fig. 1. The energy spectra for $J = 16\hbar$ in *g*-band as a function of the number of states employed in diagonalization. The energy is the absolute value.

in the calculation.

Moreover, we could not obtain the stable plateau for $J = 14\hbar$ and $J = 18\hbar$ states. The reason may be attributed to the fact that we lost many informations about high-frequency part of the wave functions which are contained in the states with small eigen values of the norm kernel. These informations can mostly be taken into account through angular momentum projection of Hartree-Fock-Bogoliubov states.⁵⁾ Calculation along this line is in progress.

In the meanwhile, we are again to make the calculation for the 1D GCM with more carefully adjusted force parameters and with much finer mesh points, since the rate of occurrence for the *zero* eigen value solutions in the diagonalization of the norm kernel are relatively small compared to the 2D case. Angular momentum projection will play less important roles in 1D GCM.

References

- 1) T. Horibata and N. Onishi: Phys. Lett. B **325**, 283 (1994).
- 2) T. Horibata and N. Onishi: Nucl. Phys. A **596**, 251 (1996).
- 3) P. M. Walker: Proc. Int. Conf. on the Future of Nuclear Spectroscopy, Crete, p. 134 (1993).
- 4) T. Horibata, M. Oi, and N. Onishi: Phys. Lett. B **355**, 433 (1995).
- 5) M. Oi, N. Onishi, and T. Horibata: RIKEN Accel. Prog. Rep. **29**, 29 (1996).

Variation of Transport Coefficients for Average Fission Dynamics with Temperature and Shape

S. Yamaji, F. A. Ivanyuk,* and H. Hofmann**

[Thermal fission, Linear response theory]

We study a slow collective motion at finite thermal excitations on the basis of linear response theory applied to the locally harmonic approximation.¹⁾ The response functions have been calculated within a realistic two-center shell model. Effects of collisions have been accounted for by using self-energies having both real and imaginary parts. The latter is allowed to depend not only on temperature but on frequency as well; in this way memory effects of the collision term can be simulated. Locally collective motion is treated self-consistently, in the sense that the structure of the associated response resembles the one known from the RPA motion. The corresponding friction γ , inertia M , and the local stiffness C are computed along a fission path of ^{224}Th within a quasi-static picture. For a damped oscillator the quantity $\eta = \gamma/2\sqrt{M|C|}$ indicates whether the motion is underdamped ($\eta < 1$) or overdamped ($\eta > 1$). Therefore, it is a good measure for the effective degree of damping. Furthermore, it is exactly this quantity, if calculated at the saddle point, which according to Kramers' famous formula

$$R_K = \left(\sqrt{1 + \eta_s} - \eta_s \right) R_{BW} \quad (1)$$

determines the deviation of the fission decay rate R_K from the R_{BW} of the Bohr-Wheeler formula. The η has been calculated as a function of T before,²⁾ but only for the case of quadrupole vibrations around the spherical minimum of lead. In the light of Eq. (1) it may suffice first to study it around the barrier. Indeed, this formula applies if, from the full dynamics across the barrier, it is only the motion around the stationary points which matters. The latter situation can be seen to be given if the height B of the barrier is much larger than the temperature:³⁾ $B/T \gg 1$. Unfortunately, often Eq. (1) is applied even in cases that this basic condition on T and B is violated.

To study these questions for our example we have calculated all relevant quantities by performing averages both around the potential minimum as well as around the barrier. The results are put together in the following Table 1.

Several inferences can be drawn immediately:

a) One of the most striking features is the weak dependence of η on the shape parameter. The temperature dependence of this quantity is similar to the one

Table 1. The quantities $\hbar\varpi = \hbar\sqrt{|C|/M}$ and η at the minimum and saddle points and the barrier height B as a function of T .

T	$\hbar\varpi_m$	η_m	B	$\hbar\varpi_s$	η_s
MeV	MeV		MeV	MeV	
1	0.82	1.1	7.20	0.50	1.2
2	0.94	2.2	5.95	0.59	2.7
3	0.93	2.5	4.31	0.59	3.2
4	0.87	2.7	2.59	0.60	3.3
5	0.79	2.9	1.18	0.67	3.0

reported previously²⁾ for vibrations of ^{208}Pb : it increases with T , to eventually reach some saturation around $T \approx 4$ MeV. This behavior is in agreement with findings,⁴⁾ at least qualitatively. Our damping rate is somewhat smaller, and its variation with the shape is weaker than that in the analysis⁴⁾ of the γ -ray multiplicity encountered in fission of ^{224}Th . However, it must be said that we have not yet striven for quantitative agreements. For instance, there is a room for a more appropriate choice of the two parameters of collisional damping. Furthermore, one should mention the influence of pairing, which still might be important at the smaller T value of 1 MeV. Moreover, the influence of angular momentum ought to be taken into account.⁵⁾

b) The basic condition on the validity of Eq. (1) is satisfied for temperatures up to 3 MeV at best. It is interesting to note that $\hbar\varpi_s$ increases with T , albeit only slightly. A closer inspection shows the quantity $2\pi T/(\hbar\varpi_s)$ to be of the order of π and thus definitely larger than unity. This implies that collective quantum effects do not contribute to fission dynamics for the examples chosen here. It should be said that in simplified studies Kramers' picture is often applied, even in cases where the barrier is too low to guaranty that the flux across the barrier can be described by Kramers' solution of the Fokker-Planck equation. This problem can only be cured by performing dynamical studies along the lines.⁶⁻⁸⁾

References

- 1) S. Yamaji et al.: to be published in Nucl. Phys.
- 2) H. Hofmann et al.: Nucl. Phys. A **598**, 187 (1996).
- 3) H. Hofmann et al.: Phys. Lett. B **317**, 489 (1993).
- 4) P. Paul and M. Thoennessen: Ann. Rev. Part. Nucl. Sci. **44**, 65 (1994).
- 5) K. Pomorski and H. Hofmann: Phys. Lett. B **263**, 164 (1991).
- 6) E. Strumberger et al.: Nucl. Phys. A **529**, 522 (1991).
- 7) P. Fröbrich et al.: Nucl. Phys. A **563**, 326 (1993).
- 8) T. Wada et al.: Phys. Rev. Lett. **70**, 3538 (1993).

* Institute for Nuclear Research of the Ukrainian Academy of Sciences, Ukraine

** Physik-Department der Technischen Universität München, Germany

The Continuity Equation of the Nuclear Four-Current

H. Kurasawa* and T. Suzuki

[Four-current, Continuity equation]

The nuclear four-current should satisfy the continuity equation,

$$\frac{\partial \rho}{\partial t} + \nabla \cdot J = 0.$$

Here, the density operator is

$$\rho(q) = \sum_{i=1}^A \exp(iq \cdot r_i) (1 - \tau_3^i) / 2,$$

and the current density is given by

$$[H, \rho] = i \nabla \cdot J,$$

for H standing for the nuclear hamiltonian. Using the eigenstate of H , the continuity equation is expressed as

$$(E_n - E_0) \langle n | \rho | 0 \rangle = \langle n | i \nabla \cdot J | 0 \rangle \quad (H | n \rangle = E_n | n \rangle). \quad (1)$$

Usually, however, we can not solve the Schrödinger equation exactly. As a result, Eq. (1) is not satisfied. It is shown below that the Hartree-Fock approximation is one of the examples in which the continuity equation is violated.

Let us assume the nuclear hamiltonian to be

$$H = T + V, \quad T = \sum_{i=1}^A t_i = \sum_{i=1}^A \frac{p_i^2}{2M}, \quad V = \frac{1}{2} \sum_{i,j} V(i, j),$$

where the nuclear interaction generally has a form:

$$V(i, j) = v_0(r) + x_\tau v_\tau(r) \tau_i \cdot \tau_j + x_\sigma v_\sigma(r) \sigma_i \cdot \sigma_j + \frac{1}{3} x_{\sigma\tau} v_{\sigma\tau}(r) \tau_i \cdot \tau_j \sigma_i \cdot \sigma_j, \quad (r = |r_i - r_j|).$$

For this hamiltonian, the isoscalar part of the four-current satisfies

$$[H, \rho^s] = [T, \rho^s] = i \nabla \cdot J^s, \quad (2)$$

and the single-particle current at $q \rightarrow 0$ should be

$$i \nabla \cdot j^s(q \rightarrow 0) = q \cdot \frac{p}{M}. \quad (3)$$

Now, the Hartree-Fock equation¹⁾ provides us with the matrix element for a particle(m)-hole(i) state;

$$\begin{aligned} (\epsilon_m - \epsilon_i) \langle m i^{-1} | \rho^s | \rangle &= \langle m | [t, \rho^s] | i \rangle \\ &+ \sum_j \langle m j | V(1, 2) \rho^s(1) - \rho^s(1) V(1, 2) | i j \rangle \\ &- \sum_j \langle m j | V(1, 2) \rho^s(2) - \rho^s(1) V(1, 2) | j i \rangle, \end{aligned} \quad (4)$$

where $| \rangle$ denotes the Hartree-Fock ground state of the nucleus, and $\rho^s(i)$ the isoscalar part of the single-particle density. In a nuclear matter approximation, we have for $p = p_F$,

$$\lim_{q \rightarrow 0} (\epsilon_m - \epsilon_i) \langle m i^{-1} | \rho^s | \rangle = q \cdot \frac{p_F}{M^*}, \quad (5)$$

where the effective mass M^* is defined by

$$\frac{1}{M^*} = \frac{1}{M} \left\{ 1 + \pi \frac{2M p_F}{\pi^2} \int v^*(r) j_1^2(p_F r) r^2 dr \right\},$$

$$v^*(r) = v_0(r) + 3x_\tau v_\tau(r) + 3x_\sigma v_\sigma(r) + 3x_{\sigma\tau} v_{\sigma\tau}(r).$$

The right hand side of Eq. (5) is different from that of Eq. (3) expressed by the free mass. Thus, in the Hartree-Fock approximation the continuity equation is violated. The reason of the violation is clear. We have obtained Eq. (3), since the nuclear interaction satisfies $[V(1, 2), \rho^s(1) + \rho^s(2)] = 0$ as in Eq. (2). Equation (4), however, takes into account only a part of the above commutator.

We can prove that in the random phase approximation (RPA) based on the Hartree-Fock approximation, the continuity equation is satisfied approximately. In RPA¹⁾ the particle-hole states are described as

$$|\omega_n\rangle = O_n^\dagger | 0 \rangle, \quad O_n^\dagger = \sum_{mi} (Y_{mi}^n a_m^\dagger a_i - Z_{mi}^n a_i^\dagger a_m),$$

and the RPA ground state defined by $O_n | 0 \rangle = 0$. We can show that the RPA equation of motion for the forward and backward amplitudes, Y_{mi}^n and Z_{mi}^n , gives

$$\begin{aligned} \omega_n \langle \omega_n | \rho | 0 \rangle &= \sum_{mi} \{ \langle m i^{-1} | [H, \rho] | \rangle Y_{mi}^{n*} \\ &+ \langle [H, \rho] | m i^{-1} \rangle Z_{mi}^{n*} \} \end{aligned} \quad (6)$$

ω_n being the excitation energy of the state $|\omega_n\rangle$. As for the isoscalar density ρ^s , the relationship of Eq. (2) gives the one-body current. Therefore, Eq. (6) can be written as,

$$\omega_n \langle \omega_n | \rho^s | 0 \rangle = \langle \omega_n | i \nabla \cdot J^s | 0 \rangle, \quad (7)$$

which is the same as the continuity equation given by Eq. (1).

For the isovector current, the Hartree-Fock approximation yields the same equation as Eq. (5) for the isoscalar current. In RPA, the isovector four-current satisfies an equation different from Eq. (7). Since we have $[V, \rho^v] \neq 0$ for the isovector density, the isovector current is given by two-body operators. Hence, we can not write the continuity equation of the isovector four-current in the form of Eq. (7).

References

- 1) D. J. Rowe: in *Nuclear Collective Motion* (Methuen Co. Ltd., London, 1970).

* Faculty of Science, Chiba University

Unstable Nuclei and the Equation of State of Asymmetric Nuclear Matter

K. Oyamatsu

[Unstable nuclei, Equation of state, Atomic masses, Nuclear radii]

We aim to extract the equation of state (EOS) of asymmetric nuclear matter from the masses and radii of unstable nuclei, which are closely related to the saturation energies and densities of asymmetric nuclear matter whose proton fraction (Y_p) is $Y_p < 0.5$. Figure 1 shows the Y_p values of various matters. We see that the unstable nuclei bridge a gap between stable nuclei and supernova matter as well as the one between stable nuclei and nuclei in inner crusts of neutron stars. As the first step of our study, we neglect surface effects and attempt to relate the EOS of asymmetric nuclear matter with the bulk properties of neutron rich nuclei.

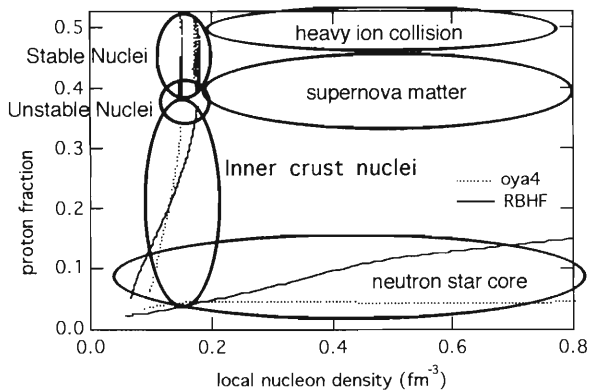


Fig. 1. Proton fractions and nucleon densities of asymmetric nuclear matter and at the centers of nuclei. The abbreviations oya4 and RBHF indicate the Thomas Fermi calculations in Refs. 1 (model IV) and 2, respectively.

For simplicity, we assume the following form for the energy per nucleon of uniform nuclear matter, whose nucleon density is n , as

$$w(n, Y_p) = w_s(n) + (1 - 2Y_p)^2 S(n), \quad (1)$$

where $w_s(n)$ and $S(n)$ are the energy per nucleon of symmetric ($Y_p = 0.5$) nuclear matter and the symmetry energy, respectively. When the density n is close to the saturation density of symmetric nuclear matter, n_0 , we can write

$$w_s(n) \approx w_0 + \frac{K_{s0}}{18 n_0^2} (n - n_0)^2 \quad (2)$$

and

$$S(n) \approx S_0 + \frac{p_{n0}}{n_0^2} (n - n_0) + \frac{K_{n0} - K_{s0}}{18 n_0^2} (n - n_0)^2. \quad (3)$$

Here, w_0 and S_0 are the saturation energy of symmetric nuclear matter and the symmetry energy at $n = n_0$, respectively. Equations (2) and (3) include density derivatives of $w(n, Y_p)$. They are the pressure of pure neutron matter, p_{n0} , and the compressibility modulus of symmetric nuclear matter (pure neutron matter), K_{s0} (K_{n0}).

In the above approximation, the saturation density, n_1 , and the energy per nucleon, w_1 , of asymmetric nuclear matter are given, respectively, by

$$n_1 = n_0 - 9 \frac{p_{n0}}{K_{s0}} (1 - 2Y_p)^2 \left[1 - \frac{K_{n0} - K_{s0}}{K_{s0}} (1 - 2Y_p)^2 \right] \quad (4)$$

and

$$w_1 = w_0 + S_0 (1 - 2Y_p)^2. \quad (5)$$

In deriving Eqs. (4) and (5), we have neglected the higher order terms than $(1 - 2Y_p)^4$. The second term in the square bracket in Eq. (4) is expected to be quite small.

From Eqs. (4) and (5), we see that the pressure of pure neutron matter primarily determines the saturation densities of asymmetric matter, while the symmetry energy at $n = n_0$ dominates their energies. We note further that the compressibility of symmetric matter also affects the saturation densities. Therefore, what we can obtain from the radii and masses of neutron rich nuclei are the energy, pressure, and possibly compressibility of pure neutron matter. However, further studies, especially on nuclear surfaces, are still necessary to determine the EOS of asymmetric matter quantitatively from the nuclear masses and radii.

References

- 1) K. Oyamatsu: Nucl. Phys. A **561**, 431 (1993).
- 2) K. Sumiyoshi et al.: Nucl. Phys. A **595**, 327 (1995).

Effect of Relativistic Equation of State on Vortex Pinning to the Nuclei in Neutron Star Crusts

Y. S. Mochizuki

[Neutron stars]

The inner crust of a neutron star consists of a body-centered cubic (*bcc*) lattice of neutron rich nuclei, relativistic degenerate electrons, and a neutron superfluid. Since the star is rotating, there are a number of quantized vortices in the superfluid. The vortex lines are expected to be nearly parallel to the axis of rotation.

Each vortex line possesses a normal fluid core over a distance ξ , the coherence length of the superfluid. We take a view that the BCS pairing is prohibited completely inside the vortex core. The pairing energy is rather large. In the superfluid, the pairing energy per neutron is given by $\varepsilon_p = (3/8) \Delta^2/E_F$, where Δ is the superfluid energy gap and E_F the Fermi energy of superfluid neutrons. For simplicity we assume that the superfluidity does not exist in the nuclei. Then the pairing energy can be gained by increasing overlap of the vortex core line with nuclei. This is simply the origin of the vortex pinning.

The pinning energy (the energy gain when a vortex line pins to nuclear materials) is given by $E_p = \varepsilon_p n_n^{out} V$, where V is the overlap volume of the vortex core and the nuclear materials, and n_n^{out} is the superfluid neutron number density outside the nuclei. Hence, the pinning energy depends on the Δ and also on the size of the nuclei. The pinning energy is a key physical quantity to explain frequency of neutron star glitches (sudden spinups in pulsars).

So far, the nuclear size dependence on E_p has not been considered except by Takatsuka (1984).¹⁾ Usually, the following parametric form²⁾

$$E_p = 0.87 k_F \Delta^2 \quad (1)$$

is used to estimate E_p . Here, $k_F = (3\pi^2 n_n^{out})^{1/3}$ is the Fermi wave number. It should be noted that in Eq. (1) the radius of nuclei is fixed as $R_N = 7$ fm.

Recently, Sumiyoshi, Oyamatsu, and Toki (1995)³⁾ calculated a nuclear lattice structure in the inner crust, adopting the equation of state based on the relativistic Brueckner-Hartree-Fock theory. It has been known, from the analysis of laboratory nuclei, that calculations in the relativistic framework produce larger radii of neutron distributions in the nuclei than conventional calculations as the neutron richness increases. In fact, the nuclear size obtained in Ref. 3 is quite large in the region of average baryon density, $\rho/\rho_0 \gtrsim 0.2$, as compared with those reported so far. Here $\rho_0 \equiv 0.17$ fm⁻³ denotes the normal nuclear density.

It is the purpose of present paper to examine this size effect which stems from the relativistic equation of

state on the pinning energy, using the results obtained in Ref. 3. Not only usual spherical nuclear shape, here we consider also nonspherical (cylindrical) shapes of nuclei. In particular, we consider the pinning-induced nuclear rods (PINRs) proposed by Mochizuki and Izuyama⁴⁾ (For details, see Refs. 4 and 5).

Figure 1(a) shows the result of E_p as a function of ρ/ρ_0 . In this figure, Δ is adopted from Ref. 1. E_p that was reported in Ref. 1, in which only the spherical nuclear shape was taken into account, is also shown for comparison. We found a remarkable difference between the two calculations in the high density region, $\rho/\rho_0 \gtrsim 0.25$. We note that Eq. (1) gives almost the same behavior as the E_p obtained in Ref. 1. It is thus concluded that, contrary to the conventional picture, E_p is strong enough in the deep inside of the inner crust.

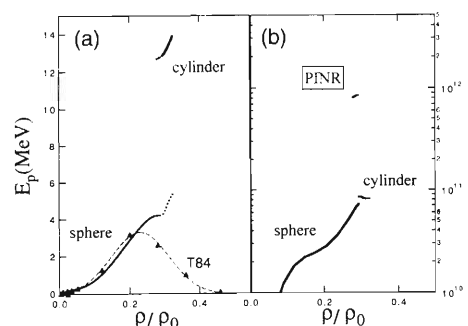


Fig. 1. (a) Pinning energy per nearest neighbor distance in the *bcc* lattice. (b) Pinning energy per unit length (1 cm) of a vortex line.

In Fig. 1(b), we show the result of E_p including that of PINR. Here, Δ is adopted from Ref. 6. From the figure we confirm the assertion in Ref. 4 which mentioned that PINRs give singularly stronger pinning. Formation of PINRs will thus be a crucial mechanism to explain neutron star glitches as discussed in Refs. 4 and 5.

References

- 1) T. Takatsuka: Prog. Theor. Phys. **71**, 6, 1432 (1984).
- 2) M. A. Alpar et al.: Astrophys. J. **346**, 823 (1989).
- 3) K. Sumiyoshi et al.: Nucl. Phys. A **595**, 327 (1995).
- 4) Y. Mochizuki and T. Izuyama: Astrophys. J. **440**, 263 (1995).
- 5) Y. S. Mochizuki et al.: submitted to Astrophys. J.
- 6) T. L. Ainsworth et al.: Phys. Lett. B **222**, 173 (1989).

Baryon Properties Based on the Chiral Quark Soliton Model[†]

M. Wakamatsu

[Nucleon spin structure, Effective theory of QCD]

The chiral quark soliton model (CQSM) is one of the simplest models of baryons, which takes account of the most important properties of low energy QCD: i.e., the spontaneous breakdown of chiral symmetry and the associated appearance of Nambu-Goldstone bosons.^{1,2)} The basic theoretical framework of CQSM consists of mean field theory and subsequent quantization of the collective rotational motion based on the cranking method; which are both familiar techniques in the theory of deformed nuclei. With this framework, the bound state problem for a baryon can be solved nonperturbatively under a full inclusion of the negative-energy Dirac-sea quark degrees of freedom in addition to the three valence quarks. A unique feature of this model is that it predicts a quite small fraction of quark spin to the nucleon spin.²⁾ It means that in this model a sizable part of the total nucleon spin is carried by the orbital angular momentum of quarks. Undoubtedly, this is a natural consequence of the basic dynamical assumption of the model: i.e., a physical baryon as a rotating hedgehog object.

By extending the model further to the case of flavor SU(3), we can study the properties of strange baryons like the Λ and Σ , and can also study the strangeness contents of nonstrange baryons like the nucleon.^{3,4)} Table 1 shows the prediction of the flavor SU(3) CQSM as for the flavor decomposition of quark spin fractions to the nucleon spin.

Table 1. The flavor decomposition of quark spin fractions.

	$O(\Omega^0)$	$O(\Omega^0 + \Omega^1) + \Delta m_s$	experiment
Δu	0.34	0.87	0.83
Δd	-0.26	-0.35	-0.43
Δs	-0.08	-0.03	-0.10
$\Delta \Sigma$	0	0.49	0.31

Here, the column represented by $O(\Omega^0)$ shows the mean field predictions, or equivalently, the contributions of the zeroth order term in the collective angular velocity, Ω . On the other hand, the column represented by $O(\Omega^0 + \Omega^1) + \Delta m_s$ gives the final predictions of the SU(3) CQSM, which takes account of the first order rotational correction in Ω as well as the flavor SU(3) breaking effects caused by the mass difference between the strange and nonstrange quarks. One can see from this table that one of the characteristic predictions of the SU(3) CQSM is the negative polarization of the strange quark sea with respect to the direction of the nucleon spin. This feature is also interpreted as an evidence of the formation of the symmetry breaking hedgehog mean field. As the terminology “hedgehog mean field” indicates, the model (CQSM) naturally has close connections with the Skyrme model. In fact, the correspondence between these two models become almost exact in the fictitious limit of $N_c \rightarrow \infty$. However, we have recently found that this correspondence seriously breaks down at the next leading order in N_c .^{5,6)} This observation resolves the long-standing g_A problem of the Skyrme model, thereby confirming the superiority of the CQSM to the Skyrme model as a realistic low energy model of baryons.

References

- 1) D. I. Diakonov, V. Yu. Petrov, and P. V. Pobylitsa: Nucl. Phys. B **306**, 809 (1988).
- 2) M. Wakamatsu: Nucl. Phys. A **524**, 561 (1991).
- 3) H. Weigel, R. Alkofer, and H. Reinhardt: Nucl. Phys. B **378**, 638 (1992).
- 4) A. Blotz, D. I. Diakonov, K. Goeke, N. W. Park, V. Yu. Petrov, and P. V. Pobylitsa: Nucl. Phys. A **555**, 765 (1993).
- 5) M. Wakamatsu and T. Watabe: Phys. Lett. B **325**, 467 (1994).
- 6) M. Wakamatsu: Prog. Theor. Phys. **95**, 143 (1996).

[†] Invited talk at the XIII International Seminar on High Energy Physics Problem, Dubna, 2-7 September, 1996.

QCD Corrections to the Structure Function g_2

J. Kodaira

[Deeply inelastic scattering, Spin structure]

Recently there has been much interest in the nucleon spin structure function, g_2 . In the framework of the operator product expansion, not only the twist-2 but also the twist-3 (higher-twist) operators contribute to g_2 in the leading order of $1/Q^2$. The general features characteristic to the higher-twist operators are; (1) the occurrence of the operators which are proportional to the equation of motion (EOM operators) and several operators are related through the EOM operators;¹⁾ (2) some gauge non-invariant EOM operators will mix under the procedure of the renormalization.²⁾ These facts bring about some complication for the higher-twist operators through the course of renormalization.

The anomalous dimensions of the composite operators, which are obtained from the renormalization constant, control the Q^2 dependence of the structure functions. We examine what happens to the renormalization if there are several operators which are related through the EOM operators. We illustrate the points with the scalar field theory. Assume that we have two composite operators R_1 and R_2 which are related through the equation of motion:

$$R_1 = R_2 + E, \quad (1)$$

where E is an EOM operator. Since we have three composite operators with a constraint of Eq. (1), we can choose any two operators among three as an independent basis.

First we choose R_1 and R_2 . Then renormalization takes the following form:

$$\begin{pmatrix} R_1 \\ R_2 \end{pmatrix}_R = \begin{pmatrix} Z_{11} & Z_{12} \\ Z_{21} & Z_{22} \end{pmatrix} \begin{pmatrix} R_1 \\ R_2 \end{pmatrix}_B. \quad (2)$$

Here, the suffix R (B) denotes the renormalized (bare) operator. Next, we change the operator basis to R_i ($i = 1$ or 2) and E . Then, the renormalization matrix should become triangular,³⁾

$$\begin{pmatrix} R_i \\ E \end{pmatrix}_R = \begin{pmatrix} Z_{ii}^E & Z_{iE} \\ 0 & Z_{EE} \end{pmatrix} \begin{pmatrix} R_i \\ E \end{pmatrix}_B, \quad (3)$$

since the counterterm to the E operator should vanish by the equation of motion. From Eqs. (2) and (3), we can derive the following relations among the renormalization constants, Z 's:

$$\begin{aligned} Z_{11}^E &= Z_{11} + Z_{12} = Z_{21} + Z_{22} = Z_{22}^E, \\ Z_{EE} &= Z_{22} - Z_{12} = Z_{11} - Z_{21}, \end{aligned}$$

$$Z_{1E} = -Z_{12}, \quad Z_{2E} = Z_{21}. \quad (4)$$

Equation (4) is a consistency condition for the renormalization of the operators satisfying Eq. (1).

We note that the arbitrariness in the choice of the operator basis does not enter into the physical quantities. This fact can be explicitly confirmed by noting that the physical matrix element of the E operator vanishes:^{1,3)} $\langle p|E|p' \rangle = 0$. Taking the physical matrix element of Eq. (3), we conclude that the renormalization constant of Z_{ii}^E is only relevant. We reach the same conclusion also from Eq. (2).

The anomalous dimensions of twist-3 operators in QCD at the one-loop level have been studied in Ref. 4. However it is not clear how the EOM operators are dealt with and their results do *not* coincide each other. We have reanalyzed the operator mixing problems by keeping the EOM operators. We have clarified the role of the EOM operators and given a correct answer for the anomalous dimensions by calculating the off-shell Green's functions.²⁾

Finally let us make a comment on the Burkhardt-Cottingham sum rule. The operator product expansion naively suggests:

$$\int_0^1 dx g_2(x, Q^2) = 0.$$

We have shown that this sum rule does not receive any corrections in QCD.⁵⁾

We expect that future measurements on g_2 will clarify the effect of twist-3 operators which share some common feature with more general higher-twist effects in QCD.

References

- 1) H. D. Politzer: Nucl. Phys. B **172**, 349 (1980).
- 2) J. Kodaira, T. Uematsu, and Y. Yasui: Phys. Lett. B **344**, 348 (1995); J. Kodaira, K. Tanaka, T. Uematsu, and Y. Yasui: Phys. Lett. in press.
- 3) J. C. Collins: in *Renormalization* (Cambridge Univ. Press, 1984); and references therein.
- 4) E. V. Shuryak and A. I. Vainshtein: Nucl. Phys. B **199**, 951 (1982); A. P. Bukhvostov, E. A. Kuraev, and L. N. Lipatov; JETP Lett. **37**, 483 (1984); X. Ji and C. Chou: Phys. Rev. D **42**, 3637 (1990).
- 5) J. Kodaira, S. Matsuda, K. Sasaki, and T. Uematsu: Phys. Lett. B **345**, 527 (1995).

Next-to-Leading-Order Q^2 Evolution Program for Spin-Dependent Structure Functions

M. Hirai,* S. Kumano, and M. Miyama*

[Q^2 evolution, Structure function]

Spin-dependent structure functions are measured in the polarized lepton-nucleon scattering. They depend on two kinematical variables, x and Q^2 . The Q^2 dependence is calculated within perturbative QCD, and it is described by integrodifferential equations so called DGLAP equations. Next-to-leading-order (NLO) splitting functions for spin-dependent parton distributions are evaluated recently.¹⁾ Therefore, we can study numerical solution of the NLO spin-dependent Q^2 evolution equations.²⁾

Although we used a Laguerre-polynomial method³⁾ for solving the equations of unpolarized case, a brute-force method can be employed as an alternative one. This method was already investigated for solving the spin-independent evolution equations with or without parton-recombination effects.⁴⁾ The same method is applied to the spin-dependent case. We divide variables into small steps (N_x steps in the Bjorken variable $\ln x$, and N_t steps in the variable $t \equiv -(2/\beta_0) \ln[\alpha_s(Q^2)/\alpha_s(Q_0^2)]$) and calculate the differentiation and integration in the evolution equations after rewriting them by $df(x)/dx = [f(x_{m+1}) - f(x_m)]/\Delta x_m$ and $\int dx f(x) = \sum_{m=1}^{N_x} \Delta x_m f(x_m)$. In this way, the integrodifferential equations are solved step by step if the initial parton distributions are provided.

We use the Gehrman-Stirling set-A⁵⁾ as the input distributions given at $Q^2 = 4 \text{ GeV}^2$. We study evolution of nonsinglet, singlet, and gluon distributions from $Q^2 = 4 \text{ GeV}^2$ to $Q^2 = 200 \text{ GeV}^2$ with $N_f = 4$ and $\Lambda_{\overline{MS}} = 231 \text{ MeV}$. Numerical results depend on the step numbers, N_t and N_x . First, N_t is varied from 20 to 1000 steps with a fixed $N_x = 1000$. We find that the evolved distributions are almost the same. It means that merely $N_t = 50$ steps are enough for obtaining accurate evolution. This conclusion is expected because the scaling violation is a small logarithmic effect. Next, N_x is varied from 100 to 4000 steps with a fixed $N_t = 200$. The result is shown in Fig. 1. From this figure, we find that several hundred of x steps are necessary for obtaining good accuracy. Namely, if we choose the parameters $N_t = 200$ and $N_x = 1000$,

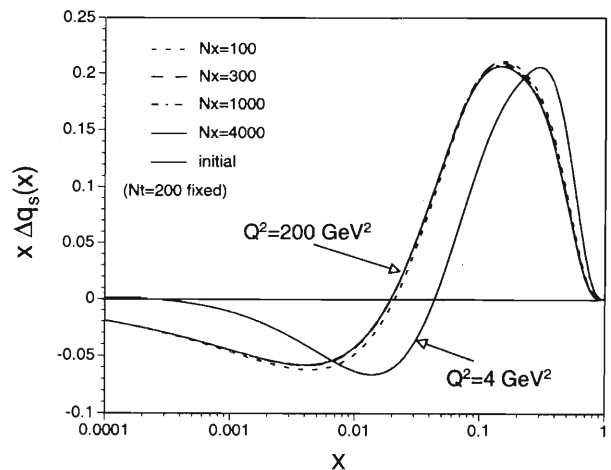


Fig. 1. N_x dependence in the $x\Delta q_s$ evolution.

the evolution results are good enough. We also analyzed evolution of the nonsinglet and gluon distributions. The obtained results show the similar accuracy.

Our numerical analysis is still in progress, particularly in comparison with scaling violation data of g_1 . However, the results indicate that an accurate solution can be obtained in the region $10^{-4} < x < 0.8$ by taking more than two-hundred t steps and more than one-thousand x steps.

References

- 1) W. Vogelsang: Phys. Rev. D **54**, 2023 (1996), RAL-TR-96-020; R. Mertig and W. L. van Neerven: Z. Phys. C **70**, 637 (1996).
- 2) M. Hirai, S. Kumano, and M. Miyama: research in progress.
- 3) R. Kobayashi, M. Konuma, and S. Kumano: Comput. Phys. Commun. **86**, 264 (1995).
- 4) M. Miyama and S. Kumano: Comput. Phys. Commun. **94**, 185 (1996).
- 5) T. Gehrman and W. J. Stirling: Phys. Rev. D **53**, 6100 (1996).

* Department of Physics, Saga University

Q^2 -Evolution of the Chiral-Odd Twist-3 Parton Distributions $h_L(x, Q^2)$ and $e(x, Q^2)$ in the Large N_c Limit

I. I. Balitsky,* V. M. Braun,** Y. Koike, and K. Tanaka

[Nucleon structure functions, Chiral-odd, Twist-3, Large N_c QCD]

The nucleon has three independent twist-3 parton distributions: $g_2(x, Q^2)$, $h_L(x, Q^2)$, and $e(x, Q^2)$ ¹⁾ which are the functions of the Bjorken variable x and large momentum squared Q^2 characterizing relevant hard processes. Here, g_2 is chiral-even while h_L and e are chiral-odd. The increasing experimental precision requires understanding of these higher twist effects induced by correlations of partons. In particular, g_2 and h_L play a distinguished role in spin physics, since they can be measured as leading effects for certain asymmetries.¹⁾

Q^2 -evolution of the twist-3 distribution is generally quite sophisticated due to mixing with quark-antiquark-gluon operators, the number of which increases with spin (moment of the distribution). For the flavor-nonsinglet part of g_2 , a crucial simplification has been pointed out in the large N_c limit of $SU(N_c)$ color to neglect $O(1/N_c^2)$ corrections:²⁾ $g_2(x, Q^2)$ obeys a simple Gribov-Lipatov-Altarelli-Parisi (GLAP) evolution equation and the corresponding anomalous dimension is known in analytic form.

In this work³⁾ we have proved that the same pattern is obeyed by chiral-odd distributions $h_L(x, Q^2)$ and $e(x, Q^2)$ and that the simplification at large N_c is of universal nature. We have obtained the renormalization group (RG) equation in the leading logarithmic approximation for the twist-3 nonlocal operators $\bar{\psi}(uz)\sigma_{\mu\xi}\Lambda g G_{\nu\xi}(tz)z_\mu z_\nu\psi(vz)$ with $\Lambda = 1$ and $i\gamma_5$; which are relevant respectively for e and h_L , and express quark-gluon correlations. Here, ψ denotes the quark field, $G_{\nu\xi}$ the gluon field strength tensor, z_μ the light-like vector ($z^2 = 0$). We have found analytic solutions of the RG equation in the limit $N_c \rightarrow \infty$, and obtained the Q^2 -evolution for the moments:

$$\mathcal{M}_n[e(Q^2)] = L^{\gamma_n^+/b} \mathcal{M}_n[e(\mu^2)] \quad (1)$$

$$\mathcal{M}_n[h_L(Q^2)] = L^{\gamma_n^-/b} \mathcal{M}_n[h_L(\mu^2)], \quad (2)$$

where the anomalous dimensions equal respectively

$$\gamma_n^\pm = 2N_c \left\{ S_n - \frac{1}{4} - \frac{1}{n+1} \left(-\frac{1}{2} \pm 1 \right) \right\}. \quad (3)$$

Here, $\mathcal{M}_n[e(Q^2)] \equiv \int_{-1}^1 dx x^n e(x, Q^2)$, $b = (11N_c - 2N_f)/3$ with N_f the number of flavors, $S_n = \sum_{j=1}^n 1/j$, and $L = \alpha_s(Q^2)/\alpha_s(\mu^2)$ with $\alpha_s(Q^2)$ the running coupling constant of QCD. The results (1)–(3) show that h_L and e both obey simple GLAP evolution equations with the corresponding anomalous dimensions given in analytic form and with no complicated operator mixing. Our results are valid to $O(1/N_c^2)$ accuracy.

One can check the above results (1)–(3) directly by using the anomalous dimension matrix which are obtained in Refs. 4 and 5 by renormalization of the twist-3 local operators. In particular, by comparing our solution of (3) with the spectrum of anomalous dimensions which is obtained by the numerical diagonalization of the mixing matrix in Refs. 4 and 5, we conclude that our solutions always correspond to operators with the *lowest* anomalous dimension in the spectrum (for more detail, see Refs. 3 and 5).

Since the $1/N_c^2$ corrections are small, our solutions solve the problem of the Q^2 -evolution of twist-3 nonsinglet parton distributions for all practical purposes, providing a powerful framework both in confronting with experimental data and in model-building. From a general point of view, our solutions are interesting as providing an example of an interacting three-particle system in which one can find an exact energy of the lowest state. For phenomenology, the main lesson is that inclusive measurements of twist-3 distributions are complete (to our accuracy) in the sense that knowledge of the distribution at one value of Q_0^2 is enough to predict it at arbitrary Q^2 , in the spirit of GLAP evolution equation.

References

- 1) R. L. Jaffe and X. Ji: Nucl. Phys. B **375**, 527 (1992).
- 2) A. Ali, V. M. Braun, and G. Hiller: Phys. Lett. B **266**, 117 (1991).
- 3) I. I. Balitsky, V. M. Braun, Y. Koike, and K. Tanaka: Phys. Rev. Lett. **77**, 3078 (1996).
- 4) Y. Koike and K. Tanaka: Phys. Rev. D **51**, 6125 (1995).
- 5) Y. Koike and N. Nishiyama: hep-ph/9609207; RIKEN Accel. Prog. Rep. **30**, 29 (1997).

* Center for Theoretical Physics, MIT, U.S.A.

** NORDITA, Denmark

Q^2 -Evolution of Chiral-Odd Twist-3 Structure Function and Fragmentation Function: $e(x, Q^2)$ and $\hat{e}(z, Q^2)$

Y. Koike and N. Nishiyama*

[Structure function, Twist-3, Chiral-odd, Large- N_c]

The nucleon has three independent twist-3 quark distributions; $g_2(x, Q^2)$, $h_L(x, Q^2)$, and $e(x, Q^2)$.¹⁾ The Q^2 -evolution of these twist-3 distributions is generally very complicated due to the mixing among quark-antiquark-gluon operators, the number of which increases with spin (the moment of the distributions). So far, the anomalous dimension matrices for $g_2(x, Q^2)$ and $h_L(x, Q^2)$ have been calculated in the one-loop level. In our recent work,²⁾ we have completed the calculation of the one-loop anomalous dimension matrix for $e(x, Q^2)$. Our method follows closely the one in³⁾ which discussed the Q^2 dependence of $h_L(x, Q^2)$. In the large- N_c limit, we have confirmed that the Q^2 evolution is solely governed by the lowest eigenvalues of the anomalous dimension matrix, as was found in⁴⁾ by a different method. Taking the n -th moment of e , the Q^2 dependence at $N_c \rightarrow \infty$ becomes

$$\mathcal{M}_n[e(Q^2)] = L^{\gamma_n^e/b} \mathcal{M}_n[e(\mu^2)]$$

$$\text{with } \gamma_n^e = 2N_c \left(S_n - \frac{1}{4} - \frac{1}{2(n+1)} \right), \quad (1)$$

where $\mathcal{M}_n[e(Q^2)] = \int_{-1}^1 dx x^n e(x, Q^2)$, $L = \alpha_s(Q^2)/\alpha_s(\mu^2)$, $b = (11/3)N_c - (2/3)N_f$ and $S_n = \sum_{j=1}^n 1/j$. This shows that $e(x, Q^2)$ evolves slightly

slower than the other two twist-3 distributions.

For phenomenological applications, the twist-3 fragmentation function $\hat{e}(z, Q^2)$ is more interesting, since it appears as a leading contribution to the pion production cross section in the transversely-polarized deep inelastic scattering from the nucleon⁵⁾: $\hat{e}(z, Q^2)$ of the pion appears with the transversity distribution, $h_1(x, Q^2)$, of the nucleon. Our present study is expected to supply useful information about the Q^2 evolution of $\hat{e}(z, Q^2)$. In particular, if the so-called Gribov-Lipatov reciprocity relation⁶⁾ holds true even for the twist-3 distribution and fragmentation functions, the problem of Q^2 dependence of $\hat{e}(z, Q^2)$ has virtually been solved.

References

- 1) R. L. Jaffe and X. Ji: Nucl. Phys. B **375**, 527 (1992).
- 2) Y. Koike and N. Nishiyama: hep-ph/9609207, Phys. Rev. D, in press.
- 3) Y. Koike and K. Tanaka: Phys. Rev. D **51**, 6125 (1995).
- 4) I. I. Balitsky, V. M. Braun, Y. Koike, and K. Tanaka: Phys. Rev. Lett. **77**, 3078 (1996).
- 5) R. L. Jaffe and X. Ji: Phys. Rev. Lett. **71**, 2547 (1993).
- 6) V. N. Gribov and L. N. Lipatov: Sov. J. Nucl. Phys. **15**, 675 (1972).

* Graduate School of Science and Technology, Niigata University

Quark Helicity Distributions Using QCD Sum Rule Approach

H. Kitagawa and T. Hatsuda

[Quark helicity, QCD sum rule]

“Spin Crisis”, raised in the 1980’s from the data of $g_1(x)$ for the proton (in the polarized lepton-proton inclusive experiment), is a problem that the quarks do not carry all of the spins of the proton. This problem has not been solved yet. Experimentally, one of the main purposes of the RHIC-SPIN project (by the polarized proton-proton collider) is to investigate the helicity of quarks and gluons in the proton. Theoretically, the spin contents of quarks are being discussed qualitatively using “effective” models of QCD. In order to compare the data, however, it is necessary to evaluate them quantitatively.

QCD sum rule is a useful tool to evaluate physical quantities. It was applied to the (spin-averaged) quark distribution functions by Kolesnichenko¹⁾ and Belyaev and Blok.²⁾ They evaluated the second moments of quark distributions:

$$M_2^{(q)} = \int x q(x) dx.$$

We have followed the method of Ref. 2 for the quark helicity distribution.

The second moment of quark appears in the response of constant external field, which is introduced by the lagrangian term, $\Delta\mathcal{L}_q = -i\bar{\psi}D_\mu\gamma_\nu\psi S^{\mu\nu}$, where ψ represents quark and $S^{\mu\nu}$ is a tensor external field. This form is determined by the operator product expansion (OPE). In the spin-polarized case, by OPE we can derive lagrangian term, $\Delta\mathcal{L}_q^{\text{pol.}} = -i\bar{\psi}D_\mu\gamma_5\gamma_\nu\psi S_{\text{pol.}}^{\mu\nu}$.

For the spin-averaged quark distributions, the second moment M_2^q can be obtained, by comparing coefficients of $p_\rho p_\lambda p^\mu \gamma_\mu S^{\rho\lambda}$ in both theoretical and phenomenological sides. After the Borel transformation, we obtain (in the leading order):

$$M_2^{(d)} + C^{(d)}M^2 = \frac{3}{20(2\pi)^4\lambda_N^2}M^6 E_2(s_0/M^2)e^{m_N^2/M^2}$$

$$M_2^{(u)} + C^{(u)}M^2 = \frac{7}{20(2\pi)^4\lambda_N^2}M^6 E_2(s_0/M^2)e^{m_N^2/M^2}.$$

Here M and m_N are the Borel mass and the nucleon mass respectively, and

$$\langle 0|\eta|N\rangle = \lambda_N v$$

$$v \otimes \bar{v} = p^\mu \gamma_\mu + m_N$$

$$E_n(x) = 1 - e^{-x} \sum_{k=0}^n \frac{x^k}{k!}$$

for η being an interpolating field of the nucleon and s_0 being the threshold of the continuum.

For the quark helicity distributions, the second moment $\Delta M_2^{(q)}$ can be obtained, by picking up terms

which contains $s_\rho p_\lambda S_{\text{pol.}}^{\rho\lambda}$ (where s_ρ is the spin of the nucleon). After the Borel transformation, we obtain (in the leading order):

$$\Delta M_2^{(d)} + \Delta C^{(d)}M^2 = -\frac{3}{10(2\pi)^4\lambda_N^2 m_N^2}M^8$$

$$\times E_3(s_0/M^2)e^{m_N^2/M^2} \quad (1)$$

$$\Delta M_2^{(u)} + \Delta C^{(u)}M^2 = \frac{2}{5(2\pi)^4\lambda_N^2 m_N^2}M^8$$

$$\times E_3(s_0/M^2)e^{m_N^2/M^2}. \quad (2)$$

Results of calculations are shown in Fig. 1. The left hand sides (l.h.s.) of the above Eqs. (1) and (2) are approximated by the straight line at $M^2 = 1.5 \text{ GeV}^2$. Extrapolation of this line into the point $M^2 = 0$ gives $\Delta M_2^{(u)} = 0.3$ and $\Delta M_2^{(d)} = -0.24$.

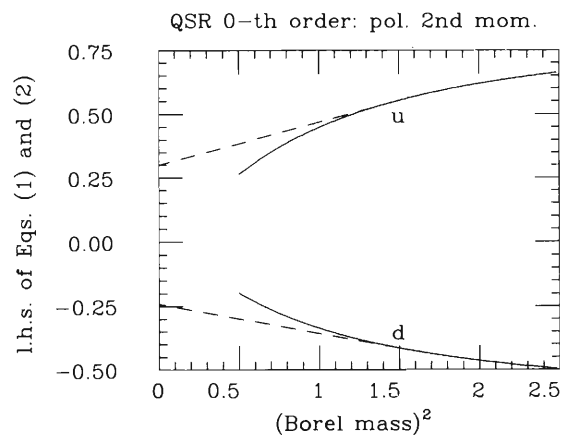


Fig. 1. The Borel mass, M , dependence of the left hand sides of Eqs. (1) and (2) denoted by u and d , respectively. The dashed lines are the extrapolation to the point $M^2 = 0$.

The first moment of quarks corresponds to the value of the spin of the nucleon, which are calculated by Balitsky and Ji³⁾ using QCD sum rule technique. On the other hand, these second moments are not measured by the inclusive reaction. They can be measured by exclusive reactions, such as RHIC-SPIN.

Further calculation including gluon corrections are now in progress.

References

- 1) A. V. Kolesnichenko: Sov. J. Nucl. Phys. **39**, 968 (1984).
- 2) V. M. Belyaev and B. Yu. Blok: Z. Phys. C **30**, 279 (1986).
- 3) X. Ji: MIT-CTP-2517 Hep-ph/9603249, Mar. 1996.

Quark Helicity in Proton by Semi-Inclusive Asymmetries of Kaons

H. Kitagawa and Y. Sakemi

[Quark helicity, Semi-inclusive]

High-energy inclusive lepton-hadron reactions have made clear the contents of the hadrons, i.e., much of knowledge on quark distributions in the proton and neutron was gained owing to perturbative QCD techniques as well as high precision data. However, as for the distributions of gluons and sea quarks, which cannot be observed directly by the inclusive processes, we have not obtained a unified view. This is the problem of the moment.

A semi-inclusive reaction, in which the scattered lepton and a produced hadron are detected simultaneously, provides many kinds of information on the target depending on the tagged hadron, and is expected to solve the above problem. The HERMES collaboration at Deutsches Elektronen-Synchrotron (DESY) is measuring the quark and gluon distributions by the semi-inclusive reaction with polarized positron beam and polarized gas targets tagging the pion and neutral kaon. Data with pions are now under analysis, and data with kaons will appear in 1997. Here we formulate relationships between the quark distributions and the observed spin asymmetries.

We follow the formulation by Gllenstern¹⁾ and Frankfurt²⁾ who investigated the pion-tagged case. We use the quark-parton model to assume factorization. Fragmentation function, $D_f^h(z)$, is assumed to be spin-independent, isospin-symmetric, and different between strange quarks and light quarks.

Negatively charged pion, π^- , is composed of d and \bar{u} quarks. For the proton target, we use a favored fragmentation function, $D(z)$, for d and \bar{u} , and an unfavored fragmentation function, $\bar{D}(z)$, for u , \bar{d} , s , and \bar{s} quarks. These fragmentation functions were obtained by fitting the e^+e^- scattering data. Combining the data with π^- and with π^+ , we obtain the spin asymmetry:

$$A_p^{\pi^+\pi^-} - \frac{g_1^p}{F_1^p} = \frac{g_1^p}{F_1^p} \kappa \left(-\frac{\Delta s}{18g_1^p} + \frac{s}{18F_1^p} \right), \quad (1)$$

where

$$\kappa = \frac{\int_{z_{min}}^1 \frac{z}{1+z} D(z) dz}{\int_{z_{min}}^1 \frac{1}{1+z} D(z) dz} \sim 0.34 \quad (2)$$

with $z_{min} = 0.2$. The distributions, s and Δs , can be derived from the above equation.

On the other hand, neutral kaon, K_0^S , contains s -quark $K_0^S = (d\bar{s} + s\bar{d})/\sqrt{2}$. Fragmentation function of s -quark is assumed to be factorized as $D_s(z) = D(z)/\lambda$, where $\lambda \sim 0.3$. Spin asymmetry for this case is

$$A_p^{K_0^S} = \frac{8\Delta u + \kappa_1\Delta d + \kappa_2\Delta s}{8u + \kappa_1d + \kappa_2s}, \quad (3)$$

where $\kappa_1 \sim 3.05$ and $\kappa_2 \sim 7.84$. Note that we can extract the distributions, s and Δs , with less ambiguity, since their coefficients are large.

Next, we estimate the spin asymmetries which will be measured by the HERMES collaboration. We use the existing parametrization for the quark distributions: CTEQ3L for the unpolarized quark distribution and Gehrmann-Stirling A(LO) for the polarized quark distribution. Results of the calculations are shown in Fig. 1. In the case of kaon tagging, we can see a significant difference from zero at $x \geq 0.1$ (x is the Bjorken scaling variable.) which corresponds to the s -quark contribution.

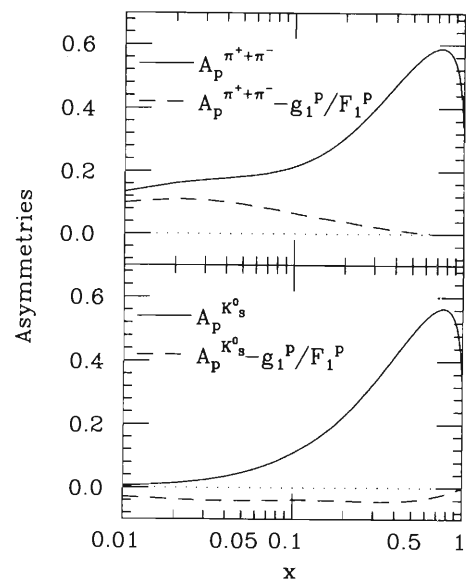


Fig. 1. Estimated spin asymmetries for the cases of pion tagging (upper figure) and kaon tagging (lower figure). The existing parametrizations for the quark distributions are used.

We can obtain much information on the hadrons from semi-inclusive reactions. This reaction contains the fragmentation processes, which have not been studied so much as the quark distributions. It is necessary to study the fragmentation functions experimentally and theoretically, in order to remove ambiguity in the semi-inclusive process.

References

- 1) St. Gllenstern et al.: Phys. Lett. B **312**, 166 (1993).
- 2) L. L. Frankfurt et al.: Phys. Lett. B **230**, 141 (1989).

Test of Δg in Spin Correlations between Target Protons and Produced Λ_c^+ at COMPASS Experiment

T. Yamanishi and T. Morii*

[Gluon, Polarized gluon, Spin structure, Charmed baryon]

Recent measurement of the spin-dependent proton structure function implies that little (only 15%) of the proton spin is carried by quarks.¹⁾ The result is far from the prediction by the naive quark/parton model. On the other hand, a spin sum rule,

$$\frac{1}{2} = \frac{1}{2}\Delta\Sigma + \Delta g + \langle L_Z \rangle_{q+g} \quad (1)$$

suggests that in addition to quarks, the gluons and orbital angular momenta of quarks and gluons contribute to the proton spin. In Eq. (1), $\Delta\Sigma$ and Δg are the amount of the proton spin carried by quarks and gluons, respectively; and $\langle L_Z \rangle_{q+g}$ denotes the orbital angular momentum of quarks and gluons. In order to understand the proton spin structure, it is very important to measure the density and behavior of spin-dependent gluon distribution in a proton for various reactions.

Here, we study a semi-inclusive production of polarized Λ_c^+ baryons from a longitudinally polarized proton, $\ell\vec{p} \rightarrow \ell'\vec{\Lambda}_c^+ X$, in order to deduce Δg in a proton. The correlation between the spin of the Λ_c^+ (produced in the target fragmentation region, $x_F < 0$) and that of the target proton is expected to be significantly affected by the polarized gluon contents, because the process can occur only via photon-gluon fusion mechanism in the lowest order as shown in Fig. 1. Since a charm is created by a gluon and has its spin parallel to the gluon spin, the direction of Λ_c^+ spin, which must preserve the charm quark spin, depends on that of gluon spin. Therefore, the spin correlation between the produced Λ_c^+ and target proton gives a good information on gluon polarizations in a proton.

In order to estimate the sensitivity of this process for Δg , we calculate a spin correlation asymmetry, A_{LL} defined as

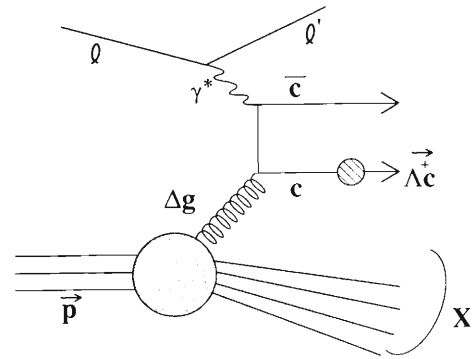


Fig. 1. The lowest order QCD diagram for the inelastic Λ_c^+ leptonproduction in unpolarized lepton-polarized proton scatterings.

$$A_{LL} = \frac{[d\sigma_{++} - d\sigma_{+-} + d\sigma_{--} - d\sigma_{-+}]}{[d\sigma_{++} + d\sigma_{+-} + d\sigma_{--} + d\sigma_{-+}]}, \quad (2)$$

where $d\sigma_{+-}$, for an instance, denotes that the spin of the target proton is positive while that of the produced Λ_c^+ is negative. Calculating the A_{LL} with various examples of Δg , we have found that the A_{LL} strongly depends on the density and behavior of Δg . It is concluded that the process considered here, $\ell\vec{p} \rightarrow \ell'\vec{\Lambda}_c^+ X$, can give a quite useful information on the behavior of gluon polarizations.

References

- 1) J. Ashman et al.: Phys. Lett. B **206**, 364 (1988); Nucl. Phys. B **328**, 1 (1989); B. Adeva et al.: Phys. Lett. B **302**, 533 (1993); Phys. Lett. B **320**, 400 (1994); P. L. Anthony et al.: Phys. Rev. Lett. **71**, 959 (1993); D. Adeva et al.: Phys. Lett. B **329**, 399 (1994); K. Abe et al.: Phys. Rev. Lett. **74**, 346 (1995).

* Faculty of Human Development and Graduate School of Science and Technology, Kobe University

RHIC Spin Project

H. En'yo, Y. Goto, K. Hatanaka, N. Hayashi, T. Ichihara, K. Imai, M. Ishihara, T. Katayama,
A. Luccio, Y. Mao, A. Masaike, Y. Nakada, M. Okamura, N. Saito, Y. Sakemi, H. Sato,
T. Shibata, Z. Sun, Y. Watanabe, H. Wu, and M. Yoso

[*pp* interaction, Structure function, Spin, Asymmetry, Polarized beam]

We are promoting the RHIC spin project.¹⁾ The main physics goals of the project are to elucidate the spin structure of proton, and to test the standard model mainly via the parity violating process, in collaboration with Brookhaven National Laboratory (BNL). The Relativistic Heavy Ion Collider (RHIC) and the PHENIX detector at BNL will provide us an opportunity of experiments taking advantages of high energy (up to 250 GeV), high luminosity ($\sim 10^{32}$ cm⁻²s⁻¹), and high polarization ($\sim 70\%$) of proton beam. The project includes not only the physics research but also the development and construction of accelerators and detectors.

The present article summarizes all the progress made for the project in this year. Detailed description of each subject is carried out in this issue separately. The preparation for physics experiments is one of the main subject of the project. First of all, it should be mentioned specifically that construction of the PHENIX detector was started during this year (Fig. 1). The photo of Fig. 1 shows the Muon arm section which RIKEN contributes much effort for its construction. The remaining Muon Magnet South (MMS) has been fabricated by Mitsubishi Electric Co. and RIKEN with

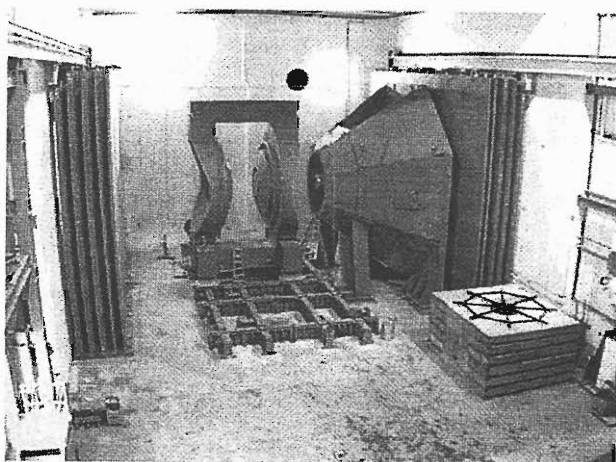


Fig. 1. A photo of the PHENIX construction at present, showing the Central Magnet, an arm of the Muon Magnet (Muon Magnet North), and a pair of iron walls for Muon Identifier (MuID).

technical supports of Lawrence Livermore National Lab. (LLNL).

The investigation of Limited Streamer Tube (LST) is proceeded, which forms the MuID with iron walls. We are testing the LSTs with the high energy (~ 2 GeV) muon and pion beams at National Lab for High Energy Phys. (KEK), and also with cosmic ray and radioactive sources. Fabrication of the LSTs will start in the next year according to the results of this test experiment at KEK.

Simulation studies are underway to establish the analysis methods as well as on-line trigger scheme. Sensitivity of the measurements of polarized parton distributions is evaluated using the results of resolution and acceptance studies. For these studies we have three coherent activities with collaboration of theorists: (1) summarize both unpolarized and polarized cross sections for various reactions expected in RHIC;²⁾ (2) evaluate the yields and statistical uncertainties; (3) develop polarized parton distributions based on the currently available experimental data. Details of the simulation studies and studies of polarized parton distributions are described in separate papers.

We, responsible for accelerator field, concentrate on accelerating polarized proton, by using the RHIC accelerator, up to 250 GeV without a depolarization. The main effort is R&D of the special superconductive magnet (so called Siberian Snake magnet) to flip the spin of the proton, which is the main component to keep the polarization of protons in the RHIC accelerator. The magnetic field calculation in three dimensions is well established, which is an indispensable technique to design the Siberian Snake magnet in an optimized form. The "Spin Tracking" is also well established, which calculates the behavior of the proton spin in the RHIC accelerator. Furthermore, a model magnet of the Siberian Snake was made, whose maximum current reached 470 A (planned maximum 420 A) which corresponds 4 T of magnetic field at the central region.

As we described above, the project is proceeding very well. We will put further effort in the coming year toward the first beam scheduled in 1999.

References

- 1) H. En'yo et al.: RIKEN Accel. Prog. Rep. **29**, 80 (1996).
- 2) R. L. Jaffe and N. Saito: Phys. Lett. B **382**, 165 (1996).

Spin Physics with PHENIX Detector System at RHIC

H. En'yo, Y. Goto, N. Hayashi, T. Ichihara, K. Imai, Y. Mao, A. Masaïke, Y. Nakada,
N. Saito, Y. Sakemi, T. Shibata, Y. Watanabe, M. Yosoi, and M. Ishihara

[pp interaction, Structure function, Spin, Asymmetry, Polarized beam]

We are studying the spin physics possible with the PHENIX detector system at Relativistic Heavy Ion Collider (RHIC) in Brookhaven National Laboratory.¹⁾ Here we report the results of our recent studies on prospective measurements of the gluon helicity distribution ΔG and of the anti-quark helicity distribution $\Delta\bar{q}$. Measurements of these two distributions are crucial for understanding the spin structure of nucleon.

One of the promising methods to determine ΔG is to measure the asymmetry for the production of a prompt photon (γ) with the high transverse momentum p_T . In proton-proton (pp) collisions at the energy of RHIC, about 90% of the photon production comes from the quark-gluon Compton scattering process ($q + g \rightarrow q + \gamma$), and the rest originates from the quark annihilation process ($q + \bar{q} \rightarrow g + \gamma$). We define a double longitudinal-spin asymmetry as $A_{LL} = \frac{\sigma(++) - \sigma(+-)}{\sigma(++) + \sigma(+-)}$, where σ represents the photon production cross section and the signs indicate the helicity states of two colliding protons. Since the quark-gluon Compton process dominates in the production of a high p_T photon, the asymmetry is dominantly governed by that process. The asymmetry for the Compton process is given by $A_{LL} = \frac{\Delta q}{q} \cdot \frac{\Delta G}{G} a_{LL}$, where a_{LL} is an asymmetry in partonic level and is calculable; q and G are the unpolarized quark and gluon distribution functions, respectively; $\frac{\Delta q}{q}$ is fixed by other experiments; and G is determined from an unpolarized cross section of the photon production. Thus, one can extract ΔG by measuring A_{LL} . We have estimated the yield of prompt photons by using a QCD event generator named *PYTHIA*²⁾ in a wide p_T range assuming the integrated luminosities 320 and 800 pb⁻¹ for the colliding energy $\sqrt{s} = 200$ and 500 GeV, respectively. From this study we have confirmed a correlation between probed Bjorken's x of gluon and p_T of photon, which allows us to study the x dependence of ΔG . Expected errors on $\frac{\Delta G}{G}$ were calculated from the photon yield and A_{LL} formula, which are indicated by error bars in Fig. 1 together with the preliminary results of the J/ψ production process. It is shown clearly that a very precise measurement can be made around $x \sim 0.1$ where a recent theoretical model depicts a maximum in the magnitude of $\frac{\Delta G}{G}$.

$\Delta\bar{q}$ can be determined from the single longitudinal-spin asymmetry $A_L = \frac{\sigma(+)-\sigma(-)}{\sigma(+)+\sigma(-)}$ for production of a weak boson, W^\pm . Here $\sigma(+)$ stands for the cross section for a W production in collision of the unpolarized proton and the proton with positive helicity, and $\sigma(-)$ denotes the same as $\sigma(+)$ but with negative helicity. Since the W^+ is produced dominantly by $u\bar{d} \rightarrow W^+$, the asymmetry for its production $A_L(W^+)$ is sensitive to both Δu and $\Delta\bar{d}$. Similarly, $A_L(W^-)$ is sensitive to Δd and $\Delta\bar{u}$. As in the case of ΔG , we have evaluated the statistical error of our measurements of

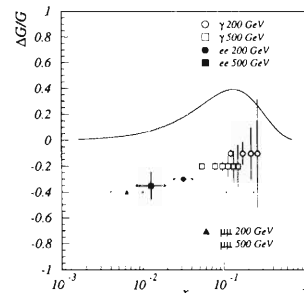


Fig. 1. Prospective measurements of the $\frac{\Delta G}{G}$ calculated from prompt photon and J/ψ ($ee, \mu\mu$) yield.

the $\frac{\Delta\bar{q}}{q}$ and $\frac{\Delta q}{q}$ which were calculated from the boson yield estimated by *PYTHIA*. The results are plotted in Fig. 2. Curves in the figure show theoretical predictions performed separately on $\frac{\Delta\bar{q}}{q}$ and $\frac{\Delta q}{q}$ for different flavors of two independent groups. The filled and open circles show the points to be determined from productions of W^+ and W^- , respectively. Obviously, we can select one of the models from our measurements.

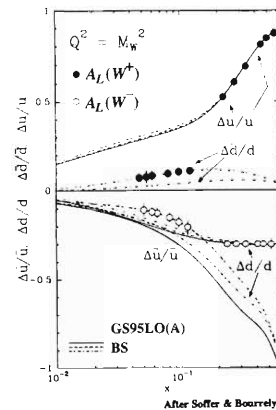


Fig. 2. Flavor decomposition of the quark and anti-quark polarizations for a W production.

In summary, we have estimated the yields for pp reactions, from which we could determine the helicity distributions of gluon and of anti-quark in the proton. The statistical error on the measurement of $\frac{\Delta G}{G}$ will be in between 0.01 to 0.1 at $0.05 < x < 0.20$. $\frac{\Delta\bar{q}}{q}$ can be determined with the statistical error of 0.02 to 0.05 at $0.05 < x < 0.10$.

References

- 1) H. En'yo et al.: RIKEN Accel. Prog. Rep. **29**, 80 (1996).
- 2) T. Sjöstrand: Comput. Phys. Commun. **82**, 74 (1994).

Study of Polarized Parton Distribution Functions in the Nucleon

Y. Goto, N. Hayashi, M. Hirai, S. Kumano, M. Miyama, T. Morii,
N. Saito, T. Shibata, and T. Yamanishi

[Polarization, Structure functions, Spin structure, Nucleon]

In 1995, RIKEN started the RHIC-spin project in collaboration with Brookhaven National Laboratory (BNL). The main goal of the project is to elucidate the spin structure of the nucleon. The Relativistic Heavy Ion Collider (RHIC), which is designed to give a luminosity of $2 \times 10^{32} \text{ cm}^{-2} \text{ sec}^{-1}$, an energy of $\sqrt{s} = 50\text{--}500 \text{ GeV}$, and a proton beam polarization of about 70% for polarized pp collisions, is under construction at BNL. To meet the goal of planned experiments and to propose crucial measurements to constrain the spin structure of the nucleon, a working group on the polarized parton distribution functions (pol-pdf's) was formed.

The spin structure of the nucleon has been studied in polarized lepton scattering off the polarized nucleon target (pol-DIS). As revealed in the “*proton spin crisis*”, our understanding of the spin structure is not sufficient yet. In particular, the gluon polarization, sea-quark polarization, and flavor decomposition are not tightly constrained by the pol-DIS experiments.

On the other hand, the experiments on the spin structure are entering to new stages:

- further precision measurement in inclusive pol-DIS,
- semi-inclusive pol-DIS, and
- polarized proton-proton collision.

The goals of these experiments are to determine:

- gluon polarization,
- sea-quark polarization, and
- flavor decomposition.

The working group is composed of three subgroups with respective subject:

- data analysis group,
to summarize the current experimental and theoretical knowledges on the spin structure
- parametrization group,
to develop the best polarized parton distribution functions (pol-pdf) which fit well to all available experimental data including new one

- Q^2 -evolution group,
to develop computer programs on the pol-pdf up to any Q^2 with the splitting functions to include next-to-leading-order α_s corrections.

The first stage of the program is in progress.

As the second stage, we would like to suggest crucial measurements for pol-pdf. Based on the results obtained from these subgroups, we will study the processes sensitive to the polarized strange quarks and gluons, and predict the physics for di-muon productions in the final state, prompt photon productions, heavy flavor productions, weak boson productions, etc. at the RHIC energies.

We are opening the home page on WWW for virtual conference at the address,
<http://www.rarf.riken.go.jp/rarf/rhic/theory/>.

We are grateful to Prof. T. Hatsuda, Dr. H. Kitagawa, Dr. K. Tanaka, Dr. S. Ohta, and Prof. Y. Koike for useful discussions.

Working Group on Polarized Parton Distribution Functions (Pol-PDF)

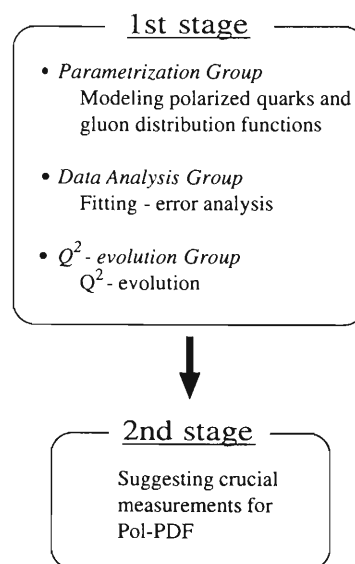


Fig. 1. Flow chart of the program of our working group. The first stage is in progress.

R&D of Iarocci Tube for RHIC Spin Project

Y. Mao, Y. Nakada, H. En'yo, K. Imai, N. Saito, N. Hayashi,
Y. Watanabe, Y. Goto, T. Ichihara, and M. Ishihara

[Iarocci tube, Working mode, Time spread]

A clean identification of muon is a key issue for RHIC spin project. The production of weak bosons W , which is sensitive to the anti-quark contents of the proton, can be identified by the detection of high transverse momentum muons. The production of heavy quark system, which is sensitive to the gluon contents of the proton, can be tagged with the detection of dimuon in the proper mass range.

To meet the goal of the experiments, the muonID in PHENIX detector system should have the following characteristics: (i) time resolution ≤ 100 ns, (ii) stability in detection efficiency, and (iii) low cost to cover a wide area. Iarocci tube¹⁾ has been selected as a candidate for such detector. As a part of PHENIX' muonID R&D, we have investigated the Iarocci tube's plateau range and time response in different conditions to specify its operation mode and operation gas. In addition, we have compared performance of the tubes from Italy and from China; both of them are candidates for mass production in future.

Figure 1 shows a cross-sectional view of two Iarocci tubes which mainly comprise three parts: a 8-cell comb extrusion with the inner wall painted by graphite, an outer jacket and a set of silver-plated Cu-Be wires of 100 μm diameter. Iarocci tubes can be operated in either streamer mode or proportional mode. It is one of urgent issues to select one mode out of two. By using a mixture of $\text{Ar}:\text{C}_4\text{H}_{10} = 1:3$ ($\text{Ar}-\text{C}_4\text{H}_{10}$, hereafter) as the working gas, we measured the pulse height spectra of cosmic ray and ^{90}Sr radioactive source under the HV from 3.9 to 5.0 kV. The transition from the proportional to streamer modes has been clearly observed at about 4.5 kV. An comparison of streamer mode with proportional mode has been made as described below. Although the plateau range, detection efficiency and time spread of the proportional mode are similar to those of the streamer mode, the pulse height is quite different in two modes. Since the average pulse height of streamer mode is over 10 times larger than that of proportional mode, we may be able to use a low-gain pre-amplifier to reduce the cost. In addition, a larger signal output allows a higher discrimination level. Consequently, a higher noise level is acceptable.

In operation, a streamer occurs when electrons drift close to the anode wire after the primary ionization. The drift time depends on the position where the primary ionization occurred in a cell. Therefore, there exists a time uncertainty or time spread. We investigated the time spread with cosmic ray and ^{90}Sr source by a triple coincidence setup which consisted of two

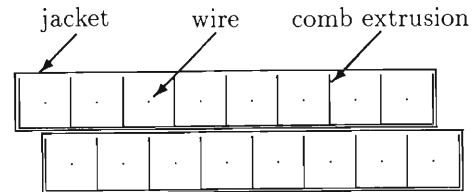


Fig. 1. The cross-section of two Iarocci tubes.

scintillation detectors one above and another below the tube. The FWHM of time spread was about 75 ns for $\text{Ar}-\text{C}_4\text{H}_{10}$, and was 40 ns for $\text{CF}_4:\text{C}_4\text{H}_{10} = 1:1$.

Using the same method, we also measured the time spread for two tubes shifted each other by half-cell (as shown in Fig. 1). The result confirmed that the time spread decreased to about 40 ns for $\text{Ar}-\text{C}_4\text{H}_{10}$, which is half of that for a single layer tube. Namely, when two tubes are layered and shifted by half-cell, one can meet the requirement (< 100 ns) of PHENIX trigger system.

To compare Chinese tubes with Italian ones, we first made a quality index (Table 1) to define a better tube. We started the evaluation work from comparing Italian tubes and Chinese assembled ones. The result showed that Chinese tubes are as stable as Italian ones after we examined all items listed above.²⁾ We are going to receive 80 of genuine Chinese made tubes for further comparison.

Table 1. Quality index of Iarocci tube.

Pressure drop	< 1 mbar after 10 min. at 30 mbar over-pressure.
Current leakage	$< 1 \mu\text{A}$ without a source
HV tolerance	> 5.0 kV with $\text{Ar}-\text{C}_4\text{H}_{10}$
Plateau range	> 400 V beyond about 4.5 kV

Based on our R&D work, we suggest that Iarocci tubes are to be operated in the streamer mode for PHENIX muonID for a better noise tolerance and there is no need to use CF_4 since the time spread already met the requirement when two tubes were layered and shifted by half-cell. In order to evaluate the muon identifier system as a whole, especially in muon detection efficiency and pion rejection rate, we are going to perform test experiment at KEK.

References

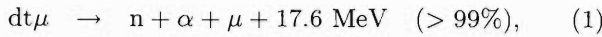
- 1) E. Iarocci: Nucl. Instrum. Methods Phys. Res. A **217**, 30 (1983).
- 2) Y. Nakada and Y. Mao: Report of MuonID Chamber R&D at Kyoto, PHENIX-muon-96-11, Aug. 1996.

Measurement of Neutrons from Muon Catalyzed dt Fusion Reaction at RIKEN-RAL Muon Facility

N. Kawamura, S. N. Nakamura, K. Nagamine, T. Matsuzaki, K. Ishida, S. Sakamoto, M. Tanase, M. Kato, K. Kurosawa, K. Kudo,* N. Takeda,* and G. H. Eaton**

[Muon catalyzed fusion, Fusion produced neutron]

In this article, we report on the muon catalyzed fusion (μ CF) produced neutron detection system at the RIKEN-RAL Muon Facility. For each dt- μ CF cycle, one 14.1 MeV neutron is created via the following reactions:



The muon cycle rate (λ_c) and the muon loss probability per cycle (W), which is mainly caused by the reaction (2), were deduced from the neutron yield (Y_n) and the decreasing time constant of neutron yield (λ_n). These values are associated each other as follows:

$$\lambda_n = \lambda_0 + W\phi\lambda_c, \quad (3)$$

$$Y_n = \int \phi\lambda_c \exp(-\lambda_n t) dt = \frac{\phi\lambda_c}{\lambda_n}, \quad (4)$$

where $\lambda_0 = 0.455 \times 10^6 \text{ s}^{-1}$ is the muon free decay rate, and ϕ is the DT-target density.

In our setup two neutron counters, that have been calibrated by the standard neutron source at the ETL-Tsukuba, were placed 82 cm away from the DT-target along the μ^- beam axis (Fig. 1). The neutron events via μ CF cycle were separated from γ -ray events and from pile-up events by signal processing. We determine λ_n and the total neutron number due to μ CF, which is the product of Y_n and the μ^- stopping number in the target, from the neutron spectra.

Preliminary analysis on 28% tritium (T) concentrated pure DT-system shows:

$$\lambda_n = 1.262(6) \times 10^6 \text{ s}^{-1} : \text{Liquid (20K)}, \quad (5)$$

$$= 1.414(6) \times 10^6 \text{ s}^{-1} : \text{Solid (15K)}. \quad (6)$$

According to Eq. (3), the above-obtained difference of λ_n between the liquid and solid targets comes from the

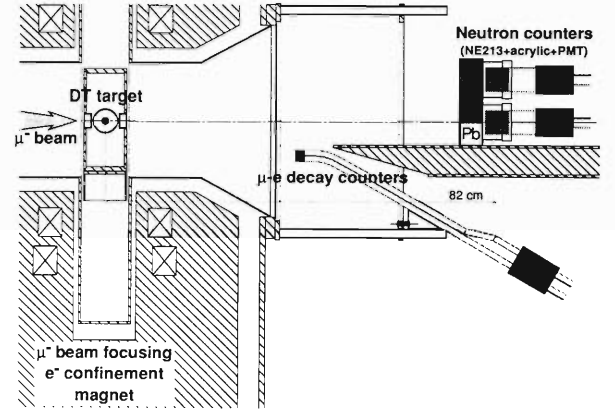


Fig. 1. The cross-sectional view of the neutron detection system along the beam axis. The μ^- beam injected from the left is focused on the DT-target under 2.4 T magnetic field. Two neutron counters were placed 82 cm down-stream from the DT-target. In front of the neutron counters, 5 cm thick lead blocks were placed, so that μ -e decay electrons do not enter the neutron counters.

difference in the target density ($\phi_{\text{solid}}/\phi_{\text{liquid}} = 1.14$), and λ_c and W do not depend on the DT-system phases. However, only in the solid phase target we observed the increases of λ_n as a function of the time after the solidification. This was not possible to observe in the liquid phase target. We consider that this effect is due to the accumulation of the ^3He decayed from tritium, which can not diffuse nor go out from the solid DT-system. If once a μ^- transfers from $d\mu$ or $t\mu$ to this residual ^3He , in which binding energy of μ^- is about four times deeper than those of the hydrogen isotopes, such a μ^- can not contribute to the μ CF cycle, and as a result λ_n increases.

* Electrotechnical Laboratory

** Rutherford-Appleton Laboratory, U.K.

Muon Transfer in Excited States of Muonic Hydrogen Atoms Observed with X-ray Measurement

S. Sakamoto, K. Nagamine, and K. Ishida

[Exotic atom, Muonic hydrogen X ray, Muon transfer]

The muon transfer between hydrogen isotopes [e.g., $(p\mu) + d \rightarrow (d\mu) + p$] is one of the vital processes in the muon catalyzed fusion (μCF). Muons may transfer from the excited states of muonic hydrogen atoms. The population of the muonic hydrogen atoms in the ground state is, therefore, different from the composition of the hydrogen isotopes. The parameter q_{1s} ,¹⁾ defined by the probability of a muonic atom with lighter nucleus to reach its ground state after its initial formation, has been introduced to express this muon transfer rate relative to the atomic cascade rate. Although theoretical studies²⁾ predicted low q_{1s} , the first indirect measurements³⁾ for a d - t mixture have reported rather high q_{1s} values.

The fraction of the non-radiative transition to the ground state is negligibly small⁴⁾ in gaseous hydrogen. The number of muonic hydrogen atoms that reach the ground state can be estimated by observing Lyman X-rays from muonic hydrogen atoms (1.9 ~ 2.7 keV). The most crucial point is to detect and resolve X-rays from different muonic hydrogen isotopes, whose energy separation is only ~ 0.1 keV. A lithium-drifted silicon detector (Si(Li)) adopted for our experiment was managed to achieve the energy resolution of 112 eV at the energy around 2 keV.

The experiment has been initiated at the Port-3 of RIKEN's Pulsed Muon Facility at the Rutherford Appleton Laboratory (RAL). A gas target chamber of 1.5 liter capacity was filled with protium gas, deuterium gas, or their mixture. The gas density ϕ was 0.01 of liquid hydrogen density (LHD) when the chamber was cooled down to ~ 80 K. The first experimental run was successfully carried out in September, 1996. Figure 1 shows X-ray energy spectra in a prompt time interval. Peaks of the K_α , K_β , and K_γ X-rays originated from muonic hydrogen atoms are clearly seen in pure protium and pure deuterium spectra. By referring these spectra for the exact energies and widths of peaks, the peaks of X-rays from different muonic hydrogen isotopes are easily resolvable in the spectra of the mixtures of protium and deuterium.

Our previous result,⁵⁾ along with a similar experiment⁶⁾ at Paul Scherrer Institute (PSI), has suggested a high q_{1s} when the deuteron concentration $C_d \leq 0.5$. There are some theoretical and experimental suggestions that muonic hydrogen atoms may have a rather high kinetic energy (~ 1 eV) during their atomic cascade process, which might explain this discrepancy

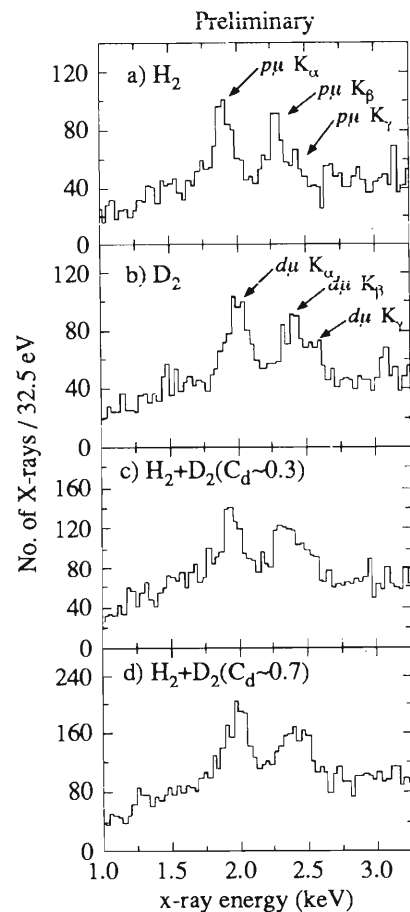


Fig. 1. Energy spectra of prompt X-rays ($\phi = 0.01$ LHD). The events detected within 100 nsec of each muon beam pulse were selected.

between measured and predicted q_{1s} 's. The analysis is now in progress and the second run is scheduled in February, 1997 for more systematic measurements.

References

- 1) C. Petijean: Nucl. Phys. A **543**, 79 (1992).
- 2) A. V. Kravtsov: Phys. Lett. A **132**, 124 (1988).
- 3) S. E. Jones et al.: Phys. Rev. Lett. **56**, 588 (1986).
- 4) E. C. Aschenauer and V. E. Markushin: to be published in Hyperfine Interact.
- 5) S. Sakamoto and K. Nagamine: to be published in Hyperfine Interact.
- 6) B. Lauss et al.: Phys. Rev. Lett. **76**, 4693 (1996).

Measurement of X-rays from α -Sticking in Muon Catalyzed dt Fusion Reaction at RIKEN-RAL Muon Facility

K. Ishida, K. Nagamine, T. Matsuzaki, S. N. Nakamura, N. Kawamura, S. Sakamoto, M. Tanase, M. Kato, K. Kurosawa, and G. H. Eaton*

[Muon catalyzed fusion, Muonic X-ray]

Direct knowledge of the muon to alpha sticking probability (ω_s) in the Muon-Catalyzed Fusion (μ CF) is one of the most important observable in all the μ CF studies, since the ω_s draws a stringent upper limit on the energy-production capability from the μ CF reaction. The ω_s can be determined directly by measuring the characteristic muonic X-ray from the recoiling $(\mu\alpha)^+$ ions. The 8.2 keV K_α X-ray with a Doppler broadening of around 0.5 keV is expected to be observed. A serious difficulty in this X-ray measurement in a high density and high tritium fraction D-T mixture is a huge radiation background of bremsstrahlung up to 17 keV from the tritium decay in a D-T mixture. With a strong pulsed muon beam, the X-ray detection system needs to be operational only during the presence of muon pulse, so that the signal to noise ratio is drastically increased. This type of μ CF experiment was initiated at the Meson Science Laboratory, University of Tokyo, located at the National Laboratory for High Energy Physics (UTMSL/KEK).¹⁾

At the RIKEN-RAL Muon Facility recently completed,²⁾ an advanced experiment was performed with the strongest pulsed muon beam and using the tritium handling system which can remove the ^3He impurity produced from tritium decay.³⁾ A backward negative muon with a double pulsed structure (each 70 ns in duration with a 320 ns separation and 50 Hz repetition frequency) was introduced into the liquid $\text{D}_{0.72}\text{T}_{0.28}$ target.

The typical energy spectrum is shown in Fig. 1, which was measured by a Si(Li) detector placed 12.4 cm away from the target. A clear Doppler broadened K_α peak is seen at 8.2 keV. The disappearance rate of the K_α peak was found to be consistent with that of neutrons.⁴⁾ Also, the K_β/K_α ratio was preliminary obtained to be 0.076 ± 0.027 . Further measurements are planned to determine this ratio more precisely.

Through calibration works of the X-ray detection

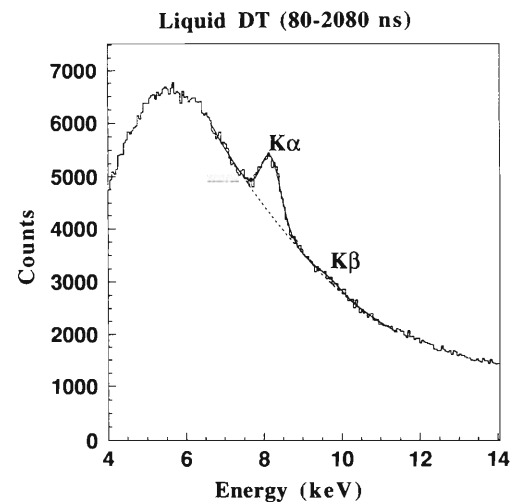


Fig. 1. Energy Spectrum of the observed delayed part of the X-ray from muon catalyzed fusion in liquid $\text{D}_{0.72}\text{T}_{0.28}$. The time range is from 80 ns to 2080 ns after the second muon beam pulse.

system, the number of occurrence X-ray emission was obtained to be around 0.32 ± 0.03 per muon stopped in the target. A detailed analysis of fusion neutron data is now under progress to deduce the value of sticking probability.

References

- 1) K. Nagamine, T. Matsuzaki, K. Ishida et al.: Muon Catalyzed Fusion **5**, 1239 (1990); Hyperfine Interact. **82**, 343 (1993).
- 2) K. Nagamine, T. Matsuzaki, K. Ishida, I. Watanabe et al.: Hyperfine Interact. **85**, 1091 (1994).
- 3) T. Matsuzaki et al.: RIKEN Accel. Prog. Rep. **30**, 151 (1997).
- 4) N. Kawamura et al.: RIKEN Accel. Prog. Rep. **30**, 37 (1997).

* Rutherford Appleton Laboratory, Chilton, DIDCOT, Oxon, U.K.

Experimental Study of CSB Force in N-d Scatterings at 12 MeV

N. Nishimori, K. Sagara, T. Fujita, H. Akiyoshi, F. Wakamatsu, K. Maeda, H. Nakamura, and T. Nakashima*

[NUCLEAR REACTION: $D(\bar{n},n)D$, Polarized-neutron beam, $E_n = 12$ MeV; Charge symmetry breaking]

Angular distribution of analyzing power $A_y(\theta)$ of $D(\bar{n},n)$ scattering at $E_n = 12$ MeV was measured in the CM angular range from 59.8° to 146.5° to study the charge symmetry breaking (CSB) in the P-state nucleon-nucleon (NN) interaction. The experimental method and the preliminary result have been described elsewhere.¹⁾ The statistical accuracy of the $A_y(\theta)$ was about 1.5% around the A_y maximum. The systematic uncertainty of the $A_y(\theta)$ is the sum of the uncertainty of the \bar{n} -beam polarization plus the other systematic uncertainty in the $D(\bar{n},n)$ experiment. To determine the \bar{n} -beam polarization uncertainty, we made a separate experiment on the polarization transfer coefficient $K_y^{y'}(0^\circ)$ of the $D(\bar{d},\bar{n})$ reaction by which a polarized neutron (\bar{n}) beam was produced. The systematic uncertainty of the present $A_y(\theta)$ was estimated to be 1.0%, and the most accurate \bar{n} -d data of $A_y(\theta)$ was obtained.

We compared our data with Triangle University National Laboratory (TUNL) data.²⁾ Though the global structure of the angular distribution was nearly the same, a small difference was found around the peak of A_y . The difference was $1.9 \pm 3.6\%$ at the A_y peak. The difference was mainly attributed to the difference of $3.9 \pm 1.0\%$ between the adopted values for the $K_y^{y'}(0^\circ)$ of the $D(\bar{d},\bar{n})$ reaction. The $K_y^{y'}(0^\circ)$ value adopted in the TUNL experiment³⁾ was obtained using one set of the n - ^4He phase shifts, whereas the value adopted in the present experiment was determined absolutely without using the phase shifts.

In Fig. 1 we compared the present \bar{n} -d data of $A_y(\theta)$ with the \bar{p} -d data of $A_y(\theta)$ measured at the same energy.⁴⁾ A distinct difference was found in the angular distribution. The \bar{n} -d $A_y(\theta)$ is smaller than the

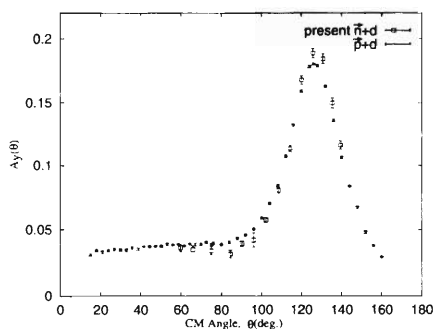


Fig. 1. $A_y(\theta)$ of N-d scattering at 12 MeV. The squares are the present \bar{n} -d data. The crosses are \bar{p} -d data obtained at Kyushu University Tandem Laboratory (KUTL).

\bar{p} -d $A_y(\theta)$ in the CM angular range from 60° to 110° , and is larger in the CM angular range above 110° . If the incident proton energy in the p -d scattering is assumed to decrease by 0.64 MeV due to the Coulomb barrier, the angular dependence of $\Delta A_{Nd}(\theta)$ is considerably well explained. At present we can not extract any quantitative conclusion from the energy shift.

We extracted the difference in the A_y maxima between \bar{n} -d and \bar{p} -d scatterings (ΔA_{Nd}) to study CSB of N-N interaction, because it was considered that the A_y has a large value of about 0.19 at the peak and seems to be sensitive to a possible small change in N-N forces such as caused by CSB. We obtained ΔA_{Nd} value of 0.0083 ± 0.0028 at 12 MeV, which was slightly smaller than that derived from the TUNL data as shown in Fig. 2. This small value of ΔA_{Nd} is still higher than that by the approximate Coulomb calculation.⁵⁾

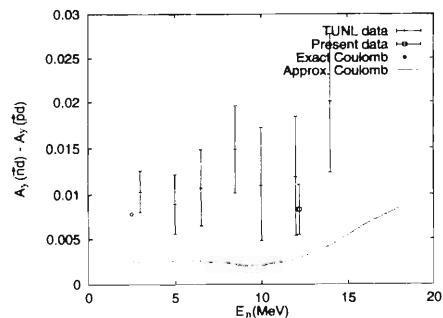


Fig. 2. Energy dependence of $A_y(\theta)$ difference between \bar{n} -d and \bar{p} -d scatterings at their peaks. The experimental TUNL data are marked by + symbols. The square is the present data. The diamond shows an exact Coulomb calculation.⁶⁾ The dotted line indicates an approximate Coulomb calculation.

It is necessary to evaluate the contribution of Coulomb force on ΔA_{Nd} in order to draw a conclusion on CSB of N-N interaction from the present experiment. If the energy shift by Coulomb force can be explained by an exact Coulomb calculation at 12 MeV, some conclusion may be possible to be drawn.

References

- 1) N. Nishimori et al.: RIKEN Accel. Prog. Rep. **29**, 58 (1996).
- 2) C. R. Howell et al.: Few Body Systems **2**, 19 (1987).
- 3) P. W. Lisowski et al.: Nucl. Phys. A **242**, 298 (1975).
- 4) K. Sagara et al.: Phys. Rev. C **50**, 576 (1994).
- 5) T. Takemiya: Prog. Theor. Phys. **86**, 975 (1991).
- 6) G. H. Berthold et al.: Phys. Rev. C **41**, 1365 (1990).

* Department of Physics, Kyushu University

Cross Sections of αxn Channels in the $^{40}\text{Ar} + ^{209}\text{Bi}$ Reaction

Y. Pu, K. Morita, T. Nomura, Y. Tagaya, T. Uchibori, T. Minemura, M. Kurokawa,
T. Motobayashi, M. G. Hies, T. Ariga, A. Yoshida, and K. Sueki

[Nuclear reaction, α -decay, $^{209}\text{Bi} (^{40}\text{Ar}, \alpha xn) ^{245-x}\text{Es}$, $E_{\text{lab}} = 207 \text{ MeV}$]

In an effort to search for a more effective method for the synthesis of super heavy elements, an experiment was performed to measure the cross sections of αxn channels in the reaction of $^{40}\text{Ar} + ^{209}\text{Bi}$. Even though a similar measurement was carried out by Nomura et al. a few years ago,¹⁾ the present experiment was done with an improved focal-plane detector, where a 2D position sensitive detector (PSD) was used to measure both the single α -decays as well as the possible correlations of subsequent decays. From this experiment, a more decisive conclusion is expected regarding the prospect of using αxn channels as an alternative tool for the production of super-heavy elements through heavy ion reactions.

A pulsed ^{40}Ar beam with energy of 7.6 MeV/nucleon from the RIKEN Ring Cyclotron was passed through a thin aluminum-foil energy degrader to bombard a 0.8 mg/cm^2 ^{209}Bi target. The bombarding energy at the center of the target was adjusted to be 207 MeV to optimize the production of $\alpha 2n$ channels. The key point is to compare the production cross section of αxn channels with that of xn channels. The evaporation residues were separated from the beam and the other reaction products by using the gas-filled isotope separator (GARIS)²⁾ at the cyclotron lab. The primary beam was pulsed typically with a sequence of 1 sec on and 2 sec off mode in order to achieve a good separation between the long-lived evaporation residues of interest and some short-lived transfer products when their α -decay energies are close. The average beam current on the target was around 30 pA during a period of 4.5 days.

The result of the beam-off alpha spectrum obtained in the present experiment is shown in Fig. 1(a), and the same beam-off alpha spectrum but measured 0.9 sec after the beam was switched off is in Fig. 1(b) over the same alpha decay energy region. In Fig. 1(a), about 21 counts of alpha decays which are assigned to be transfer product of $^{212\text{m}}\text{At}$ are clearly seen, while in Fig. 1(b), only a few events located around 7855–7895 keV survived. Due to the short life time of $^{212\text{m}}\text{At}$, only an average of 0.1 events of $^{212\text{m}}\text{At}$ decay could remain in the delayed spectrum. Because the energies of these events are very close to the $E\alpha$ of ^{242}Es or ^{243}Es , the

4 events in Fig. 1(b) are most likely originated from the alpha decay of ^{242}Es or ^{243}Es isotopes produced through the $^{209}\text{Bi}(^{40}\text{Ar}, \alpha 2n)$ or $^{209}\text{Bi}(^{40}\text{Ar}, \alpha 3n)$ reactions. From a preliminary correlation analysis of the present data, we obtained a cross section of approximately 200 pb for the xn channels and obtained an approximate cross section of 10 nb for the αxn channels. The former value is consistent with the 4 n cross section in the same reaction reported in Ref. 3 and the later values confirmed the previous result reported by Nomura et al. in Ref. 1. A more complete analysis of the data is under way.

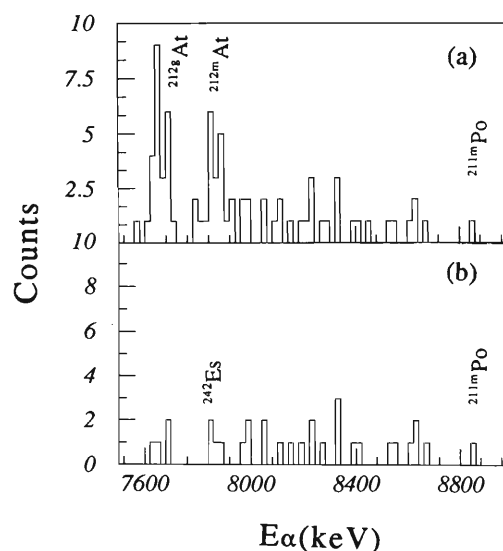


Fig. 1. The α -decay energy spectrum measured in the reaction $^{40}\text{Ar} + ^{209}\text{Bi}$, at $E_{\text{lab}} = 207 \text{ MeV}$ (a) during the beam-off period and (b) 0.9 sec after switch-off of the beam.

References

- 1) T. Nomura et al.: RIKEN Accel. Prog. Rep. **24**, 25 (1990).
- 2) K. Morita et al.: Nucl. Instrum. Methods Phys. Res. B **70**, 220 (1992).
- 3) S. Hofmann: Proc. Tours Symp. on Nucl. Phys. II, Aug. 30–Sept. 2, p. 362 (1994).

High-Spin States in ^{146}Eu

E. Ideguchi, Y. Gono, S. Mitarai, T. Morikawa, A. Odahara, M. Kidera, M. Shibata, H. Tsuchida,
T. Kishida, X. Zhou, M. Oshima, Y. Hatsukawa, S. Hamada,* H. Iimura,*
T. Ishii,* and M. Ishihara

[NUCLEAR REACTION: $^{140}\text{Ce}(^{10}\text{B},4n)^{146}\text{Eu}, E(^{10}\text{B}) = 50 \text{ MeV};$
 $^{139}\text{La}(^{13}\text{C},5n)^{146}\text{Eu}, E(^{13}\text{C}) = 98 \text{ MeV}; \gamma\text{-}\gamma \text{ coincidence measurement}$]

In the $N = 83$ isotones high-spin isomers have been found systematically, i.e., ^{144}Pm ,¹⁾ ^{145}Sm ,²⁾ ^{146}Eu ,³⁾ ^{147}Gd ⁴⁾ and ^{148}Tb .⁵⁾ Among them the half-life of the high-spin isomer in ^{146}Eu is much shorter than those of the adjacent isotones, ^{145}Sm and ^{147}Gd , although the excitation energies of these three isomers are similar, $\sim 8.5 \text{ MeV}$. This large deviation of half-life from the systematics suggests a different origin in the isomerism or an abrupt change of the level structure at high-spin states in ^{146}Eu .

On the other hand, isomers with the spin of $27/2$ are also found in the $N = 83$ odd isotones systematically. The excitation energies of the states decrease gradually with increase of the mass number. The parities of these states, however, change suddenly from positive to negative between ^{145}Sm ⁶⁾ and ^{147}Gd .⁴⁾ This trend also appears in the spin 10 states of $N = 82$ doubly-even isotones between ^{144}Sm ⁷⁾ and ^{146}Gd .⁸⁾ Since ^{146}Eu is located in the middle of ^{145}Sm and ^{147}Gd , it is meaningful to study the level structure of ^{146}Eu in order to understand the reason why the change of parity in $27/2$ state happened. The spins and parities of corresponding states in ^{146}Eu are estimated to be 16^- or 15^+ by coupling 1 proton hole to the $27/2^-$ state in ^{147}Gd or 1 proton to the $27/2^+$ state in ^{145}Sm , respectively.

Although the level scheme of ^{146}Eu was reported previously⁹⁾ up to the excitation energy of 3.5 MeV, the 15^+ state was only tentatively assigned and the 16^- state was not found yet. The existence of 10 ns isomer at $\sim 8.5 \text{ MeV}$ was also reported,³⁾ but the decay scheme from the high-spin isomer was not established well.

In order to clarify the low lying states in ^{146}Eu , an in-beam γ -ray measurement was made by using $^{140}\text{Ce}(^{10}\text{B},4n)^{146}\text{Eu}$ reaction at the tandem laboratory of Kyushu University. The ^{10}B beam with energy of 50 MeV was bombarded on a natural Ce target with thickness of 1.6 mg/cm^2 . The level scheme of excited states below 5 MeV was made based on this γ - γ coincidence data.

For the purpose of constructing the level scheme up to high-spin states, $\sim 8.5 \text{ MeV}$, another γ - γ coincidence measurement was carried out by using $^{139}\text{La}(^{13}\text{C},6n)^{146}\text{Eu}$ reaction. The ^{13}C beam of 98 MeV was provided by the JAERI tandem accelerator. In order to obtain the time information of γ -rays the pulsed beam was used in the experiment. The dura-

tion and the repetition of the pulsed beam were 40 ns and 4 MHz, respectively. A self-supporting ^{139}La foil target with the thickness of 11 mg/cm^2 was used. Gamma-rays were detected by using six HPGe detectors with BGO Anti-Compton shields. These detectors were placed at four different angles with respect to the beam axis, so that the information of the angular distribution could be obtained. Fifty new γ -rays were identified to originate from ^{146}Eu by setting gates on the previously reported γ -rays.⁹⁾ Figure 1 shows the level scheme so far constructed. Spins above 14^+ state were tentatively assigned based on the angular distribution of γ -rays. The data analysis is still in progress.

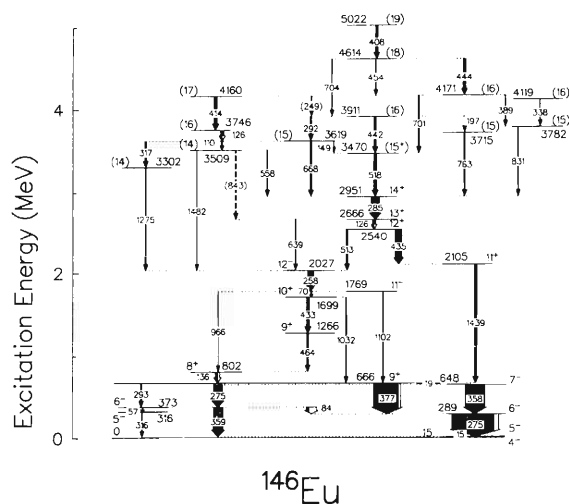


Fig. 1. Proposed level scheme of ^{146}Eu .

References

- 1) T. Murakami et al.: *Z. Phys. A* **345**, 123 (1993).
- 2) A. Ferragut et al.: *J. Phys. Soc. Jpn.* **62**, 3343 (1993).
- 3) E. Ideguchi et al.: *Bull. Phys. Soc. Jpn.*, p. 108 (1993).
- 4) M. W. Drigert et al.: *Nucl. Phys. A* **515**, 466 (1990); and references therein.
- 5) R. Broda et al.: *Proc. Symp. on High-Spin Phenomena in Nuclei*, Argonne, p. 397 (1979).
- 6) A. Odahara et al.: *Z. Phys. A* **350**, 185 (1994).
- 7) E. Ott et al.: *Z. Phys. A* **348**, 57 (1994).
- 8) H. Wolters et al.: *Z. Phys. A* **333**, 413 (1989).
- 9) A. Ercan et al.: *Z. Phys. A* **329**, 63 (1988).

* Japan Atomic Energy Research Institute

Study of High-Lying States in ^{147}Eu

X. H. Zhou, E. Ideguchi, Y. Gono, T. Kishida, S. Mitarai, T. Morikawa, H. Tsuchida,
M. Shibata, H. Watanabe, M. Miyake, M. Oshima, Y. Hatsukawa, S. Hamada,*
H. Iimura,* M. Shibata,* T. Ishii,* and M. Ishihara

[NUCLEAR REACTION: $^{13}\text{C} + ^{139}\text{La}$ at $E_{lab} = 98$ MeV; γ - γ coin. measurement; Level scheme]

Extensive γ -ray spectroscopies of odd-mass nuclei in the neighborhood of the doubly-magic ^{146}Gd nucleus have resulted in a well-developed understanding of the coupling between a valence nucleon and an even-even spherical core nucleus.¹⁻⁵⁾ The weak coupling model was suggested to interpret the observed yrast level (the yrast level is the lowest level in energy at a given angular momentum) structures in odd-A europium isotopes³⁾ which exhibit a level structure with the spin sequence and energy spacing very similar to the yrast level scheme of the adjacent even-even nuclei. Prior to the present work the level structure in ^{147}Eu had been studied mainly via fusion-evaporation reactions with rather light projectiles.^{3,6)} Therefore, the previous investigations have only provided information on states with excitation energies less than 4.2 MeV. In this paper we present the preliminary results for the higher-lying states in ^{147}Eu .

The excited states in ^{147}Eu were populated by the reaction of $^{139}\text{La}(^{13}\text{C}, 5n)$ at the ^{13}C beam energy of $E_{lab} = 98$ MeV provided by the Tandem Accelerator at JAERI. A γ - γ coincidence measurement was performed with six HPGe detectors with anti-Compton shields. Based on the coincidences with the known γ rays in ^{147}Eu , sixteen new γ rays were identified to belong to ^{147}Eu . Therefore, the previously reported level scheme for ^{147}Eu was extended from 4174 keV to 7064 keV in the excitation energy. The level scheme for ^{147}Eu proposed from the present work is shown in Fig. 1. The spin and parity assignments were adopted from the previous work for low-lying states.³⁾

In the weak coupling framework, it could be expected that states in ^{147}Eu arise from the stretched coupling of $d_{5/2}^{-1}$ and $g_{7/2}^{-1}$ proton holes to $^{148}\text{Gd}^{(7)}$ and of $h_{11/2}$ protons to ^{146}Sm .⁸⁾ Previous experiments identified that the $d_{5/2}^{-1}$ and $g_{7/2}^{-1}$ proton hole states are located at 0 and 229 keV, respectively, and that the $h_{11/2}$ proton state occurs at 625 keV. With the zero-order approximation, the energy of a state in ^{147}Eu is calculated to be the sum of the energy of the correct particle or hole state and the energy of the corresponding state of the even-even core. The predictions of the weak coupling calculation are compared with the experimental results in Fig. 1. The weak coupling calculation indicates that the low-lying yrast states in ^{147}Eu can be formed by the coupling of $h_{11/2}$ proton

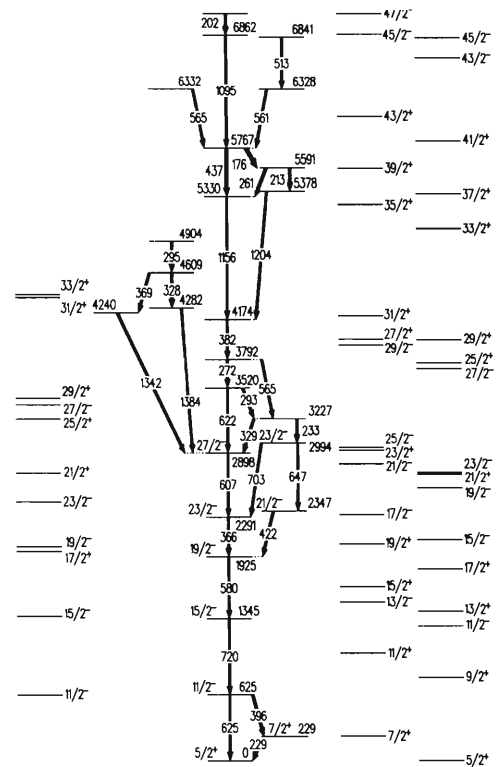


Fig. 1. Comparison of experimentally observed levels in ^{147}Eu with the zero-order weak coupling calculations shown on the left for the $h_{11/2}$ proton state and on the right for the $d_{5/2}^{-1}$ and $g_{7/2}^{-1}$ proton hole states, respectively.

to ^{146}Sm , but the $d_{5/2}^{-1}$ and $g_{7/2}^{-1}$ proton holes should play an important role in the high-lying yrast states. We are planning an experiment to assign the spin and parity values to the newly established levels in ^{147}Eu .

References

- 1) S. M. Aziz et al.: Phys. Rev. C **41**, 1268 (1990).
- 2) T. Glasmacher et al.: Phys. Rev. C **47**, 2586 (1993).
- 3) J. G. Fleissner et al.: Phys. Rev. C **16**, 227 (1977).
- 4) A. Odahara et al.: Z. Phys. A **350**, 185 (1994).
- 5) E. Ideguchi et al.: Z. Phys. A **352**, 363 (1995).
- 6) G. L. Bianco et al.: J. Phys. **7**, 219 (1981).
- 7) S. Lunardi et al.: Phys. Rev. Lett. **53**, 1531 (1984).
- 8) J. Kownachi et al.: Nucl. Phys. A **337**, 464 (1980).

* Japan Atomic Energy Research Institute

High Spin Isomer Beam Line

T. Kishida, Y. Gono, E. Ideguchi, T. Morikawa, M. Kidera, M. Shibata, H. Tsuchida, K. Miyazaki, H. Watanabe, H. Wu, A. Tanokura, S. S. Yamamoto, A. Yoshida, S. Mitarai, A. Odahara, T. Murakami, M. Oshima, H. Kusakari, M. Sugawara, M. Kubo, T. Murata, M. Shimura, H. Kumagai, and M. Ishihara

[NUCLEAR REACTIONS: $^{12}\text{C}(^{140}\text{Ce},5n)$, $^{24}\text{Mg}(^{136}\text{Xe},\alpha9n)$,
 $E_p = 7\text{--}10\text{ MeV/u}$; Recoil separator; High-spin isomer beams]

The high spin isomer beam line of RIKEN Accelerator Facility is a unique apparatus in the world which provides a high spin isomer as a secondary beam. In general, the intensity of a secondary beam is much smaller than its primary beam. It is, therefore, very important to study characteristics of high spin isomer beam and to develop a beam line with a high transport efficiency. In this report, discussions are made on some general requirements for the construction of a high spin isomer beam line.

First, Requirement for the Primary Beam. The mechanism of inverse kinematics should be used, which means that a heavy ion is the incident and a light atom is the target. For this case, the reaction products recoil in the forward direction, maintaining the kinetic energies high enough to induce the secondary reactions. In general, the energy range required for the primary beam is 6–10 MeV/nucleon for the mass region of 140.

Next, Requirement for the Reaction Mode. There are many reaction modes for the production of high spin isomer states. In general, when the production target is heavier, the separation between the primary beam and the reaction products by their magnetic rigidity becomes better, and the angular divergence of the reaction products becomes larger; and vice versa. To see this more quantitatively, some calculations were made for ^{147}Gd produced by the reactions of $^{12}\text{C}(^{140}\text{Ce},5n)$ and $^{24}\text{Mg}(^{136}\text{Xe},\alpha9n)$. From the results of the angular distributions of ^{147}Gd calculated for these two cases, it is concluded that the angular acceptance of $\pm 40\text{ mr}$ is large enough to transport Gd efficiently even when the production target is heavy. Calculations were also made for the charge state distributions of ^{147}Gd and of the primary beam as a function of the magnetic rigidity. The yield of ^{140}Ce is 10^3 times as large as that of ^{147}Gd at the magnetic rigidity with which the charge state distribution of ^{147}Gd becomes maximum, while the yield of ^{147}Gd is 10^5 times as large as that of ^{136}Xe in the latter reaction. And in our energy region, it is concluded that a high spin isomer beam line must cover the range magnetic rigidity 0.8–1.3 Tm.

There are some other requirements for high spin isomer beams: 1) The optics should be dispersive at the first focal plane. 2) The optics should have small dispersion after the first focal plane. 3) Double stage

spectrometer system is desirable. 4) The path length of the beam line should be as short as possible.

RIKEN Accelerator Facility has two beam lines which have been used as a high spin isomer beam line: E1C and RIPS.

E1C was a gas filled beam line in the first stage. A gas filled system makes it possible to transport several different charge states efficiently to the experimental area. But the problem of this system was its beam size. The diameter of the beam spot was more than 40 mm. It does not fit for the secondary reactions. By evacuating the beam line, the diameter of the beam spot became much less than 10 mm. E1C has an angular acceptance of $\pm 7\text{ mr}$.

In order to improve the transmission efficiency, a large acceptance beam line, RIPS, was recently used as a high spin isomer beam line. Though the RIPS is well known as a high energy RI beam line using a projectile fragmentation method, it can be used also successfully as a low energy isomeric beam line by using a fusion-evaporation method. RIPS has an angular acceptance of $\pm 40\text{ mr}$.

By considering all the requirements described above, it is concluded that RIPS is more suitable for a high spin isomer beam line than E1C. RIPS has an advantage in every characteristics except the path length between the production target and the final focal plane. RIPS has a long path length which corresponds to the time of flight of about 860 ns, while E1C has that of about 220 ns.

For a quantitative comparison, some considerations are made here for the case of $^{12}\text{C}(^{140}\text{Ce},5n)$. When the magnetic rigidity is set at the value corresponding to the charge state $48+$ of ^{147}Gd , the acceptance for each charge state is calculated as ($47+$: 5.1%, $48+$: 29%, $49+$: 5.1%) for E1C, and ($46+$, $47+$, $48+$, $49+$, $50+$: 100%) for RIPS. Then, by taking into account of the charge state distribution, the total acceptance of E1C becomes 9.4%, and that of RIPS 89%, which is almost 10 times larger than E1C. But, due to the flight decay of the isomer (^{147m}Gd ; $t_{1/2} = 0.55\ \mu\text{s}$), the resulting transmissions are 6.4% and 19% for RIPS and E1C, respectively. Then the ratio of transmission between RIPS and E1C is calculated to be 3. The experimental ratio was 4, which agrees with the calculation.

Measurement of Deuteron Spin-Flip Probability in the $^{12}\text{C}(\vec{d}, \vec{d}')^{\prime}$ Reaction at $E_d = 270$ MeV

Y. Satou, H. Sakai, H. Okamura, S. Ishida, N. Sakamoto, H. Otsu, T. Uesaka, T. Wakasa, T. Oonishi, T. Nonaka, G. Yokoyama, H. Ohnuma, T. Niizeki, T. Ichihara, and K. Hatanaka

[NUCLEAR REACTION: $^{12}\text{C}(\vec{d}, \vec{d}')^{\prime}$ at $E_d = 270$ MeV; Isoscalar spin excitation]

Inelastic scattering of polarized deuterons is one of the promising processes to study isoscalar spin-dependent excitation modes in nuclei, such as coherent particle-hole states and isoscalar spin strength in the continuum. To perform the $(\vec{d}, \vec{d}')^{\prime}$ reaction, we have developed a focal plane Deuteron POLarimeter (named DPOL)¹⁾ which utilizes the $^{12}\text{C}(d, d)$ and $^1\text{H}(d, pp)$ reactions to cope with the simultaneous determination of all the vector and tensor polarizations of the scattered deuterons. Effective analyzing powers and double scattering efficiencies of these reactions have been measured by a calibration experiment and have already been reported.²⁾

Here we present new data obtained by the measurement of $^{12}\text{C}(\vec{d}, \vec{d}')^{\prime}$ reaction using DPOL. Eight spin observables in the reaction ($A_y, A_{yy}, P^{y'}$, $P^{y'y'}$, $K_y^{y'}$, $K_{yy}^{y'}$, $K_{yy}^{y'y'}$) and differential cross sections (σ) were measured over an angular range from 2° to 8° and an excitation energy range from 2 to 25 MeV.

A 270 MeV polarized deuteron beam from the RIKEN Ring Cyclotron was used to bombard a 87.2 mg/cm²-thick ^{12}C target. Typical beam intensity was 10 nA. Details of the polarized deuteron beam are described elsewhere.³⁾ The scattered deuterons were momentum analyzed by a magnetic spectrometer SMART and their positions were determined by a multiwire drift chamber (MWDC) located at the second focal plane. Plastic trigger counters accompanied with a 2.5 cm-thick polyethylene plate were used as the secondary targets. The $^{12}\text{C}(d, d)$ and $^1\text{H}(d, pp)$ reactions took place in the targets were identified by a plastic counter hodoscope (2 m \times 2 m \times 6.5 cm) which was placed 4 m downstream from the secondary targets. Polarizations of the scattered deuterons were deduced from the scattering asymmetry of these reactions.

Figure 1(a) shows the excitation energy spectrum of ^{12}C . The unnatural parity 1^+ (12.7 MeV) and 2^- (18.3 MeV) states are clearly excited as well as the natural parity 2^+ (4.44 MeV), 0^+ (7.65 MeV), and 3^- (9.64 MeV) states. All these are isoscalar states. Figure 1(b) shows the spin-flip probability S_1 ($\Delta S_z = 1$) plotted every 500 keV bins. S_1 is derived from the tensor spin observables by using the relationship:

$$S_1 = \frac{1}{9}(4 - A_{yy} - P^{y'y'} - 2K_{yy}^{y'y'}). \quad (1)$$

The result is based on the analysis of 60% of the total data collected. The errors given are statistical ones

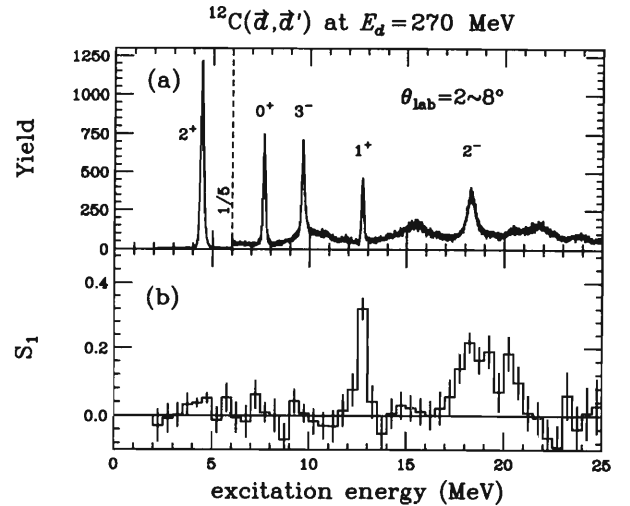


Fig. 1. Experimental results of the deuteron polarization transfer measurement on ^{12}C . (a) Measured excitation energy spectrum. (b) Spin-flip probability S_1 .

only. It is to be noted that this is the first case in which S_1 is presented as a spectrum. The spin-flip 1^+ state at 12.7 MeV is strongly enhanced compared to the other natural parity transitions. This shows that S_1 is a good signature of the isoscalar spin transfer strength.

From the recent analysis of the $^{12}\text{C}(\vec{d}, \vec{d}')^{\prime}$ experiment performed at SATURNE, Johnson et al. have reported a previously unknown isoscalar state of a 1^+ nature at 20.5 MeV.⁴⁾ They have measured a vector polarization of the scattered deuterons to extract a signature S_d^y .⁵⁾ It would be of interest to see that our data shown here seem to suggest as well an existence of some spin-flip structure at the corresponding excitation energy region.

Further analysis to estimate the systematic errors as well as to extract the double spin-flip probability S_2 ($\Delta S_z = 2$) is now in progress.

References

- 1) S. Ishida et al.: AIP Conf. Proc. **343**, 182 (1995).
- 2) S. Ishida et al.: RIKEN Accel. Prog. Rep. **29**, 179 (1996).
- 3) H. Okamura et al.: AIP Conf. Proc. **343**, 182 (1995).
- 4) B. N. Johnson et al.: Phys. Rev. C **51**, 1726 (1995).
- 5) M. Morlet et al.: Phys. Lett. B **247**, 228 (1990).

Measurement of Polarization Correlation Coefficient for the ${}^3\text{He}(d,p){}^4\text{He}$ Reaction

T. Uesaka, H. Okamura, T. Oonishi, Y. Satou, S. Ishida, N. Sakamoto, H. Otsu, T. Wakasa, T. Nonaka, G. Yokoyama, K. Itoh, T. Wakui, and H. Sakai

[NUCLEAR REACTIONS ${}^3\text{He}(d,p){}^4\text{He}$, $E = 270$ MeV; Measured polarization correlation coefficient, Polarized beam, Polarized target]

A structure of deuteron is still an important subject in nuclear physics. In particular, the D-state wave function in the high $p-n$ relative momentum region is not well studied.

Recently, we have proposed a new approach to study the D-state wave function, by measuring the polarization correlation coefficient, $C_{//}$, for the ${}^3\text{He}(d,p){}^4\text{He}$ reaction. Here, $C_{//}$ is defined as a ratio of the differential cross section at forward angle when d - and ${}^3\text{He}$ -spins are parallel each other to that when spins are unpolarized,

$$C_{//} = \frac{d\sigma_{\uparrow\uparrow}}{d\sigma_{\text{unpol}}}. \quad (1)$$

Assuming that s-wave is dominant in the neutron capture process by ${}^3\text{He}$, the $C_{//}$ is expressed under plain wave Born approximation by

$$C_{//} = \frac{9}{4} \frac{w^2(k)}{u^2(k) + w^2(k)}, \quad (2)$$

where k , $u(k)$ and $w(k)$ are the $p-n$ relative momentum, the S-state deuteron wave function, and the D-state one, respectively. It is important to point out that $C_{//}$ is directly proportional to the D-state density at k .

The present experiment was performed at E3-room of RIKEN Accelerator Research Facility. This is the first experiment to use the polarized ${}^3\text{He}$ gas target developed at RIKEN.¹⁾ The polarized ${}^3\text{He}$ gas with a thickness of about 10 mg/cm^2 was bombarded by a polarized deuteron beam of 270 MeV. Protons at 4° were detected by NaI(Tl) detectors with $2''\phi \times 3''$ in size, which were placed at a distance of 2.6 m downstream from the target. Figure 1 shows a measured energy spectrum. A peak corresponding to the ${}^3\text{He}(d,p){}^4\text{He}$ reaction, which has a large positive Q-value, is isolated from a large bump which is most probably due to deuteron breakup events.

The coefficient $C_{//}$ is a linear combination of the tensor analyzing powers, A_{xx} and A_{yy} , and the vector polarization correlation coefficients, $C_{x,x}$ and $C_{y,y}$:

$$C_{//} = 1 + \frac{1}{4}(A_{xx} + A_{yy}) + \frac{3}{4}(C_{x,x} + C_{y,y}). \quad (3)$$

Figure 2 shows a preliminary result of the measured asymmetry. This asymmetry corresponds to

$$\frac{1}{4}P_{yy}(A_{xx} + A_{yy}) + \frac{3}{4}P_x P_y^T (C_{x,x} + C_{y,y}), \quad (4)$$

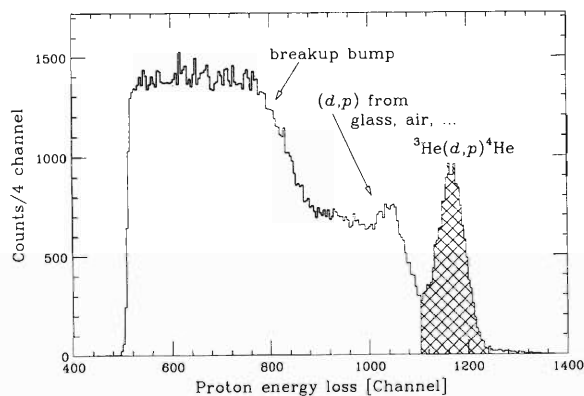


Fig. 1. Proton energy loss spectrum in NaI.

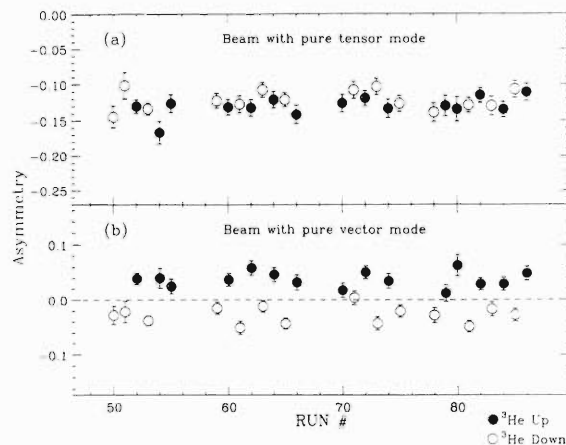


Fig. 2. A preliminary result of the measured asymmetry. Error bars included statistical errors only. Each run took approximately for 2-hours.

where P_{yy} , P_y , and P_y^T are the beam tensor, the vector polarization, and the target vector polarization, respectively. Figure 2(a) is the asymmetry for the beam with the pure tensor mode ($P_{yy} \sim -0.9$, $P_y \sim 0$). It does not depend on the ${}^3\text{He}$ polarization. On the other hand, Fig. 2(b) shows the asymmetry by the beam with the pure vector mode ($P_y \sim -0.45$, $P_{yy} \sim 0$), which changes its sign depending on the ${}^3\text{He}$ polarizations "Up" or "Down".

Further analysis to obtain $C_{//}$ is in progress.

References

- 1) T. Uesaka et al.: RIKEN Accel. Prog. Rep. **30**, 139 (1997).

Spin-Flip Dipole State of ^{90}Y Studied by the $^{90}\text{Zr}(d, ^2\text{He})$ Reaction at $E_d = 270$ MeV

H. Okamura, T. Uesaka, T. Wakasa, Y. Satou, T. Oonishi, T. Nonaka, H. Sakai, S. Ishida, N. Sakamoto, T. Ichihara, T. Niizeki, and H. Ohnuma

[NUCLEAR REACTION: $^{90}\text{Zr}(\text{polarized } d, ^2\text{He})$; $E_d=270$ MeV;
Measured σ , A_y , A_{yy} , and A_{xx} ; Multipole decomposition analysis]

In spite of the extensive study made by using the charge exchange reactions at intermediate energies, the understanding of the spin- and isospin-flip states other than the Gamow-Teller state ($L=0$) is still rather limited. The $(d, ^2\text{He})$ reaction is considered to be a promising tool for the study of higher multiplicities, because (a) it exclusively excites the spin-flip state, (b) the background Gamow-Teller transition is Pauli-blocked for heavy nuclei, and (c) the tensor analyzing powers, A_{yy} and A_{xx} , are useful in identifying J^π of the final state. The last feature (c), which was theoretically pointed out first,¹⁾ has experimentally been established by the previous study of the $^{12}\text{C}(d, ^2\text{He})^{12}\text{B}$ reaction.²⁾

The aim of the present experiment is a study of the spin-dipole state ($S=1, L=1$) of ^{90}Y , making the most of the feature (b). The angular distributions of the differential cross section, A_y , A_{yy} , and A_{xx} for the $^{90}\text{Zr}(d, ^2\text{He})$ reaction at 270 MeV have been obtained in the range of $\theta_L=0^\circ-15^\circ$. The typical spectra of the differential cross section and A_{xx} are shown in Fig. 1. It should be noted that a fine structure of low-lying levels observable in Fig. 1(a) was smeared out in the (n, p) spectra obtained at TRIUMF because of the lack of energy resolution.³⁾ The (n, p) spectra also suffered from the large amount of hydrogen contamination caused by the complicated target system.

Since the simple one-step distorted-wave Born approximation (DWBA) was proved to be successful in the analysis of the $^{12}\text{C}(d, ^2\text{He})^{12}\text{B}$ reaction,¹⁾ the multipole decomposition of the spectra has been performed based on the DWBA prediction for various L -transfers. The result is shown in Fig. 1(b). The dipole component is dominant up to the excitation energy of about 20 MeV. This allows us to discuss the analyzing powers with small ambiguities.

Concerning the spin-dipole states, the DWBA prediction is summarized as following: $A_{xx} \sim -2$ for 0^- , $A_{xx} \sim +1$ for 1^- , and $A_{xx} \sim 0$ for 2^- . The observed A_{xx} shows, however, a structure-less distribution with a positive but small value in the whole region measured. It suggests that there exists no concentrated distribution of the 0^- or 1^- state and that the dipole component mainly consists of the 2^- state. This is consistent with the recent result of the (p, n) measurement.⁴⁾ Further analysis is in progress.

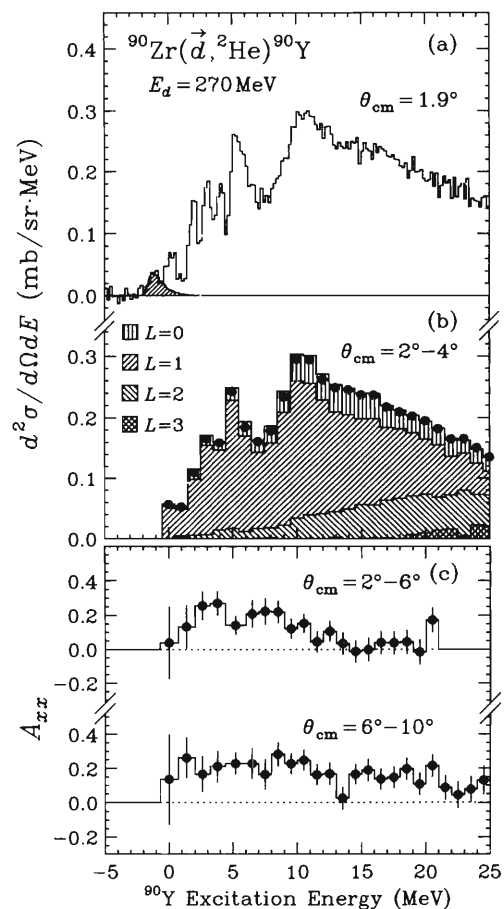


Fig. 1. (a) Spectrum of the differential cross section at the mean center-of-mass angle of 1.9° . The contribution of the hydrogen contamination is shown by the shaded area. (b) Multipole decomposition of the spectrum at $2^\circ-4^\circ$. The contributions of each L -transfer component are indicated by the shaded regions. The total spectrum reconstructed is in good agreement with the data shown by the closed circle. (c) Spectra of the tensor analyzing power A_{xx} at $2^\circ-6^\circ$ and $6^\circ-10^\circ$.

References

- 1) D. V. Bugg and C. Wilkin: Nucl. Phys. A **467**, 575 (1987).
- 2) H. Okamura et al.: Phys. Lett. B **345**, 1 (1995).
- 3) K. J. Raywood et al.: Phys. Rev. C **41**, 2836 (1990).
- 4) T. Wakasa et al.: Nucl. Phys. A **599**, 217c (1996).

Production Cross Sections of Projectile-like Fragments in the $^{48}\text{Ca} + ^{64}\text{Ni}$ and $^{48}\text{Ca} + ^{181}\text{Ta}$ Reactions at 70A MeV

M. Notani, N. Aoi, D. Beaumel, N. Fukuda, M. Hirai, E. Ideguchi, M. Ishihara, H. Iwasaki, T. Kishida, T. Kubo, H. Kumagai, S. M. Lukyanov, T. Nakamura, Y. T. Oganessian, Y. E. Penionzhkevich, H. Sakurai, T. Teranishi, Y. Watanabe, Y. Watanabe, K. Yoneda, and A. Yoshida

[NUCLEAR REACTIONS: $^{64}\text{Ni}, ^{181}\text{Ta}(^{48}\text{Ca}, X)$, $E(^{48}\text{Ca}) = 70A$ MeV;
Production cross sections of projectile-like fragments.]

The particle stability of extremely neutron-rich nuclei close to the drip-line can be used for testing various mass predictions. For the efficient production of extremely neutron-rich nuclei, we have investigated the target dependence on production rates of the projectile-like fragments¹⁾ with a 70A MeV ^{48}Ca beam. In addition, we made an attempt to estimate cross sections and yields for ^{33}Ne , ^{34}Ne , and ^{36}Na , and to argue their particle stabilities. We expect the target dependence to give a clue of elucidating the production mechanism of projectile-like fragments at intermediate energies (10 ~ 100 A MeV).²⁾

To investigate the target dependence on production cross sections, we used two energy-loss-equivalent production targets, ^{64}Ni and ^{181}Ta , with thickness of 244 and 400 mg/cm², respectively. The experimental setup is described in Ref. 3. Table 1 shows the ratio of the yield for ^{181}Ta target to that for ^{64}Ni target with $B\rho = 3.68$ Tm setting of the RIPS spectrometer. We found that the ^{181}Ta target provides larger yields than ^{64}Ni for the fragments with $A = 3Z + 2$. Thus, we employed the ^{181}Ta target for the next new isotope search experiment. By using the transmission calculated with the INTENSITY code,^{4,5)} we deduced the production cross sections from the production rates of projectile-like fragments for $^{19-23}\text{N}$, $^{21-24}\text{O}$, $^{23-29}\text{F}$, $^{24-32}\text{Ne}$, $^{29-35}\text{Na}$, $^{34-38}\text{Mg}$, and $^{35-41}\text{Al}$ as shown in Fig. 1.

Table 1. Ratios of the yields for ^{181}Ta to ^{64}Ni targets in neutron-rich fragments production in the F-Na region.

A	$3Z - 1$	$3Z$	$3Z + 1$	$3Z + 2$
F	0.42 ± 0.03	0.62 ± 0.04	(unstable)	1.6 ± 0.3
Ne	0.21 ± 0.07	0.36 ± 0.05	0.84 ± 0.03	2.0 ± 0.5
Na	0.26 ± 0.16	0.29 ± 0.08	0.44 ± 0.22	1.5 ± 0.7

At the new isotope search experiment with the ^{181}Ta target, we found no events associated with ^{33}Ne , ^{34}Ne , and ^{36}Na . No observed events of these isotopes insists on either their particle instabilities or insufficient statistics due to low cross sections. Thus, we have estimated the cross sections and total yields with all of our data sets for the new isotope search. In this estimation, we assumed that isotope and isotone dependencies on

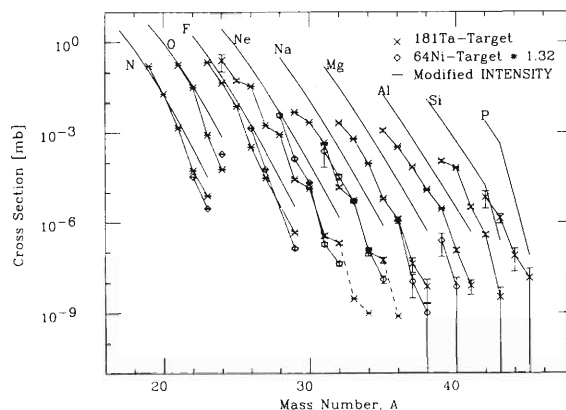


Fig. 1. Production cross sections of projectile-like fragments for the ^{64}Ni and ^{181}Ta targets, compared with those calculated by the INTENSITY code.⁴⁾

the cross sections are described in an exponential form with consideration of even-odd effects. The estimated cross sections and total yields are tabulated in Table 2. At present, due to low statistics or large uncertainties of the cross sections, we could not conclude their particle instabilities.

Table 2. Estimated production cross sections and yields under present experimental conditions with the ^{181}Ta target for three nuclei, ^{33}Ne , ^{34}Ne , and ^{36}Na .

Nuclei	Cross section [pb]	Yield [counts]
^{33}Ne	1 - 6	1.5 - 8.7
^{34}Ne	0.6 - 3	0.8 - 4.0
^{36}Na	0.4 - 1	0.6 - 1.6

References

- 1) M. Notani et al.: RIKEN Accel. Prog. Rep. **29**, 50 (1996).
- 2) D. Guerreau: Nucl. Phys. A **447**, 37c (1985).
- 3) H. Sakurai et al.: RIKEN Accel. Prog. Rep. **30**, 49 (1997).
- 4) J. A. Winger, B. M. Sherrill, and D. J. Morrissey: Nucl. Instrum. Methods Phys. Res. B **70**, 380 (1992).
- 5) Y. Doki: JAERI-M 94-028, p. 70; Master thesis, Univ. Tokyo (1994).

New Neutron-Rich Isotopes ^{38}Mg , ^{40}Al , and ^{41}Al Produced by Fragmentation of a 70A MeV ^{48}Ca Beam

H. Sakurai, N. Aoi, D. Beaumel, N. Fukuda, M. Hirai, E. Ideguchi, M. Ishihara, H. Iwasaki, T. Kishida, T. Kubo, H. Kumagai, S. M. Lukyanov, T. Nakamura, M. Notani, Y. Ts. Oganessian, Y. E. Penionzhkevich, T. Teranishi, Y. Watanabe, Y. Watanabe, K. Yoneda, and A. Yoshida

[NUCLEAR REACTIONS: $^{181}\text{Ta}(^{48}\text{Ca},X)$, $E(^{48}\text{Ca})=70A$ MeV; Evidence for ^{38}Mg , ^{40}Al , ^{41}Al]

The results of an experiment by the RIKEN–JINR collaboration on search for the new Ne, Na, Mg and Al isotopes close to the neutron drip-line are presented. We found, for the first time, three new neutron-rich nuclei: ^{38}Mg and $^{40,41}\text{Al}$.

These nuclei were produced by the projectile fragmentation of a 70A MeV ^{48}Ca beam. The 64% enriched ^{48}Ca oxide powder was used to produce the ^{48}Ca ions at the ECR source of the AVF cyclotron. The ^{48}Ca beam reacted with a ^{181}Ta target of 400 mg/cm² thickness. The reaction fragments were collected and analyzed with the RIPS spectrometer¹⁾ operated in the achromatic mode. Taking into account the energy loss in the target for both the beam and fragments with $A/Z \sim 3.2$, the magnetic rigidity of the RIPS was set to be 3.438 Tm. Particle identification was performed event-by-event by measuring the magnetic rigidity ($B\rho$), time-of-flight (TOF), energy loss (ΔE), and total kinetic energy (TKE).²⁾

The positions of fragments at the momentum-dispersive focal plane were measured using a parallel plate avalanche counter (PPAC) in order to determine the $B\rho$ value. The PPAC with the sensitive area of 15 cm(W) \times 10 cm(H) was larger than the one used at a previous experiment:²⁾ it covered the full rigidity acceptance of RIPS (6%). All of the other detectors were located at the final focal point (F3), involving a 0.5 mm thick plastic scintillation counter (PL), a four-element silicon-detector telescope, and an 1 mm thick plastic scintillation veto counter. The TOF of each fragment over the 27.5 m flight-path between the target and F3 was determined from the PL timing and RF signal of the cyclotron. The silicon telescope consisted of two 0.5 mm thick surface-barrier-type silicon detectors, and 3 mm and 4.2 mm thick lithium-drift silicon detectors. This configuration provided two or three independent ΔE measurements and all the silicon detectors combined provided a TKE measurement. The veto counter was used for rejecting such events as piled up due to light fragments. The measured values of $B\rho$, TOF, ΔE , and TKE were combined to give redundant particle identifications for obtaining the proton number (Z), charge (Q), and mass number (A) of

the fragment, as described in Ref. 2.

Figure 1 shows a two-dimensional plot of events, A/Z versus Z . The result was obtained from the data accumulated for one day with an average beam intensity of ~ 2 pnA. Significant numbers of events were observed for new isotopes, ^{38}Mg (18 events), ^{40}Al (34 events), and ^{41}Al (4 events). We observed no events associated with ^{33}Ne . We took also the data with different $B\rho$ settings, e.g., for $A/Z \sim 3.3$ and 3.4, and with a higher beam intensity up to 4 pnA, where no ^{33}Ne events were observed, either. These data were evaluated to estimate the expected yields of ^{33}Ne , which may lead to arguments on particle instability of ^{33}Ne . The related discussion is found in Ref. 3.

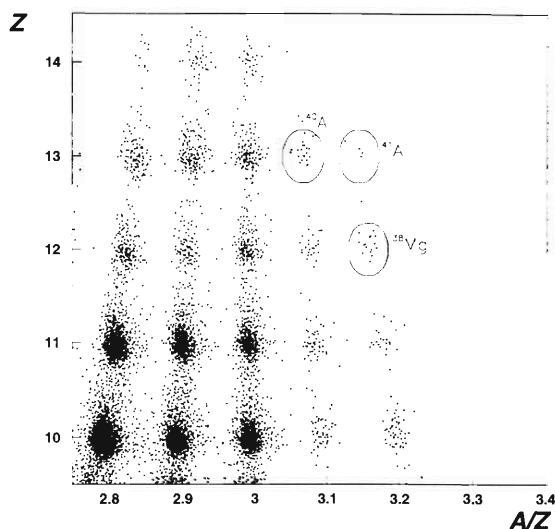


Fig. 1. Two-dimensional A/Z versus Z plot. Three ^{38}Mg , ^{40}Al , and ^{41}Al isotopes are clearly visible. See text for further details.

References

- 1) T. Kubo et al.: Nucl. Instrum. Methods Phys. Res. B **70**, 309 (1992).
- 2) H. Sakurai et al.: Phys. Rev. C. **54**, R2802 (1996).
- 3) M. Notani et al.: RIKEN Accel. Prog. Rep. **30**, 48 (1997).

Isomer Production in Fragmentation Reactions Induced by a 70A MeV ^{48}Ca Beam

H. Iwasaki, N. Aoi, D. Beaumel, N. Fukuda, M. Hirai, E. Ideguchi, M. Ishihara,
T. Kishida, T. Kubo, H. Kumagai, S. M. Lukyanov, T. Nakamura, M. Notani, Y. Ts. Oganessian,
Y. E. Penionzhkevich, H. Sakurai, T. Teranishi, Ya. Watanabe, Yu. Watanabe,
K. Yoneda, and A. Yoshida

[NUCLEAR REACTION: $^{64}\text{Ni}, ^{181}\text{Ta}(^{48}\text{Ca}, X), E(^{48}\text{Ca}) = 70\text{A MeV}$; Measured (fragment)gamma-coin;
Reviewed small $T_{1/2}$ isomer production for ^{26m}Na and ^{32m}Al .]

Recently the projectile-like fragmentation has been used as a method for production of long-lived isomers¹⁾ as well as radio-active beams. The study on isomeric states of the reaction fragments is important for understanding the reaction mechanism of projectile-like fragmentation. We have made an attempt to search for new isomers in neutron-rich nuclei in the $7 \leq Z \leq 18$ region, and have deduced isomer ratios of the known isomers, ^{26m}Na and ^{32m}Al , with two different targets.

The neutron-rich nuclei were produced by using the projectile fragmentation of a 70A MeV ^{48}Ca beam. We used two targets, ^{181}Ta and ^{64}Ni , with thickness of 400 mg/cm² and 244 mg/cm², respectively. The reaction fragments were collected and analyzed by RIKEN projectile-fragment separator (RIPS).²⁾ The magnetic rigidity of RIPS was set to be 2.78 Tm to optimize for $A/Z \sim 2.6$ nuclei, while the momentum acceptance was restricted to 0.2%. The reaction fragments were implanted into a 2 mm thick Al stopper, which was located between the first and second silicon detectors at the final focal plane (F3), as described in Ref. 3. The particle identification was performed event by event by measuring the ΔE and TOF. The γ rays from the implanted ions were measured by using a Clover-type Ge detector⁴⁾ placed 20 cm apart from the stopper. The Ge detector was calibrated with standard ^{152}Eu and ^{133}Ba γ -ray sources. The summed photo-peak efficiency of the Ge detector was obtained about 0.2% at 1 MeV. The detector covered the energy range from 20 keV to 3 MeV. The timing spectra of γ rays were obtained using a unit called TDC (Lecroy 4208) whose gate opened for 30 μs after the arrival of a fragment at the stopper.

Implanted fragments were $^{17-19}\text{N}$, $^{18-21}\text{O}$, $^{20-23}\text{F}$, $^{23-26}\text{Ne}$, $^{25-28}\text{Na}$, $^{28-31}\text{Mg}$, $^{31-34}\text{Al}$, $^{34-36}\text{Si}$, $^{37-39}\text{P}$, $^{39-42}\text{S}$, $^{42-45}\text{Cl}$, and $^{46-47}\text{Ar}$. These fragments were accumulated from 50,000 to 800,000 events with the ^{181}Ta target. The statistics obtained with the Ta target was about seven times larger than that with the ^{64}Ni target. Among them, we could find no characteristic peaks indicating the new isomers.

On the other hand, we have observed known γ rays from ^{26m}Na ($E_\gamma = 82.5$ keV) and ^{32m}Al ($E_\gamma = 221.6, 734.1$ keV).¹⁾ The sensitivity of this experiment for new isomer search was limited. For instance, more than 10% of isomer ratio is necessary for detecting the associates of 200 keV γ rays.

We deduced a half-life of ^{32m}Al to be 185 ± 15 ns by analyzing a timing spectrum gated by the γ ray at energies of 221.6 keV and 734.1 keV. This half-life is consistent with that previously reported, 200 ± 20 ns.¹⁾ Taking account of the γ -ray detection efficiency and the isomer decay in its flight, we have deduced the isomer ratios of ^{26m}Na and ^{32m}Al for each target. In this evaluation, the half-lives used for ^{26m}Na and ^{32m}Al were, 9.2 μs and 185 ± 15 ns, respectively. Table 1 shows the measured isomer ratios for ^{26m}Na and ^{32m}Al , compared with the results measured at GANIL.¹⁾ High isomer production is evident in the systems of $^{48}\text{Ca} + ^{181}\text{Ta}$ and $^{48}\text{Ca} + ^{64}\text{Ni}$ as high as that in the $^{40}\text{Ar} + ^9\text{Be}$ system obtained at GANIL.

Table 1. Isomer ratios (F) obtained for ^{26m}Na and ^{32m}Al with two different targets, compared with the results for ^{32m}Al measured at GANIL.

Isomer	Beam	Target	E/A (MeV)	F (%)
^{26m}Na	^{48}Ca	^{181}Ta	70	16 (1)
	^{48}Ca	^{64}Ni	70	13 (3)
^{32m}Al	^{48}Ca	^{181}Ta	70	78 (7)
	^{48}Ca	^{64}Ni	70	68 (13)
$^{32m}\text{Al}^{1)}$	^{36}S	^9Be	75	32 (3)
	^{40}Ar	^9Be	61	93^{+7}_{-12}

References

- 1) M. Robinson et al.: Phys. Rev. C **53**, 1465 (1996).
- 2) T. Kubo et al.: Nucl. Instrum. Methods Phys. Res. B **70**, 309 (1992).
- 3) H. Sakurai et al.: RIKEN Accel. Prog. Rep. **30**, 49 (1997).
- 4) Catalog of Eurisy Mesures (France, 1994).

Angular Distribution of the ^8B Dissociation and E2 Components[†]

T. Motobayashi, T. Kikuchi, N. Iwasa,*¹ Y. Ando, M. Kurokawa, S. Moriya,
H. Murakami, T. Nishio, J.-Z. Ruan, S. Shirato, S. Shimoura, T. Uchibori, Y. Yanagisawa, T. Kubo,
H. Sakurai, T. Teranishi, Y. Watanabe, M. Ishihara, M. Hirai, T. Nakamura, S. Kubono, M. Gai,*²
R. H. France III,*³ K. Inskik Hahn, T. Delbar, P. Lipnik, and C. Michotte

[$^{208}\text{Pb}(^8\text{B},^7\text{Be}p)^{208}\text{Pb}$, Coulomb dissociation, E2 component, Angular distribution]

Breakup of ^8B in the Coulomb field of ^{208}Pb was performed for the first time at RIKEN.¹⁾ The results demonstrated that this Coulomb dissociation provides an alternative method for studying the $^7\text{Be}(p,\gamma)^8\text{B}$ reaction at low energies. This reaction is important for estimating the high-energy neutrino flux relevant to the “solar neutrino puzzle”, defined as the discrepancy between the measured and predicted neutrino yields from the sun.

A question remains for possible contribution of E2 transitions to the Coulomb dissociation results, whereas astrophysical S_{17} -factors were extracted by assuming pure E1 transitions in the analysis reported in Ref. 1. In the $^7\text{Be}(p,\gamma)^8\text{B}$ reaction, the E2 amplitudes are very small, but they are enhanced in the Coulomb dissociation process. It is known that the differential cross section ($d\sigma/d\theta$) near the grazing angle is sensitive to the E2 component. The nuclear excitation, which introduces an uncertainty in the analysis, is important also for the angular momentum transfer $\ell = 2$ in addition to the E2 Coulomb excitation.

We performed new measurements of the dissociation of ^8B in order to elucidate E2 contributions.²⁾ The RIPS separator provided radioactive ^8B beams of 2×10^4 particles per second, which bombarded a 50 mg/cm^2 ^{208}Pb target. The averaged incident energy was 51.9 MeV/u. The breakup fragments, ^7Be and proton, were detected in coincidence after traveling through the 3.1 m flight-path filled with helium gas. In order to increase the sensitivity of the measurement to the E2 amplitude, the detector system covered a larger angular range up to $\theta_8 \approx 10^\circ$ compared with that in the the first experiment where the efficiency was essentially zero in the vicinity of $\theta_8 = 6^\circ$.

Figure 1 shows the experimental yields as a function of the scattering angle θ_8 for two relative energy bins. The yield labelled as $\epsilon \cdot d\sigma/d\theta$ is related to the original cross section $d\sigma/d\theta$ via the response function that takes into account the detection efficiency and all sorts of experimental resolution. The response function was obtained by a Monte-Carlo simulation and used also in calculating the theoretical E1 and $\ell = 2$ curves. Nuclear contribution for $\ell = 2$ transitions was evaluated

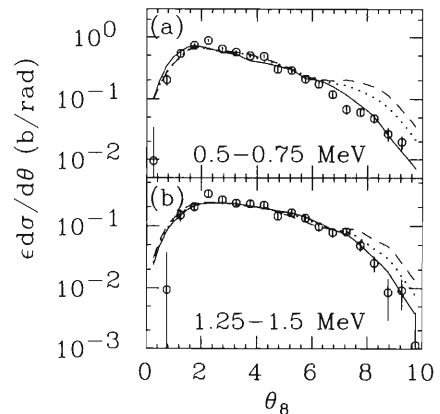


Fig. 1. Observed cross sections, $\epsilon d\sigma/d\theta$, defined by the product of the detection efficiency and differential cross section, as a function of the scattering angle θ_8 for two relative energy bins of 500–750 keV (a) and 1250–1500 keV (b). The theoretical best fits (solid curves) are in favour of the pure E1 transitions. Dashed and dotted curves correspond to the results calculated with $\ell = 1$ [E1] and $\ell = 2$ [E2 and nuclear] components predicted by two different theoretical models, respectively.

by a quantum mechanical calculation with a collective form factor, where the deformation length was set to be the same as the Coulomb one.

The curves for the pure E1 transition fit to the data of Fig. 1, thereby suggesting very small $\ell = 2$ amplitudes at low relative energies. In fact, the best fits are in favour of essentially no mixture of $\ell = 2$ amplitudes below 1.75 MeV. The curves calculated with a mixture of the $\ell = 2$ amplitudes (obtained by applying two different theoretical models^{3,4)} on ^8B) are also shown in the figure for comparison. The small $\ell = 2$ component verified here may support our previous analysis with pure E1 transition in deducing the S_{17} factors from the Coulomb dissociation data.¹⁾

References

- 1) T. Motobayashi et al.: Phys. Rev. Lett. **73**, 2680 (1994); N. Iwasa et al.: J. Phys. Soc. Jpn. **65**, 1256 (1996).
- 2) T. Kikuchi et al.: RIKEN Accel. Prog. Rep. **29**, 73 (1996).
- 3) B. T. Kim, M. H. Park, and K. H. Kim: Phys. Rev. C **35**, 363 (1987).
- 4) S. Typel and G. Baur: Phys. Rev. C **50**, 2104 (1994).

[†] Condensed from an article in Phys. Lett. B, in print.

*¹ GSI, Germany

*² Department of Physics, University of Connecticut, U.S.A.

*³ Institut de Physique Nucléaire, Université Catholique de Louvain, Belgium

Charge Exchange Reactions of Neutron-Rich Nuclei

S. Shimoura, T. Teranishi, Y. Ando, M. Hirai, N. Iwasa, T. Kikuchi, S. Moriya, T. Motobayashi, H. Murakami, T. Nakamura, T. Nishio, H. Sakurai, T. Uchibori, Y. Watanabe, Y. Yanagisawa, and M. Ishihara

[NUCLEAR REACTIONS: $^1\text{H}(^{11}\text{Li}, ^{11}\text{Be}^*)$, $^1\text{H}(^9\text{Li}, ^9\text{Be}^*)$, 63 A MeV;]
 [Charge exchange reaction; Isobaric analog state; Neutron halo.]

Charge exchange reactions of (p,n) and (d,2n) have been measured for the ^{11}Li and ^9Li nuclei employing the inverse kinematics and invariant mass methods at 63 A MeV.

The experiments have been performed at the RIKEN secondary beam line called RIPS. The detector setup is described in elsewhere.¹⁾

We have observed the isobaric analog state (IAS) of ^{11}Li nucleus in the relative energy spectrum of the $^9\text{Li}+p+n$ system produced by the $^1\text{H}(^{11}\text{Li}, ^{11}\text{Be}^* \rightarrow ^9\text{Li}+p+n)$ reaction. The IAS has been identified by the comparison between the relative energy spectra for the ^1H and ^2H targets¹⁾ and the angular distribution (Fig. 1) of the $^9\text{Li}+p+n$ center-of-mass system.

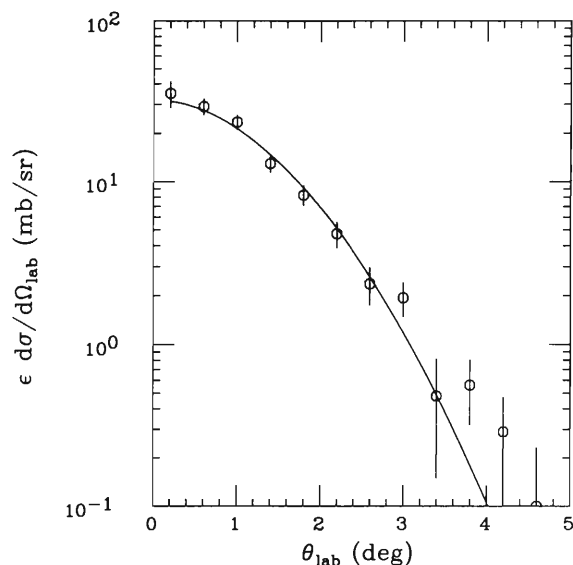


Fig. 1. Angular distribution of the observed differential cross-section in the laboratory system for the $^9\text{Li}+p+n$ center-of-mass system. Solid line denotes a Gaussian fit.

The decay mode of IAS is analyzed from relative energy spectra of the two-body systems $^9\text{Li}+n$ and $p+n$. The angular correlation of p and n is also analyzed for the angular momentum of the decay process. It is found that the IAS mainly decays, through an *s*-wave proton emission, to *s*-wave scattering states of the $^9\text{Li}+n$ system; which may be identified as an

s-wave resonance.

The excitation energy and width of the IAS of ^{11}Li nucleus are deduced to be $E_x = 21.14 \pm 0.03$ MeV and $\Gamma = 0.25_{-0.1}^{+0.2}$ MeV, respectively, by an *R*-matrix analysis (Fig. 2). The Coulomb displacement energy estimated from the above E_x is smaller than that for the ^9Li nucleus, which is attributed to the extend nature of the wave function of halo nucleons. The magnitude of width of the IAS indicates an importance of the *s*-wave component of the halo nucleon in the IAS, which is consistent with the result of the angular correlation analysis.

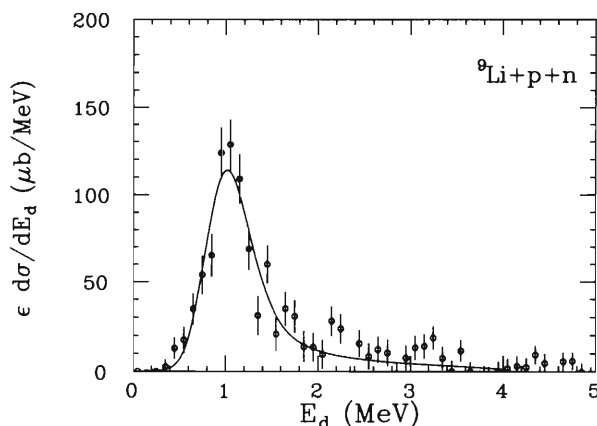


Fig. 2. Relative energy spectrum of the $^9\text{Li}+p+n$ system for the Fermi transition. Solid line denotes a prediction of an *R*-matrix analysis

In order to study the optical potentials and effective interactions for the neutron-rich nuclei, analyses on the absolute magnitudes of the cross sections are now in progress for the $^1\text{H}(^9\text{Li}, ^9\text{Be}^*(\text{GTS}, \text{IAS}))$ reactions followed by the $2\alpha+n$ channels, observed in β -decay.²⁾ The angular correlation of the three-body system is also being analyzed for the study of intermediate channels and their angular momenta.

References

- 1) T. Teranishi et al.: RIKEN Accel. Prog. Rep. **29**, 72 (1996)
- 2) G. Nyman et al.: Nucl. Phys. A **510**, 189 (1990).

Quasifree Nucleon-Knockout Reactions from ${}^6\text{He}$ and ${}^{11}\text{Li}$

T. Kobayashi, A. Ozawa, K. Yoshida, A. Korshennikov, I. Tanihata,
E. Y. Nikolski, and T. Nakamura*

[NUCLEAR REACTIONS $p({}^6\text{He},\text{pn}){}^5\text{He}$, $p({}^{11}\text{Li},\text{pn}){}^{10}\text{Li}$,
 $p({}^6\text{He},\text{pp}){}^5\text{H}$, $p({}^{11}\text{Li},\text{pp}){}^{10}\text{He}$; $E/A = 83\text{ MeV}$]

The quasifree nucleon-knockout reactions, $(p,2p)$ and $(e,e'p)$, by proton or electron beams have been used to study the single-particle properties, such as the binding energy or the momentum distribution, of bound nucleons inside the nucleus.¹⁾ We have applied this method to the neutron-knockout reactions (p,pn) and proton-knockout reactions $(p,2p)$ from neutron-rich nuclei on a proton target with inverse kinematics. The former reaction was used for studying the single-particle properties of valence neutrons in ${}^6\text{He}$ and ${}^{11}\text{Li}$, and the latter for producing neutron-rich resonances beyond the neutron drip line.

The measurement was performed using secondary beams of p , d , ${}^6\text{He}$, and ${}^{11}\text{Li}$ at 83 A MeV. Targets used were a CH_2 plate as a proton target, and a C plate for background subtraction. Two nucleons (pn or pp) from the quasifree p -N scattering were detected at $\Theta_{\text{lab}} = \pm 45^\circ$ using plastic-scintillator telescopes with MWPC's. Forward fragments, from the decay of the $(A-1)$ system produced in the nucleon-knockout process, were detected at 0° by a magnetic spectrometer. Detection of the forward fragments provides information on the decay properties of the $(A-1)$ system.

Separation-energy spectra are shown in Fig. 1, when the forward fragment was detected in coincidence. The separation-energy resolution, evaluated by the $p(d,\text{pN})$ and $p(p,2p)$ reactions, was 1.1 MeV and 1.5 MeV for the (p,pn) and $(p,2p)$ processes, respectively. Known resonances, ${}^5\text{He}$ and ${}^{10}\text{He}$, were clearly observed. Two states in ${}^{10}\text{Li}$ were observed. From the characteristics of the (p,pn) reaction, two states at $S_n = 0.42\text{ MeV}$ and 5.2 MeV were assigned as $(\nu p_{1/2})^{-1}$ and $(\nu p_{3/2})^{-1}$ hole states, respectively. A peak for the $p({}^6\text{He},\text{pp}){}^3\text{H}$ process was assigned as the ${}^5\text{H}$ resonance.

By gating on the separation-energy distribution, the momentum distribution of the valence neutron in a specific orbit was obtained (Fig. 2). The momentum resolution evaluated by the $p(p,2p)$ reaction was 8 MeV/c (rms) in one direction. It was noticed that the momentum distribution was isotropic in the projectile rest frame. The momentum distribution obtained by the present method is roughly free from the final-state interaction, which was turned out to be the dominant process in the projectile fragmentation processes.²⁾ By comparing the width of the neutron momentum distribution and that of the core fragment in the projec-

tile fragmentation processes, the momentum correlation $(\vec{p}_1 \cdot \vec{p}_2)$ between two valence neutrons in ${}^6\text{He}$ and ${}^{11}\text{Li}$ was turned out to be negative, indicating that the two valence neutrons are moving in the opposite direction.

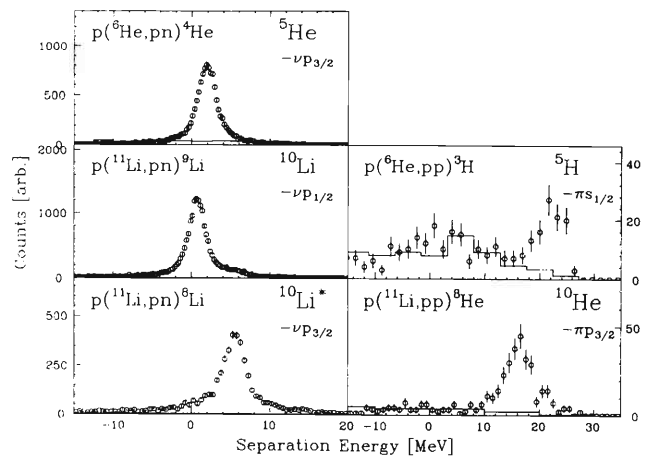


Fig. 1. Separation-energy spectra for the (p,pn) and $(p,2p)$ processes from ${}^6\text{He}$ and ${}^{11}\text{Li}$. Contribution from ${}^{12}\text{C}$ in a CH_2 target is shown by a solid histogram.

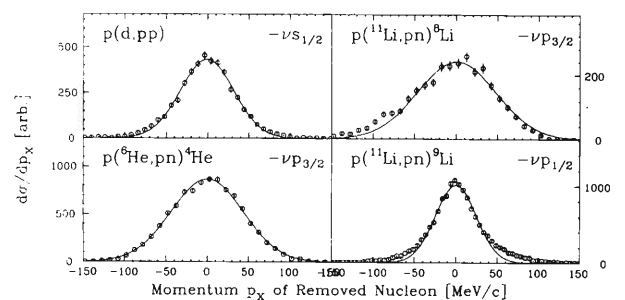


Fig. 2. Momentum distributions of valence neutron. Gaussian fittings are shown by solid lines.

References

- 1) G. Jacob and T. Maris: Rev. Mod. Phys. **38**, 121 (1966).
- 2) M. Zinser et al.: Phys. Rev. Lett. **75**, 1719 (1980).

* Department of Physics, University of Tokyo

Reaction Cross Sections Measured for ^8B to Obtain Its Density Distribution

M. Fukuda, M. Mihara, T. Fukao,* M. Tanigaki, T. Onishi, K. Matsuta, Y. Nojiri, T. Minamisono, T. Ohtsubo, S. Fukuda, S. Ito, T. Kobayashi, S. Momota, A. Ozawa, T. Suzuki, I. Tanihata, K. Yoshida, M. Ishihara, and T. Nakamura

[NUCLEAR REACTION $\text{Be}(^{12}\text{C}, ^8\text{B})$; $E = 135$ MeV/nucleon; Measured ^8B reaction cross sections; Deduced ^8B density distribution.]

In order to investigate the density distribution of ^8B , we measured the reaction cross sections for ^8B on Be, C, and Al targets at the beam energies of 40 and 60 MeV/nucleon using the transmission method. The unstable nuclear beam of ^8B was produced by the projectile fragmentation of the 135 MeV/nucleon ^{12}C primary beam provided from the RIKEN Ring Cyclotron; the nuclide selection was made through the RIPS (RIKEN Projectile fragment Separator). The beam energy of 40 MeV/nucleon was chosen to gain the large nucleon-nucleon total cross sections that are about three times of the ones at the LBL energy of 790 MeV/nucleon.¹⁾ At 60 MeV/nucleon the cross section is about in the middle of the values at these two energies. The ^8B secondary-beam energy was roughly adjusted by a combination of the thickness of production target and that of wedge degrader at the first focus point of the RIPS. The fine tuning of the beam energy was done by adjusting the magnetic field of the second dipole of the RIPS.

The particle counting and identification before the reaction target was done by a thin Si counter for ΔE measurement and three parallel plate avalanche counters (PPACs) that provide the time and position information. Downstream of the reaction target, the identification was made from ΔE taken by Si counters and from time-of-flight (TOF) taken in between the PPAC and plastic counters. The thickness of the reaction targets were chosen so that the energy loss in the target was about 20 MeV/nucleon for both energies.

In order to connect the experimental σ_R to the density distribution of ^8B , we employed the Glauber-type calculation²⁾ with an enhancement factor at the intermediate energy range. This factor was deduced from the σ_R data for other stabler nuclides such as ^6Li , ^7Be , and ^{12}C , whose densities can well reproduce the interaction cross sections at high energies.¹⁾ We assumed a shape of the density distribution of ^8B and fitted it to the σ_R data including the high-energy data through the Glauber-type calculation. The assumed shape for protons in ^8B was a Gaussian at the core and a Yukawa-square tail at the outer region, while that for neutrons was a Gaussian with the same width as proton core. In the χ^2 -fitting procedure unrealistic tail slopes corresponding to negative binding energies were rejected.

The preliminary result is shown by the shaded region in Fig. 1, where the error is indicated as the width of the region. The density calculated by Kitagawa and Sagawa³⁾ (KS) is also shown in the same figure by the solid line. The present density deduced from the experimental σ_R is in agreement with the theoretical calculation though it seems to have a little bit smaller amplitude at the tail part.

In addition to the reaction cross sections, the fragmentation cross sections $\sigma_F(^8\text{B} \rightarrow ^7\text{Be})$ were observed and found to be quite large as about 15% of the reaction cross sections. If the tail shown in Fig. 1 consists of proton and $\sigma_F(^8\text{B} \rightarrow ^7\text{Be})$ is governed by the probability of the removal of the tail proton, $\sigma_F(^8\text{B} \rightarrow ^7\text{Be})$ becomes nearly equal to $\sigma_R(^8\text{B}) - \sigma_R(^7\text{Be})$. Using the experimental values of $\sigma_R(^8\text{B})$ and $\sigma_R(^7\text{Be})$, the fragmentation cross sections, $\sigma_F(^8\text{B} \rightarrow ^7\text{Be})$, were found to be almost equal to $\sigma_R(^8\text{B}) - \sigma_R(^7\text{Be})$. This fact supports the existence of the proton tail in the ^8B density distribution as shown in Fig. 1

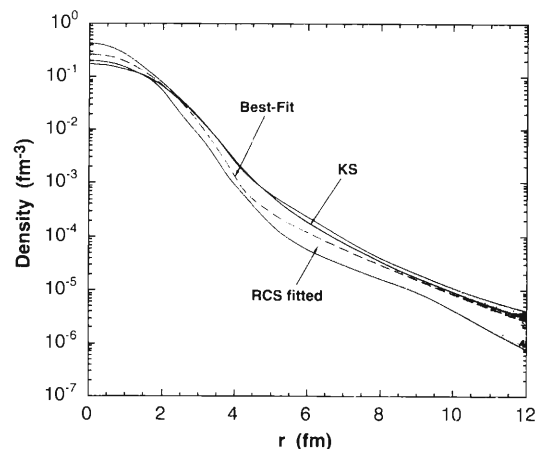


Fig. 1. Density distribution of ^8B deduced by a fitting to the σ_R data (shaded region) and by the calculation in Ref. 3 (solid line denoted as KS).

References

- 1) I. Tanihata et al.: Phys. Lett. B **206**, 592 (1988).
- 2) P. J. Karol: Phys. Rev. C **11**, 1203 (1975).
- 3) H. Kitagawa and H. Sagawa: Phys. Lett. B **299**, 1 (1993).

* Present address: Mitsubishi Electric Inc.

Momentum Distribution of ${}^7\text{Be}$ Produced through ${}^8\text{B}$ Fragmentation

M. Mihara, M. Fukuda, T. Fukao, M. Tanigaki, T. Onishi, K. Matsuta, Y. Nojiri, T. Minamisono, T. Ohtsubo, M. Ishihara, T. Nakamura, S. Fukuda, S. Ito, T. Kobayashi, S. Momota, A. Ozawa, T. Suzuki, I. Tanihata, K. Yoshida, and Y. Ogawa

[NUCLEAR REACTION $\text{Be}({}^{12}\text{C}, {}^8\text{B})$; $E = 135$ MeV/nucleon, Be , C , $\text{Al}({}^8\text{B}, {}^7\text{Be})$; $E = 38$ and 60 MeV/nucleon, $\text{Si}({}^8\text{B}, {}^7\text{Be})$ and Be , C , $\text{Al}({}^7\text{Be}, {}^6\text{Li})$; $E = 50$ MeV/nucleon, Measured momentum distributions.]

The momentum distribution of ${}^7\text{Be}$ produced through fragmentation of the ${}^8\text{B}$ which is a proton-halo candidate was measured. The momentum distribution is sensitive to the spatial wave function of a removed proton near the nuclear surface as well as the reaction cross sections of ${}^8\text{B}$ at several tens of MeV/nucleon, which have shown a large enhancement.¹⁻³⁾

We measured both the longitudinal and transverse momentum distributions of ${}^7\text{Be}$ on a thin Si target at 50 MeV/nucleon. The transverse distributions were measured also for thick Be, C, and Al targets at 38 and 60 MeV/nucleon. The ${}^8\text{B}$ beam was produced through the ${}^{12}\text{C} + {}^9\text{Be}$ collision with a 135 MeV/nucleon ${}^{12}\text{C}$ beam provided by the RIKEN ring cyclotron, and was separated by RIPS. A schematic view of the experimental setup is shown in Fig. 1. The ${}^7\text{Be}$ nuclei were identified by a combination of their energy loss in thin Si detectors and a large plastic scintillator, with the time of flight (TOF) between the parallel-plate avalanche counters (PPACs) and the plastic scintillator. The Si detectors D1 and D2 were used as targets when a reaction target was removed, and then the next detectors (D2 and/or D3) were used for particle identification. The longitudinal momentum of ${}^7\text{Be}$ was obtained from TOF and the transverse one was from the horizontal positions of PPACs and from the plastic scintillator which gives light outputs with both left and right sides.

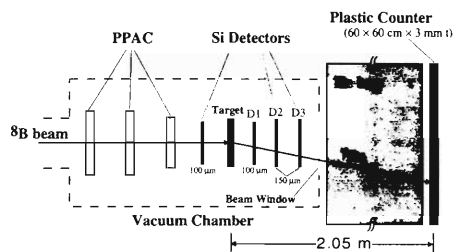


Fig. 1. Schematic view of the experimental setup.

Typical momentum spectra of ${}^7\text{Be}$ are shown in Fig. 2. A Lorentzian function was fitted to each spectrum. The width obtained for the longitudinal distribution is preliminarily 75 ± 8 MeV/c, which is in agreement with the previous data measured at 1471 MeV/nucleon with C, Al and Pb targets by Schwab et al.⁴⁾ The result at 38 MeV/nucleon with Si tar-

get by Negoita et al.³⁾ is about 20% larger than the present result. The widths for the transverse momentum distributions are about 110 MeV/c independent on the energy and targets within the uncertainties of 10%, which are about 40% larger than that for the longitudinal one. The present values are, however, much smaller than the value expected from Goldhaber theory⁵⁾ (~ 210 MeV/c) that accounts for the momentum distribution of stable nuclei. The transverse momentum spectra of ${}^6\text{Li}$ after the break up of ${}^7\text{Be}$ on Be, C, and Al targets at 50 MeV/nucleon were also measured. A typical result of ${}^6\text{Li}$ for Be target is inserted in Fig. 2. The width 217 ± 20 MeV/c from a Gaussian fitting is in good agreement with the Goldhaber theory.

The experimental momentum spectra of ${}^7\text{Be}$ were compared with the calculation within the Glauber theory. In the calculation, the proton radial wave function with a long tail obtained from the nucleon density distribution of ${}^8\text{B}$, which was in turn deduced from the reaction cross section data,²⁾ was used. The result is consistent with the experiment as shown by solid line in Fig. 2. This supports the existence of a proton halo in ${}^8\text{B}$.

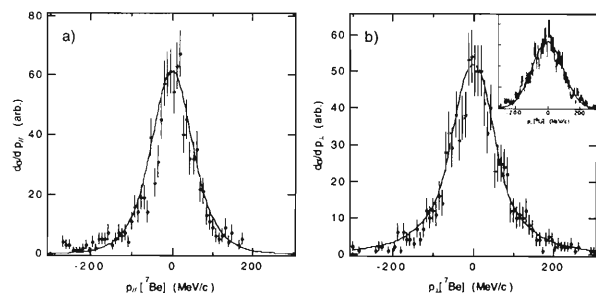


Fig. 2. a) Longitudinal and b) transverse momentum distributions of ${}^7\text{Be}$ at 50 MeV/nucleon on a Si target. The solid line shows the Glauber calculation. The insert shows the transverse momentum distribution of ${}^6\text{Li}$.

References

- 1) R. E. Warner et al.: Phys. Rev. C **52**, R1166 (1995).
- 2) M. Fukuda et al.: OULNS Annual Report 1995, p. 47 (1995).
- 3) F. Negoita et al.: Phys. Rev. C **54**, 1787 (1996).
- 4) W. Schwab et al.: Z. Phys. A **350**, 283 (1995).
- 5) A. S. Goldhaber: Phys. Lett. B **53**, 306 (1974).

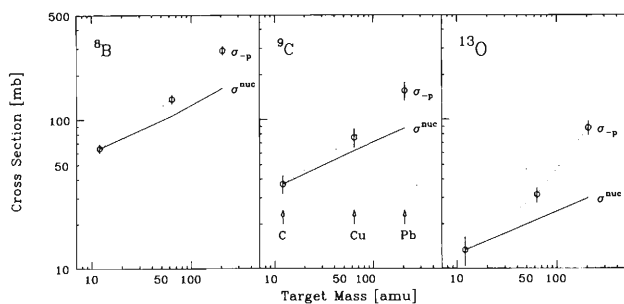
Electromagnetic Dissociation of ^8B at 2A GeV

T. Kobayashi, A. Ozawa, K. Yoshida, I. Tanihata, K. Matsuta, D. Olson,* and H. Wieman*

[NUCLEAR REACTIONS $^8\text{B}, ^9\text{C}, ^{13}\text{O} + \text{C}, \text{Cu}, \text{Pb}$; $E/A = 2$ GeV; Electromagnetic dissociation.]

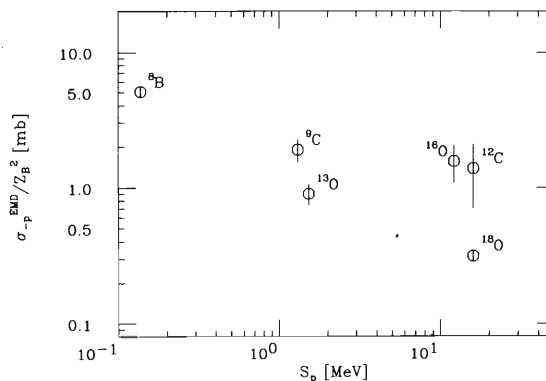
Interaction of high-energy nuclear beams with a high-Z target is characterized by the interaction of virtual photons from the target with the projectile. This process, called the electromagnetic dissociation (EMD), provides the information concerning the Giant dipole resonance in the projectile. In order to study the GDR in β -unstable proton-rich nuclei, we have studied the EMD of proton-rich projectiles. Experiments were performed at LBL, using secondary nuclear beams of ^8B , ^9C , and ^{13}O at 2 A GeV. Targets used were C, Cu, and Pb. Particles in the final state were measured, inclusively or exclusively, by the HISS spectrometer composed of drift chambers and plastic-scintillator hodoscopes.

Firstly, one-proton-removal cross sections (σ_{-p}) from the projectile were measured inclusively by detecting each of the leading fragments ^7Be , ^8B , and ^{12}N , produced from the breakup of ^8B , ^9C , and ^{13}O projectiles, respectively. Target-mass dependences are shown in Fig. 1. The cross section caused by the nuclear interaction (σ^{nuc}) was estimated by scaling the cross sections into He isotopes, as shown by solid lines in Fig. 1. The EMD cross sections (σ^{EMD}) were obtained by a subtraction: $\sigma^{\text{EMD}} = \sigma_{-p} - \sigma^{\text{nuc}}$.

Fig. 1. Target-mass dependence of σ_{-p} .

The EMD cross sections on a Pb target, normalized by the square of the projectile charge Z_B , are shown in Fig. 2 as a function of the proton-separation energy (S_p), together with those of ^{12}C , ^{16}O , and ^{18}O measured at the same energy.¹⁾ In contrast to the EMD cross sections of neutron-rich nuclei, dependence on the separation energy is small. The large enhancement by the low-energy continuum were not observed, presumably due to the Coulomb and centrifugal barriers.

Secondly, the breakup of ^8B into multi-particle final states ($^7\text{Be} + p$, $^6\text{Li} + 2p$, $^4\text{He} + ^3\text{He} + p$,

Fig. 2. Normalized σ^{EMD} on a Pb target as a function of S_p .

$^4\text{He} + d + 2p$) were measured on C and Pb targets. The Q-value dependence is shown in Fig. 3. Firstly, one-proton-removal cross section ($^8\text{B} \rightarrow ^7\text{Be} + p$) on a C target is reduced by about a factor of 3 compared with the inclusive cross section, due to the large contribution from the pion production. Secondly, it is noted that the Q-value dependence is characterized by an inverse slope of 4 MeV, except for the process into $^7\text{Be} + p$ on a Pb target. The nuclear part of the cross section was estimated using the average ratio of $\sigma_{-p}(\text{Pb})/\sigma_{-p}(\text{C})$. The EMD cross section $\sigma^{\text{EMD}}(^8\text{B} + \text{Pb} \rightarrow ^7\text{Be} + p)$ obtained by this method is 120 mb, which agrees well with $\sigma^{\text{EMD}}(^8\text{B} + \text{Pb} \rightarrow ^7\text{Be} + X)$ of 127 mb from the inclusive measurement.

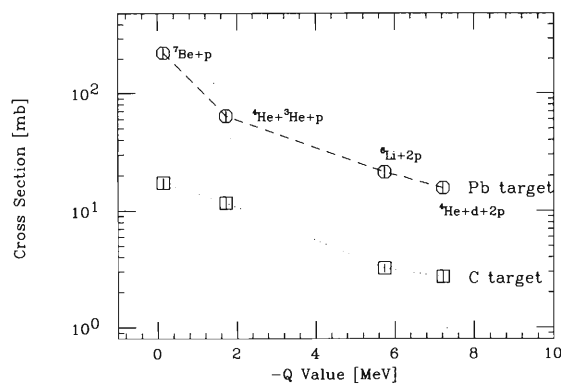


Fig. 3. Q-value dependence of breakup cross sections.

References

- 1) D. L. Olson et al.: Phys. Rev. C **28**, 1602 (1983).

* Nuclear Science Division, Lawrence Berkeley Laboratory, U.S.A.

Nuclear Radii of Na and Mg Isotopes

T. Suzuki, H. Geissel,* O. Bochkarev,** L. Chulkov,** N. Fukunishi, M. S. Golovkov,**
 D. Hirata, H. Irnich,* Z. Janas,* H. Keller,* T. Kobayashi, G. Kraus,* G. Münzenberg,*
 S. Neumaier,* F. Nickel,* A. Ozawa, A. Piechaczek,* E. Röckl,*
 W. Schwab,* K. Sümmerer,* K. Yoshida, and I. Tanihata

[Heavy-ion collision, Radioactive beam, *rms* radii]

The effective root-mean-square matter radii ($\tilde{r}_m \equiv \langle r_m^2 \rangle^{1/2}$) of ${}^A\text{Na}$ ($A = 20\text{--}23, 25\text{--}32$) and ${}^A\text{Mg}$ ($A = 20, 22, 23, 27, 29\text{--}32$) were deduced from the measured interaction cross sections (σ_I). The experiment was performed at the projectile fragment separator facility at GSI. We related σ_I to \tilde{r}_m by a Glauber model employing the Fermi-type distribution: $\rho(r) = \rho_0/[1 + \exp((r-r_0A^{1/3})/\alpha)]$.

We did not assume the existence of a neutron skin in the present analysis. The manner of the analysis is slightly different from the previous report, where we observed a growth of a neutron skin as a function of the Fermi-energy difference, $S_p - S_n$.¹⁾ We calculated the loci for constant \tilde{r}_m and for constant σ_I in the α vs. r_0 plane. Thus-determined \tilde{r}_m of Na isotopes agreed with those calculated from neutron-skin data by: $A\tilde{r}_m^2 = Z\tilde{r}_p^2 + N\tilde{r}_n^2$ within error bars.²⁾ Therefore, measurements of \tilde{r}_m themselves are not sufficient to discuss a neutron skin. However, the \tilde{r}_m of Mg isotopes do not contradict from what we observed in Na isotopes as seen in Fig. 1.

In Fig. 1, the spherical nuclear radii normalized by $A^{1/3}$ are plotted against $S_p - S_n$. The spherical radii can be written as:³⁾ $\langle r_m^2 \rangle \equiv \langle r_m^2 \rangle [1 + (5\pi/4)\langle \beta_2^2 \rangle]$. This assumes that the nuclear shapes can be parametrized as rotational ellipsoids with the deformation being limited to the quadrupole contribution. The deformation parameter $\langle \beta_2 \rangle$ of the nuclei under consideration were taken from relativistic mean field (RMF) calculation. The common tendency of decreasing spherical radii as the function of $|S_p - S_n|$ is seen for both Na and Mg isotopes. This fact can be explained by a model where the valence nucleons are responsible for the changes in nuclear radii.⁴⁾ The spherical part of the nucleus decreases when neutrons are added in the $d_{5/2}$ subshell and increases when $s_{1/2}$ subshell is filled. The fact that the $\tilde{r}_m^2 A^{-1/3}$ takes minimum around $S_p - S_n \approx 0$ veri-

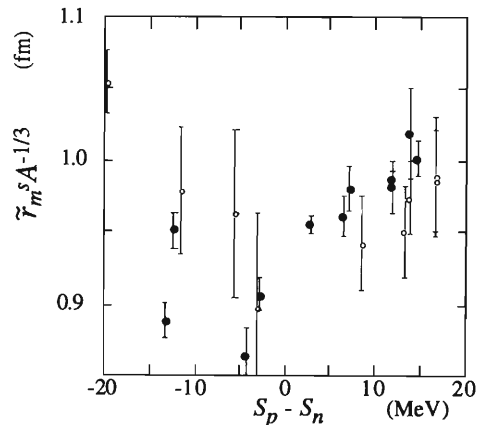


Fig. 1. Dependence of $\tilde{r}_m^2 A^{-1/3}$ on the difference between the minimal energies necessary to remove one proton or neutron from a nucleus of Na (closed circles) or Mg (open circles) isotopes.

fies that no neutron/proton skin is formed in stable nuclei. The deviation of $S_p - S_n$ from zero may be explained by the difference of Coulomb displacement energy, $\Delta E_c = 6Ze^2/(5\tilde{r}_m)$. Note that the tendency did not change essentially except for the steepness of the radius of curvature when we took another deformation parameter by Möller et al.⁵⁾

The present data thus support the idea of growth of neutron skin not only in Na but also in Mg isotopes. A thick proton skin of 0.4 fm in ${}^{20}\text{Mg}$ is reported.⁴⁾

References

- 1) T. Suzuki et al.: Phys. Rev. Lett. **75**, 3241 (1995).
- 2) T. Suzuki et al.: in preparation.
- 3) G. Fricke et al.: Phys. Rev. C **45**, 80 (1982).
- 4) L. Chulkov et al.: Nucl. Phys. A **603**, 219 (1996).
- 5) P. Möller et al.: At. Data Nucl. Data Tables **59**, 185 (1995).

* GSI, Darmstadt, Germany

** Kurchatov Institute, Moscow, Russia

Beta Decay of ^{11}Li

K. Yoneda, N. Aoi, H. Miyatake, H. Ogawa, Y. Yamamoto, E. Ideguchi, T. Kishida, T. Nakamura, M. Notani, H. Sakurai, T. Teranishi, H.-Y. Wu, S. Yamamoto, Y. Watanabe, A. Yoshida, and M. Ishihara

[RADIOACTIVITY $^{11}\text{Li}(\beta^-)$, measured β -delayed neutron, deduced $\log ft$, and deduced Ex in ^{11}Be .]

We have investigated β decay of the neutron drip-line nucleus ^{11}Li . For determination of the decay scheme of ^{11}Li , detection of the delayed neutrons as well as γ rays is critical because the β -delayed neutron emission probability of ^{11}Li is large ($P_{1n} = 85\%$) reflecting its large Q_β -value (20.68 MeV) and small neutron separation energy of the daughter nucleus ^{11}Be (0.504 MeV). We have performed for the first time a β -n- γ triple coincidence measurement and have determined the decay scheme associated with a single neutron and/or γ -ray emission.

^{11}Li beam was produced by the projectile-fragment separator RIPS and was implanted into the stopper material (1 mm-thick Si detector). The emitted β rays were detected by ΔE - E plastic-scintillator telescopes placed above and below the stopper. Delayed γ rays were detected by a Ge detector and two NaI(Tl) scintillators. For delayed neutron detection, two sets of plastic scintillators were used to cover wide range of neutron energies: one for high-energy neutrons above about 1 MeV, the other for low-energy neutrons below 1 MeV.¹⁾ Neutron energy was determined from its time-of-flight (TOF), which was deduced from the difference between the detection times of β ray and neutron.

The main panel of Fig. 1 shows the neutron TOF spectrum obtained by the high-energy neutron detectors and the inset by the low-energy neutron detectors. Eight neutron groups labeled by the number 1 to 8 were observed. In the γ -ray spectrum obtained in coincidence with the β ray, five peaks associated with the decay of ^{11}Li were identified.

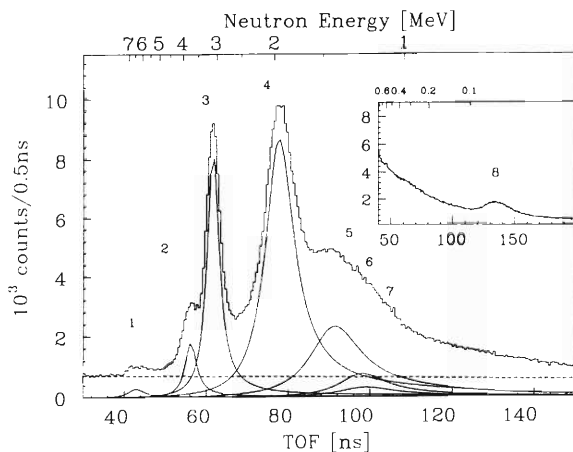


Fig. 1. TOF spectra of the neutron emitted in the β decay of ^{11}Li (see text in detail).

From the β -n- γ triple coincidence analysis, we determined the decay scheme as shown in Fig. 2. The branch leading to the state of ^{11}Be ($Ex = 8.03 \pm 0.05$ MeV) is newly identified. From the obtained $\log ft$ values indicated in Fig. 2, all the observed transitions are classified as the Gamow-Teller (GT) transitions. The spin and parity of the final states of ^{11}Be are confined to $1/2^-$, $3/2^-$ or $5/2^-$ from the selection rule of the GT transitions. Among the observed five states of ^{11}Be , the three states ($Ex = 2.69, 3.96, 8.03$ MeV) have significant neutron emission components leading to the 0^+ ground state of ^{10}Be . Since the neutron emissions connect different parity states, it is most probable that these neutron emissions are due to p -wave neutrons. We can thus assign the spin and parity of these neutron emitting states to be $1/2^-$ or $3/2^-$.

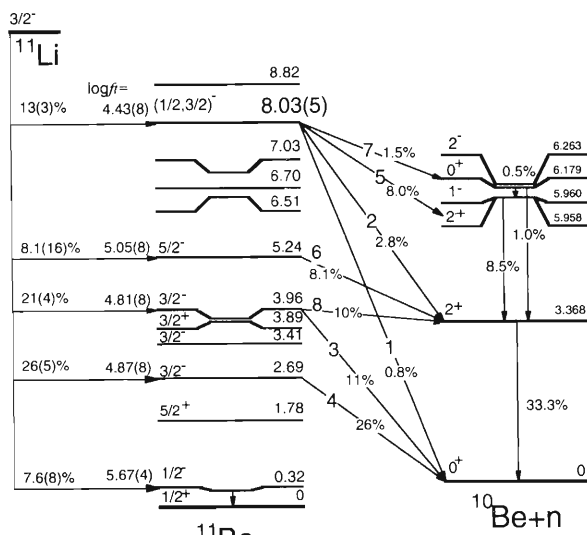


Fig. 2. Deduced ^{11}Li decay scheme. Excitation energies are indicated in MeV.

The $\log ft$ value of the GT transition to the first excited state of ^{11}Be ($J^\pi = 1/2^-$, $Ex = 0.32$ MeV) is sensitive to the wave function of the two halo neutrons of ^{11}Li .²⁾ The wave function of the halo neutrons can be described as $\alpha|(2s_{1/2})^2_v\rangle + \beta|(1p_{1/2})^2_v\rangle$. From the present $\log ft$ value, 5.67 ± 0.04 , $|\beta|^2$ is deduced to be $51 \pm 6\%$.

References

- 1) K. Yoneda et al.: RIKEN Accel. Prog. Rep. **29**, 182 (1996).
- 2) T. Suzuki and T. Otsuka: Phys. Rev. C **50**, 555 (1994).

β -Delayed Neutron Decay of Spin Polarized ^{17}B

H. Miyatake, Y. Yamamoto, T. Shimoda, S. Tanimoto, S. Mitsuoka, H. Ueno, H. Izumi,
H. Ogawa, K. Asahi, N. Aoi, Y. Mizoi, M. Notani, K. Yoneda, M. Ishihara,
E. Ideguchi, A. Ozawa, T. Kubo, and T. Kishida

[RADIOACTIVITY spin polarized $^{17}\text{B}(\beta^-)$, Measured β -delayed neutrons, γ -rays]

The nucleus ^{17}B is known as one of halo nuclei on the neutron drip-line and its valence proton occupies a p-shell, different from the valence neutrons in a sd-shell. The final states of allowed β -transitions are non-normal parity states in ^{17}C . Hence, we can obtain systematic information about the strengths of cross-shell interactions by the decay study of ^{17}B together with the magnetic moment experiment.¹⁾ In the previous measurement,²⁾ the decay scheme was constructed assuming the ground state in ^{16}C as a final state of delayed neutron transitions. This assumption should be confirmed experimentally. In our measurement, therefore, all possible transitions to the excited states in ^{16}C were studied by detecting the subsequent γ -rays. Moreover, J^π of excited states in ^{17}C were studied to determine the decay scheme clearly. A new experimental method of J^π assignment, which was deduced from detection of the asymmetric β -rays coincident with respective delayed particles using the polarized parent nucleus,³⁾ was applied. The polarized ^{17}B obtained in the same manner of Ref. 1 was implanted into the Pt-foil. The polarization of individual β -transition was measured by applying the β -NMR method. The energies of neutrons were measured by means of the time of flight method with two different sets of plastic scintillators; one set had 1.5 m flight path for the measurement of high-energy neutrons and another set had 0.5 m for the low-energy neutron measurement, respectively, as shown in Fig. 1. A clover Ge detector (4×470 cc) and NaI(Tl) scintillators (4×960 cc) were placed 5 cm from the Pt-foil to observe the γ -rays with a high detection efficiency. Figure 2 shows the energy spectrum of γ -rays, measured by the Ge detector. The γ -ray peak of 1.77 MeV, which corresponds to the excitation energy of the first 2^+ state in ^{16}C , was clearly found. From the lifetime analysis, the half life of this transition was 5.5(6) ms, which agrees with the half life of ^{17}B [$T_{1/2} = 4.9(2)$ ms].²⁾ Therefore, it indicates that the 2^+ state in ^{16}C is fed by some delayed neutrons. The more detailed analysis for polarization of the individual β -transition as well as neutron TOF spectrum is in progress. A revised decay scheme will be constructed including these results.

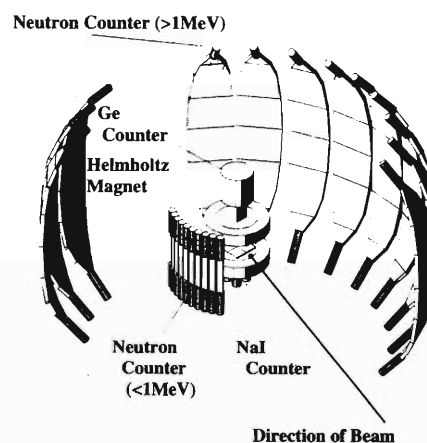


Fig. 1. A schematic drawing of the detector set-up around the Pt-foil (not shown). The clover Ge detector and NaI(Tl) scintillators are located inside the Helmholtz magnet.

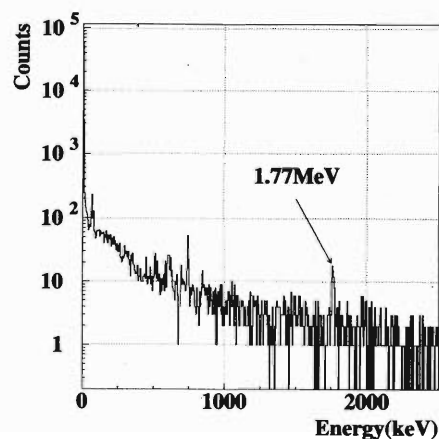


Fig. 2. The γ -ray spectrum coincident with the β -ray and neutron signals.

References

- 1) H. Ueno et al.: Phys. Rev. C **53**, 2142 (1996).
- 2) G. Raimann et al.: Phys. Rev. C **53**, 453 (1996).
- 3) H. Miyatake et al.: RIKEN Accel. Prog. Rep. **29**, 64 (1996).

Measurement of β -decay Branching Ratio of ^{17}Ne into the First Excited State of ^{17}F

A. Ozawa, M. Fujimaki, S. Fukuda, S. Ito, H. Kitagawa, T. Kobayashi, G. Kraus, S. Momota, G. Münzenberg, T. Suzuki, I. Tanihata, and K. Yoshida

[RADIOACTIVITY $^{17}\text{Ne}(\beta^+ \gamma)$; Measured β -decayed γ , Deduced branching ratios]

The β -decay branching ratio of ^{17}Ne into the first excited state of ^{17}F has been measured by a direct method. In the previous report,¹⁾ the motivation and experimental setup for the present experiment were described in detail; so that only the experimental results and discussions are described here.

The branching ratio with $E_\gamma = 495$ keV (denoted by $Br(495)$) was deduced by the following equation:

$$N_\gamma(495) \times \varepsilon_{\text{time_bin}} = \varepsilon \Omega(495) \times Br(495) \times N_{\text{beam}}(^{17}\text{Ne}),$$

where $N_\gamma(495)$ is the peak intensity of the $E_\gamma = 495$ keV, $\varepsilon_{\text{time_bin}}$ is the correction for the time used for the measurement since we observed γ -rays only in the beam-off period, $\varepsilon \Omega(495)$ is the 495 keV γ -ray detection efficiency, and $N_{\text{beam}}(^{17}\text{Ne})$ is the number of ^{17}Ne implanted in the stopper. The $\varepsilon_{\text{time_bin}}$ can be calculated using the known $T_{1/2}$ of ^{17}Ne and the beam-on and -off cycle. Since no excited state feeds to the first excited state in ^{17}F , the deduced $Br(495)$ corresponds to the β -decay branching ratio of ^{17}Ne into the first excited state of ^{17}F . The $\varepsilon \Omega(495)$ was deduced from the on-line detection efficiency, which was measured using ^{10}C beam. For the deduction, energy dependence on efficiency determined by point γ -ray sources was used. Since the branching ratios obtained by using two Ge detectors were consistent each other within the error bars, we determined a branching ratio of $1.44 \pm 0.16\%$ by averaging the two values.

The present value of branching ratio determined above is consistent with the previous one ($1.65 \pm 0.16\%$)²⁾ within their error bars. From the branching ratio, we have deduced the β -decay ft value to obtain $\log ft = 6.43 \pm 0.07$. The β -decay branching ratio for the corresponding state of ^{17}N , the mirror nuclei of ^{17}Ne , is well known. Thus, we have deduced the ft value for ^{17}N in the same way. Using the ft values for ^{17}Ne and ^{17}N , we obtained the asymmetry given by the δ -value defined by $\delta = (ft)^+ / (ft)^- - 1$, where $(ft)^+$ and $(ft)^-$ are the ft values for positron and electron decays, respectively. The δ -value obtained in the present study is -0.57 ± 0.10 . This value shows a large deviation from zero, thus suggesting an anomalous nuclear structure for the pair.

In order to understand the large anomaly, we performed theoretical calculations for the β -decay strength, as follows. The δ is given by the overlapping of the valence nucleon in the initial nuclei and a core part in the final nuclei. In our calculations, the

valence nucleon of the initial nuclei can be described by only the configuration of the $2s_{1/2}$ and $1d_{5/2}$ orbits. Thus, the observed δ is sensitive to the fraction of the $2s_{1/2}$ component in the valence nucleon and to the radial part of the component. The wave functions obtained by the spherical Skyrme Hartree-Fock equations with the SGII interaction are used, except for the valence nucleons. The wave functions of the valence nucleons are obtained in the Woods-Saxon potential, whose depth is adjusted in order to reproduce the empirical separation energies: for example, 0.48 MeV (a half of the empirical S_{2p}) for ^{17}Ne , and 4.19 MeV (a half of the empirical S_{2n}) for ^{17}N . We performed this procedure for both the $2s_{1/2}$ and $1d_{5/2}$ orbits. Thus, in our calculations δ can be given by fractions of the $2s_{1/2}$ component in ^{17}Ne and ^{17}N . The results of calculation are shown in Fig. 1. In the figure, the calculated δ is shown as a function of the fraction of $2s_{1/2}$ component for the valence nucleons in ^{17}Ne and ^{17}N . The δ observed in the present experiment is indicated by the hatched area on the figure. The area is located at the region where the fraction of $2s_{1/2}$ component in ^{17}Ne is higher than that in ^{17}N by a factor of six. This supports the occurrence of an s - d inversion in the ^{17}Ne and ^{17}N mirror pair, as described in Ref. 3.

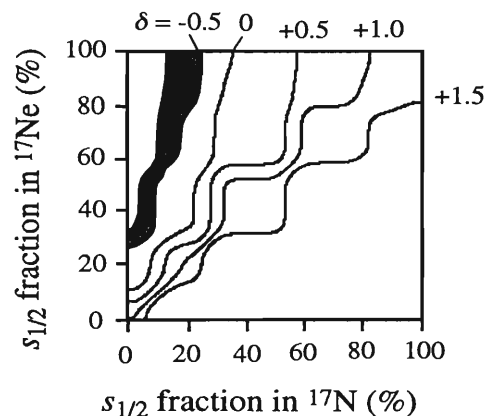


Fig. 1. Calculated δ as a function of the fraction of $2s_{1/2}$ component in ^{17}Ne and in ^{17}N .

References

- 1) A. Ozawa et al.: RIKEN Accel. Prog. Rep. **29**, 66 (1996).
- 2) M. J. G. Borge et al.: Phys. Lett. B **317**, 25 (1993).
- 3) A. Ozawa et al.: Phys. Lett. B **334**, 18 (1994).

Magnetic Moments of ^{17}N and $^{17}\text{B}^\dagger$

H. Ueno, K. Asahi, H. Izumi, K. Nagata, H. Ogawa, A. Yoshimi, H. Sato, M. Adachi, Y. Hori, K. Mochinaga, H. Okuno, N. Aoi, M. Ishihara, A. Yoshida, G. Liu, T. Kubo, N. Fukunishi, T. Shimoda, H. Miyatake, M. Sasaki, T. Shirakura, N. Takahashi, S. Mitsuoka, and W.-D. Schmidt-Ott

[NUCLEAR STRUCTURE: Magnetic moments, Ground state ^{17}N and ^{17}B]

The magnetic moments of ^{17}N and ^{17}B were measured by using spin-polarized radioactive nuclear beams which were obtained from the projectile fragmentation reaction. The result for the ^{17}N magnetic moment, $\mu(^{17}\text{N}) = (-0.352 \pm 0.002) \mu_N$, where μ_N is the nuclear magneton, shows an outward deviation from the Schmidt value. Hereafter, the experimental $\mu(^{17}\text{N})$ will be assigned a negative sign taken from the Schmidt value. By virtue of a simplifying feature of nuclear structure inherent in a $p_{1/2}$ -valence nucleus, the deviation is reliably attributed to admixing of the configurations in which two neutrons in the sd shell are coupled to $J^\pi = 2^+$. This interpretation is confirmed in standard shell-model calculations. In Fig. 1 the experimental $\mu(^{17}\text{N})$ value is compared with the results of shell-model calculations. The shell-model calculations were made with two different sets of effective interactions, "PSDMK"^{1,2)} and "PSDWBT"^{1,3)}. These calculations reproduce fairly well the experimentally inferred amount of 2^+ admixture, as well as the experimental magnetic moment itself.

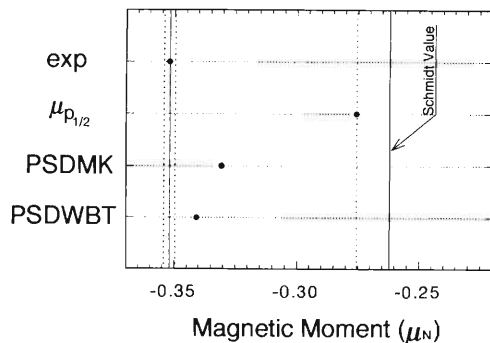


Fig. 1. Comparison of the experimental μ value (denoted by exp) for ^{17}N with the theoretical predictions. For the abbreviations denoting the theories, see text.

The magnetic moment for ^{17}B was determined to be $\mu(^{17}\text{B}) = (2.545 \pm 0.020) \mu_N$. Hereafter, the experimental $\mu(^{17}\text{B})$ will be assigned a positive sign taken from the Schmidt value. The experimental value and shell-model calculations of μ for ^{17}B are plotted in Fig. 2, together with those for odd-mass B isotopes. The result is substantially smaller than the $\pi p_{1/2}$

single particle value, and the shell-model calculations indicate that the quenching of μ largely stems from $J^\pi = 2^+$ configurations of the sd neutrons. The experimentally observed amount of quenching is, however, larger than the shell-model predictions, suggesting an enhanced contribution of the 2^+ neutron configurations. This result is explainable if the pairing energy (V_{01}) for neutrons in the sd shell of a neutron-rich nucleus is assumed to diminish by about 30%, as indicated by the curve of dotted line in Fig. 2. We also found that the use of the reduced pairing energy improves agreements in not only the magnetic moment but low-lying level energies of ^{17}N as well.

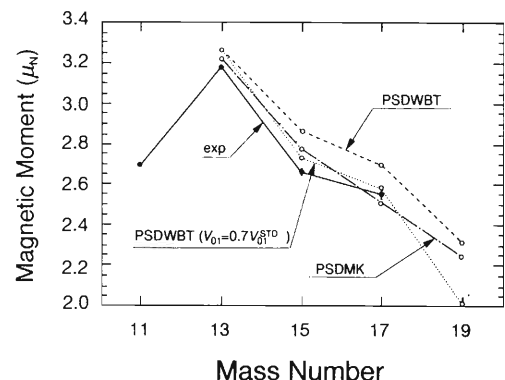


Fig. 2. The experimental and theoretical values of μ for the odd-mass B isotopes. exp: the experimental values. PSDWBT: the shell model calculations with the PSDWBT interaction. PSDWBT ($0.7V_{01}^{STD}$): the PSDWBT calculations with $|V_{01}|$ values reduced by 30% (i.e., the three matrix elements, $\langle(d_{5/2})^2|V|(d_{5/2})^2\rangle^{J^\pi=0^+}$, $\langle(s_{1/2})^2|V|(s_{1/2})^2\rangle^{J^\pi=0^+}$, and $\langle(d_{3/2})^2|V|(d_{3/2})^2\rangle^{J^\pi=0^+}$, are multiplied by a common factor 0.7). PSDMK: the shell model calculations with the PSDMK interaction.

References

- 1) B. A. Brown, A. Etchegoyen, and W. D. M. Rae: OXBASH, MSU Cyclotron Laboratory Report No. 524 (1986).
- 2) D. J. Millener and D. Kurath: Nucl. Phys. A **255**, 315 (1975).
- 3) E. K. Warburton and B. A. Brown: Phys. Rev. C **46**, 923 (1992).

[†] Condensed from the article in Phys. Rev. C **53**, 2142 (1996)

Quadrupole Moment of ^{23}Mg

K. Matsuta, T. Onishi, M. Fukuda, M. Mihara, M. Sasaki, T. Yamaguchi, T. Miyake,
K. Sato, K. Minamisono, Y. Nojiri, T. Minamisono, T. Ohtsubo, A. Ozawa, S. Fukuda, S. Momota,
K. Yoshida, T. Suzuki, T. Kobayashi, I. Tanihata, G. F. Krebs,*
J. R. Alonso,* and T. J. M. Symons*

[NUCLEAR STRUCTURE: Nuclear magnetic resonance,
Measured quadrupole moment of ^{23}Mg ground state.]

The quadrupole(Q) moment is an important nuclear property for the study of the nuclear structure, especially for the halo structure of proton-rich nuclei.¹⁾ As a step toward the systematic studies, the Q moment of ^{23}Mg ($I^\pi = 3/2^+$, $T_{1/2} = 11.3$ s) has been measured for the first time using combined technique of the polarized nuclear beams and β -NMR at RIKEN.

Experimental procedure was similar to the previous works.^{1,2)} A 100 A MeV ^{24}Mg beam extracted from the RIKEN ring cyclotron was used to bombard a 1-mm thick Be target. Considering energy loss in the target, the average beam energy was 91 A MeV. The polarized ^{23}Mg fragments emerging from the target at $1.5^\circ \pm 0.6^\circ$ were separated and momentum analyzed by the RIPS (RIKEN Projectile fragment Separator). Momentum window was set at $\Delta p/p = (1.5 \pm 0.5)\%$ relative to the beam velocity. The separated ^{23}Mg nuclei were then implanted in a 500- μm -thick MgF_2 catcher placed in a magnetic field H_0 of 6.5 kOe. The c axis or the $\langle 110 \rangle$ axis of the MgF_2 (tetragonal) catcher was set parallel to H_0 . The polarization of ^{23}Mg was detected through the β -ray counting asymmetry.

For the efficient NMR measurement, NNQR (New Nuclear Quadrupole Resonance) method¹⁾ combined with the Adiabatic Fast Passage (AFP) method was used, where a set of 6 rf fields (a sequence of the 3 frequencies split by the eqQ interaction) was applied to invert the polarization. Split frequencies for given eqQ were programmed based on the known q and η . The programmed Δf , a half of the full split, is very close to $\Delta f = |(1 + \eta)eqQ/4h|$ or $|(1 - \eta)eqQ/4h|$ for $H_0 // c(V_{yy})$ or $H_0 // \langle 110 \rangle (V_{xx})$, respectively. Here, Larmor frequency $\nu_L = 1.7691$ MHz, $|eqQ(^{25}\text{Mg})/h| = (3.450 \pm 0.015)$ MHz, $\eta = 0.28 \pm 0.04$ and $Q(^{25}\text{Mg}) = (201 \pm 3)$ mb are given from the literature.

Two eqQ spectra were obtained as shown in Fig. 1 for two different crystal orientations. From the spectra, the eqQ coupling frequencies and the Q moment of ^{23}Mg were determined as shown in Table 1. The last column $V_{xx} + V_{yy} (= |V_{zz}|)$ in Table 1, is the most accurate because it is insensitive to the ambiguity of η .

The obtained Q moment $|Q(^{23}\text{Mg})| = (114.2 \pm 2.2)$

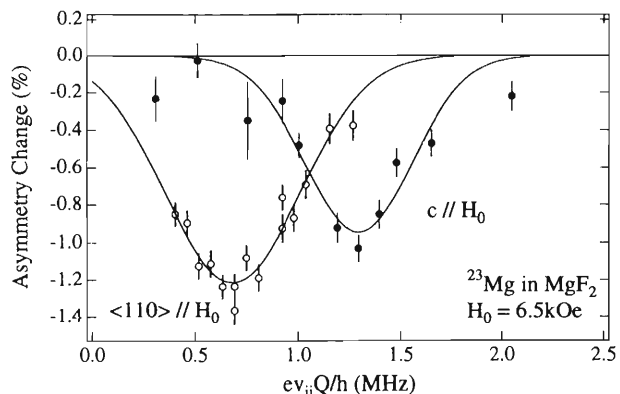


Fig. 1. eqQ spectra of ^{23}Mg in MgF_2 .

Table 1. The eqQ couplings and the Q moment of ^{23}F .

orientation	$c//H_0$	$\langle 110 \rangle // H_0$	
FG	V_{yy}	V_{xx}	V_{zz}
$ eV_{ii}Q/h $	1.282(17)	0.678(12)	1.960(21)
$Q^{23}\text{Mg}/Q^{25}\text{Mg}$	0.581(20)	0.546(32)	0.568(7)
	W.M. 0.571(17)		
$Q(^{23}\text{Mg})$ (mb)	114.8(3.8)		114.2(2.2)
Theory (mb)			
Cluster			118
Shell(Kuo)			122
Shell(PW)			112

mb is compared with the theoretical calculations as shown in Table 1. The Q moment values predicted from the cluster model³⁾ and from the shell model⁴⁾ with Kuo and PW interactions are in good agreement with the present experimental Q moment.

References

- 1) T. Minamisono et al.: Phys. Rev. Lett. **69**, 2058 (1992).
- 2) K. Matsuta et al.: Nucl. Phys. A **588**, 153c (1995); Nucl. Phys. A **377**, 361 (1982).
- 3) A. Kabir and B. Buck: Nucl. Phys. A **518**, 449 (1990).
- 4) B. J. Cole, A. Watt, and R. R. Whitehead: J. Phys. G: Nucl. Phys. **1**, 303 (1975).

* LBL, Berkeley, CA94720, U.S.A.

Asymmetry Parameter of ^{23}Mg Beta Decay

K. Matsuta, T. Onishi, M. Fukuda, M. Mihara, T. Yamaguchi, T. Miyake, M. Sasaki, Y. Nojiri, T. Minamisono, T. Izumikawa, M. Tanigaki, M. Nakazato, A. Harada, T. Ohtsubo, S. Fukuda, S. Momota, K. Yoshida, A. Ozawa, T. Suzuki, T. Kobayashi, I. Tanihata, J. R. Alonso,* G. F. Krebs,* and T. J. M. Symons*

[NUCLEAR STRUCTURE: Nuclear magnetic resonance, Measured]
 asymmetry parameter of ^{23}Mg ground state transition.

Study of the weak vector coupling constant G_V with mixed transitions provides a sharp test for CVC (conserved vector current) theory. The G_V is determined for mixed transitions from the asymmetry parameter A and the half life. In the early measurement, the A of ^{35}Ar showed apparent violation of CVC,¹⁾ i.e., the deduced G_V differed significantly (by 3%) from the one precisely determined for the pure Fermi transitions.²⁾ Although this long standing problem seems to have been solved by the recent data from the LBL group and from the Wisconsin group, the A 's of neutron and ^{19}Ne still show significant discrepancy. This may suggest incompleteness of our knowledge on the nuclear structure dependent correction, if it is not really a CVC violation. In order to clarify this interesting problem from the mass number dependence, the A of the ^{23}Mg ($I^\pi = 3/2^+$, $T_{1/2} = 11.32$ sec) β -decay has been measured in the present experiment.

Spin polarized beta-emitting ^{23}Mg fragment was produced through the projectile fragmentation process with the 91-AMeV ^{24}Mg beam on Be target. The ^{23}Mg fragments emerging from the target at $1.5^\circ \pm 0.6^\circ$ were selected by a slit and separated it out from the other various fragments using the RIPS (RIKEN Projectile Fragment Separator). The ^{23}Mg nuclei were then implanted into a thin Pt catcher (15–50 μm thick). The catcher was placed in a strong magnetic field H_0 of 2.15 kOe and was cooled down to 14 K to maintain the polarization produced in the projectile fragmentation process. The β -ray asymmetry AP (P : polarization) was measured by means of asymmetric β -ray emission for both ground state transition and the decay branch to the first excited state, which was tagged by the β -delayed γ rays ($E_\gamma = 440$ keV).

The β -ray asymmetries obtained from β -ray singles (AP_0) and the β - γ coincidence (AP_{ex}) with several different conditions are shown in Fig. 1a. Although the absolute AP values are different for different conditions, the ratio AP_{ex}/AP_0 consistently stays constant as shown in Fig. 1b. The average value of the ratio is

0.838 ± 0.009 . Correcting the β - γ angular correlation, β -ray scattering effect, and γ -ray background, the true ratio $A_{ex}/A_0 = 0.990 \pm 0.012$ was obtained. Since the transition to the excited state is pure Gamow-Teller, A_{ex} is precisely predicted to be $-3/5$. Thus the preliminary result for the asymmetry parameter was obtained as $A_0 = -0.606 \pm 0.007$.

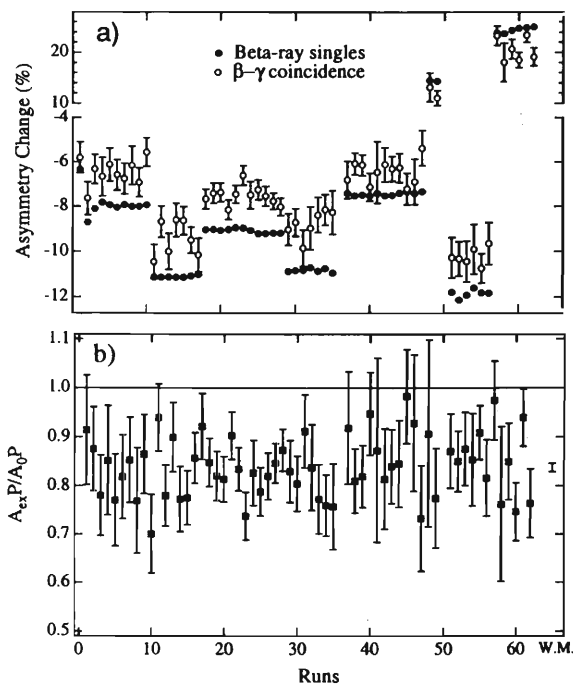


Fig. 1. Asymmetries for the β -ray single and β - γ coincidence events.

References

- 1) F. P. Calaprice, E. D. Commins, and D. A. Dobson: Phys. Rev. **137**, 1453 (1965).
- 2) J. C. Hardy and I. S. Towner: Nucl. Phys. A **254**, 221 (1975).

* LBL, Berkeley, CA94720, U.S.A.

Development of Polarized ^{129}Xe Solid for Polarizing Unstable Nuclei

H. Sato, M. Tsuda, A. Yoshimi, H. Izumi, H. Ogawa, N. Kurokawa, K. Sakai, M. Adachi, K. Asahi,
H. Okuno, T. Kubo, S. Fukuda, A. Yoshida, M. Ishihara, K. Yoneda, and M. Notani

[Nuclear magnetic moment, ^{129}Xe solid stopper]

Measurements of nuclear moments provide useful information in the study of microscopic structure of the nuclei far from stability.¹⁻⁴⁾ In such experiments, producing a spin polarization in the objective nuclei plays a key role. We have proposed a new method to produce the spin polarization, which comprises an implantation of unstable nuclei into a highly polarized stopper and subsequent transfer of the host nuclear polarization to unstable nuclei through dipole-dipole interaction. To use for the host material, we are developing a polarized ^{129}Xe solid stopper for which a large spin polarization as well as a long relaxation time can be attained.⁵⁾ In order to obtain a large nuclear polarization, the ^{129}Xe gas atom is polarized by spin exchange with an optically polarized Rb atom. After the ^{129}Xe polarization (P_{Xe}) reaches its equilibrium, the gas cell is cooled down in contact with liquid nitrogen to obtain a polarized ^{129}Xe solid. P_{Xe} is determined by measuring an NMR signal.

Previously, we reported on the development of a polarized Xe cell.⁶⁾ A cylindrical glass cell, 4 cm long and 2 cm in diameter, was filled with a natural Xe gas of a partial pressure p_{Xe} , a N_2 gas of 100 Torr, and a small amount of Rb vapor. The cell was illuminated by the circularly polarized light from a Ti-Sapphire laser (~ 1 W in laser power). As a result, a polarization as large as $P_{\text{Xe}} = 59\%$ was obtained at $p_{\text{Xe}} = 10$ Torr. At a high pressure $p_{\text{Xe}} = 800$ Torr, which corresponded to $5 \times 5 \times 1 \text{ mm}^3$ volume of solid Xe, the polarization attained was $P_{\text{Xe}} = 1\%$. The wall relaxation time (T_w), which represents the effect of relaxation due to collisions of Xe atoms against the cell wall, was 5 min in average.⁶⁾

As a matter of fact, the above achieved Xe polarization and pressure, $P_{\text{Xe}} = 1\%$ at $p_{\text{Xe}} = 800$ Torr, are not satisfactory for realization of a practical volume nor for polarization as a practical ^{129}Xe solid stopper. In order to obtain a larger P_{Xe} and a higher p_{Xe} , we have developed a new ^{129}Xe cell system. We

employed an optical pumping scheme with two diode lasers (~ 15 W each) which are suitable to polarization in a high pressure cell. In order to suppress the wall relaxation, an inner surface of the glass cell was coated with SurfaSil.⁷⁾ We made several coated as well as uncoated cells, and measured T_w in them. Although T_w 's were found to differ from cell to cell, $T_w > 20$ min was achieved within some of the coated ones. As a result, we obtained $P_{\text{Xe}} = 11\%$ at 800 Torr and $P_{\text{Xe}} = 5.6\%$ at 2300 Torr of an enriched (79.2%) ^{129}Xe gas.

In the new system, the glass cell has a rectangular part ($8 \times 20 \times 2 \text{ mm}^3$) at the bottom. After polarizing the ^{129}Xe gas in a dewar, the ^{129}Xe solid was made in the rectangular part within 5 minutes by directly immersing it into the liquid nitrogen. We also made an experiment to test the performance of apparatus with the beam of unstable nuclei ^{11}Be which was provided from Riken Ring Cyclotron and separated by the projectile fragment separator (RIPS) at Riken. Almost 100% of ^{11}Be particles incident on the system could be implanted into a solid ^{129}Xe stopper of $1.5 \times 8 \times 1.5 \text{ mm}^3$ in size, and β -rays thus detected were identified as those from ^{11}Be atoms properly stopped inside the ^{129}Xe stopper. Because of a trouble occurred in the polarizing laser system during the last beam time, so far we have not yet succeeded in observing ^{11}Be polarization. Repairs have been done, and we are now developing an apparatus for the measurement of the magnetic moment of ^{11}Be .

References

- 1) H. Okuno et al.: Phys. Lett. B **354**, 41 (1995).
- 2) H. Izumi et al.: Phys. Lett. B **336**, 51 (1995).
- 3) H. Ueno et al.: Phys. Rev. C **53**, 2142 (1996).
- 4) K. Asahi et al.: Nucl. Phys. A **588**, 135c (1995).
- 5) M. Gatzke et al.: Phys. Rev. Lett. **70**, 690 (1993).
- 6) H. Sato et al.: RIKEN Accel. Prog. Rep. **29**, 181 (1996).
- 7) X. Zeng et al.: Phys. Lett. A **96**, 191 (1983).

Production of a Low Energy ^{12}B Beam and Observation of its Nuclear Polarization

A. Ozawa, M. Fujimaki, S. Fukuda, G. Kalnins, S. Momota, T. Suzuki, I. Tanihata, and H. Yamazaki

[RADIOACTIVITY $^{12}\text{B}(b^-)$, Measured β^- rays, Deduced nuclear polarization]

A low-energy secondary beam ($E/A < \text{few MeV}$) is indispensable for studying the nuclear reactions relevant to astrophysical interests and to β , γ spectroscopy for unstable nuclei. For such studies, recoil mass spectrometers have been constructed combined with heavy-ion accelerators, such as the Tandem Van de Graff. On the other hand, a polarized secondary beam is indispensable for measuring the nuclear moments for unstable nuclei and studying the hyperfine interactions in material.

In RIKEN, a heavy-ion linear accelerator (RILAC) has mainly been used for injecting the beam into the RING Cyclotron, and for experiments using low-energy primary beams. The RILAC is also suitable for producing low-energy secondary beams, since it can accelerate various primary beams (He to Bi) with variable energies (for example, $E/A = 0.6\text{--}3.0$ MeV for ^{11}B) and high intensities (for example, a few 100 nA for ^{11}B). Thus, based on the above motivations, we started to construct the secondary beam line in RILAC from 1994.

The beam line comprises a set of QDQQ magnets, as shown in Fig. 1. The line has two focusing points. The angular and momentum acceptances are 2.6 msr and $\pm 1.0\%$, respectively. The momentum dispersion is 1.4 cm/% at the intermediate focus. A small dipole magnet is located upstream of the target chamber, which is used to deflect the primary beam. The primary beams can be bent on the target by two magnets, thus providing a deflection angle of up to 5° . Between the first Q-doublet and the intermediate dipole magnet thin foils can be placed so as to create the nuclear polarization (P_N) by beam-foil interactions. A magnetic field of up to 600 G can be applied to the foils. At the first focus, devices for the β -NMR and momentum slits are located. The scattering chamber,

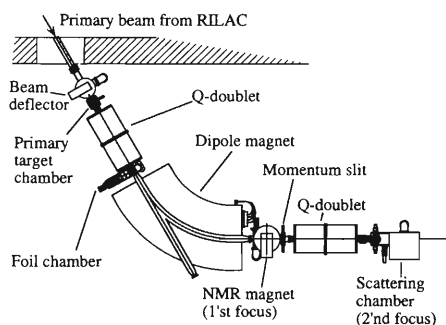


Fig. 1. Layout of the secondary beam line in RILAC.

located at the second focus, can be used for reaction experiments using a secondary beam.

We obtained a ^{12}B ($T_{1/2} = 20$ ms) beam with $E/A \approx 1.8$ MeV; the typical production rate was about 50 cps/nA. The ^{12}B beam was produced by the reaction $d(^{11}\text{B}, ^{12}\text{B})p$ with a $E/A = 2.5$ MeV ^{11}B beam accelerated by RILAC and a 1.5 mg/cm 2 thick CD_2 target. The production of ^{12}B was confirmed by its β -decay time spectrum. The spectrum was composed of an exponential curve of signal plus a constant background. Also, we finally obtained $T_{1/2} = 19.6 \pm 0.3$ ms, which is consistent with that in the literature.¹⁾ The intensity of the ^{12}B beam was estimated based on the β -ray intensity. We can also obtain a good separation for different charge states of the secondary beam.

We measured P_N of the $^{12}\text{B}^{5+}$ produced by the reaction process under the above conditions. In this case, the primary beam was deflected by magnets. The ^{12}B beam was collected at a scattering angle of 4° with $\pm 1^\circ$ of acceptance, which corresponds to 10° scattering in the inverted reaction: $^{11}\text{B}(d,p)^{12}\text{B}$. P_N was measured as a function of the momentum of the ^{12}B beam by the β -NMR method. We observed a decisive P_N at the high-energy side of the ^{12}B beam, as shown in Fig. 2. Here, the sign of P_N is defined to be positive for the direction parallel to $\vec{p}_i \times \vec{p}_f$, where \vec{p}_i and \vec{p}_f are the momentum vectors of incoming and outgoing particles. The P_N integrated in the total momentum distribution is about 1.5%; consistent with that observed in the inverted reaction in Ref. 2.

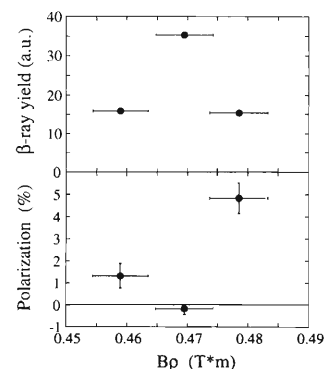


Fig. 2. Momentum dependence of the polarization of a ^{12}B beam.

References

- 1) F. Ajzenberg-Selove: Nucl. Phys. A **506**, 1 (1990).
- 2) M. Tanaka et al.: Nucl. Phys. A **263**, 1 (1976).

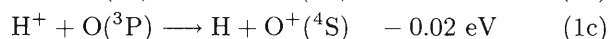
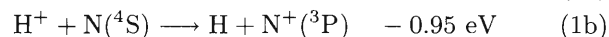
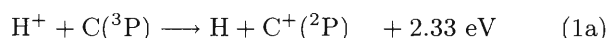
2. Atomic and Solid-State Physics

Inelastic Processes in Collisions of H⁺ Ions with C, N, and O Atoms below 1 keV

M. Kimura, J.-P. Gu,* G. Hirsch,* R. J. Buenker,* and I. Shimamura

Electron capture reactions resulting from collisions of protons with carbon, nitrogen and oxygen atoms are known to play an important role in earth's atmosphere,¹⁾ interstellar space,²⁾ and astrophysical plasmas,³⁾ and are fundamental for other relevant applied fields.⁴⁾ Yet, accurate rates of these collision processes are rarely known except some crude and limited attempts for evaluation. Rate coefficients for the [H⁺ + N] and [H⁺ + O] collision processes were theoretically evaluated by Steigman et al.⁵⁾ and Field and Steigman,⁶⁾ respectively, based on an orbiting approximation with corresponding values of 2.5×10^{-14} cm³/s and 7.4×10^{-10} cm³/s at 10,000 K, respectively. Chambaud et al.⁷⁾ carried out a more rigorous study on electron capture in the [H⁺ + O] collisions using a molecular orbital method with the spin-orbit coupling as a driving force and determined the rate coefficient as 4.8×10^{-10} cm³/s at 10,000 K. There is no large-scale theoretical study on the [H⁺ + C] and [H⁺ + N] collision systems except for an exploratory calculation by Butler and Dalgarno⁸⁾ for the [N⁺ + H] system.

In this paper, we attempt to investigate collision dynamics, and to evaluate electron capture cross sections and corresponding rate coefficients for the three (C, N, O) target atoms rigorously based on a molecular representation within a semiclassical framework for HC⁺, HN⁺, and HO⁺. The processes studied are as follows, with corresponding asymptotic energy defects given between the closest states:



The multireference single- and double-excitation (MRD-CI) configuration interaction method was employed.⁹⁾ A semiclassical MO expansion method with a straight-line trajectory of the incident ion was employed to study the collision dynamics.¹⁰⁾ Substituting the total wave function into the time-dependent Schrödinger equation, we obtain a set of first-order coupled equations. By solving the coupled equations numerically, we obtain the scattering probabilities for transitions, and integration of this probability over the impact parameter gives the cross section. In adiabatic potentials obtained, for the CH⁺ system, the ground [H⁺ + C(³P)] channel lies above the dominant electron capture [H + C(²P)] channel, whereas all the target-excitation [H⁺ + C(¹D,¹S)] channels lie slightly above the ground state. For the NH⁺ system,

the [H⁺ + N(⁴S)] channel is the ground state with the electron capture [H + N(³P)] channel nearby. Above this electron capture channel, a series of target excitation channels follows. For OH⁺ system, the [H⁺ + O(³P)] channel is the lowest level similarly for the NH⁺ system and then, the electron capture [H + O(⁴S)] channel and the target excitation [H⁺ + O*(¹D)] channel follow. Because of a small asymptotic energy defect (near-resonant processes) between the initial and closest electron capture channels for almost all systems, the electron capture cross sections from the ground-state atoms are very large: approximately 10^{-16} – 10^{-15} cm² for all systems at above 100 eV. The rate coefficients for electron capture from the ground-state C(³P), N(⁴S), and O(³P), and some representative values are given in Table 1. The rates increase with temperature (T) from less than 10^{-14} cm³/s to 2×10^{-11} cm³/s for CH⁺, 3.5×10^{-11} cm³/s to 2×10^{-9} cm³/s for NH⁺ and 6.1×10^{-11} cm³/s to 7×10^{-9} cm³/s for OH⁺, when T is raised from 10,000 K to 100,000 K, respectively.

Table 1. Representative rate coefficients for electron capture at temperatures above 10,000 K resulting from collisions of H⁺ ions with C, N, and O target atoms.

Temp. (K)	Targets		
	C(³ P)	N(⁴ S)	O(³ P)
10,000	—	3.51×10^{-11} ⁽⁵⁾ 5.3×10^{-10}	6.10×10^{-11} ⁽⁶⁾ 9.1×10^{-10}
50,000	2.61×10^{-12}	4.80×10^{-10}	2.91×10^{-9}
100,000	2.34×10^{-11}	2.03×10^{-9}	7.02×10^{-9}
200,000	2.08×10^{-10}	6.73×10^{-9}	1.39×10^{-8}

References

- 1) R. F. Stebbings, A. C. H. Smith, and H. Ehrhardt: *J. Geophys. Res.* **69**, 2349 (1964).
- 2) J. H. Black and A. Dalgarno: *Astrophys. J.* **206**, 132 (1976).
- 3) G. E. Geisler: *J. Geophys. Res.* **72**, 81 (1967).
- 4) R. A. Phaneuf, F. W. Meyer, and R. H. McKnight: *Phys. Rev. A* **17**, 534 (1974).
- 5) G. L. Steigman, M. W. Werner, and F. M. Geldon: *Astrophys. J.* **168**, 373 (1971).
- 6) G. B. Field and G. Steigman: *Astrophys. J.* **166**, 59 (1971).
- 7) G. Chambaud et al.: *J. Phys. B* **13**, 4205 (1980).
- 8) S. E. Butler and A. Dalgarno: *Astrophys. J.* **234**, 765 (1979).
- 9) R. J. Buenker and S. D. Peyerimhoff: *Théo. Chim. Acta* **35**, 33 (1974); R. J. Buenker: *Intern. J. Quantum Chem.* **29**, 435 (1986).
- 10) M. Kimura and N. F. Lane: in *Advanced Atomic Molecular Optical Physics* Vol. 26, edited by D. R. Bates and B. Bederson (Academic Press, NY, 1989) p. 76.

* Theoretische Chemie, Universitaet Wuppertal, Wuppertal, Germany

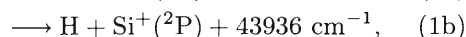
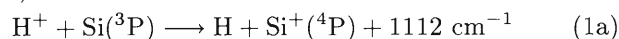
Electron Capture Rates in Collisions of H^+ Ions with Si Atoms: Capture by the ground and excited state

M. Kimura, A. B. Sannigrahi,* J.P. Gu,* G. Hirsch,* R. J. Buenker,* and I. Shimamura

Baliunas and Butler¹⁾ examined the effect of charge transfer in conjunction with the silicon spectral lines, and estimated the value of the rate coefficient as 10^{-11} cm^3/s for the charge transfer process in collisions of H^+ ions with $\text{Si}(^3\text{P})$ ground state atoms. From this, they suggested a possible importance of the ionization process of silicon atoms. Apart from this case study, to the best of our knowledge, there is no theoretical or experimental determination of the charge transfer cross section.

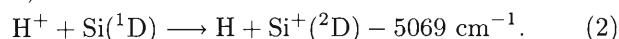
We have carried out a theoretical investigation for charge transfer in collisions of H^+ ions with neutral Si atoms both in the ground and metastable states at collision energies from 10^{-3} eV to 10 keV. The processes we have studied are as follows, with corresponding asymptotic energy defects:

i) Ground state Si ions:



and

ii) Metastable Si ions:



The metastable ^1D state in Eq. (2), which lies at 50235 cm^{-1} higher in energy than the $[\text{Si}^+(^2\text{P}) + \text{H}]$ state, is considered to compete with the ground state as the collision energy increases to keV regime. Hence, it is important to understand the electron capture mechanism of the both ground and metastable states. The adiabatic potential curves of SiH^+ are obtained by employing the *ab initio* multireference single- and double-excitation configuration interaction (MRD-CI) method.²⁾ From the bottom of adiabatic potentials, they correspond asymptotically to the atomic states $[\text{H} + \text{Si}^+(^2\text{P})]: 1^3\Pi, 1^3\Sigma^+$, $[\text{H} + \text{Si}^+(^4\text{P})]: 2^3\Pi, 1^3\Sigma^-$ and $[\text{H}^+ + \text{Si}(^3\text{P})]: 3^3\Pi, 2^3\Sigma^-$ for triplet manifold, and $[\text{H}^+ + \text{Si}(^1\text{D})]: 2^1\Pi, 2^1\Sigma^+$ and $[\text{H} + \text{Si}^+(^2\text{D})]: 3^1\Pi, 3^1\Sigma^+$ for singlet manifold. A semiclassical molecular orbital expansion method with a straight-line trajectory of the incident ion was employed to study the collision dynamics.³⁾ By solving the coupled equations numerically, we obtain the scattering probability for transitions, and integration of this probability over the impact parameter gives the cross section. The molecular states included are the two sets of states: separating to $[\text{H}^+ + \text{Si}(^3\text{P})]: (2^3\Sigma^-, 3^3\Pi)$, $[\text{H} + \text{Si}^+(^4\text{P})]: (1^3\Sigma^-, 2^3\Pi)$, $[\text{H} + \text{Si}^+(^2\text{P})]: (1^3\Sigma^+, 1^3\Pi)$ for the charge transfer from the initial ground state, and $[\text{H}^+ + \text{Si}(^1\text{D})]$

$(2^1\Sigma^+, 2^1\Pi)$, $[\text{H} + \text{Si}^+(^2\text{D})]: (3^1\Sigma^+, 3^1\Pi)$ for the electron capture from the initial metastable state. A fully quantum mechanical representation of the MO expansion method was employed for collision energies below 30 eV. The coupled equations are solved numerically to obtain the scattering matrix. The molecular states included are two sets of channels: (i) $[\text{Si}^+(^4\text{P}) + \text{H}]: (3^3\Pi)$ and $[\text{Si}(^3\text{P}) + \text{H}^+]: (2^3\Pi)$ and (ii) $[\text{Si}^+(^2\text{D}) + \text{H}]: (3^1\Pi)$ and $[\text{Si}(^1\text{D}) + \text{H}^+]: (2^1\Pi)$. The cross sections obtained are shown in Fig. 1. Because of a small asymptotic energy defect between the initial and closest electron capture channels, and because of the exothermicity in nature for the transition, the electron capture process from the ground state $\text{Si}(^3\text{P})$ atoms is extremely efficient. Therefore, the present cross section for the $\text{Si}^+(^4\text{P})$ formation are found to have a broad peak with a value of $1 \times 10^{-14} \text{ cm}^2$ between 10 eV and 10 keV. It gradually decreases as the collision energy decreases, but it still has a value of 10^{-15} cm^2 even at 1 eV. The present cross section for the $\text{Si}^+(^2\text{P})$ formation is comparable with those of the $\text{Si}^+(^4\text{P})$ formation above 1 keV, but it sharply decreases below 0.5 keV because of a larger energy defect from the initial state. The $\text{Si}^+(^2\text{D})$ formation in the singlet-state collision is also large with the charge transfer cross section of $3 \times 10^{-15} \text{ cm}^2$ above 1 eV.

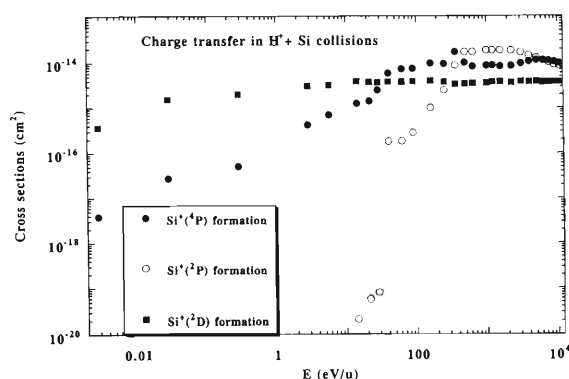


Fig. 1. Charge transfer cross sections below 10 keV. Filled circles: $\text{Si}^+(^4\text{P})$ formation; open circles: $\text{Si}^+(^2\text{P})$ formation; filled squares: $\text{Si}^+(^2\text{D})$ formation.

References

- 1) S. L. Baliunas and S. E. Butler: *Astrophys. J.* **235**, L45 (1980).
- 2) A. B. Sannigrahi, R. J. Buenker, G. Hirsch, and J. P. Gu: *Chem. Phys. Lett.* **237**, 204 (1995).
- 3) M. Kimura and N. F. Lane: in *Advanced Atomic Molecular Optical Physics* Vol. 26, edited by D. R. Bates and B. Bederson (Academic Press, NY, 1989) p. 76.

* Theoretische Chemie, Universität Wuppertal, Wuppertal, Germany

Charge Transfer in Collisions H^+ Ions with Ground State Mg Atom at Low keV Collision Energies

C. M. Dutta,* P. Nordlander,* and M. Kimura

Charge transfer cross sections of the process $Mg + H^+ \rightarrow Mg^+ + H$ were measured for the range of 1–2 keV collision energies.^{1–3)} Most of the theoretical work were performed by using either classical approximations or semi-empirical approaches.^{4,5)} The only quantum mechanical *ab-initio* calculation at keV energies was performed by Olson and Liu.⁶⁾ They calculated charge transfer cross sections by using a molecular orbital (MO) expansion method within a semiclassical framework and by employing straight-line trajectories. They obtained a good agreement with experiments around the maximum of the cross section at ~ 8 keV, but at the lower energies their calculated values appear to overestimate the electron capture. Therefore, it seems appropriate at this time to carry out an *ab-initio* calculation of charge transfer cross sections by taking couplings to more MO states than previous calculations into account.

We have employed the semi-classical impact parameter method based on a MO expansion. This approach was explained in detail elsewhere.⁷⁾ The $(MgH)^+$ molecule is treated as a quasi two-electron system by representing the $Mg^{++}(1s^2 2s^2 2p^6)$ ion core by a Gaussian-type pseudopotential. The configuration interaction (CI) method with linear combinations of Slater determinants consisting of Slater-type orbitals is used to obtain Born-Oppenheimer MO's and eigenenergies of the system. Substituting the total wavefunction into the time-dependent Schroedinger equation, we obtain a set of first-order coupled equations in time. By solving the coupled equations numerically, we obtain the scattering amplitudes for transitions, and integration of the probability over the impact parameter gives the cross section for the process concerned.

Figure 1 shows the adiabatic potential energies of the lowest fourteen states of the $(MgH)^+$ system as a function of the internuclear separation, R . Figure 2 shows the total single-charge transfer cross sections calculated by inclusion of the lowest fourteen MO's, together with some other theoretical results and experimental data. Our calculated charge transfer cross sections (depicted by a solid-line curve in the figure) are in fairly good agreement above $E \sim 3$ keV with most of experimental data. At lower collision energies, however, the calculated cross sections become larger by 30% than measurements, although ours are smaller than the values (dashed-line curve in the figure) by Olson and Liu. At lower energies, these measurements were carried out by using D^+ or He^+ ions instead of

H^+ ions. Therefore, if the claim that when H^+ ions are used, the cross sections obtained become uniformly larger than those by D^+ and He^+ at low energies still holds and is taken into account, then we would expect that the discrepancy between the calculated cross sections and measurements should be somewhat reduced. More experimental efforts are desirable in this energy region ($E < 3$ keV) in order to verify the theoretical results.

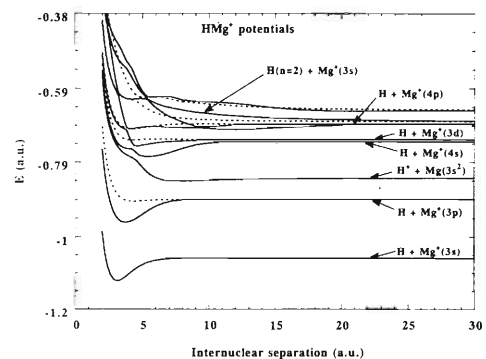


Fig. 1. Adiabatic potentials for the MgH^+ .

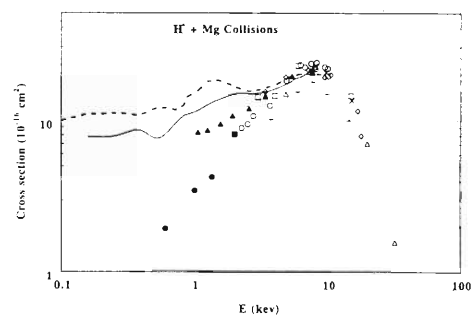


Fig. 2. Charge transfer cross sections in collisions of H^+ ions with Mg atoms. Solid-line: the present, dashed-line: Olson and Liu. All symbols are the experimental results (Ref. 1–3).

References

- 1) R. D. DuBois and L. H. Toburen: *Phys. Rev. A* **31**, 3603 (1985).
- 2) R. D. DuBois: *Phys. Rev. A* **34**, 2738 (1986).
- 3) J. Eriksen: *Phys. Rev. A* **19**, 2185 (1979).
- 4) D. R. Bates and R. A. Mapleton: *Proc. Phys. Soc. (London)*, **87**, 657 (1966).
- 5) R. A. Mapleton and N. Crossbaard: *Phys. Rev.* **188**, 228 (1969).
- 6) R. E. Olson and B. Liu: *Phys. Rev. A* **20**, 1366 (1979).
- 7) M. Kimura and N. F. Lane: in *Advanced Atomic Molecular Optical Physics* Vol. 26, edited by D. Bates and B. Bederson (Academic Press, NY, 1989) p. 76.

* Department of Physics, Rice University, Houston, TX, U.S.A.

Triple-Center Expansion Study of Ionization Processes

N. Toshima

The triple-center expansion method was first applied to ion-atom collisions by Anderson et al.¹⁾ in order to incorporate the united atom wave functions explicitly into the basis functions used for the coupled-channel method. The method was studied further by Lin et al.²⁾ and Winter and Lin.³⁾ Under the recognition that the united atom wave functions have sizable overlap with the continuum states of the target and projectile atoms, Winter and Lin⁴⁾ and Winter⁵⁾ applied it to the calculations of ionization cross sections. In this report we extend the two-center Gaussian-type-orbital-basis (GTO) coupled-channel method to a triple-center description in order to study ionization processes.

We adopt the impact parameter method; the relative motion of the heavy particles is described classically by a rectilinear trajectory with a constant velocity v in the impact-parameter representation. We solve the time-dependent Schrödinger equation of a single-electron system,

$$\left[H - i \frac{\partial}{\partial t} \right] \Psi(\mathbf{r}, t) = 0 \quad (1)$$

by introducing an expansion:

$$\begin{aligned} \Psi(\mathbf{r}, t) = & \sum_{i=1}^{N_T} a_i(t) \psi_i^T(\mathbf{r}_T, t) \\ & + \sum_{i=N_T+1}^{N_T+N_P} a_i(t) \psi_i^P(\mathbf{r}_P, t) \\ & + \sum_{i=N_T+N_P+1}^N a_i(t) \psi_i^C(\mathbf{r}_C, t), \end{aligned} \quad (2)$$

in terms of the target wave functions:

$$\psi_i^T(\mathbf{r}_T, t) = \phi_i^T(\mathbf{r}_T) \exp(-iE_i^T t), \quad (3)$$

the projectile wave functions:

$$\begin{aligned} \psi_i^P(\mathbf{r}_P, t) = & \phi_i^P(\mathbf{r}_P) \\ & \times \exp(-iE_i^P t + i\mathbf{v} \cdot \mathbf{r}_T - \frac{i}{2}v^2 t), \end{aligned} \quad (4)$$

and wave functions of a virtual atom on the third center C:

$$\begin{aligned} \psi_i^C(\mathbf{r}_C, t) = & \phi_i^C(\mathbf{r}_C) \\ & \times \exp(-iE_i^C t + i\mathbf{p}\mathbf{v} \cdot \mathbf{r}_T - \frac{i}{2}p^2 v^2 t). \end{aligned} \quad (5)$$

Here, ϕ_i^T , ϕ_i^P and ϕ_i^C are the hydrogenic eigenfunctions with eigenvalues E_i^T , E_i^P and E_i^C of the Hamiltonians of the target T, projectile P and virtual atom C, respectively; and \mathbf{r}_T , \mathbf{r}_P , \mathbf{r}_C and \mathbf{r} are the electron coordinates measured from the three centers T, P, C, and

from the coordinate origin, respectively. The third center C and its nuclear charge are arbitrary in principle. We choose C as the equiforce saddle point between the two nuclei, and the charge as that of the united atom, i.e.,

$$p = \frac{\sqrt{Z_T}}{\sqrt{Z_T} + \sqrt{Z_P}}, \quad (6)$$

$$Z_C = Z_T + Z_P. \quad (7)$$

Here, p is the ratio of the distances between T and C and between T and P, while Z_T , Z_P and Z_C stand for the charges on T, P and C, respectively. The eigenfunctions of each center are further expanded in terms of the Gaussian-type basis functions as

$$\phi_{nlm}(\mathbf{r}) = \sum_{\nu} c_{\nu}^{n\ell} e^{-\alpha_{\nu} r^2} r^{\ell} Y_{\ell m}(\hat{r}), \quad (8)$$

where the nonlinear parameters α_{ν} are generated as a modified geometrical progression. The coefficients $c_{\nu}^{n\ell}$ are determined so as to diagonalize the atomic Hamiltonians of the target, projectile and virtual atom. Substitution of Eq. (2) into Eq. (1) gives coupled equations in a matrix form:

$$i\mathbf{S} \frac{d\mathbf{a}}{dt} = \mathbf{V}\mathbf{a}, \quad (9)$$

where \mathbf{a} is the column vector of the expansion coefficients, while \mathbf{S} and \mathbf{V} are the overlap and interaction matrices defined as

$$S_{ij} = \langle \psi_i | \psi_j \rangle, \quad (10)$$

$$V_{ij} = \langle \psi_i | H - i\partial/\partial t | \psi_j \rangle. \quad (11)$$

All the matrix elements of \mathbf{S} and \mathbf{V} are calculated analytically in the same way as stated for the two-center expansion.⁶⁾ This high analyticity is a great advantage of the GTO expansion method since three-center matrix elements appearing in V_{ij} are very complicated to handle and since the calculation in the representation of the Slater-type-orbital (STO) expansion is time-consuming.

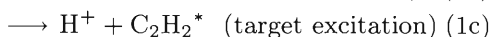
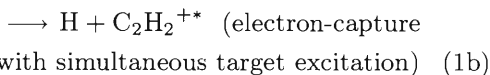
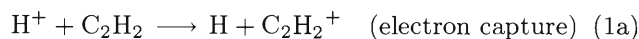
References

- 1) D. G. M. Anderson, M. J. Antal, and M. B. McElroy: J. Phys. B **7**, L118 (1974).
- 2) C. D. Lin, T. G. Winter, and W. Fritsch: Phys. Rev. A **25**, 2395 (1982).
- 3) T. G. Winter and C. D. Lin: Phys. Rev. A **29**, 567 (1984).
- 4) T. G. Winter and C. D. Lin: Phys. Rev. A **29**, 3071 (1984).
- 5) T. G. Winter: Phys. Rev. A **37**, 4656 (1988).
- 6) N. Toshima and J. Eichler: Phys. Rev. A **46**, 2564 (1992).

Elastic and Inelastic Processes in $H^+ + C_2H_2$ Collisions below 1.5 keV Regime

M. Kimura, Y. Li,* G. Hirsch,* and R. J. Buenker*

In the present note, we report the results for electron capture and direct elastic scattering in collisions of H^+ ions with C_2H_2 molecules for energies below 1.5 keV. Contribution from electron-capture accompanied with simultaneous target excitation is also examined. Hence, the processes studied are:



Two molecular configurations are specifically considered to study the effects of molecular orientations on collision dynamics: (i) a proton approaches an H atom along the molecular axis of the C-C bond and (ii) it approaches perpendicularly toward the midpoint of the C-C bond in C_2H_2 . The interference arising from different molecular orientations is investigated. The adiabatic potential energy curves are calculated by means of the multireference single- and double-excitation configuration interaction (MRD-CI) method.^{1,2)} A fully quantum mechanical representation of the MO expansion method was employed; that is, dynamical transitions were driven by nonadiabatic couplings.³⁾ The

coupled equations are solved numerically to obtain the scattering S^1 matrix for each partial wave l .³⁾ The differential cross section is then obtained from the standard formula. In the present calculation, we have employed two- and three-state close-coupling treatments with molecular orbitals (MOs) corresponding to the initial [$H^+ + C_2H_2$] and electron capture [$H + C_2H_2^+$] channels. Adiabatic potential curves are displayed in Figs. 1a and 1b. The differential cross sections obtained are shown in Figs. 2a and 2b both for C_{2v} and C_{00v} symmetries, respectively, for scattering angles 0 – 180° at 1.5 keV. Collision dynamics for C_{2v} and C_{00v} symmetries were found to be effective in nearly the same small scattering-angle regions. Hence, the interference arising from these two molecular configurations occurs rather strongly at narrow regions of scattering angle, and unambiguous structures in differential cross sections arising from the interference are observed.

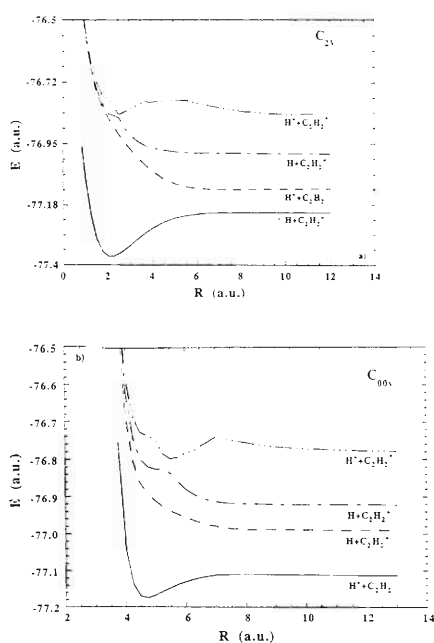


Fig. 1. a) Adiabatic potentials for C_{2v} symmetry in the [$H + C_2H_2$] $^+$ system. b) Adiabatic potentials for C_{00v} symmetry in the [$H + C_2H_2$] $^+$ system.

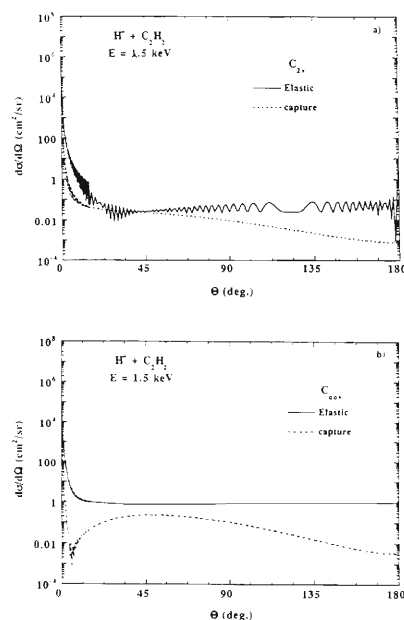


Fig. 2. a) Differential cross sections for elastic and electron capture processes for C_{2v} symmetry at 1.5 keV. b) Differential cross sections for elastic and electron capture processes for C_{00v} symmetry at 1.5 keV.

References

- 1) M. Kimura, Y. Li, G. Hirsch, and R. J. Buenker: Phys. Rev. A **52**, 1196 (1995).
- 2) R. J. Buenker and S. D. Peyerimhoff: Theoret. Chim. Acta **35**, 33 (1974); **39**, 217 (1975); R. J. Buenker: Int. J. Quantum Chem. **29**, 435 (1986).
- 3) M. Kimura and N. F. Lane: Adv. At. Mol. Phys. Vol. 26, Eds. D. R. Bates and B. Bederson (Academic Press, NY, 1989) p. 79.

* Theoretische Chemie, Universitaet Wuppertal, Germany

Double Electron Detachment from Negative Hydrogen Ions under High Energy, Highly Charged Ion Impact

H. Tawara, L. P. Presnyakov,* and D. B. Uskov*

Phenomena of the electron detachment from negative hydrogen ions in collisions with highly charged ions (HCI) are not only interesting in basic collision aspects but also important in applications such as fusion plasma heating technology.

So far, the single electron detachment from H^- ions resulting in the production of neutral hydrogen beam, H^0 , has been studied at HCI collisions, but only under relatively low energy.¹⁾ Namely, there are no such experimental studies under a high energy (MeV/amu) HCI collision. We have thus started to investigate the electron detachment from H^- ions under such collisions at MeV/amu region and to measure their cross sections.²⁾ It should be noted that no investigation on the double electron detachment from H^- ions has been reported yet, except for that under the electron impact.³⁾

In the present work, we describe some results of our calculations of the cross sections for the double electron detachment from H^- ions under the MeV/amu HCI ion impact. The present approach in calculating the double electron detachment from H^- ions is based on a modified version of our method previously applied to the double electron removal from a neutral He atom.⁴⁾

Assuming that two electrons ($1s, 1s'$) in a H^- ion are independent, the one-electron continuum wavefunctions in the final channel have different forms for the "outer" ($1s'$) and "inner" ($1s$) electrons. The function for the "outer" electron is in the Volkov-Keldysh state, given as

$$\Psi_1 = \Psi_{\mathbf{k}_1}(t) = (2\pi)^{-3/2} \exp[i\mathbf{p}_1(t)\mathbf{r}_1 - \frac{i}{2} \int_0^t d\tau p_1^2(\tau)], \quad (1)$$

where

$$\mathbf{p}_i = \mathbf{k}_i - \mathbf{A}(t), \quad \mathbf{A}(t) = q \int_0^t d\tau \mathbf{R}(\tau)/[\mathbf{R}(t)]^3. \quad (2)$$

Here, \mathbf{k}_i is the momentum of the i -th electron at the distance r_i from nucleus, $\mathbf{R}(t) = \mathbf{b} + \mathbf{v}t$ is the inter-nuclear distance depending on the impact parameter b and the relative velocity v , and q is the projectile charge.

On the other hand, the wavefunction for the "inner" electron describes the electron motion in the Coulomb field of proton and the dipole field of projectile ion, given as:

$$\Psi_2 = \Psi_{\mathbf{k}_2}(t)G, \quad (3)$$

where

$$G = \exp(\pi\nu/2)\Gamma(1+i\nu)F(-i\nu, 1, i(p_2r_2 + \mathbf{p}_2\mathbf{r}_2)), \quad (4)$$

$$\nu = 1/p_2.$$

Here, Γ and F are the gamma function and the confluent hypergeometric function, respectively.

Using these functions, the second-order perturbation theory, similar to the independent-event model,⁵⁾ results in the following cross sections for the double electron detachment from a H^- ion:

$$\sigma_d = R_{SO}\sigma_s + \sigma_{TS} \quad (5)$$

where σ_s is the single electron detachment cross section, R_{SO} the shake-off constant which represents the ratio of the cross sections for double-to-single-electron detachment at asymptotic collision energies, and σ_{TS} the cross section of a two-step process in terms of one-electron event. R_{SO} can be estimated, from the experimental data available under electron impact,³⁾ to be $(2.3 - 4.0) \times 10^{-3}$.

σ_s has been calculated in the previous study¹⁾ to be

$$\sigma_s = 51.6(q/v)^2 \ln\{2.03v^2/(1 + 0.139v^2)^{1/2} + 1.01\} [10^{-16} \text{ cm}^2] \quad (6)$$

where q is the charge of a HCI and v the H^- ion velocity in atomic units. Equation (2) agrees with the *ab initio* Bethe-Born calculation at asymptotic region.⁶⁾ On the other hand, using a similar treatment of Refs. 4 and 7, the present analysis for the two-step process results in the following analytical expression for σ_{TS} given to be

$$\sigma_{TS} = 2.9(q/v)^4 \exp(-0.41q/v^2 - 1.1/v) [10^{-16} \text{ cm}^2]. \quad (7)$$

It should be noted that the single-electron detachment cross section scales as $(q/v)^2$, whereas that for the double electron detachment does as $(q/v)^4$.

The contribution from the interference term between two wavefunctions has been estimated and found to be less than the cross sections given by Eq. (5).

References

- 1) F. Melchert, M. Benner, S. Krüdener, R. Schultze, S. Meuser, S. Petri, S. Pfaff, E. Salzborn, D. B. Uskov, and L. P. Presnyakov: Phys. Rev. Lett. **74**, 888 (1995).
- 2) H. Tawara, T. Tonuma, H. Kumagai, and T. Matsuo: RIKEN Accel. Prog. Rep. **29**, 91 (1996).
- 3) D. J. Yu, S. Rachafi, J. Jureta, and P. Defrance: J. Phys. B **25**, 4593 (1992).
- 4) L. P. Presnyakov, H. Tawara, I. Yu. Tolstikhina, and D. B. Uskov: J. Phys. B **28**, 85 (1995).
- 5) N. C. Deb and D. S. F. Crothers: J. Phys. B **23**, L799 (1990).
- 6) Y. K. Kim and M. Inokuti: Phys. Rev. A **33**, 665 (1971).
- 7) L. P. Presnyakov and D. B. Uskov: Sov. J.- JETP **59**, 515 (1984).

* Lebedev Physics Institute, Moscow, Russia

Theoretical Study for Absorption and Emission Spectra of Alkali Atom and Liquid-He Composite System

J. Z. Tang,* M. Kimura, and I. Shimamura

Spectroscopic studies of atoms and molecules in the superfluid He have provided a new and exciting research subject not only in the atomic and molecular physics, but also in the condensed-matter physics.¹⁻⁵⁾ Because the electron-He interaction is uniformly repulsive in nature, atomic electrons of the impurity atom push the surrounding He away, forming a nearly spherical vacuum space, or so-called a "bubble" around the impurity atom. A general size of the bubble is as large as 10-30 a.u. The atomic state and dynamics inside the bubble are expected to be significantly different from those of a free atom, and this type of study (given below) should provide an important knowledge for fundamental physics. Experimental attempts to explore these physics have been very active recently, and have deepened our level of understandings for the bubble. There were several problems formerly for understanding what were observed, but very recently some theoretical works have been performed to shed much light on them.⁶⁻⁸⁾

Earlier, we presented the result of a comparative study of absorption and emission spectra from Mg through Be and showed a good agreement with measurements in general.⁵⁾ In present report, we extend the calculation to alkali atoms in the liquid-He, explain our results of each absorption and emission spectra resulted from transitions between the ground state and optically-allowed first excited state, and discuss characteristics of spectrum shift and half-width seen in each spectrum.

The system of an impurity atom in the liquid-He is a complicated many-body problem if all particles involved are treated fully quantum mechanically. Since we are interested in studying a perturbation of the liquid-He on the optical transitions of the impurity atom, we employ here a simple bubble model of the liquid-He as fully documented earlier.⁵⁾ Atomic units are used throughout.

Density distribution: The density distribution of atoms in liquid-He around the impurity atom may be described by a bubble model.⁶⁾ The shape of the bubble depends on the electronic distribution of the impurity atom. For the study of absorption spectra, the bubble may be assumed to be spherically symmetric if the atom is initially in an s state. For studying emission, however, the bubble is considered to be of a non-symmetric shape because of the unsymmetric nature of an excited π state.

Total energy and the breathing bubble oscillation: An impurity atom is introduced into the liquid-He of the temperature below 3K. For simplicity, we assume the spherical symmetric structure for the bubble here.

The total energy of this composite system of the impurity atom and liquid-He is given as

$$E_{\text{tot}} = E_{\text{atm}} + E_{\text{surf}} + E_{\text{pv}} + E_{\text{int}},$$

where E_{atm} is the free-atom energy; E_{surf} represents the surface tension energy of the bubble; E_{pv} describes the pressure-volume work at the surface of the bubble; and E_{int} is the interaction between the impurity and surrounding He atoms.

Adiabatic line-broadening theory: The spectral intensity for an optical transition of atoms may be obtained by the Fourier transformation of the transition dipole correlation function.

Absorption and emission spectra: The conventional procedure to evaluate absorption and emission spectra is based on the line-broadening theory.^{1-5,9)} This theory is based on the collisional broadening of the spectrum through the interaction with liquid-He. In the present study, we modify the standard line broadening theory by including the effect of the bubble oscillation. Then, the spectrum can be described as

$$I(\omega) = \int dR_0 I_a(\omega, R_0) |\chi(R_0)|^2,$$

where I_a and χ are the line-broadening based on the adiabatic theory and distribution of the bubble size (i.e., bubble nuclear wavefunction), respectively.

Diatomic molecular states: Molecular states of a two-body adiabatic system are obtained by using the configuration-interaction (CI) method. We believe that the present precision is considered to be reasonably sufficient for *ab initio* calculations of spectra, in which experimental shifts were found to be in a range of 200 cm^{-1} to 700 cm^{-1} .

Based the theory above, a theoretical study of the atomic absorption and emission spectra of alkaline atoms (Li, Na, K, Rb and Cs) in the superfluid He (a bubble) was carried out, and their shifts and half-widths were also examined to be compared with measured spectra. The results for the absorption and emission spectra agree very well with measurements for most cases in spectral shapes and give rationales to some of unexpected observations.

References

- 1) Special issue of Zeit. fuer Physik B, 98 (1995).
- 2) A. Fujisaki et al.: Phys. Rev. Lett. **71**, 1039 (1993).
- 3) Y. Takahashi et al.: Phys. Rev. Lett. **71**, 1035 (1993).
- 4) T. Kinoshita, Y. Takahashi, and T. Yabusaki: Phys. Rev. B **49**, 3648 (1994).
- 5) J. H. M. Beijersbergen, Q. Hui, and M. Takami: Phys. Lett. A **181**, 393 (1993).
- 6) J. Dupont-Roc: Z. Phys. B **98**, 383 (1995).
- 7) J. L. Persson et al.: Phys. Rev. Lett. **76**, 1501 (1996).
- 8) T. Kinoshita, K. Fukuda, and T. Yabusaki: Phys. Rev. B **54**, 6600 (1996).
- 9) J. Z. Tang, M. Kimura, and I. Shimamura: Chem. Phys. Lett. **256**, 327 (1996).

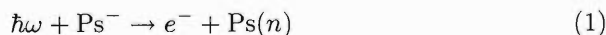
* Department of Physics, University of Tennessee, Knoxville, TN, U.S.A.

Photodetachment Cross-Sections of the Positronium Negative Ion

A. Igarashi

The positronium negative ion, $\text{Ps}^- (e^- e^- e^+)$, is the special system in which three particles with same mass are interacting through Coulomb potentials. The Ps^- system has only one bound state of the symmetry $1S^e$. Its existence has been confirmed and the decay rate has been measured to be $2.09 \pm 0.09 \text{ ns}^{-1}$,¹⁾ which is in good agreement with theories. As for Ps^- photodetachment, there is no experimental measurement and there are little theoretical works enough to discuss their reliability of cross-sections.

Thus in present report, we calculated photodetachment cross-sections of Ps^- in the process:



up to just above the $n=2$ threshold by use of the hyperspherical-coupled-channel (HCC) method. The HCC method is a powerful tool to describe the strong electron-electron correlations in a two-electron system, such as He and H^- , and was successfully applied to the calculation of photoionization cross-sections.²⁾ The photodetachment cross-section can be written as

$$\sigma(\omega) \propto | \langle \psi_f | D | \psi_i \rangle |^2. \quad (2)$$

Here, ψ_i is the initial bound state of $1S^e$ symmetry and ψ_f the continuum state of $1P^o$ symmetry, and D the dipole operator in either the velocity or length form.³⁾

The initial and final wave functions are calculated in the HCC method with an expansion in terms of the channel functions which converge to atomic states of $\text{Ps}(n=1 \sim 4)$ at the asymptotic region. Our binding energy for the initial state is 0.011997 a.u., which is sufficiently accurate for our purpose compared with the best variational value of 0.012005 a.u.⁴⁾ The results obtained in the velocity and length forms agree within less than about 1%, and only results calculated with the length form are shown in figure.

Present photodetachment cross-sections for the process (1) are shown in Fig. 1 in the energy region near the $\text{Ps}(n=2)$ threshold. Two prominent spikes, just below $e^- + \text{Ps}(n=2)$ threshold, are the first two of the infinite series of Feshbach resonance. These resonances are attributed to an attractive potential between e^- and Ps , which decays as $1/R^2$ owing to the Stark effect for the degenerate $\text{Ps}(n=2)$ states. Another peak above the $\text{Ps}(n=2)$ threshold is the shape resonance of $1P^o$ symmetry predicted by Botero et al.⁵⁾

It is interesting to compare the photodetachment spectrum of Ps^- with those of H^- (for example, Fig. 4(a) in Ref. 2). A close qualitative resemblance

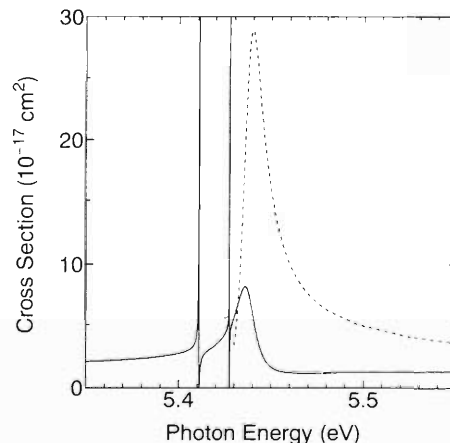


Fig. 1. Photodetachment cross-sections by $\hbar\omega + \text{Ps}^- \rightarrow \text{Ps}(n) + e^-$ near the energy of the $\text{Ps}(n=2)$ threshold. $\text{Ps}(1)$ production: solid curve; $\text{Ps}(2)$ production: dotted curve.

can be seen. A qualitative discussion based on the hyperspherical adiabatic potential curves has been made in Ref. 5.

The resonance energies and widths around $\text{Ps}(n=2)$ threshold of $1P^o$ symmetry are tabulated in Table 1. The lowest resonance position by the complex-coordinate calculation of Bhatia et al.⁶⁾ is in good agreement with the present value. The results of adiabatic treatment in the hyperspherical coordinates⁵⁾ are reasonable, since it is a simple, single channel calculation.

Table 1. Resonance energies E_r and widths Γ (in a.u.) of Ps^- of $1P^o$ symmetry, where $9.8[-7] \equiv 9.8 \times 10^{-7}$.

	Present		Botero et al. ⁵⁾		Bhatia et al. ⁶⁾	
	$-E_r$	Γ	$-E_r$	Γ	$-E_r$	Γ
1.	0.063156	9.8[-7]	0.062587		0.063156	1.0[-6]
2.	0.062543	2.8[-7]	0.062506			
3.	0.062137	5.4[-4]	0.0621	4.[-4]		

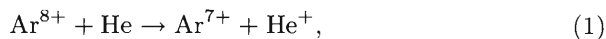
References

- 1) A. P. Mills Jr.: Phys. Rev. Lett. **46**, 717 (1981).
- 2) J.-Z. Tang et al.: Phys. Rev. A **49**, 1021 (1994).
- 3) A. K. Bhatia et al.: Phys. Rev. A **32** 3745 (1985).
- 4) Y. K. Ho: J. Phys. B **16**, 1503 (1983).
- 5) J. Botero et al.: Phys. Rev. Lett. **56**, 1366 (1986).
- 6) A. K. Bhatia et al.: Phys. Rev. A **42**, 1119 (1990).

Recoil-Ion Momentum Spectroscopy of 0.25 MeV/nucleon Ar-He Collisions

T. Kambara, Y. Awaya, Y. Kanai, T. M. Kojima, Y. Nakai, R. Dörner, V. Mergel,
H. W. Schmidt-Böcking, M. Jäger, and B. D. DePaola

Final-state distribution of single-electron capture by 0.25 MeV/nucleon Ar^{8+} ions from He atom,



have been measured with COLd Target Recoil Ion Momentum Spectroscopy (COLTRIMS).¹⁻³ In single-electron capture processes without an emission of free electrons, the binding energy of the captured electron to a nl -orbital of the projectile is related to the longitudinal component (parallel to the beam direction) of the recoil ion momentum $p_{\parallel R}$ by the relationship:

$$p_{\parallel R} = -[(\epsilon_{nl} - \epsilon)/v + m_e v/2], \quad (2)$$

where m_e is the electron mass, v is the projectile velocity, ϵ is the electron binding energy of He atom, and ϵ_{nl} is the binding energy of captured electron in the nl orbit. In this and next articles, the recoil-ion momentum is expressed by atomic unit (au) which correspond to 300 m/s for a He ion.

The experiments were performed at RILAC with a setup which was almost same as that described previously,² but was improved in the resolution of the recoil-ion momentum measurement. The slow recoil ions produced in the intersection region were analyzed by an electrostatic spectrometer,³ where the three components of the recoil-ion momentum vector were determined by the recoil-ion trajectory and its time-of-flight (TOF) in coincidence with the projectile. In the present measurements, a non-uniform electric field was used to achieve a position focusing effect of the same momenta from the whole collision volume (lens effect). The lens effect has improved the resolution of the longitudinal momentum component to about ± 0.2 au (atomic unit) from the resolution of ± 0.5 au without it. In the present collision system, this momentum resolution corresponds to about ± 17 eV of resolution for the binding energy of the captured electron. The overall resolution of the transverse component $p_{\perp R}$ was about ± 0.2 au.

Figure 1 shows a $p_{\parallel R}$ distribution by Ar^{8+} ions, where the yield is integrated over $p_{\perp R} \leq 4$ au. Since the projectile of Ar^{8+} ion is a neon-like system where the orbitals with $n \leq 2$ are closed, the electron is cap-

tured to the orbitals with $n \geq 3$. The figure also shows the final electron orbitals and the excitation energies relative to the ground $3s$ state of the Ar^{7+} ion. The present resolution of the final state binding energy is enough to separate the capture to the $n = 3$ states from those to the $n \geq 4$ states. The capture to the $n = 4$ states also appears as a shoulder of the peak due to the capture to the $n = 5$ states. The $n = 5$ states are dominantly populated by single-electron capture in the present collision system and this result agrees with a classical overbarrier model.⁴

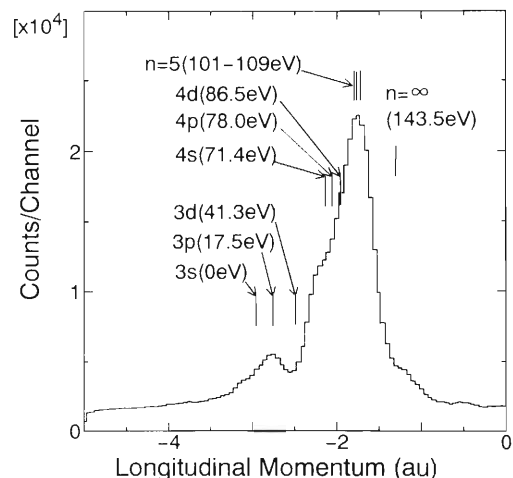


Fig. 1. The longitudinal momentum distribution of recoil ions for one-electron capture from He by 0.25 MeV/nucleon Ar^{8+} ions. The electronic states of the captured electron and respective excitation energies are also indicated.

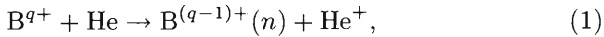
References

- 1) K. Ullmann et al.: Proc. 4th US/Mexico Symp. on Atomic and Molecular Phys., San Juan del Río, Mexico, 1994, World Scientific, 1995, p. 269.
- 2) T. Kambara et al.: J. Phys. B **28**, 4593 (1995).
- 3) V. Mergel et al.: Phys. Rev. Lett. **74**, 2200 (1995).
- 4) H. Ryufuku, K. Sasaki, and T. Watanabe: Phys. Rev. A **21**, 745 (1980).

Recoil-Ion Momentum Analyses of Single-Electron Capture of He by $B^{4+,5+}$ at 0.5–1 MeV/nucleon

T. Kambara, A. Igarashi, N. Watanabe, Y. Nakai, T. M. Kojima, and Y. Awaya

We have made state-selective measurements of differential cross sections of one-electron capture processes from helium atoms by fast boron ions ($Z = 5$),



where n is the principal quantum number of the captured electron. The projectiles were fully-stripped B^{5+} ions at energies of 0.75 and 1 MeV/nucleon and were hydrogen-like B^{4+} ions at 0.567, 0.75, and 1 MeV/nucleon.

We have measured all the momentum components of the recoil He^+ ions applying COLd Target Recoil Ion Momentum Spectroscopy (COLTRIMS)^{1,2)} in coincidence with the projectiles which captured one electron. From the longitudinal component of the recoil-ion momentum, we have deduced the binding energy of the final states of the captured electron. The differential cross sections for these final states have been obtained as functions of the transverse component.

The experimental setup was almost same as that of the previous study.²⁾ A collimated boron beam from RILAC intersected a target of He gas jet. Before the formation of the gas jet, the target He gas was precooled to 35–40 K at a pressure of 500 mbar.

The projectile ions which captured one electron in the target gas were selected by a deflecting magnet and were detected with a position-sensitive parallel-plate avalanche counter. The recoil ions were analyzed by an electrostatic spectrometer with a uniform extraction field and the charge state and three components of the momentum vector were determined in coincidence with the detected projectile ions.

Figure 1 shows the measured longitudinal momentum distribution of the recoil He^+ ions. The final states of the captured electron were separated to the ground state ($n = 1$) and to the excited states ($n > 1$) as shown in the figure. A peak around 0 au was produced by chance coincidences between projectile charge change and target ionization. The electron capture predominantly occurs into the excited states, but

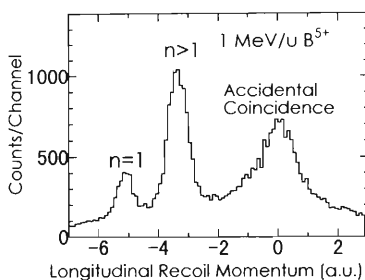


Fig. 1. Longitudinal recoil-momentum distribution of He^+ by 1 MeV/nucleon B^{5+} projectiles.

the relative intensity of the capture into the ground state increases rapidly with the collision energy.

Figure 2 shows the differential cross section of single-electron capture by 1 MeV/nucleon B^{5+} projectiles. The results are normalized to the theoretical total cross sections of an eikonal approximation.³⁾ The capture cross sections to the excited states have an almost same dependence on the transverse momentum regardless of the charge state and energy of the projectile; with a peak around 1 au and a monotonous decrease at the higher transverse momentum and a slower decrease above 3 au. The capture cross section to the ground state, on the other hand, has a different feature: It depicts a peak at about 1.5 au and a broad tail or a hump at the higher transverse momentum. The shape of the hump depends on the collision velocity and projectile charge.

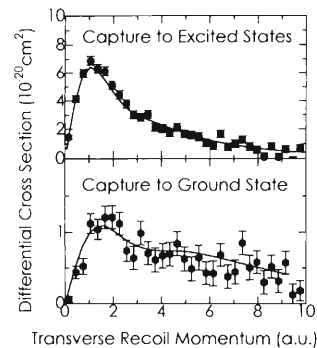


Fig. 2. Differential cross section of one-electron capture to the ground (lower figure) and excited (upper figure) states by 1 MeV/nucleon B^{5+} ions. Dots are experimental results and solid lines are the calculation results.

The experimental results of the differential cross sections were compared with calculations of the eikonal approximation.³⁾ The results are shown in Fig. 2 by curves of solid lines. The theoretical predictions for the capture to the excited states agree well the experimental results at all the projectile velocities and charge states. The theory can well reproduce the hump structure in the differential cross section for the capture to the ground state. The agreement is better for the higher velocity and charge state of the projectile. The details of this work are reported elsewhere.⁴⁾

References

- 1) K. Ullmann et al.: Proc. 4th US/Mexico Symp. on Atomic and Molecular Phys., San Juan del Río, Mexico, 1994, World Scientific, 1995, p. 269.
- 2) T. Kambara et al.: J. Phys. B **28**, 4593 (1995).
- 3) K. Kobayashi, N. Toshima, and T. Ishihara: Phys. Rev. A **32**, 1363 (1985).
- 4) T. Kambara et al.: J. Phys. B in press.

Beam Foil Spectra of Highly Charged Argon Ion in Visible Region

K. Ishii, T. Nishida,* Y. Kimura, M. Fujiwara, T. Nakano,
S. Kawae, K. Ando, and Y. Awaya

Beam-foil spectra of highly charged Ar ion at the energy of 1.0 and 2.0 MeV/amu were recorded in the region between 200 and 700 nm. Photons emitted from the Ar ion after its passage through a thin carbon foil were dispersed by a monochromator and detected by a liquid nitrogen cooled CCD camera (Princeton Instruments, Inc.). The CCD detectors cover the wavelength range of about 80 nm. The recording of the spectra for each range were successively repeated at least twice while keeping the conditions unchanged, e.g., the beam current and the exposure time. The spectra thus recorded contain several spurious spikes, whose height is often as large as the intense spectral lines. Most of them originate from the cosmic rays and the others from X-rays from the beam transport. The spikes due to the X-rays were reduced by covering the detector with lead sheets. Still some were left and therefore the exposure time for each run was limited to less than three minutes. The remaining spikes were eliminated in the data processing by comparing the two successively recorded spectra.

Using the hydrogenic term energies, the wavelengths and the transition probabilities for the Rydberg transitions were calculated.^{1,2)} Most of the intense lines are thus classified as transitions of high n, l levels in Ar X to Ar XVII.

In Fig. 1 the observed argon spectra in the range 210–250 nm at 1.0 MeV/amu beam energy are displayed. It is noted that a satellite line on the longer wavelength side of the $n = 9-10$ transition in Ar XIII appears only at the observation in the close vicinity of the foil and moves to the longer wavelength side as the foil was translated upstream relative to the observation line.

The short-lived and broad feature of the satellite line suggests that this line is due to the multiply excited Rydberg transition. We have tentatively attributed this to the Ar XII $1s^2 2s^2 2p 9l n'' l'' - 1s^2 2s^2 2p 10 l' n''' l'''$ transition, where $l = 8$, $l' = 9$, and n'' is larger than 10. As a first approximation, we have calculated the level energies of $[\text{core}]9_8 n'' l''$ and the $[\text{core}]10_9 n''' l'''$ using the modified Rydberg formula.³⁾ We have also calculated them by use of the atomic structure calculation code.⁴⁾

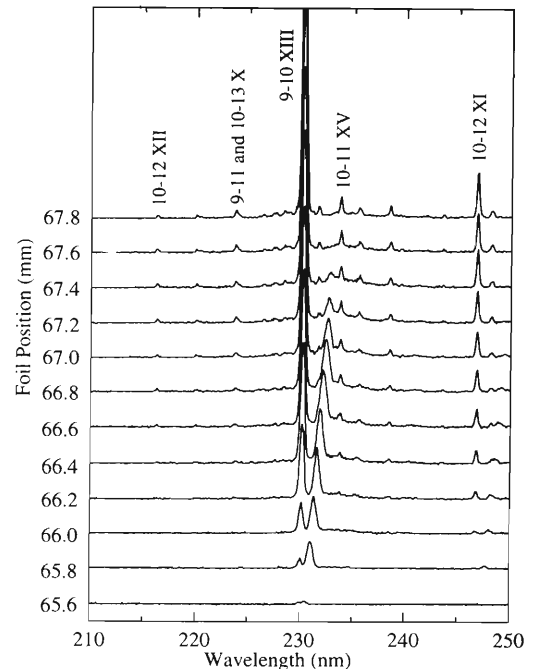


Fig. 1. A portion of Ar ion spectra at 1.0 MeV/amu energy at a sequence of successive foil position. The prompt spectrum is at the bottom and the delayed ones are shown upwards.

The calculated wavelength varies from 230.7 to 236.7 nm when n'' was changed from 22 down to 12. The further study both in experiment and in calculation is now in progress.

References

- 1) H. A. Bethe and E. E. Salpeter: in *Quantum Theory of One- and Two-Electron Atoms* (Springer-Verlag, Berlin, 1957), p. 262.
- 2) B. Edlén: in *Handbuch der Physik*, edited by S. Flügge, (Springer-Verlag, Berlin, 1964) Vol. XXVII, p. 80.
- 3) F. H. Read: *J. Phys.* **B10**, 449 (1977).
- 4) R. D. Cowan: in *The Theory of Atomic Structure and Spectra*, University of California Press, Berkeley (1981).

* Department of Engineering Science, Kyoto University

Beam Foil Spectra of Highly Charged Neon Ion in Visible Region

K. Ishii, T. Nishida,* Y. Kimura,* M. Fujiwara,* S. Kawae,*
T. Nakano,* K. Ando, and T. Kambara

Beam-foil spectra of highly charged Ne ion at the beam energy of 0.5 and 1.0 MeV/amu were recorded in the region between 200 and 700 nm. Photons emitted from the Ne ion after a passage through a thin carbon foil were dispersed by a monochromator and detected by a photomultiplier (PMT). In the early Summer of 1996, the PMT was replaced by a liquid nitrogen cooled CCD detector (Princeton Instruments, Inc.). The data acquisition time was largely reduced. In the previous years, it took 24 hours to scan the spectral range from 200 to 450 nm by use of a single channel photomultiplier. Now, the efficiency was improved by a factor of almost one hundred.

In the spectra thus far recorded, most of the lines are classified as transitions of high n, ℓ levels in Ne V to Ne X, where n ranges from 5 to 11. The lines due to transition of $2s7\ell-2s8\ell'$ in Be-like Ne VII were found split into ℓ -components by the perturbation of the nearby lying doubly excited $2p5\ell$ configuration to $2s8\ell$. The energy levels, the transition wavelengths, and the transition probabilities were computed by use of the atomic structure code.¹⁾ In the calculation, relevant configurations were included as many as possible. In addition to the main configurations of $2s7\ell$ and $2s8\ell$, the perturbing $2p3\ell$, $2p4\ell$, $2p5\ell$, $2p6\ell$, $2p7\ell$ and $2s6\ell$ were included with all the possible ℓ . In Fig. 1 the observed neon spectrum in the range 360–400 nm at 0.5 MeV/amu beam energy is compared with the calculated spectrum. Note that the agreement is good not only in the line positions, but also in the relative intensities. The identification was confirmed by the decay measurements of individual lines.

The use of the CCD detector made it possible to record the spectra at the different foil positions. The integrated beam current collected in the Faraday cup and also the non-dispersed photons counted by a photomultiplier at the fixed position close to the foil through an optical fiber were used to normalize the spectra. The CCD camera covers the spectral range of about 80 nm. The recording of spectra for each range was repeated successively at least twice under the same conditions in order to eliminate the spurious spikes caused by cosmic rays. A broad satellite line at 390 nm on the longer wavelength side of Ne VII $2s7i-2s8k$ transition was found to decay as soon as the observation position goes downstream from the foil. Strikingly, it moves towards the longer wavelength side.

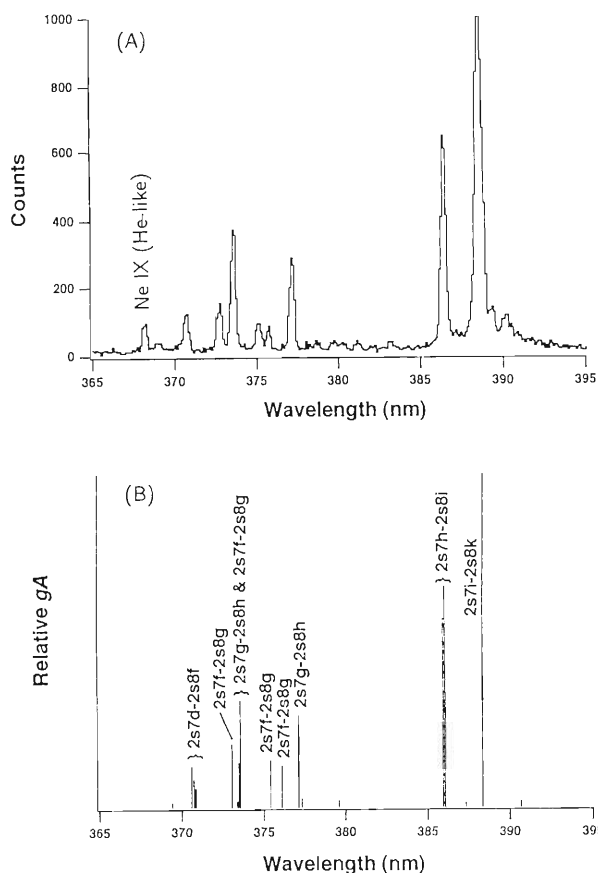


Fig. 1. Comparison of observed and calculated spectra in the range of 360–400 nm. (A) Observed at the beam energy of 0.5 MeV/amu. (B) Calculated lines are due to the transition of Ne VII $1s^22s7\ell-1s^22s8\ell'$.

The broad and short-lived features suggest that this line originates from the multiply excited transitions. This line is tentatively assigned as the transition of Ne VI $1s^22s7\ell n\ell'-1s^22s8\ell n\ell'$, where n ranges from 12 to 18 with highest ℓ' . This is not a special case. Most of the Rydberg transitions with $\Delta n = 1$ are accompanied by a short-lived, broad line on the longer wavelength side. They show the same feature as described for the Ne VI $n = 7-8$ transition.

References

- 1) R. D. Cowan: in *The Theory of Atomic Structure and Spectra*, University of California Press, Berkeley (1981).

* Department of Engineering Science, Kyoto University

Intercombination Line Oscillator Strengths for High-Z Mg- and Al-like Ions

R. Hutton, L. Engström, S. Huldt, I. Kink, B. Nyström, Y. Zou,
I. Martinson, P. Bengtsson, K. Ando, T. Kambara, Y. Kanai,
T. M. Kojima, Y. Nakai, and Y. Awaya

Intercombination line transition rates have been investigated for various ions belonging to the Mg- and Al-like sequences. The investigation has been performed using the ion beams from RILAC and the techniques of beam-foil spectroscopy. The procedure for doing these measurements has been described elsewhere.¹⁾ The results of the measurements show a consistent deviation from the generally accepted theoretical trend. This is summarized in Figs. 1 and 2. In Fig. 1 the (scaled) $3s^2\ ^1S_0 - 3s3p\ ^3P_1$ transition oscillator strength (f) in Mg-like ions is shown for ions up to Mg-like Au as a function of the effective charge $\zeta = q + 1$ of the ion, where q is the charge state. The experimental results are compared to theoretical values.

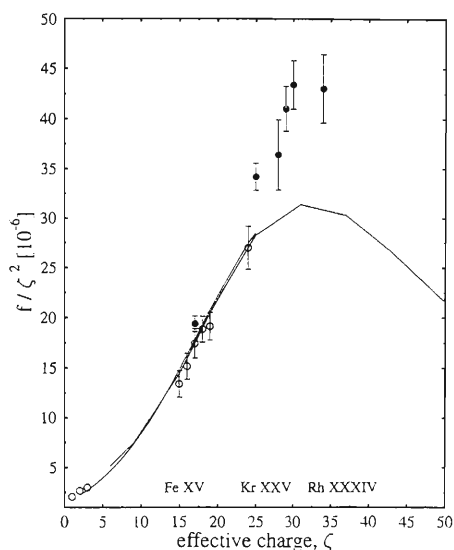


Fig. 1. Scaled oscillator strength for the Mg-like intercombination line as a function of the effective charge. The darkened points were measured at RIKEN. The full curve represents theoretical values.²⁾ References to the data represented by open circles and to other theoretical works can be found in Ref. 3.

The points represented by filled circles are the data obtained at RIKEN. A clear discrepancy between theory and experiment is observed. A similar plot but for the $3s^23p\ ^2P_{3/2} - 3s3p^2\ ^4P_{5/2}$ transition in Al-like ions is presented in Fig. 2, where the open circles represent data obtained at RIKEN. The origin of this discrepancy is not understood at present; there are no known experimental problems which could result in such deviations.

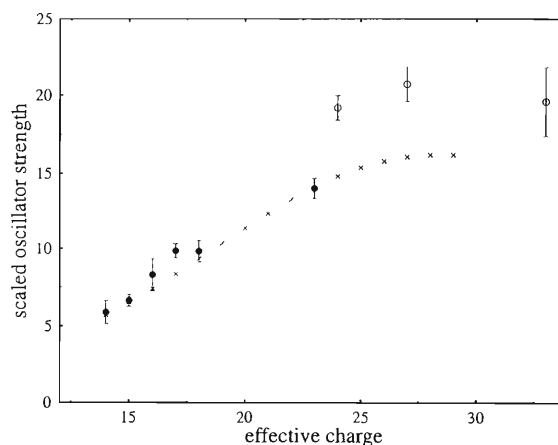


Fig. 2. A similar picture to Fig. 1 but for the $3s^23p\ ^2P_{3/2} - 3s3p^2\ ^4P_{5/2}$ transition in Al-like ions. The points measured at RIKEN are represented by open circles. The theoretical data denoted by \times are from Ref. 4. References to the data represented by filled circles can be found in Ref. 5.

References

- 1) R. Hutton: Proc. 8th Int. Conf. on the Physics of Highly Charged Ions, Sept. 1996, Omiya, Japan, to be published in Physica Scripta.
- 2) L. J. Curtis: Physica Scripta **43**, 137 (1991).
- 3) E. Träbert et al.: Z. Phys. D **32**, 295 (1995).
- 4) K.-N. Huang: At. Data Nucl. Data Tables **34**, 1 (1986).
- 5) E. Träbert: Phys. Rev. A **47**, 3805 (1993).

Lifetimes for the Be- and B-like Fe Intercombination Lines

R. Hutton, B. Nyström, I. Martinson, K. Ishii, M. Jäger,
K. Ando, P. Bengtsson, T. Kambara, and Y. Awaya

The $2s^2\ ^1S_0 - 2s2p\ ^3P_1$ intercombination line in Be-like ions is of considerable interest. This is reflected in the amount of work, both theoretical and experimental, done on the intercombination rate for ions in this sequence. The main reason for the interest is due to the fact that the intercombination lines in C III and O V are used in the diagnostics of astrophysical plasmas. Given the amount of theoretical data available for the decay rate of the $2s2p\ ^3P_1$ level, there is surprisingly little amount of experimental data for the ions of this sequence. The $2s2p\ ^3P_1$ lifetime has been measured for only four ions in the sequence, namely C III, Fe XXIII, Kr XXXIII, and Xe LI. The measurement for Fe XXIII¹⁾ was not in agreement with the currently recommended theoretical result.²⁾ However, the previous Fe XXIII beam-foil measurement suffered from rather large error estimates. With this in mind a re-measurement of the $2s2p\ ^3P_1$ lifetime was initiated for Fe XXIII. The measurement was made using a beam of 2.5 MeV/nucleon Fe ions provided by the RILAC. The measurement procedure has been described in a number of previous articles (e.g., Ref. 3) and will not be discussed here. The experimentally determined lifetime was found to be 17.5 ± 1.5 ns which is in reasonable agreement with the recommended theoretical value of 19.6 ± 0.8 ns.²⁾ The scaled $2s2p\ ^3P_1$ lifetime is shown in Fig. 1 for a number of ions in the Be I sequence. More details of this figure can be found in Ref. 4. Using the same ion beam a measurement was made for the $2s2p^2\ ^4P_{5/2}$ lifetime in B-like Fe. No measurements of the B-like intercombination line transition rates have been previously reported for high- Z ions. The experimentally determined value for the $^4P_{5/2}$ lifetime is 14.8 ± 1 ns which is in good agreement with the most recent theoretical result of 13.4 ns.⁵⁾

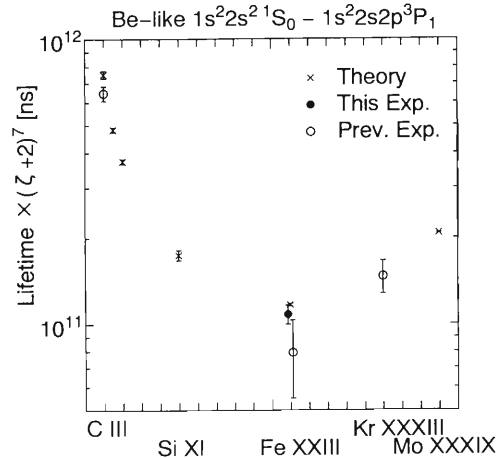


Fig. 1. A comparison between theoretical and experimental values for the $2s2p\ ^3P_1$ lifetime in Be-like ions. $\zeta = q + 1$ is the effective charge where q is the charge state of the ion. The new Fe²²⁺ data point (filled circle) was measured at RIKEN; see Ref. 4 for details. The remaining experimental data are taken: C²⁺ from Ref. 6, Fe²²⁺ from Ref. 1, and Kr³²⁺ from Ref. 7. The theoretical data are from Ref. 8.

References

- 1) D. Deitrich et al.: Phys. Rev. A **18**, 208 (1978).
- 2) T. Brage, J. Flemming, and R. Hutton: manuscript in preparation for Mon. Not. R. Astron. Soc.
- 3) R. Hutton et al.: Phys. Rev. A **51**, 143 (1995).
- 4) R. Hutton et al.: accepted for publication in Physica Scripta.
- 5) G. Merkelis et al.: Physica Scripta **51**, 233 (1995).
- 6) V. H. S. Kwong et al.: Astrophys. J. **411**, 431 (1993).
- 7) D. Deitrich et al.: Phys. Rev. A **22**, 1109 (1980).
- 8) A. Ynnerman and C. Froese-Fischer: Phys. Rev. A **51**, 2020 (1995).

Oscillator Strengths for Resonance Transitions in Na-like Kr

I. Kink, R. Hutton, B. Nyström, I. Martinson, K. Ishii, K. Ando, T. Kambara, Y. Nakai, T. M. Kojima, and Y. Awaya

We have measured the lifetime of the $3p^2P_{3/2}$ level in Na-like Kr^{25+} , using beam-foil excitation and cascade corrected analysis. The Kr beam at 2 MeV/nucleon was provided by RILAC. Our result, $\tau = 45 \pm 2$ ps, has half the uncertainty as compared to the previous experimental data taken for highly ionized Na-like ions, and permits an important test of theoretical methods. Recently, Hutton *et al.*¹⁾ pointed out a seemingly systematic one standard deviation ($1\sigma_s$) difference between theoretical and experimental f -values of the $3s^2S_{1/2} - 3p^2P_{3/2}$ transitions for Na-like ions with the charge state $Z > 20$. More precise result of ours indicates that these small differences ($\sim 1\sigma_s$) are coincidental and insignificant, confirming the reliability of theoretical calculations for this Na-like system. A review of the scaled line strength for the $3s^2S_{1/2} - 3p^2P_{3/2}$ transition is shown in a graphical form in Fig. 1. Here, the quantity Z^2S/C is plotted against $1/(Z-10)$, where S is the line strength in a.u. and C is a relativistic correction. The measured point for Kr^{25+} is shown by a filled black square and indicates that there is no remaining discrepancy between theory and experiment. References to the other experimental points can be found in Ref. 1. The theoretical data were produced using the Coulomb approximation Hartree-Slater method; cf., Ref. 2. More details can be found in a recent publication by Kink *et al.*³⁾

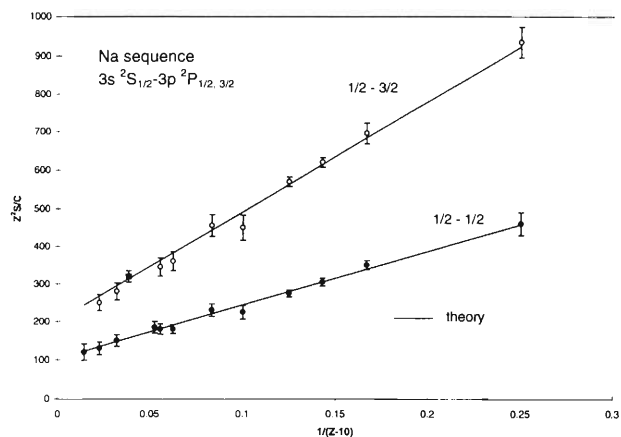


Fig. 1. The quantity Z^2S/C as a function of $1/(Z-10)$ for Na-like ions: Dots show the experimental results and lines show the theoretical results.

References

- 1) R. Hutton, S. Huldt, B. Nyström, I. Martinson, K. Ando, T. Kambara, Y. Kanai, Y. Nakai, and Y. Awaya: Phys. Rev. A **51**, 143 (1995).
- 2) L. J. Curtis, D. G. Ellis, and I. Martinson: Phys. Rev. A **51**, 251 (1995).
- 3) I. Kink, R. Hutton, B. Nyström, I. Martinson, K. Ando, T. Kambara, Y. Nakai, T. M. Kojima, and Y. Awaya: accepted for publication in Phys. Rev. A, Nov. 1996.

Wavelengths for Al- and Si-like Intercombination Lines

R. Hutton, P. Bengtsson, K. Ando, T. Kambara, and Y. Awaya

In a number of previous articles, intercombination rates for the Mg-like lines have been discussed for ions ranging from Ni to Nb.¹⁾ Those previous works have concentrated on lifetime measurements as the intercombination line wavelengths were already known. However, although the Mg-like $3s^2\ ^1S_0 - 3s3p\ ^3P_1$ transition wavelength is well known for ions up to $Z = 54$ the situation for Al- and Si-like ions is not so well documented. By using the beam-foil spectroscopy and in particular the techniques of delayed-spectroscopy, the wavelengths for Al-like and Si-like intercombination lines in ions up to Nb ($Z = 41$) have been determined. Some deviations from calculated wavelengths and from previous experimental data were noticed. An example of such a deviation can be seen in Fig. 1, where $(E_{obs} - E_{cal})/(Z - 13)$ is plotted as a function of $(Z - 13)$. Here E_{obs} is observed transition energy and E_{cal} is calculated transition energy. When all relevant effects are included for E_{cal} this difference is expected to converge to a constant value. The method used to find the Al- and Si-like intercombination lines is based on the fact that the $3s^2\ ^1S_0 - 3s3p\ ^3P_1$ wavelength is already known up to Xe ($Z = 54$).³⁾ Then, a simple isoelectronic plot of wavelength differences allows easy extrapolation for

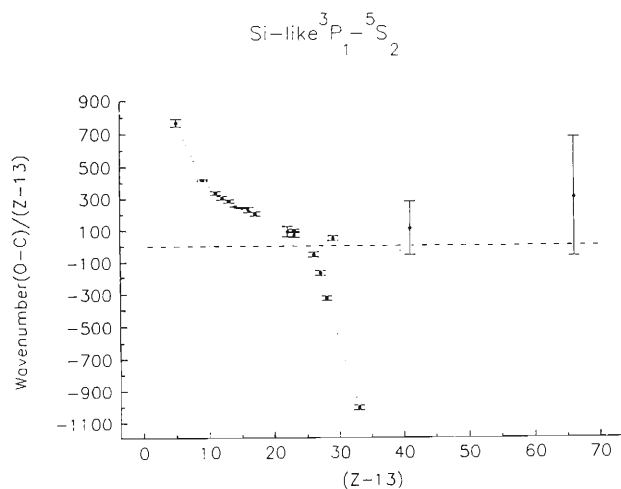


Fig. 1. The difference between the (scaled) observed and calculated transition energies for one of the Si-like intercombination lines. The data for Y, Zr, and Nb were obtained at RIKEN.

the Al- and Si-like lines (See, Fig. 2). In Fig. 2 the difference between Al-like and Mg-like intercombination line wavelengths are plotted. The identifications were confirmed by choosing different beam energies to vary the charge state fractions after the exciter foil. The results of this work are discussed in more detail in Ref. 2.

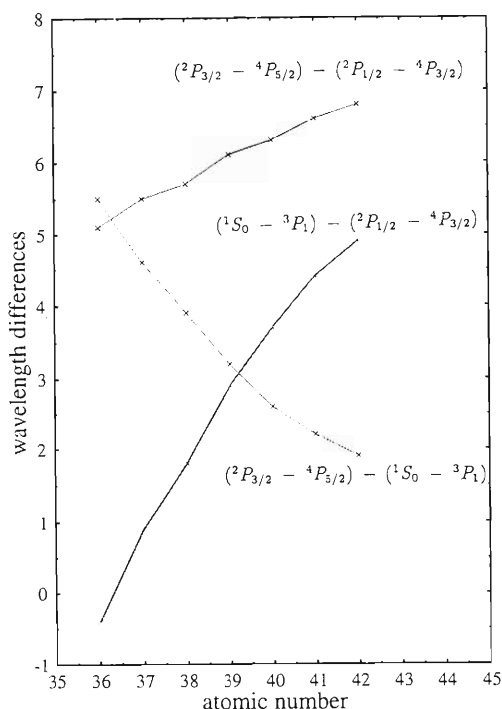


Fig. 2. Wavelength differences for Mg- and Al-like intercombination lines are plotted against the atomic number. The Al- and Si-like wavelengths were determined at RIKEN and the Mg-like intercombination line wavelength is known for ions up to Xe.³⁾

References

- 1) R. Hutton: Proc. 8th Int. Conf. on the Physics of Highly Charged Ions, Sept. 1996, Omiya, Japan, to be published in Physica Scripta, see references therein.
- 2) P. Bengtsson et al.: Proc. 8th Int. Conf. on the Physics of Highly Charged Ions, Sept. 1996, Omiya, Japan, to be published in Physica Scripta.
- 3) J. F. Seely et al.: J. Opt. Soc. Am. B 5, 602 (1988).

Charge Transfer Cross Sections of Low-Energy Highly Charged Ions with N₂

Y. Kanai, Y. Nakai, M. Kitajima, T. Kambara, and Y. Awaya

To study the charge transfer processes of the low-energy highly charged ion and atom (or molecule) collisions, we started to measure the charge transfer cross sections of highly charged ions. Low-energy highly charged ions from the 14.5 GHz Caprice¹⁾ ion source were energy-analyzed and focused on the gas cell. The cell length was 5 cm. The entrance and exit apertures of the gas cell were 1 and 2 mm, respectively. After the collisions, the ion charge states were analyzed by an electrostatic analyzer and a position sensitive detector (MCP + wedge and stripe anode).

Here, we report the total single electron capture cross section σ_1 of highly charged ions in the collisions with N₂ molecules. Present results are shown in Fig. 1. We used the Ar^{3,7+}, O^{3,6+} and N³⁺ ions in the energy range of 2–10,000 eV/u. In this energy range, the energy dependence of the σ_1 is small. This type of energy dependence can be explained by a simple model called absorbing sphere model.²⁾ In this model, when the highly charged ions come to a critical distance from the target, all the ions capture the target electrons. To compare our experimental results with this model, we show the broken and solid lines in Fig. 1: the values calculated with this model divided by some factors (2.8 and 1.6). The energy dependence of our results, except for the N³⁺ ions, is in good agreement with this model made for the single electron capture processes. In the case of collisions of the highly charged ions with targets, an ion can capture multiple electrons (> 2) inside the critical distance. Therefore, for the absolute values of the capture cross sections, we have to compare the values calculated by the absorbing sphere model with the total capture cross section $\sigma_{\text{tot}} = \sum_i \sigma_i$. For Ar⁷⁺ collisions, we measured the total capture cross section and found $\sigma_{\text{tot}} = 1.7 \times \sigma_1$. These values are almost same as those calculated by the absorbing sphere model. For the collisions of high charge ($q = 6, 7$) ions, we can obtain the total cross sections by this model. For the low charge ($q = 3$) ions, however, absolute values of our results are not in agreement with this model. For the low charge ion collisions, we need

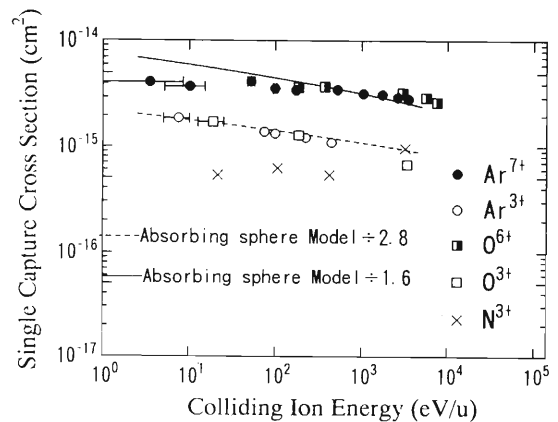


Fig. 1. Single electron capture cross sections of highly charged ions with N₂. Solid and broken lines show the values calculated by the absorbing sphere model divided by 1.6 and 2.8, respectively.

more experimental results to discuss about the applicability of this model.

For the lower energy region (< 10 eV/u), our results contain a couple of experimental uncertainties due to (A) the beam energy spread of the low-energy ion beams and (B) the limitation of the scattering angle of scattered ions by the exit aperture of gas cell. To solve these problems, we are planning the following new experiments: (a) to set the energy selector before the collisions region, (b) to use the gas jet as target, and (c) to measure the angular dependence of charge transfer cross sections to obtain the total cross sections. After these new experiments, we may be able to discuss more detail of the charge transfer processes of highly charged ions.

References

- 1) Y. Kanai et al.: RIKEN Accel. Prog. Rep. **30**, 168 (1997).
- 2) R. E. Olson and A. Salop: Phys. Rev. A **14**, 579 (1976).

Diode-Laser Spectroscopy of Atomic Beams

T. Wakui, W.-G. Jin, T. Minowa, H. Katsuragawa, H. Uematsu,* and M. Wakasugi

Measurements of the isotope shift and hyperfine structure in atomic transitions by means of laser spectroscopy give us information about atomic structures and nuclear properties. Using RIKEN accelerator facility, we are performing laser spectroscopy of atoms with unstable nuclei. Therefore, test experiments with stable isotopes using a new laser spectroscopic technique are necessary, and development of such a technique using a diode-laser instead of the conventional complicated and expensive ring-dye laser is particularly desirable for nuclear laser spectroscopy. This paper reports measurements of the isotope shift and hyperfine structure obtained by means of a high-resolution diode-laser spectroscopy.

As a light source, we used single-mode diode lasers with power of 15–50 mW in the wavelength region of 670–800 nm. Both the temperature and current of the diode-laser were controlled by a controller. Frequency scanning of laser was made by modulation of the current. An atomic beam was ejected from a molybdenum oven with a small hole of 1 mm in diameter. The oven was heated to 600 °C for Ba beam with a tungsten filament. The atomic beam then passed through another collimation orifice of 2 mm in diameter. The laser beam was crossed with the atomic beam orthogonally so that the Doppler broadening is reduced. The resonant fluorescence from the atomic beam was focused by a spherical mirror onto a cooled photomultiplier to be measured. A Fabry-Perot interferometer (FPI) with a free spectral range of 300 MHz was used for the calibration of the relative frequency. The fluorescence and the transmitted signal of the FPI were simultaneously recorded with a multichannel scaler.

Figures 1 and 2 show laser-induced fluorescence spectra of the 791.1-nm transition in Ba I and the 680.3-nm transition in Sm I, respectively. In Fig. 1, small peaks indicated by a, b, and c are hyperfine transitions in ^{135}Ba while α , β , and γ are those in ^{137}Ba . The peaks of both ^{130}Ba and ^{132}Ba isotopes are overlapped with ^{138}Ba . In Fig. 2, the peaks indicated by * are hyperfine transitions in ^{147}Sm and ^{149}Sm . The FWHM of peaks is about 50 MHz for Ba and about 70 MHz for

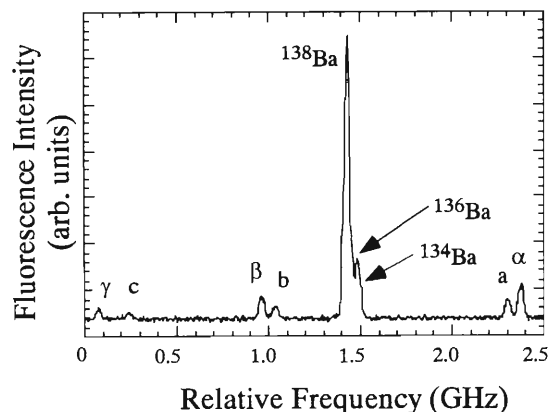


Fig. 1. Observed spectrum of the 791.1-nm transition in Ba I.

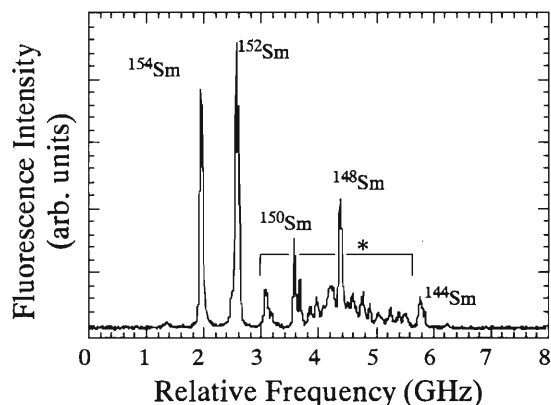


Fig. 2. Observed spectrum of the 680.3-nm transition in Sm I.

Sm. This shows that the resolution of our experimental setup is enough for the measurements of hyperfine structure and isotope shift. From the observed hyperfine spectra, the hyperfine structure constants for the $^3\text{P}_1$ state of ^{135}Ba and ^{137}Ba were determined. The isotope shifts in Ba I and Sm I were also obtained, and the electron density at the nucleus was derived.

* Tokyo Gakugei University

Laser Spectroscopy of AgHe₂ Exciplex in Liquid Helium

Q. Hui,* J. L. Persson,** Z. J. Jakubek,** M.-P. Coquard,** M. Nakamura, and M. Takami

We are currently studying the physical properties of neutral atoms in liquid helium by laser spectroscopy.^{1,2)} One of the aims of this work is to explore the feasibility of using liquid helium for the on-line spectroscopic study of the unstable nuclei produced by Riken ring cyclotron (RRC). For this purpose, it is crucial to understand the behavior of stable neutral and ionic atoms trapped in liquid helium and their interaction with the surrounding liquid. A neutral atom is known to be trapped in a bubble-like cavity due to a strong repulsive force between the impurity and the surrounding helium atoms.³⁾ The coupling of the cavity with the trapped atom induces a large shift and broadening of the atomic absorption spectra, while the shift and broadening are relatively small in the emission stage. In our recent study of Ag in liquid helium, we found a new feature as described here in the observed spectra,^{4,5)} which should be important for the study of atomic ions with unstable nuclei.

Figure 1 shows the observed emission spectrum of Ag in liquid helium. The excitation laser wavelength was 322.5 nm, which corresponds to the peak of the broad and blue-shifted D2 absorption line of Ag. Only the D1 emission line was observed close to the position of the free atomic line. In addition, an extra broad emission band was observed around 382 nm with a

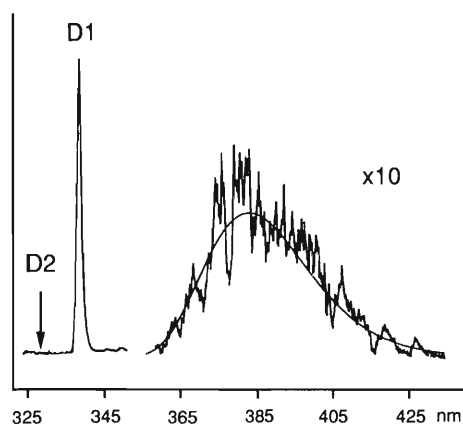


Fig. 1. Emission spectrum from Ag in liquid helium. In addition to the D1 emission line, a weak and broad emission band is observed on the red side of the D1 line. A simulated emission band is drawn by a solid line.

35 nm (FWHM) band-width. The excitation spectra measured by monitoring the D1 line and the broad band emission showed a significant difference between the two: the D1 emission was observed by exciting the D1 and D2 absorption lines, while the broad emission was observed only when the D2 line was excited. These observations indicate that the Ag atoms excited to the $P_{3/2}$ fine structure component relax to the $P_{1/2}$ state and also to an unknown state from which the broad emission occurs.

The absence of D2 emission in liquid helium has been reported for Rb and Cs.⁶⁾ Dupont-Roc⁷⁾ has proposed that in the $P_{3/2}$ states of these alkali atoms, two helium atoms may attach to the atom along the nodal line of the doughnut-like $P_{3/2}$ electron distribution, thereby forming an exciplex, by the attractive force from their exposed ion cores. He predicted a red-shifted, bound-free emission band from the exciplex, but observation of the emission has not been reported till today. We assigned the observed broad emission from Ag to the counterpart of the red-shifted emission expected for the alkali atoms. To confirm this assignment, we have made an extensive *ab initio* calculation on the AgHe₂ potential energy curves and have simulated the emission spectrum. The simulated emission band is drawn in Fig. 1 with a solid curve over the observed band. An excellent agreement between the calculation and observation has confirmed that the Dupont-Roc's model is correct.

This discovery is of particular importance for the study of charged atoms in liquid helium, because they are expected to have stronger attractive interaction with helium atoms, and because any atomic ion with one valence electron should show exactly the same behavior. Extension of the present work to atomic ions is in progress.

References

- 1) Q. Hui et al.: Z. Phys. B **98**, 353 (1995).
- 2) J. L. Persson et al.: Phys. Rev. A **52**, 2011 (1995).
- 3) H. Bauer et al.: Phys. Lett. A **146**, 134 (1990).
- 4) J. L. Persson et al.: Phys. Rev. Lett. **76**, 1501 (1996).
- 5) M. Nakamura et al.: RIKEN Accel. Prog. Rep. **28**, 77 (1995); RIKEN Accel. Prog. Rep. **29**, 124 (1996).
- 6) Y. Takahashi et al.: Phys. Rev. Lett. **71**, 1035 (1993).
- 7) J. Dupont-Roc: Z. Phys. B **98**, 383 (1995).

* Inorganic Chemical Physics Laboratory; Saitama University, Graduate School of Science and Engineering.

** Inorganic Chemical Physics Laboratory; STA Fellow.

Temperature Dependence of Al-LVV Auger Electron Spectra (I)

A. Koyama, A. Yoneda, K. Ogiwara, and M. Uda*

Al-L₂₃VV Auger electron spectra induced by fast Ar¹²⁺-ions (1 MeV/amu) were measured at the target temperatures of 40 and 300 °C. Figure 1 shows the difference between the Al-LVV Auger spectrum at 300 °C and that at 40 °C for an incident angle of 25° with respect to the surface of the target. The spectrum at 300 °C is also shown as reference. At energies high and low sides of the peak energy, E_m , the difference is negative, and at energies where the spectrum is steepest it is almost zero; indicating only a slight narrowing of the spectrum, but no decrease of E_m at 300 °C compared to that at 40 °C. Figure 2 shows the difference of spectra for a grazing incident angle of 4°. At energies higher than E_m , the difference is negative, and at lower energies it is positive. At energies where the spectra is

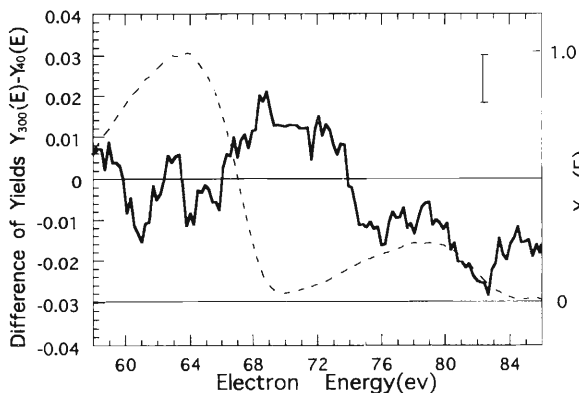


Fig. 1. Difference between the energy spectrum of Al-LVV Auger electrons at the target temperature of 300 °C and that at 40 °C, $Y_{300}(E)-Y_{40}(E)$, for the impact of Ar¹²⁺-ions (1 MeV/amu) at the incident angle of 25° with respect to the surface. Scattering of data is ± 0.005 as indicated by a segment in the figure. The energy spectrum for 300 °C is shown by the dotted curve. The difference is negative at energies around E_m , which means the narrowing of the peak at 300 °C compared to that at 40 °C, but no energy shift.

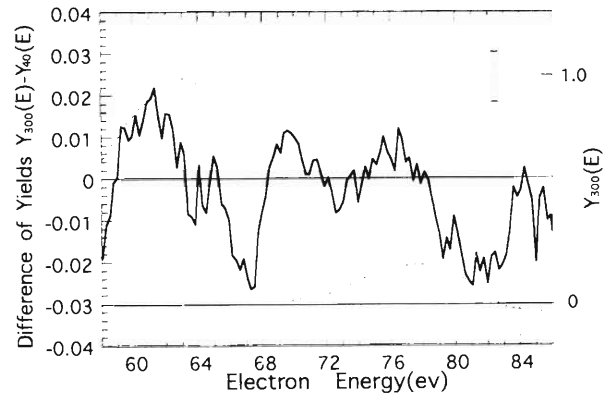


Fig. 2. Difference between the energy spectra at 300 °C and 40 °C, $Y_{300}(E)-Y_{40}(E)$, for the grazing incident angle of 4°. The dotted curve is the Auger spectrum at 300 °C. Scattering of data is ± 0.005 as indicated by a segment in the figure. The difference is negative at the high energy part of the peak and positive at the low energy one, which means the decrease of the peak energy for 300 °C compared to that for 40 °C. The energy decrease is deduced to be about 0.2 eV from the comparison of the spectra.

steepest, the negative difference is most pronounced; indicating that E_m for 300 °C is lower than that for 40 °C. The magnitude is about 0.2 eV.

This temperature dependence strongly supports the multiple-hole (MH) transportation model. The model states that; the energy decrease of E_m is caused by the increase of binding energy of the valence electrons (VE), which is induced by the Coulomb potential due to MH. The MH are created by the emission of VE from the surface due to an impact of a projectile. Diffusing out of the MH is delayed at high target temperature because transportation of valence electrons is slow at high temperature compared to low. That is, lowering of the energy of Auger electrons continues for a long time at high temperature compared to the case of low temperature.

* Department of Materials Science and Engineering, Waseda University

Temperature Dependence of Al-LVV Auger Electron Spectra (II)

A. Koyama, A. Yoneda, K. Ogiwara, and M. Uda*

Multiple electron-holes (MH) created in the valence band composed of s- or p-like electrons are annihilated promptly, and their effect on Auger electron spectra was scarcely observed for the impact of various projectiles incident at large angles with respect to the surface of a target. However, we observed clear projectile-dependence of Al- and Si-LVV Auger electron spectra for small incident angles near 4° . We also observed temperature-dependence on Al-LVV Auger electron spectra induced by the impact of Ar^{12+} ions (1 MeV/amu) incident at 4° ; decrease of the most probable energy of 0.2 eV at 300°C compared to 40°C . Such temperature-dependence as well as those projectile- and incident angle-dependences can be explained by using a model of transportation of MH in the valence band.

Binding energies of valence electrons are considered to increase with existence of those holes via Coulomb potential and kinetic energy of Auger electrons, E_m , decreases; it is because of the relationship approximately given by $E_m = B_L - B_V - B_{V'}$. That is, the energy decrease is given by

$$\Delta E_m = -\Delta(B_L - 2B_V) \sim 2\Delta B_V. \quad (1)$$

When a projectile excites a L-shell electron of an Al atom located the top-most layer of the surface, valence electrons are also excited, emitted from the surface, and MH are left behind. Density of them is proportional to the projectile's stopping power. It is the cause of the projectile-dependence. For grazing angle incidence, they are created in a semicylindrical region on the surface with its radius a and its length infinite. For normal incidence, they are created in a cylindrical region on the surface with its radius a and its depth d . Values of a and d should be nearly equal to the dynamic screening distance of 6Å. The area is much larger for grazing angle incidence than for normal incidence, and it takes long time for the holes to diffuse out in the case of grazing angle incidence compared to normal incidence, which gives rise to the incident angle-dependence.

MH will begin to diffuse from the created region, and after t sec the density of them at the excited Al location will be approximately given by

$$\rho_g(t) = \rho_0 \{1 - \exp(-a^2/4Dt)\}, \quad (2)$$

for grazing angle incidence. For the normal incidence, on the other hand,

$$\rho_n(t) = 2\rho_0/(4\pi Dt)^{3/2} \int_0^d \exp(-Z^2/4Dt) dx \\ \times \int_0^a 2\pi r dr \exp(-r^2/4Dt). \quad (3)$$

The diffusion constant D of MH is nearly equal to that of valence electrons and is approximately given by

$$D \sim \lambda v/3, \quad (4)$$

where λ is the mean free path of valence electrons, and v is their velocity. λ is dependent on target temperature, which is the origin of the temperature-dependence, and can be estimated from the electrical resistivity. Then we can calculate the value of D as $D = 2.41 \times 10^{17} \text{Å}^2/\text{sec}$ at 40°C , and $D = 1.6 \times 10^{17} \text{Å}^2/\text{sec}$ at 300°C .

The energy decrease of Auger electrons averaged over the time is given by

$$\Delta E\nu = 2 \int n_A \Delta B\nu(t) dt / \int n_A dt, \quad (5)$$

where ν is meant n or g, and $n_A = \exp(-t/\tau_A)$ is the number of Auger electrons emitted in the time interval from t to $t+dt$. $\Delta B\nu$ is approximately given by Qe^2/r , where r is the screening distance of the Coulomb potential due to MH, and Q is the total number of MH in the hemispherical region with the radius r around the excited Al atom, and $Q = (2\pi/3)r^3\rho(t)$ with the hole density $\rho(t)$.

By substituting Eqs. (1), (2), (3), and (4) into Eq. (5), we can estimate the energy decrease to be $\Delta E_g = 1.3 \text{ eV}$ (300°C) and $\Delta E_g = 1.0 \text{ eV}$ (40°C) for those values of $a = 9\text{Å}$, $r = 6\text{Å}$, and $d = 6\text{Å}$. That is $\Delta E_g(300^\circ\text{C}) - \Delta E_g(40^\circ\text{C}) = 0.3 \text{ eV}$, which is almost equal to the experimental value of 0.2 eV. The value of r is put to be equal to that of the dynamic screening distance, and $\Delta E_n(40^\circ\text{C}) = 0.2 \text{ eV}$, which is also the same with the previously obtained experimental value. Thus, we can reproduce the projectile-, incident angle-, and temperature-dependences of Al-LVV Auger electrons, by using the multiple hole transportation model.

* Department of Materials Science and Engineering, Waseda University

Mössbauer Spectroscopy using ^{57}Mn Beam from RIPS

Y. Kobayashi, Y. Yoshida, J. Nakamura, K. Yukihiro,* K. Hayakawa,* A. Yoshida, Y. Watanabe, N. Aoi, N. Inabe, M. Kase, A. Goto, Y. Yano, M. Ishihara, and F. Ambe

Radioisotope beams (RI-beams) are becoming recently very attractive in the field of materials science. So far, radioisotopes have been used as nuclear probes to obtain the atomistic information by the implantation technique. In addition to that, the RI-beams are expected to change physical and chemical properties of materials and even to synthesize new materials in a limited part of samples due to their very high energies. In this year (1996), new in-beam Mössbauer experimental apparatus has been constructed at the E6 hall at RIKEN Ring Cyclotron Facility to use the ^{57}Mn beam provided by the projectile fragmentation reaction in RIPS. Besides the ^{57}Co used for conventional Mössbauer experiments, ^{57}Mn is long known to be another source nuclide of ^{57}Fe with a short half-life of 1.45 m.

Among the applications of RI-beams to materials science, the in-beam Mössbauer spectroscopy has been one of the most powerful method to study isolated ^{57}Fe atoms and their dynamics in metals and semiconductors.¹⁾ We report here a preliminary result from the in-beam Mössbauer experiment on ^{57}Fe ($\leftarrow^{57}\text{Mn}$) in a single crystal of Si. Since we implant ^{57}Mn as highly charged ions with high energy into the Si crystal, the ^{57}Fe atoms decayed from ^{57}Mn in the sample may be expected at exotic valence states.

A ^{57}Mn beam was produced by the projectile fragmentation reaction of ^{59}Co ($E = 80$ MeV/nucleon) with a Be target. After the ^{57}Mn beam was slowed down through a degrader with an appropriate thickness, its final implantation energy and intensity were estimated to be several tens MeV/nucleon and about 10^5 particles/s, respectively. The beam irradiated the Si sample through a lead collimator with a hole of $\phi 30$ mm. The Si wafer with thickness of 0.5 mm was placed 45° against the beam direction in the vacuum chamber. In order to confirm the ^{57}Mn nuclei stopping in the sample, two solid-state-detectors were placed before and behind the sample, and the γ -rays of 14.4 and 122 keV were monitored by a CdZnTe detector through a Mylar window of the chamber. The energy spectrum of γ -rays is shown in Fig. 1. The background level was considerably low, so that the γ -peaks of 14.4 and 122 keV originating from the excited states of ^{57}Fe could be clearly seen in the spectrum.

The Mössbauer spectrum of ^{57}Fe ($\leftarrow^{57}\text{Mn}$) in Si at room temperature is shown in Fig. 2. The γ -rays from the 14.4 keV Mössbauer level of ^{57}Fe atoms were detected by a parallel-plate avalanche counter (PPAC)

with a ^{57}Fe enriched stainless steel as an absorber. The fast-timing signals from the PPAC were used for the Mössbauer measurements. Although the quality of the spectrum was still rather low due to extremely low counting rate (~ 0.06 cps), broad lines can be seen around zero Doppler velocity and at high velocity range. The peaks near zero correspond to the Mössbauer spectrum observed at 300 K after Coulomb-excitation and recoil-implantation.²⁾ The satellite lines around ± 3 mm/s and ± 11 mm/s are entirely different from other components of ^{57}Fe in Si. If they are real ones, the present result might suggest the existence of an exotic ionic state and/or the appearance of novel physical property of ^{57}Fe having decayed from ^{57}Mn .

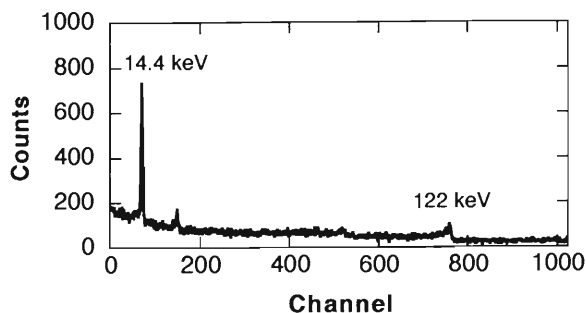


Fig. 1. The γ -ray spectrum of the Si wafer during Mössbauer measurement.

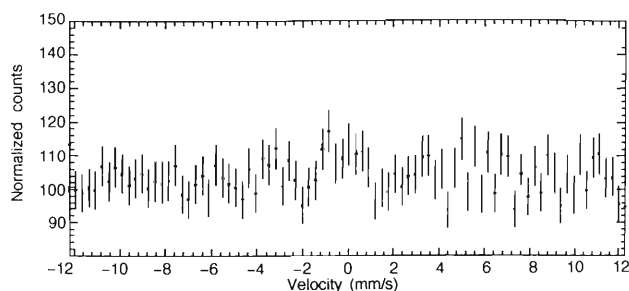


Fig. 2. The in-beam Mössbauer spectrum of ^{57}Fe ($\leftarrow^{57}\text{Mn}$) in Si using the RIPS at room temperature.

References

- 1) R. Sielemann and Y. Yoshida: *Hyperfine Interact.* **68**, 119 (1991).
- 2) P. Schwalbach et al.: *Phys. Rev. Lett.* **64**, 1274 (1990).

* Shizuoka Institute of Science and Technology

Hyperfine Interactions of ^{61}Ni in Distorted Spinel Chromites

J. Nakamura, T. Okada, Y. Noro,* Y. Kobayashi, H. Kitazawa,** and F. Ambe

A huge value of hyperfine magnetic field (H_{hf}) of $^{61}\text{Ni}^{2+}$ on the spinel A-sites (tetrahedral sites) in NiCr_2O_4 was first reported by Sekizawa et al.¹⁾ Recently, Okada et al.²⁾ have applied a ^{61}Ni Mössbauer spectroscopy to various spinel chromite including $M_{0.9}\text{Ni}_{0.1}\text{Cr}_2\text{O}_4$ ($M = \text{Mn}, \text{Co}, \text{or Zn}$) and $\text{Cu}_{1-x}\text{Ni}_x\text{Cr}_2\text{O}_4$, in which much larger H_{hf} have observed. The largest value of $|H_{hf}|$ observed was about 800 kOe in the tetragonally distorted spinel chromite $\text{Cu}_{0.9}\text{Ni}_{0.1}\text{Cr}_2\text{O}_4$ (when $c/a = 0.92$). Furthermore, they have found a linear dependence between $|H_{hf}|$ and bulk distortion given by c/a . Namely, the huge value of $|H_{hf}|$ decreased linearly with increase of c/a around $c/a = 1.0$.

Freeman and Watson calculated the Fermi contact term in H_{hf} to be about $-200 \sim -300$ kOe for Ni^{2+} ion. The huge value observed in these spinel compounds was not possible to be interpreted by only the Fermi term. Love and Obenshain have applied the ^{61}Ni Mössbauer spectroscopy on several spinel compounds, and have reported that degenerated Ni^{2+} electronic state should produce a finite orbital angular momentum.³⁾ They proposed that the unquenched orbital angular momentum originates H_{hf} . In these chromites, this orbital term will be the major one, and is written as

$$H_{\text{orb}} = 2\mu_B \langle r^{-3} \rangle_{av} \langle L_z \rangle_{av} .$$

Here, $\langle L_z \rangle_{av}$ is the mean value of unquenched orbital angular momenta for degenerated Ni^{2+} electronic states and is calculable from ligand theory. The huge value of H_{hf} was able to be interpreted using calculated $\langle L_z \rangle_{av}$.²⁾ However, there is still a controversy, because Gütllich et al.⁴⁾ have reported a negative sign of H_{hf} , which denies the H_{orb} origin mentioned above.

The purpose of this study is to obtain an interpretation of both the huge H_{hf} and electric field gradient (EFG), using $\langle L_z \rangle_{av}$. The $\text{Cu}_{1-x}\text{Ni}_x\text{Cr}_2\text{O}_4$ system has attracted our attention because it exhibits the largest at H_{hf} compound (at $x = 0.1$) and has a wide solubility range corresponding to a variety of c/a . We prepared the samples with several compositions ($x = 0.5, 0.8$ and 0.9) and measured the ^{61}Ni Mössbauer spectra at 4 K. The detailed experimental procedure is described in Ref. 2.

The present spectra indicate the same relationship between $|H_{hf}|$ and c/a observed previously.²⁾ The EFG

parameter e^2qQ_g was derived under the assumption of θ , the angle between a principal axis of EFG and the direction of spin, being fixed to 0° and 90° for $c/a < 1$ and $c/a > 1$, respectively. The theoretical value of EFG using an orbital angular momentum was reported by Okiji and Kanamori for Fe^{2+} in some oxides.⁵⁾ We extended their theory to the Ni^{2+} case, and derived the uniaxial EFG, eq_z , as;

$$eq_z = -\frac{2}{105} |e \langle r^{-3} \rangle_{av}| [3 \langle L_z^2 \rangle_{av} - L(L+1)] .$$

Then, we calculated eq_z with $\langle r^{-3} \rangle_{av}$ of 6.1 a.u., and the derived relation between H_{hf} and e^2qQ_g is shown with solid lines in Fig. 1.

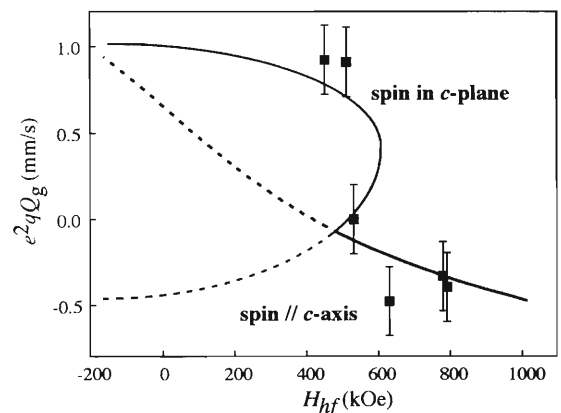


Fig. 1. Correlation between H_{hf} and e^2qQ_g for several chromite spinels. The Fermi term was assumed to be -200 kOe.

In the figure, the experimentally observed values are also plotted, which are found to be on the theoretical solid line. The present result indicates that the unquenched orbital angular momentum gives an account of the huge H_{hf} and EFG.

References

- 1) H. Sekizawa et al.: J. de Physique **32**, C1-326 (1971).
- 2) T. Okada et al.: Phys. Lett. A **209**, 241 (1995).
- 3) J. C. Love and F. E. Obenshain: AIP Conf. Proc. **18**, 513 (1973).
- 4) P. Gütllich et al.: J. de Physique **41**, C1-185 (1980).
- 5) A. Okiji and J. Kanamori: J. Phys. Soc. Jpn. **19**, 908 (1964).

* Hitachi Multimedia Systems R & D Division

** National Institute for Metals

Magnetic Properties of $\text{YSr}_2\text{Cu}_{3-x}\text{Fe}_x\text{O}_{7+\delta}$ and Effects of Hot Isostatic Pressing

T. Fuwa,* N. Ikeda,** J. Nakmura, T. Okada, K. Kohn,** and N. Yamada*

We have studied the effect of heat-treatment on the magnetic properties of Fe-doped $\text{YSr}_2\text{Cu}_3\text{O}_{7+\delta}$,¹⁾ especially for $x = 0.4$ and $x = 1.0$, by the magnetic susceptibility measurements and ^{57}Fe Mössbauer spectroscopy. The room temperature Mössbauer spectra are shown in Fig. 1(a)-(d). Doublet A originates from the Fe-ions substituting Cu(II) sites. Other doublets B, B' and C are attributed to the Fe-ions substituting Cu(I) sites.

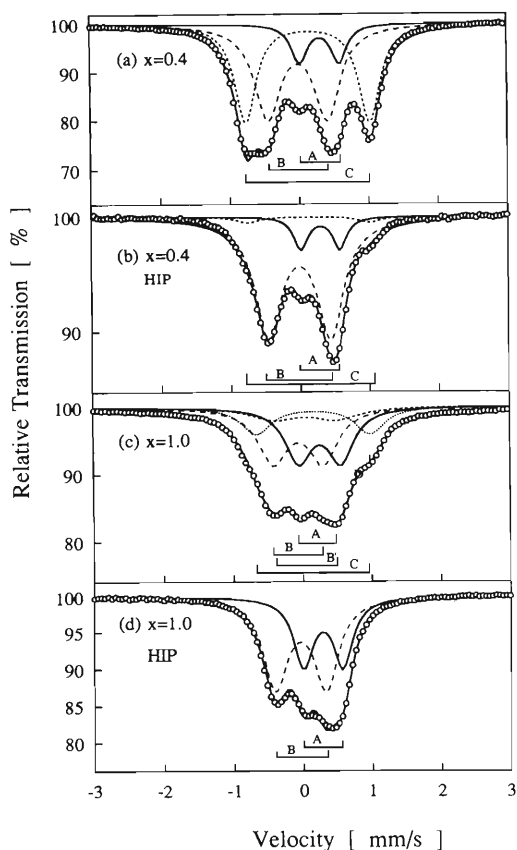


Fig. 1. The room-temperature Mössbauer spectra of $\text{YSr}_2\text{Cu}_{3-x}\text{Fe}_x\text{O}_{7+\delta}$.

The measured Mössbauer parameters are listed in Table 1.

(1) $\text{YSr}_2\text{Cu}_2\text{Fe}_{0.4}\text{O}_{7+\delta}$: The sample synthesized in 1 atm oxygen environment (NON-HIP sample) was not a superconductor, while the Hot Isostatic Pressing (HIP) sample prepared under oxygen partial pressure of 40 MPa²⁾ was found to be a superconductor with $T_c = 37$ K. At low temperature ($T < 14$ K), the hyperfine mag-

Table 1. Mössbauer parameters measured for $\text{YSr}_2\text{Cu}_{3-x}\text{Fe}_x\text{O}_{7+\delta}$.

x	site	IS[mm/s]	Q.S.[mm/s]	Area[%]
0.4	A	+0.254	0.578	15
	B	-0.042	0.848	40
	C	+0.125	1.761	45
0.4 HIP	A	+0.292	0.584	17
	B	-0.018	0.893	78
	C	+0.170	1.711	5
1.0	A	+0.256	0.610	32
	B	-0.056	0.725	36
	B'	+0.047	0.914	13
1.0HIP	C	+0.169	1.646	19
	A	+0.287	0.574	38
	B	-0.036	0.733	62

netic fields larger than 280 kOe were observed. This means that for the HIP sample the superconductivity and the magnetic ordering can coexist in that low temperature region.

(2) $\text{YSr}_2\text{Cu}_2\text{Fe}_{1.0}\text{O}_{7+\delta}$: From the susceptibility measurement, it was observed that the sample prepared under 1 atm oxygen environment is antiferromagnetically ordered near 70 K. By the HIP process, the magnetic ordering temperature of the same sample went down to about 55 K, but unlike the case of $\text{YSr}_2\text{Cu}_{2.6}\text{Fe}_{0.4}\text{O}_{7+\delta}$ this sample did not show any sign of superconductivity. The room temperature Mössbauer spectra show that the spectrum of the NON-HIP sample is composed of four doublets (See Fig. 1(c)) and that the spectrum of the HIP sample changed two doublets (See Fig. 1(d)). The magnetic ordering temperature obtained by the Mössbauer spectroscopy was different from that by the susceptibility measurements. Namely, the magnetic ordering temperature of the NON-HIP sample was about 240 K and that of the HIP sample was ordered below about 77 K.

In summary, we can consider two possibilities on the effect of HIP process. One is that more oxygen was introduced into the sample. Another is that the redistribution of Fe-ions between Cu(I) and Cu(II) sites took place. The latter is supposed to be a more important effect in the HIP process. But in order to discuss the HIP effects in detail, it is necessary to do more experiments with a series of $\text{YSr}_2\text{Cu}_{3-x}\text{Fe}_x\text{O}_{7+\delta}$ samples at $x \leq 1.0$ prepared by the HIP process.

References

- 1) M. Pissas, G. Kallias, E. Moraitakis, D. Niarchos, and A. Simopoulos: *Physica C* **234**, 127 (1994).
- 2) B. Okai: *Jpn. Appl. Phys.* **29**, L2180 (1990).

* Dept. Appl. Phys. and Chem., Univ. of Electro-Comm.

** Dept. Phys., Waseda University

^{57}Fe Mössbauer Spectroscopy of $\text{Cu}_{1-x}\text{Fe}_x\text{GeO}_3$

T. Okada, H. Kitazawa,* J. Nakamura, Y. Kobayashi, and F. Ambe

A spin-Peierls (SP) transition in inorganic compounds was first found in CuGeO_3 by Hase et al.¹⁾ The oxide, CuGeO_3 , is a quasi-one-dimensional antiferromagnet (AF) with $S = 1/2$ for the linear structure of this compound. As the temperature is lowered below the SP transition temperature (T_{sp}), the magnetic susceptibility decreases rapidly. This SP transition can be described as a progressive dimerization of $S = 1/2$ AF chains. It is quite attractive that the dimerization of AF chains can be controlled by replacement of the other ions.^{2,3)} From this point of view we doped Fe ions in CuGeO_3 .

Polycrystalline specimens were obtained by heating the mixture of CuO , GeO_2 and $\alpha\text{-Fe}_2\text{O}_3$ for 10 days in air. The ^{57}Fe Mössbauer effect and magnetic measurements of $\text{Cu}_{1-x}\text{Fe}_x\text{GeO}_3$ ($x = 0.005, 0.01$ and 0.03) with the SP transition around 14 K were made at various temperatures. The isomer shift (IS) refers to the one of metallic irons. The Mössbauer spectra of $\text{Cu}_{0.99}\text{Fe}_{0.01}\text{GeO}_3$ measured at various temperatures are shown in Fig. 1. The spectrum at 297 K consists of three doublets due to the quadrupole splitting (QS). The first doublet (A) (17% in population) has $QS = 2.08$ mm/s and $IS = +0.95$ mm/s. The second doublet (B) (45%) has $QS = 1.38$ mm/s and $IS = +0.25$ mm/s. The third doublet (C) (38%) has $QS = 0.61$ mm/s and $IS = +0.27$ mm/s. The values of IS indicate that Fe ions in (A) site are in the divalent state and those in (B) and (C) sites are in the trivalent state. Lowering temperature below 30 K, the component of (B) site becomes broad and shows the broad sextet at least at 2 K as for a magnetic splitting. The spectra of (A) and (C) sites remain quadrupole doublets even at 2 K. The Fe ions of (A) and (C) sites are paramagnetic at the whole temperature range measured. However, no Mössbauer parameters change appreciably near T_{sp} . In the Fe rich composition (e.g., $x = 0.03$), although not shown here, one part of Fe ions do not dissolve into the CuGeO_3 . Thus the solubility range of Fe ions in CuGeO_3 is found very narrow. The curves of temperature dependence of the magnetization are shown in Fig. 2. The values of T_{sp} for 0.005, 0.01 and 0.03 are obtained as 14.5, 14.0 and 13.0 K, respectively. These compounds are in the SP state. The values of T_{sp} decrease more gradually by replacing Fe ions than by non magnetic ions. The increase of the magnetization at very low temperature is due to paramagnetic Fe ions (C).

The Fe ions replaced in CuGeO_3 are both in trivalent (83%) and divalent (17%) states. One part of Fe^{3+} ions orders magnetically at low temperature. It means

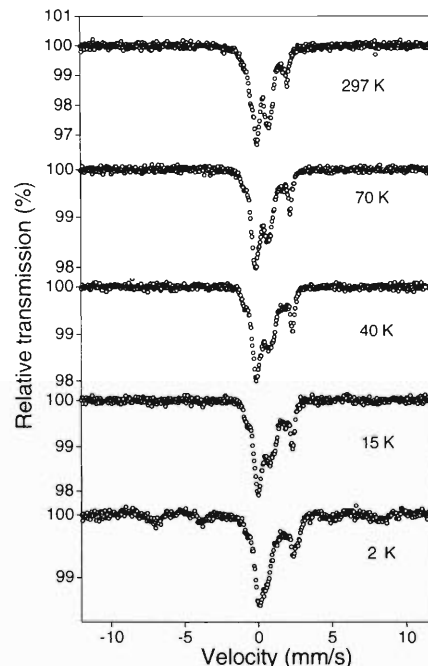


Fig. 1. Mössbauer spectra of $\text{Cu}_{0.99}\text{Fe}_{0.01}\text{GeO}_3$ ($x = 0.01$) measured at various temperatures.

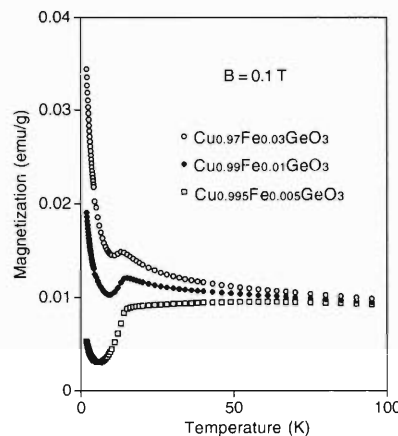


Fig. 2. Temperature dependence of the magnetization of $\text{Cu}_{1-x}\text{Fe}_x\text{GeO}_3$ ($x = 0.005, 0.01$ and 0.03) under an external field strength $B = 0.1$ T.

that the SP state and the long-range antiferromagnetic order can coexist in this system.

References

- 1) M. Hase et al.: Phys. Rev. Lett. **70**, 3651 (1993).
- 2) S. B. Oseroff et al.: Phys. Rev. Lett. **74**, 1450 (1995).
- 3) M. Hase et al.: Phys. Rev. **54**, R3722 (1996).

* National Research Institute for Metals

^{61}Ni Mössbauer Spectroscopy of LiNiO_2 and NaNiO_2

T. Okada, Y. Noro,* J. Nakamura, Y. Kobayashi, and F. Ambe

^{61}Ni Mössbauer measurements are made to elucidate the magnetic properties of LiNiO_2 and NaNiO_2 with a two-dimensional (2-D) magnetic layer.

The 2-D triangular lattice antiferromagnet with $S = 1/2$ is much interested in the relation of the new magnetic ordering model¹⁾ (RVB model) which assumes that the antiferromagnetic spin pairs move in the 2-D magnetic layer. Hirakawa²⁾ proposed LiNiO_2 as a material adapted to the RVB model. However, it is not yet testified, though many studies are made by various methods. On the other hand, a transition to the antiferromagnetic state in NaNiO_2 was observed at $T_N = 20$ K by Bongers and Enz.³⁾ A two sublattice model with an ordinary antiferromagnetic order between the ferromagnetic layers of Ni^{3+} ions was proposed by them. The Ni ions in LiNiO_2 and NaNiO_2 are in the trivalent and in the low spin 2E state, $t_{2g}^6 e_g^1$, with $S = 1/2$ based on the magnetic susceptibilities observed at high temperature range.

The crystal structures of LiNiO_2 and NaNiO_2 are an ordered rock salt type (R3m) and a slightly distorted one (C2/m), respectively. The Ni ions are occupied in the octahedral sites.

The single line source of ^{61}Cu ($\rightarrow ^{61}\text{Ni}$) for the Mössbauer spectroscopy was produced by the RIKEN AVF cyclotron. Experimental procedure was reported in detail in previous papers.⁴⁾

Mössbauer spectra of LiNiO_2 and NaNiO_2 taken at 5 K are shown in Fig. 1. Each spectrum consists of a broadened line caused by the hyperfine magnetic fields (H_{hf}). Values of H_{hf} amount approximately 80 and 66 kOe for LiNiO_2 and NaNiO_2 , respectively. Values of the isomer shift (IS) are -0.18 and -0.17 mm/s for LiNiO_2 and NaNiO_2 , respectively, relative to the one of metallic Ni. This is the first report on IS of Ni ions in the trivalent state.

The magnitude of Fermi term in H_{hf} is roughly proportional to the number of the polarized electrons.⁵⁾ The g-value observed from ESR measurements on LiNiO_2 indicates that the orbital angular momentum is completely quenched. The observed values of H_{hf} of $^{61}\text{Ni}^{3+}$ ions in LiNiO_2 and NaNiO_2 are almost same as

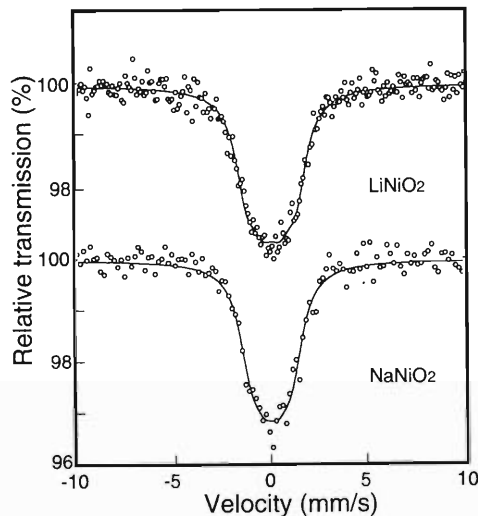


Fig. 1. ^{61}Ni Mössbauer spectra of LiNiO_2 and NaNiO_2 at 5 K.

100 kOe expected in the low spin state. We discuss in detail the values of these H_{hf} in the following paper.⁶⁾

In the RVB model the antiferromagnetic spin pairs move quite rapidly in the 2-D magnetic layer. Then, the broadened line caused by H_{hf} is expected sharp due to the motional narrowing. However, experimental results of the nearly same H_{hf} in LiNiO_2 and NaNiO_2 indicate the existence of an ordinary magnetic order in both oxides at least at 5 K. It suggests that the RVB model is not adapted to the LiNiO_2 .

References

- 1) P. W. Anderson: Mater. Res. Bull. A **8**, 153 (1973).
- 2) K. Hirakawa et al.: J. Phys. Soc. Jpn. **54**, 3526 (1985).
- 3) P. E. Bongers and U. Enz.: Solid State Comm. **4**, 153 (1966).
- 4) T. Okada et al.: Phys. Lett. **209**, 241 (1995).
- 5) R. E. Watson and A. J. Freeman: Phys. Rev. **123**, 2027 (1961).
- 6) T. Okada et al.: RIKEN Accel. Prog. Rep. **30**, 93 (1997).

* Hitachi Multimedia Systems R&D Division

Effect of 4s Electrons on the Electronic State of Ni³⁺ Ions in LiNiO₂ and NaNiO₂

T. Okada, Y. Noro,* J. Nakamura, Y. Kobayashi, and F. Ambe

The hyperfine magnetic fields (H_{hf}) and isomer shifts (IS) of Ni³⁺ ions in LiNiO₂ and NaNiO₂ with two dimensional (2-D) magnetic layer structure were measured by ⁶¹Ni Mössbauer spectroscopy. The effect of 4s electron on H_{hf} is discussed relating to the measured large IS . They indicate a significant role of 4s electron in the electronic state of Ni³⁺ ions in LiNiO₂ and NaNiO₂.

The 2-D magnetic layer made with Ni³⁺ ions in the octahedral ligands is interesting because 1) it may support a new magnetic ordering model¹⁾ (RVB model) and 2) it must have a strong relation with high T_c superconductor made of Cu²⁺ ion layers. There is only a little report on the electronic state of Ni³⁺ ions and no report on Mössbauer measurements on it.

Mössbauer spectra of LiNiO₂ and NaNiO₂ measured at liquid-helium temperature show a broadened line caused by the hyperfine magnetic fields.²⁾ The values of them amount around 80 and 66 kOe for LiNiO₂ and NaNiO₂, respectively. The values of IS are -0.18 and -0.17 mm/s for LiNiO₂ and NaNiO₂, respectively, relative to metallic Ni.

The 4s-electron dependence on IS for three different electron configurations of ⁶¹Ni calculated by Travis and Spijkerman³⁾ is shown in Fig. 1, where our data are shown by the circles. The observed values of IS of Ni³⁺ ions in LiNiO₂ and NaNiO₂ are on the line of 3d⁷-4s electron configuration. This is the first report on IS of Ni³⁺ ions. The measured values of IS are much larger than that for NiO. They indicate presence of a large fraction of 4s electrons in the electronic state of Ni³⁺ ions. The horizontal axis of Fig. 1 shows the 4s electron contribution to each state. They are about 15% in NiO

and 28% in LiNiO₂ and NaNiO₂, respectively. The typical value of 4s electron contribution for Fe³⁺ ions is less than 5%. So, the contribution for LiNiO₂ and NaNiO₂ have 20% larger than that for Fe³⁺. This large fraction of 4s electrons in Ni³⁺ ions must play a significant role in the magnetic properties of LiNiO₂ and NaNiO₂.

The H_{hf} is induced mainly from Fermi contact (core polarization) and the orbital angular momentum.⁴⁾ The electronic state of Ni³⁺ ions in the octahedral sites is t_{2g}⁶e_g¹ with one unpaired electron. It is similar to Ni²⁺ in the octahedral sites as seen below;

Valence	Electronic state	Spin	H_{hf} (kOe)
Ni ³⁺	t _{2g} ⁶ e _g ¹	1/2	+ or - 66/80
Ni ²⁺	t _{2g} ⁶ e _g ²	1	-100.

As a first approximation, H_{hf} coming from the core polarization and the orbital angular momentum is proportional to the number of unpaired electrons. The value of H_{hf} of Ni³⁺ ions can be estimated as -50 kOe from -100 kOe of Ni²⁺ ions in NiFe₂O₄. Next, we consider the effect of covalency on H_{hf} . Fraction of covalent 4s electrons is known to induce the positive H_{hf} in the case of Fe³⁺ ions. Evans concluded that a difference of 0.10 mm/s in the isomer shifts corresponds to a difference of 30 kOe in H_{hf} .⁵⁾ A difference in IS can be transfer to a difference in 4s electron contribution by using Walker chart;⁶⁾ 2.8% of 4s electron contribution corresponding to 0.10 mm/s of IS . Assuming that the relation between the 4s contribution and the correction for H_{hf} can maintain in ⁶¹Ni, we deduce about +140 kOe for a difference of 13% of fraction of 4s electron between NiO and LiNiO₂. As a result, we obtain about +90 kOe for ⁶¹Ni³⁺ ions in LiNiO₂. Experimental results of 80 kOe and 66 kOe in LiNiO₂ and NaNiO₂ show fairly good agreement with them. So we conclude that contrary to ordinary transition ions, the dominant mechanism for H_{hf} of Ni³⁺ ions is Fermi contact term induced from the 4s electron.

References

- 1) P. W. Anderson: Mater. Res. Bull. A **8**, 153 (1973).
- 2) T. Okada et al.: RIKEN Accel. Prog. Rep. **30**, 92 (1997).
- 3) J. C. Travis and J. J. Spijkerman: in *Mössbauer Effect Methodology* Vol. 3, edited by I. J. Gruverman (Plenum press, 1968) p. 237.
- 4) A. Okiji and J. Kanamori: J. Phys. Soc. Jpn. **21**, 2732 (1966).
- 5) B. J. Evans and S. Hafner: J. Appl. Phys. **38**, 694 (1968).
- 6) L. R. Walker et al.: Phys. Rev. Lett. **6**, 98 (1961).

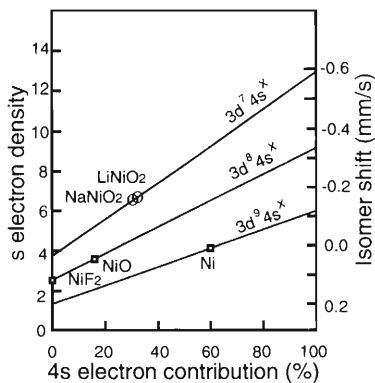


Fig. 1. The 4s-electron dependence on the isomer shift of ⁶¹Ni, calculated for three electron configurations, with typical examples and our data (the circles).

* Hitachi Multimedia Systems R & D Division

Channeling Study on H in Nb-Mo Alloys

E. Yagi and S. Koike*

In previous studies we investigated the lattice location of H in Nb-3(at%)Mo-2(at%)H, Nb-3(at%)Mo-5(at%)H, and Nb-10(at%)Mo-6(at%)H alloys by means of a channeling method using a nuclear reaction $^1\text{H}(^{11}\text{B}, \alpha)2\alpha$ with a ^{11}B beam of the energy about 2 MeV.^{1,2)} In this method, hydrogen is detected by measuring the emitted α -particles.

In Nb-3(at%)Mo alloys, when the H concentration is lower than that of Mo, H atoms are located at room temperature at the sites displaced from tetrahedral sites (T sites) by about 0.6 Å towards one of their nearest neighbor lattice points, while they become located at T sites at 373 K.¹⁾ The result demonstrates the trapping of hydrogen by an undersized Mo atom. We concluded that, at this low Mo concentration, the trapping of H by Mo is very effective as a mechanism for the enhancement of the terminal solubility of H in Nb on alloying with the undersized Mo atoms.^{3,4)} In this alloy one Mo atom traps approximately 0.7–1.0 H atoms, i.e., the trapping efficiency is 70–100%. However, in an Nb-10(at%)Mo alloy the efficiency decreases to 20–30%, suggesting a change in the lattice location of H in the more concentrated Nb-Mo alloys.²⁾ Therefore, in the present study the lattice location of hydrogen in Nb-20(at%)Mo alloys has been investigated.

Figure 1(a) shows channeling angular profiles obtained at room temperature for the Nb-20(at%)Mo-2.6(at%)H alloy. The profiles of α -particles exhibit a central peak superimposed on a shallow dip for the $\langle 100 \rangle$ channel, a broad peak consisting of three sub-peaks superimposed on a shallow dip for the $\langle 110 \rangle$ channel, and a small central peak superimposed on a shallow dip for the $\{100\}$ channel. The angular positions of peaks expected for the T -site occupancy are indicated by arrows in the figure. They coincide with the observed peak positions. The overall features are similar to those for the T -site occupancy, indicating that a large portion of H atoms are located at T sites. The point to be noted as a difference from the profiles for the T -site occupancy is that a shallow dip is observed for the $\langle 100 \rangle$ and $\langle 110 \rangle$ channels. This

result suggests that a portion of H atoms are located at the sites which are shadowed by both $\langle 100 \rangle$ and $\langle 110 \rangle$ atomic rows. They are octahedral sites (O sites). By fitting the calculated angular profiles of α -particles for various distributions of H atoms between T and O sites to the observed ones, it is concluded that 20–30 percent of H atoms become located at O sites and remains are at T sites. The occupancy at the trapped sites, which was observed in Nb-3(at%)Mo alloys (Fig. 1(b)), is no more observed.

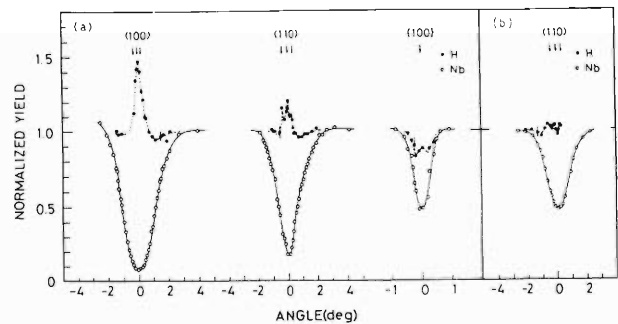


Fig. 1. Channeling angular profiles of α -particle yields (\bullet) and yields of ^{11}B ions backscattered by host metal atoms (\circ) obtained at room temperature for (a) the Nb-20(at%)Mo-2.6(at%)H alloy, and (b) the Nb-3(at%)Mo-2(at%)H alloy. The full curves and the dashed curves have been drawn to guide the eye.

References

- 1) E. Yagi, S. Nakamura, F. Kano, T. Kobayashi, K. Watanabe, Y. Fukai, and T. Matsumoto: Phys. Rev. B **39**, 57 (1989).
- 2) E. Yagi, T. Kobayashi, K. Watanabe, Y. Fukai, and T. Matsumoto: Proc. Jpn. Acad. B **65**, 38 (1989).
- 3) T. Matsumoto, Y. Sasaki, and M. Hihara: J. Phys. Chem. Solids **36**, 215 (1975).
- 4) J. F. Miller and D. G. Westlake: Trans. Jpn. Inst. Metals **21**, suppl., 153 (1980).

* Department of Physics II, Faculty of Science, Science University of Tokyo

μ^+ SR Study of Polaron Motion in Polyaniline[†]

F. L. Pratt, K. Ishida, and K. Nagamine

Fundamental to the understanding of conducting polymer systems are the nature and properties of their charge and spin excitations which are strongly coupled to the underlying molecular structure of the polymer. The muon is a particularly sensitive probe of such soliton and polaron excitations, as the muon implantation process itself can generate an excitation whose dynamical properties can be studied via the evolution of the muon spin polarization. This was first demonstrated in polyacetylene¹⁾ and subsequent studies were reported for a range of conducting polymers.²⁾ In earlier studies the muon spin relaxation was fitted to an exponential decay function which does not describe the relaxation so well over a wide time range. Risch and Kehr recently derived a relaxation function that more properly describes the 1D diffusion of the spin defect.³⁾ Their longitudinal muon spin relaxation function in finite field strengths has the form: $G(t) = \phi(\Gamma t)$ for $\lambda T \gg 1$ with $\phi(x) = \exp(x) \operatorname{erfc}(\sqrt{x})$, where erfc signifies the complementary error function, λ the electron spin flip rate, T the experimental timescale and Γ a relaxation parameter. This relaxation function goes as $t^{-1/2}$ at long times rather than decaying exponentially. When the intrachain diffusion rate D_{\parallel} is large compared to $\omega_0^2/\sqrt{2\omega_e\lambda}$ (ω_0 is the muon-electron hyperfine coupling and ω_e is the electronic Larmor frequency), the relaxation parameter follows the $1/B$ field dependence $\Gamma = \omega_0^4/2\omega_e D_{\parallel}^2$, which is independent of the spin flip rate λ and depends sensitively on D_{\parallel} . At low field strengths there will be a cutoff to the $1/B$ field dependence at B_c which may be due to crossover to a 3D diffusion regime when ω_e becomes smaller than the interchain diffusion rate D_{\perp} .

We have carried out muon spin relaxation measurements on samples of undoped polyaniline (PANI:EB) at the RIKEN-RAL muon facility in order to study the motion of the polarons in this system. We have found that the measured relaxation is well described by the Risch-Kehr function over a wide range of experimental conditions. The data are fitted with only two parameters; the initial amplitude and the relaxation parameter Γ . Some results for PANI:EB are shown in Fig. 1.

It can be seen in Fig. 1 that at 6 K the one-dimensional $1/B$ regime holds down to below 10 G, whereas at 300 K the $1/B$ regime only holds down to 300 G or so. This suggests that D_{\perp} increases by around two orders of magnitude between 6 K and 300 K, where it reaches a value of $\sim 5 \times 10^9$ rad/s. Since at 500 G and above the $1/B$ field dependence is obeyed over a wide range of temperature, a field of 1 kG was chosen for a more detailed study of the temperature dependence of the relaxation. This is shown in Fig. 2.

From Fig. 2 it can be seen that there is a rapid increase in the relaxation above 150 K. This is believed to be associated with the excitation of phenyl ring librations which are known to couple strongly to the electronic excitations.⁴⁾ Using the value for the hyper-

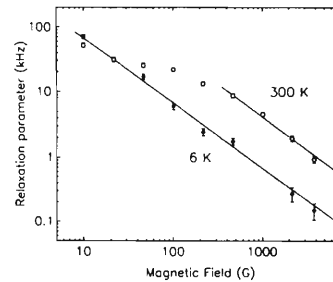


Fig. 1. Relaxation parameter Γ versus magnetic field B for PANI:EB at 6 K and 300 K. The lines show the regions where Γ obeys the $1/B$ law.

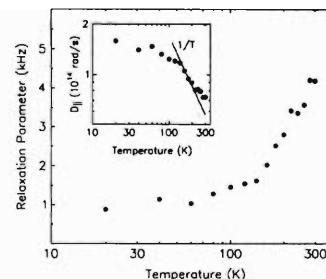


Fig. 2. Temperature dependence of the relaxation parameter Γ for PANI:EB at 1 kG. The inset shows the polaron intrachain diffusion rate D_{\parallel} derived from the 1 kG relaxation using the value $\omega_0 = 2\pi \times 150$ MHz.

fine frequency $\omega_0 = 2\pi \times 150$ MHz estimated from the longitudinal decoupling field of the initial muon asymmetry, the diffusion rate D_{\parallel} was calculated from Γ and is shown in the inset to Fig. 2. The diffusion rate shows a weak metallic temperature coefficient at low temperatures which becomes rather stronger above 150 K. Between 150 K and 200 K the diffusion rate is inversely proportional to temperature, which is suggestive of phonon limited metallic transport. In contrast to D_{\parallel} , the interchain diffusion D_{\perp} increases sharply above 150 K, suggesting that ring rotation assists interchain transport but hinders intrachain motion. The values for D_{\parallel} at 300 K and for the temperature dependence of D_{\perp} are quite similar here to an earlier ESR study of spin dynamics in metallic polyaniline,⁵⁾ but the fully metallic temperature dependence of D_{\parallel} seen here is in marked contrast to the semiconducting behaviour reported below 150 K in the doped case.⁵⁾

References

- 1) K. Nagamine et al.: Phys. Rev. Lett. **53**, 1763 (1984); K. Ishida et al.: Phys. Rev. Lett. **55**, 2009 (1985).
- 2) F. L. Pratt et al.: Synth. Met. **55**, 677 (1993); F. L. Pratt et al.: Synth. Met. **69**, 231 (1995); F. L. Pratt et al.: Hyperfine Interactions (1996, to be published).
- 3) R. Risch and K. W. Kehr: Phys. Rev. B **46**, 5246 (1992).
- 4) J. M. Ginder and A. J. Epstein: Phys. Rev. B **41**, 10674 (1990); A. J. Milton and A. P. Monkman: J. Phys. D: Appl. Phys. **26**, 1468 (1993).
- 5) K. Mizoguchi and K. Kume: Sol. St. Comm. **89**, 971 (1994).

[†] Condensed from an article to appear in Synthetic Metals.

Magnetic State of $\text{TlBa}_2\text{Y}_{1-x}\text{Ca}_x\text{CuO}_y$ Studied by $\mu^+\text{SR}$

I. Watanabe, S. Nakajima,* S. Ohira,** K. Nishiyama, and K. Nagamine

$\text{TlBa}_2\text{Y}_{1-x}\text{Ca}_x\text{CuO}_y$ (Tl-1212) is one of the high- T_c superconducting (SC) oxides and shows the highest transition temperature, $T_c = 106$ K at $x = 0.6$.¹⁾ In previous studies, we reported that an antiferromagnetically (AF) ordered state of Cu-spins with the transition temperature of about 400 K can exist for $0 \leq x \leq 0.5$ ²⁻⁵⁾ and that an abrupt transition from the AF state to the SC state occurred at around $x = 0.5$. In a present paper, the results of detailed analysis of the zero-field muon spin resonance (ZF- $\mu^+\text{SR}$) experiments including low temperature measurements down to 30 mK are reported. The ZF- $\mu^+\text{SR}$ experiments down to 1.5 K were carried out at RIKEN-RAL Muon Facility in Rutherford-Appleton Laboratory, UK and the ZF- $\mu^+\text{SR}$ ones down to 30 mK was carried out at UTMSL in KEK by using a top loading type dilution refrigerator. A pulsed muon beam with the momentum of 27 MeV/c was used.

As described in previous reports,^{2,3)} the ZF- $\mu^+\text{SR}$ time spectrum observed in the AF ordered state consists of three asymmetry components. Because an implanted muon prefers to stop near by an oxygen atom, three muon sites are expected in the Tl-1212 crystal: a CuO-plane oxygen site (A_{pl}), an apical oxygen site (A_{ap}), and TlO-plane oxygen site (A_{Tl}).³⁾

Saturated internal field of 23 and 170 Oe which were due to the AF ordering of the Cu-spins were observed at A_{ap} - and A_{pl} -sites, respectively. An asymmetry amplitude of the A_{ap} -component is about four times larger than that of A_{pl} -component. The asymmetry amplitudes of both A_{pl} - and A_{ap} - components decrease linearly with increasing x and vanish in the SC state, indicating that the fraction of the AF spin alignment decreases with x .

A randomly distributed static field was observed at the A_{Tl} -site.^{2,3)} It was confirmed from the longitudinal-field experiment that the distributed field is also induced by the AF ordering. The asymmetry amplitude of the A_{Tl} -component increases with increasing x up to $x = 0.5$ and vanishes in the SC state. Figure 1 shows the x -dependence of the depolarization rate of the muon spin of the A_{Tl} -component obtained at 5 and 300 K. The depolarization rates decrease rapidly with increasing x . Since the muon spin at the A_{Tl} -site is depolarized by the distributed static internal field, the width of the field distribution can be roughly estimated from the depolarization rate to be about 70 Oe at $x = 0$ and 7 Oe for $x \geq 0.3$. The reduction of internal field at the muon site which originates from randomization of spin directions may be enhanced with increasing x .

Volume fraction of the SC state was estimated from the transverse-field $\mu^+\text{SR}$ measurements to be approximately zero, up to $x = 0.5$. It increased suddenly to be

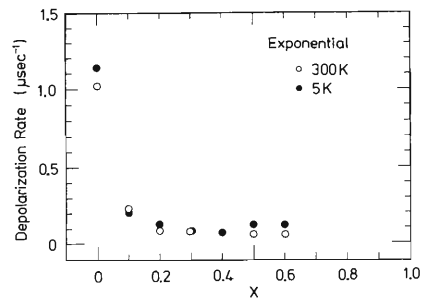


Fig. 1. Ca-Concentration of the depolarization rate of the muon spin at the A_{Tl} -site, obtained at 5 and 300 K.

50% at $x = 0.6$ and showed more than 80% at $x = 1.0$.

These results give us an aspect that the AF spin alignment is partially destroyed by the hole-doping. When the randomly distributed region overwhelms the AF ordered region, the system changes to the SC state.

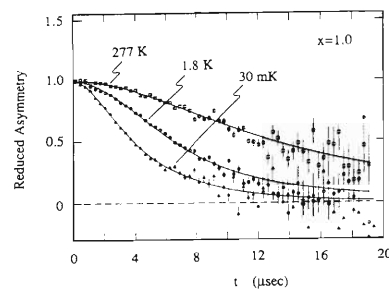


Fig. 2. Zero-field $\mu^+\text{SR}$ time-spectrum at $x = 1.0$ and $T = 277$ K, 1.8 K, and 30 mK. No sign of a magnetic ordering was observed.

Figure 2 shows the ZF- $\mu^+\text{SR}$ time-spectra obtained when for $x = 1.0$ ($T_c = 86$ K) and $T = 277$, 1.8 K and 30 mK. The spectra are well described by the dynamical Kubo-Toyabe function, indicating that the muon spin is depolarized only by randomly-distributed nuclear dipolar fields at the muon sites. The motional narrowing effect which was due to the diffusion of muons through the crystal was observed with increasing temperature. Any sign of the magnetically ordered state was not observed down to 30 mK. Thus, the co-existence between the SC state and the magnetically ordered state is unlikely for $x = 1.0$ in the Tl-1212 system.

References

- 1) S. Nakajima et al.: *Physica C* **182**, 89 (1991).
- 2) I. Watanabe et al.: RIKEN Accel. Prog. Rep. **29**, 113 (1996).
- 3) I. Watanabe et al.: to be published in *Hyperfine Interactions* (1996).
- 4) I. Watanabe et al.: *Czech. J. Phys.* **46**, 2673 (1996).
- 5) I. Watanabe et al.: to be published in *J. Low Temp. Phys.* (1996).

* Fac. Sci., Tohoku University

** Meson Science Laboratory (UTMSL), Department of Physics, Faculty of Science, University of Tokyo

Evidence for Muonium Passivation in n-Doped Ge

R. Kadono, R. M. Macrae, K. Nishiyama, and K. Nagamine

The current state of knowledge about the dynamical properties of atomic defects under thermal/electronic excitations (including defect metastability and associated site change) in semiconductors is still rather limited compared with the situation regarding their equilibrium structure. In this regard, hydrogen isotopes are no exception despite their apparent simplicity; the accumulated knowledge largely relates to the electronic structure of isolated (paramagnetic) muonium centers, for which high-resolution μ SR (Muon Spin Rotation, Relaxation, and Resonance)¹⁾ spectroscopic techniques analogous to EPR (electron paramagnetic resonance) and ENDOR (electron-nuclear double resonance) are available. The situation is more difficult where the study of diamagnetic muon states (Mu^\pm , i.e., μ^+ or Mu^-) is concerned, as such high-resolution spectroscopy is not possible due to the absence of the electron-muon hyperfine interaction.

Recently, we have shown that charge/spin exchange interaction between implanted muons and excess carriers may serve as a probe of the electronic state of diamagnetic muons in semiconductors.²⁾ We found that a Mu^\pm state formed slowly at lower temperatures in n-Ge does not interact with photo-induced excess carriers, suggesting that the electronic level associated with the Mu^\pm state is not in the band gap. Since the Mu^\pm state seems to be Mu^- formed by a process $\text{Mu}_T^0 + d^0 \rightarrow \text{Mu}_T^- d^+$ (where Mu_T^0 is the muonium at the tetrahedral interstitial site), the result is strong evidence that the observations correspond to the passivation of donor levels by Mu_T^0 centers, a phenomenon of crucial importance in determining the electronic transport properties of semiconductors.³⁾

The experiment was conducted primarily at the RIKEN-RAL Muon Facility in the Rutherford Appleton Laboratory which provides a pulsed beam of nearly 100% spin-polarized muons. A part of the measurement was performed at the Meson Science Laboratory, University of Tokyo (UTMSL, located at KEK). The single crystal Ge specimen described in Ref. 4) (subsequently discovered to be n-doped with Sb, with $[\text{Sb}] \sim 10^{14} \text{ cm}^{-3}$ estimated from $\rho \sim 15 \Omega\text{cm}$) was used again in the current experiment. The observed time-dependent muon polarization at 12 K in Fig. 1 indicates that there is a fraction of implanted muons which exhibits moderate depolarization only weakly affected by illumination. Moreover, the spectra in Fig. 1 consist of a relaxing and a non-relaxing component with relative amplitudes dependent on the applied longitudinal field, a feature characteristic of slow irreversible conversion from a state undergoing spin/charge exchange interaction to the final non-relaxing state. The detailed analysis of the field dependence indicates that

almost 50% of the non-relaxing component is a Mu^\pm state (the rest is attributed to a stationary Mu_T^0 state). Taking into account that Mu_T^0 is known to be a very fast diffuser in this temperature range, such a “delayed” Mu^\pm state strongly suggests the formation of a Mu-donor complex (which is akin to Mu^\pm) by diffusion-controlled reaction between Mu and donor atoms. More importantly, the absence of charge exchange interaction between the final Mu^\pm centers and excess carriers under illumination (as inferred by the absence of spin relaxation) supports the presumption that there is no electronic level in the band gap associated with this complex state, i.e., passivation of the donor level by muonium.

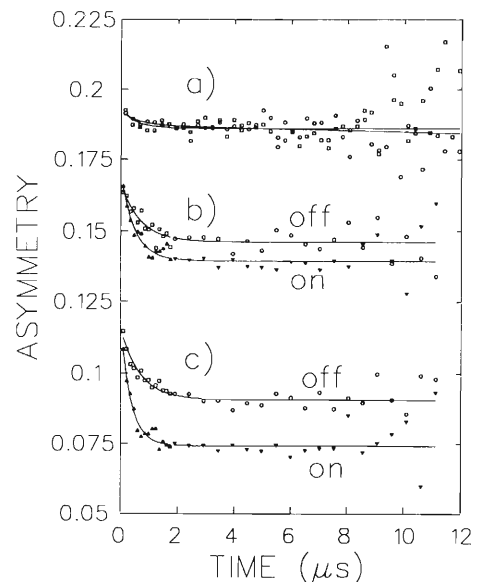


Fig. 1. Time spectra of decay positron asymmetry in Ge at 12 K with (“on”) and without (“off”) illumination when a) Longitudinal Field=0.34 T, b) 0.1 T, and c) 0.01 T.

References

- 1) For recent reviews, see for example, B. D. Patterson: Rev. Mod. Phys. **60**, 69 (1988); R. F. Kiefl and T. L. Estle: in *Hydrogen in Semiconductors*, Academic Press, San Diego, p. 547 (1991).
- 2) R. Kadono et al.: Phys. Rev. B **55**, 4035 (1997).
- 3) For recent reviews, see for example, S. J. Pearton, J. W. Corbett, and M. Stavola: *Hydrogen in Crystalline Semiconductors*, Springer, Berlin (1992); J. I. Pankove and N. M. Johnson eds.: *Hydrogen in Semiconductors*, Academic Press, San Diego (1991).
- 4) R. Kadono et al.: Phys. Rev. Lett. **73**, 2724 (1994).

μ SR Study on the Two-Leg Ladder Compound, $\text{La}_{1-x}\text{Sr}_x\text{CuO}_{2.5}$

J. Akimitsu, A. Yamashita, K. Ishii, K. Ohishi, R. Kadono, N. Kobayashi,*
Z. Hiroi,* M. Takano,* and K. Nagamine

$\text{LaCuO}_{2.5}$ is a new two-leg ladder compound recently discovered by Hiroi and Takano¹⁾ under a high pressure. The temperature dependence of the susceptibility suggests that the ground state of this compound is the spin liquid state with a finite spin gap. However, the recent NMR²⁾ and μ SR³⁾ measurements clearly indicate the antiferromagnetic long-range order of this system, contrary to the previous suggestion.

Recently, we have performed the muon spin relaxation (μ SR) measurements on hole-doped $\text{La}_{1-x}\text{Sr}_x\text{CuO}_{2.5}$ for $x=0.025, 0.05, 0.10, 0.15,$ and 0.20 , to confirm whether the superconducting correlation is suppressed by weak but non-negligible inter-ladder interactions. In zero external field, a rapid decrease of the initial asymmetry was observed, indicating that Cu spins are antiferromagnetically ordered at Néel temperature ($T_N \approx 150$ K). And surprisingly, there appears no change of T_N for the different Sr concentrations, x , as shown in Figs. 1 and 2. Figure 3 shows the concentration dependence of the internal magnetic fields at muon sites measured by applying an axial magnetic field. They are almost constant at $B \sim 800$ G in the insulating phase ($x = 0 \sim 0.10$), and gradually decrease to $B \sim 300$ G in the metallic phase ($x = 0.20$). However, time spectra is different between $x = 0.20$ (metallic phase) and the other concentrations (insulating phase); a fast relaxation function was clearly observed in the former samples, although it was not observable in the latter ones.

Our preliminary conclusion is that magnetic order

can not be destroyed by the increase of hole concentration, contrary to our initial expectation.

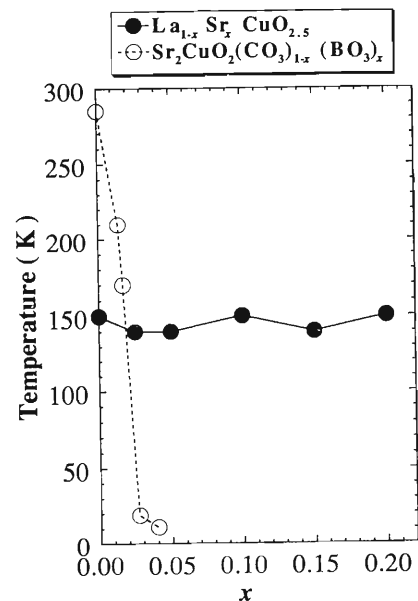


Fig. 2. The phase diagram of the two-leg ladder system $\text{La}_{1-x}\text{Sr}_x\text{CuO}_{2.5}$ and oxycarbonate superconductor $\text{Sr}_2\text{CuO}_2(\text{CO}_3)_{1-x}(\text{BO}_3)_x$.⁴⁾ In contrast a rapid decrease of T_N for the oxycarbonate superconductor, it is almost constant for the ladder compound.

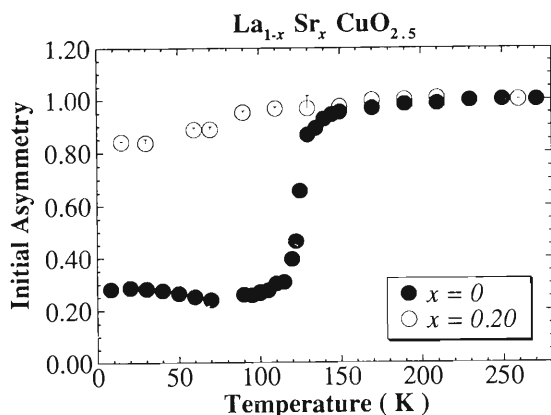


Fig. 1. Temperature dependence of the initial asymmetry for two different Sr concentrations x , indicating that the magnetic transition temperature ($T_N \sim 150$ K) did not change.

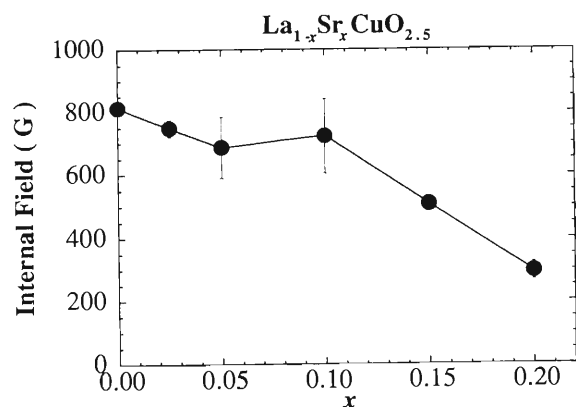


Fig. 3. Internal magnetic field at the muon site *vs.* Sr concentration, x .

* Department of Physics Aoyama Gakuin University;
Institute for Chemical Research, Kyoto University

References

- 1) Z. Hiroi and M. Takano: Nature **377**, 41 (1995).
- 2) S. Matsumoto et al.: Phys. Rev. B **53**, 11942 (1996).
- 3) R. Kadono et al.: Phys. Rev. B **54**, 9628 (1996).
- 4) H. Nakata et al.: Physica C **263**, 344 (1996).

Bose-Glass Transition of the Heavy-Ion Irradiated $\text{La}_{1.85}\text{Sr}_{0.15}\text{CuO}_4$ Single Crystal[†]

G. Tatara, M. Matsuda, K. Katsumata, T. Kambara, Y. Awaya, T. Mitamura, M. Terasawa, Y. Endoh, K. Yamada, and S. Hosoya

Recently the vortex system in high- T_c superconductors has been attracting much attention because of its rich phase structure.¹⁾ We report on the study of phase structure of a vortex system in the heavy-ion irradiated $\text{La}_{1.85}\text{Sr}_{0.15}\text{CuO}_4$ single crystal. The ions created tracks work as columnar pinning centers, resulting in a new Bose-glass phase.²⁾

Unirradiated (or pre-irradiation) sample, grown by the traveling solvent floating zone (TSFZ) method, has a sharp superconducting transition at 37.5 K. One of such samples was irradiated parallel to the c -axis by the 3.4 GeV Xe ions produced from the RIKEN Ring Cyclotron. The density of irradiation for this sample was $2.7 \times 10^{10} \text{ cm}^{-2}$, which corresponds to the vortex density at the field of $B_\Phi = 0.5 \text{ T}$.

Figure 1 shows the hysteresis curve of the samples with $B_\Phi = 0$ (i.e., unirradiated) and $B_\Phi = 0.5 \text{ T}$ at 15 K. It is notable that the absolute value of the magnetization of the sample with $B_\Phi = 0.5 \text{ T}$ is enhanced by a factor of about 2.8 compared to the unirradiated (open circles) one.

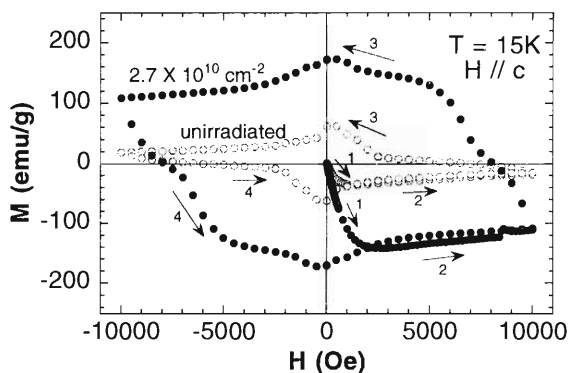


Fig. 1. Hysteresis curve of the unirradiator ($B_\Phi = 0$) and irradiated ($B_\Phi = 0.5 \text{ T}$) samples at 15 K. Closed circles: Irradiated by the intensity $2.7 \times 10^{10} (\text{cm}^{-2})$. Open circles: Unirradiator sample.

The imaginary part, $\chi''(T)$, of the AC susceptibility

of the unirradiated sample shows a peak at a temperature below the critical temperature T_c . The behavior of χ'' of the $B_\Phi = 0.5 \text{ T}$ sample below a crossover field of $B_{cr} \sim 0.5 \text{ T}$ is similar to that of the unirradiated sample, although the peak temperature is shifted to the higher field side (Fig. 2). Above B_{cr} , χ'' of the irradiated sample becomes asymmetric and has another small broad peak at a lower temperature.

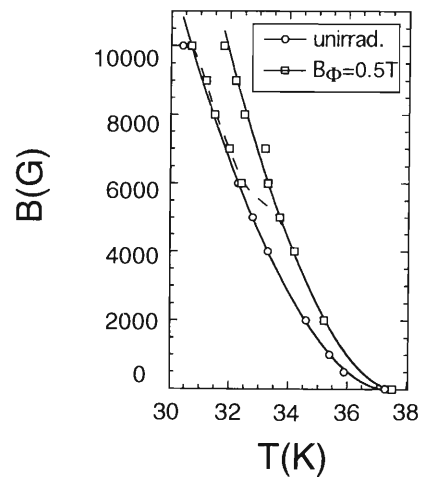


Fig. 2. The irreversibility line determined from the position of the peak of χ'' for the samples with $B_\Phi = 0$ (open circles) and 0.5 T (open squares). Solid lines are the fits of the low field region ($B \leq 0.5 \text{ T}$) with a function of $B \propto (T_c - T)^\alpha$ with $\alpha = 1.8$. Dotted line is a guide to the eye.

The origin of the two peaks for $B > B_{cr}$ of $B_\Phi = 0.5 \text{ T}$ sample may be due to the co-existence of columnar defects and intrinsic point defects.

References

- 1) G. Blatter et al.: Rev. Mod. Phys. **66**, 1125 (1994).
- 2) D. R. Nelson and V. M. Vinokur: Phys. Rev. B **48** 13060 (1993); A. I. Larkin and V. M. Vinokur: Phys. Rev. Lett. **75** 4666 (1995).

[†] Condensed from the article in Czech. J. Phys., **46**, 1555 (1996).

Heavy-Ion Irradiation Effects on the Super-Conducting Material, $\text{La}_{1.85}\text{Sr}_{0.15}\text{CuO}_4$

T. Mitamura, M. Terasawa, X.-J. Fan, T. Kohara, K. Ueda, T. Kambara, Y. Awaya, M. Matsuda, G. Tatara, N. Takezawa,* and K. Fukushima*

Practical application of the high-temperature superconductor is strongly dependent on the efforts to achieve a high critical current density under high magnetic fields, because, by a free motion of vortices, the critical current density tends to decrease rapidly when the temperature approaches the critical temperature. The introduction of columnar defects by a swift irradiation of heavy-ions is one of the most promising approaches to create effective defects which pin the magnetic fluxes. Enhancement of the pinning strength in high- T_c cuprates introducing parallel or multi-direction columnar defects of high-energy heavy-ions has been reported.¹⁻⁵⁾ In the present study, the effect of columnar defects on the critical current density of a polycrystalline high- T_c cuprate is investigated.

The polycrystalline $\text{La}_{1.85}\text{Sr}_{0.15}\text{CuO}_4$ bulk material was produced by an usual sintering method. The critical temperature, T_c , was measured to be 38 K. Specimens with the size of about 2 mm \times 10 mm and thickness of 0.1 mm were irradiated at room temperature in a high vacuum by the 3.5 GeV, $^{136}\text{Xe}^{31+}$ ions which were obtained from RIKEN Ring Cyclotron. Ion irradiations were carried out by two ways: a single direction irradiation perpendicularly to the surface of specimen (parallel irradiation), and a multi-direction irradiation (splay irradiation) at angles of $0, \pm 5$ and ± 10 degrees with respect to the normal vector to the surface. Considering ion range and electronic stopping power of the target material to this ion, defects with cylindrical structure can be assumed to have formed along the ion trajectories. By a high-resolution transmission microscopy, columnar defects were found almost amorphous phase and its damaged region was about 5 nm in mean diameter.⁶⁾ The measurements of magnetization hysteresis were performed using a SQUID magnetometer of Quantum Design, and irreversibility line was deduced in the temperature-magnetization plane, which corresponds to the boundary dividing the pinning region of the magnetic flux lines (vortices) from complete depinning one.

As shown in Fig. 1, the irreversibility lines for the $B_\phi = 6.0$ T specimens are improved to a higher magnetic field. In the figure, B_ϕ is the field-equivalent irradiation dose. The irradiation dose of 1.0×10^{11} Xe/cm² corresponds to the vortex density at the field of $B_\phi = 2.0$ T. Especially, the splay-irradiated specimen shows more improvement than the parallel-irradiated one, indicating that the splay configuration of columnar defects is more effective to pin the vortex. A sudden collapse of the irreversibility line observable near T_c , i.e., at $T = 37.5$ K, for only the irradiated specimens may be the evidence of the existence of another type of vortex pinning mechanism which is enhanced under the irradiation. Krusin-Elbaum et al.⁷⁾ found a similar behavior of the irreversibility line for

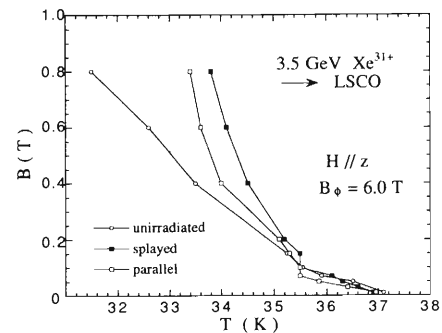


Fig. 1. Change of irreversibility line before and after the 3.5 GeV, Xe ion irradiation.

YBCO in their ac susceptibility observation, and proposed that this change is an evidence of the thermal softening boundary, which is theoretically predicted by Feigel'man and Vinokur.⁸⁾ At the moment, we have no decisive explanation about this.

From the crystal orientation point of view, there should be no difference between the parallel and splay irradiations to the polycrystalline materials, because the crystal axes of various grains are randomly distributed with respect to the direction of a columnar defect. Hence, it is natural to mention that the direction of ion beam does not play an important role. In the present study, however, it was found that the splay irradiation is more effective to introduce defects for vortex pinning than the parallel irradiation, suggesting that entangled states of vortices, which result from random exchanges of vortices between columnar defects, are more easily attained in the configuration of randomly oriented columnar defects. As a result, even in the polycrystalline high- T_c cuprates, the vortex pinning strength may be more enhanced in the case of the splay irradiation.

References

- 1) V. Hardy et al.: Nucl. Instrum. Methods Phys. Res. B **54**, 472 (1991).
- 2) Th. Becker et al.: Physica C **245**, 273 (1995).
- 3) M. Terasawa et al.: Physica C **235-240**, 2805 (1994).
- 4) T. Hwa, P. Le Doussal, D. R. Nelson, and V. M. Vinokur: Phys. Rev. Lett. **71**, 3545 (1993).
- 5) Th. Schuster et al.: Phys. Rev. B **51**, 16358 (1995).
- 6) M. Terasawa et al.: Trans. Mat. Res. Soc. Jpn. **17**, 383 (1994).
- 7) L. Krusin-Elbaum et al.: in *Progress in High Temperature Superconductivity*, Vol. 30 (World Scientific, 1992) p. 62.
- 8) M. V. Feigel'man and V. M. Vinokur: Phys. Rev. B **41**, 8986 (1990).

* Toshiba Research and Development Center

Studies of Columnar Defects in $\text{Bi}_2\text{Sr}_2\text{CaCu}_2\text{O}_x$ by TEM and STS

N. Nishida, S. Kaneko, Y. Ono, H. Sakata, K. Satoh,
T. Kambara, and Y. Awaya

High-energy heavy ions are known to produce columnar defects (3–10 nm in diameter) in high- T_c oxide superconductors along their tracks.¹⁾ As the diameter is the order of the superconducting coherence length, columnar defects can act as pinning centers in high- T_c superconductors. It is interesting and important to study the microscopic electronic states at and around columnar defects. We have generated columnar defects in $\text{Bi}_2\text{Sr}_2\text{CaCu}_2\text{O}_x$ at a (E5a) beam line by impacting 3.4 GeV $^{136}\text{Xe}^{31+}$ ions from RIKEN ring cyclotron, and studied them by applying transmission electron microscope (TEM) and scanning tunneling microscope (STM). In STM experiment a clean surface of $\text{Bi}_2\text{Sr}_2\text{CaCu}_2\text{O}_x$ was prepared by cleaving the single crystal of $\text{Bi}_2\text{Sr}_2\text{CaCu}_2\text{O}_x$ at 4.2 K in vacuum. Scanning tunneling spectroscopic (STS) method has also been successfully applied to study columnar defects.

In Fig. 1, a high resolution TEM photograph is shown, where we can see that a columnar defect has an amorphous structure and has a sharp boundary in atomic scale. In Figs. 2 one of our STM observations of columnar defects on $\text{Bi}_2\text{Sr}_2\text{CaCu}_2\text{O}_x$ is shown. Figure 2(a) exhibits a constant-current STM image of a columnar defect. The image corresponds to the vertical movement of a STM needle probe against $\text{Bi}_2\text{Sr}_2\text{CaCu}_2\text{O}_x$ surface in order to keep a tunneling current constant at a constant applied voltage between the needle and the sample. In Fig. 2(b) the movement of the needle is plotted across the columnar defect; it can be seen that a STM needle comes closer to the surface abruptly at the region of columnar defect. This means that the columnar defect is an insulator. This is

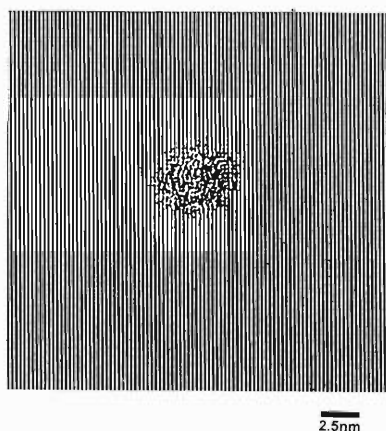


Fig. 1. Columnar defects in $\text{Bi}_2\text{Sr}_2\text{CaCu}_2\text{O}_x$ observed by a high-resolution TEM.

the first experimental evidence shown microscopically of the insulating electronic state of columnar defects in high-temperature oxide superconductors. Recent theories²⁾ have discussed that boundary effects in d-wave superconductors depend on kinds of the surface, such as (1,1,0) or (1,0,0) surface boundary of CuO_2 plane, and are quite different from those in s-wave superconductors. In order to study the boundary effects, the local density of states around a columnar defect in $\text{Bi}_2\text{Sr}_2\text{CaCu}_2\text{O}_x$ has been measured by using our LT-STs at 2.2 K. The analysis is now in progress and expected to give us back valuable information about the symmetry of Cooper-pairing in high- T_c copper-oxide superconductors.

We acknowledge JEOL for kindly taking a high-resolution TEM photograph.

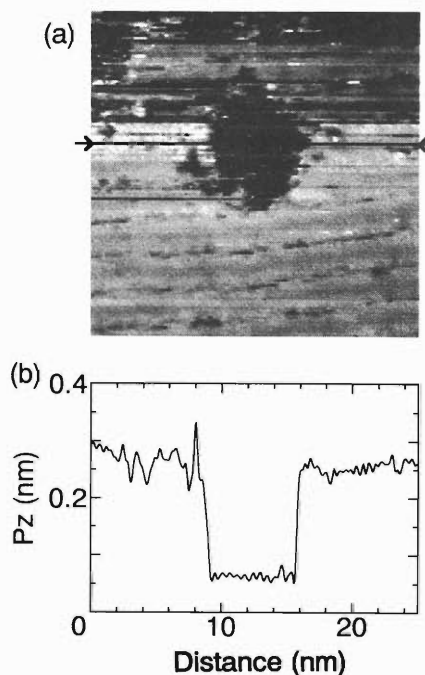


Fig. 2. (a): A constant-current STM image of a columnar defect in $\text{Bi}_2\text{Sr}_2\text{CaCu}_2\text{O}_x$ at a bias voltage of 1 Volt. (b): The columnar defect revealed by moving STM-needle across it.

References

- 1) M. Toulemonde, S. Bufford, and F. Studer: Nucl. Instrum. Methods Phys. Res. B **91**, 108 (1994).
- 2) M. Matsumoto and H. Shiba: J. Phys. Soc. Jpn. **64**, 1703 (1995).

An Evaluation of Single Event Upset on Memories

S. Matsuda, T. Akutsu, S. Shugyo, M. Nakamura, K. Sugimoto, T. Hirose, H. Ohira, Y. Nagai, T. Kohno, N. Inabe, M. Kase, A. Goto, and Y. Yano

Semiconductor devices, which are essential in artificial satellites and spacecrafts, degrade by radiation in space. The radiation environment around the earth includes the electrons and protons trapped by the earth's magnetosphere, solar protons, and heavy ions in galactic cosmic rays. It is well known that the impingement of high energy heavy ions on semiconductor devices causes so-called single event phenomenon (SEP) like single event upset (SEU) on memory devices, single event latch-up (SEL) on CMOS and LSI etc., and single event burnout (SEB) by the heavy ion going through the active area of POWER MOSFET. The author's affiliation NASDA (National Space Development Agency of Japan) previously studied SEB and Single Event Gate Rapture (SEGR) on POWER MOSFET by using the heavy ions from the RIKEN Ring Cyclotron.

During this reporting period, we performed irradiation test on two types of memory chips (256kSRAM and 16MDRAM) with a beam of ^{40}Ar at 90 MeV/u (3600 MeV). The LET of the ion in the material(Si) is 2.02 MeV/(mg/cm²) and its range is 4330 μm (Si). We have performed several irradiation tests on 256kSRAM in use of TIARA (Takasaki Ion Accelerators for Advanced Radiation Application) and measured the cross section of SEU as a function of LET. In this irradiation test at RIKEN, we acquired a new set of data on the cross section. The results are plotted in Figs. 1 (write data = '0000') and 2 (write data = '1111'). At TIARA, we had to open the lid of the devices since the range of the ions was not long enough. In this test at RIKEN, we irradiated the devices both with lid and without lid. This result gives an evidence that the ion beam with the same LET evokes SEU with the same cross section even at different energies of the ion beam. Therefore, we could acquire the correlation data of the SEU on 256kSRAM by the beam with different LETs.

Recently, memory devices are getting smaller and lighter, and special type of package structure such as LOC (Lead on Chip structure) is used to shrink the de-

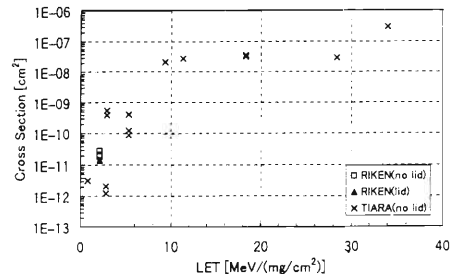


Fig. 2. Test result of 256kSRAM (write data = '1111').

vice. For this type of package, the chip surface is partly covered with its lead-flame. The heavy ion beam does not reach the chip surface in usual way of its irradiation. But by the use of a long-range ion beam and by irradiating from backside of chip, the observation of SEU is possible.

We has performed a few irradiation tests on 16MDRAM (assembled inside an ordinary package and opened the lid) in TIARA to measure the cross section as a function of LET. In this irradiation test at RIKEN, we used a LOC structure 16MDRAM and irradiated from backside of the chip to obtain a new data of SEU cross section as a function of LET, as plotted in Fig. 3. There is a disagreement between the Ar-3600 MeV data at RIKEN and the Ne-260 MeV data at TIARA. In the case of irradiating from the backside of chip, LET changes because of the energy loss of ions before the ions reach the sensitive area. But, in this irradiation test, the beam range was long enough, so that the change of LET does not effect the test result. Moreover, the data at TIARA were on 8bit 16MDRAM and the data at RIKEN is on 4bit 16MDRAM. From our experience, the memory-bit composition of devices does not effect the SEU test result. We are under discussion on the discrepancy of test result and have a plan to continue the irradiation test from backside of the chip for storing more data.

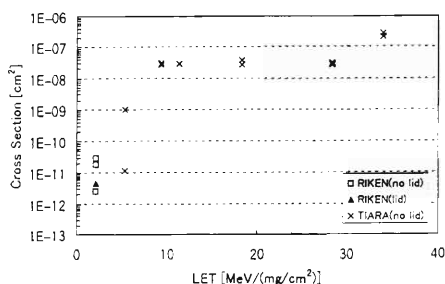


Fig. 1. Test result of 256kSRAM (Write data = '0000').

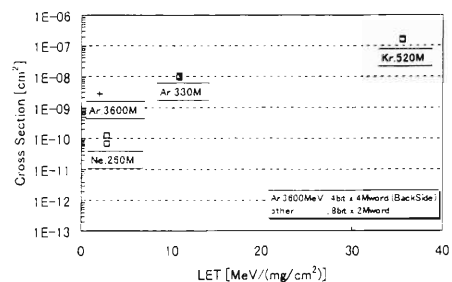


Fig. 3. Test result of 16MDRAM.

3. Radiochemistry and Nuclear Chemistry

In-Beam Mössbauer Study on Jump Processes of Self-Interstitial in Pure Iron after $^{56}\text{Fe}(d, p)^{57}\text{Fe}$ Reaction

Y. Yoshida, Y. Kobayashi, J. Nakamura, F. Ambe, E. Yagi, R. Sielemann,* H. Häßlein,*
A. Feinauer,** T. Grund,** and A. Seeger**

In order to elucidate the dynamical effects due to jump processes of the interstitial ^{57}Fe atoms produced by the $^{56}\text{Fe}(d, p)^{57}\text{Fe}$ reaction, we measured the angular dependence of Mössbauer spectrum at different crystal orientations.^{1,2)} The iron single crystal ($5 \times 10 \text{ mm}^2$ with 1 mm thick) was oriented so that the surface was (001) and the long axis of the rectangle was [001]. The deuteron beam ($E = 8 \text{ MeV}$) was introduced into the specimen with an angle of 45° to the surface from the direction of [110] and stopped about $100 \mu\text{m}$ of depth inside the sample. This means that both the deuterons and the radiation damage were accumulated during the measurement. To reduce any effects caused by this accumulation, we used a low intensity of 50 nA (one fourth of the full current) and the sample was annealed above 350 K after every measurement. The spectra were measured between the pulsed beams to avoid the prompt peaks because the time-structure of the beams was not suitable for our measurement.

The emission direction of the Mössbauer γ -radiation can be varied from parallel to [100] to [110] by changing the position of the detector. Figure 1 shows the Mössbauer spectra of single crystal iron along [100] direction between 60 and 420 K. It is clearly seen that the peak intensities of the 2nd and 5th lines decrease as the temperature decreases. This means that the direction of the magnetization changed, roughly speaking, from parallel to perpendicular to the surface shallower than

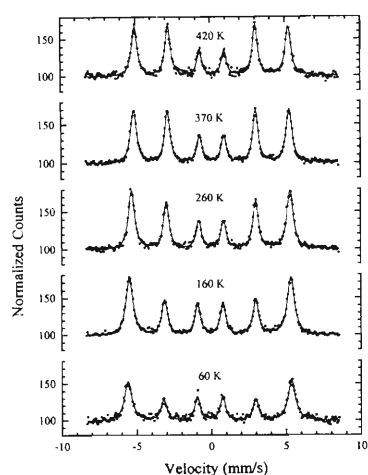


Fig. 1. In-beam Mössbauer spectra of ^{57}Fe in single crystal Fe along [100] after $^{56}\text{Fe}(d, p)^{57}\text{Fe}$ reaction. The spectra were measured between 60 and 420 K.

* Hahn-Meitner-Institut Berlin, Germany

** Max-Planck-Institut für Metallforschung & Max-Planck-Institut für Physik, Stuttgart, Germany

the region where the deuterons were stopped. The total area intensity of the spectrum at 60 K is much smaller than those of the other spectra at higher temperatures. It suggests the existence of a broad component. The origin of such effects are not clear at this experiment, but one possible explanation may be due to an internal stress which would arise from the accumulation of deuterons and defects and would become stronger in lower temperatures.

The angular dependence of the Mössbauer spectra at 370 K and 160 K is shown in Fig. 2(a) and (b), respectively. The angles of -11 and $+34$ degrees correspond to the directions of [110] and [100], respectively. The hyperfine splitting of the spectrum at [110] is considerably higher than those at another angle both at 370 K and 160 K, indicating the existence of the defect lines in addition to the substitutional line. The γ -rays emitting from the ^{57}Fe atoms which are stopping on the substitutional sites will be strongly self-absorbed by the ^{57}Fe atoms existing with a natural abundance of 2% in the sample. This is why the intensity of the substitutional line depends on the detection angle. On the other hand, the γ -rays emitting from the ^{57}Fe atoms ending up on a defect site, for instance, on the interstitial sites, will not be resonantly absorbed inside the sample. Accordingly, the intensity of the defect lines will not depend so much on the angles.

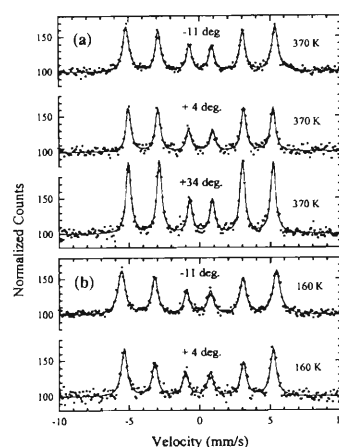


Fig. 2. Angular dependence of Mössbauer spectra at 370 and 160 K.

References

- 1) Y. Yoshida et al.: RIKEN Accel. Prog. Rep. **29**, 111 (1996).
- 2) A. Feinauer et al.: HMI-Berlin Ann. Rep. B **540**, 111 (1995).

In-Beam Mössbauer Spectroscopy on ^{57}Fe in Solid Ar and Solid Xe after Coulomb-Excitation and Recoil-Implantation

Y. Yoshida, Y. Kobayashi, K. Hayakawa,* K. Yukihiro,* H. Häßlein,*
J. Nakamura, S. Nasu, E. Yagi, and F. Ambe

The inert gas solid has been often used for a matrix to study isolated ions using Mössbauer spectroscopy at a low temperature. This technique is usually called “matrix isolation”, and often combined with a coevaporation¹⁾ or with an implantation technique at a low energy of several 10 keV²⁾ to introduce Mössbauer probes into the inert gas solids.

In the present study, we implanted ^{57}Fe into solid Ar and solid Xe immediately after the Coulomb-excitation via a pulsed Ar ion beam with energy of 120 MeV from the AVF-cyclotron at RIKEN, and simultaneously measured Mössbauer spectra of ^{57}Fe in the solid Ar and Xe samples. This in-beam Mössbauer technique is supposed to be more appropriate to study isolated ^{57}Fe atoms on different lattice sites and their dynamic behavior in the inert gas solids. This is because the high recoil implantation energy of several MeV, the low ^{57}Fe concentration of 10^{10} necessary for one measurement, and the short measuring time of several hundreds nano seconds make us possible to study the completely isolated ^{57}Fe -states even at elevated temperatures. The same technique has been developed and applied to the studies of atomic jump processes in metals and semiconductors³⁾ at the Hahn-Meitner-Institute in Berlin. A preliminary result was reported in the last year.⁴⁾

The solid samples were prepared by condensation of Ar and Xe gases on a copper substrate in 40×30 mm rectangular shape, which was cooled by a continuous-He-flow cryostat down to 50 and 90 K, respectively, in a small chamber directly connected to the measuring chamber. Mössbauer spectrum was measured by two Parallel-Plate-Avalanche Counters (PPAC), which were mounted on the Mössbauer driving units. The beam intensity of ^{40}Ar was only 3 pA, yielding the γ -ray count rate of about 0.3 s^{-1} per each detector. This rather low intensity was mainly due to a poor condition of the ion source, which will be improved in the next experiment.

Figures 1 (a) and (b) show the ^{57}Fe Mössbauer spectra in the solid Ar and Xe samples, respectively, in comparison with the ^{57}Fe spectrum in the bare Cu substrate (Fig. 1(c)). Each spectrum was measured at 10 K for 18, 20, and 6 hours, respectively. Although the accumulation time for the spectrum of ^{57}Fe in Cu was the shortest, the spectrum can be seen most clearly and be analyzed by a sharp single Lorentzian. The center shift is $-0.37(3) \text{ mm/s}$, which corresponds to the isomer shift of $0.26(3) \text{ mm/s}$ at the room tempera-

ture. This component can, therefore, be assigned as Fe atoms on the substitutional site in Cu. On the other hand, the quality of the spectra for solid Ar and solid Xe is rather poor, which is supposed to be mainly due to the small Debye-Waller factors in both systems, due to the low beam intensity of Ar (about 3 pA), and due to a short repetition time of beam pulses of 160 ns. In both spectra, there seems to be at least two different components: in the spectrum of solid Ar, at around $1.0(2)$ and $-0.48(8) \text{ mm/s}$, and in the spectrum of solid Xe, at around $0.5(1)$ and $-1.3(2) \text{ mm/s}$. The component at the right hand side of each spectrum appears to be due to the “ Fe^0 monomer state (configuration $3d^6 4s^2$)”, which was reported and assigned as “substitutional” in the experiments^{1,2)} after the coevaporation of ^{57}Fe and ^{57}Co and implantation of ^{57}Co . When we compare the isomer shifts of these components with the values obtained from the in-beam Mössbauer measurements on metals,³⁾ however, it may be more plausible to assign them as the interstitial sites in solid Ar and solid Xe.

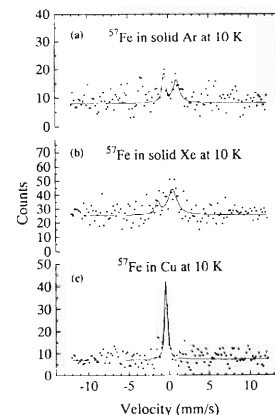


Fig. 1. Mössbauer spectra of ^{57}Fe in (a) solid Ar, (b) solid Xe, and (c) bare Cu-substrate after the Coulomb-excitation and its recoil-implantation at 10 K.

References

- 1) P. H. Barrett and T. K. McNab: Phys. Rev. Lett. **25**, 1601 (1970); H. Micklitz and P. H. Barrett: Phys. Rev. Lett. **28**, 1547 (1972).
- 2) M. Van Rossum et al.: Phys. Lett. A **75**, 241 (1980).
- 3) Y. Yoshida et al.: Phys. Rev. Lett. **61**, 195 (1988); Y. Yoshida: Hyperfine Int. **47**, 95 (1989); R. Sielemann and Y. Yoshida: Hyperfine Int. **68**, 119 (1991); B. Keck, R. Sielemann, and Y. Yoshida: Phys. Rev. Lett. **71**, 4178 (1993).
- 4) Y. Yoshida et al.: RIKEN Accel. Prog. Rep. **29**, 111 (1996).

* Shizuoka Institute of Science and Technology

Simultaneous Determination of Biobehavior of Sc, Mn, Fe, Co, Zn, Se, Rb, Y, and Zr in Mice Bred under Different O₂ Gas Percentage Circumstance

R. Amano, S. Oishi,* S. Seto,* N. Fukumoto,* S. Enomoto, and F. Ambe

Radioactive multitracer has been utilized and proved its versatility for simultaneous tracing of many elements in various biological systems.¹⁾ We have also been applying the multitracer technique to study the tissue and subcellular behavior of many trace elements in mice. We have described that the multitracer solution, which was prepared from an Ag target irradiated with heavy ion beams in RIKEN Ring Cyclotron, is effective for simultaneous tracing of biotrace elements such as Mn, Co, Zn, Se, and Rb over the experimental period up to 2 months.^{2,3)} The present work aimed to examine the simultaneous evaluation of biobehavior of Sc, Mn, Fe, Co, Zn, Se, Rb, Y, and Zr in mice bred in different O₂ gas percentage circumstance.

A no-carrier-added multitracer solution was obtained from an Ag (purity: more than 99.99%) target irradiated by heavy-ion beam in RIKEN Ring Cyclotron. The multitracer solution was prepared according to the method of S. Ambe⁴⁻⁶⁾ in Radioisotope Center, Kanazawa University. This animal experiment started one month after cyclotron bombardment and thereby produced 10 radioisotopes (⁴⁶Sc, ⁵⁴Mn, ⁵⁹Fe, ⁵⁷Co, ⁵⁸Co, ⁶⁵Zn, ⁷⁵Se, ⁸³Rb, ⁸⁸Y, and ⁸⁸Zr) of 9 elements were utilized as the tracers. Male Crj: CD-1(ICR) mice weighing 20–22 g (4 weeks old) were used. Physiological saline solutions (0.001N HCl, pH 2-3) containing the radioactive multitracer were intraperitoneally injected (0.2 ml/mouse). The injected mice were housed in the steel net cages, which were placed into the box with a constant gas flow (2 l/min) from a cylinder. In this way, the mice were bred under 4 different O₂ gas percentage circumstances.

At 48 hrs after injection of the multitracer, the mice were sacrificed under ether anesthesia and approximately 0.2 ml of blood was collected. After this, brain, cardiac muscle, lung, liver, spleen, pancreas, kidney, skeletal muscle, and bone were excised. The 9 tissues and blood were weighed and freeze-dried. The dried samples were subjected to γ -ray spectrometry using a Ge detector in reference to an appropriate standard in order to obtain the tissue uptake rate of each tracer, which was expressed as the radioactivity percentage of the injected dose per gram of tissue (% dose/g).

The tracers of Mn, Zn, Se, Rb, Y, and Zr were simultaneously detected in all liver samples at 48 hrs after the intraperitoneal injection under 4 different O₂ gas percentage circumstances (10, 20, 80, and 100%). Each liver uptake rate is expressed as the mean value with its standard deviation from five mice bred under same circumstance. Figure 1 compares the liver uptake rates of the 6 tracers. Although all the liver

uptake rates except those of Rb were observed to be equal within the standard deviations under the 4 different circumstances, the uptake rate of Rb tracer under 10% O₂ circumstance is higher than those under the other circumstances (20, 80, and 100%). The tracers of Se and Rb were observed in all blood and soft tissue samples except in bone. The uptake rates of Se and Rb tracers in all tissues and blood can be compared under 4 different circumstances. Figure 2 shows the uptake rates of Se and Rb tracers in blood and brain. It was found that the Rb uptake rates of all soft tissues and blood under 10% O₂ circumstance is only higher than those under the other 3 circumstances (20, 80, and 100%).

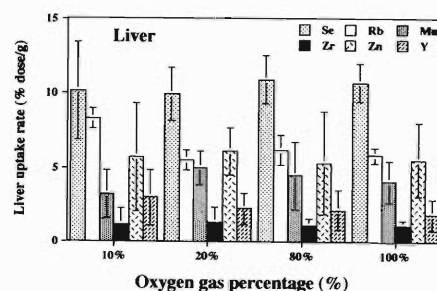


Fig. 1. Liver uptake rates of Mn, Zn, Se, Rb, Y, and Zr in mice at 48 hrs after injection under 4 different O₂ gas percentage circumstances.

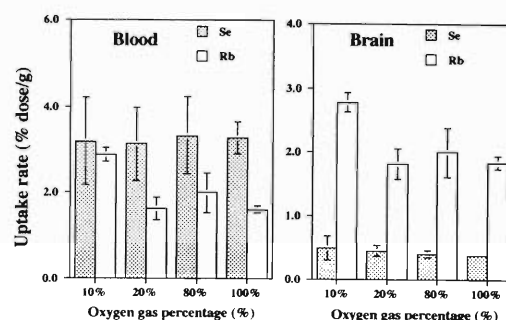


Fig. 2. Uptake rates of Se and Rb tracers at 48 hrs after injection in blood and brain of mice bred under 4 different O₂ gas percentage circumstances.

References

- 1) In RIKEN Review No. 13 (1996).
- 2) R. Amano et al.: *J. Trace Elements Med. Biol.* **10**, 145 (1996).
- 3) R. Amano et al.: *Ann. Cli. Lab. Sci.* **26**, 531 (1996).
- 4) S. Ambe et al.: *Chem. Lett.* **1991**, 149.
- 5) S. Ambe et al.: *Anal. Sci.* **7**, Suppl., 317 (1991).
- 6) S. Ambe et al.: *J. Radioanal. Nucl. Chem.*, Articles **195**, 297 (1995).

* School of Health Sciences, Faculty of Medicine, Kanazawa University

Uptake Behavior of Multitracers in LEC Rats before Jaundice Development (II)

S. Oishi,* R. Amano, A. Ando,* T. Takada,* R. Takafuji,* S. Enomoto, and F. Ambe

Unusual Cu accumulation in LEC (Long Evans Cinnamon) rats has been known to be involved in the development of jaundice, hepatic injury, and hepatocellular carcinoma. Previously, we examined the distribution of multitracers in tissue of LEC rats, and described the age-dependence on increased uptake of Zn by liver and kidneys before jaundice development.¹⁾ In present work, we have mainly studied the subcellular fractionation and gel-filtration pattern of the Zn and Se trace elements in the supernatant fraction in livers of the LEC and Wistar rats having the same 7 weeks of age.

A no-carrier-added radioactive multitracer was obtained from an Ag target irradiated with the 135 MeV/nucleon N-14 beam which was accelerated by RIKEN Ring Cyclotron. The preparation for a multitracer solution was carried out in the Radioisotope Center, Kanazawa University, following to the method of Ambe et al.²⁻⁴⁾ This animal experiment started 2 months after the cyclotron-produced ion bombardment, and therefore four radioisotopes of ⁵⁴Mn, ⁶⁵Zn, ⁷⁵Se and ⁸³Rb were mainly served as tracers.

One fifth of ml of the final radioactive multitracer solution (pH 2-3, physiological saline solution) was intraperitoneally (i.p.) injected in to LEC and Wistar rats. At 12 hr after the i.p. injection containing the radioactive multitracer solution, these rats were sacrificed after ether anesthesia. Then, the liver was excised and treated by subcellular distribution method followed by Sephadex G-75 gel filtration method. The excised liver were homogenized in a cold (5 °C) 0.25 M sucrose solution containing 0.01 M Tris(hydroxymethyl)aminomethane-HCl buffer of pH7.6 (10% weight per volume) by a Potter-Elvehjem type homogenizer, following to a modified method of Hogeboom and Schneider. Separation of the supernatant solution was performed on Sephadex G-75 gel-filtration column (25 mmϕ × 500 mm length) using a 0.001 M Tris-HCl buffer (pH 8.6) solution and a flow rate of 0.6 ml min⁻¹. The 5.5 ml aliquot obtained from the filtration was freeze-dried and its radioactivity (gamma-ray spectrometry) was measured by using pure Ge semi-conductor detectors.

From the results of subcellular distribution as shown in Fig. 1, there were no significant age-dependent changes for both Se and Zn uptake cellular distributions in the liver of LEC rats. It shows high percentages of Zn and Se in the supernatant fraction. Figure 2 compares the elution curves of Se and Zn tracers in the

supernatant by use of Sephadex G-75 gel filtration. We find that Se behaves in a similar manner in both LEC and Wistar rats, but Zn behaves different way. The amount of Zn tracer in LEC rat was higher than that of Wistar rat, especially for fraction numbers 18-26 as shown in Fig. 2. Moreover, we think that the high accumulation of Zn in the liver of LEC rat is involved in metallothionein, because the solutions of the 18-26 fraction numbers were estimated to contain proteins of 7000-10000 molecular weights, which are almost equal to the molecular weight of metallothionein.

Further study is required to discuss the relationship between metallothionein and high uptake of Zn in the liver and kidneys.

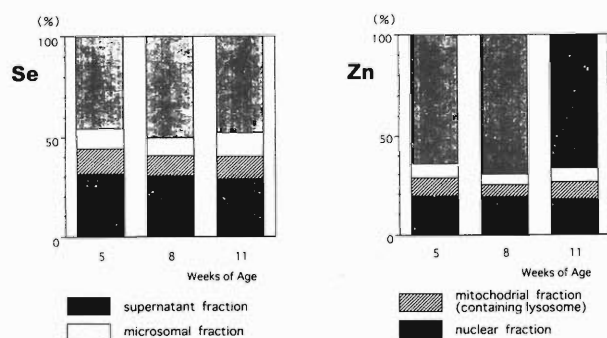


Fig. 1. Subcellular distribution of Se and Zn in the liver of LEC rat.

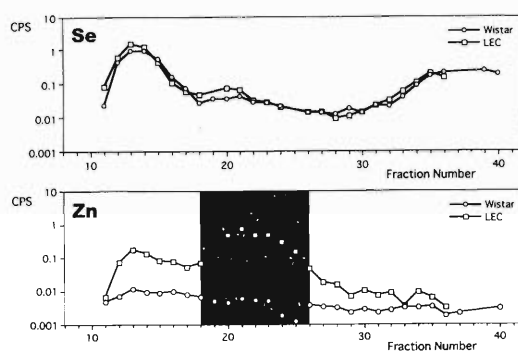


Fig. 2. Elution curves of Se and Zn for the supernatant fraction in the liver of the LEC and Wistar rats on Sephadex G-75 gel-filtration.

References

- 1) S. Oishi et al.: RIKEN Accel. Prog. Rep. **29**, 155 (1996).
- 2) S. Ambe et al.: Chem. Lett. **1991**, 149.
- 3) S. Ambe et al.: Anal. Sci. **7**, Suppl., 317 (1991).
- 4) S. Ambe et al.: J. Radioanal. Nucl. Chem., Articles **195**, 297 (1995).

* School of Health Sciences, Faculty of Medicine, Kanazawa University

In vivo Behavior of Various Elements in Hepatopathic Animals (I) Metabolic study of trace elements in acute alcoholic mice

S. Enomoto, R. G. Weginwar, S. Ambe, and F. Ambe

Recently, the research of adult diseases such as cancer, diabetes mellitus, and hypertension is widely carried out. The hepatopathy is focused as a chronic disease in the present so called age of satiation, and the research from various phases to liver cancer and liver cirrhosis has been done. Alcoholic hepatopathy has various types such as fatty liver, acute alcoholic hepatitis, liver cirrhosis, and the ZIEVE syndrome. In the current idea, the reason why the fatty liver develops to the liver cirrhosis is doubtful, and it is dominant to the idea of inducing by the overlap of acute alcoholic hepatitis. In the present paper, we discuss the dysbolism of trace elements by the hepatopathy using a model mouse which induced the acute alcoholism.

The acute alcoholic hepatopathy model and normal mice used ddY strain in 7 weeks of ages. Three ddY mice were treated intraperitoneally with alcohol for 3 hrs before, and for 3, 11, 19, 27, 35, 43, 51, 59, 67 and 71 hrs after injection of the multitracer solution described below. Each mouse received 0.025 ml/g body weight of 25 (V/V) % alcohol each time. The injection schedule and experimental procedure are shown in Ref. 1.

Figure 1 shows the comparison of biodistribution on the acute alcoholic hepatopathy and normal mouse livers at 24 hrs after the multitracer administration. In the liver of the acute alcoholic hepatopathy mouse, the uptake of Be, Sc, Mn, Se, Rb, Y, and Zr increased further than the normal one. The uptake of Be, Cr, and Y in the acute alcoholic hepatopathy mouse increased about 3 times of the normal one. This tendency was seen even in 72 hrs after the multitracer administration, and especially, Be and Y were increased after 72 hrs by about 8.5 times than the normal mouse. *In vivo*, Be exists as Be^{2+} , and it seems to be similar to Al^{3+} , and Sc, Cr, Mn, Y, and Zr exist *in vivo* at 3 valences. The alcohol seemed to give some effects on there because of an increase for the uptake of these elements of 3 valences. On the other hand, Be and Y are the bone seeking elements, and these elements are easy to accumulate in the liver which induced the hepatopathy.

We observed many fat granulations and fiberization in the diabetes mellitus model mouse, and it was reported that the bone seeking elements are stored in the part of fiberization. It was estimated that such a change had been generated by the crisis of the hepatopathy in the alcoholism model mouse, and the uptake of Be and Y was suggested to increase by this reason. In the liver of the alcoholism model mouse, the uptake of As decreased remarkably. In the alcoholism model mouse, the hemoglobin concentration was 9.23 ± 0.23 g/dl, and that in the normal mouse was 13.21 ± 0.56 g/dl. The anaemia seemed to have been caused in the alcoholism model mouse. In general, the As incorporated in the internal mainly shifts in the erythrocyte. By the anaemia, a decrease in number of erythrocyte was induced, and the As uptake quantity seemed to decrease in the liver, since the number of the erythrocyte which transports to the liver decreases.

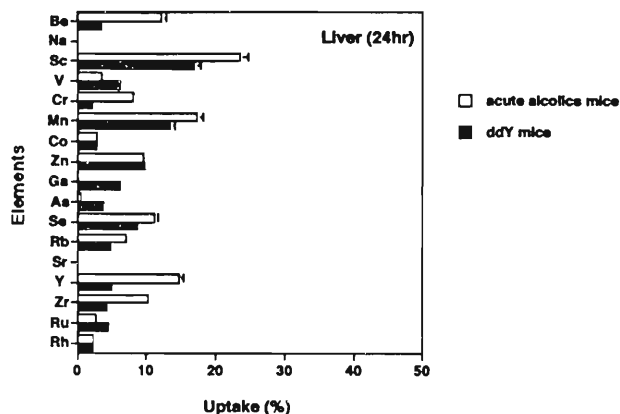


Fig. 1. Uptake (%) of various elements in the acute alcoholic and normal mice.

References

- 1) S. Enomoto et al.: RIKEN Accel. Prog. Rep. 29, 145 (1996).

In vivo Behavior of Various Elements in Hepatopathic Animals (II) Metabolic study of trace elements in liver-cancer bearing rat

S. Enomoto, N. Hayakawa, K. Endo, S. Ambe, and F. Ambe

The Long Evans Cinnamon (LEC) rat genetically contracts the jaundice at 4 ~ 5 months which causes acute hepatitis, and approximately the half dies. Survived rat passes through chronic hepatitis, liver cirrhosis, and it contracts the liver cancer. Critical causes of the hepatitis were examined in detail, and it was found that the copper abnormally accumulates in the liver and that the copper concentration reaches about 50 times of the sound rat. It became clear that concentration of the ceruloplasmin in the blood remarkably lowered and that it is very similar to human's Wilson disease. The LEC rat seems to be able to become not only model animal of the Wilson disease but also that of the human liver disease. In this paper, we discuss dysbolism and accumulation of the trace element using LEC rats as a model animal of liver cancer that derives from Wilson disease.

The liver-cancer bearing rat used a LEC strain in 80 weeks old and normal rat used a Wistar strain in 12 weeks old. The 0.1 ml of multitracer solution was dissolved in the physiological saline, and was injected to each rat intravenously. After 24 hrs from the administration, we sacrificed and liver, kidney, spleen, and brain were collected. The gamma ray was measured by a Ge semiconductor detector.

In the liver, the uptake of Sc, V, Mn, Zn, Rb, As, and Zr on LEC rat increased compared with normal one as shown in Fig. 1. The uptake of Sc, V, Zn, and As by LEC rat increased by two times while that of Mn was increased by 1.5 times, that of Ga by 3 times, and that of Zr by 4 times. On the other hand, the uptake of Se and Y decreased. In the kidney, the uptake of Sc, Ga, As, and Zr increased compared with normal rat. The uptake of As and Zr increased by 3 times. The uptake of Mn, Zn, Se, Rb, Ru, and Rh decreased. There was no change for V, Cr, and Co. The liver of LEC rat cancerated, and liver tissue grew a large number of false bile ducts in the leaflet marginal zone, and hepatic duct fibrous disease surrounded in the fibroblast was recognized frequently. Because Ga has a tumor seeking property, the uptake of Ga by LEC rat increased. In the liver, As is methylated by S-adenosyl methionine, and becomes monomethyl arsonic acid and dimethylarsinic acid, and it is excreted from the kidney. LEC rat caused various enzymatic abnormalities by the Cu dysbolism; especially, in our result, there were remarkable decrease with the ceruloplasmin and increase in copper and metallothionein. In LEC rat, the lowering of the concentration of glutathione peroxidase and cytochrome P-450 is reported. It is consid-

ered that As may increase in liver and kidney; because of an enzymopathy and a dysbolism, the methylation does not work completely. In the liver of LEC rat, the uptake of the essential elements such as Mn, Co, and Zn increased, since the essential element is closely related to the enzyme. In the organs such as kidney, spleen, and brain, there was also a change on the uptake of Mn, Co, and Zn. In these organs, this tendency seems to originate the enzymatic abnormalities as well as to result in the liver cancer. The uptake of essential elements is remarkably different from the liver data of acute alcoholic hepatopathy mouse¹⁾ and LEC rat. On mouse which contracted an acute alcoholic hepatopathy, the initial state of the hepatic disorder, the abnormalities of enzymatic system and other proteins are not directly connected with the dysbolism of the essential elements. However, in the LEC rat of the last stage of cancer, our result suggested that the uptake of the essential elements was increased, since the homeostasis maintenance mechanism of the trace elements in the internal is collapsed by a remarkable liver injury. Uptake of the bone seeking elements such as Sc and Zr increased. These results and previous papers¹⁻²⁾ suggested that the hepatopathy and the storage of bone seeker in the liver have a close relation through the fiberization of the liver.

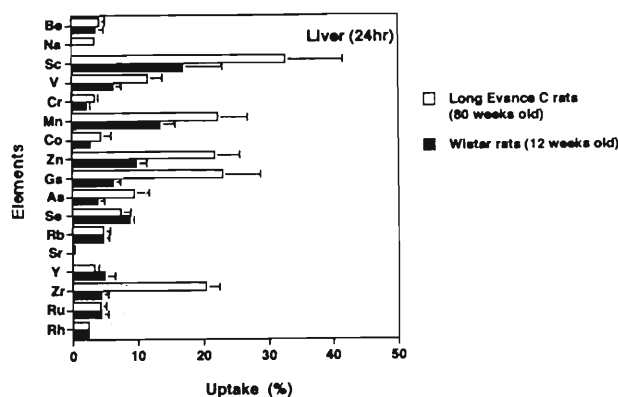


Fig. 1. Uptake (%) of various elements in the LEC and Wistar rats liver.

References

- 1) S. Enomoto et al.: RIKEN Accel. Prog. Rep. 30, 107 (1997).
- 2) S. Enomoto et al.: RIKEN Rev. No. 13, p. 31 (1996).

Accumulation of Inorganic Elements in the ddY Mice Implanted with Ehrlich Sarcoma

S. Enomoto, B. Liu, S. Ambe, R. Amano, and F. Ambe

Investigation of the metabolism of inorganic compounds in tumor will help develop anti-tumor drugs and tumor diagnosis agents. We have investigated the short-term metabolism of 16 radioactive elements in the mice implanted with Ehrlich sarcoma. A discussion of the transportation, accumulation, and metabolism of radioactive elements and their relation with muscle and tumor is given.

The experimental ddY mice underwent implantation of Ehrlich sarcoma in the thigh. After one week when the tumor diameter grew about 1–2 cm, a multitracer solution in physiological saline was administered intraperitoneally to the tumor-bearing mice. At 3, 24, and 48 hrs after injection, three mice were sacrificed and samples of blood, liver, muscle and tumor were excised. These tissues and the blood were weighed and applied for radioactivity measurements.

In this study, the radioisotopes of following elements were used as multitracers: Be^{2+} , Sc^{3+} , Zn^{2+} , Rb^+ , Y^{3+} , Zr^{4+} , TeO_3^{2-} , Ba^{2+} , Hf^{4+} , Ir^{6+} , Pt^{6+} , Ce^{3+} , Eu^{3+} , Gd^{3+} , Yb^{3+} , Tm^{3+} , and Lu^{3+} . In saline, Zr, Hf, Pt, and Ir exists as a mixture of chloro-complexes, while other metal ions are kept as simple free ions.

In order to elucidate a selective tumor accumulation, the tumor/muscle ratios were calculated. The radioactivity of 16 elements in muscle and tumor was compared in Fig. 1. At 3 hrs after the administration, only Be, Y, Ba, Eu, Gd, Yb, and Lu showed a the tumor/muscle ratio higher than 1. At 24 hrs after the injection of tracers, only Rb, Te, and Hf gave a tumor/muscle ratio less than 1. At 48 hrs, Rb, Zr, and Hf still showed the tumor/muscle ratio less than 1, while the rare-earth element (REE) revealed a higher tumor/muscle ratio than other elements showed. Generally speaking, among the 16 elements used in this study, alkaline metals Rb and bivalent cations Be, Ba, and Zn showed relatively low tumor/muscle ratio. Trivalent cations REE revealed a high tumor/muscle ratio. On the other hand, Zr and Hf, Pt and Ir also showed low tumor/muscle ratio.

Most elements showed a lower uptakes in tumor and higher uptakes in liver. It demonstrated that the compounds injected *in vivo* accumulated more quickly into liver than those into tumor. During the whole time studied, a low tumor/liver ratio was observed for most of elements studied. However, we may noticed that 24 and 48 hrs after injection, the accumulation difference between liver and tumor becomes smaller gradually. Comparing the distribution in blood and tumor, a high radioactivity in blood did not result in a high uptake in tumor tissue. On the contrary, REE that have a

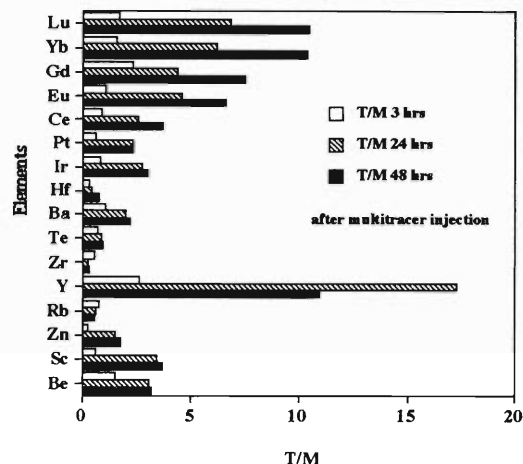


Fig. 1. Time dependence of the ratio of the uptake in tumor to that in muscle (T/M) for each element.

fast or metabolism in blood show a high uptake by tumor. From this experiment, it seems that the REE were transported to the tumor location in around 24 hrs and accumulated there.

It is thought that the transportation process has a closed relation with the tumor uptake. It is surely true that blood or serum played an important role in the distribution of the trace elements in the living body. The two proteins of major importance for transport of metal ions are albumin and transferrin. It has been well discussed that trivalent REE has been found to displace Fe^{3+} in transferrin.

In general, tumor cells exhibit a high amount of transferrin receptors. As a result of pathological stain on a tumor tissue slice which were used by fluorescence labeled anti-transferrin receptor polyclonal antibody, we observed that Ehrlich sarcoma solid tumor cell had a lot of transferrin receptor. It is presumed that the trivalent REE interacts with transferrin and is then carried to the tumor transferrin receptor.

On the other hand, alkali metal and alkaline earth metal did not accumulate in tumor. This maybe from the two reasons: first, it may interact with the serum albumin that is responsible for transport of Ca, Co, and Zn and for metabolism in the liver. Second, they can not replace Fe^{3+} on the transferrin.

As for Pt, Ir, Zr, and Hf, their lower tumor/muscle ratio maybe due to that, first, they form a complicated chemical form or complex and second, they have a strong affinity with some substance before they reached the tumor and this substance metabolism point is not high in tumor cells.

Metabolic Study of Trace Elements in Se-deficient Rats

R. Hirimuma, N. Sotogaku, K. Endo, S. Enomoto, S. Ambe, and F. Ambe

A number of studies on the role of Se in biochemistry are found in literatures.¹⁻³⁾ Selenium is one of the essential trace elements and is known as the central ion in glutathione peroxidase. It is also reported that Se is in a competitive or synergetic relationship with several metals such as Mn, Fe, Co, Zn, and As. Therefore, it is very important to clarify the distribution of trace elements in various organs of Se-deficient rats. However, no systematic study has been reported on the behavior of trace elements in Se-deficient rats.

In the present study, the uptake and distribution of trace elements in Se-deficient rats were examined by a multitracer technique, which can be used to evaluate the behavior of many elements under a same experimental condition.

A multitracer solution containing 20 different radioisotopes was prepared from a silver target irradiated by a heavy ion beam of 135 MeV/nucleon from RIKEN Ring Cyclotron. After chemical separation, this multitracer was dissolved in saline. Mother rats were fed with Se-deficient diet (produced by Oriental

Yeast Co., LTD.) since their 14th day of pregnancy until the weanling period of their baby rats. The weanling rats were separated from their mothers, and were fed with Se-deficient diet until the age of 12 weeks. As a reference, 12-week-old normal rats were used. A tenth ml of saline containing the multitracer was injected by intravenously in the tail vein of all the rats. The Se-deficient and normal rats were sacrificed at 3, 12, 24 and 72 hours after injection, and the radioactivities of their organs and body fluids were determined by γ -ray spectrometry. The observed γ -rays were assigned on the basis of their energies and half-lives. The behavior of Be, Na, Ca, Sc, V, Cr, Mn, Fe, Co, Zn, Ga, As, Se, Rb, Sr, Y, Zr, Tc, Ru, and Rh was examined. There were little individual differences in each group of rats.

Figure 1 shows the uptake of various elements in the kidney, liver, and spleen of Se-deficient and normal rats, as typical examples. At 24 hours after injection, the uptake of Se was larger in the brain, intestine, kidney, spleen, and ovary of the Se-deficient rats than in those of the normal ones.

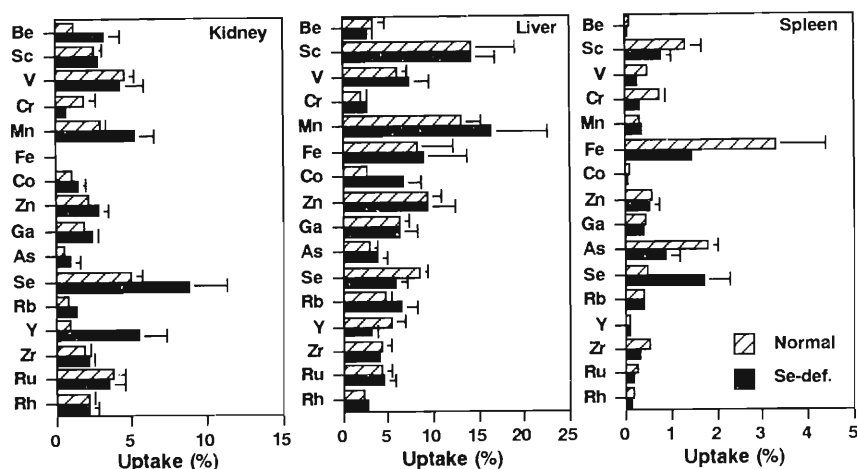


Fig. 1. Tissue uptake of various elements in normal and Se-deficient rats at 24 hours after the elements injection.

In the kidney, the uptake of Be, Mn, and Y of the Se-deficient rats was larger than that of the normal ones. In case of the liver, there was little difference in the uptake of the elements except Co between the Se-deficient and normal rats. In the spleen, the uptake of Fe and As of the Se-deficient rats was smaller than that of the normal ones.

The elements, Se, Fe, and As, are closely related to hemoglobin. Arsenic is bound to a globin part of hemoglobin in erythrocytes, and Fe is a constituent of hemoglobin. Glutathione peroxidase has a greater affinity for hemoglobin. The observed decrease of the

uptake of Fe and As by the spleen in Se-deficiency suggests that the deficiency causes hemopoietic hypofunction of this organ.

References

- 1) J. N. Thompson and M. L. Scott: *J. Nutr.* **97**, 335 (1969).
- 2) H. G. Seiler, A. Sigel, and H. Sigel: in *Handbook on metals in clinical and analytical chemistry* (Marcel Dekker, New York, 1994), p. 551.
- 3) E. Glattre et al.: *Biol. Trace. Elem. Res.* **49**, 177 (1995).

Metabolic Study on Ca-deficient Rats Using a Multitracer

R. Hirunuma, K. Endo, S. Enomoto, S. Ambe, and F. Ambe

Calcium is the fifth most abundant element in the living body.¹⁾ The most important Ca compound is hydroxyapatite *in vivo*, which constitutes the mechanical strength of bone and teeth. Calcium homeostasis is maintained by hormonal regulation of the intestinal absorption and renal reabsorption. Calcium is absorbed in the whole small intestine, preferentially from duodenum and the upper part of jejunum. The intestinal absorption is regulated by hormones and vitamin D. The excretion in the kidneys is influenced by local factors like the glomerulus and tubulus functions and by the amount of filterable Ca^{2+} as well as by other factors such as cortisol, parathyroid hormone, vitamin D, and calcitonin. Vitamin D is necessary for normal absorption of Ca and phosphate from both the intestine and the skeleton. In the present study, the uptake and distribution of trace elements in various organs of Ca-deficient rats were examined by a multitracer technique, by which one can determine the behavior of various elements under a given experimental condition.

A multitracer solution was prepared from a gold target irradiated with a heavy-ion beam of 135 MeV/nucleon from RIKEN Ring Cyclotron. Ca-deficient rats were fed with Ca- and vitamin D-deficient diet (produced by Oriental Yeast Co., LTD.) for three weeks. The purpose of this vitamin D-deficiency in the diet was to inhibit Ca absorption

from the small intestine. Three male Ca-deficient rats weighing 105 g on average were used, while three six-week-old male normal ones weighing 190 g on average were used as a reference. A tenth ml of a saline containing the multitracer was injected intravenously in the tail vein of each rat. The Ca-deficient and normal rats were sacrificed at 24 hours after the injection, and the radioactivities of organs and body fluids were determined by γ -ray spectrometry.

In order to examine the physiological condition of the rats fed with Ca-deficient food, the contents of Ca in their plasma were measured. The Ca contents were found to be 10.8 ± 0.2 mg/dl and 3.4 ± 0.2 mg/dl, respectively, for the normal and the Ca-deficient rats; proving that the latter were really deficient in Ca.

The behavior of Be, Ca, V, Mn, Zn, As, Se, Rb, Sr, and Ba was examined using the multitracer. The results on Rb, V, and Mn are shown in Fig. 1. The tracer of Ca was found predominantly in bones of both Ca-deficient and normal rats. However, its uptake by bones of the Ca-deficient rats was only slightly higher than that of the normal rats. This observation is interpreted that Ca was acutely required and taken up not only by the bone but also by the other organs and body fluids of the rats, because Ca concentration in them was much lower than that expected by the homeostasis.

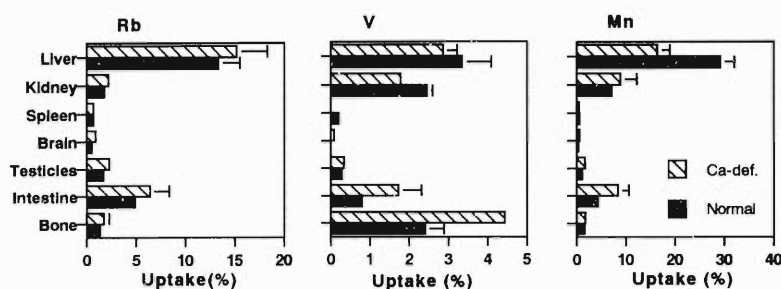


Fig. 1. Tissue uptake of Rb, V, and Mn in Ca-deficient and normal rats.

There was little difference in the uptake of Zn, As, Se, and Rb between the Ca-deficient and normal rats. The uptake of V was larger by the intestine and bone of the Ca-deficient rats than by those of the normal ones, while the uptake by the kidneys of the former was smaller than by those of the latter. Manganese was found mainly in the liver of both the Ca-deficient and normal rats, and the uptake of the former rats was smaller than that of the latter. Manganese accumulates in the liver and excretes to bile. It is known that Mn controls catalysis of the enzyme (for example, pyruvate carboxylase²⁾), to which it is combined and that Mn^{2+} is antagonistic to Ca^{2+} (for example, Ca

contained in calmodulin³⁾). The decrease of Mn in the liver of Ca-deficient rats suggests that an enzyme such as pyruvate carboxylase must be influenced by Ca deficiency.

References

- 1) H. G. Seiler, A. Sigel, and H. Sigel: in *Handbook on metals in clinical and analytical chemistry* (Marcel Dekker, New York, 1994), p. 299.
- 2) M. C. Scrutton and A. S. Mildvan: *Biochemistry* **7**, 1490 (1968).
- 3) D. J. Wolff et al.: *J. Biol. Chem.* **252**, 4108 (1977).

In vitro Binding Assay of the Trace Elements in Bovine Serum Proteins

N. Sotogaku, R. Hirunuma, K. Endo, S. Enomoto, S. Ambe, and F. Ambe

Since Pribram¹⁾ studied the interaction of Ca^{2+} ions with plasma proteins, a number of works have been done on the affinity of biotrace elements to various proteins.^{2,3)} The elements investigated are however limited. Once absorbed, metal ions enter into the blood and are mostly bound to blood cells and/or to plasma proteins; for example, Fe and Cu bind to transferrin and ceruloplasmin, respectively. Metals are widely distributed in the body via bloodstream. Although metal ions *in vivo* are known to play important roles for various enzyme reactions, the information of affinity of respective metal ions to various proteins of living body is required in order to understand the mechanisms of transfer of energy and/or electrons in the system. In the present work, we examined the pH-dependence of binding affinity of various elements with serum proteins using a multi-tracer technique. Their dependence in the range of pH 6.4–8.5 was examined by ethanol sedimentation method. The serum proteins used were albumin, β -globulin, γ -globulin, apotransferrin, and holotransferrin, which means iron-free and monoferric- or diferric-transferrin, respectively. These purified bovine serum proteins were purchased from Wako Pure Chem. Ind., Ltd. and were used without further purification. As a sample buffer, N-[2-hydroxyethyl]piperazine-N'-[2-ethanesulfonic acid] (HEPES) was used, and the each protein (1.0 mg) was dissolved in 50 mM-HEPES solution. The pH value of protein solution was adjusted to be 6.4, 6.8, 7.4, 8.0, and 8.5 by adding a diluted NaOH solution. Then, each protein solution was mixed with 50 μl of a buffer solution containing the multitracer, and the final mixed solution was mildly incubated at 37 °C for 20 min. After the incubation, excess ethanol was added and then centrifuged at 3,000 rpm for 10 min. The γ -ray radioactivities of the sediment were measured by a pure Ge detector, and compared with those of the standard multitracer solution. From the analysis of the γ -ray energy spectra, the affinities of Be, Cr, Mn, Co, Zn, Rb, Sr, Ba, Ir, and Pt were determined.

Figure 1 shows the effect of pH on the binding percentage of Be, Mn, Co, Zn, and Sr to each serum pro-

tein. Among them, high binding percentages (more than 70%) of Be and Sr to albumin were observed in the pH range investigated. Carboxyl and imidazole groups of albumin play an important role to bind these metals, because these groups are both ionized in this pH range. Alkaline-earth metal ions are bound to the carboxyl groups, since alkaline-earth metal ions have little affinity for imidazole groups.¹⁾ Binding of Co and Zn to both types of transferrin increased with an increase of the pH values above 6.8. Transferrin is known to possess two metal-binding sites, and therefore highly specific structural changes occur as the pH values rise. On the basis of our results, the structural changes of protein was confirmed to affect its affinity of metals.

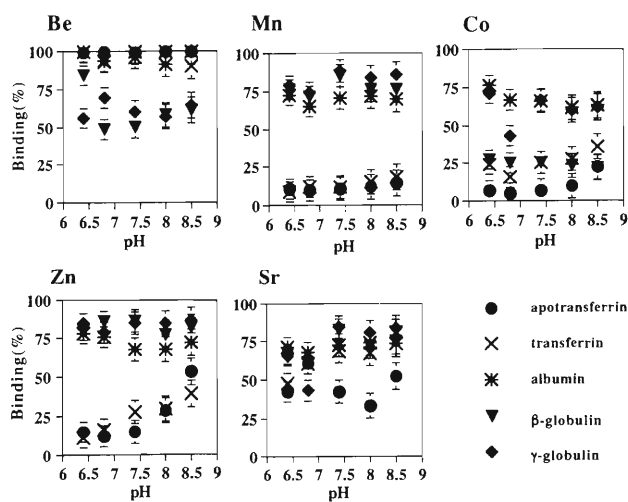


Fig. 1. Effect of pH on the binding of various elements to bovine serum proteins.

References

- 1) L. I. Iron and D. J. Perkins: *Biochem. J.* **84**, 152 (1962).
- 2) D. C. Ross, T. J. Egan, and L. R. Purves: *J. Biol. Chem.* **21**, 12404 (1995).
- 3) K. Ichimura, H. Kihara, T. Yamamura, and K. Satake: *Biochem. J.* **106**, 50 (1989).

Binding Activity of Various Metallic Elements to Blood Components

N. Sotogaku, R. Hirunuma, K. Endo, S. Enomoto, S. Ambe, and F. Ambe

Metallic ions which are absorbed into body from digestive organs are passed into blood and are transported to organs. The blood is composed of plasma and corpuscles, both of which affect transportation of metal ions. The transport and chemical state of metallic ions are of basic importance in bio-inorganic chemistry, but they have not yet been understood completely. In this work, we have studied binding activities of blood components for various metallic ions using the multitracer technique.

A multitracer was prepared by employing an established procedure. Fifty ml of blood was drawn from rats and was mixed with 50 ml of a buffer solution (4.2 mM-Citrate, 8.5 mM-Sodium Citrate, 12.2 mM-glucose; pH 7.4). The procedure for separation of blood components was essentially the same as that described by Kasahara et al.¹⁾ but was modified for a small scale experiment. In this study, blood components used were plasma, corpuscles, and erythrocyte ghost. One ml of the buffer solution containing the multitracer was mixed with a buffer solution (1 ml) containing a component of blood. These samples were incubated for 20 min at 37 °C in an incubator and were centrifuged at 3,000rpm for 10 min. The radioactivities of sediments were determined by the γ -ray spectrometry.

The results are given in percentage compared to a standard. In this experiment, Be, Na, V, Mn, Fe, Co, Zn, Ga, As, Se, Rb, Sr, Ru, Rh, and rare earth elements (REEs) were analyzed. However, the other possible elements Na, Fe, Co, Ga, As, Rb, Ru, and Rh were not analyzed and will not be discussed in this paper. Figure 1 shows the binding percentage of Be, V, Mn, Zn, Se, Sr, and REEs for each component of the blood. It is seen from Fig. 1a that the binding activity of Be, Mn, Zn, and Sr are high for the plasma component. The binding assay for serum proteins in vitro shows that Mn, Zn, and Sr are bound to albumin, β -globulin, and γ -globulin.²⁾

These observations suggest that Mn (II) is bound to the proteins in plasma. Beryllium is known to be a toxic element, and its high binding affinity to serum

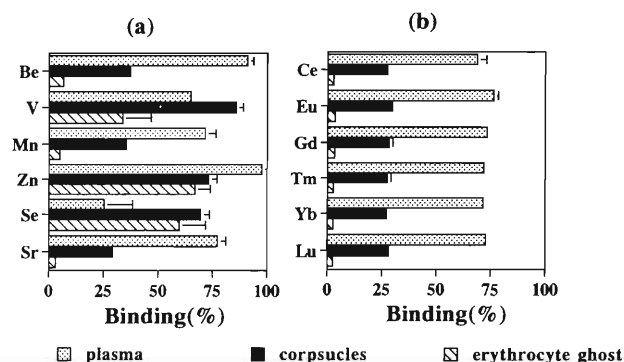


Fig. 1. Binding (%) of various elements to blood components. (a) Typical elements other than (b) rare earth elements, REE.

proteins was found.²⁾ The results on Zn and Sr agree with those reported in the literature.³⁾ On the other hand, Se and V are highly bound to the component of corpuscles, and the former to that of erythrocyte ghost too. As a component of glutathione peroxidase, Se is known to reduce lipid peroxides in living body. This element undergoes reductive metabolism in the erythrocyte. We presume that the binding site of Se to the erythrocyte ghost is the phospholipid, because the element is highly concerned with the lipid of bio-membrane. The constitution of erythrocyte ghost is water-19.5%, protein-39.6%, glucide-5.8%, and lipid-35.1%, while the lipid consists of phospholipid and cholesterol. The REEs were mainly found in the plasma, and binding percentages are similar to one another (Fig. 1b).

References

- 1) M. Kasahara and P. C. Hinkei: Proc. Nat. Acad. Sci. **73**, 396 (1976).
- 2) N. Sotogaku et al.: RIKEN Accel. Prog. Rep. **30**, 112 (1997).
- 3) H. Sigel, A. Sigel, and H. G. Seiler: in *Handbook on metals in clinical and analytical chemistry*, (Marcel Dekker, New York, 1994), p. 577; p. 667.

Beneficial Effect of Rare Earth Elements on the Growth of *Dryopteris erythrosora*

T. Ozaki, S. Enomoto, Y. Minai, S. Ambe, F. Ambe, and T. Tominaga

For a long time, most biochemists have considered the rare earth elements (REE) to be harmful, interrupting physiological functions involving Ca antagonistically. This is mainly because of the similarities in the ionic radii of Ca and REE.¹⁾ Many works to determine the amount of REE in plants were performed recently by chemists.²⁾ Some of them reported very high concentration of REE in plants, but they seldom pursued their research up to biological roles of the elements. In the present paper, we describe determination of REE in a fern, *Dryopteris erythrosora*, by the instrumental neutron activation analysis (INAA) and describe the effect of La on the growth of *Dryopteris erythrosora*.

For the growth rate experiment, small sporophytes about 2 cm high above the ground were chosen. Those sporophytes originated from the same fern and grew naturally on the same soil without receiving any artificial treatment. After washing with distilled water, sterilization was conducted by immersing them in 70% (v/v) ethanol for 30 seconds followed by three rinses in ultra-purified water. The Murashige-Skoog (MS) basal medium³⁾ was used throughout this study. The culture medium was dissolved in ultra-purified water and the pH was adjusted to be 5.7 with 0.5-N NaOH or 0.5-N HCl. After adding 1.0% (w/v) agar to the above solution, we dissolved it by autoclaving for 15 min at 121 °C and each 30 ml of the agar was poured into 100 ml plastic wares. A La-containing medium (hereafter referred to as a LA-medium) was prepared by adding 10 mM LaCl₃ to the MS basal medium before the pH adjustment. A Ca-containing medium (CA-medium) and a Na-containing medium (NA-medium) were prepared in the same way. Growth condition was maintained as 12hr light / 12hr dark photoperiod, at a light intensity of about 10,000 lux and 25 ± 2 °C. After 2 months of cultivating, the fresh weight of the samples was measured to obtain the growth rate defined as follows: Growth rate

$$= \frac{\text{Fresh weight after 2 months of cultivation}}{\text{Fresh weight at the start of cultivation}}$$

Here, we define the concentration ratio as follows:
Concentration ratio

$$= \frac{\text{Concentration in plant}}{\text{Concentration in soil}}$$

in order to make it easier to grasp the image how highly the ferns absorb REE from the soil. Ferns in a LA-medium for the growth experiment showed a high concentration of La (more than 2 ppm) at the end of the growth period. On the other hand, the concentrations of La were under detection limit (less than 10 ppb) for the case of ferns in a control (MS), NA-, and CA-media. Growth rate was drastically accelerated by

the addition of La (Fig. 1). This strongly suggests a beneficial effect of La on the growth of *Dryopteris erythrosora*. The effect is neither the same nor alternative one of Ca because the average of growth rates of ferns in a LA-medium exceeded the one in a CA-medium.

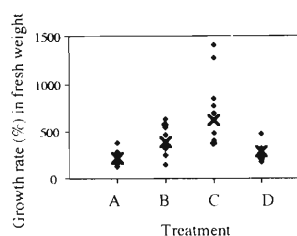


Fig. 1. Growth of *Dryopteris erythrosora* affected by Na(A), Ca(B), La(C), and control(D). Treat. A: MS+Na, Treat. B: MS+Ca, Treat. C: MS+La, Treat. D: MS(control), × Average of each treatment.

The concentrations of Ca and La measured for each fern were plotted in Fig. 2. No correlation can be seen between the concentrations of La and Ca, suggesting different responses of the fern to REE and to Ca. Furthermore, the concentration ratio of lighter rare earth elements sometimes exceeded 1 which was larger than that of Ca, although Ca is an essential elements and has many functions in plants. This also indicates that the sample ferns required REE for some biological functions and absorbed REE quite aggressively.

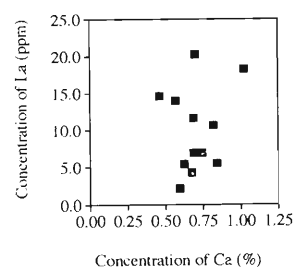


Fig. 2. Concentration of La vs. Ca.

A multitracer from an Au target irradiated in RIKEN Ring Cyclotron contains many kinds of radioisotopes of REE. Application of the multitracer technique should be useful for elucidation of the uptake mechanisms of REE and their roles in the growth of ferns.

References

- 1) R. J. P. Williams: Biochem. Soc. Trans. **7**, 481 (1970).
- 2) M. Koyama et al.: J. Radioanal. Nucl. Chem. **112**, 789 (1987).
- 3) T. Murashige et al.: Physiol. Plant. **15**, 473 (1962).

Influence of Aluminum on the Uptake of Various Cations from a Solution into Carrots

T. Ozaki, S. Enomoto, Y. Minai, S. Ambe, F. Ambe, and Y. Makide*

In these days, increased acidification of rain has become a serious problem, particularly for agriculture. The dominant harmful effect caused by acidification is thought to be exerted due to H^+ ions, or otherwise Al^{3+} ions produced more as lowering pH of the soil. Incidentally, one of the strikingly conspicuous features of salt absorption by plant roots is the stimulatory effect of polyvalent cations, which was first reported by Viets¹⁾ for barley roots. This is indicative that the Al^{3+} may do harm plants not only by existence of itself but via the other ions affected by Al^{3+} . Many researchers have been trying to reveal the riddle of this effect; their interests have been in the interactions among essential or beneficial elements. This must be caused from the background of this discovery; that is, Ca, one of the most important elements for plant cells, was first reported to have this scenario. Since then, many researchers have paid their attention only to essential or beneficial elements and not to toxic ones. However, kinds of elements existing in the soil are abundant, and there must be some influence of Al on the uptake of other elements from soils into plants.

For producing multitracers, plates of gold, silver, and titanium were irradiated with the 135 MeV/nucleon ^{12}C beam from the RIKEN Ring Cyclotron. Procedures for the preparation of multitracer solutions from Au and Ag targets are described in Ref. 2 and 3. For Ti also will be reported elsewhere the procedures of separation of a multitracer solution containing valuable nuclides as ^{28}Mg or ^{47}Ca . The influence of Al on the uptake of Be, Na, Mg, K, Sc, Ti, V, Mn, Fe, Co, Ni, Zn, Rb, Sr, Y, Zr, Ce, Eu, Gd, Yb, Lu, and Hf was examined. A standard solution of $AlCl_3$ (0.001N) for atomic absorption analysis was purchased from Wako-Junyaku.

Carrots (*harumakigosun*) were germinated and grown at 25 ± 2 °C on soil for 20 days. Light was provided by fluorescent lamps of 10000 lux with a photoperiod of 12h. The carrots which became 7 cm long from root to top were transplanted, after washing with ultra-purified water, into the aerated ultra-purified water. They were kept there before absorption of the multitracer for 3 days in order to remove the soil on the root surfaces as much as possible. The water was

renewed every several hours. For the uptake experiments, the multitracer solution was once evaporated to dryness, and the tracers were dissolved into the ultra-purified water with pH adjusted to 4.5 ± 0.1 using 0.01N HCl only.

Figure 1 shows the uptake of Be into intact roots and leaves grown in the multitracer solutions with various concentrations of $AlCl_3$. A maximum was found at the concentration of 0.002 ppm of Al for the uptake of Be by the root. This phenomenon may be explained as Viets' effect. The similar effect was observed even for rare earth elements (REE). Both of these lead us to the idea that the Viets' effect is sometimes not favorable for plants because Be and REE are toxic for plants. Increase of the uptake into leaves was not observed for all the elements including essential or beneficial ones, presumably because this experiment was conducted for a short period. This suggests that the influences of Al on the toxic element uptake may appear at different times between roots and leaves: the former because of the increase in harmful elements and the latter, due to the decrease of beneficial ones.

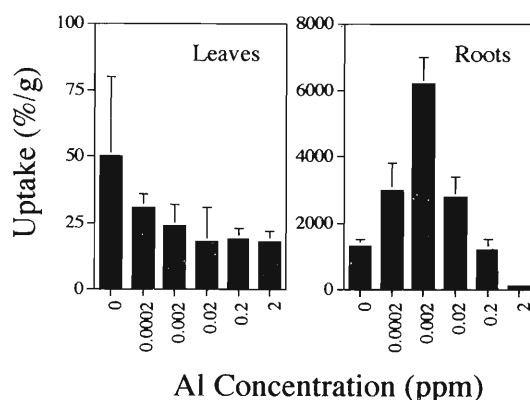


Fig. 1. Uptake of Be into roots and leaves

References

- 1) F. G. Viets, Jr. et al.: *Plant Physiol.* **19**, 466 (1944).
- 2) S. Ambe et al.: *Anal. Sci.* **7**, 317 (1991).
- 3) S. Ambe et al.: *Chem. Lett.* **1991**, 149.

* University of Tokyo, School of Science, Radioisotope Center

Translocation and Re-distribution of Radionuclides from the Leaf Surface in Plants

T. Watanabe, K. Matsumoto, S. Ambe, and I. Yamaguchi

The cuticle that covers the outermost surfaces of the aerial parts of growing plants is thought to play an important role to protect the plants against invasion by microbes and against penetration of foreign substances. Our previous study on translocation of radionuclides, performed using the multitracer,^{1,2)} showed in a couple of plants a possibility that the cuticle possesses a selection mechanism in foliar-uptake of radionuclides and that the translocation pattern in plants can relate to an intrinsic nature of each radionuclides.

This study deals with the transcuticular translocation and re-distribution of the multitracer from leaf surfaces in a wide range of plants like red clover (*Trifolium pratense* L.), orchard grass (*Dactylis glomerata* L.), Japanese radish (*Raphanus sativus* L.),

and mung bean (*Phaseolus mungo* L.) at the 5th leaf stage. In order to determine their selection mechanism, a radioactive multitracer technique was used.

Ten micro liter (5 micro liter \times 2) of the multitracer selection was applied onto the central region of upper surface of the 2nd leaf of a plant. The translocation of radionuclides was periodically assayed by determining the radioactivity of five fractions; the surface residue of applied site, the cuticular layer beneath the applied site, the residual area outside the applied site on the 2nd leaf, the other aerial parts except the 2nd leaf, and the roots.

The results revealed that the translocation is a site-sequential process and that a stable state distribution is reached 14 days after application, as shown in Table 1.

Table 1. Uptake and translocation of radionuclides 14 days after application in red clover, orchard grass, mung bean, and Japanese radish.

Element	Residue on leaf surface (%)				Penetration into cuticle (%)				Accumulation in the treated leaf outside of the applied site(%)				Accumulation in the non-treated leaves and stem(%)				Root(%)			
	red clover	orchard grass	mung bean	Japanese radish	red clover	orchard grass	mung bean	Japanese radish	red clover	orchard grass	mung bean	Japanese radish	red clover	orchard grass	mung bean	Japanese radish	red clover	orchard grass	mung bean	Japanese radish
Ca	100	99	100	100	0	1	0	0												
Te	76	100	51	100	24	0	49	0												
Be	72	0	32	44	28	68	68	55	0	32	0	0								
Y	73	98	68	85	26	2	32	15	1	0	0	0								
Ce	64	95	60	84	36	5	40	16	0	0	0	0								
Pm	80	-	10	84	20	-	99	16	0	0	0	0								
Gd	75	97	71	68	25	3	29	32	0	0	0	0								
Yb	37	96	65	86	62	4	35	14	0	0	0	0								
Lu	81	97	74	95	19	3	26	5	0	0	0	0								
Os	31	100	72	70	69	0	28	30	0	0	0	0								
Ir	33	100	36	11	67	0	64	89	0	0	0	0								
Pt	42	0	28	18	50	100	72	82	0	0	0	0								
Mn	4	37	58	14	82	3	42	38	6	54	0	42	8	6	0	6				
Sr	2	44	41	26	98	22	58	61	0	33	1	13	0	0	0	0				
Ba	28	81	48	47	72	19	51	49	0	0	1	4	0	0	0	0				
Hf	37	82	55	12	63	18	42	84	0	0	2	4	0	0	0	0				
Sc	74	67	44	55	6	13	41	6	12	10	3	10	8	5	8	16	0	6	4	13
Zn	9	49	72	10	32	2	28	35	7	3	0	5	45	41	0	20	7	6	0	29
Co	7	39	52	18	12	1	48	7	2	0	0	2	31	22	0	28	48	38	0	44
Se	13	72	77	61	48	4	19	19	0	0	0	0	21	15	1	4	17	15	3	17
Eu	69	77	69	73	11	2	31	11	0	0	0	0	8	8	0	4	12	13	0	12
Rb	2	27	4	10	7	2	32	5	14	6	11	9	56	51	38	21	21	15	16	56

The radionuclides of Be*, Ca*, Y*, Te*, Ba*, Ce*, Pm*, Gd*, Yb*, Lu*, Hf*, Os*, Ir*, and Pt* have tented to remain on the cuticle or to move within an area close to the application site, but Sc*, Zn*, Co*, Se*, Eu*, Rb*, and probably Cs* have easily migrated to accumulate into various parts of the plant including roots. Mn* and Sr* were slightly ambiguous and intermediate in behavior, but possibly they are more mobile over a longer period.

The selection mechanisms at both the transcuticular uptake stage and the metabolic migration stage (apoplast-symplast transport) inside the plant tissues

can work in the overall process of uptake and translocation of radionuclides from the air into the plant tissues.

References

- 1) T. Watanabe, K. Matsumoto, S. Ambe, and I. Yamaguchi: Proc. 32th Ann. Meeting on Radionuclides in the Physical Science and Industry, Tokyo, July, p. 129 (1995).
- 2) K. Matsumoto, T. Watanabe, S. Ambe, and I. Yamaguchi: Proc. of Nuclear Cross-Over Research International Workshop, Tokyo, 1996-2, p. 274 (1996).

Studies on Some Parameters that May Influence the Uptake of Radioisotopes by Plants from the Soil

S. Gouthu, T. Arie, and I. Yamaguchi

Much research has been extended towards decreasing the radiation burden of soil using plants during the past decade.^{1,2)} Uptake by plants or transfer coefficients of all radioisotopes are widely varying due to differences in plant species and soil types, and many other reasons. Also the reported uptake percentages of many isotopes by plants are too low for the effective and fast removal of isotopes from soil. So, we attempted to test several plant species for their relative uptake capabilities of radioisotopes under uniform laboratory conditions. Our objective is to identify which plant species shows a general high uptake ability over others and to explore the possibility of improving it by:

A) soil amendments like varying pH conditions, nutrient mineral content, organic matter content, etc. B) the introduction of some soilborne non-pathogenic fungal and bacterial species. This is attempted since some microorganisms, associated with roots of plants, are

known to absorb nutrients from the soil and supply them to the host plants and also alter soil conditions, which in turn may augment the uptake capability of plants.

As the first step of this project, we are now testing several plants for their relative uptake capabilities using multitracer as the source of radioisotopes. Use of multitracer enables us to test uptake percentages of several isotopes at the same time under the same conditions.

To the multitracer solution an appropriate amount of ^{137}Cs was added and diluted to the desired concentration with distilled water. This solution was supplied to the soil in which seeds are sown. After thirty days of growing period, the aerial plant part was taken and the uptake of radioactive isotopes of interest were detected using a Ge detector. So far, we have tested thirty-five plants and the screening is still under way. The data of the first set of five tested plants is presented in Table 1.

Table 1. Uptake percentage of the multitracer elements and cesium from the soil by some plants.

	Uptake percentage (per gram dry weight of plant)				
	^{22}Na	^{58}Co	^{83}Rb	^{85}Sr	^{137}Cs
Turnip ¹⁾	6.08 ± 0.80	0.37 ± 0.17	8.76 ± 0.91	0.66 ± 0.20	0.19 ± 0.18
Chinese cabbage ²⁾	5.09 ± 1.08	0.33 ± 0.22	10.14 ± 3.55	0.58 ± 0.22	0.07 ± 0.08
Soybean ³⁾	8.76 ± 0.91	0.01 ± 0.01	1.80 ± 0.27	0.15 ± 0.01	0.05 ± 0.01
Black mungbean ⁴⁾	11.80 ± 1.31	0.09 ± 0.02	3.45 ± 1.20	0.15 ± 0.13	0.04 ± 0.04
Maize ⁵⁾	0.00	0.03 ± 0.01	7.51 ± 4.63	0.13 ± 0.00	0.20 ± 0.08

Multitracer A2 (0.40 kbq) and cesium (0.93 kbq) were given to a pot containing 160 g of soil and a seed of plant was sown.

Uptake was calculated as percentage of total amount given to each pot. The values are shown along with the standard deviations.

1) *Brassica campestris* L. (capitata group) cv. Hinona (Average dry weight was 0.98 ± 0.16 g/plant)

2) *B. campestris* L. (pekinensis group) cv. Oosaka-shirona (Average dry weight was 1.46 ± 0.36 g/plant)

3) *Glycine max* Merr. (Average dry weight was 3.40 ± 0.26 g/plant)

4) *Vigna radiata* R. Wilcz. (Average dry weight was 1.77 ± 0.05 g/plant)

5) *Zea mays* L (Average dry weight was 1.99 ± 0.48 g/plant)

After screening, we plan to select some plants with higher uptake rates and proceed to the second part of the experiment by manipulating several soil parameters including microorganisms to further increase the uptake.

References

- 1) W. Kuhn, J. Handl, and P. Schuller: Health Phys. **46**, 1083 (1984).
- 2) D. C. Lauria, I. A. Sachett, J. C. Pereira, and R. Zenaro: J. Radioanal. Nucl. Chem., Articles **182**, 91 (1994).

Uptake Rate of Trace Elements by Soybean Plant

T. Shinonaga, S. Ambe, and I. Yamaguchi

Toxic radionuclides released into atmosphere are trapped and eventually deposited on the soil and leaves of plants. They are absorbed through roots from the soil and directly through leaves, and are translocated also into the edible part of plants. Such problems of pollution have been aggravated in these years. Concerning these problems, there are many studies not only on the uptake of toxic elements but also on the influence of co-existent elements on it. In the previous multitracer study, we demonstrated that the trace elements in the atmosphere are absorbed by the leaves of soybean plants and are translocated into the edible parts.¹⁻³⁾

In the present study, the uptake rate, translocation, and distribution of Sc, Mn, Co, Zn, As, Se, Rb, Sr, Y, Tc, and Re by the soybean (*Glycine max* L. Merrill cv. Okuharawase) root have been investigated using the multitracer technique. The soybean plants were cultivated in soil for 39 d at 26 °C under exposure to 17000-lux of light from fluorescent lamps for 12 h a day in a growth chamber. After that, the multitracer solution was added to the soil near to each soybean plants which were further cultivated under the diurnal condition (8000 lux, 25 °C in a draft chamber). They were harvested after 2, 6, 10, 16, 26, 42, 68, 120, 190, and 247-h culture. Leaves, stems and beans originating from the same node were collected together.

The γ -ray measurement was performed for the roots, leaves, stems, and beans with HP-Ge detectors. Among the elements, Rb and Tc were found to be quickly translocated into each part of a soybean plant.

The γ -ray intensity of ^{95m}Tc in the first leaf is shown as a function of time in Fig. 1. The other data are currently being analyzed.

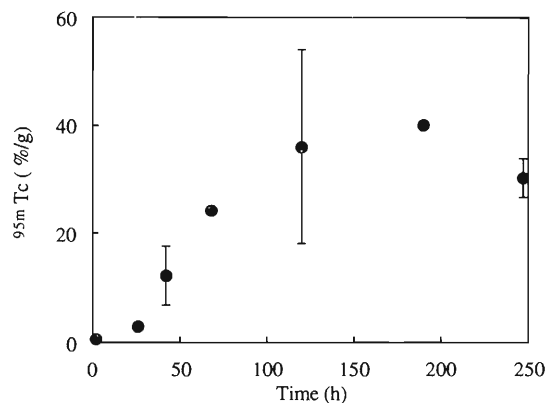


Fig. 1. Uptake of ^{95m}Tc by the first leaf of soybean plants during 2 to 247 h.

References

- 1) T. Shinonaga and S. Ambe: *Water, Air, and Soil Poll.*, in press.
- 2) T. Shinonaga, S. Ambe, S. Enomoto, H. Maeda, M. Iwamoto, T. Watanabe, and I. Yamaguchi: *J. Radioanal. Nucl. Chem., Lett.* **212**, 163 (1996).
- 3) T. Shinonaga, S. Ambe, T. Watanabe, and I. Yamaguchi: *RIKEN Rev. No. 13*, p. 19 (1996).

Multitracer Studies on the Extraction of Noble Metals with N,N-Dialkyl Aliphatic Amides from Nitric Acid Solutions

N. Ito, Y. Saito, K. Kimura, H. Narita,* T. Yaita,**
S. Tachimori,** S. Ambe, and F. Ambe

Distribution ratios of noble metals with N,N-dialkyl aliphatic amides from nitric acid solutions were determined by using a fraction of multitracer solutions. Multitracer solutions were prepared from an irradiated silver or gold target¹⁻³) by removing the target metal. A platinum group and oxoacid-forming metal fraction separated from other cation elements by cation exchange column (Dowex 50W-X8 100-200 mesh) was used for the extraction studies.

N,N-dialkyl aliphatic amides are known to be good extractants of some actinides such as U, Pu, and Th.⁴) Moreover, their stability is better than that of Tri-n-butyl phosphate (TBP), and their degradation products do not interfere unlike those of TBP. Therefore, amides were expected as alternative extractants to TBP in the reprocessing of nuclear fuels. Our investigation was carried out with 5 amides of different alkyl and aliphatic substituents focusing of fission produced noble metals such as Ru and Rh.

The amides of different structures used are: N,N-n-dioctyl butyramide (DNOBA), N,N-n-dioctyl hexanamide (DNOHA), N,N-n-dioctyl octanamide (DNOOA), N,N-dihexyl octanamide (DHOA), and N,N-dibutyl octanamide (DBOA). Concentration of amides was chosen 1 mol·dm⁻³ in a diluent of dodecane close to the molarity of 30% TBP.

Extraction was carried out at certain acidities of nitric acid, 1, 1.5, 2, 3, 4, 5, 6, 7 mol·dm⁻³. These acid solutions containing the multitracer were shaken with the same volume of the solvent solution for 10 minutes by using a mixer. After centrifugation, the distribution ratio was determined by γ -ray spectrometry for both organic and aqueous phases.

The distribution ratios with TBP has decreased with increasing acidity of nitric acid, whereas those with amides showed relatively flat acid dependence, but increased with decreasing in carbon numbers of alkyl group substituent.

A slope analysis of DNOOA and TBP solvent con-

centration dependent distribution ratio was carried out to obtain the solvation number and to compare it each other. Figure 1 shows the distribution ratios of the noble metals in 3 mol·dm⁻³ HNO₃ as a function of the DNOOA concentration. The slopes are 1-2 for the platinum group metals such as Ru, Rh, Ir, and Pt, and 2-3 for the Tc and Re. These results were quite similar to those of TBP, suggesting very similar extraction mechanisms each other.

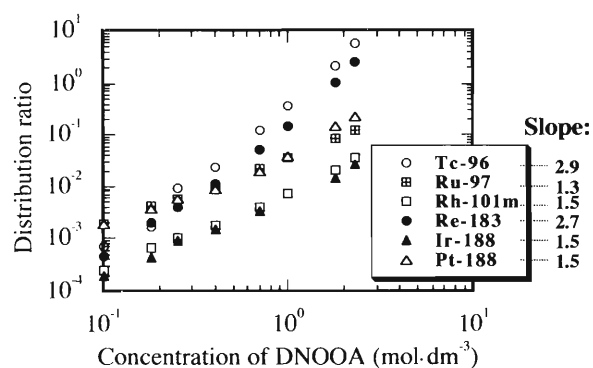


Fig. 1. Distribution as a function of DNOOA concentration.

References

- 1) S. Ambe, S. Y. Chen, Y. Ohkubo, Y. Kobayashi, M. Iwamoto, M. Yanokura, and F. Ambe: *Anal. Sci.* **7**, Suppl., 317 (1991).
- 2) S. Ambe, S. Y. Chen, Y. Ohkubo, Y. Kobayashi, M. Iwamoto, M. Yanokura, and F. Ambe: *Chem. Lett.* **1991**, 149.
- 3) S. Ambe, S. Y. Chen, Y. Ohkubo, Y. Kobayashi, H. Maeda, M. Iwamoto, M. Yanokura, N. Takematsu, and F. Ambe: *J. Radioanal. Nucl. Chem.*, Articles **195**, 297 (1995).
- 4) G. M. Gasparini and G. Grossi: *Sep. Sci. Technol.* **15**, 825 (1980).

* Faculty of Science, Ibaraki University

** Japan Atomic Energy Research Institute (JAERI)

Separation of a Multitracer from the Gold Target Irradiated with High-Energy Heavy Ions by Means of a Supported Liquid Membrane[†]

S. Ambe, M. Iwamoto, H. Maeda, and F. Ambe

The transport of Au(III) and other ions through a tributyl phosphate (TBP)/decalin membrane supported on a microporous polytetrafluoroethylene sheet was studied in order to establish a procedure for removing Au(III) ions from acid solutions of a gold target irradiated by high-energy heavy ions, leaving a multi-tracer solution in a carrier- and salt-free state.

Permeation was carried out under various conditions by changing the kind of the stripping solution, the concentrations of HCl and HNO₃ in feed solutions, and the concentration of TBP in the membrane. Figure 1 shows the transport of Au(III) ions from feed solutions of various concentrations of HCl. A feed solution of 3 mol dm⁻³ HCl gave the highest transport rate, though the difference in the initial transport rates was small among the HCl feed solutions in the 1–6 mol dm⁻³ concentration range. More than 90% of the Au(III) ions were transported to the stripping solution within 100 min. The permeability coefficient was 3×10^{-3} cm s⁻¹ for Au(III) in the 6 mol dm⁻³ HCl. On the other hand, the initial transport rates of Au(III) from feed solutions of 0.1 and 8 mol dm⁻³ HCl were smaller than those described above, though the transport from these two feed solutions was observed to increase with time.

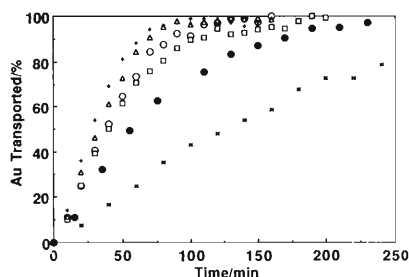


Fig. 1. The transport of Au(III) ions from the feed solutions of 0.1 (*), 1 (○), 3 (+), 5 (□), 6 (△), and 8 (●) mol dm⁻³ HCl to the distilled water through a membrane with a TBP/decalin ratio of 0.27.

Figure 2 shows the transport of Au(III) ions from feed solutions of 0.2, 1, and 2 mol dm⁻³ HNO₃. It was found that the acid concentration of the feed solutions only slightly influenced the initial rates of the transport of Au(III) ions. However, the transport reached saturation after 70, 80, and 90% of Au(III) ions had been transported from feed solutions of 2, 1, and 0.2 mol dm⁻³ HNO₃, respectively. The permeability co-

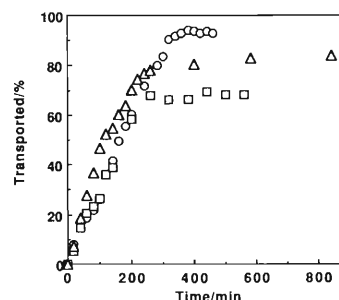


Fig. 2. Transport of Au(III) ions from the feed solutions of 0.2 (○), 1 (△), and 2 (□) mol dm⁻³ HNO₃ to distilled water through a membrane with a TBP/decalin ratio of 0.27.

efficient of Au(III) ions from the solutions was determined to be 7×10^{-4} cm s⁻¹.

As described above, Au(III) ions can be transported from both HCl and HNO₃ feed solutions. Therefore, permeation from an aqua-regia solution was examined as the final practical procedure. In this case, 4.8 g of Au target was dissolved in 20 cm³ of aqua regia. This solution was used for permeation after its dilution with distilled water to 100 cm³. In order to avoid saturation, permeation was carried out with a continuous supply of fresh distilled water to the stripping-solution compartment at a rate of 2 cm³ min⁻¹. Figure 3 shows the decrease of Au(III) in the feed solution with the permeation time. About 99% of the Au(III) ions were removed from the feed solution within 70 h. Only the peaks due to radioactive Au were detected in the stripping solution, showing selective permeation of the Au(III) ions.

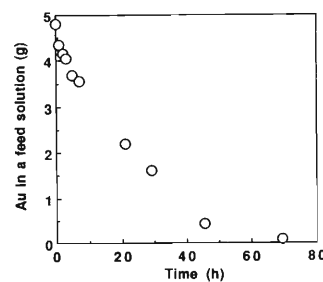


Fig. 3. Transport of Au(III) ions (4.8 g) from the feed solution of 1.8 mol dm⁻³ in HCl and 0.7 mol dm⁻³ in HNO₃ to the distilled water through a membrane with a TBP/decalin ratio of 1.

[†] Condensed from the article in *Anal. Sci.* 12, 219 (1996)

Multitracer Study for the Effect of Humate Formation on the Adsorption Behavior of Metal Ions on Kaolinite and Silica Gel[†]

Y. Takahashi, Y. Minai, T. Ozaki, S. Ambe, M. Iwamoto,
H. Maeda, F. Ambe, and T. Tominaga

Environmental behavior of the trace elements in lithosphere and hydrosphere is affected by various physicochemical processes. In particular, hydrolysis and adsorption on minerals are of primary importance in understanding their environmental behavior.¹⁾ In addition, humic substance may also be important, because it can form stable complexes with metal ions.²⁾ It is likely that the adsorption, hydrolysis, and humate formation compete for the metal ion behavior in the environment. In present work, we report application of the multitracer technique to the study of adsorption behavior of 16 trace elements on kaolinite and silica gel.

Distribution of the humic acid between the aqueous and solid phases at various pH values is shown in Fig. 1 by solid line. Photopeaks in the γ -ray spectra were assigned for 16 elements based on the analysis of γ -ray energy and its half-life. In Fig. 1 also shows the fractions of Ce, Re, Ba, Pt, and Hf remaining in the solution in contact with kaolinite. The adsorption behavior of Ce, Re, Ba, and Pt on silica gel was similar to their adsorption behavior on kaolinite. Based on the plot of dissolved fractions of humic acid and each trace element, the 16 elements can be classified into four groups by their distribution behavior, as follows.

(1) The distributions of Ce [Fig. 1(a)] between the

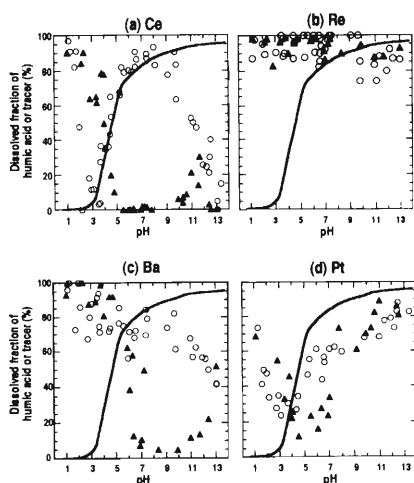


Fig. 1. Dissolved fraction of the tracer [(a)Ce, (b)Re, (c)Ba, and (d)Pt] or the humic acid when the aqueous phase (5 ml) was in contact with kaolinite (10 mg). Open circles: the tracer with humic acid, closed triangles: the tracer without humic acid, solid line: the humic acid whose initial concentration was 30 mg/l.

aqueous and solid phases were identical to that of humic acid at $3 < \text{pH} < 10$. Similar results were also obtained for other rare earth elements such as Y, Eu, Gd, Tb, Yb, and Lu. This implies that most of those elements distributed in the solution and on the surface of kaolinite or silica gel are present as humate complexes. Larger amount of rare earth elements was dissolved in contact with silica gel than with kaolinite due to the higher affinity of kaolinite than silica gel with the humic acid. The distribution behavior of humic acid may be a decisive factor controlling the distribution of those elements between mineral surface and water in the environment.

(2) The dissolved fractions of Rb, As, and Re [Fig. 1(b)] were not influenced by the addition of the humic acid. This indicates that humate formation of those elements did not affect the adsorption behavior. These elements were adsorbed neither on kaolinite nor on silica gel in the absence of the humic acid. It is likely that free Rb ion and oxo-anions of As and Re were the dissolved species in the aqueous phase. Abundances of Rb, As, and Re in seawater,³⁾ compared with those of the elements classified into the other groups in this work, were reported to be higher than those in the earth's crust.⁴⁾ It suggests that those elements are not scavenged onto the surface of minerals which is in contact with seawater. The experimental results in this work agree with the adsorption behavior of those elements estimated from their geochemistry.

(3) The fractions of dissolved Ba, Sr, Co [Fig. 1(c)], and Pt [Fig. 1(d)] increased with the addition of the humic acid in the neutral pH region. However, dissolved fractions of these elements were not identical to that of the humic acid. This implies that both the other complex formation (hydrolysis and carbonate formation) and humate formation affect the adsorption behavior of these elements. Distribution pattern of alkaline earth elements (Sr and Ba) was identical to each other. For summary, the humate formation affects, to some degree, their adsorption behavior in the environment.

References

- 1) M. Whitfield et al.: *Nature* **278**, 132 (1979).
- 2) F. J. Stevenson: in *Humus Chemistry* (John Wiley and Sons, New York, 1982).
- 3) J. P. Riley et al.: in *Chemical Oceanography*, 2nd edit. (Academic, London, 1975).
- 4) S. R. Taylor: *Geochim. Cosmochim. Acta* **28**, 1273 (1964).
- 5) C. F. Baes, Jr. et al.: in *The Hydrolysis of Cations* (Wiley, New York, 1976).

[†] Condensed from the article in *J. Radioanal. Nucl. Chem.* **205**, 255 (1996).

Model Study of Acid Rain Effect on Adsorption of Trace Elements on Soils (I)

H. Wang, S. Ambe, N. Takematsu, and F. Ambe

As a worldwide problem, acid rainfall ($\text{pH} < 5.6$) has drawn much attention of society and researchers.¹⁾ One serious effect caused by the acid rain is a disturbance of the adsorption equilibrium of elements in the soil, because the mobility and bioavailability of elements in the soil play an important role in the process of element uptake by plant. Therefore, it is essential to improve our knowledge of this process. Using a multitracer technique, effect of model acid rains on the adsorption of 11 trace elements on kaolin and soil was investigated.

Kaolin (the mineral composition is *ca.* 100% kaolinite $[\text{Al}_2\text{Si}_2\text{O}_5(\text{OH})_4]$) and Kureha soil (the particle size is < 2 mm) were used as the adsorbents. Distilled water and rain water collected in RIKEN were acidified with H_2SO_4 and used as simulated acid rains (pH 1.8–5.6). A multitracer (Be, Sc, Mn, Fe, Co, Zn, Se, Rb, Sr, Y, and Zr) was produced by the RIKEN Ring Cyclotron. It was stored as a 10^{-3} M H_2SO_4 solution. Triplicate samples of the adsorbent with the model acid rain water containing the multitracer solution were shaken at room temperature. The solid/liquid ratio was 30 mg/ml. The pH value was adjusted with H_2SO_4 or NaOH whenever necessary. After equilibrium, the mixture was separated by centrifugation. The supernatants were analyzed for pH value by a pH-meter and an aliquot of the supernatant solution was subjected to the γ -ray spectrum measurement by a HPGe detector. Subsequently, the adsorption percentage of each trace element was calculated by comparing the γ -ray intensities at a given energy before and after the adsorption, with correction for the decay.

Based on kinetic results, the equilibration period was chosen to be 3 days for kaolin/ H_2SO_4 solution system, 4 days for a kaolin/rain water system, and 6 days for a Kureha soil/ H_2SO_4 solution system.

Figure 1 shows the adsorption percentages of some trace elements on kaolin from two kinds of model acid rain water. Adsorption increases continuously with pH values, except for the anionic Se which shows unique adsorption behavior. Adsorption of Be, Mn, Co, Zn, and Sr increases sharply in the pH range 3.0–4.0. At $\text{pH} < 3.0$, their adsorption is low. And at $\text{pH} > 5.0$, their adsorption percentages are almost 100%, except for Mn (*ca.* 90%). Adsorption of Y increases gradually with pH value, and reaches 100% at pH 4.0. The elements Fe, Sc, and Zr give high adsorption yields even in the acidic pH range, amounting to almost 100% at

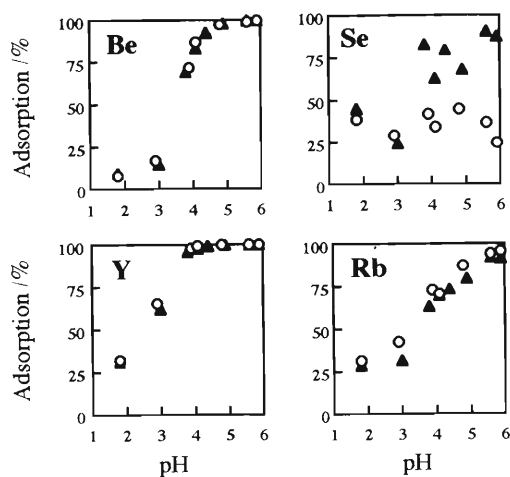


Fig. 1. pH effect of the model acid rains on the adsorption of trace elements on kaolin. Open circles: H_2SO_4 solution; and triangles: rain water.

pH 4.0. Adsorption percentage of Se in the H_2SO_4 solution is roughly constant over the pH range studied, while the adsorption percentage in the rain water is much higher at $\text{pH} > 3.0$.

There is no significant difference in the cationic ion adsorption between the two kinds of acid rain water. However, a large difference in the adsorption behavior of Se was found between the two model acid rains.

Except for Rb and Se, the adsorption behavior of the metal ions from the H_2SO_4 solution on Kureha soil is similar to that on kaolin. For Rb, the increase of adsorption on the soil with respect to pH is smaller than that on kaolin. A large difference between the soil and kaolin appears in the adsorption of Se. Adsorption percentage is about 90% below pH 5.0, and decreases slowly above pH 5.0.

We are able to conclude that the adsorption percentage-pH relationship depends strongly on the natures of the element and of the adsorbent. Acid rain reduces the retention of various cationic elements in the soil. This results in a loss of trace elements in the soil and an enrichment of trace elements in the ground water.

References

- 1) A. R. Bowers et al.: *Water, Air and Soil Pollution* **32**, 129 (1987).

Model Study of Acid Rain Effect on Adsorption of Trace Elements on Soils (II)

H. Wang, S. Ambe, N. Takematsu, and F. Ambe

As presented in the preceding paper, acid rain has significant effect on the adsorption of various elements on kaolin and soil. The adsorption behavior of trace elements can influence the availability of ions to plants. The soil is a very complicated system, which is mainly composed of aluminosiliceous materials, oxides, and humic substances. The nature of soil and the chemical properties of elements decide the adsorption behavior of various elements. Therefore, it is very important to know the adsorption process in detail. Using a radioactive multitracer technique, batch experiments have been performed to study the acid rain effect on element adsorption by soils and by the soils without organic matters or oxides.

A radioactive multitracer (Be, Sc, Mn, Fe, Co, Zn, As, Se, Rb, Sr, Y, Zr, Tc, Ru, Rh, and Re) was dissolved in solutions of different HCl concentration (pH 1.9–5.6) selected as the model acid rain. Seven soils (Kureha soil, Black soil, Forest soil, Kureha soil without oxides, Forest soil without oxides, Kureha soil without organic matters, and Black soil without organic matters) were employed as the adsorbents. These soil samples were air-dried and sieved to obtain the aggregates smaller than 0.15 mm in diameter. Three hundred mg of soil was suspended in 10 ml of the model acid rain containing the multitracer. Triplicate samples were equilibrated for 96 hours at room temperature. Suspension pH value was adjusted when necessary with HCl or NaOH solutions. The further experimental procedure is similar to that described in the preceding paper.

The pH effect of model acid rain on the adsorption of some trace elements on Kureha soils is shown in Fig. 1. The adsorption of almost all elements studied here are strongly dependent on the pH value. The adsorption trends of each element on different soils are similar. The experimental results indicate that the oxides of Kureha soil do not affect the adsorption of Be, As, Co, Zn, Zr, Tc, and Re over the pH range studied. If oxide components were removed, the adsorption percentages of Rb, Sr and Sc are higher and those of Fe and Se are lower than those on the original soil in the whole pH range. On Kureha soil and that without organic matters, the adsorption of Be, As, Se, Zr, Ru, and Rh is similar. However, the removal of or-

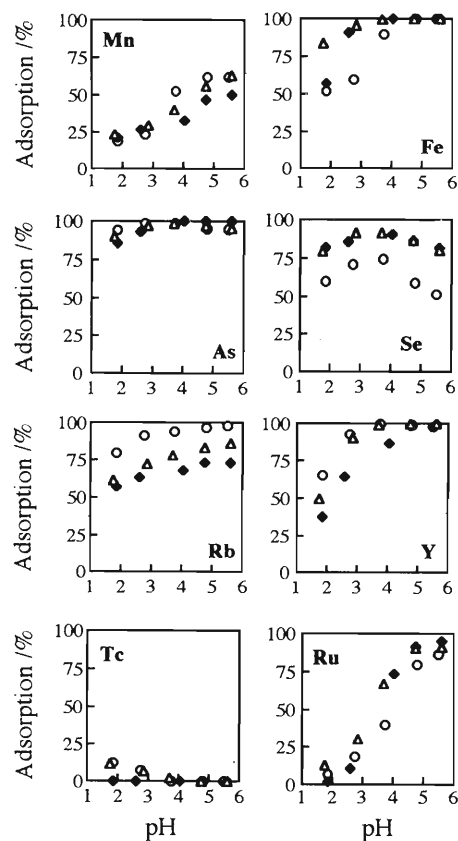


Fig. 1. The pH effect of model acid rain on the adsorption of trace elements on Kureha soils. Triangles: Kureha soil; Circles: Kureha soil without oxides; filled rhombuses: Kureha soil without organic matters.

ganic matters from Kureha soil made the adsorption percentage of the other elements much lower than that in the original soil. The removal of oxides from Forest soil made the adsorption percentage of Mn and Fe higher. However, there is no difference on adsorption of the other elements. The adsorption of elements on Black soils was similar to that on Kureha soils.

The adsorption of each trace element on different soils has similar trend, but the adsorption percentage on different soils is various, because the mineral and chemical properties of these soils are different.

Linear Momentum Transfer in the Heavy-Ion Reactions at Intermediate Energies

A. Yokoyama, K. Mukai, S. Morimoto, T. Saito, H. Baba, Y. Ohkubo,
A. Shinohara, T. Muroyama, S. Kojima, and M. Furukawa

Fusion reaction has been of much interest for many years because it is predominant in the low-energy heavy-ion reaction, and it accompanies a drastic rearrangement of nucleons in a nucleus especially for the heavy ion reaction. As the incident energy increases, the completeness of fusion reaction decreases and the incomplete fusion reaction becomes more important. The systematics of linear momentum transfer *vs.* incident energy¹⁾ has been proposed for the incomplete fusion. But the mechanism and the factors controlling incompleteness are still an open question. Therefore, we like to investigate how an incomplete fusion develops according to the increase of incident energy and what kind of factor contributes to the mechanism.

The nuclear systems studied are $^{14}\text{N}+^{165}\text{Ho}$ and $^{40}\text{Ar}+^{141}\text{Pr}$ at intermediate energies. We measured recoil momenta of the nuclides identified in experiments by using not only a thick-target-thick-catcher technique but also an angular distribution measurement. We obtained the momenta from the recoil ranges determined in the former experiment and from a fit to the angular distribution by using Monte Carlo calculations with the recoil velocity as a free parameter.

Examples of the obtained recoil velocities and the recoil momenta are listed in Tables 1 and 2. The results from the thick-target-thick-catcher method are shown in Table 1, while those from the angular distribution measurement are shown in Table 2. Both results exhibit a similar tendency that the momentum decreases as the product mass increases or as the incident energy increases in each combination of target and projectile. However, the absolute values obtained from the two methods are rather different from each other. Because complete fusion or nearly complete fusion are expected to show a forward peaking distribution, the component from such mechanism is lost to some extent for

Table 1. Recoil velocities and recoil momenta obtained from the thick-target-thick-catcher method.

System (Projectile energy)	Nuclide produced	β_{\parallel}	P_{\parallel} (GeV/c)
$^{14}\text{N}+^{165}\text{Ho}$ (35 MeV/nucleon)	$^{160}\text{Ho}^m$	0.006	0.98
	$^{106}\text{Ag}^m$	0.018	1.9
$^{14}\text{N}+^{165}\text{Ho}$ (70 MeV/nucleon)	$^{160}\text{Ho}^m$	0.0037	0.60
	$^{106}\text{Ag}^m$	0.015	1.6
$^{40}\text{Ar}+^{141}\text{Pr}$ (25 MeV/nucleon)	$^{139}\text{Nd}^m$	0.011	1.4
	$^{111}\text{In}^g$	0.019	1.9

the measurement of angular distribution. But we can assume that the incomplete fusion process is predominant as a whole as the energy increases, because we obtained a similar tendency from either one of the two experiments.

Table 2. Recoil velocities and recoil momenta obtained from the angular distribution measurement.

System (Projectile energy)	Nuclide produced	β_{\parallel}	P_{\parallel} (GeV/c)
$^{14}\text{N}+^{165}\text{Ho}$ (35 MeV/nucleon)	^{160}Er	0.0022	0.33
	$^{111}\text{In}^g$	0.0072	0.74
$^{14}\text{N}+^{165}\text{Ho}$ (70 MeV/nucleon)	^{160}Er	0.0015	0.23
	$^{110}\text{In}^m$	0.0062	0.63
$^{40}\text{Ar}+^{141}\text{Pr}$ (25 MeV/nucleon)	$^{138}\text{Pr}^m$	0.0026	0.34
	$^{111}\text{In}^g$	0.0052	0.54

In Table 3, we compare the ratios of average momenta to P_{cn} , the momenta for the case of full momentum transfer, with the calculated values by a sum rule model.²⁾ The model applies well to the incomplete fusion process and takes into consideration the characteristics of projectile such as Q values of the reaction and the difference of Coulomb energies at the entrance and exit channels. The calculated value reproduces the trend of the observed data in relation to the product mass. This means that the projectile dependence is important in the incomplete fusion reaction, that is, the characteristics of projectile should be taken into consideration as an important factor in the systematics of the incompleteness.

Table 3. Comparison of averaged recoil momenta with model calculation.

System (Projectile energy)	$\langle P_{\parallel} \rangle / P_{\text{cn}}$ Measured	Model calculation
$^{14}\text{N}+^{165}\text{Ho}$ (35 MeV/nucleon)	0.49 ± 0.06	0.16
$^{40}\text{Ar}+^{141}\text{Pr}$ (25 MeV/nucleon)	0.19 ± 0.02	0.086

References

- 1) S. Leray: J. Phys. Colloq. **47**, C4-275 (1986).
- 2) J. Wilczyński et al.: Nucl. Phys. A **373**, 109 (1982).

Preparation of Positron Emitter Sources for Slow Positron Generation by the Bombardment of a Liquid or Gas Target

T. Nozaki, Y. Itoh, P. Zi-Lin, Y. Ito, N. Nakanishi, H. Yoshida,* and A. Goto

Slow positron beams are becoming more useful. It is highly desirable that the available intensities be increased. The two approaches for achieving higher intensities of slow positrons are: (1) to increase moderator efficiencies, and (2) to generate higher intensities of fast positrons. For the latter approach, the activation of gas and liquid targets appears to have several advantages over that of solid targets. We thus intend to develop an automated system for handling gas and liquid targets. The gas or liquid target will be activated, and the product positron emitter collected on a small spot.

The technology for handling the isotopes commonly used in positron emission tomography (PET) has been well developed. The most common nuclides in use for PET are ^{11}C ($t_{1/2} = 24.4$ m), ^{15}O ($t_{1/2} = 122$ s), and ^{18}F ($t_{1/2} = 110$ m). All are pure β^+ emitters, and are produced routinely in hospitals by compact cyclotrons, using automated RI handling methods.¹⁾ Nitrogen gas target is bombarded by proton or deuteron to give either ^{11}C by the $^{14}\text{N}(p,\alpha)^{11}\text{C}$ reaction or ^{15}O by the $^{14}\text{N}(d,n)^{15}\text{O}$ reaction. The activated products are transferred together with the target gas to the place where they are used. On the other hand, the $^{18}\text{O}(p,n)^{18}\text{F}$ reaction using an ^{18}O -enriched water target is presently the best method for ^{18}F production. The yield is about 6 GBq/mA (thick target saturation activity for 15 MeV protons), which is higher than most other reactions easily accessible. The H_2^{18}O containing ^{18}F is forced to pass through a fine tube and transported into another room, where the ^{18}F is separated from the H_2^{18}O which is then returned to the target chamber.

In the synthesis of ^{11}C -labeled organic compounds, the $^{11}\text{CO}_2$ which is formed spontaneously by the reaction of the ^{11}C with impurity oxygen is often pre-concentrated by its adsorption on molecular sieves or

on liquid nitrogen-cooled substrates. For ^{18}F , either the distillation of H_2^{18}O or the trapping of ^{18}F on an anion exchange membrane filter is used for its separation from the H_2^{18}O . For our purposes it will be necessary to modify these methods slightly.

We have designed an automated apparatus for preparing the ^{18}F positron (β^+) source, which is shown in Fig. 1.

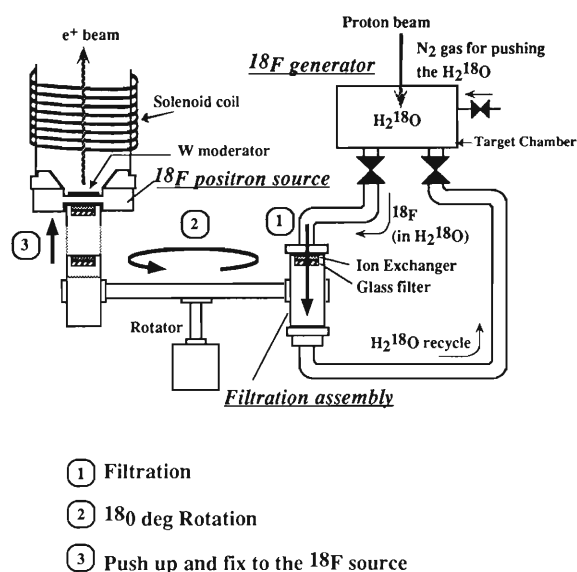


Fig. 1. Automated apparatus for preparing the ^{18}F positron (β^+) source.

References

- 1) H. N. Wagne: in *Principles of Nuclear Medicine*, 2nd edit., (W. B. Sanders, Philadelphia, 1995) p. 135 (chapters 10 and 11).

* The Japan Steel Works, Ltd.

Measurement of Spin Polarization of Positron Beam

T. Shimosaka, Y. Itoh, S. Mori, N. Nakanishi, A. Goto, M. Kase, and Y. Ito

From the viewpoint of analytical methods, the polarized slow positron beam can be expected to become a new probe for the surface characterization of materials such as surface magnetism,¹⁾ Fermi level of the magnetic material, *etc.* We have been developing slow positron beams from the various radioisotopes produced by RIKEN AVF cyclotron. We are now planning to measure the spin polarization.

The positron beam emitted from a β^+ decay process is polarized toward the direction of emission because of the parity non-conservation. The polarization, P , depends on the velocity of positron, \mathbf{v} :

$$P = (|\mathbf{v}|/c) \cos \theta,$$

where θ is the angle between the vector \mathbf{v} and the quantization axis of polarity.

The measurement is based on the mixing, in the magnetic field, of $m = 0$ states of para and ortho positroniums, whose spin direction is anti-parallel (singlet : Ψ_s) and parallel (triplet : Ψ_t) for the electrons and positrons, respectively. The mixing results changes in their lifetime and intensity.^{2,3)} The experimental setup is shown in Fig. 1. When polarized slow positrons hit the microchannel plate (MCP), they are thermalized in it, and the MCP gives a start signal to the time-to-amplitude converter (TAC). The thermalized positrons form the para and ortho positroniums. Under the magnetic field, Ψ_s and Ψ_t are perturbed to form two mixed states,

$$\begin{aligned} \Psi'_t &= \{y\Psi_s + \Psi_t(0)\}/(1+y^2)^{1/2} \\ \Psi'_s &= \{\Psi_s - y\Psi_t(0)\}/(1+y^2)^{1/2}, \end{aligned}$$

where

$$\begin{aligned} y &= x/\{1 + (1+x^2)^{1/2}\}, \\ x &= 0.0276B \text{ (where } B \text{ in kGauss)}. \end{aligned}$$

The lifetime distribution of these perturbed states are described as,

$$\begin{aligned} dN(t)/dt &= N/4[2\lambda \exp(-\lambda t) \\ &+ (1 - \varepsilon P \cos \alpha)\lambda' \exp(-\lambda' t)], \end{aligned}$$

where λ is the annihilation rate of non-perturbed triplet states, λ' is that of the perturbed state Ψ'_t , and α is the angle between the magnetic field and the quantization axis. Positron polarization (P) is obtained from the intensity of TAC or the lifetime of λ' , which will be measured by the equipment shown in Fig. 1.

We checked a decrease of the polarization inside the equipment by a simulator POEM made by Kumita et al.³⁾ Its result is presented in Fig. 2. The decrease was

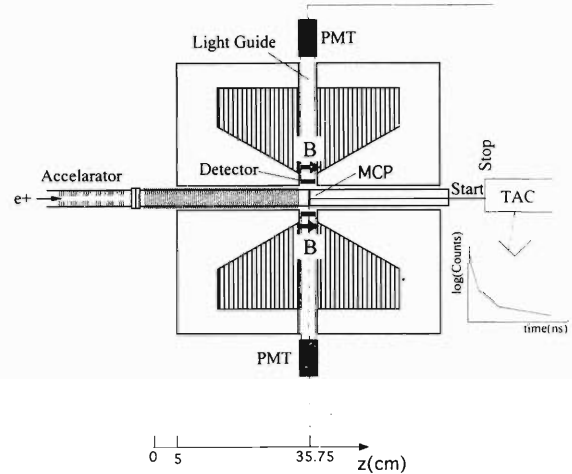


Fig. 1. Outline of the equipments for positron polarization measurement. Positrons come from the left hand side, hit the MCP, and make positroniums. The z -axis is common with Fig. 2.

approximately 5% for the positron beam whose polarization is unity at incidence. This amount is negligible. Therefore, we shall be able to obtain the polarization from the annihilation measurement.

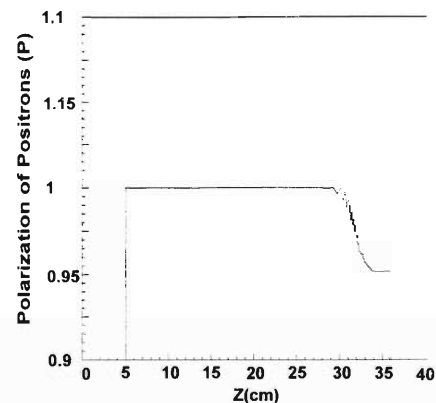


Fig. 2. Result of the simulation for positron beam polarization along z -axis inside the magnetic channel.

References

- 1) D. Gidley, A. R. Koymen, and T. W. Capehart: Phys. Rev. Lett. **49**, 1779 (1982).
- 2) P. W. Zitzewitz, J. C. Van House, A. Rich, and D. W. Gidley: Phys. Rev. Lett. **43**, 1281 (1979).
- 3) T. Kumita et al.: Appl. Sur. Sci. in press.

4. Radiation Chemistry and Radiation Biology

An Effective Mutation Method for Plants Using Heavy-Ion Beams

T. Abe, C.-H. Bae, and S. Yoshida

In the previous paper,¹⁾ we have reported that the fertilization cycle of plants is very sensitive to the irradiation of heavy-ion beams. In the present paper, tobacco embryos were irradiated with heavy-ion beams immediately after the pollination to obtain a high frequency mutation. And this new technique subjected to screening of salt-tolerant mutants.

Tobacco plants were grown for this experiment in a green house under 18-hours photoperiod at 25 to 30 °C for 3 to 4 months in the flowering period. After 24 to 108 hours of pollination, intact embryos in the flowers were irradiated with 10 to 200 [gray] of dose by heavy-ion beams (¹⁴N or ²⁰Ne: 135 MeV/u). LET of the N and Ne ion corresponded to 28.5 and 63.0 KeV/μm, respectively. One month after the irradiation, seeds of M₁ generation were harvested. The treated plants were cultivated in a green house and the resulting M₁ seeds were harvested one month after the treatment. The M₁ seeds were germinated in the 1/2 MS medium at 25 °C under continuous light. Two weeks later, morphologically abnormal plants were planted in plastic trays containing soil, and were placed in a growth cabinet under 12-hours photoperiod at 25 °C. After two weeks, the shapes of M₁ abnormal plants were observed. M₁ seeds of Xanthi (3,098) and BY-4 (7,257) were placed on the 1/2 MS medium containing 2.5% and 2.0% of NaCl, respectively, and were incubated for 4 weeks. Putatively salt-tolerant seedlings germinated under saline condition were selected and planted in soil.

High irradiation dose caused a decrease in the germination percentage (Fig. 1). The highest rate of abnormal plants at 24 to 48 hours of treatment stage after pollination was 8.3% with Ne ion and 18.1% with N

ion in Xanthi, respectively (Fig. 2). However, there is no peak in the mutation rate for BY-4. A total of 17 putatively salt-tolerant plants were selected from BY-4, whereas no salt tolerant progeny was obtained from Xanthi (Table 1). Shapes of the filament and pollen grain of salt-tolerant plants were abnormal compared with the control, and both the seed weight and fertility rate obviously decreased. One cell line induced from the three salt-tolerant seedlings indicated a salt tolerance. The cell growth and chlorophyll content were higher than those of control (wild type) in the medium containing NaCl. Above work shows that the sensitivity of plant embryos to this irradiation technique may vary by species or even by cultivars.

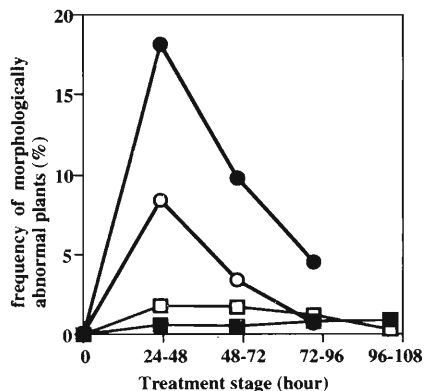


Fig. 2. Effects of embryo treatment with ion beams at different developmental stages on frequency of morphologically abnormal plants. ●N ion for Xanthi; ○Ne ion for Xanthi; ■N ion for BY-4; □Ne ion for BY-4.

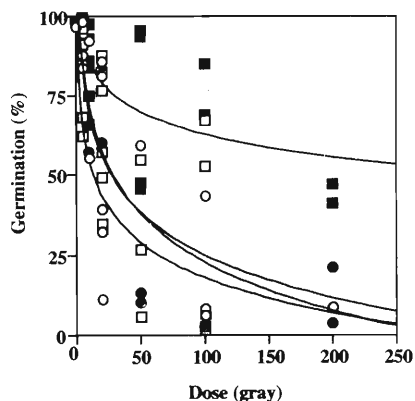


Fig. 1. Effects of embryo treatment with ion beams at different developmental stages on seed germination. ●N ion for Xanthi; ○Ne ion for Xanthi; ■N ion for BY-4; □Ne ion for BY-4.

Table 1. Effect of heavy ion beams on the seed germination of tobacco embryos under salt conditions.

Cultivar	Ion	Stage (hr)	Seed no.	Survival no.	Survival (%)
Xanthi	N	control	413	0	0
		36 - 48	277	0	0
		60 - 72	30	0	0
		84 - 96	367	0	0
		total	674	0	0
	Ne	36 - 48	1169	0	0
		48 - 60	1151	0	0
72 - 84		104	0	0	
total	2424	0	0		
BY-4	N	control	723	0	0
		24 - 60	855	9	1.05
		60 - 72	246	5	2.03
		84 - 96	1664	3	0.18
		total	2765	17	0.61
	Ne	36 - 48	1181	0	0
		48 - 60	3158	0	0
72 - 84		153	0	0	
total	4492	0	0		

References

1) T. Abe et al.: in *Modification of Gene Expression and Non-mendelian Inheritance*, ed. by K. Oono and F. Takaiwa (NIAR, Japan, 1995) p. 469.

Physical Characteristics of Irradiation Field for Proton Radiotherapy

A. Higashi, T. Kanai, H. Tomura, Y. Futami, N. Matsufuji, and F. Yatagai

We have studied physical characteristics of irradiation field using the proton beam produced at RIKEN Ring Cyclotron (RRC) facility. Proton therapy, a method of radiotherapy, has already started at several facilities. Their proton beam gantries have about one third of the source axis distance (SAD, distance between scatterer and isocenter) of the fixed port in their facilities. Therefore, data of physical characteristics obtainable with such fixed port are insufficient for designing the proton gantries. Problems are as follows: when passing through both the irradiation system and human tissue, the proton beam has a scattering angle larger than the case of heavy ions because of its lighter mass. Further, a gantry with a short SAD causes a large scattering angle. For this case, if parameters of devices in proton gantry are slightly changed, both flatness of irradiation field and depth-dose distribution will become worse than the case of carbon beam. One purpose of our experiment is, therefore, to obtain the data for designing an irradiation system, a gantry in particular, using proton beam. The other purpose is to compare the present proton data with the carbon data^{1,2)} obtained both from previous RRC experiment and from NIRS (National Institute of Radiological Sciences) with the HIMAC (Heavy Ion Medical Accelerator in Chiba)³⁾ for carbon therapy.

We used 160 and 210 MeV proton beams in the RRC-E5 area. Our setup consisted of wobbler magnets, a scatterer, a ridge filter, and a range shifter. The total length was about 4 m, which corresponds to the size of a proposed gantry.

Concerning the flat irradiation field, optimal combinations of the scatterer thickness and the wobbler radius were searched. Polyethylene plates simulating a human tissue were placed just upstream of the isocenter. A parallel plate ionization chamber was located at the isocenter. For each thickness of polyethylene, a lateral dose distribution was measured. We found that the method of the optimization developed for the carbon case at HIMAC¹⁾ can be applied for designing a proton gantry. Thickness of the scatterer and the wobbler radius, however, had to be adjusted more finely for each beam energy, irradiation-field radius, and thickness of the range shifter than the case of HIMAC.¹⁾

Penumbra size of the irradiation field was measured by using X-ray films located perpendicularly to the beam axis at the isocenter. A collimator was placed 15 or 30 cm upstream from the isocenter. Polyethylene plates were also placed just upstream of the isocenter. The penumbra size is defined as the distance between lateral position of 80% dose and that of 20% dose compared with the dose of the isocenter, which is denoted by P_{80-20} . We found that the scattering effect

in polyethylene plate dominates if the thickness exceeds 20 cm caused by the irradiation system (Fig. 1), in contrast to the carbon case.²⁾

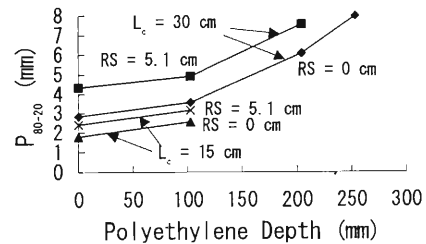


Fig. 1. Penumbra size (P_{80-20}) of 210 MeV proton beam. L_c and RS denote the distance between collimator and isocenter and the range shifter thickness, respectively.

Lateral dose distribution may be affected by the edge of the collimator. Since a beam passes through the irradiation system and since its radius is large, beam will be scattered by the edge of the collimator. The angle of the collimator to the plane perpendicular to the beam axis was set at 0, 2, 4, and 6 degrees. An X-ray film was placed at the isocenter to measure the lateral dose distribution. We found that the edge effect is negligible when the angle is smaller than 2 degrees.

Depth-dose distribution in water was measured with a parallel plate ionization chamber, by scanning the water column around the isocenter. Pristine Bragg peak and spread-out Bragg peak were measured by using a ridge filter for both 160 and 210 MeV proton beams. Results of calculation for a ridge filter developed at NIRS¹⁾ were compared with the experimental data. Analysis is now under way.

The ridge filter is composed of many bars and placed in parallel and 5 mm apart each other. At a downstream from the ridge filter, lateral dose distribution would show irregular stripes caused by differences of scattering beam by each bar and each gap. When the beam passes through the irradiation system and is scattered sufficiently, flatness of the irradiation field is satisfactory. We placed X-ray films at eight different positions downstream of the ridge filter toward the isocenter. Stripes corresponding to each gap were observable in X-ray films placed at the distances of less than 85 cm from the ridge filter, but were impossible in those placed at the distance of 135 cm.

References

- 1) T. Kanai et al.: HIMAC Report HIMAC-004 (NIRS, 1993), p. 1.
- 2) H. Tomura et al.: submitted to Med. Phys. (1996).
- 3) Y. Hirao et al.: HIMAC Report HIMAC-001 (NIRS, 1992), p. 1.

Decay Enhancement of Self-Trapped Excitons at High Excitation-Density and Low Temperature in an Ion-Irradiated BaF₂ Single Crystal

K. Kimura, T. Kohama, D. Kawakami, and W. Hong

Luminescence decay of the self-trapped exciton (STE) in an ion-irradiated BaF₂ single crystal was studied using a single-ion hitting and single-photon counting (SISP)¹⁾ with resolution of 100 ps developed by us. Another important luminescence band, the Auger-electron free luminescence, was also studied but we have reported it elsewhere.²⁾ The decay curve measured by ion irradiation was found quite different from that by photo- or electron-irradiation. The decay curve by photo- or electron-irradiation are characterized by a delayed peak i.e., a delayed growth of STE. In contrast, the decay by ion irradiation had no delayed rise, and furthermore was much more rapid at the initial stage. We could explain the peaking in the decay curves by photo- and electron-irradiation as a competing process between spontaneous luminescence-decay of STE's and a delayed regeneration of STE's by the recombination of F- and H-centers: the experimental curves were simulated by solving the rate equation. Before the explanation for the decay enhancement by ion irradiation, let us show the effect of decreasing temperature. Figures 1a through d show the decay curves measured with He, N, Ar, and Kr ions at two different temperatures in a narrow range of 20 ns in order to observe the initial stage precisely. Figure 1a shows that with decreasing temperature from 298 K to 35 K, the half lifetime was reduced from 1200 to 150 ps. This temperature effect is contrary to the known fact that STE's in photo- or electron-irradiated alkali-halides increases in the decay time with decreasing temperature. This phenomenon was explained as follows. It is noted that F and H centers and STE's are generated too close in ion irradiated BaF₂ to form a delayed peak of STE's appeared in case of photo-irradiation. At about 30 K, these centers and STE's are frozen so that the recombination does not occur and hence the decay of STE is independent of the F-H recombination. Nevertheless, the decay constant, 150 ps, is too fast to be ascribed to the spontaneous decay (cf. 600 ns in case of electron irradiation). By supposing that nonradiative decay by

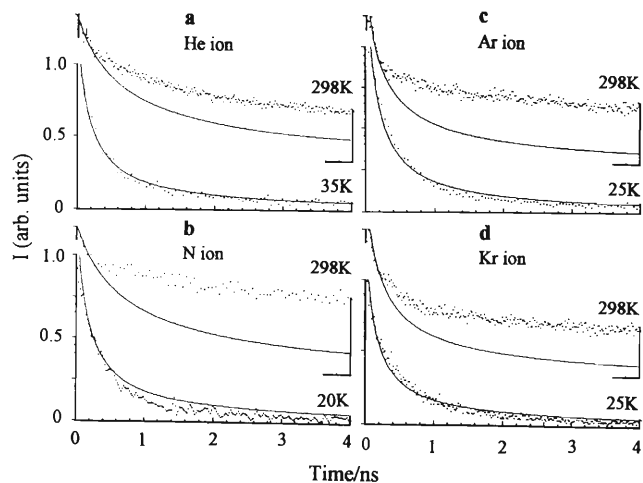


Fig. 1. Temperature-dependent decay of luminescence at 310 nm in He (a), N (b), Ar (c), and Kr (d) ions irradiated BaF₂. Solid lines are simulation curves based on the equation in the text.

STE-STE exchange interaction plays a role, we could solve the rate equations and simulate the experimental decay as shown by solid lines in Fig. 1. A solution of the rate equation is given by

$$S = \frac{1}{(a + S_0^{-1}) \exp(k_1 t) - a},$$

where S is the quantity proportional to the concentration of STE, the subscript 0 means time 0, k_1 is the rate constant of the spontaneous luminescence, and a the constant.

References

- 1) K. Kimura: Nucl. Instrum. Methods Phys. Res. B **90**, 100 (1994).
- 2) K. Kimura and J. Wada: Phys. Rev. B **48**, 15535 (1993); Phys. Rev. B **116**, 57 (1996).
- 3) K. Kimura: submitted to Phys. Rev. B.

Effects of Ne Ion Beams on Survival of *Arabidopsis thaliana*

N. Shikazono, A. Tanaka, Y. Yokota,* H. Watanabe,** S. Tano,**
T. Kanai, and S. Kitayama

The biological effects of heavy ions, estimated from the relative biological effectiveness (RBE) on lethality as a function of the linear energy transfer (LET), have been extensively studied with bacteria, yeast, and cultured mammalian cells. However, the effects of heavy ions on lethality of the multicellular organisms are not yet fully understood. *Arabidopsis thaliana* (L.) Heynh. is a multicellular organism particularly suitable for studying the effects of heavy ions and radiations. It is because the seed and plant are small, a large number of seeds are produced, and the life cycle is short.¹⁾

We previously investigated the effects of heavy ions on the survival of *Arabidopsis* using several different kinds of ions with LETs of 17 ~ 549 keV/ μ m, and found that the highest RBE is given by Ar ions at LET 252 keV/ μ m.²⁾ To further elucidate the dependence of RBE on LET, we used only the Ne ions but with several different LETs for present study.

For the particle irradiation, the dry seeds of *Arabidopsis thaliana* ecotype Columbia were carefully sandwiched between kapton films (7.5 μ m thickness) as a single layer. Seeds were exposed to the Ne ions accelerated by RIKEN Ring Cyclotron or by JAERI (Takasaki) AVF Cyclotron. The LET of Ne ions at RIKEN Ring Cyclotron was varied by placing an absorber in front of the irradiation site. The mean LETs were calculated by ELOSS code (a modified OSCAR code). After the irradiation, the plants were grown at 23 °C under a continuous light (40 μ E/m²/s). One month after sowing, those plants with expanded rosette leaves were scored as survivors.

The survival curves for the Ne ions with LET 156, 275, 352, 525, and 549 keV/ μ m are shown in Fig. 1. The Ne ions with LET of 156 keV/ μ m had the largest shoulder, while those with LET of 352 keV/ μ m had the smallest. The RBE on lethality was calculated by using the dose for 37% survival (D_{37}) for electrons as a standard and was found to give a peak at the LET around 350 keV/ μ m (Fig. 2).

In the unicellular systems, a peak was observed at the LET around 100 keV/ μ m, and heavy ions with greater LETs usually reduced the RBE value.³⁾ The difference of LET for the RBE peak between the unicellular system and *Arabidopsis* may be explained by

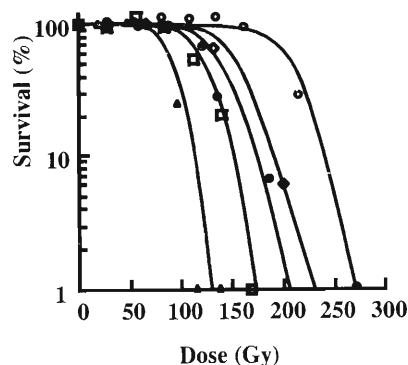


Fig. 1. Effect of the Ne ion beams with different LETs on survival. \circ : LET 156 keV/ μ m, \square : LET 275 keV/ μ m, \blacktriangle : LET 352 keV/ μ m, \diamond : LET 525 keV/ μ m, \bullet : LET 549 keV/ μ m.

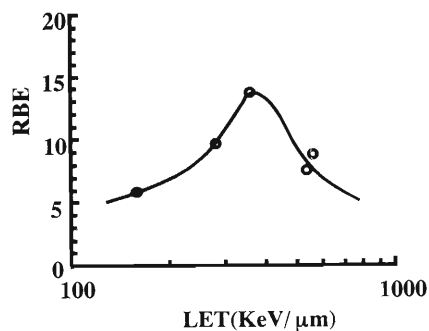


Fig. 2. RBE on lethality as a function of LET of Ne ions.

Arabidopsis' repair mechanism specific to the multicellular organisms.

Further investigations using the other heavy ions with LETs of around 300 ~ 400 keV/ μ m seem to be important in order to conclude the relationship between RBE and LET in *Arabidopsis*.

References

- 1) U. Bork et al.: Adv. Space Res. **9**(10), 117 (1989).
- 2) A. Tanaka et al.: submitted to Int. J. Radiat. Biol.
- 3) G. Kraft: Nucl. Sci. Appl. **3**, 1 (1987).

* Beam Operation Co.

** Advanced Science Research Center, JAERI

Response of Radio-Sensitive Mutant Cell Line against Heavy-Ion Beams

K. Eguchi-Kasai, H. Itsukaichi, M. Murakami, T. Kanai, F. Yatagai, and K. Sato*

It can be noted that the high LET radiations are more effective to kill cells because of a more induction of non-repairable dsb than the low LET radiations. Here, we compare the effects of charged particles on cell killing in a pair of mouse cell lines which are normal (LTA) or defective in the repair of DNA dsb (SL3-147).

Charged-particle beams were C ion of 135 MeV/u, Ar ion of 83 or 90 MeV/u, and Fe ion of 90 MeV/u. Inactivation cross sections were calculated from 37% survival dose of the survival curves fitted by a linear regression analysis to the linear quadratic model.

In the dsb repair deficient cells, relative biological effectiveness (RBE) values were close to unity for cell killing induced by charged particles with the linear energy transfer (LET) up to 200 keV/μm, and were even smaller than unity at the LET region larger than 300 keV/μm. The inactivation cross section (ICS) increased with LET for both cell lines (Fig. 1). The ICS of dsb repair deficient mutants is always larger than that of their parents for the all LET ranges. With increasing LET, the difference of ICS between the mutant and its parent became smaller. This suggests that repairable dsb decrease, and that the ratio of non-repairable dsb to the total dsb induced increases with

increasing LET. However, there still remained a small difference in ICS at the LET of about 300 keV/μm. This phenomenon may show that dsb repair still takes place at these high LET regions in the normal cell line, even its efficiency is low.

There is also other possibilities. It has been argued that the DNA content¹⁾ and geometrical cross section²⁾ of nuclei play important roles in cell inactivation by high LET radiations. Karyotypes of the both cell lines were near diploid. Chromosome number widely varies in SL3-147 cells. The average chromosome number is slightly higher in SL3-147 cells than LTA. The average nuclear area of dsb repair deficient cells is also bigger than that of their parent cell line (Fig. 2). On the other hand, R1 cells which were triploid showed similar ICS to LTA and L5178Y although they are triploid. These results suggest that DNA contents are not important for cell inactivation at high LET regions. It is not clear yet which is more important, dsb repair or nuclear area. Further study is necessary.

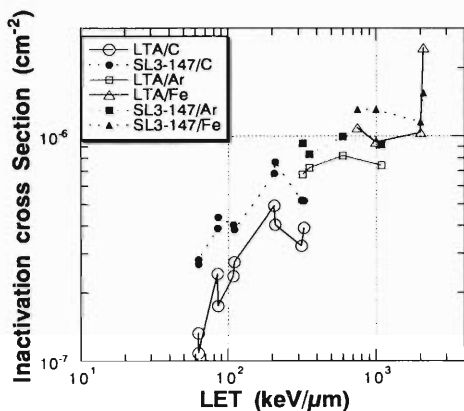


Fig. 1. Inactivation cross section of heavy ion beams. Closed symbols represent dsb repair deficient cells (SL3-147) and open symbols represent wild type cells (LTA).

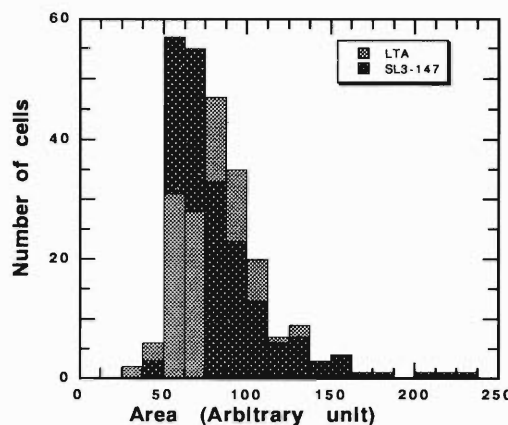


Fig. 2. Distributions of the nuclear area of dsb repair deficient cell line and its parent cell line.

References

- 1) W. Sontag et al.: *Int. J. Radiat. Biol.* **57**, 1183 (1990).
- 2) W. Kraft-Weyrather et al.: *GSI Report GSI-91-29*, C6 (1991).

* National Institute of Radiological Sciences

LET Dependence of Interphase Cell Death Induction for CHO Cells Exposed to Accelerated Heavy-Ions

H. Sasaki, F. Yatagai, T. Kanai, Y. Furusawa, and F. Hanaoka

Radiobiological studies using ionizing radiations with various LETs (Linear Energy Transfers) have shown that kill-the-cell effect of radiation depends on the ionization density (LET) and that its relative biological effectiveness (RBE) reaches a maximum around 100–200 keV/ μm . Since a high LET radiation deposits considerable energy along the primary tracks, it induces multiply damaged sites locally within a target molecule like DNA.¹⁾ Therefore, the predisposition to death before dividing (interphase death) may be higher for the high-LET than low-LET radiations. In order to verify this possibility, we have examined the LET dependence of the induction of interphase cell death using accelerated heavy-ions such as C, Ne, Ar, and Fe.

Exponentially growing asynchronous CHO-K1 (Chinese hamster ovary) cells were exposed to monoenergetic beams of heavy-ions. The dose averaged LET was selected by inserting sheets of absorber of appropriate thickness.²⁾ X-rays (200 kVp) were also used as a standard radiation source. The fraction of cells that underwent interphase cell death after irradiation was determined by observing individual cells with time-lapse photography (direct method) as well as counting the interphase death-initiated cells which were induced by caffeine (indirect method). This fraction increased linearly after exposure to X-rays with dose larger than about 10 Gy (threshold), whereas it increased at a higher rate without a threshold after exposure to high-LET heavy-ions such as 230 keV/ μm Neon (Fig. 1).

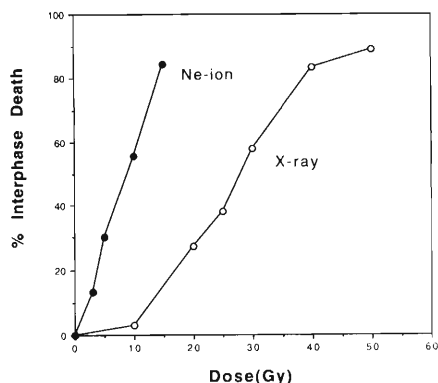


Fig. 1. Induction of interphase cell death after an exposure to X-rays or Ne ions (230 keV/ μm). The fraction of cells that underwent interphase cell death was determined by a time-lapse method.

The RBE values of heavy-ions relative to X-rays, as determined at 50% induction level, increased with LET and reached a maximum at the LET around 230

keV/ μm followed by a decay with further increase in LET (Fig. 2a). The range of LET values corresponding to the maximum RBE was narrower for the interphase death (around 230 keV/ μm) than for the reproductive death (120–230 keV/ μm) as assayed using the loss of colony-forming ability as a criterion (Fig. 2b). This suggests that targets should be more severely damaged for induction of the interphase cell death than that of reproductive cell death. On the other hand, the inactivation cross-section for interphase cell death ($\sigma = 1/F_{37}$) reached a plateau at 5–10 μm^2 .

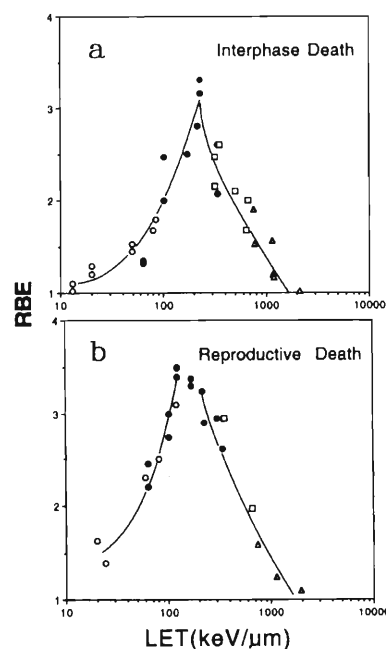


Fig. 2. RBE vs. LET relationship for the induction of (a) interphase or (b) reproductive cell deaths. (○): C-ion, (●): Ne-ion, (□): Ar-ion, (△): Fe-ion.

The present results are consistent with our previous time-lapse observations of the HeLa cells exposed to α -rays (^{241}Am),³⁾ indicating a predisposition to interphase cell death against heavy-ions irradiation. Further studies are needed to elucidate the mechanisms of interphase cell death induction by high-LET heavy-ions.

References

- 1) D. J. Brenner and J. F. Ward: *Int. J. Radiat. Biol.* **61**, 737 (1992).
- 2) T. Kanai, T. Kohno, S. Minohara, M. Sudou, E. Takada, F. Soga, K. Kawachi, and A. Fukumura: *Radiat. Res.* **135**, 293 (1993).
- 3) H. Sasaki: *Radiat. Res.* **99**, 311 (1984).

Analysis of the Mutations in Human *HPRT* Gene Induced by Heavy-ion Irradiations (III)

F. Yatagai, Y. Kagawa, N. Fukunishi, M. Hirano,* T. Shimazu,* N. Inabe, K. Eguchi-Kasai, Y. Furusawa, M. Suzuki, M. Watanabe, T. Kato,** and F. Hanaoka

To gain insight of the characteristics of the mutations induced by heavy-ion irradiation, we have analyzed the hypoxanthine phosphoribosyltransferase *hprt* mutations in human cultured cells. Both WI-L2-NS and TK6 are the human lymphoblastoid cell lines, derived from the same human spleen. The WI-L2-NS cell has a mutation in codon 237 of p53. For irradiation on these cells, the energies of C- and Ne-ions were adjusted so to irradiate the cells with three different LETs; one at the initial energy or so, one at the peak of Relative Biological Effectiveness (RBE), and one at the level just before the stop of the ions. Only the 13 keV/ μm C-ion beam was supplied by HIMAC, and others were by RIKEN Ring Cyclotron. It is interesting to determine whether the difference in X-ray sensitivity between these two cell lines can still be seen even after irradiation of such heavy ions. A difference of the type and level of the p53 protein between these two cell lines has been reported to account for the differences in their X-ray sensitivities.¹⁾ Another interest is whether the analysis of cDNA for the heavy-ion induced *hprt* mutant clones would provide a frequent recovery of exon skipping, because we often observed such type of *hprt* mutations in the human embryo (HE) cells irradiated by 230 keV/ μm C-ions.²⁾ Some knowledges on the former question were obtained as described below, but not yet for the latter.

The survival curves for both C- and Ne-ions are shown in Fig. 1. Using the D_{10} dose for X-ray irradiation as a standard, the values of RBE were calculated and the result is shown in Fig. 2. The expected LET effect on cell killing was observed with both cell lines. The *hprt* mutation frequencies at a certain survival level were also compared and the tendency of RBE for mutation seems to be similar to that for cell killing (data not shown). Isolation of genomic DNA and mRNA from the mutant clones induced by HIMAC C-ions (13 keV/ μm) were performed to identify the *hprt* mutation at the DNA sequence level. Although analysis is not yet complete, we have observed relatively fewer exon skipping. This result seems to be not contradicting with our previous results³⁾ for HE cells, but more detailed analysis is in need to judge the difference in induced mutational events between the two cell lines. We are planning to expand this line of analysis to the mutant clones obtained by the high-LET ion irradiations as mentioned above.

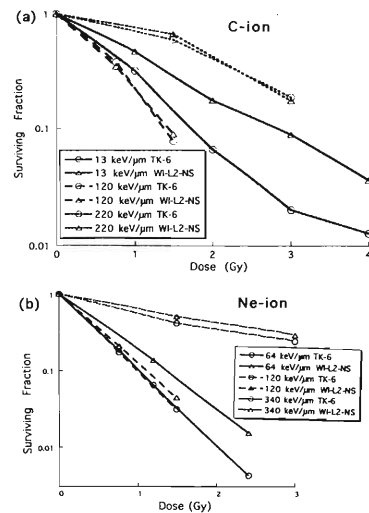


Fig. 1. LET dependence of killing effect by heavy ions (a) C-ion, (b) Ne-ion.

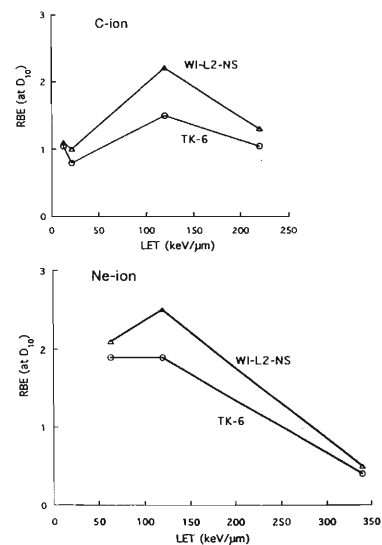


Fig. 2. RBE for a killing effect.

References

- 1) W. Zhen, C. M. Denault, K. Lovisek, S. Walter, L. Geng, and A. T. M. Vaughan: *Mutat. Res.* **346**, 85 (1995).
- 2) Y. Kagawa, F. Yatagai, M. Suzuki, Y. Kase, A. Kobayashi, M. Hirano, T. Kato, M. Watanabe, and F. Hanaoka: *J. Radiat. Res.* **36**, 185 (1995).
- 3) M. Suzuki, M. Watanabe, M. Kanai, Y. Kase, F. Yatagai, T. Kato, and S. Matsubara: *Adv. Space Res.* **18**, 127 (1995).

* Toray Research Center

** School of Medicine, Osaka University

Mutation of Human Cancer Cell-Line Caused by Heavy-Ions and X-Rays

T. Kawada,* N. Shigematsu,* H. Ito, S. Yamashita, T. Nakayama,*
K. Toya,* A. T. Yida-Sakate,* A. Kubo,* and T. Kanai

In our previous study, we reported that the mutation frequencies of V79 cells irradiated by a heavy-ion beam and X-rays increased in proportion to the irradiated dose.¹⁾ The results are shown in Fig. 1.

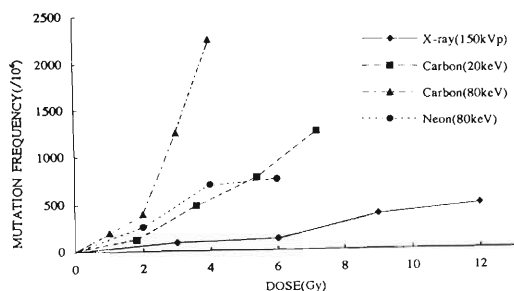


Fig. 1. Mutation frequencies of V79 per 10^6 cells irradiated by X-rays and heavy-ions (20 and 80 keV/ μ m carbon and 80 keV/ μ m neon).

The purpose of this study is to evaluate the mutation frequency of human-cell line caused by heavy-ions and X-rays. The human-cell line we used was RMG1 which was derived from human- ovarian cancer. RMG1 cells were irradiated by the heavy-ion beam from RIKEN Ring Cyclotron or by X-rays from MBR-1520R (Hitachi made) and cell survivals were calculated by colony assay. After one or two weeks of expression periods, the mutation frequencies at the *hprt* locus were calculated from the numbers of colonies formed in media supplemented with 6-thioguanine (10 μ g/ml).

Survival curves of RMG1 against the dose of heavy-ions and X-rays are shown in Fig. 2. The D_0 value for 150 kVp X-rays, 80 keV/ μ m carbon beam and 80 keV/ μ m neon beam were 1.6 Gy, 0.78 Gy, and 0.65 Gy, respectively. With the increase of linear energy transfer (LET) of a carbon beam, survival curve of RMG1 moved leftward. High LET carbon beam has more powerful kill-the-cell (KTC) effects than low LET beam. When the carbon and neon beams were used at the same LET level, they showed nearly equal KTC effects.

Mutation frequencies caused by carbon beam, neon beam and X-rays are shown in Fig. 3. In comparison with X-rays, heavy-ions result much higher mutation frequencies. As the irradiation dose of carbon beam increased, the rate of mutation frequencies further increased above a certain dose. A neon beam caused less mutation than a carbon beam under the same LET

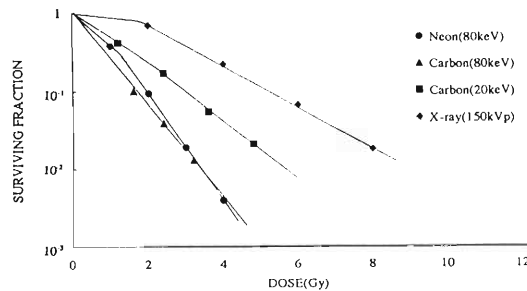


Fig. 2. Survival curves against X-rays and heavy-ions (20 and 80 keV/ μ m carbon and 80 keV/ μ m neon).

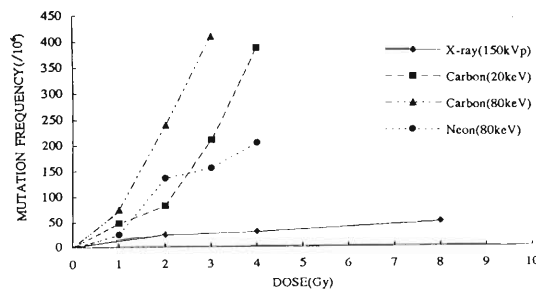


Fig. 3. Mutation frequencies against X-rays, carbon beam (20 and 80 keV/ μ m), and neon beam (80 keV/ μ m) irradiation.

level. These results were very similar to those of V79.

In conclusion with the use of the human cancer cell line (RMG1), we have evaluated the mutation caused by carbon beam, neon beam and X-rays. The results were as follows.

- 1) The mutation frequency was higher for RMG1 cells when irradiated by a heavy-ion beam than by X-rays.
- 2) Carbon beam and neon beam with the same LET level showed nearly equal KTC effects.
- 3) The mutation frequency increased when the LET of a carbon beam increased.
- 4) The mutation frequency was less for a neon than carbon beam, which suggests that neon is more favorable than carbon when a high dose therapy is needed.
- 5) As to the mutation frequencies caused by heavy-ions and X-rays, RMG1 showed the similar trend as V79.

References

- 1) N. Shigematsu et al.: RIKEN Accel. Prog. Rep. **28**, 117 (1995).
- 2) K. Toya: Nippon Acta Radiologica **56**, 736 (1996).

* Department of Radiology, Keio University School of Medicine

5. Instrumentation

A Rotating Target System for High-Intensity Heavy Ion Beams

Y. Tagaya, T. Nomura, K. Morita, Y. Pu, M. Kurokawa, and T. Motobayashi

To produce the rare nuclei whose formation crosssection is extremely low, a high-intensity heavy ion beam is required. Correspondingly, the RIKEN Ring Cyclotron facility plans to increase its accelerator's beam intensity. Then a new target system that can withstand the intense beam becomes necessary. One solution to the problem is to use multiple targets arranged on a rotating disk in such a way that one target is irradiated in a short period of time, but is cooled down during the other targets are irradiated.

We are now testing the new rotating target system and its schematic view is shown in Fig. 1. The system consists of two disks, disk-1 and disk-2. Energy degraders are mounted on the disk-1 while targets are on the disk-2. The two disks are driven by individual stepping motors and are controlled by a personal computer so as to move synchronously with pulsed ion beam. The absolute rotating angle of each disk is read by an optical encoder and is feedback to the control system for adjusting the precise position-setting. To step up the speed of disks, we adopt 1 to 5 gear ratio.

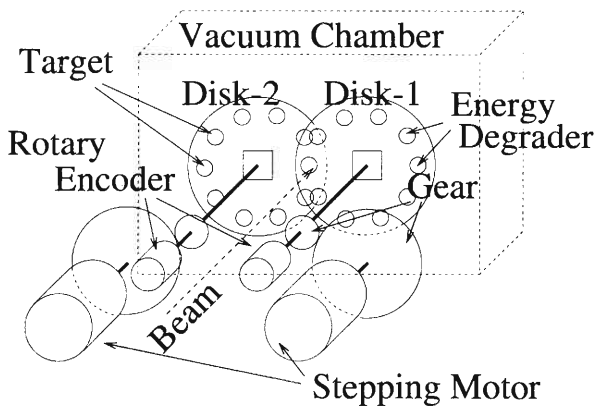


Fig. 1. Schematic view of the rotating target system. Only the two disks are inside the vacuum chamber and all the other components are outside.

Two operating modes are now prepared, one is a continual rotation mode and another is an intermittent rotation mode. In a continual rotation mode, disks are rotated at a constant speed and beam pulsing is determined by the target size. In this operating mode, fast rotation (a few hundred rpm) is possible which results

in enhanced cooling effect, but targets need to be made large to increase the time for irradiation. In an intermittent rotation mode, on the other hand, disks are rotated and stopped intermittently and therefore small targets can be used. When 10 targets are mounted on a disk in this operating mode, we can set the next target to the beam position in 50ms minimum.

We made a simple calculation of the temperature distribution of the U_3O_8 target. It was assumed that the system is operated synchronously with 50ms-on 50ms-off pulsed Ti ion beam in an intermittent rotation mode with 10 targets on a disk. This means that each target is irradiated 50ms-on and 950ms-off. The beam intensity of $1p\mu A$ (momentary value) was also assumed, which is expected to be available at the RIKEN Ring Cyclotron facility. Calculated temperature at the target center (Fig. 2) is lower than U_3O_8 sublimating temperature and thus the system is expected to work effectually at the time of the beam experiment.

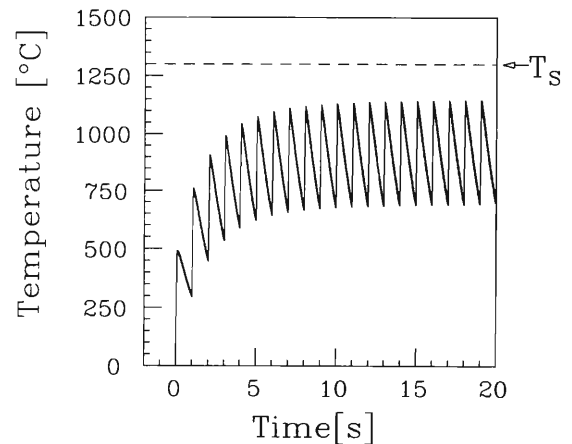


Fig. 2. Temperature at the center of U_3O_8 target. To simplify the calculation, a cubic shape target ($2 \times 2 \times 2 \text{ cm}^3$) and 1 cm thick U_3O_8 and Al degrader thickness were assumed. Boundary temperature is 20°C . Energy deposited per volume is calculated for Ti ion beam ($1p\mu A$, 247 MeV) on the 1 mg/cm^2 U_3O_8 target and $10 \mu\text{m}$ Al combination. 247 MeV is roughly estimated to be the optimum energy to produce $^{280}112$ nuclei in $\alpha 2n$ deexcitation channel. T_s (1300°C) is the U_3O_8 sublimating temperature.

Windowless Gas Target for High-Spin Isomer Beam Production

M. Shibata, Y. Gono, T. Kishida, E. Ideguchi, and M. Ishihara

Presently an upgrade of the beam intensity is under development for the heavy ion injector lineac, RILAC, and RIKEN Ring Cyclotron (RRC). Anticipated increase of their beam intensities is 10–100 times depending on the mass of ions. These high intensity beams are quite profitable for the secondary beam production, such as for the high-spin isomer beam (HSIB) production.¹⁾ However it is required to use metal foils with a high heat conductivity, such as (Be, Al, and Mg) in order to produce HSIB. Therefore it will be highly required in the future to use an windowless gas target, since any foil to separate a vessel of the gas target from the beam line vacuum would not stand against such high intensity heavy ion beams of relatively low energy.

Recently a new type windowless gas target has been developed by Sagara et al.²⁾ By using a blow-in style rather than traditional blow-out one, they succeeded to achieve more than 70 Torr of the N₂ gas pressure in the almost entire target region.

The same type of gas target has been designed for HSIB production as shown in Fig. 1. This has 10 cm of gas target region and ~ 0.6 mg/cm² of thickness at 70 Torr of gas pressure for gasses of N₂, O₂ and Ne. The reactions which will be used to produce HSIB's of ¹⁴⁴Pm, ¹⁴⁵Sm and ¹⁴⁷Gd are: ¹⁴N(¹³⁶Xe,6n)¹⁴⁴Pm, ¹⁶O(¹³⁶Xe,7n)¹⁴⁵Sm, and ²⁰Ne(¹³⁶Xe,9n)¹⁴⁷Gd.¹⁾ The cross sections of these reactions are 100 ~ 300 mb. Since the ¹³⁶Xe beam of 100 ~ 200 pnA can be expected after the upgrade of the RRC, the above mentioned thickness of gas target is enough to produce HSIB's of 10⁵ ~ 10⁶ particles/sec. The gas target has

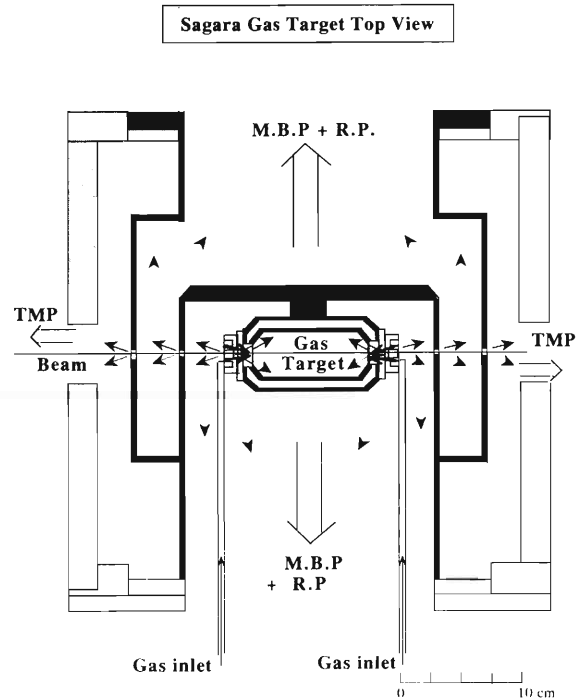


Fig. 1. A blow-in type gas target.

been designed to be placed at the entrance of the RIPS.

References

- 1) Y. Gono et al.: Nucl. Phys. A **588**, 241c (1995).
- 2) K. Sagara et al.: Nucl. Instrum. Methods Phys. Res. A **378**, 392 (1996).

Ge Telescope for γ -Ray Doppler Correction

Y. Gono, T. Morikawa, H. Tsuchida, E. Ideguchi, T. Kishida, and M. Ishihara

A germanium (Ge) counter telescope was developed for the in-beam γ -ray spectroscopy utilizing high-spin isomer beams (HSIB). The system consists of a segmented Ge (Segge) as a ΔE counter and a large volume Ge as an E counter. They were placed as shown in Fig. 1. Segge is divided into 10×10 mm squares with a 20 mm thickness. A Compton scattered γ -ray by Segge was detected by the large volume Ge detector which was a clover type Ge (Clge) in case of Fig. 1.

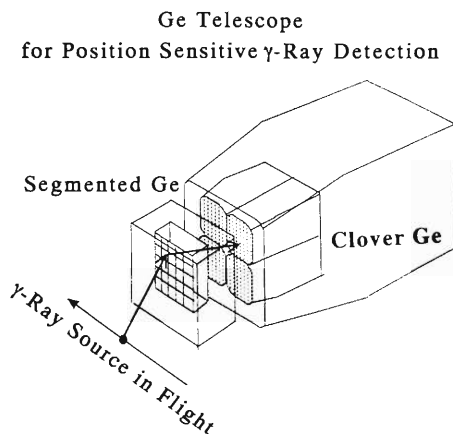


Fig. 1. A Ge telescope system.

Gamma-ray spectra of ^{152}Eu taken by this system are shown in Fig. 2. These spectra were taken by using a 50% Ge as an E counter. A telescopic spectrum shows relatively constant energy dependence of the detection efficiency comparing with those taken in a singles mode. This is reproduced by a simulation calculation made by using a computer code GEANT-IV.

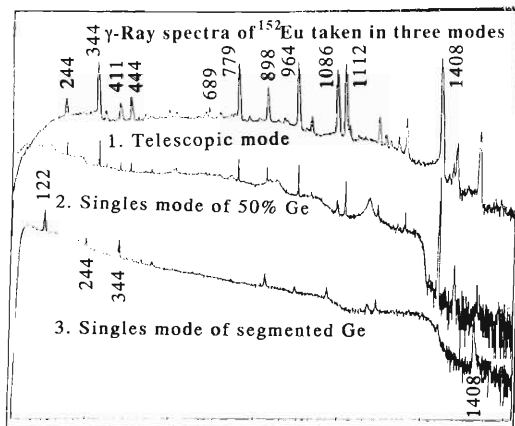


Fig. 2. γ -ray spectra taken by a Ge telescope in three different modes.

The energy dependences of γ -ray efficiencies of various detection modes are shown in Fig. 3.

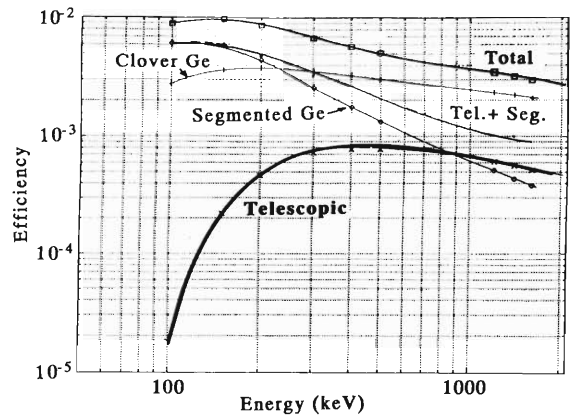


Fig. 3. γ -ray detection efficiencies of a Ge telescope in five different modes of detection.

This system was developed for Doppler correction of the γ -rays emitted from rapidly flying sources. This is the case of secondary fusion reactions by HSIB. In these reactions recoiled nuclei are anticipated to fly with a velocity of about 10% of the light velocity ($\beta \sim 0.10$). A small size of each segment in Segge allows to place it near a target, e.g. 5 ~ 10 cm, to obtain a proper energy resolution even in case of $\beta \sim 0.10$.

Gamma-ray spectra with and without Doppler corrections are shown in Figs. 4 and 5. In Fig. 4, the spectra of γ -rays emitted from the reaction products of ^{27}Al bombarded by ^{32}S at $E = 90$ MeV are displayed. This experiment was made in Kyushu University Tandem Laboratory. The recoil velocities of the

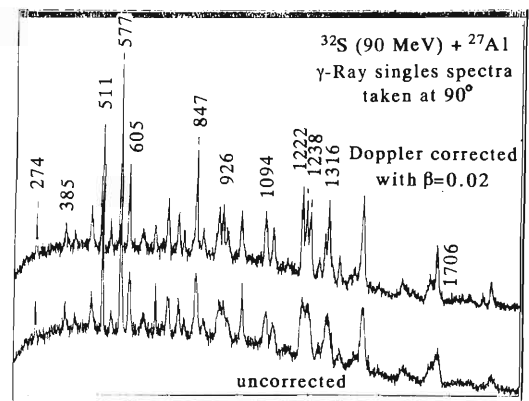


Fig. 4. γ -ray spectra taken by a Ge telescope with and without a Doppler correction for a recoil velocity of $\beta \sim 0.02$.

reaction products were $\beta \sim 0.02$. Though the Doppler correction is suffered by the effects of the emitted par-

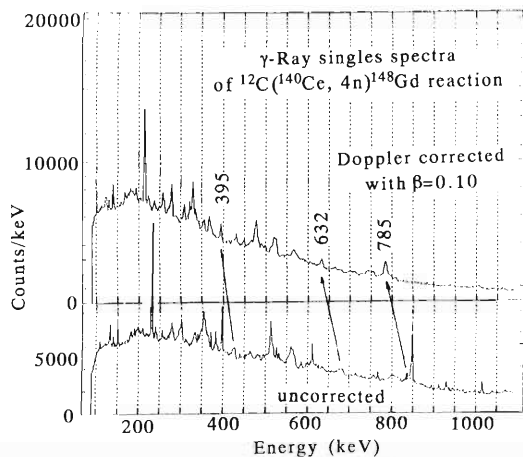


Fig. 5. γ -ray spectra taken by a Ge telescope with and without a Doppler correction for a recoil velocity of $\beta \sim 0.10$.

ticles, e.i. protons and neutrons, the energy resolution of less than 10 keV in FWHM could be obtained for the 1.7 MeV γ -ray. The γ -ray spectra shown in Fig. 5 were taken by Segge only. The γ -rays are from the $^{12}\text{C} + ^{140}\text{Ce}$ reaction under the ^{140}Ce beam energy of 7 MeV/u. In this case the velocity of the reaction products was $\beta \sim 0.10$. Peaks of 785 (2 \rightarrow 0), 632 (4 \rightarrow 2), and 395 keV (6 \rightarrow 4) of ^{148}Gd in the corrected spectrum correspond to bumps in the un-corrected spectrum as corresponded by arrows.

Since the singles spectra of each segment as well as a telescopic spectrum gives position information to make the Doppler corrections, the efficiency of this system is comparable to a 23% single crystal Ge detector as can be seen in Fig. 3. This means that 25 Ge's of 23% efficiency are necessary to achieve the same detection efficiencies as the present system when one needs the same quality of the Doppler correction. A comparison of the costs for these two systems results in a factor 3-4 better cost performance for the present system.

Further improvements in a spectrum quality can be attained by using an anti-Compton shield.

Development of a Polarized ^3He Target System

T. Uesaka, T. Wakui, T. Oonishi, M. Wakasugi, H. Sakai, and Y. Yano

A newly constructed polarized ^3He target system has been applied to a nuclear physics experiment at RIKEN Accelerator Research Facility. Figure 1 shows the photograph of the system.

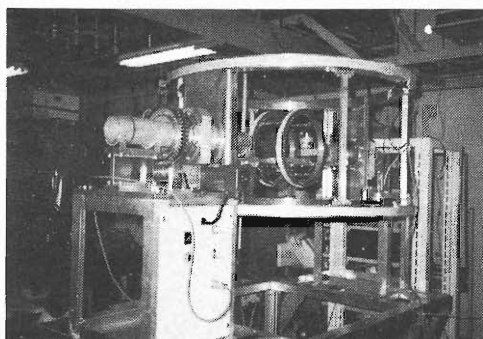


Fig. 1. Photograph of the polarized ^3He target system.

We started a performance test of the system with a few glass cells in the cigar shape of $30\text{ mm}\phi \times 100\text{ mm}$. A glass cell is filled with ^3He gas and N_2 gas of the pressure 3.3 atm and about 0.13 atm at the room temperature, respectively. The cell is also filled with Rb vapor of the density 1.0×10^{15} atoms/cm 3 at 200 °C. Polarization of the ^3He is attained by means of a spin exchange process between a ^3He nuclei and an optically pumped Rb atom. The relaxation time, which is a determining factor of the maximum polarization when a laser pumping power is sufficient, was measured for each cell. Figure 2 shows an example of a relaxation time measurement. The deduced relaxation time was 65.3 ± 6.8 hours for this case of test bench. This value is large enough to polarize the ^3He gas more than 50%.

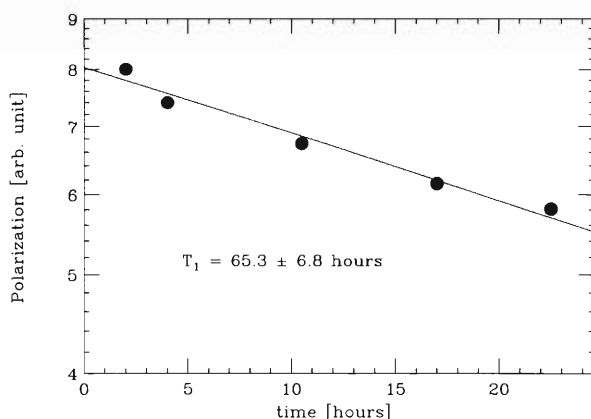


Fig. 2. Typical result of relaxation time measurement. The solid line corresponds to $T_1 = 65.3$ hours.

In order to use this target system for the experiment,¹⁾ we made a few preparations. At first, for reduction of the background events due to the entrance and exit windows of the cell, we employed thin windows as thin as $100\ \mu\text{m}$ (Fig. 3). The shape of the window was hemispherical in order to endure a high inner pressure of more than 8 atm. Among the cells of this type, the longest relaxation time was 6.8 hours. This value is smaller than one obtained before the modification by about one order. The reason for the reduction is under investigation.

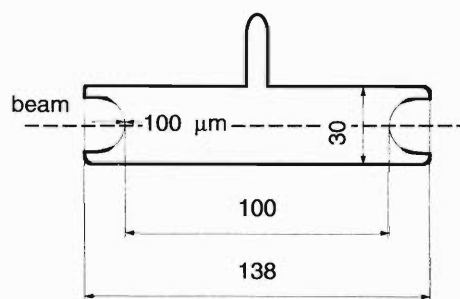


Fig. 3. The cell used in the experiment. Thickness of the entrance and exit windows is $100\ \mu\text{m}$.

Secondly, an absolute value of the polarization was calibrated by a proton NMR measurement. Namely,

$$P_{^3\text{He}} = \frac{V_{\text{NMR}}[\text{mV} \cdot \text{atm}]}{228 [\text{mV}] \times \rho[\text{atm}]}, \quad (1)$$

where $P_{^3\text{He}}$ is the polarization of ^3He , V_{NMR} the NMR signal for ^3He , ρ the ^3He density in the unit of atm at

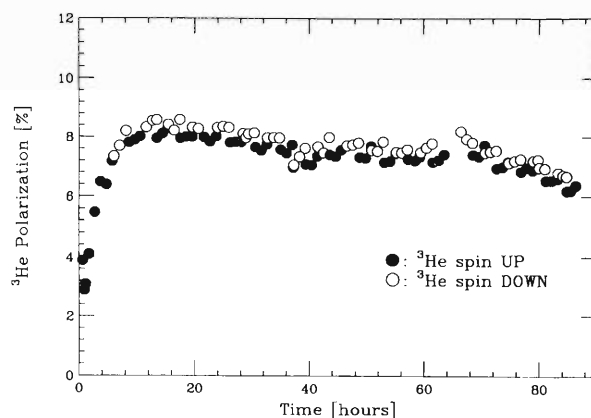


Fig. 4. The result of polarization measurement through the experiments. Open and closed circles represent the “UP” and “DOWN” states of ^3He polarization, respectively.

273 K.

Lastly, a spin-flip system was introduced. In order to reduce the systematic errors included in measured polarization observables, the direction of ^3He polarization should be reversed within a proper interval. The spin-flip system makes use of so-called Adiabatic-Fast-Passage NMR method.

Figure 4 shows a result of the polarization measurement through the experiment performed in November, 1996. This experiment was performed at the E3-room of RIKEN Accelerator Research Facility. The polarized ^3He gas target at the density of 10 mg/cm^2

was bombarded by a polarized deuteron beam of 270 MeV .¹⁾ Open and closed circles are for the spin "UP" and "DOWN" states, respectively. The spin-flip system worked well. A problem of the small difference between "UP" and "DOWN" is, however, still remained. We are now conducting an off-line measurement to correct this difference.

References

- 1) T. Uesaka et al.: RIKEN Accel. Prog. Rep. **30**, 46 (1997).

Performance Study of a Phoswich Detector in the Mixed Field of Neutrons and Charged Particles

T. Nakamura, M. Takada, S. Taniguchi, N. Nakao, T. Shibata, Y. Uwamino, and N. Nakanishi

The contribution of neutrons to the radiation exposure of astronauts still remains vague, because the neutron detection in the spacecraft is difficult due to the intense charged particle field in the space.

In order to measure an accurate neutron spectrum in the mixed field of neutrons and charged particles, we have developed a phoswich detector composing of a 50.8 mm diameter and 50.8 mm long NE213 organic liquid scintillator contacted with a 5 mm thick NE115 plastic scintillator via an optical glass, as shown in Fig. 1. If a charged particle enters into the detector, fast and slow pulses come out from NE213 and NE115, respectively. If neutron or γ -ray enters into the detector, only the fast pulse from NE213 comes out. Light flashes in both scintillators are registered by one-photomultiplier. Using a technique of pulse-shape discrimination based on the decay time differences of the light flash (the decay times of NE213 and NE115 are a few nsec and a few hundred nsec, respectively), this detector is able to discriminate neutron events from charged particle events.

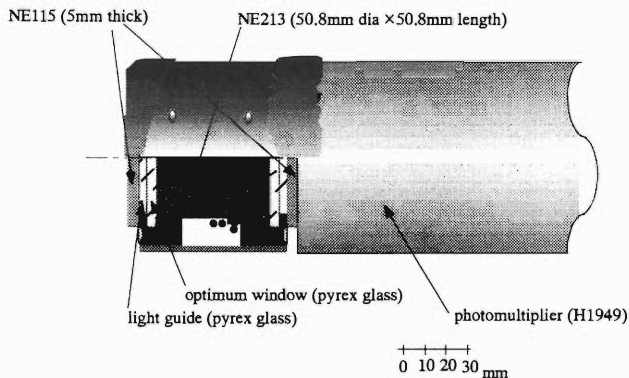


Fig. 1. The phoswich detector consisting of a NE115 plastic scintillator optically coupled with a NE213 liquid scintillator.

We produced a mixed field of neutrons and protons by bombarding 135 MeV protons on a 10 mm thick Li

target at an angle of 30 degrees relative to the proton beam direction in the E4 beam line of RIKEN Ring Cyclotron.

A two-dimensional plot of slow- versus total-component pulses detected with this phoswich detector in a mixed field of neutrons and protons is shown in Fig. 2. Five areas labelled from 'A' to 'E' can be seen in Fig. 2. The area 'A' refers to γ rays, while the area 'B' refers to the neutrons which did not interact with NE115 but with NE213. The area 'C' indicates the protons which stopped inside the NE115 scintillator or the glass, whereas the area 'D' indicates the protons interacted with both NE115 and NE213 scintillators. The area 'E' shows electrical noise events caused by a too high voltage supplied to the photomultiplier.

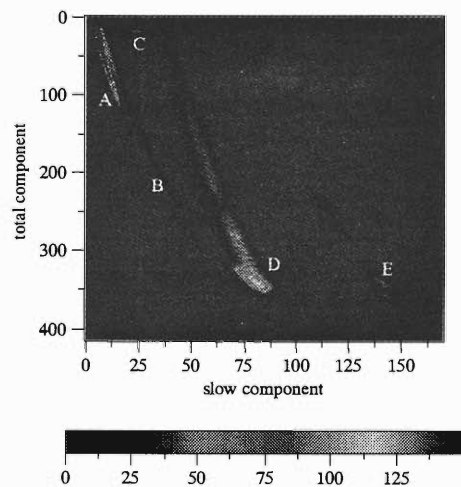


Fig. 2. Two-dimensional map [total component, slow component] obtained with the phoswich detector in a mixed field of neutrons and protons. The area 'A' is due to γ rays, 'B' is due to neutrons, 'C' and 'D' are due to protons, and 'E' is due to electrical noises.

This phoswich detector can clearly discriminate neutron events from proton events, and is useful to measure neutrons in the mixed field with protons.

Proton-Knockout (p,2p) Reactions from ^{12}C with Normal and Inverse Kinematics

T. Kobayashi, S. Ito, A. Ozawa, K. Yoshida, K. Miki, and E. Takada*

Quasifree (p,2p) proton-knockout reaction by proton beams has been used to study the single-particle properties, such as the binding energy or the momentum distribution, of bound protons in the nucleus.¹⁾ Using inverse kinematics, i.e., a heavy-ion beam on a proton target, this method can be applied to any β -unstable nuclei. For the experiments using secondary nuclear beams, we have studied a feasibility of the (p,2p) reaction with inverse kinematics, comparing the same process by two kinds of kinematics: (1) $^{12}\text{C}(p,2p)$ reaction with a proton beam on a ^{12}C target at 210 MeV, and (2) $p(^{12}\text{C},2p)$ reaction with a ^{12}C beam on a proton target at 230 A MeV.

A two-arm detector system is shown in Fig. 1. It is composed of drift chambers, a thin plastic scintillator, and a NaI (6" diam. by 5" thick) which can stop protons up to 210 MeV.

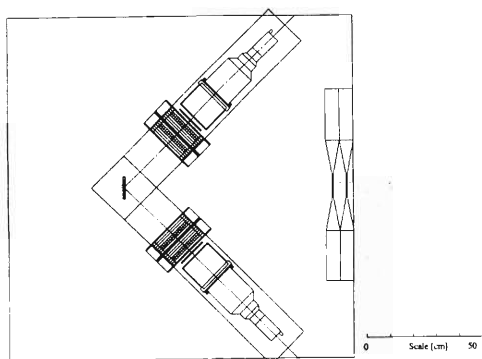


Fig. 1. Two-arm detector system.

Measurements using proton beams were performed at RIKEN. The detector was calibrated using the $p(p,2p)$ reaction. The energy resolution for a 100 MeV proton was 0.6 MeV (rms) evaluated by the $^{12}\text{C}(p,p)$ reaction. The missing-energy resolution for two protons was 1.0 MeV (rms) evaluated by the $p(p,2p)$ reaction.

The $^{12}\text{C}(p,2p)$ reaction using proton beams on a 0.1 g/cm²-thick CH₂ was studied at 135 and 210 MeV. The separation energy spectra are shown in Fig. 2. A sharp peak at 16 MeV ($\pi p_{3/2}$ knockout) and a broad peak around 35 MeV ($\pi s_{1/2}$ knockout) were clearly observed, with a resolution of 1.2 MeV (rms). Momentum distributions of $\pi s_{1/2}$ and $\pi p_{3/2}$ protons are shown in Fig. 3. The momentum resolution, evaluated by the $p(p,2p)$ reaction, is 3.5 MeV/c (rms) shown by the solid histogram. Characteristic shapes for $L = 0$

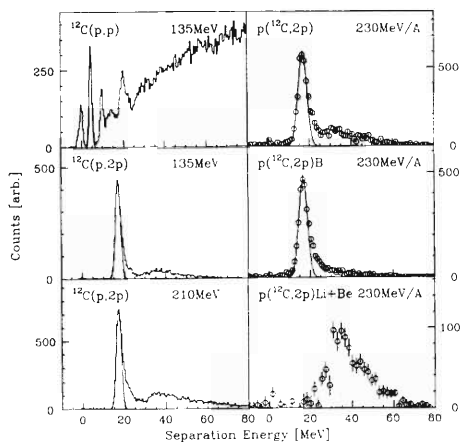


Fig. 2. Separation-energy spectra.

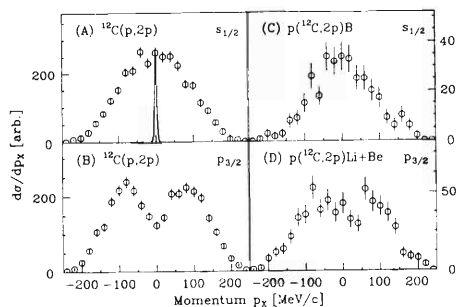


Fig. 3. Momentum distributions of knockout protons.

and $L = 1$ can be seen.

The proton-knockout reaction with inverse kinematics, $p(^{12}\text{C},2p)$, was performed using a 230 A MeV ^{12}C beam from HIMAC on a CH₂ target at NIRS. A plastic scintillator was placed at 0° in order to detect particles from the decay of the (A-1) system formed in the (p,2p) process. As shown in Fig. 2, $\pi p_{3/2}$ - and $\pi s_{1/2}$ -knockout peaks were associated with fragments with $Z = 5$ and $Z = 3,4$, respectively. The separation-energy resolution was 1.9 MeV (rms), which was dominated by the target thickness of 0.2 g/cm². As shown in Fig. 3, momentum distributions of knockout protons in the projectile-rest frame were similar to those of the $^{12}\text{C}(p,2p)$ reaction.

In summary, it was proved that the (p,2p) proton-knockout reaction can be studied using inverse kinematics with a reasonable separation-energy resolution by a simple scintillator-based two-arm telescope.

References

- 1) G. Jacob and T. Maris: Rev. Mod. Phys. **38** 121 (1966).

* National Institute of Radiological Sciences

Development of a MUSIC (Multi-Sampling Ionization Chamber)-type Detector for Identification of Low Energy Nuclear Reactions

Y. Mizoi, T. Miyachi, Y. Matsuyama, T. Fukuda, H. Miyatake, N. Aoi, K. Yoneda, Y. Watanabe, M. Notani, N. Fukuda, H. Sakurai, A. Yoshida, Y. Watanabe, and M. Ishihara

We have developed a MUSIC-type detector system and tested its performance by using beams from the RILAC and AVF cyclotron at RIKEN. We also performed an experiment to measure the ${}^8\text{Li}(\alpha, n){}^{11}\text{B}^*$ reaction at energies of astrophysical interest¹⁾ with RIPS at the RIKEN Ring Cyclotron. Analysis of the data is now in progress.

This detector is based on MUSIC (Multi-Sampling Ionization Chamber)-type detectors,²⁾ which can measure the energy loss along the particle trajectory. A main advantage of the present MUSIC-type detector is the capability of a time-projection chamber (TPC) employing a flash ADC to identify multi-track events. The vertical position is determined by the drift time of the electrons, and the horizontal position is determined by employing a backgammon-type cathode (PADs).³⁾ The other feature is that the gas in the chamber works as both a detection medium and a gas target, resulting in a high detection efficiency. Owing to these features of the MUSIC-type detector, we can measure reactions induced by RI beams with low intensities.

Figure 1 shows a cross-sectional view of the MUSIC-type detector, which consists of a field cage and 64 backgammon-type cathode PAD cells. The field cage has a 70 cm long, 15 cm high, and 20 cm wide active area, and the field wires are wound doubly to obtain a better uniformity of the drift field. To prevent cross talk between adjacent anode wires, three planes of cathode PADs surround the anode wire. Each cathode PAD cell is 1 cm long, 1 cm high, and 20 cm wide.

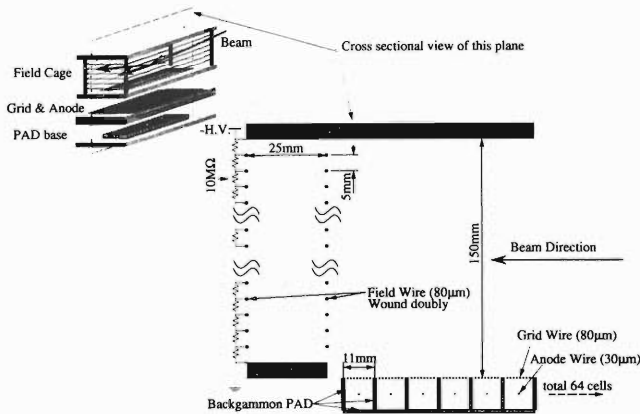


Fig. 1. Cross-sectional view of the MUSIC-type detector. The field wires are wound doubly with a 5 mm pitch.

Figure 2 shows a three-dimensional plot of the averaged energy loss in each PAD for the ${}^8\text{Li}$ beams with various energies. The x-axis represents the time-of-flight of incident ${}^8\text{Li}$ beams. The TOF at 200 nsec equals about 3 MeV/nucleon, and the shorter TOF corresponds to the higher incident energy. The y-axis represents the PAD numbers, which are aligned along the beam direction from upstream to downstream. The width of one PAD is 1.1 cm. The gas ingredients are

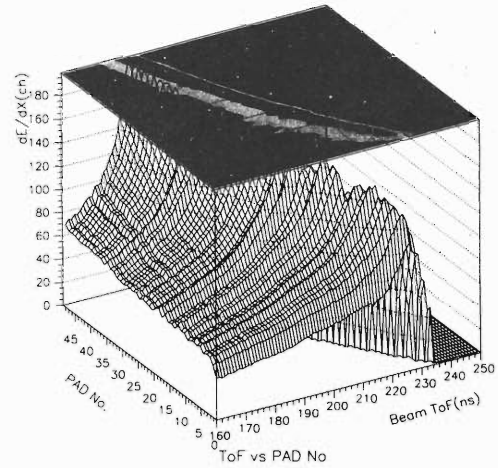


Fig. 2. Bragg curve of ${}^8\text{Li}$.

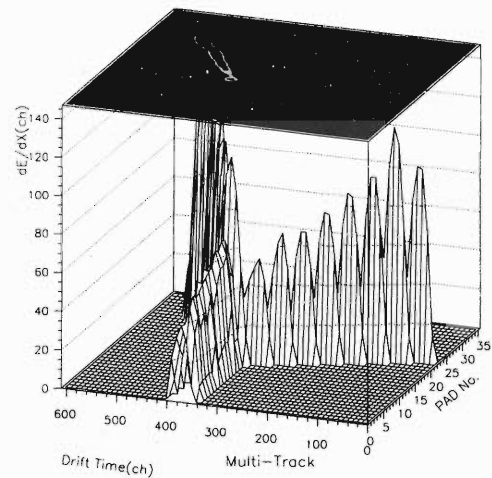


Fig. 3. Typical multi-track event: a candidate for an elastic scattering.

^4He (90%) and iso-butane(10%), and gas pressure is about 400 torr. While this plot clearly shows Bragg curves for various incident energies, higher energy particles go through the detector. A contour plot (Fig. 2) shows an energy-range curve. To select the reaction events, we can use these Bragg curves as a reference. We show two examples of the reaction events which were selected by this method. Figure 3 shows the raw data of flash ADCs of a typical multi-track event. The y-axis represents the drift time of electrons ionized by charged particles under electric field. The drift velocity of the electrons equals about $1 \text{ cm}/\mu\text{sec}$, and the unit of the y-axis equals 25 nsec/channel. This event is a candidate for an elastic event, $^8\text{Li}(\alpha, \alpha)^8\text{Li}$. The right track may be an α particle, because of its long range and lower dE/dX . The left track may be a ^8Li .

Figure 4 shows a typical fusion-like event. The dotted-line histogram is a reference Bragg curve relevant to the beam energy of this event, and the solid-line histogram is a reaction event. This is a candidate for the $^8\text{Li}(\alpha, n)^{11}\text{B}$ reaction because of a sudden change in dE/dX and the very short range. We can guess from kinematics calculations that a ^{11}B may run forward and a neutron may run backward. We have measured not only charged particles but also a neutron in this experiment. We can thus derive further information about the $^8\text{Li}(\alpha, n)^{11}\text{B}^*$ reaction; for example, the branching ratio of the excited states($^{11}\text{B}^*$) as well as the ground state of ^{11}B , by performing fur-

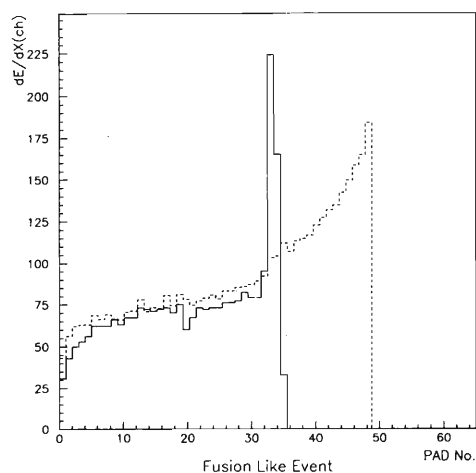


Fig. 4. Typical fusion-like event: a candidate for $^8\text{Li}(\alpha, n)^{11}\text{B}$ reaction. Dotted line is a Bragg curve for reference and solid line is a reaction event.

ther analyses.

References

- 1) X. Gu et al.: Phys. Lett. B **343**, 31 (1995).
- 2) K. Kimura et al.: Nucl. Instrum. Methods Phys. Res. A **297**, 190 (1990).
- 3) R. Allemand et al.: Nucl. Instrum. Methods **137**, 141 (1976).

Toroidal Spectrometer for Measurement of Emitted Electron Spectra Arising from Collisions between Highly Charged Ions and Neutral Atoms

Y. Tamagawa, D. Chiba, T. Takayanagi, K. Wakiya, Y. Kanai,
T. Kambara, and Y. Awaya

We have constructed a toroidal-mirror-type electron energy analyzer¹⁾ which can measure electron spectra arising from the collisions between highly-charged ions and neutral atoms. An eminent character of this analyzer is the capability to measure the angular distribution of emitted electrons without a moving part.

Figure 1 shows a sketch of the apparatus. The wall radius and the toroidal (axis) radius of the analyzer are 104 mm and 136.8 mm, respectively. The ion (or electron) beam passes through the target region perpendicular to this figure. Electrons ejected from the target region are energy-analyzed by the toroidal prism and focused on the position-sensitive detector indicated as MCP. A TOF recoil ion analyzer is set inside to study their charge states.

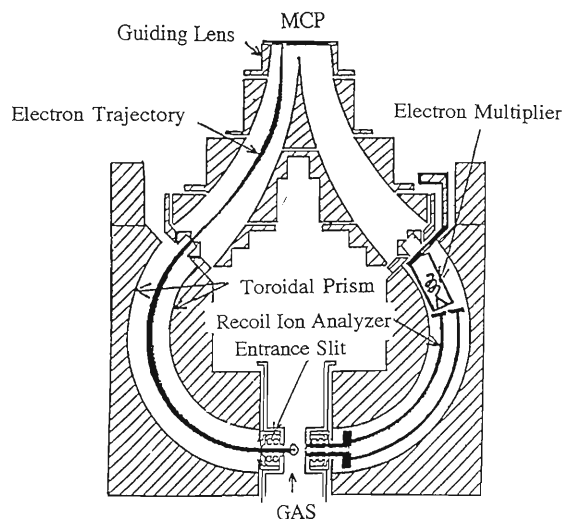


Fig. 1. A sketch of the toroidal analyzer. Distance from the center axis of toroid to the entrance slit is 32.8 mm. Spacing between the inner and outer electrodes of the analyzer is 40 mm.

As a test of the apparatus, we have measured elastic e-Ar scattering at an electron energy of 100 eV in an angular range of 20–120 degrees (See, Fig. 2). At this stage, we used the channel electron multiplier (CEM) instead of the position-sensitive MCP detector, and have not set the recoil ion analyzer yet. In present setup, the angular distribution of the scattered electrons was measured by rotating the CEM. In Fig. 2, our result is compared with that of Srivastava et al.²⁾ We have measured only a relative distribution of elas-

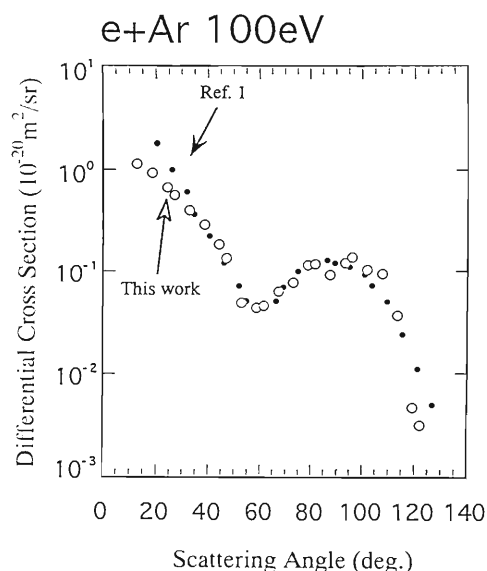


Fig. 2. The double differential cross section for the elastic scattering of 100 eV electrons by Ar. Open circles: present results, closed circles: Ref. 1.

tic scattering and normalized our data to the referred data at 90 degrees. Our result agrees well with that of Srivastava et al. except below 30 degrees. This demonstrates that our analyzer can measure the angular distribution of the emitted electrons from ion-atom collisions for a wide angular range (30–140 degrees with respect to the beam direction).

In March of 1996, we set our analyzer at the beam line of RIKEN 14.5 GHz ECR ion source (Caprice), and have tried to measure the Auger electrons from the N^{4+} ($1s^23l\ 3l'$) produced by the collisions of 50 keV N^{5+} on Ar. At that time, we could not get a clear spectrum of those Auger electrons, because of a large background noise. The background signals are considered as the low energy electrons produced near the collision region. To reduce the background noise, we are currently trying to improve our analyzer and beam transport systems.

References

- 1) H. A. Engelhardt, W. Back, and D. Menzel: *Rev. Sci. Instrum.* **52**, 835 (1981).
- 2) S. K. Srivastava, H. Tanaka, A. Chutjian, and S. Trajmar: *Phys. Rev. A* **23**, 2156 (1981).

Mounting of a CCD Detector on the Rowland Circle of a Grazing-Incidence Spectrometer for Use in Beam-Foil Spectroscopy

R. Hutton, S. Huldt, I. Martinson, Y. Zou, K. Ando, T. Kambara, and Y. Awaya

A back illuminated CCD detector has been tested on a 2.2 meter McPherson/Nikon grazing incidence spectrometer. This spectrometer is used in beam-foil spectroscopy experiments at RIKEN. The geometry of the grazing-incidence mounting would require the CCD chip to be positioned with a high angle of incidence with respect to the incoming analyzed photons. However, this would present 2 practical problems; (a) the CCD chip would reflect a high percentage of the incoming photons and (b) the chip dead layer would be effectively enlarged at such high angle α by $1/\cos(\alpha)$. For these reasons the CCD chip was positioned normal to the incoming photons. This alleviates the 2 above problems, but introduces imaging problems either side of the CCD chip center. These imaging problems were investigated using geometrical arguments and also by imaging light from a vacuum spark source. The grazing-incident geometry is shown in Fig. 1.

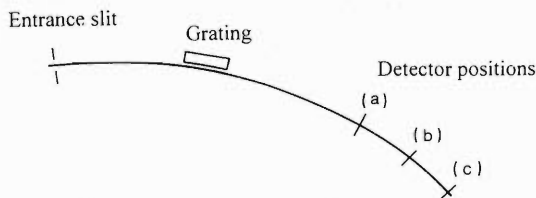


Fig. 1. Schematic diagram of the grazing-incidence geometry.

The results of the spark spectra are summarized in Figs. 2a, b, and c. Two strong lines are seen from the spark. These are Ne-like Al lines, namely the $2p^6 - 2p^5 3s$ resonance and intercombination lines at 160.07 and 161.69 Å, respectively. Figure 2b shows

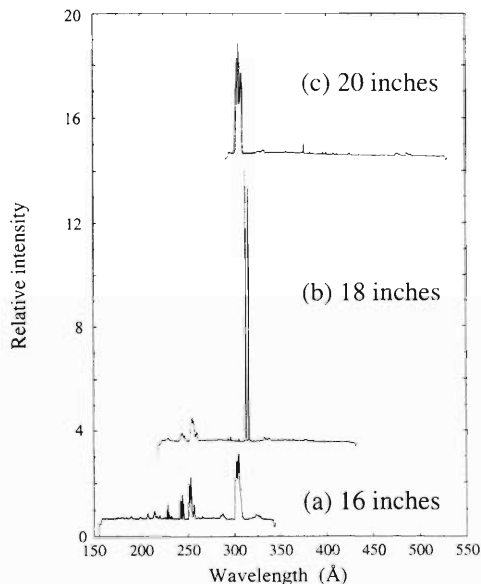


Fig. 2. Spectra recorded at various positions around the Rowland circle of a 2.2 meter grazing incidence spectrometer (i.e. 16, 18, and 20 inches). The 2 strong lines seen at the center of the CCD chip recorded at the 18 inch position are separated by 1.6 Å. The imaging is seen to degenerate as the lines move away from the center of the chip.

data recorded with the CCD center placed at 18 inches along the Rowland circle. Here, the 2 lines are almost centered on the CCD chip and the resolution is seen to be good. The other 2 images are taken at 16 and 20 inches (2a and 2c respectively) around the Rowland circle. Here, the imaging is acceptable for lower resolution beam-foil work.

Proton Beam Test of Cosmic Ray Telescope for the First Brazilian Scientific Satellite

T. Kohno, H. Kato, and K. Nagata

We are promoting a joint collaboration program¹⁾ of cosmic ray observation with USA group and Brazilian group, aboarding instrumentation on the first Brazilian scientific microsatellite. Our main objective of this observation is heavy ions of the solar and anomalous cosmic rays. For this purpose, we designed a telescope with a large geometric factor ($2.5 \text{ cm}^2 \cdot \text{sr}$) since the flux of these heavy ions is very low in comparison with protons and electrons in space. The heavy ion beam test of this telescope named MAIN by RIKEN Ring Cyclotron was performed in 1995.²⁾ The protons and electrons have been widely observed so far. But, their fluxes at the district near Brazil are not yet measured correctly due to its extraordinary high intensity. This phenomenon arises from the anomalously weak geomagnetic field of that area called South Atlantic Anomaly (SAA). The above described MAIN telescope is not favorable for the observation of protons and electrons at SAA since the counting rate would rapidly saturate due to its large geometric factor and the very high intensity. Therefore, we have designed a dedicated small telescope (we call it PRE) with very small geometric factor ($5 \times 10^{-3} \text{ cm}^2 \cdot \text{sr}$) for the purpose to observe protons, electrons, and alphas in the SAA region. The basic design of this PRE telescope is shown in Fig. 1.

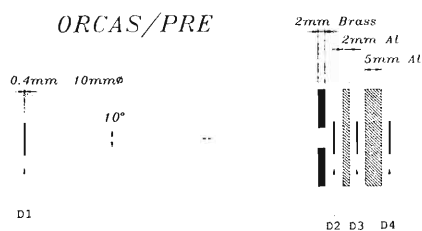


Fig. 1. Cross sectional view of the telescope. Each detector consists of two PIN diodes with thickness of 200 micron.

In order to observe a wide energy region, we used aluminum absorbers in between D2 and D3, D3, and D4. The response curves of this telescope for protons is shown in Fig. 2. Using many discriminators having various levels we can obtain counting rates of fixed energy ranges with four channels for electrons, five channels for protons, and four channels for alphas. As seen from Fig. 2, the observable energy range is from 3 MeV to 60 MeV for protons. However, we used 70 MeV proton beam, which is the lowest energy available at Riken Ring Cyclotron, for the first calibration experiment of the telescope.

The main purpose of this first calibration experiment was to check the response of each detector to the beam at various energy levels. The beam was injected from

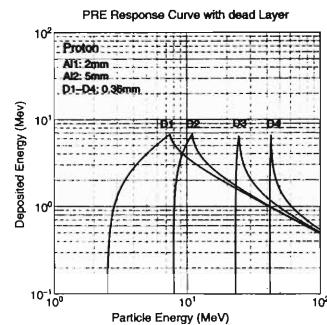


Fig. 2. Response curves of the telescope for protons. Vertical incidence is assumed. The nominal thickness of each detector is 400 micron, but it contains a dead layer having 40 micron thickness.

left hand side in Fig. 1 and we took pulseheight analysis data for each detector. In order to take data for various input energies, we used Al absorbers in front of D1 with various thicknesses as an energy degrader. We plotted the observed peak energy and calculated energy deposition in the detector vs. Al absorber thickness (Fig. 3).

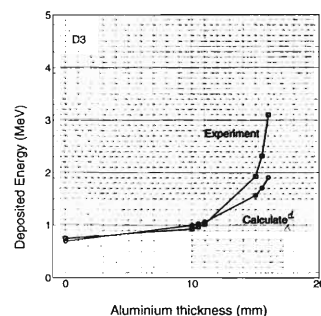


Fig. 3. Experimentally observed peak energies and calculated energies deposited in D3 vs. thicknesses of the Al absorber.

Agreement of the two values is good for the thin absorbers, but discrepancy increases at thick absorber region. Specially, at the very point where the range of proton beam is nearly same as the physical length of absorber, a slight error in the detector or absorber thicknesses can produce some amount of residual energy after the absorber. But this is not a so serious problem for the real observation because its probability is rather low.

References

- 1) T. Kohno et al.: RIKEN Accel. Prog. Rep. **28**, 132 (1995).
- 2) T. Kohno et al.: RIKEN Accel. Prog. Rep. **29**, 189 (1996).

Development of a Liquid Argon Ionization Chamber with Excellent Energy Resolution for High Energy Heavy Ions

A. Yunoki, T. Doke, M. Kase, T. Kato, J. Kikuchi, K. Masuda,
M. Niimura, Y. Piao, E. Shibamura, and I. Tanihata

An experiment was carried out for estimation of the energy resolution of the detector which was constructed for measuring the precise energy of heavy ion particles at the beam energy (E_b) around 100 MeV/nucleon.

The detector medium was liquid argon doped with 80 ppm allene (C_3H_4). Allene is a photosensitive molecule, which can be photoionized by absorbing a VUV photon emitted from argon. A high-energy particle passing through the liquid argon produces many electron-ion pairs and excitons along the particle track. Electrons can be collected to the anode by applying an electric field (E). Excitons and neutralized ions become self-trapped molecules to emit VUV photons. The VUV photons are absorbed by the allene molecules to be photoionized, and the resultant electrons are also collected to the same anode. Consequently, more numbers of electrons can be collected and a better energy resolution can be obtained in the allene-doped liquid argon than in the pure liquid argon.¹⁾ Hitachi et al.²⁾ measured the energy resolution (FWHM) in the allene-doped liquid argon to obtain 0.37% for 33.5 MeV/nucleon ^{18}O and 0.57% for 31.9 MeV/nucleon ^{36}Ar .

Recently, it is required to measure the precise energy of heavy ions at around 100 MeV/nucleon. So, we have developed a gridded ionization chamber suitable for this requirement. Figure 1 shows the chamber and its cryostat. The beam window of the chamber is made of 48 mm \times 48 mm Havar foil with thickness of 130 mg/cm², which works at the same time as a cathode electrode. A screen grid consists of 10 μ m ϕ tungsten wires soldered to the frame with 150 μ m pitch. An anode electrode is a stainless steel plate connected to hermetic feedthroughs, which are connected to a high-voltage (HV) module and to a preamplifier through a coupling capacitor. A distance from the cathode to grid is 40 mm, longer than the range of the high-energy ions to be measured. Shielding inefficiency of the screen grid is <1%, which is negligible in measuring the energy resolution but might cause a little disturbance in the linearity of pulse heights against the particle energies.

The gridded ionization chamber is fixed inside of a stainless-steel vacuum vessel for the thermal insulation. The outside of the chamber is surrounded by about four layers of superinsulators. To keep the chamber at a low temperature, liquid argon at the upper

part of the stainless-steel vessel is utilized as a coolant.

Argon and allene gas were purified through preconditioned molecular sieves at liquid oxygen temperature. They were condensed into the chamber. The measurement started over 30 hours after the liquefaction.

The charge signal from the anode was fed into a linear amplifier (ORTEC 450) through a charge-sensitive preamplifier. The shaping time constant of the linear amplifier is 10 μ s to ensure the entire charge collection.

Figure 2 shows the energy spectrum for 94 MeV/nucleon ^{40}Ca experimentally observed. The energy resolution was obtained by subtracting in quadrature the width of test pulses from that of the charge signal. At $E = 2.5$ kV/cm, the energy resolution was 0.6% (FWHM). The fraction of collected charge was 27% of the total charge produced.

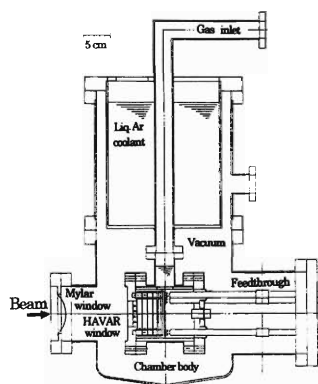


Fig. 1. Cross sectional view of experimental apparatus.

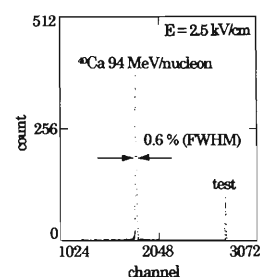


Fig. 2. Experimental energy spectrum obtained with detector of Fig. 1.

Contribution of the fluctuation of energy loss into the windows to the energy resolution was estimated to be 0.26% (FWHM). The experimental result was worse than this estimation by a factor of 2. Further study is needed to understand and improve the limitation of the energy resolution.

References

- 1) S. Suzuki: Ph. D. thesis, Waseda University, 1986.
- 2) A. Hitachi et al.: Nucl. Instrum. Methods Phys. Res. A **340**, 546 (1994).
- 3) K. Masuda et al.: Nucl. Instrum. Methods Phys. Res. A **279**, 560 (1989).

Collinear Laser Spectroscopy of Li-like ^{11}B Beam

S. Ozawa, M. Hies, N. Inabe, T. Katayama, T. Kubo, H. Okuno, I. Tanihata,
M. Wakasugi, Y. Watanabe, Y. Yano, and A. Yoshida

A new on-line laser spectroscopy system for the highly-charged and high-energy ion beam is now in development to study systematically the nuclear charge radii of unstable isotopes. In order to test the system, we measured D1 transition of Li-like $^{11}\text{B}^{2+}$ ion (primary beam) with the beam energy of 15 MeV/nucleon.

Figure 1 shows the experimental setup. The laser pulse having the repetition rate of 100Hz is synchronized with the ion beam to collide each other at the interaction region. The RF signal of the cyclotron is used as a trigger of the laser. The $^{11}\text{B}^{2+}$ ions are excited by the laser from the ground state $2S_{1/2}$ to the excited state $2P_{1/2}$. The D1 transition energy is 48358.5 cm^{-1} ($\lambda = 207\text{ nm}$),¹⁾ and the laser wavelength is required to be 247 nm because of the Doppler shift. The laser beam is provided with a pulsed dye laser excited by an excimer laser and a second harmonic generator. After the interaction, the excited ions are separated from the laser beam line using a bending magnet. A fluorescence photon detector, which consists of twelve photomultipliers (PM) and two cylindrical mirrors, is put on the ion beam line behind the magnet to suppress a huge noise from the laser. The time of flight from the interaction region to the detector is about 40 ns. Before measurement, the spatial overlapping between the laser and the ion beam is checked using two viewers made of ZnS, and the time overlapping is also checked with a plastic scintillator (PL1).

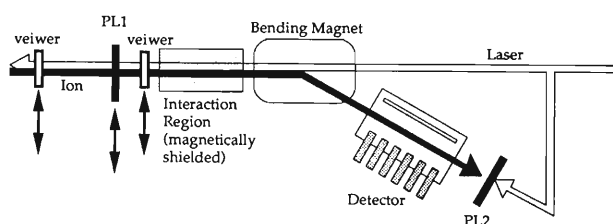


Fig. 1. Experimental setup.

The fluorescence photon counts normalized by the ion beam intensity are plotted in Fig. 2. Resonance peaks are clearly observed. By making a least square fitting to the data with Lorentz function, the center of gravity of the spectrum line is derived to be 247.489(8) nm. Using the velocity of the ion $\beta = 0.1779(8)$ measured with dipole magnets of RIPS, the transition energy is obtained to be $48365(24)\text{ cm}^{-1}$. This is in agreement with NBS value.¹⁾ Because of an ambiguity of the β value, the present accuracy is not enough to measure the isotope shift. To suppress the ambiguity,

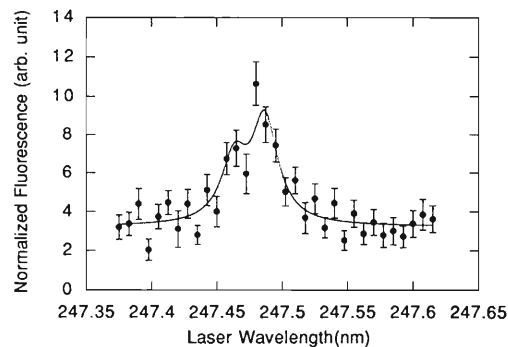


Fig. 2. Fluorescence spectrum of D1 transition. The solid curve shows the fitted line shape including hyperfine components.

ity, the measurement should be made using two lasers propagating parallel and antiparallel to the ion beam. Then, the accuracy of the result should be sufficient for the isotope shift measuring.

Since PMs are put along the beam line, the decay curve of the $2P_{1/2}$ state is measured as shown in Fig. 3. The life time is estimated to be 9(2) ns. The error is estimated without the systematic error.

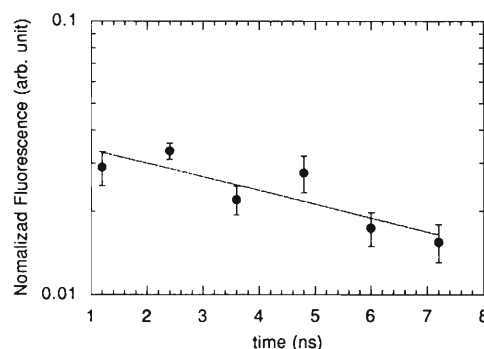


Fig. 3. Decay curve of the $2P_{1/2}$ state.

The detection efficiency of the present system is $8.1(8) \times 10^{-8}$. The improvement of the $2P_{1/2}$ state at the detector is the easiest way to get a higher detection efficiency. Thus, we are now constructing a new detection system that is put just after the interaction region.

References

- 1) C. E. Moor: in *Atomic Energy Levels* (NBS, Washington D.C. 1949), p. 19.

Development of an On-Line Laser Ion Source

T. Ariga, M. G. Hies, T. T. Inamura, T. Ishizuka, W.-G. Jin,
K. Morita, T. Murayama, Y. Pu, and M. Wakasugi

An on-line laser ion source to employ a resonance ionization scheme has been developed at RIKEN GARIS/IGISOL facility to investigate the nuclear charge radii and electromagnetic moments of unstable nuclei in the refractory element region.^{1,2)}

The ion source was tested for the short lived isotopes $^{161-157}\text{Hf}$ produced with the $^{nat}\text{Sn} (^{48}\text{Ti}, xn)$ reaction using a 7.6-MeV/nucleon ^{48}Ti beam from RIKEN Ring Cyclotron.³⁾ These Hf isotopes are α -emitters. A target of natural Sn was used and the target thickness was 1.0 mg/cm^2 . This target was put at the entrance of the gas-filled recoil isotope separator (GARIS). To estimate the number of produced Hf isotopes, the ^{48}Ti ions elastically scattered from the Sn target were monitored. The Hf isotopes were collected at the ion guide isotope separation on-line (IGISOL) gas cell with the GARIS. The Hf isotopes are thermalized and neutralized in the gas cell filled with a buffer gas of He and Ar. The typical gas pressures were 150 Torr for He and 120 Torr for Ar.

The Hf atoms are selectively ionized by a two-step ionization process using two-color lasers as shown in Fig. 1, and are extracted together with the gas flow. The wavelengths of lasers are 368.195 nm for the first step (laser 1), and 357.408 nm for the second step (laser 2). The wavelength of the laser 2 is fixed, while that of the laser 1 is scanned to find out the resonance wavelength of unstable Hf isotopes.

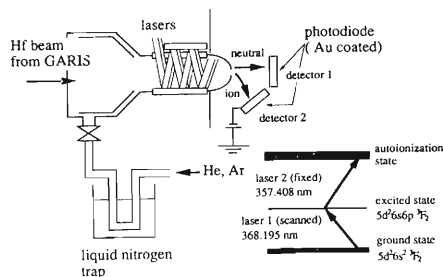


Fig. 1. Experimental setup and the resonance ionization scheme of Hf isotopes.

To prevent chemical reactions caused by the impurities in the buffer gas, highly purified gas (over 99.9999%) was used, and a liquid nitrogen trap was used to remove water in the gas line. To measure the α -decay of Hf isotopes, two photodiodes ($10 \times 10 \text{ mm}^2$) were put in front of the nozzle of the gas cell (Fig. 1). The detector 1 was put on the beam axis, whereas the detector 2 was put off axis, and a negative voltage (-40 V) was applied in order to catch only the ionized Hf isotopes.

A measured α -spectrum in the gas cell is shown in

Fig. 2. If the wavelength of laser 1 is on resonance, the intensities of the α -peaks of Hf at detector 2 are enhanced. The measurement of the α -spectrum is repeated by changing the laser wavelength. In Fig. 3, the count rate of α -particles emitted from ionized Hf isotopes, which is measured with the detector 2, is shown as a function of the laser wavelength. The count rate are normalized with the monitor counts of elastic scattering of ^{48}Ti beam. The deviation of the resonance wavelength for the unstable Hf isotopes from that for the stable isotopes is expected to be around -0.007 nm . A small enhancement is observable near -0.005 nm , but not clear because of the poor count rate.

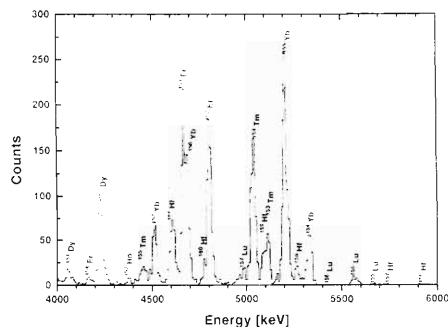


Fig. 2. The α -spectrum measured in the gas cell.

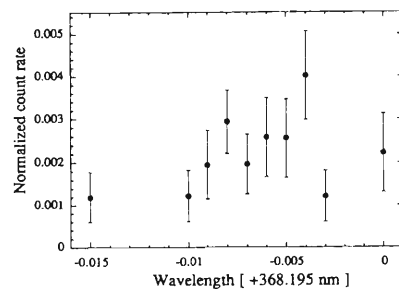


Fig. 3. The resonance ionization spectrum for $^{161-157}\text{Hf}$ isotopes.

In the present experiment, the enhancement of the yield of the α -decay of Hf isotopes due to laser resonance ionization is much smaller than that in the cases of off-line test experiment.¹⁾ It seems that the purification of the buffer gas was insufficient; a small amount of O_2 may still be contained in the buffer gas. In the future, the gas purifier system shall be improved in order to increase the yield.

References

- 1) M. Hies et al.: RIKEN Accel. Prog. Rep. **29**, 177 (1996).
- 2) M. Hies et al.: RIKEN Accel. Prog. Rep. **29**, 198 (1996).
- 3) M. Hies et al.: RIKEN Accel. Prog. Rep. **29**, 46 (1996).

Completion of Tritium Gas Handling System for Muon Catalyzed Fusion Experiment at RIKEN-RAL Muon Facility

T. Matsuzaki, K. Nagamine, K. Ishida, S. N. Nakamura, I. Watanabe, M. Kato, K. Kurosawa, M. Hashimoto, and M. Tanase

We have completed a tritium gas handling system (TGHS) for the muon catalyzed fusion (μ CF) experiment at RIKEN Muon Facility of Rutherford Appleton Laboratory (RAL) in U.K. This system enables us, at the experimental site, to purify the target gas by removing ^3He component, to change the D/T mixing ratio, and to measure hydrogen isotope components, in the target gas.

Detailed description of the system was given in Refs. 1 and 2.

The RAL staffs were called to Japan during the factory test to confirm the safe operation of TGHS before its transportation to U.K. The TGHS installation including various tests and inspections, a tertiary house construction as the third container of the target gas, and the interlock system assembly were completed at RAL in December 1995.

The tritium gas for the μ CF experiment has been produced, enriched, and filled in gas cylinders at JAERI. Two cylinders, containing 700 Ci (26 TBq) tritium gas in each, were transported and installed in the TGHS at RAL in January 1996.

Gas operation procedure of the TGHS was simulated by using deuterium gas. Then, a small quantity of tritium gas (14 Ci or 0.5 TBq) was introduced to repeat all the operations including the gas analysis procedure to assure the safety. After some modification of the system together with a titanium-getter's performance test at RAL, a tritium gas of 100 Ci (3.7 TBq) was introduced further to the system to prove the safety during the gas operation in May 1996. Finally, tritium gas was added up to 700 Ci (26 TBq) to confirm the safety operation again, and then the μ CF experiment with 28% tritium concentration was commenced in June 1996, where the total D/T gas quantity was about 950 ml.

The schematic diagram of TGHS displayed on screen of the control computer is shown in Fig. 1. The D/T target-gas purification was performed in every five days approximately during the experiment according to the following procedure, where the D/T gas was liquefied in the target.

1. Target warm-up and the D/T gas vaporization to buffer tank.

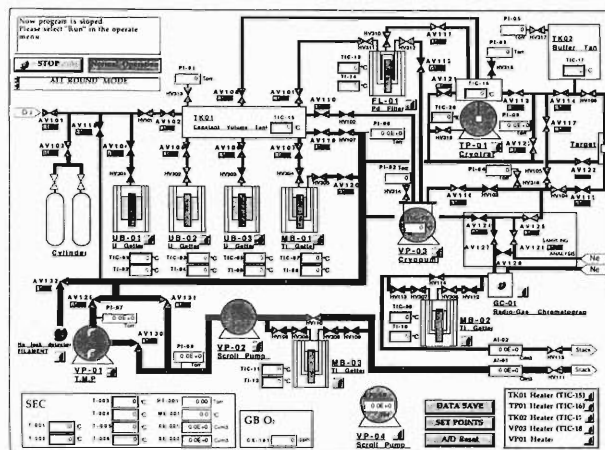


Fig. 1. Schematic diagram of the TGHS.

2. The D/T gas collection to an uranium getter at room temperature.
3. Recovery of residual gas in the system to cryopump.
4. System evacuation by turbo molecular pump and scroll pump.
5. The D/T gas release to constant volume from the uranium getter by heating.
6. Gas purification by passing the D/T gas through Pd-filter to cryotrap.
7. The D/T gas liquefaction in the target by cooling.

The gas quantity was calculated by PVT method, where P, V, and T are pressure, volume, and temperature, respectively. The tritium-release to stack during the system evacuation was monitored by an ion-chamber (AI01) in the exhaust line.

The μ CF experiment with 28% tritium concentration has been conducted and some results are reported in present volume.

References

- 1) T. Matsuzaki et al.: RIKEN Accel. Prog. Rep. **28**, 134 (1995).
- 2) T. Matsuzaki et al.: RIKEN Accel. Prog. Rep. **29**, 194 (1996).

Compact CAMAC Data Acquisition System with ACC K3976 and PC-Linux

S. N. Nakamura and M. Iwasaki*

We have developed a CAMAC data acquisition system (*EXP95*) with ACC K3976 and workstation (DEC AXP200-4/166) at RIKEN-RAL Muon Facility.¹⁾ This data acquisition system (DAQ system) had following characteristics:

- Data acquisition and on-line analysis are performed by two computers (ACC and a host computer), and heavy duty of on-line analysis on the host computer will not disturb data acquisition.
- It is especially suitable for pulsed beam facility, because the data transfer from ACC to the host computer can be carried out during the spill off cycle.
- Acquired data quality can be monitored from a remote station via network.
- Off-line analysis can be performed by the same software which is used for the on-line analysis.
- Commands to DAQ system can be given from a user-friendly graphical interface.

The *EXP95* DAQ system is compact and highly flexible but the workstation is still too expensive (a few million yen) to use for just test or very simple experiments. Recently, performance of the personal computers (PCs) increased rapidly and multi-user, multi-task operating systems (*e.g.*, PC-UNIX) became available. Practically, there is no large difference in performances between workstations (WSs) and PCs, even though PC is one order less expensive than WS. Therefore, we de-

signed a compact CAMAC DAQ system (*EXP96*) for PC with all advantages of *EXP95*. We chose Linux as the operating system (OS) of PC. Linux is a freely distributable implementation of UNIX for Intel 80X86 machines (Recently, Linux project supports other platforms as DEC-Alpha and SUN-sparc). It is very stable OS, and X window system is also available (XFree86 and Accelerated X). Most of CERN Library including PAW++ has been already ported to Linux and furthermore software developing environment is also well prepared.

1) Hardware Configuration

Hardware configuration is exactly the same as *EXP95*, except that WS was replaced by PC. The system consists of two computers: One is a CAMAC Auxiliary Crate Controller (ACC: Kinetics K3976) with MC68030 40MHz CPU and 1MB memory (upgradable to 4MB). The ACC concentrates on data collection from CAMAC modules, and the acquired data are transferred to PC via CAMAC-SCSI interface (Kinetics K3929). CAMAC DAQ part was not changed from *EXP95* and its ability is the same. Typically, one CAMAC word data acquisition takes 1.6 μ sec.

In present paper, PC means so-called AT clone which is supported by Linux. Detail of the required PC specifications can be found in Ref. 2. There are many options of hardware for AT clone, but the selections of SCSI interface board and video card are crucial. Table 1 shows hardware specifications of our PC on which *EXP96* has been developed.

Table 1. Hardware configuration of the PCs used for development.

	PC 1	PC 2
CPU	Intel Pentium 100MHz	Pentium-Pro 200MHz
Memory	32 MB	32 MB
Hard Disk	EIDE 1GB, SCSI 1GB	EIDE 2GB, SCSI 2GB
SCSI Interface	BT-946C	AHA-2940
Video Card	Number Nine Motion 771	Matrox Millennium

CPU power and DAQ performance have no direct relation since the ACC collects data from CAMAC modules. Even 80486 CPU can be used for *EXP96*, however, more powerful CPU is desirable for quick response in on-line analysis. Memory should be more important than CPU power. In order to use X window system, 16MB RAM is prerequisite. As a DAQ host computer, 32MB or more is preferable. We used

an EIDE harddisk as well as a SCSI harddisk during development, because a bug of the software related to the SCSI device driver disabled us to access SCSI harddisk. We believe that there is no more serious bug and one SCSI harddisk should be enough for now. Any SCSI interface card on the Linux supporting list is usable. However, it should be noted that the performance of SCSI interface has direct relation to data transfer rate from ACC to PC. The *EXP96* requires X window system and the video card should be supported

* Meson Science Laboratory, Faculty of Science, University of Tokyo

by XFree86 (free port of MIT X Window System for 80X86) or by Accelerated X (commercial X Window System for 80X86).

2) Software Configuration (See, Fig. 1)

On ACC K3976, the program which manages CAMAC functions is running. This program is written by MC68030 assembly language. Cross 68030 assembler was written by Fortran and compiled with f2c+gcc on PC. A user can easily write CAMAC commands sequence using macro library without any knowledge on MC68030 CPU. This ACC machine code has 100% compatibility between *EXP96* and *EXP95*.

On the host PC, several processes are running on Linux to receive data from ACC. Main programs of *EXP96* are written from scratch by C, not using the code from *EXP95* written in Fortran. The CAMAC function driver uses a generic SCSI device driver (a part of Linux kernel) and it does not depend on a particular hardware. Therefore, any SCSI interface board can be used if it is supported by Linux kernel. It should be noted that even PCMCIA SCSI interface card can be used for *EXP96* and thus even laptop PC can serve as the host computer.

On-line and off-line analysis were performed by PAW++ software developed at CERN.³⁾ Stored data can be analyzed after the experiment with the same software used for the on-line analysis. The off-line analysis can be performed on PC as well as WS.

The graphical user interface was constructed on X-Window system with Tcl/Tk and the same look-and-feel was realized between *EXP95* and *EXP96*.

3) Performance Test

ACC can acquire one CAMAC word data per 1.6 μ sec

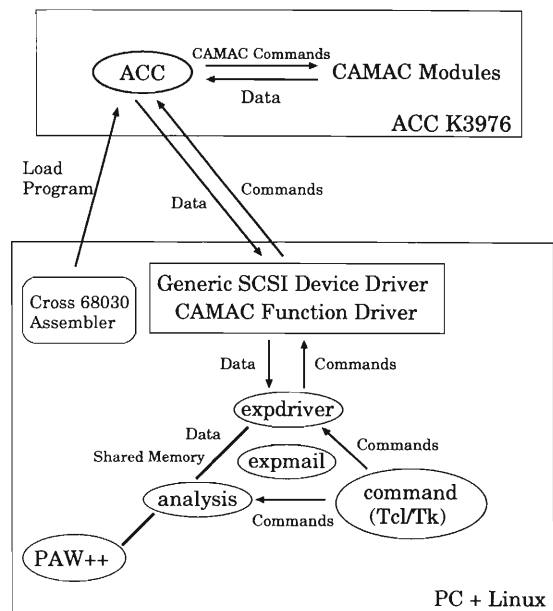


Fig. 1. Three processes (*expdriver*, *analysis* and *command*) run on the host PC communicating with each other by *expmail* process which uses UNIX message. Acquired data by the ACC are transferred to PC via generic SCSI device driver and stored on a hard disk by *expdriver*. These data are shared with *analysis* using UNIX shared memory function and some of them are analyzed and passed to it PAW++.

and it does not depend on the host computer. Contrarily, SCSI data transfer rate depends on the hardware. Three different computers, DEC AXP200-4/166 (WS), Pentium 100MHz (PC), and Pentium-Pro 200 MHz (PC) were tested.

Computer	OS	SCSI Interface	Block Transfer Rate (kB/sec)
DEC AXP200-4/166MHz	OVMS 6.1H2	Originally equipped	750
Pentium 100MHz	Linux 2.0.0	BT-946C (ISA)	790
Pentium-Pro 200MHz	Linux 2.0.0	AHA-2940 (PCI)	912

As seen in the table, PC performance is better than WS against our expectation. Linux is much smaller and lighter OS than Open VMS, and thus it might have better performance for low-level I/O accesses. In addition, a new SCSI card (*e.g.*, AHA-2940) with better performance will be supported quickly by Linux because it is improved constantly.

We developed a compact CAMAC DAQ system with ACC and PC + Linux. This DAQ system inherits all advantages of the workstation version, and shows better performance even though PC is one order less expensive than workstation. PC will be useful as a part

of DAQ system for the medium and small experiments with the best cost performance.

References

- 1) S. N. Nakamura and M. Iwasaki: RIKEN Accel. Prog. Rep. **29**, 192 (1996); Nucl. Instrum. Methods Phys. Res. in press.
- 2) FRiC: Linux Hardware Compatibility HOWTO, <http://sunsite.unc.edu/mdw>.
- 3) CERN Application Software Group: CERN Program Library **Q121**, (1995).

Evaluation of UNIX DAQ System (UNIDAQ) on VME

Y. Watanabe, H. Kobinata,* Y. Mizoi, Y. Watanabe, A. Yoshida,
T. Miyachi, T. Fukuda, M. Notani, and M. Ishihara

We are now developing a MUSIC-type detector¹⁾ in order to research fusion reactions with unstable nuclei. The UNIX DAQ (Data AcQuisition) system on a VME (Versa Module Europa) board computer was introduced to deal with a large amount of data at a high-speed, and its ability was evaluated.

Our MUSIC-type detector²⁾ measures the drift time and the energy loss of incident charged particles. This makes it possible to locate the particles in the three dimensional space so that their plural tracks can be detected at the same time.

For that purpose, we employ Flash-ADC TKO (TRISTAN/KEK Online system) modules which read out pulse signals from the cathode pads as a time series data. A single Flash-ADC module contains eight Flash-ADC channels and each one will sample the pulse shape every 25 ns during 25.6 μ s. The dynamic range of the Flash-ADC is 8 bits. We use 128 Flash-ADC channels and the TKO crate controller, SCH, extends 8 bits data to 32 bits data, so the total data size of all Flash-ADC's is 512 kbytes per event. Although SCH has the ability to suppress the data beneath a certain threshold and hence to reduce the total size of data (threshold suppression), the total data size was yet too large. We have thus introduced TKO-VME DAQ system to deal with these enormous data swiftly. The TKO interface of VME, SMP, has two buffers. The data from TKO is stored on one buffer; another buffer is accessed through the VME dataway. They are able to be swapped. Thus, simultaneous two data transfers make the data acquisition rate enhance. The SMP is controlled by the UNIX DAQ system, UNIDAQ,³⁾ which runs on the HP743rt/HP-RT v2.02 board computer placed in a VME module. Figure 1 illustrates a schematic of the UNIX DAQ system. The workstation, HP-UX v9.05, controls the DAQ system and analyzes data.

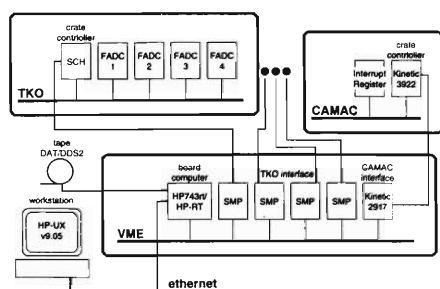


Fig. 1. A schematic illustrating the UNIX DAQ system.

* Micro-Fabrication Process Dev. Lab., ULSI Device Development Laboratories, NEC Corporation

The UNIDAQ contains three computer processes: collector, recorder, and analyzer. The collector process and the recorder process run on the HP-RT board computer. The analyzer process runs on the HP-UX workstation. The collector process fetches data from the CAMAC and TKO modules; the recorder process writes down the data on the DAT (Digital Audio Tape); and the analyzer process analyzes them.

We evaluated the data acquisition rate using only four units of Flash-ADC modules with random pulse triggers.⁴⁾ The only half size of the data (12.8 μ s) was read from each Flash-ADC for the evaluation. Figure 2 shows the time required by each stage of the data acquisition. From Fig. 2 we can expect the data acquisition rate without (with) the DAT to be 90 cps (17 cps). The measured data acquisition rates are shown in Table 1, and they were only slightly smaller than the expectation values. In the present circumstances, the threshold value of the threshold suppression was zero and the total data size was about 24 kbytes. So, the data transfer rate without the DAT is 1.8 Mbytes/sec. Adjustment of the threshold value and the adoption of a high-speed data storage device may improve the data acquisition rate.

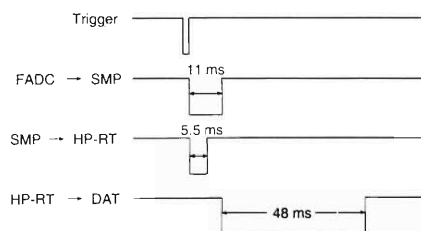


Fig. 2. Time required by each stage of the data acquisition.

Table 1. Data acquisition rate by four units of Flash-ADC modules. Only half size of the data was read from each Flash-ADC for the evaluation. The data size of one event was compressed from 64 kbytes into about 24 kbytes by the threshold suppression.

	w/o DAT	w/ DAT
Expectation	90 cps	17 cps
Measurement	75 cps (1.8 Mbytes/sec)	15.5 cps (0.4 Mbytes/sec)

References

- 1) K. Kimura et al.: Nucl. Instrum. Methods Phys. Res. A **297**, 190 (1990).
- 2) Y. Mizoi et al.: RIKEN Accel. Prog. Rep. **30**, 143 (1997).
- 3) Unidaq Documentation Set, SDC-93-478, Superconducting Super Collider Laboratory (1993).
- 4) H. Kobinata: Master's thesis, University of Tokyo, 1996.

Computing Environment around the Accelerator Research Facility

T. Ichihara, Y. Watanabe, and A. Yoshida

In this report, we describe the recent update and improvement of the computing environment around the RIKEN Accelerator Research Facility (RARF). The updates of the computers in this year are indicated by the underline. General description of the data acquisition system at the RARF can be found elsewhere.¹⁾

(1) On-line data acquisition system

Currently, seven VAX's are used for CAMAC-based on-line experiments at the RARF. The node names and locations are as follows:

<u>GALIS::</u>	<u>Alpha station (B2F E1)</u>
<u>GALISF::</u>	<u>VAX 4000/106A(B2F E1)</u>
<u>SMART::</u>	<u>Alpha Station (B2F E4)</u>
<u>SMARTF::</u>	<u>VAX 4000/106A(B2F E4)</u>
RIPSVX::	VAX 4000 (B2F RIPS)
RIKMOV1::	Micro VAX II (1F)
RIKMOV2::	Micro VAX II (B2F E3)
RIKMOV3::	Micro VAX II (Linac)
RIKMOV4::	Micro VAX II (B2F E6)

Two new VAX 4000/106A computers (GALISF::, SMARTF::) were installed for data acquisitions, and two new Alpha stations (GALIS, SMART) were installed for on-line data analysis and display. Independent measurements and detector tests can be performed without interference. The current version of the data-acquisition system supports a CAMAC multi-crate parallel-readout using multi-J11's (starbursts). Digital audio tapes (DAT) of 2 GB capacity are used for the standard on-line data recording media.

(2) Off-line data processing system -1

The following Alpha/VMS and VAX/VMS workstations are available for the off-line data analysis and for

<u>RIKAXP::</u>	<u>Alpha server 5/250 (Ring 1F) 4 CPU</u>
<u>RIKAX1::</u>	<u>Alpha Station 255/233 (Ring 1F)</u>
<u>RIKAX2::</u>	<u>Alpha Station 255/233 (Ring 1F)</u>
<u>RIKAX3::</u>	<u>Alpha Station 255/233 (Ring 1F)</u>
RIKAX4::	DEC 3000-300 (Linac Lab.)
RIKAX5::	DEC 3000-300 (Atomic Lab.)
RIKAX6::	DEC 3000-300 (Ring, nuclear theory)
RIKAX7::	DEC 3000-300 (Radiation Lab.)
RIKEN::	(virtual node name of the VAX cluster)
<u>RIKVAX::</u>	<u>VAX-4000/106A(Ring 1F)</u>
RIKVS0::	DEC 3000-400 (Ring 1F)
RIKVS2::	VAX Station 4000-60 (Ring 2F)
RIKVS3::	VAX Station 4000-60 (Ring 1F)
RIK835::	DEC 3000-400 (Radiation Lab.)
RIKLV1::	VAX Station 3100 M76 (Linac Lab.)
RIKLV2::	DEC 3000-400 (Linac Lab.)

general purpose calculations.

Two CPU modules were added in the Alpha server 5/250. As a result, the server equips four CPU's and 512 MB memory. This is utilized as a home machine for the experimental users and also a boot server for AXP workstations. File servers for the experimental data of RIKAX1-3 were replaced from DEC 3000-400 by Alpha Station 255/233. In total eleven alpha workstations and three VAX workstations are used for the data analysis etc. These computers are connected by LAVC (Local Area VAX Clusters) via the FDDI or ethernet. They are also connected to the HEPnet (DECnet) and STA/IM Internet (IP/DECnet) and reachable from all over the world.

(3) Off-line data processing system -2

Following FACOM VPP 500 Massive Parallel computers and DEC OSF/1 server and workstation groups have been also used for the off-line data analysis, simulations, and theoretical calculation:

FACOM VPP 500	(RIKEN computing center)
DEC 7000 (OSF/1)	(RIKEN computing center)

(4) Wide area computer network connectivities

The TISN (Todai International Science Network) was terminated in May 1996. RIKEN is now connected to the STA/IMnet at the speed of 1.5Mbps. This will be increased to 6Mbps in 1997. Also the RIKEN accelerator research facility is connected to the world-wide network of HEPnet (High Energy Physics NETWORK) / SPAN (Space Physics Analysis Network) as Area 40, which is a part of the DECnet Internet. In order to support these wide area network connections, following three leased lines are used:

1.5 Mbps	to STA/IMnet (IP, Decnet)
64 kbps	to KEK, Tsukuba (DECnet)
9.6 kbps	to Tokyo Institute of Technology (DECnet)

(5) Address of the electric-mail

The address of the electric-mail for a general user of the RIKEN accelerator research facility is described as follows, where the userid should be replaced by a proper name.

```
(Internet)
  userid@rikaxp.riken.go.jp
(HEPnet/DECnet)
  rikaxp::USERID (or 41823::userid)
```

References

- 1) T. Ichihara et al.: IEEE Transaction on Nuclear Science **35-6**, 1628 (1989).

Fabrication of the Muon Magnet for the RHIC Spin Project

T. Ichihara, H. Enyo, Y. Goto, N. Hayashi, K. Imai, A. Masaike, N. Saito,
T. Shibata, Y. Watanabe, and M. Ishihara

Relativistic Heavy Ion Collider (RHIC) will be completed in 1999 at the Brookhaven National Laboratory (BNL). The Siberian snakes and spin rotator magnets will be installed in the RHIC main ring, according to the RIKEN-BNL spin physics collaboration.¹⁾ These make it possible to accelerate the polarized protons up to 250 GeV for collision to investigate the origin of the nucleon spin.

Muon magnet (MM) is one of the detector magnets to be installed in the PHENIX detector in order to analyze the momenta of muon and muon-pair with high resolution. It is about 8 m tall and weighs approximately 200 metric tons. RIKEN is taking a role of fabricating it. Basic design²⁾ of the magnet has been carried out in collaboration with Lawrence Livermore National Laboratory (LLNL). The results has been presented by means of 3D CAD (Pro/ENGINEER) data.

The contract between RIKEN and Mitsubishi Elec-

tric Cooperation (Melco) was concluded in March 1996 for the fabrication of the magnet. After the completion, the whole magnet will be transported to the BNL in April 1997. A part of the magnet (coil) was already shipped to the BNL in August 1996.

As shown in Fig. 1, the muon magnet consists of basic part and attachments. The whole magnet is put on a track system and can be moved by a Hilman roller and hydraulic cylinder system for the installation and maintenance of the tracking detector.

The basic part of the muon magnet consists of steel and coils. Its main components are shown in Fig. 2. The piston core is mounted on the backplate. The counter weight is made of lead bricks, which is necessary to keep the center of the gravity low and to make sure of the stability in traveling.

A cross section of the magnet is shown in Fig. 3. Two coils, the front and rear coils, will be installed on

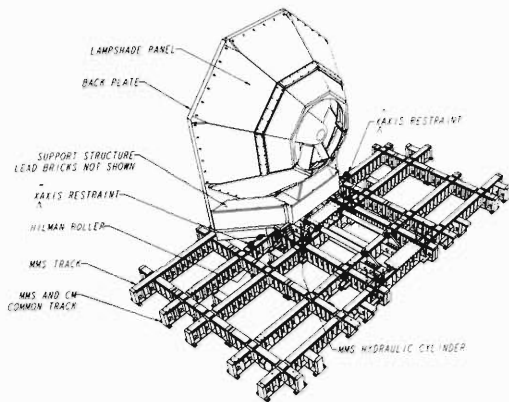


Fig. 1. Muon magnet on the track system.

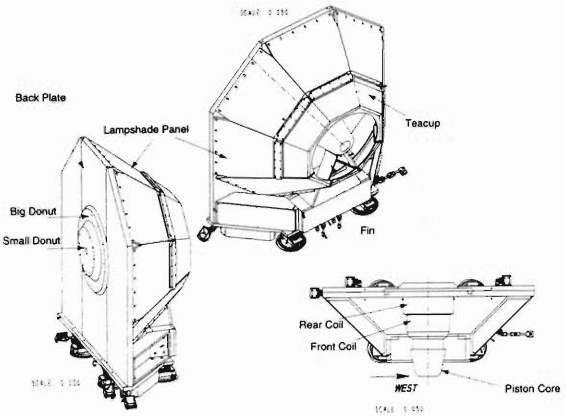


Fig. 2. Basic component of the muon magnet.

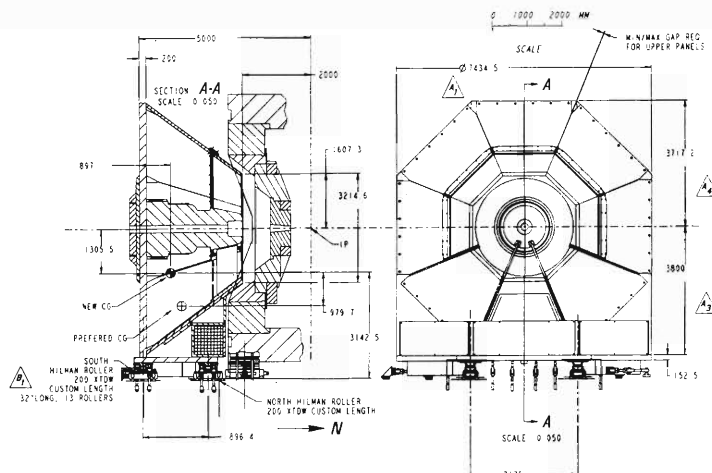


Fig. 3. Front view and cross section of the muon magnet.

Table 1. Specifications of the coil.

Item	Front Coil	Rear Coil
AT	131, 100AT	262, 200AT
Current	2, 300A	2, 300A
Number of Turns	57turn/coil	114turn/coil
Inner Diameter	$\phi 1413.0mm$	$\phi 1617.0mm$
Outer Diameter	$\phi 1499.4mm$	$\phi 1787.4mm$
Coil Length	586mm	606/567mm
Conductor cross section	$18.5 \times 18.5mm^2$	$18.5 \times 18.5mm^2$
	$\phi 11.5$	$\phi 11.5$
Conductor Material	OFC	OFC
Resistance (at 20°C)	19.0m Ω	44.4m Ω
Voltage	44.4V	104.1V
Joule Loss	102.1kW	239.5kW
No. of Water Cir.	8	16
Water Flow Rate	179l/min	331l/min
Water Temp. Rise	8.1°C	10.2°C
Flow Velocity	3.6m/sec	3.3m/sec

the piston core of the magnet. Insulation of the coils will be done by pre-pregnant method. The windings of each coil will be connected electrically in series.

The specification of the MM coils are as shown in Table 1.

The muon magnet is presently under construction at Melco Kobe Works and will be completed in March 1997. The news on current status of the magnet fabrication can be obtained by the WWW server at the URL of

<http://www.rarf.riken.go.jp/rarf/rhic/mms/>.

References

- 1) See the WWW server of <http://www.rarf.riken.go.jp/rarf/rhic/>.
- 2) PHENIX Muon Magnet South-Preliminary Design Review, LLNL-PHENIX-96-002, May 1 1996, *unpublished*.

6. Material Analysis

Development of an In-Air High-Resolution PIXE System

K. Maeda, K. Ogiwara, H. Hamanaka,* and K. Hasegawa*

We have constructed a compact, wavelength-dispersive spectrometer system for the high-resolution PIXE (particle induced X-ray emission) analysis in the air of atmospheric pressure.

An experimental setup for the PIXE system is schematically shown in Fig. 1.¹⁾ A proton beam (~ 2.5 MeV) generated by a tandem accelerator is taken out of the vacuum line to the air through a $7\ \mu\text{m}$ -thick Al-foil, which collides against a sample target placed in the air. The distance between the exit Al-foil and the target surface is 15 mm. Passing through the air and Al-foil reduces the proton energy by 0.3 MeV. X-rays emitted from the target are analyzed with a flat single crystal and detected by a position-sensitive proportional counter (PSPC).

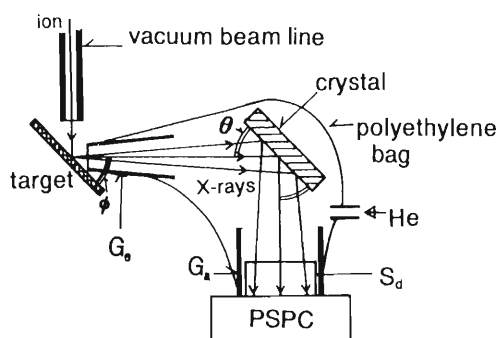


Fig. 1. A compact, in-air, high-resolution PIXE system: S_d , the divergence slit; G_e and G_a , the guide frames for X-ray path; and ϕ , the X-ray take-off angle.

The analyzing crystal and PSPC are both mounted on a θ - 2θ goniometer. A guiding frame (entrance guide G_e) for the path of X-rays is placed between the source and crystal, and another frame (acceptance guide G_a) is placed between the crystal and PSPC. The top of the entrance guide is covered with a thin ($1.5\ \mu\text{m}$ -thick) Mylar window. The whole path of X-rays from the entrance guide to the PSPC window via the crystal is enveloped with a commercial polyethylene bag. The total path length of the X-rays is fixed by 35 cm. Helium gas is introduced through a small hole made on the bag. It requires a few minutes to fully replace the air in the bag by He gas. No serious loss of He gas was observed during the θ - 2θ rotation of the crystal and PSPC. The top part of the entrance guide is so small that the entrance window can be placed very close to the X-ray source, as close as 3 mm of distance.

The PSPC used here is a home-made, single resistive anode type. It employs a carbon fiber of $7\ \mu\text{m}$ -diameter as the anode. The cathode is the window and

walls of the counter tube. We have also constructed a charge-division type multichannel analyzer. The output pulses of the PSPC are converted into position signals by a digital divider and accumulated in the memory of the analyzer.^{2,3)} The system control and data processing are carried out with a personal computer. The size of the PSPC is very small, i.e., $10\ \text{cm} \times 3.5\ \text{cm} \times 4\ \text{cm}$. Its sensitive window is 30 mm in width and 8 mm in height, and its spatial resolution is 0.3 mm with a 1 bar of P-10 counter gas. For the present geometry, the simultaneously detectable angular range ($\Delta\theta$) is 5° , and 1 channel in the PSPC corresponds to 0.094 mm in position and 0.0157° in the angle θ . An aluminized 4 or $1.5\ \mu\text{m}$ -thick Mylar sheet is used for the PSPC window.

Considering the absorption factors of X-rays by the spectrometer window, PSPC window, helium gas, and air, the lower limit of X-ray energy detectable with this system is estimated to be around 1 keV. Until now, we have measured $K\alpha$ and $K\beta$ spectra of Al, Si, P, S, and Cl in several compounds. It took only a few minutes to one hour to obtain one spectrum which was induced by 100 nA of 2.2 MeV protons. For examples, the observed intensity of Si $K\alpha$ from a crystalline Si wafer was 5000 counts/ μC and that of P $K\alpha$ from pressed powders of boron phosphide (BP) was 3500 counts/ μC , using an InSb (111) analyzing crystal.

As representative spectra measured with this system, Si $K\alpha$ and $K\beta$ of a fused quartz (SiO_2) and a crystalline silicon (c-Si) are shown in Figs. 2 and 3, respectively. These spectra were induced by a 2.2 MeV

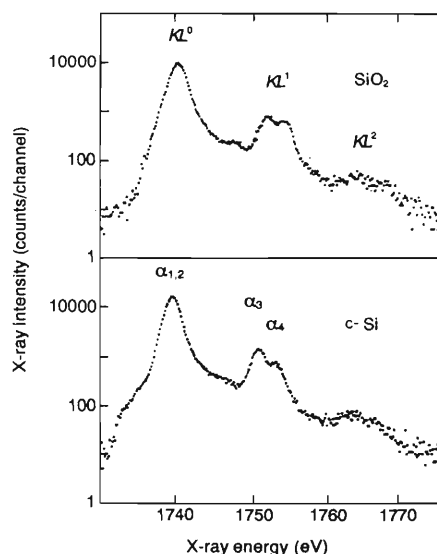


Fig. 2. Si $K\alpha$ spectra of SiO_2 and c-Si. Accumulated beam charge = $50\ \mu\text{C}$.

* College of Engineering, Hosei University

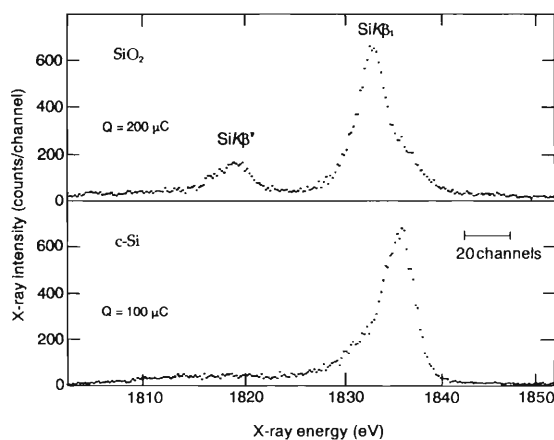


Fig. 3. Si $K\beta$ spectra of SiO_2 and c-Si, where Q is the accumulated beam charge.

proton beam of 3 mm-diameter and analyzed with an InSb (111) crystal of interplaner spacing of $d=0.374$ nm. The X-ray take-off angle was 10° . The angle 2θ at the center of the PSPC was set at 141° for the Si $K\alpha$ and 129° for the Si $K\beta$.

The line ($\alpha_{1,2}$) of $K\alpha$ emitted from a singly ionized state, KL^0 , and the $K\alpha$ satellites emitted from multiply ionized states, KL^1 and KL^2 , were well resolved as shown in Fig. 2. Moreover, fine structures in the KL^1 satellite (α_3 and α_4) were clearly distinguished.

FWHM (full width at half maximum) for the Si $K\alpha_{1,2}$ of c-Si estimated from Fig. 2 was 1.8 eV. This value is reasonable considering the following factors: (1) natural width of each component of the Si $K\alpha_{1,2}$ doublet is 0.49 eV and splitting of the doublet is 0.60 eV, and (2) line broadening due to the angular resolution ($d\theta$) of the spectrometer is 0.9 eV. The $d\theta$ is determined mainly by the X-ray source width, the spatial resolution of the PSPC, and by the path length of X-rays from the source to PSPC. The $d\theta$ was estimated to be 0.094° for the experimental condition of

Figs. 2 and 3, corresponding to 0.9 eV and 1.4 eV in the energy ranges of Si $K\alpha$ (1.74 keV) and Si $K\beta$ (1.84 keV), respectively.

The $K\beta$ spectra reflect the nature of the chemical bonding more prominently than the $K\alpha$ spectra, as can be seen from Fig. 3. A satellite line denoted by $K\beta'$ appears on the low-energy side of the main line $K\beta_1$ in the spectrum of SiO_2 . The $K\beta'$ line is not observed in the spectrum of the c-Si. The energy difference between the $K\beta'$ and $K\beta_1$ lines is 14 eV. This value approximately equals to the energy difference between O $2s$ and O $2p$ orbitals. While the $K\beta_1$ main line is due to the molecular-orbitals composed of both Si $3p$ and O $2p$, the $K\beta'$ satellite is originated from the molecular-orbital composed mainly of O $2s$. Thus, fine structures of $K\beta$ spectra can represent well the chemical environments of atoms in compounds.

PIXE measurements in non-vacuum, especially in the atmospheric air, are quite useful for biological, environmental, and archeological substances because the *in-air* PIXE has many advantages such as: 1) the sample handling is simple, 2) there is no limit of sample size, 3) the vaporization of a volatile component is suppressed. We have made a compact, in-air high-resolution PIXE system in reality. Using this system, *in-situ* chemical state analysis of delicate samples is now possible. Since the PIXE system requires only a small amount of samples (≤ 1 mg and/or ≤ 10 mm²) and a short data acquisition time (≤ 1 h for a spectrum), a two-dimensional mapping of chemical states for an example is promising.

References

- 1) K. Maeda, H. Hamanaka, and K. Hasegawa: Int. J. PIXE in press.
- 2) H. Hamanaka, K. Hasegawa, and Y. Yamamoto: Int. J. PIXE **1**, 141 (1990).
- 3) M. Koike and K. Hasegawa: Nucl. Instrum. Methods Phys. Res. A **272**, 840 (1988).

Positron/Positronium Annihilation in Nanocrystalline Si

X. Zhao* and Y. Itoh

Positron and positronium annihilation investigations were applied to nanocrystalline silicon (nc-Si) thin films, for the first time. The nc-Si thin films with average crystallite diameters of 3–5 nm show intense blue luminescence at room temperature. The nanometer-sized Si crystallites formed in amorphous Si (a-Si) matrix give rise to this luminescence caused by a quantum size effect.¹⁾ Because of the nc-Si layer is formed by a crystallization of a-Si and is a mixture of a-Si and nc-Si phases combined by a grain boundary, it is interesting to observe the positron (Ps) annihilation effect in such new materials, especially to observe the phase transition from amorphous to crystalline in nanometer scale.

S-parameter-positron energy curves were measured for the samples crystallized for 10 s to 1 h as well as for the as-grown a-Si, as shown in Fig. 1. Very Large S-parameters up to 0.62 were observed in the as-grown a-Si thin film, and then, the S-parameters dropped suddenly to 0.53 by crystallization of the thin film at 800 °C for 10 s, which was almost the same to the value observed in the c-Si (100) substrate. Further crystallization from 60 s to 1 hour showed smaller change in the S-parameters than that from the a-Si to 10 s, as shown in the figure. The large S value for the as-grown a-Si sample indicates that a great number of *para*-Ps

(p-Ps) annihilates in the structural defects, such as nanometer-sized voids. The a-Si layer was deposited on Si substrate at room temperature, which introduces a high strain field if there is a structural defect. The defect seems to disappear by a relaxation of the strain during annealing at 800 °C, no matter how short the annealing time is. The relaxation of the strain, on the other hand, induces a nucleus generation in the strain-induced crystallization process. Thus, the vanishing of the Ps formation indicates the growth of the nanocrystallites in the a-Si matrix. This suggests that positron is a sensitive probe for structural investigations of the nc-Si materials.

In order to obtain additional information on the nature of Ps formed in a-Si, positron lifetime measurements were carried out by using an accelerator-based pulsed positron beam at Electrotechnical Laboratory, Japan. It is interesting that there is no long-lived *ortho*-Ps component (> ns) in the as-grown a-Si layer. The average lifetime of the Ps is estimated from the spectra to be 520 ps, which is close to the spin-averaged lifetime of the Ps. The absence of the long-lived component might be attributed to a fast spin conversion effect of o-Ps to p-Ps. Because no H was involved in the deposition process,¹⁾ there may be a lot of dangling bonds in the as-grown a-Si layer. It is proposed that upon the collision with the unpaired electron of the dangling bond o-Ps undergoes the spin conversion and annihilates with the short lifetime of about 520 ps. The lifetime for the sample annealed for 10 s was determined to be 310 ps which is close to the value of positron annihilating in a divacancy defect in c-Si²⁾ indicating an annealing out effect of the larger size defects. The sample annealed for 1 h showed a longer lifetime component besides the 310 ps one. This should be due to the growth of the crystallites from the nuclei which introduces additional structural defects in the grain boundaries.

We would like to thank K. Hirata and Y. Kobayashi of National Institute of Materials and Chemical Research and T. Ohdaira, R. Suzuki, and T. Mikado of Electrotechnical Laboratory for the collaboration.

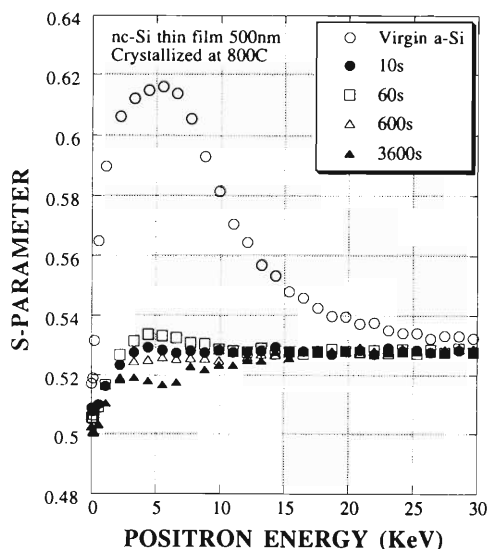


Fig. 1. S-parameters of a-Si and nc-Si thin films as functions of the positron energy. S-values at energies higher than 25 keV are close to that measured from the c-Si substrate.

References

- 1) X. Zhao, O. Schoenfeld, S. Komuro, Y. Aoyagi, and T. Sugano: Phys. Rev. B **50**, 18654 (1994).
- 2) M. Kwete, D. Segers, M. Dorikens, L. Dorikens-Vanpraet, and P. Clauws: Phys. Status Solidi A **122**, 129 (1990).

* Laboratory for Nanoelectronics Materials, Frontier Research Program

Development of a TOF-ERDA System for Wide Mass Range

W. Hong, S. Hayakawa,* K. Maeda, S. Fukuda, M. Yanokura, M. Aratani,
K. Kimura, Y. Gohshi,* and I. Tanihata

Elastic recoil detection analysis (ERDA) is one of the most promising methods for determination of light and medium elements in a heavy matrix, such as trace hydrogen analysis. Though a conventional ERDA employing a stopper foil in front of the detector has been performed at RIKEN,^{1,2)} a new ERDA system using time of flight (TOF) detection was set up to realize both higher mass resolution and lower detection limit.

The experimental arrangement is shown in Fig. 1. ⁴⁰Ar ions accelerated to 41.5 MeV by the RILAC were used as a probe. Incident angle of the beam was 55°. A tantalum collimator having 3 mm ϕ hole was used. A time detector composed of two MCPs and 10 $\mu\text{g}/\text{cm}^2$ carbon foil³⁾ was assembled and installed between the sample and the SSB detector. The time resolution of the detector was better than 100 ps. Detector angle was 55° and the physical length of flight was 314 mm. A CAMAC system was used to control counting system by KODAQ code⁴⁾ on a personal computer. Figure 2 shows the spectra of a Si wafer. High channel of the time axis represents short time because the start and stop signals are reversed to each other. Oxygen is from natural oxide layer of the Si wafer surface. Carbon appears because of low vacuum (3×10^{-7} torr) of the target chamber. The energy and time resolutions were 530 keV at 13.2 MeV and 0.9 ns at 33.0 ns respectively. The mass resolution was calculated to be 1.9 at mass 28. The energy and time resolutions may be overestimated because of the carbon and silicon oxide layers at surface.

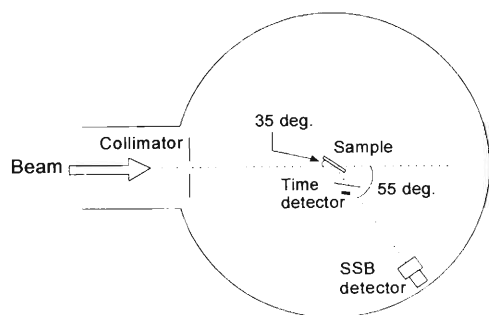


Fig. 1. Setup of the TOF-ERDA spectrometer.

After the measurement, the spectra are reconstructed with the region of interest determined by an input gate defined anew on the scatter plot, Fig. 2(a). The gate established on the scatter plot affects the other windows, Fig. 2(b), (c) so that the only data corresponding to the selected data of the scatter plot appear in the energy and time spectra. With this

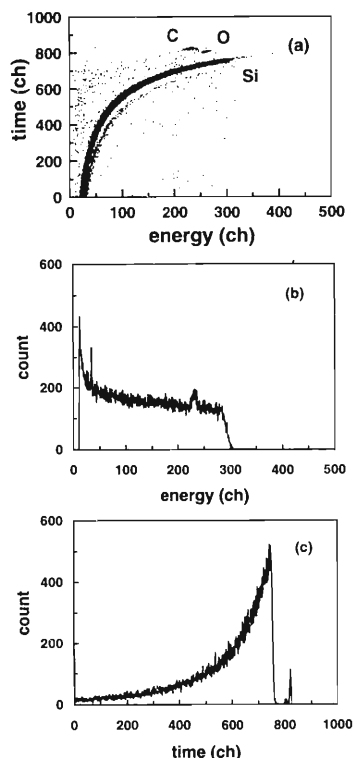


Fig. 2. Raw spectra for a Si wafer. (a) TOF-Energy scatter plot, (b) energy spectrum, (c) time spectrum. Counting time: 20 min.

method, a peak can be separated from the other peaks and background in the energy and time spectra.

By using the TOF system the mass resolution of ERDA was improved remarkably. The main results are: (1) Hydrogen, carbon, nitrogen and oxygen were detected simultaneously. (2) The mass resolution of the system was 1.9 for silicon of the mass 28. (3) Carbon, nitrogen and oxygen peaks were separated in TOF-E scatter plot, and energy spectra of individual elements were obtained with use of KODAQ code. Resultant low-background spectra are promising for detecting trace elements whose peaks are difficult to be detected by conventional ERDA.

References

- 1) H. Nagai, S. Hayashi, M. Aratani, T. Nozaki, M. Yanokura, I. Kohno, O. Kuboi, and Y. Yatsurugi: Nucl. Instrum. Methods B **28**, 59 (1987).
- 2) K. Kanazawa, M. Yanokura, M. Aratani, and H. Akiyama: Vacuum **44**, 7 (1993).
- 3) K. Kimura and J. Wada: Phys. Rev. B **48**, 15535 (1993).
- 4) K. Omata, Y. Fujita, N. Yoshikawa, M. Sekiguchi, and Y. Yoshida: IEEE Trans. Nucl. **39**, 143 (1992).

* Department of Applied Chemistry, University of Tokyo

7. Miscellaneous

Strong X-Ray Emission due to a Charge-Up Effect

J. Kawai, N. Inada, and K. Maeda

We have found that strong x-rays are emitted from charged-up targets when MeV ion is bombarding.¹⁻³⁾ The electrified insulator target was ionized by electron beam as well as ion beam. X-ray emission cross section of the electron excitation is much higher than that of the ion excitation for such an experimental condition. This charge-up X-ray emission effect was first discovered by Terasawa⁴⁾ almost 30 years ago.

To clarify the mechanism of the charge-up effect, we applied DC 3 kV between a copper pin and copper plate in a 10^{-5} Torr vacuum (see Fig. 1). The distance between the pin and the plate was 8 mm. The plate was coated by fluorescent powder. A tungsten filament to supply thermionic electrons was set in the vacuum chamber. Once the filament was switched on, electrons were supplied from the filament to the vacuum chamber, and X-rays began to generate after one strong spark between the pin and the plate. The X-rays were detected by a Si(Li) solid state detector. Just after the spark, we switched off the filament, but the X-rays were still emitting. The X-rays continued for several minutes or say thirty minutes, and stopped by another strong spark. There observed a few bright spots on the fluorescent powder coated on the copper plate during this X-ray emission. Thus, the X-rays emitted after the filament had been switched off was a field emission from the sample. The details of the mechanism of the

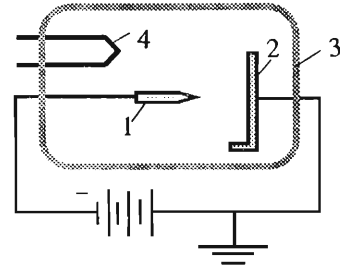


Fig. 1. Schematic illustration of the experimental setup.
1. Copper pin, 2. Copper plate coated by fluorescent powder, 3. Vacuum chamber, and 4. Tungsten filament.

strong X-ray emission from a charged-up insulator has not yet been clarified, but it has been demonstrated that the 3 kV DC field emission can generate strong X-rays.

References

- 1) J. Kawai, K. Maeda, N. Sakauchi, and I. Konishi: *Spectrochim. Acta B* **50**, L1 (1995).
- 2) K. Maeda and H. Hamanaka: *Spectrochim. Acta B* **51**, 343 (1996).
- 3) J. Kawai, K. Maeda, N. Sakauchi, and I. Konishi: *Nucl. Instrum. Methods Phys. Res. B* **109/110**, 206 (1996).
- 4) M. Terasawa: *J. Phys. Soc. Jpn.* **25**, 1199 (1968).

Residual Radioactivity Produced by 2.9 MeV/nucleon α -Particles

Y. Uwamino, S. Kagaya, S. Shinohara, K. Harasawa, and T. Kambara

The maximum energy of RILAC is above 2.5 MeV/nucleon, but any experiment should be performed with the energy below or equal to 2.5 MeV/nucleon at present because of the radiation safety. The main purpose of this experiment is to get an accurate information on radiation safety for the abolishment of the above energy adjustment.

Residual radioactivity produced by 2.864 MeV/nucleon alpha (α) particles was measured with thick targets of graphite, aluminum, copper, lead, and stainless steel. The targets were separately irradiated for an hour with about 1 μ A of beam current, and the gamma rays were measured by a Ge detector.

We observed very weak 511 keV gamma rays only from the graphite target. Induced radioactivity in lead was not detected at all.

Gamma-ray emission from the aluminum target was

also weak, and only the radioactivity found was what were produced by the impurities: that is, ^{72}As and ^{57}Ni .

^{66}Ga and ^{67}Ga were intensely produced in the copper target via the $^{63}\text{Cu}(\alpha, n)$ and $^{63}\text{Cu}(\alpha, \gamma)$ reactions. The Q values of these reactions are -7.5 MeV and 3.7 MeV, and the reaction rates were estimated to be 6×10^{13} and 8×10^{11} [coulomb $^{-1}$], respectively.

The induced radioactivity was strong in the copper target, and a slight contamination was observed with the wipe test which was performed immediately after the irradiation.

In the stainless steel target, ^{58}Co and ^{57}Ni were observed, and the latter seems to be produced by the $^{54}\text{Fe}(\alpha, n)$ reaction. The secondary neutron and gamma rays were also measured by an NE213 scintillator, and the data are presently under analysis.

IV. NUCLEAR DATA

Status Report of the Nuclear Data Group

Y. Tendow, A. Yoshida, A. Hashizume, and K. Kitao

The Nuclear Data Group has been continuing the data related activities described below since the previous year.¹⁾

(1) Nuclear reaction cross-section data (EXFOR)

Compilation of the charged particle nuclear reaction cross sections has been continued. The reaction cross sections to produce 20 radioisotopes of medical use: ^{11}C , ^{13}N , ^{15}O , ^{18}F , ^{28}Mg , ^{52}Fe , ^{67}Ga , ^{68}Ge , ^{74}As , ^{77}Br , ^{82}Br , ^{77}Kr , ^{81}Rb , $^{82\text{m}}\text{Rb}$, ^{111}In , ^{123}Xe , ^{127}Xe , ^{123}I , ^{124}I , and ^{125}I as well as related old data which have not been included in the EXFOR master file up to now and new data appeared in recent journals are continued to be collected and compiled into EXFOR files. This year, we have transmitted two so-called 'TRANS' files to the International Atomic Energy Agency (IAEA) Nuclear Data Section (NDS). One is named 'TRANS R010' containing the revised 'R0038' entry which had been combined into the EXFOR master previously. The other is 'TRANS R011' containing three new entries with a total of 86 subentries (excitation curves), that is the entry 'R0051' with 50 curves for (α, x) reactions on several natural targets, the entry 'R0052' with 9 curves for (α, xn) and (α, pxn) reactions on lanthanide targets, and the entry 'R0053' with 27 curves for (α, xn) and $(^3\text{He}, x)$ reactions on Ta and Bi targets.

(2) Evaluated Nuclear Structure Data File (ENSDF)

We have been participating in the ENSDF compilation network coordinated by the Brookhaven National Nuclear Data Center (NNDC). The evaluation and compilation of $A = 129$ mass chain and updated evaluation of $A = 127$ have been completed and published in the Nuclear Data Sheets this year.^{2,3)} Mass chain $A = 120$ evaluation has also been completed and the draft is now under the review at the NNDC. The ENSDF, as well as the other databases, is supposed to be listed more and more by the on-line service through the network like WWW, and can be updated more frequently hereafter. We are expecting to update $A = 129$ mass chain partially whenever new data come out after this day.

(3) Nuclear Science References (NSR)

We are engaged in collecting and compiling secondary references (annual reports, conference proceedings, etc.) appeared in Japan since the previous year into the Nuclear Science References (NSR) file and sending it to NNDC.

The Nuclear Science References (previously Nuclear Structure References) Coding Manual was revised this year with small modifications and improvements from the old version.⁴⁾

The compilation of 1995 annual reports has been completed and sent to the NNDC. Japanese secondary sources surveyed this year are as follows (in code name in NSR):

RIKEN (*RIKEN Accel. Prog. Rep.*),
 JAERI-TV (*JAERI Tandem & V.D.G.*),
 JAERI-TIARA (*JAERI Takasaki Ion Acc. Advanced Rad. Appl.*),
 INS (*INS Univ. Tokyo*),
 UTTAC (*Univ. Tsukuba Tandem Accel. Center*),
 RCNP (*Res. Center Nucl. Phys. Osaka Univ.*),
 OULNS (*Osaka Univ. Lab. Nucl. Study*),
 CYRIC (*Cyclo. Radioisot. Center, Tohoku Univ.*).

(4) Others

The biennial IAEA Advisory Group Meeting on the Coordination of the Nuclear Reaction Data Centers (NRDC) was held at the Brookhaven National Laboratory, National Nuclear Data Center (NNDC) on 3-7 of June 1996. Participants were the heads and observers from 11 nuclear data centers: IAEA NDS, NEA Data Bank, CJD (Nuclear Data Center, Obninsk), CAJaD (Kurchatov Inst.), CDFE (Photonuclear Data Center, Moscow), RIKEN, JAERI, JCPRG (Sapporo), CNDC (China Nuclear Data Center, Beijing), ATOMKI (Hungary) and NNDC (Brookhaven) who served the host of the meeting. In addition to the authorized members mentioned above, two centers attended the meeting for the first time this year: NIEF Nuclear Data Group (Sarov, previously Arzamas-16, Russia) and Institute for Nuclear Research (Kiev, Ukraine). A major topic discussed at the meeting was the challenge from the rapid advance of computer network technologies and its impact on the data dissemination methods by the centers. Both NNDC and NDS agreed to take actions for expanding their on-line services under the WWW technology. Because the on-line information can be updated frequently, new problems on the archiving of database and accurate referencing of data extracted from on-line services will be expected. It was agreed to establish new citation guidelines.

References

- 1) Y. Tendow, A. Yoshida, A. Hashizume, and K. Kitao: RIKEN Accel. Prog. Rep. **29**, 205 (1996).
- 2) Y. Tendow: Nuclear Data Sheets **77**, 631 (1996).
- 3) K. Kitao and M. Oshima: Nuclear Data Sheets **77**, 1 (1996).
- 4) S. Ramavataram and C. L. Dunford: BNL-NCS-51800, Rev. 08/96 (1996).

V. DEVELOPMENT OF ACCELERATOR FACILITIES

Production of ^{48}Ca Ions in 10 GHz ECRIS

T. Nakagawa, T. Kageyama, J. Fujita, M. Kase, A. Goto, and Y. Yano

For an experiment to search new isotopes, an intense beam of ^{48}Ca was strongly demanded. To produce such beams, it is effective to use its enriched materials, because its natural abundance is very low. As the enriched ^{48}Ca are normally sold as oxides, the method to produce highly charged ions from oxide materials as described in Ref. 1 is one of the best ways. However, it is not advantageous to make a rod of oxide materials of the enriched isotopes in view of the cost. From these reasons, we put the oxide powder into an Al_2O_3 tube (2 mm inside diameter, 4 mm outside diameter) and inserted it directly into the plasma as shown in Fig. 1.

The support gas was oxygen. The vacuums of the first, second, and extraction stages were 6.0×10^{-6} , 6×10^{-7} , and 7×10^{-8} Torr, respectively. The microwave power supplied into the second stage was 600 W. Figure 2 shows the charge state distribution as a function of the analyzing magnet current. The ECRIS was tuned for producing $^{48}\text{Ca}^{11+}$ ions. The ^{48}Ca ions were accelerated by the AVF- Ring Cyclotron complex up to 70 MeV/u. The maximum beam intensity was 40 e μA for a short time. The average beam intensity of 15 e μA ($^{48}\text{Ca}^{11+}$) was produced from the ECRIS and 100 enA was on the target for the experiment. The powder consumption rate was 0.3 mg/h.

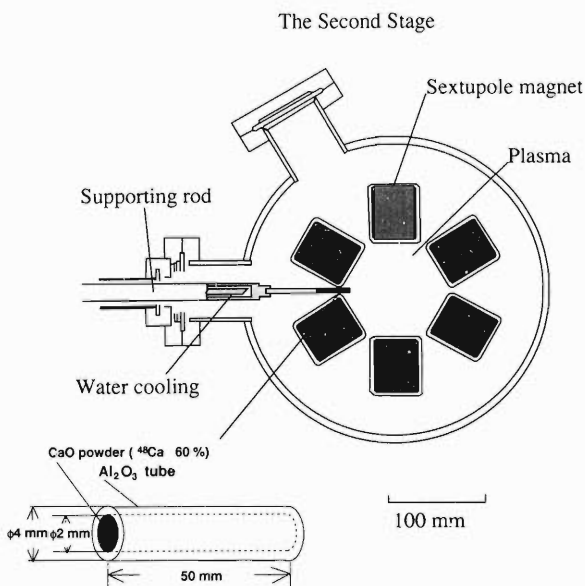


Fig. 1. Cross sectional view of the RIKEN 10 GHz ECRIS.

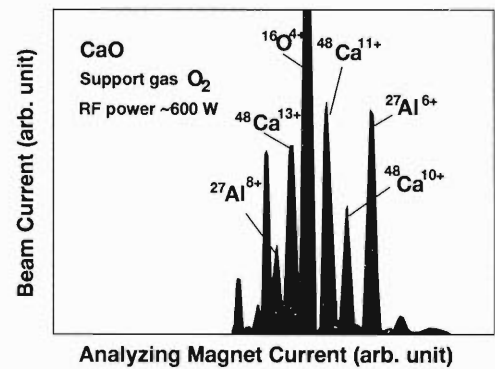


Fig. 2. Charge state distributions as a function of analyzing magnet current. The source was tuned for producing the $^{48}\text{Ca}^{11+}$ ions.

References

- 1) T. Nakagawa, T. Kageyama, A. Goto, M. Kase, and Y. Yano: Jpn. J. Appl. Phys. **32**, 2463 (1995).

Present Status of RIKEN 14.5 GHz Caprice

Y. Kanai, Y. Nakai, T. M. Kojima, T. Kambara, and Y. Awaya

In order to study the low energy highly-charged ion and atom collision processes, and to study the excited states of highly-charged ions, we installed a 14.5 GHz ECRIS (Caprice) and constructed the beam lines in 1995.¹⁾ This year (1996), we have made some improvements of the ion source itself and beam transport system: (1) we placed an aluminum tube inside the plasma chamber, and (2) we transported the low energy highly-charged ion beams to the experimental chamber.

Hitz^{2,3)} and Nakagawa⁴⁾ reported that by using an aluminum chamber, or using an aluminum tube inside the plasma chamber, they have improved the efficiency of the ECRIS. We used an almost same aluminum tube (1 mm thickness) as Nakagawa used for RIKEN 18 GHz ECRIS, and obtained some improvement in the efficiency. In Fig. 1, we show the Ar ion current extracted from the Caprice and measured after the analyzing magnet. We obtained higher currents at higher charge states with the aluminum tube inside the plasma chamber. This tendency is same as re-

ported by Nakagawa et al. They reported that they did not need the support gas to achieve the high performance with the aluminum tube. For our case, however, to obtain the best result, we needed the support gas (oxygen gas).

To obtain the low energy highly-charged ion beams, we have designed and made the whole beam lines of Caprice isolated from the ground.¹⁾ From January 1996, we have tried to transport the low energy highly-charged ion beams to the experimental chamber. We used the Ar⁷⁺ ion beams for this test. We could transport the 140 eV Ar⁷⁺ ion beams to the experimental chamber. The Ar⁷⁺ ions were extracted by the voltage difference V_g between the plasma chamber V_p and the beam line V_b (e.g., $V_g = 1020$ V when $V_p = 20$ V and $V_b = -1000$ V), transported, and were decelerated to the ground potential just before the chamber. After the deceleration lens, we used the einzel lens to focus the beam at the experimental chamber. The beam spot size on the target position was 1 mm in diameter. Typical current of the 140 eV Ar⁷⁺ ions was 0.1 enA. Higher energy (>4 keV) Ar⁷⁺ ions could be transported to the experimental chamber without the deceleration method: $V_g = V_p$ and $V_b = 0$ V. Lower energy (<4 keV) Ar⁷⁺ ions could not be transported to the chamber without the deceleration method. For lower energy beams, the energy spread due to the plasma potential is compatible to the final beam energy. We are preparing an electrostatic energy analyzer to place after the deceleration lens, which will determine the precise beam energy of lower energy ions.

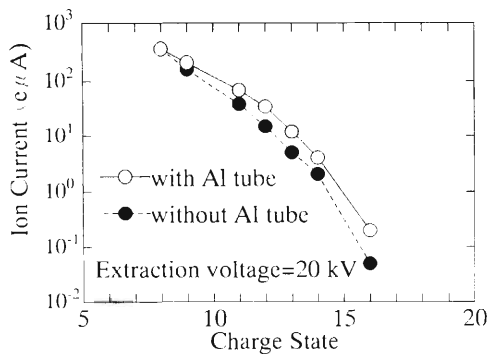


Fig. 1. Charge state distribution of Ar ions from RIKEN 14.5 GHz Caprice. Open circles: with aluminum tube, closed circle: without aluminum tube.

References

- 1) Y. Kanai et al.: RIKEN Accel. Prog. Rep. **29**, 208 (1995).
- 2) D. Hitz et al.: Proc. 12th Int. Workshop on ECR Ion Sources, p. 126 (1995).
- 3) D. Hitz et al.: Rev. Sci. Instrum. **67**, 883 (1996).
- 4) T. Nakagawa et al.: Jpn. J. Appl. Phys. **35**, 4077 (1996).

I_{beam} was found to be scaled by $V_{\text{ex}}^{2.5}$ as shown by dotted curves, regardless of discharge conditions. Such a sharp rise to exceed the scaling ($V_{\text{ex}}^{1.5}$) of space-charge limited current, followed by a saturation, can be explained due to a sharp convergence of the beam divergence (caused by the expansion cup) as V_{ex} is raised, thus reducing beam loss to the extraction electrode.

Figure 3 indicates that the optimum working gas pressure (p) to maximize I_{beam} is around 7×10^{-4} Torr-Ar independent of V_{ex} . The Paschen's minimum pressure at which the arc start voltage (V_s) is minimum was $p_{\text{min}} = 5 \times 10^{-3}$ [Torr] for the working gas of hydrogen. When the filament current $I_f \geq 18\text{A}$, the V_s was found to decrease drastically than the voltage predicted by Paschen's law:

$$V_s[\text{V}] = 165 \frac{p/p_{\text{min}}}{1 + \ln(p/p_{\text{min}})} \quad (1)$$

No arc initiated at $p \leq 5 \times 10^{-3}$ [Torr] with anode potential $V_a \leq 250\text{V}$. Throughout the paper, the pressure is the one measured near Faraday cup, which is 2 ~ 3 orders lower than the pressure at the anodic (IE-K) plasma region. The arc resistance was $R_{\text{arc}} \sim 20\Omega$ when V_a was at Paschen's minimum (165V) at $p = 5 \times 10^{-3}$ Torr. Interestingly, I_{beam} depicts its maximum at this $V_a = 165\text{V}$.

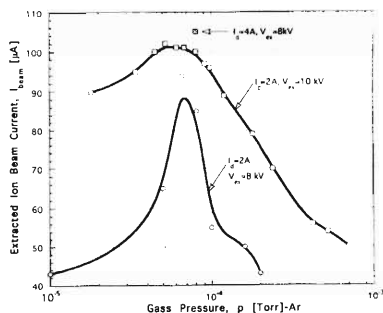


Fig. 3. Pressure dependent I_{beam} at various V_{ex} and I_d .

Figure 4 shows a linear growth of I_{beam} with respect to I_d ($\equiv I_K \equiv I_a + I_{\text{IE}}$) independent of V_{ex} . Namely, for small I_d , the next formula was found:

$$I_{\text{beam}}[\text{A}] = 55.7 \times 10^{-6} I_d[\text{A}]. \quad (2)$$

The scaling of Eq. (2) agrees with the sheath model by Lejeune²⁾ based on the theory by Langmuir.³⁾ Electric potential of the anode column becomes positive in reference to the grounded (HV-GND) anode, when the total ion generation exceeds 2.86 times of the number of ions contributing the ion current density j_i . With the positive potential the ions can be extracted from the anode column even when $V_{\text{ex}} = 0$ or without a penetration of the extraction electric field into the column. At the both sheath boundaries of anode column ends, the ion flux should be given by the same j_+ if there were no loss. Now, the electron current density j_e permitted to pass the anode column depends upon the j_i arrived at the sheath boundary; which is

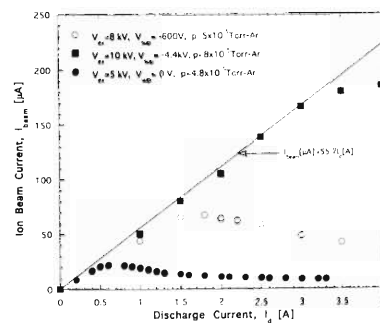


Fig. 4. Discharge current (I_d) dependent I_{beam} .

a stability condition given by $j_e = j_i(m/M)^{1/2}$. Therefore, $j_+ = j_i = j_e(m/M)^{1/2}$ without loss. However, if $j_i = \gamma j_+$ due to a loss, where γ (≤ 1) is a parameter describing the loss into IE, we have $j_+ = (j_e/\gamma)(m/M)^{1/2}$. Obviously, $I_+ \sim j_+ d^2$ (d : anode orifice diameter) and $I_d \sim j_e D^2$ (D : anode column diameter), then

$$I_+ \equiv I_{\text{beam}} = I_d(m/M)^{1/2} (d/D)^2 \gamma^{-1} \quad (3)$$

This I_+ can explain the scaling of Eq. (2): $I_{\text{beam}} \sim I_d$. Our case, $(d/D)^2 = (0.8/5)^2 = 2.6 \times 10^{-2}$ and $(m/M)^{1/2} = 3.7 \times 10^{-3}$ for argon so that Eq. (3) gives $\gamma \sim 1$ since $I_{\text{beam}}/I_d = 55.7 \times 10^{-6}$ from Eq. (2). This means that we have still a room to achieve the higher I_{beam} by decreasing the γ to IE.

A decay is observable for large I_d ($\geq I_{d0}$) in Fig. 4. This can be a transition from a normal arc mode to a so-called ‘‘arc-starvation’’ mode where D and γ increase suddenly, thereby decreasing I_{beam} via Eq. (3). We have observed, however, a linear increase of the dark current (I_{dark}) in to the extraction electrode, which started exactly at $I_d = I_{d0}$. This phenomenon is therefore attributable as an increase of new D and γ definable for the beam in between anode and extraction electrode. Increase of D can be suppressed increasing the axial field B since $D \sim B^{-1/2}$. Indeed, we have observed $I_{\text{beam}} \sim B$. This and our another observation $I_{\text{beam}} \sim p$ as seen by Fig. 4 support the sheath model of Eq. (3). Also observed was the effect of suppressor voltage (V_{sup}), which decreases I_{dark} , thereby increasing the beam current: $I_{\text{beam}} \sim V_{\text{sup}}^{1/2}$.

Data of the pre-arc phase demonstrates that the production of I_{beam} takes place only after $I_{\text{IE}} = 0$, or when IE is floating at around $V_{\text{IE}} = -50\text{V}$. The $I_d \equiv I_a + I_{\text{IE}}$ should not be too large for the sake of I_{beam} .

Longevity of the filament (presently around 11 hrs with W) is the most crucial factor for DPIS to evolve a practical source. Use of a tantalum (150 hrs), composite (oxidized Ni-mesh), or LaB_6 (850 hrs max in high vacuum) cathode and pulsing of the anode potential (V_a) are in progress.

References

- 1) M. von Ardenne: Atomkernenergie **1**, 2015 (1956).
- 2) L. L. Lejeune: Nucl. Instrum. Methods **116**, 417 (1974).
- 3) I. Langmuir: Phys. Rev. **33**, 945 (1929).

Recent Progress in ECRIS Physics Study: Radial distribution of negative potential, hot ring, and instability

M. Niimura, T. Nakagawa, A. Goto, and Y. Yano

Progress was made in understanding the physics of electron cyclotron resonance (ECR) ion source. Actual distribution of the electric potential inside an ECR ion source (ECRIS) was derived based upon an experimental¹⁾ data, with which distributions of the highly charged ions (HCI) trapped electrostatically inside the ECR-zone were calculated. These profiles revealed a shell-like ring structure of hot electrons distributed right on the ECR-surface. It was evident from the localized area of less-space charge and less-trapped ions than the vicinity. The ECR-zone which is a 'nucleus' of an ECRIS plasma is shown to possess an internal structure: hot electron ring (HER) distribution, inside of which the warm electrons, responsible for the ionization and/or trapping of HCI, occupy as core. The extra-nucleus cold electrons also trap some ions radially due to the negative potential. The purpose of study is to discover better methods of ECR-heating (ECRH) to the right electron temperature (T_e), of HCI cooling to mitigate the driftwave instability, and of positive potential lowering to extract HCI out of the potential-well. In the present paper, we demonstrate that ECRIS potential profiles can be deduced by a simple ion endloss current (or ion confinement time) measurement, without employing costly heavy-ion beam techniques. The 'dia-magnetic' current (i_{dm}) accounted for the HER heating is shown to help stabilize the instability, thereby allowing more absorption of RF power across the ECR surface.

Before ECRH: The 'thermal' motion of the axially magnetized ions and electrons is a gyration motion along the field line (B_z) going back and forth, because the velocity ($v_{//}$) parallel to B_z remains same even after the perpendicular velocities (v_{\perp}) undergo gyrations around B_z . Therefore, both ions and electrons will be bounced back together toward the midplane by the mirror magnetic field (MMF) whose maximum field is B_m , unless their pitch-angles at the midplane $\theta \equiv \sin^{-1} v_{\perp}/v$ (where $v^2 = v_{//}^2 + v_{\perp}^2$) were smaller than the critical angle $\theta_m \equiv \sin^{-1} (R_m^{-1/2})$. Therefore, the charge neutrality prevails inside the MMF: no axial space charge before RF. Here, $R_m \equiv B_m/B_o \geq 1$ is the mirror ratio and subscript "o" denotes midplane (Min- B_z) quantities. This situation is consistent with the experimental fact: a HCI trapping negative potential has never been evidenced before applying the RF for ECRH.

After ECRH: Once RF is applied at the frequency $\omega_c = eB_z/m_e$, only the electrons of mass m_e can increase the v_{\perp} component. This ensures $\theta \gg \theta_m$ and thus can start trapping more electrons than off-

resonant ions within MMF in the matter of nano-seconds. In practice, most of the ECR-heated electrons tend to be reflected at B_{ECR} ($\leq B_m$) before reaching the point of B_m , as confirmed by a study of Coulomb collisions in the RF-diffusion velocity space.¹⁾ This means that all the MMF confined electrons will eventually achieve $v_{//} = 0$ at $B = B_{ECR}$; i.e., there the total kinetic energy W ($\equiv W_{//} + W_{\perp}$) becomes $W_{\perp} \equiv (1/2)mv_{\perp}^2$. The W_{\perp} relaxes as the particle migrates along the field line toward the lower- B_z region (core heating) following the invariance of the magnetic moment $\mu_e \equiv W_{\perp}/B_z$.

Axial Distribution of Negative Potential, $\phi(z) < 0$: This origin is the space charge of ECRH electrons, as clear from the above discussion, accumulated inside the zone $B_o \leq B \leq B_{ECR}$. Another experimental fact, that a negative potential-well deepened from 10 to 30V proportional to the RF input power,²⁾ can be accounted for an increase of the electron space charge (not of the T_e) by RF.

Axial Distribution of Positive Potential, $\phi_{//A} \geq 0$: Length of ECR-zone is necessarily shorter than or equal to that of MMF. The electrons outside the MMF are what have fallen into the loss cone and thus left cold. They drift along field lines to be lost on endwalls at a higher rate than the ions. In order to retard the fast diffusion of electrons a positive ambipolar potential ($\phi_{//A} \geq 0$) is induced outside ECR-zone. The positive $\phi_{//A}$ is a problem for the HCI extraction out of a negative potential-well.

Radial Distribution of Negative Potential, $\phi_{\perp A} \leq 0$: If the radial diffusion (\perp to B_z) is classical, the cross-field diffusion of ions is faster than that of electrons, thereby establishing a negative ambipolar potential ($\phi_{\perp A} \leq 0$) to retard ion diffusion. Therefore, $\phi(r) < 0$ prior to RF power application inside and outside of the ECR-zone.

Semi-Experimental Derivation of the $\phi(r)$ under RF: We have tried to derive $\phi(r)$ based from the ion endloss current-densities $J_{//i}(r)$ measured by a Faraday cup and time-of-flight detector which was scanned radially outside the ECR-zone.³⁾ Let us discuss briefly the ion endloss flux ($\Gamma_{//i}$) because of the relationship $J_{//i}(r) \equiv Z_i e \Gamma_{//i}(r)$. The $\Gamma_{//i}$ is defined by the number of ions escaping every second per unit area from two ends of an ECR cylinder with cross-section S_{end} and length L_p ($//$ to MMF). The volume of cylinder is $V \equiv L_p S_{end}$ being filled with the averaged ion density $\langle n_i \rangle$. Namely, $\Gamma_{//i} = (1/2)\langle n_i \rangle \langle v_i \rangle$, where $\langle v_i \rangle$ is the arithmetically averaged ion velocity. Substitution of this $\Gamma_{//i}$ into the continuity equa-

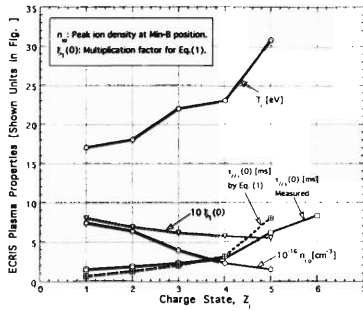


Fig. 1. Parameters of an ECRIS, Constance-B.¹⁾

tion, $\partial\langle n_i \rangle / \partial t + \Gamma_{//i} / L_p = 0$, yields the ion confinement time $\tau_{//i} = L_p / v_i$. Here, the ion escaping velocity $v_i \equiv \langle v_i \rangle / 2 \equiv \sqrt{2kT_i / \pi M}$. If $n_i(0) \equiv n_{i0}$ is known to be the peak ion density, we can always write $\langle n_i \rangle$ as $\langle n_i \rangle \equiv \xi_i n_{i0}$ so that $\Gamma_{//i} = \xi_i n_{i0} v_i$, using a multiplication factor $\xi_i (\leq 1)$. Then $\tau_{//i} \equiv \langle n_i \rangle L_p / \langle n_i \rangle v_i$ can be expressed:

$$\tau_{//i}(r) = \xi_i(r) \frac{n_{i0} L_p}{\Gamma_{//i}(r)} \equiv \xi_i(r) Z_i e \frac{n_{i0} L_p}{J_{//i}(r)}. \quad (1)$$

With our simple-minded formula $\xi_i(0) = 0.5[1 + \exp(-0.5Z_i)]$ together with the experimental data of $J_{//i}(0)$, n_{i0} , and $L_p = 20$ cm, above Eq. (1) gives the $\tau_{//i}(0)$ in good agreement with measured one as shown in Fig. 1.

Imagine now a radial distribution of $\phi(r) \leq 0$ at the midplane of an ECR-zone, in which ions are electrostatically trapped. Radial equation of motion for the trapped ion mass density is, at the steady-state $dv_i/dt = 0$, nothing but a balance equation between the two force densities of $-kT_i \nabla_r n_i(r)$ and $-Z_i e n_i \nabla_r \phi(r)$. Within the present paper, we assume the ion temperature (T_i) to be isotropic although it may differ at different charge states, $Z_i (=1, 2, 3, \dots$ when $i = 1, 2, 3, \dots$). The integration under the conditions $\phi(\text{wall}) = 0$ and $n_i(\text{wall}) = n_{iw}$ gives:

$$\phi(r) = -\frac{kT_i}{Z_i e} \ln \frac{n_i(r)}{n_{iw}} \quad \text{or} \quad \frac{n_i(r)}{n_{iw}} = \exp \frac{-Z_i e \phi(r)}{kT_i}. \quad (2)$$

Due to the potential barrier $|\phi(r)|$, the trapped ions are confined much longer than the parallel drift time L_p / v_i by a factor of $\exp(Z_i e |\phi(r)| / kT_i)$; as much as

$$\tau_{//i}(r) = \frac{L_p}{v_i} \exp \left(\frac{Z_i e |\phi(r)|}{kT_i} \right). \quad (3)$$

Equating this with Eq. (1), we have

$$\phi(r) = -\frac{kT_i}{Z_i e} \ln \frac{R J_{//i}(r)}{Z_i e \xi_i(r) n_{i0} v_i}. \quad (4)$$

Notice that $\xi_i(r) n_{i0}$ is the axially averaged ion density at the radius r . Using Eq. (4), $\xi_i(0)$, and measured $J_{//i}(0)$ we can obtain an accurate $\phi(0) \sim -15.5$ eV. However, since we can not know $\xi_i(r)$ at arbitrary r , $|\phi(r)|$ is best to be derived using Eq. (3) and measured data of $\tau_{//i}(r)$ by

$$|\phi(r)| = \frac{kT_i}{Z_i e} \ln \frac{\tau_{//i}(r) v_i}{L_p}. \quad (5)$$

Figures 2(a) and (b) show the distributions of $\phi(r)$ and $n_i(r)/n_w$ at the midplane derived from Eqs. (5) and (2), respectively. It is straight forward to derive the space charge distribution $\Delta n_e(r)$ of the warm and hot electrons using Fig. 2(a).

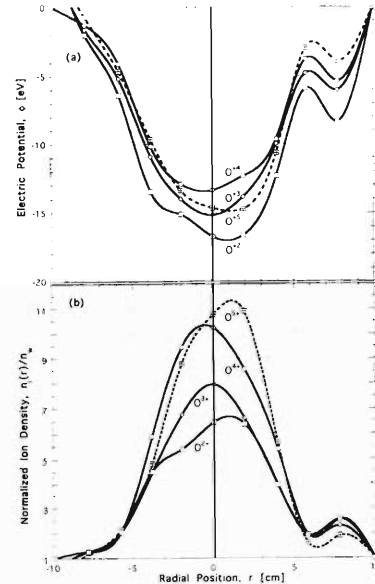


Fig. 2. Radial distributions of (a) electric potential and (b) trapped HCI, derived from an experimental data.¹⁾

Discussions: Figure 2(a) shows that the radius of the ECR-cylinder is $r_0 = 6$ cm. When this cylinder is filled with an uniform excess-electron density Δn_e , the negative potential maximum should be given by $\phi(0) \equiv (\Delta n_e e / 4\epsilon_0) r_0^2 = 4.52 \times 10^{-9} n_e (\text{m}^{-3}) r_0^2 (\text{m})^2$ in Volts, which calculates $\Delta n_e = 9.53 \times 10^5 (\text{cm}^{-3})$ for $|\phi(0)| = 15.5$ V. This parabolic potential is due to the n_{ew} inside the ECR core. A hole-burning visible at $r_0 = 6$ cm in Fig. 2a indicates a shell-like HER with the excess electron density Δn_{eh} less than Δn_{ew} . Shell's half width (Δr) is close to 1 cm, giving the aspect ratio ($\Delta r / r_0$) of 6. The Δn_{eh} modifies the otherwise parabolic potential profile at around $r = 6$ cm. The shell-like HER must be heated via the i_{dm} generated by $v_{ph} \times B_z$ mechanism (v_{ph} : radially outward phase velocity of an electrostatic wave) that can accelerate electrons up to a relativistic energy. The i_{dm} has a stabilizing effect against the resistive driftwave instabilities because it can reduce the core magnetic pressure, similarly to gas mixing which can reduce the core thermal pressure; thereby giving a room to increase the HCI particle density inside the core.

References

- 1) A. Girard et al.: Proc. ECR-12, INS-J-182, p. 164 (1995).
- 2) K. S. Golovanivsky: Rev. Sci. Instr. **63**, 2886 (1992).
- 3) C. C. Petty et al.: J. Phy. Colloq. **50**, C1-783 (1989).

Beam Optics Study of Superconducting Solenoid Focusing in RI Beam Production Beamline

J.-W. Kim and T. Kubo

The use of a strong focusing element has been suggested to obtain a small beam spot on the RI-beam production target located at the entrance of the RIPS (Riken Projectile-fragment Separator).¹⁾ The focused spot size which can be obtained at present is around 2 mm, but some nuclear experiments require even smaller spot size to realize a point-like source of RI beams.

Two kinds of focusing elements were considered: quadrupole triplet and superconducting solenoid. After a series of comparison work we chose to use a superconducting solenoid partly because of its symmetric optical properties.

A high field superconducting solenoid can produce a strong focusing even for the heavy ions of relatively high energy. The solenoid is intrinsically a weak focusing element, but the high magnetic field produced by a superconducting coil overcomes its weakness. The focal length by the solenoidal magnetic field (B) is $f = \frac{4p^2}{q^2 \int B^2 dz}$, where p is the particle momentum and q is the charge state.

We chose a superconducting solenoid employing a conduction cooling method since we wanted to avoid difficulties of maintaining a cryogenic system utilizing liquid helium. In order to provide a sufficient operation margin for such type, the field strength on axis is decided to be 6.2 tesla. Considering the dimension of the RI-beam production target-chamber and the strong stray fields of the solenoid, the distance between solenoid and target is chosen to be around 1 meter.

Beam optics calculations have been carried out using a first- and second- order matrix multiplication program 'TRANSPORT' to optimize the solenoid location and to find out the magnetic parameters and dimensions. The design particle is $^{12}\text{C}^{6+}$ with a beam energy of 135 MeV/u which is the most rigid beam from RRC. From these conditions the solenoid length is calculated to be 1.1 meter. The beam envelopes are calculated with TRANSPORT when the beam emittance is 3.2π mm mrad., which is plotted in Fig. 1. The diameter of the focused beam spot is 0.4 mm.

To examine the settings of optical elements for different beam spot sizes, optics calculations have been carried out assuming 1 mm of spot size. Since the beam parameters at the solenoid can be adjusted by the upstream beamline quadrupoles, a range of the present solenoid fields can be actually used to produce a 1 mm diameter spot. With a field of 5.6 T, a 1 mm beam-spot can be comfortably achieved, where the beam envelopes look similar to those in Fig. 1. Even with 5.2

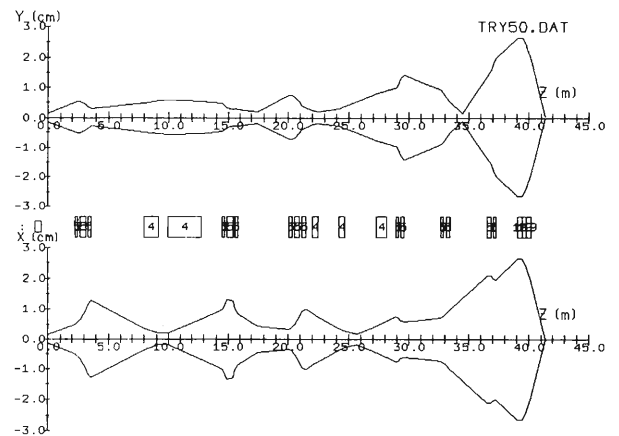


Fig. 1. Beam envelopes when the solenoid field on axis is 6.2 tesla. The beam spot size on target is 0.4 mm, and the drift space from the edge of the solenoid coil to the target is 1.2 m.

It is possible to focus the beam down to 1 mm, but at the cost of transmission efficiency.

The beam spot-size at the focal plane is calculated assuming aberration free for optical elements. However, in focusing the beam to a small dimension, such as in our application, the aberration effects could be of appreciable concern. Especially, if even a smaller beam is needed such as in microbeam applications, aberrations have to be carefully examined since they are the limiting factors to the focusing.²⁻⁴⁾ Lens errors limiting the performance of a lens system are following: spherical, chromatic, and parasitic aberrations. Ray tracing programs can be used for accurate calculations of these errors. In our case, however, only rough error estimations are made using simple analytic expressions found in Ref. 2.

The spherical aberration is described as $d_s = C_s \alpha^3$, where d_s is the diffusion diameter of beam spot, C_s is the aberration coefficient, and α is the half angle of convergence in the image side. The C_s is roughly $90 \text{ rad}^{-3}\text{m}$, and then d_s is 0.3 mm when α is 15 mrad. This appears to be rather large, but since our solenoid is a thick lens, unlike the Glaser type field of Ref. 2, the result may be overestimating.

The chromatic aberration depends on the energy spread of beam. A description of the chromatic aberration is $d_c = C_c \alpha \Delta E/E$. The C_c is $1.2 \text{ rad}^{-1}\text{m}$, which is roughly the focal length. Assuming $\Delta E/E$ is 0.1%, d_c is 0.02 mm, which does not appear detrimental.

On the other hand, misalignment which is a main source of parasitic error can be divided into two compo-

nents: lateral displacement and tilting about its center. This error is known to be sensitive for microbeams⁴, but expected to be less sensitive for a half-millimeter size of beam.

In conclusion, aberrations seem not to be a serious limiting factor in our application, although we need an elaborate ray-tracing calculation for a more definite conclusion.

References

- 1) J. Kim et al.: RIKEN Accel. Prog. Rep. **30**, 175 (1997).
- 2) A. Stephan et al.: Nucl. Instrum. Methods Phys. Res. B **89**, 420 (1994).
- 3) C. J. Maggiore: Nucl. Instrum. Methods **191**, 199 (1981).
- 4) H. Koyama-Ito et al.: Nucl. Instrum. Methods **174**, 331 (1980).

A Liquid He-Free Solenoid for RI Beam Production

J.-W. Kim, T. Kubo, and T. Kawaguchi

A superconducting solenoid has been designed and under construction by Mitsubishi Electric Corporation for use at the entrance of RIKEN projectile-fragment separator (RIPS). The solenoid which utilizes a conduction cooling method will focus heavy ion beams on target for the production of radioactive isotope (RI) beams. Advantages of the superconducting solenoid as a final focusing element, such as symmetric beam optical properties and easy operation, were the reason for our choice over usual multipllets typically quadrupole magnets. The maximum magnetic field on axis is 6.2 tesla (T), and the coil length is 1.05 m. A Gifford-McMahon (GM) refrigerator is employed together with high- T_c material current leads. Some detailed solenoid parameters are listed in Table 1. A test coil has been wound, its performance being tested. We expect the complete solenoid to be delivered in early 1997.

Table 1. Design parameters of the solenoid.

B_{max} on axis	6.2 T
$\int B \cdot dl$	6.8 T·m
J_{ave}	9,800 A/cm ²
Amp·turn	5.5 MA·turn
I_{op}	41 A
Stored Energy	450 kJ
Inductance	534 H
Superconducting Wire	Cu/NbTi=1.3, $\phi = 0.60$ mm

The solenoid is divided into three equal-length coils as shown in Fig. 1. Its purposes are to limit the length of coil-winding and to distribute the stored energy. When the solenoid quenches, the current of each coil decays individually through three diodes in a parallel connection with each coil. Since the coil is epoxy impregnated and radially thin, a high voltage problem becomes negligible only by adopting the diode protection. According to calculations with the program QUENCH,¹⁾ the normal region reaches the radial boundary of the coil prior to the axial boundary in usual quench situations, so that the inter-layer voltage is not of concern.

The refrigerator is a Gifford-McMahon type, and its

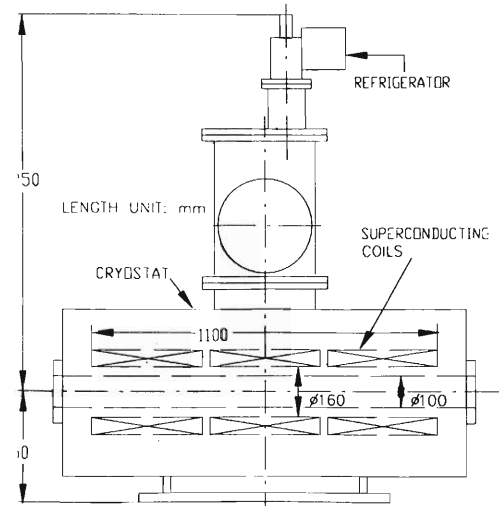


Fig. 1. A schematic view of the solenoid.

cold head is directly attached the central coil. To improve the conduction cooling efficiency, copper plates are placed between the coil and the coil end flanges. Since the cold mass of 300 kg is rather large for a GM refrigerator of 1 W at 4.5 K, the cooling time is expected to be longer than one week. A low operating-current (41 A) was chosen to reduce the heat load through the high- T_c material current leads, resulting in a large coil inductance of 534 H. The current ramping time will be about 2 hours with a 3 volt power supply. We have accepted this slow cooling and ramping times since the solenoid operation will usually not require frequent adjustments of solenoid current.

The solenoid doesn't have a flux return yoke. The stray field on the RI beam production target is around 140 gauss when the maximum field on the solenoid axis is 6.2 T. Those instruments sensitive to the magnetic fields such as turbo pump will have their own shields, which seems to be the most effective shielding method for our case.

References

- 1) M. N. Wilson: Rutherford Laboratory Report RHEL/M-151 (1968).

Study of Spin Dynamics for RHIC Spin Project

H.-Y. Wu, T. Katayama,* A.-U. Luccio,** K. Hatanaka,*** N. Saito, and M. Ishihara

The RHIC collider consists of two rings of superconducting magnets. Each ring consists of three inner arcs and three outer arcs and six insertions joining the inner and outer arcs. Each arc is composed of 11 FODO cells. These kinds of periodic structure will produce a periodic structure on the beam orbit, which will cause the depolarization resonance of polarized beam. During acceleration process, such a resonance occur when the number of spin precession rotations per revolution $G\gamma$ ($G = 1.793$ is the anomalous magnetic moment of the proton, γ is the relativistic factor) is equal to an integer (imperfection resonance) or equal to $kP \pm \nu_y$ (intrinsic resonance), where k is an integer, and P the superperiodicity of ring, and ν_y the vertical betatron tune.

The motion of spin vector is described by BMT equation, and the orbital motion of particle obeys the Lorentz equation. The individual magnet will kick out the spin direction at the place where $\vec{S} \times \vec{B}$ is not zero, where \vec{S} is spin vector.¹⁾ The change of spin direction can be recovered by a periodic magnet setup. But, when the beam energy is at depolarization resonance area, the polarization will be lost.

To avoid the depolarization resonance during the acceleration and colliding experiments, a pair of Siberian snakes will be installed in each ring. One Siberian snake consists of four helical magnets. The perfectly working Siberian snake in one side of the ring rotates spin 180° and the Siberian snake in the other side of the ring would restore the spin to the initial direction. Because this process makes the spin tune value change suddenly at depolarization resonance point, the lost polarization can be recovered and depolarization resonance is easily crossed.

A search of the working points of Siberian snake was made by an analysis for the first order magnetic field and by tracking in both the first and second order magnetic field. The results are given in Table 1, and of course, we use the lowest value set.

The depolarization is mainly decided by vertical motion. The vertical displacement of the particle can be decomposed into two parts: (1) the closed orbit distortion (COD) due to a misalignment of the magnet system and (2) the betatron amplitude of a particle. Intrinsic depolarization resonance is caused by betatron motion, and imperfection depolarization resonance is caused by closed orbit errors. For a perfectly aligned machine, the vertical COD is zero and the strengths of imperfection depolarization resonance are zero, although the energy dispersion produces the horizontal

Table 1. Field strengths of perfectly working Siberian snakes. ($B_2 = -B_3$, $B_4 = -B_1$) at 25 GeV polarized proton. Units by Tesla.

		1	2	3	4
First order	B_1	1.2319	3.2282	5.0892	5.3788
	B_3	3.9580	5.5300	2.3861	8.8272
First order	B_1	1.2336	3.2265	5.0865	5.3769
	B_3	3.9570	5.5273	2.3836	8.8225
Second order	B_1	1.0723	3.3872	5.1324	5.5050
	B_3	3.9328	5.6587	2.2711	8.9256

COD, which is the second order effect of imperfection depolarization.

We used the MAD program to search the closed orbit, and to deduce the transport matrix of the orbit from the lattice output. The BMT equation is given by the matrix formulation:

$$\begin{vmatrix} 1 - (B^2 + C^2)c & ABc - Cs & ACc - Bs \\ ABc - Cs & 1 - (A^2 + C^2)c & BCc + As \\ ACc + Bs & BCc - As & 1 - (A^2 + B^2)c \end{vmatrix}$$

with

$$\begin{cases} c = 1 - \cos\omega\delta s \\ s = \sin\omega\delta s \end{cases}, \quad A = \frac{P_x}{\omega}, \quad B = \frac{P_y}{\omega}, \quad C = \frac{P_s}{\omega},$$

$$\omega^2 = P_x^2 + P_y^2 + P_s^2.$$

Here, the spin rotation strengths are P :

$$\begin{aligned} P_x &= \frac{h}{(B\rho)} [(1 + G\gamma)(-x'B_s + B_x) \\ &\quad + (1 + G)x'(x'B_x + B_s + y'B_y)], \\ P_s &= \frac{h}{(B\rho)} [(1 + G\gamma)(-x'B_x + y'B_y) \\ &\quad + (1 + G)(x'B_x + B_s + y'B_y)], \\ P_y &= \frac{h}{(B\rho)} [(1 + G\gamma)(-y'B_s + B_y) \\ &\quad + (1 + G)y'(x'B_x + B_s + y'B_y)]. \end{aligned}$$

The matrices for each kind of magnet are given for the first order and the second order approximations.^{3,4)}

For the arrangement of magnet system of the lattice of RHIC, a spin tracking of intrinsic depolarization was made with both vertical and horizontal displacements in all elements (dipoles, quadrupoles, sextuples, Siberian snakes, RF's, etc.). The result for the first

* INS, University of Tokyo

** Brookhaven National Laboratory, U.S.A.

*** RCNP, Osaka University

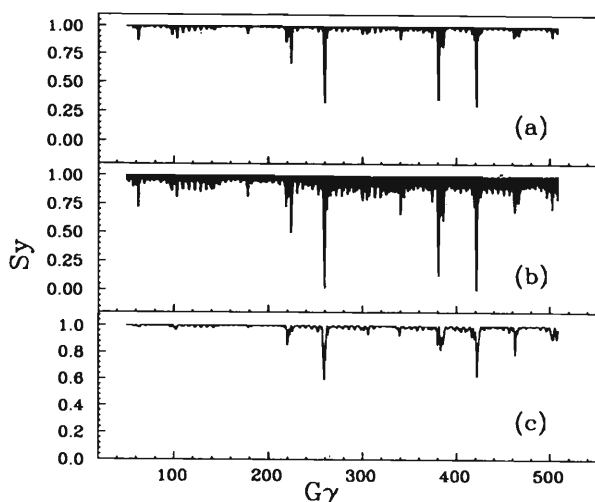


Fig. 1. The intrinsic depolarization spectrum (a) for the first order at $7 \pi \text{ mm} - \text{mrad}$ and (b) for the second order spin tracking at $7 \pi \text{ mm} - \text{mrad}$, compared with (c) the imperfection depolarization spectrum.

order is shown in Fig. 1(a). Here, the first order spin rotation strengths P_x, P_s, P_y , second order magnetic field in Siberian snake, and one spin transport matrix for each element are used.

Spin tracking of the second order is needed for high precision result (Fig. 1(b)), in which the second order terms of spin rotation strength, higher orders of magnetic field in Siberian snake, and spin matrix for slices of an element are involved. A more noise in the background of depolarization spectrum and a larger strength of depolarizing peaks are observed. With larger emittance than $7 \pi \text{ mm} - \text{mrad}$, it is difficult to keep the polarization.

The imperfection depolarization (Fig. 1 (c)) was studied by tracking a particle of zero normal emittance, with the COD at 5 mm rms^5 which is produced by a random misalignment of magnets ($\pm 0.1 \text{ mm rms}$ in length, $\pm 0.1 \text{ mrad rms}$ in angle).

When both the imperfection resonance and intrinsic resonance are taken into account, the alignment error was required to be less than $\pm 0.01 \text{ mm rms}$ in length and $\pm 0.01 \text{ mrad rms}$ in angle; which are too small values to realize in the alignment of magnet system. Although the alignment error can be improved to 0.1 mm rms , the COD correction system can improve the COD as small as $\pm 0.2 \text{ mm rms}$. Figure 2 shows that the polarization spectrum was stable at the vertical COD of $\pm 0.2 \text{ mm rms}$, but becomes unstable at the COD of $\pm 0.3 \text{ mm rms}$ for the normalized emittance $20 \pi \text{ mm} - \text{mrad}$.

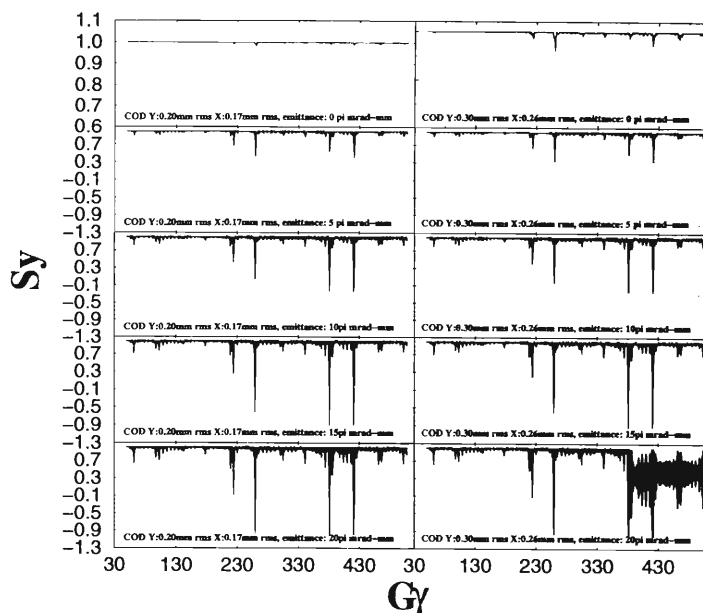


Fig. 2. The intrinsic depolarization coupled with the imperfection depolarization.

References

- 1) H. Wu: AGS/RHIC/Spin Note, BNL, No. 23 (1996).
- 2) H. Wu et al.: AGS/RHIC/Spin Note, BNL, No. 25 (1996).
- 3) H. Wu et al.: AGS/RHIC/Spin Note, BNL, No. 26 (1996).
- 4) A. Luccio: AGS/RHIC/Spin Note, BNL, No. 13 (1996).
- 5) H. Wu et al.: AGS/RHIC/Spin Note, BNL, No. 36 (1996).

Optimization Method Using 2D Analysis in Helical Dipole Magnets for RHIC

M. Okamura, T. Kawaguchi, T. Tominaka, and T. Katayama

The Relativistic Heavy Ion Collider (RHIC) - Spin Project, a joint project between Brookhaven National Laboratory (BNL) and RIKEN, started in 1995. We are collaborating with the BNL-accelerator group to promote research in the Siberian Snake which consists of helical dipole magnets. In present report, a distortion of the dipole field caused by the spiral structure of helical coils is discussed.

In the helical dipole magnets, a large longitudinal field can exist. Therefore we started to compute the longitudinal as well as transverse fields in these magnets using three dimensional (3D) analysis numerical code, OPERA-3d/TOSCA. The results of this work can predict the fraction of longitudinal fields,¹⁾ and are being used successfully in the orbit-spin tracking. On the other hand, to optimize the cross sectional dimensions, the two-dimensional (2D) analysis is more convenient than the 3D analysis which obviously requires time consuming procedures and long computing times. In fact, 2D magnetic field calculation at BNL has been used to optimize the positions of conductors and yokes. However, we need to investigate a difference between the 2D and 3D analysis due to the helical structure.

In order to confirm the effect of helical structure, two types of coils were analyzed by OPERA-3d. Figure 1 shows the first-type which is a full-length Snake Magnet based on the half-length model now being fabricated at BNL. The second-type coil shown in Fig. 2 was drawn by untwisting the first coil. The calculation of this second coil corresponds to the 2D analysis. In order to optimize the configuration of magnets for the RHIC project, calculated azimuthal fields, B_θ , along a

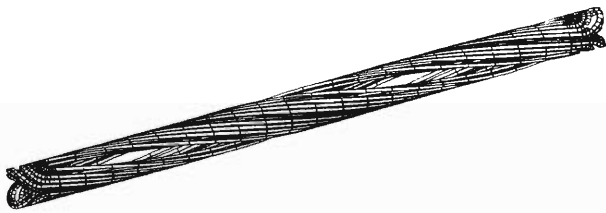


Fig. 1. Helical coil.



Fig. 2. Untwisted helical coil.

circular arc have been expanded in terms of the multipole coefficients of Fourier series in the cylindrical coordinates. In this method, the multipole components by OPERA for both the first and second coils are almost same. Yet, there must be an effect due to the longitudinal fields in the helical magnet. We have analyzed this by using the vertical fields, B_y . The ratio of the sextupole component to the dipole component in the first coil was predicted to be 0.076% larger than that in the second coil.

In case of helical dipole magnets, the expressions of the field are given ignoring skew components as follows.

$$B_r = B_0 \sum_0^n f_n I'_{n+1}((n+1)kr) \tilde{b}_n \sin(n+1)\theta \quad (1)$$

$$B_\theta = \frac{1}{kr} B_0 \sum_0^n f_n I_{n+1}((n+1)kr) \tilde{b}_n \cos(n+1)\theta \quad (2)$$

$$B_z = -B_0 \sum_0^n f_n I_{n+1}((n+1)kr) \tilde{b}_n \cos(n+1)\theta, \quad (3)$$

where,

$$f_n = \frac{2^{n+1}(n+1)!}{(n+1)^{n+1}} \frac{1}{r_0^n k^n}, \quad k = \frac{2\pi}{\lambda}. \quad (4)$$

Here, I and λ are the modified Bessel function and helical pitch of helix, respectively. As mentioned above, according to our 3D analysis, there is no obvious effect of helical structure on multipole components in the cylindrical coordinates. Then, the above series can be converted into the Cartesian coordinates,

$$B_x = B_0 \sum_0^n f_n \tilde{b}_n \left[I'_{n+1}((n+1)kr) \sin(n+1)\theta \cdot \cos\theta - \frac{I_{n+1}((n+1)kr)}{kr} \cos(n+1)\theta \cdot \sin\theta \right] \quad (5)$$

$$B_y = B_0 \sum_0^n f_n \tilde{b}_n \left[I'_{n+1}((n+1)kr) \sin(n+1)\theta \cdot \sin\theta + \frac{I_{n+1}((n+1)kr)}{kr} \cos(n+1)\theta \cdot \cos\theta \right]. \quad (6)$$

Here, we assume that the helical dipole magnet can be optimized only using B_θ components. Then $b_n = 0$ for $n > 0$. So, these expressions can be transformed into,

$$B_x = B_0 \tilde{b}_0 \left[I'_1(kr) - \frac{I_1(kr)}{kr} \right] \sin 2\theta \quad (7)$$

$$B_y = B_0 \tilde{b}_0 \left[\left(I'_1(kr) + \frac{I_1(kr)}{kr} \right) - \left(I'_1(kr) - \frac{I_1(kr)}{kr} \right) \cos 2\theta \right]. \quad (8)$$

These expressions show that the B_x component consists of a single sextupole term. Also, the B_y component is expressed as a sum of the dipole and sextupole terms. Accordingly, when the magnet is optimized using Fourier expansion of only B_θ , it appears a sextupole component in the Cartesian coordinates. In our magnets, the ratio of the sextupole component to the dipole component is predicted to be 0.0771% at $r = 3.0$ cm. This value, which is caused by the b_0 coefficient explains the results of the 3D analysis. Of course, in a real magnet there are effects caused by higher order coefficients, $n = 1, 2, 3, \dots$ but these terms can be ignored because the $n = 0$ or b_0 , term is dominant in the Snake Magnet.

To optimize the configuration of helical dipole magnets by using 2D calculations, it will be effective to set b_2 so as to offset the helical effect due to b_0 . As a result, the azimuthal angle dependence θ dependence of magnetic fields will be eliminated, and the only remaining effect of being helical is the radial dependence expressed by the first term in Eq. (8). We plan to achieve the ideal field uniformity limit of $\pm 0.077\%$ due to this radial dependence in our helical magnet designs.

References

- 1) M. Okamura et al.: Proc. 5th Eur. Part. Accel. Conf., p. 2261 (1996).

High Current Design of Superconducting Helical Dipole Magnets for RHIC Spin Project

T. Kawaguchi, T. Tominaka, M. Okamura, K. Hatanaka, and T. Katayama

The RHIC spin project¹⁾ under RIKEN-BNL collaboration is planning to use 48 superconducting helical dipole magnets as Siberian Snakes and spin rotators. The construction of superconducting helical dipole magnets is the first trial in the world. The magnets have its straight length of 2.4 m and helical angle of 360 degrees, which needs to generate the maximum magnetic field of 4.0 T in the beam orbit area.

BNL has designed low-current helical dipole magnets its operation current around 400 A.^{2,3)} The principal idea of designing the low current magnet is to decrease the cooling capacity for the power leads which connect the current-carrying lines between the room temperature and 4.5 K regions. But this low current design is risky to achieve such a high magnetic field, because the low current coil requires fine-round wires and hence more turn numbers, which is liable to cause wire motions that may induce a coil quench. Thus, all of the superconducting dipole magnets (of straight type) existed in the world are operating at currents higher than 5000 A, and are using Rutherford type cables formed in a rectangular shape. From the above point of view, we have decided to design the high-current helical dipole magnets as one of the backups to the BNL low current design.

In our design we selected the operation current to be 3000 A which enables to use Rutherford type cable, satisfactory in the cooling capacity. Table 1 shows a comparison of the basic design parameters among the BNL standard dipole (straight type), the BNL helical model, and the RIKEN helical model. The merits of our high current design are as follows: (1) wire arrangement is accurate because of the small turn number and of the rectangular wire shape; (2) the first

point makes the coil tough against the quench because wire motions can hardly occur; (3) the first point also makes the magnetic field accurate due to the precise wire arrangement; (4) applying a pre-stress during the coil winding is easy compared with the low current coil, and the pre-stress can give a further quench toughness; (5) the small turn number reduces the construction cost and time. The demerits are as follows: (1) the cooling capacity increases (although acceptable); (2) the power supplies and the bus bar system between the power supplies and the magnets are much more expensive than those in the low current design.

The basic design was made by RIKEN,⁴⁾ and the technical design study was done by Hitachi Ltd. Corp.⁵⁾ and Mitsubishi Electric Corporation.⁶⁾ Figure 1 shows the coil shape of model magnet, used for three dimensional magnetic field calculation. Cross section of designed coils is shown in Fig. 2. During the design, we have studied the wire arrangements

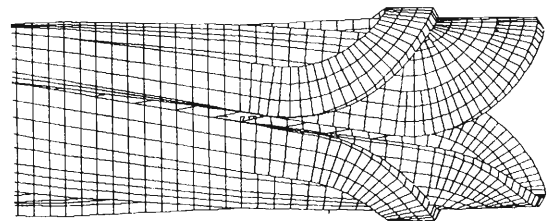


Fig. 1. Helical coil structure (for 3D magnetic field calculation).

Table 1. Comparison among RHIC dipole coil and two model snake coils by BNL & RIKEN designs.

Items	RHIC dipole coil	Model snake coil	
		BNL design	RIKEN design
Central field with yoke, B ₀ (T)	3.5	4.0	4.0
Coil inner dia. (mm)	80	100	100
Yoke inner dia. (mm)	119.4	182.8	139.4
Length of straight section (m)	9.266	1.1	2.0
Helical angle (degree)	0	180	360
Operation current (A)	5000	382	3000
Superconducting cable	Rutherford (rectangular)	round cable	Rutherford (rectangular)
	d 0.648 mm x 30	d 0.33 mm x 7	d 0.648 mm x 18

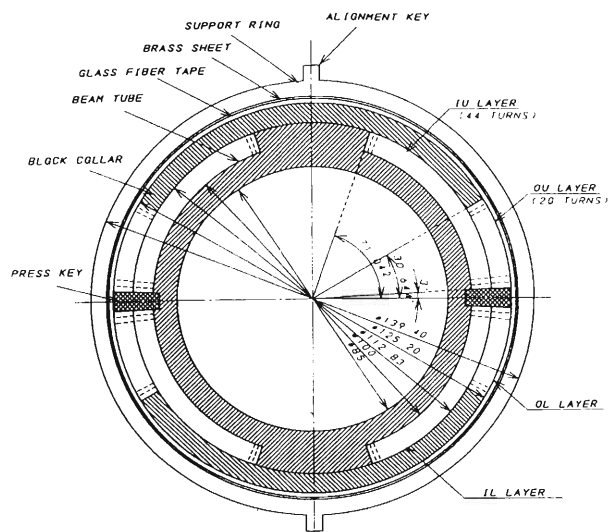


Fig. 2. Helical dipole coil cross section (unit: mm).

resulting in better magnetic field distributions, winding procedures, pre-stress application methods, electrical insulation systems for the coil, magnetic forces of the coil, and so on. The pre-stress application method for the helical dipoles is very different from that for normal straight dipoles, and we need more elaborate technical designs before the real construction of the model magnet.

BNL had already constructed the first model coil in 1995 based on the low current design, when our design work was initiated. After our design study, we decided to postpone the construction of our model magnet, because the second and third model magnets were being constructed at BNL. In November 1996, one of the two model magnets reached 4 T after 12 quenches. This magnet should be improved from the view points of the quench toughness and of the accurate magnetic field, but it succeeded to achieve the required magnetic field (of 4.0 T) which was thought risky. As described above, the BNL low current design allows to make economical systems. Though our design will be finished

as only a design work, we have studied many aspects through this design work and we can give our comments to BNL for the next prototype magnet design and for the real magnets to be constructed through the RIKEN-BNL collaboration.

References

- 1) RHIC spin project: Proposal on spin physics using the RHIC polarized collider, Sep. (1993).
- 2) R. Gupta et al.: Design and status of helical magnet at BNL, BNL internal workshop, Sep. (1994).
- 3) R. Meinke: Helical dipole magnets using advanced manufacturing technology, BNL internal report, Apr. (1996).
- 4) T. Kawaguchi: Preliminary study for superconducting snake coil, RIKEN internal workshop, Dec. (1995).
- 5) Hitachi Ltd. Corp.: Design study for Siberian snake coil in RHIC, RIKEN internal report, Mar. (1996).
- 6) Mitsubishi Electric Corp.: Design report of a superconducting helical coil (Siberian snake) for the relativistic heavy ion collider (RHIC), RIKEN internal report, Mar. (1996).

Field Analysis of a Helical Dipole Magnet

K. Hatanaka, T. Katayama, T. Kawaguchi, M. Okamura, and T. Tominaka

Superconducting helical dipole magnets will be used in RHIC as Siberian snakes and rotators.¹⁾ Extensive investigations are performed on the orbit and spin trackings to examine whether the spin polarization of the proton will be conserved up to the highest energies with the help of Siberian snakes. During the first stage, the numerical tracking was performed using an analytical expression for the magnetic field in the snake. It is now required to use a more realistic description for the magnetic field in the snake. Beam trajectory and spin motion can numerically be calculated, provide that the magnetic field map is given along the beam path. However, it is not practical to store the whole field strengths along the helical magnets. Besides, the map has usually some errors. Calculated or measured magnetic field maps may not always satisfy Maxwell's equations. This causes errors in numerical calculations of the orbit and spin matrices; orbit matrices should be symplectic, and spin matrices be unitary. There are following three methods to improve the situation. (1) An approximately symplectic matrix calculated from a field map is transformed into an exactly symplectic one, (2) Small modifications to the field values are performed so as to bring the field satisfy Maxwell's equation. (3) The field is made more Maxwellian by reading only one or two field components from the map and deriving the other components by using appropriate expansion coefficients.

The method (3) is physically more sound²⁾ and should produce a more symplectic matrix. This strategy was applied to examine three dimensional (3D) magnetic field calculated by the computer code TOSCA including the fringing field region. In the central region of a finite-length helical dipole magnet or in the whole region if the length was infinite, the magnetic field has a cylindrical symmetry, and a solution of the Laplace equation $\Delta\Psi = 0$ is given by

$$\Psi = -B_0 \left\{ \sum_{n=0}^{\infty} \frac{2^{n+1}(n+1)!}{(n+1)^{n+2}} \frac{1}{r_0^n k^{n+1}} I_{n+1}((n+1)kr) \right. \\ \left. \times [\tilde{a}_n \cos((n+1)\tilde{\theta}) + \tilde{b}_n \sin((n+1)\tilde{\theta})] \right\}.$$

Here I_n is the modified Bessel function and $\tilde{\theta} = \theta - kz$, where $k = 2\pi/\lambda$ and λ is the wave length of the helix.

In the analysis of the magnetic field, above expansion was assumed to be applicable at the fringing field region as well as at the magnet center. The coefficients \tilde{a}_n and \tilde{b}_n were determined by fitting the radial field B_r and azimuthal field B_θ in the median plane ($\theta = 0$ or π), respectively. In the fitting procedure, the maximum value of n was taken to be 6, and odd n values were included as well. The longitudinal field B_z in the median plane was derived from the obtained coefficients. Differences between the 3D calculated and fitted/derived fields are shown in Fig. 1. Off median plane magnetic field distributions were derived with the same coefficients and are also compared with the 3D calculations by TOSCA in Fig. 1. The magnetic field in the median plane is seen from the figure to have magnetic field well simulated by a simple function. For the off median plane magnetic field, however, the difference is quite large: contributions from the coils should be taken into account for the function used.³⁾

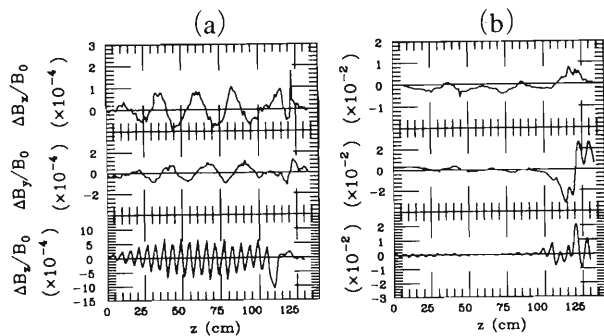


Fig. 1. Differences between the 3D-calculated and fitted/derived fields normalized by B_0 , (a): in the median plane $x = 3$ cm and $y = 0$ cm, and (b): off median plane $x = 0$ cm and $y = 3$ cm.

References

- 1) E. Courant et al.: AGS/RHIC/Spin Note, BNL, No. 40 (1996).
- 2) A. Luccio et al.: AGS/RHIC/Spin Note, BNL, No. 41 (1996).
- 3) K. Hatanaka et al.: AGS/RHIC/Spin Note, BNL, No. 37 (1996).

Analytical Field Calculation of Helical Coils for RHIC Spin Project

T. Tominaka, M. Okamura, T. Kawaguchi, K. Hatanaka, H. Sato, and T. Katayama

The purpose of this paper is to give the analytical expression of multipole expansion for a single helical current conductor, and to give that for a helical dipole magnet. These analytical expressions may be useful for not only design but also field analysis of a helical dipole magnet.

The field in the current-free and iron-free regions of a helical magnet can be obtained by using the scalar potential Ψ . The 3-dimensional (3D) Laplace's equation in circular cylindrical coordinates is expressed as:

$$\nabla^2 \Psi = \frac{\partial^2 \Psi}{\partial r^2} + \frac{1}{r} \frac{\partial \Psi}{\partial r} + \frac{1}{r^2} \frac{\partial^2 \Psi}{\partial \theta^2} + \frac{\partial^2 \Psi}{\partial z^2} = 0.$$

Since the winding is periodic in z -direction with a pitch length L , the general solution of Laplace's equation is,¹⁾

$$\Psi_h(r, \theta, z) = \sum_{n=1}^{\infty} (c'_n I_n(nkr) + d'_n K_n(nkr)) \times \{a'_n \cos(n(\theta - kz)) + b'_n \sin(n(\theta - kz))\} + e'z + f'\theta.$$

Here, $k = 2\pi/L$, $I_n(nkr)$ is the modified Bessel function of the first kind of order n , and $K_n(nkr)$ is the modified Bessel function of the second kind of order n . The helical scalar potential can be determined from the requirement that the non-helical scalar potential Ψ_h is equal to the 2D scalar potential. As a result, the interior ($r < a$) helical scalar potential and magnetic field generated by a single helical conductor of radius a , angle ψ and current I are given by

$$\Psi_{h,in}(r, \theta, z) = \frac{\mu_0 I}{2\pi} \sum_{n=1}^{\infty} (n-1)! \left[\frac{2}{nka} \right]^n I_n(nkr) \times \{-a_n(k) \cos(n(\theta - kz)) + b_n(k) \sin(n(\theta - kz))\} - \frac{\mu_0 I}{2\pi} kz$$

$$\left\{ \begin{array}{l} B_r(r, \theta, z) = \frac{\mu_0 I}{\pi} k^2 a \sum_{n=1}^{\infty} n K'_n(nka) I'_n(nkr) \times \sin(n(\theta - \psi - kz)) \\ B_\theta(r, \theta, z) = \frac{\mu_0 I}{\pi} ka \sum_{n=1}^{\infty} n K'_n(nka) \frac{I_n(nkr)}{r} \times \cos(n(\theta - \psi - kz)) \\ B_z(r, \theta, z) = -\frac{\mu_0 I}{\pi} k^2 a \sum_{n=1}^{\infty} n K'_n(nka) I_n(nkr) \times \cos(n(\theta - \psi - kz)) + \frac{\mu_0 I}{2\pi} k. \end{array} \right.$$

Similarly, the exterior ($r > a$) helical scalar potential and magnetic field are:

$$\Psi_{h,ex}(r, \theta, z) = \frac{\mu_0 I}{2\pi} \sum_{n=1}^{\infty} (n-1)! \left[\frac{2}{nka} \right]^n \frac{I'_n(nka)}{K'_n(nka)} K_n(nkr) \times \{-a_n(k) \cos(n(\theta - kz)) + b_n(k) \sin(n(\theta - kz))\} - \frac{\mu_0 I}{2\pi} \theta$$

$$\left\{ \begin{array}{l} B_r(r, \theta, z) = \frac{\mu_0 I}{\pi} k^2 a \sum_{n=1}^{\infty} n I'_n(nka) K'_n(nkr) \times \sin(n(\theta - \psi - kz)) \\ B_\theta(r, \theta, z) = \frac{\mu_0 I}{\pi} ka \sum_{n=1}^{\infty} n I'_n(nka) \frac{K_n(nkr)}{r} \times \cos(n(\theta - \psi - kz)) + \frac{\mu_0 I}{2\pi} \frac{1}{r} \\ B_z(r, \theta, z) = -\frac{\mu_0 I}{\pi} k^2 a \sum_{n=1}^{\infty} n I'_n(nka) K_n(nkr) \times \cos(n(\theta - \psi - kz)) \end{array} \right.$$

The above expressions for the magnetic field of a helical coil are the functions of r and $(\theta - kz)$, and are helically symmetric. However, the sum \sum to a finite order of the above expressions of the interior and exterior magnetic fields do not approach the same value at $r = a$. This discontinuity of the magnetic field at $r = a$ can be overcome with application of the Cesàro's method of summation.¹⁾

For a single helical conductor with current $I = 100$ A, radius $a = 0.33$ mm, angle $\psi = 30^\circ$, and pitch length $L = 9.51$ mm, a comparison between the analytical and numerical calculations was made. Since an agreement was confirmed between the analytical and numerical calculations, the field was calculated for the whole space except for the located point of a single helical conductor, as shown in Fig. 1.

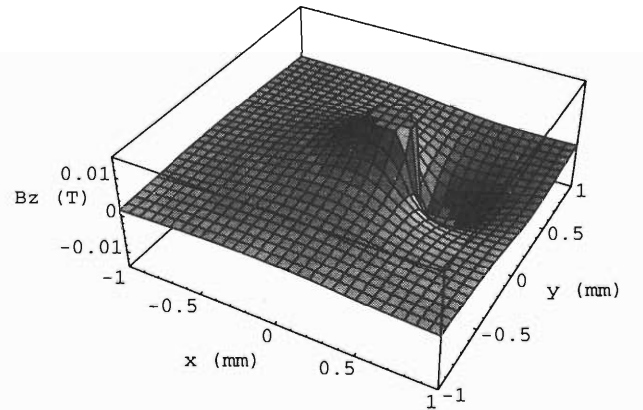


Fig. 1. 3D plot of the analytically calculated B_z at $z = 0$, which is consistent with the numerical calculation with Biot-Savart Law.

Using the above expression for $r < a$, the interior magnetic field of helical dipole coil with an infinite length can easily be derived as the summation of four(4) helical line currents with dipole symmetry as follows:²⁾

$$\left\{ \begin{array}{l} B_r(r, \theta, z) = B_{\text{ref}}(k) r_0 \sum_{n=1}^{\infty} n! \left[\frac{2}{n k r_0} \right]^n k I'_n(n k r) \times \\ \quad \{-a_n(k) \cos(n(\theta - k z)) + b_n(k) \sin(n(\theta - k z))\} \\ B_\theta(r, \theta, z) = B_{\text{ref}}(k) r_0 \sum_{n=1}^{\infty} n! \left[\frac{2}{n k r_0} \right]^n \frac{I_n(n k r)}{r} \times \\ \quad \{a_n(k) \sin(n(\theta - k z)) + b_n(k) \cos(n(\theta - k z))\} \\ B_z(r, \theta, z) = B_{\text{ref}}(k) r_0 \sum_{n=1}^{\infty} (-k) n! \left[\frac{2}{n k r_0} \right]^n I_n(n k r) \times \\ \quad \{a_n(k) \sin(n(\theta - k z)) + b_n(k) \cos(n(\theta - k z))\}, \end{array} \right.$$

where r_0 is the reference radius.

The above expression can be obtained as the extension of the following interior magnetic field of 2D dipole coil in the European definition,

$$\left\{ \begin{array}{l} \lim_{k \rightarrow 0} [B_{r,h}(r, \theta, z)] = B_{r,2d}(r, \theta) = \\ \quad B_{\text{ref}} \sum_{n=1}^{\infty} \left(\frac{r}{r_0} \right)^{n-1} (-a_n \cos n\theta + b_n \sin n\theta) \\ \lim_{k \rightarrow 0} [B_{\theta,h}(r, \theta, z)] = B_{\theta,2d}(r, \theta) = \\ \quad B_{\text{ref}} \sum_{n=1}^{\infty} \left(\frac{r}{r_0} \right)^{n-1} (b_n \cos n\theta + a_n \sin n\theta) \\ \lim_{k \rightarrow 0} [B_{z,h}(r, \theta, z)] = B_{z,2d}(r, \theta) = 0. \end{array} \right.$$

Therefore, the normal and skew multipoles due to many helical line currents with current I_i , radius a_i , angle ψ_i are

$$\left\{ \begin{array}{l} B_n(k) = B_{\text{ref}}(k) b_n(k) = -\frac{\mu_0}{\pi} \frac{1}{2^n (n-1)! r_0} (n k r_0)^n \times \\ \quad \sum_i I_i (k a_i K_{n-1}(n k a_i) + K_n(n k a_i)) \cos n\psi_i \\ A_n(k) = B_{\text{ref}}(k) a_n(k) = -\frac{\mu_0}{\pi} \frac{1}{2^n (n-1)! r_0} (n k r_0)^n \times \\ \quad \sum_i I_i (k a_i K_{n-1}(n k a_i) + K_n(n k a_i)) \sin n\psi_i. \end{array} \right.$$

With the definition of $b_1(k) = 1$ (=constant), naturally $B_{\text{ref}}(k) = B_1(k)$. Then, the asymptotic forms for the reference field $B_{\text{ref}}(k)$ and for these helical multipole coefficients $a_n(k)$ and $b_n(k)$ are given in the limit $k \rightarrow 0$ (or $L \rightarrow \infty$) by,

$$\left\{ \begin{array}{l} \lim_{k \rightarrow 0} [B_{\text{ref}}(k)] = B_{\text{ref}} \\ \lim_{k \rightarrow 0} [a_n(k)] = a_n \\ \lim_{k \rightarrow 0} [b_n(k)] = b_n. \end{array} \right.$$

Therefore, the twisting from the 2D dipole to helical dipole gives mathematically two changes. One is in the character of the function describing the field, and another is in the values of multipoles determined by the current and position of the conductor.

This analytical method was used to obtain the contents of multipoles expected for both helical dipoles of slotted and direct-wind types.^{3,4)} For the helical dipole

of slotted type designed in BNL, the twist (or k) dependence of the reference field $B_{\text{ref}}(k)$ and of the helical sextupole coefficient $b_3(k)$ are shown in Fig. 2, while the dipole field distribution without iron yoke is shown in Fig. 3. In addition, it was confirmed that this analytical calculation is consistent with the numerical calculation by the 3D magnetic field numerical code, OPERA-3d/TOSCA.^{2,3,5)}

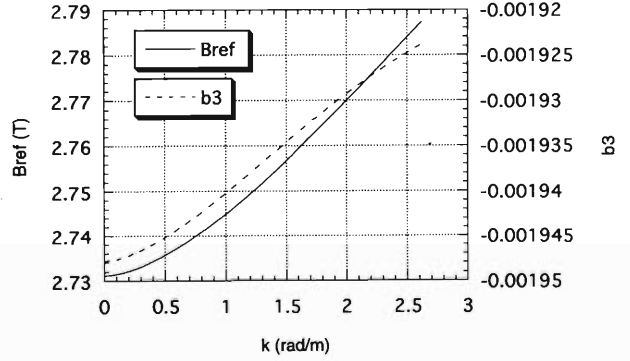


Fig. 2. Twist dependence of the reference field $B_{\text{ref}}(k)$ and of the normal sextupole coefficient $b_3(k)$.

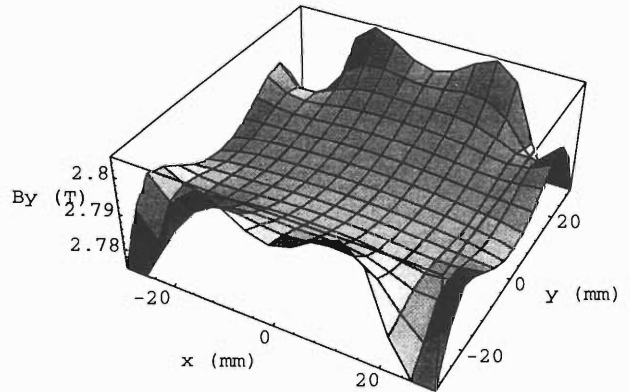


Fig. 3. Dipole field distribution of the BNL helical dipole magnet of slotted type without an iron yoke.

References

- 1) T. Tominaka: AGS/RHIC/Spin Note, BNL, No. 49 (1996).
- 2) T. Tominaka: AGS/RHIC/Spin Note, BNL, No. 24 (1996).
- 3) T. Tominaka: AGS/RHIC/Spin Note, BNL, No. 47 (1996).
- 4) T. Tominaka: AGS/RHIC/Spin Note, BNL, No. 48 (1996).
- 5) M. Okamura: AGS/RHIC/Spin Note, BNL, No. 46 (1996).

Observation of Slow Transient Effect of Magnetic Field Gradient in RIKEN Ring Cyclotron Magnet

M. Kumada* and M. Kase

In a cyclotron, it is known that during the startup a kind of sophisticated initialization of magnets is necessary. The way of initialization seems to vary from Institute to Institute. Even with the best way acquired during the startup, it is common that operator has to wait for a couple of hours until a circulating beam stabilizes. This waiting period is much longer than that of synchrotron. This long waiting time is usually ascribed to the magnetic after-effect, warm-up effect of magnet iron, or a temperature effect of cooling water. These causes, however, can not explain the difference between a cyclotron and a synchrotron, as the causes affect similarly for both. The major difference between the cyclotron and synchrotron is in the thickness of iron material. The cyclotron uses a block solid magnet, whereas the synchrotron in many cases uses laminated magnet. The adoption of a laminated magnet in a synchrotron is to avoid an eddy current effect. Since a cyclotron magnet operates by DC, it is believed that the eddy current effect does not exist.

The time constant of the eddy current scales as square of the thickness of the iron width. Thickness of 0.5 mm lamination is common in synchrotron. The width of a block of the cyclotron ranges upto a few meter. Even in a DC magnet, one has to turn on its current from zero to a finite value or has to change the field strength in need for tuning. The question is whether the time constant of a response of the DC block magnet is negligible or not. The ratio of the time constant between the laminated magnet and the typical cyclotron magnet is $(3 \times 10^{-3}/3)^2 = 10^{-6}$, whose large difference in magnitude makes us uneasy. It can be shown that the time constant can be calculated analytically for a simple magnet of simple geometry and is an order of tens of minutes. The measurement was done in DC magnets of various sizes at NIRS.¹⁾ For further detailed study of transient effect, we have measured the time response of the RIKEN sector magnet during the summer shut down period. Analysis of the eddy current predicts a transient response of the field distribution as well as strength. Therefore, we have set three hall probes at different locations inside the gap of the sector magnet. The magnet excitation current whose shape is trapezoidal was also measured at the same time.

Figure 1 shows the time response of the ratio of the magnetic strengths at two locations, and the shape of excitation current. It is apparent that the field distribution changes with time. Figure 2 shows the field strength (B_{in}) and at the same time the ratio of this

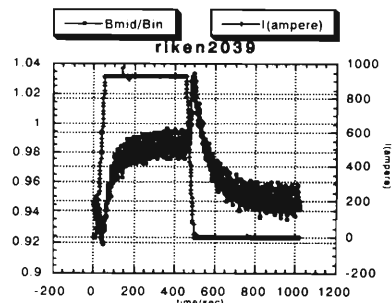


Fig. 1. Time response of the Ratio of field.

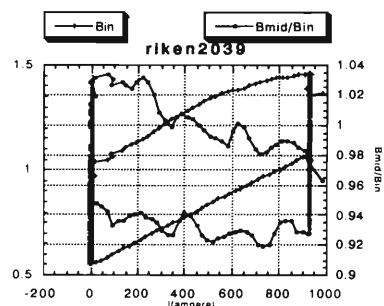


Fig. 2. Hysteresis of the ratio of the field and the strength of the field.

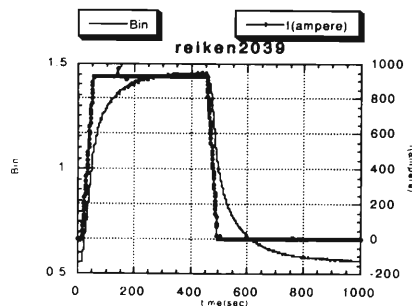


Fig. 3. Time response of the field strength.

field strengths (B_{mid}/B_{in}) as a function of the exciting current. It shows a large hysteresis: characteristics never seen in the existing literature. Finally, Fig. 3 shows the time response of the field strength and excitation current. From this data, it can be shown that the decaying time constant is not composed from a single component, but at least from several component, as predicted by the theory. They are 1.8, 6.25, 34.7 and 81.8 minutes respectively. Further study by computer calculation is currently underway by the code of OPERA2D.

References

- 1) Kumada et al.: Pres. at 1996 Fall Meet. Phys. Soc. Jpn., to be also submitted to PAC97.

* National Institute of Radiological Sciences

Commissioning Run of a New Injector System for RILAC

A. Goto, Y. Miyazawa, M. Hemmi, O. Kamigaito, T. Nakagawa, M. Kase, T. Chiba, S. Kohara, E. Ikezawa, T. Kageyama, S. Numata, Y. Batygin, and Y. Yano

Installation of a new injector system for RILAC on site was made during the August and September '96 after its one-year test on the test bench. The commissioning run of the system then started in October, 1996.

Figure 1 shows a photograph of the new injector system consisting of an 18 GHz ECR ion source¹⁾ and a variable-frequency folded-coaxial (FCRFQ) linac,²⁾ along with the beam transport line from the existing 450 kV Cockcroft-Walton terminal to a new beam matching section³⁾ installed in between the FCRFQ linac and RILAC.

During the commissioning runs, beam acceleration tests through RILAC have been performed successfully for $^{14}\text{N}^{2+,3+}$, $^{36}\text{Ar}^{5+}$, $^{40}\text{Ar}^{2+4+5+}$, $^{56}\text{Fe}^{8+}$, $^{84}\text{Kr}^{5+}$, and $^{129}\text{Xe}^{7+}$ ions at the frequencies of 18.8, 22.3, 28, 32, 35, and 36 MHz. High beam intensity and high beam transmission efficiency both better than ever before were obtained; the maximum efficiency of 51% was attained for transmission from the ion source till the end of RILAC. An $^{36}\text{Ar}^{5+}$ ion beam was further delivered to and accelerated through RRC. We have achieved for the first time the beam intensity of $1\ \mu\text{A}$ from RRC, which is the maximum intensity required for the RI Beam Factory project. Results of beam acceleration tests are summarized in Table 1.



Fig. 1. Photograph of the new injector system along with the beam transport line starting from the existing 450 kV Cockcroft-Walton terminal.

Table 1. Results of the acceleration tests through RILAC using the new injector system.

Ion	Frequency (MHz)	Intensity ($e\ \mu\text{A}$)			Transmission efficiency (%)	Energy (MeV)	Beam Power (W)
		after ECRIS	before RILAC	after RILAC			
$^{14}\text{N}^{2+}$	28.0	88	51	22	25	22.0	296
$^{14}\text{N}^{3+}$	32.0	96	66	37	39	28.6	352
$^{14}\text{N}^{3+}$	35.0	120	84	40	33	34.3	457
$^{14}\text{N}^{3+}$	36.0	68	45	30	44	36.4	364
$^{36}\text{Ar}^{5+}$	18.8	28	16	11	38	16.5	35
$^{40}\text{Ar}^{2+}$	18.8	93	45	25	27	28.2	352
$^{40}\text{Ar}^{5+}$	18.8	27	19	10	38	25.0	50
$^{40}\text{Ar}^{4+}$	22.3	40	22	14	34	40.0	135
$^{56}\text{Fe}^{8+}$	28.0	20	14	10	51	87.7	110
$^{84}\text{Kr}^{5+}$	18.8	22	10	6.3	29	59.3	75
$^{129}\text{Xe}^{7+}$	18.8	10	3	2.2	22	91.2	28

Beam services using the new injector system are planned to start from the Spring of 1997.

We have decided to raise the maximum extraction voltage of the ECR ion source from 10 kV (the initial designed value) to 20 kV in order to obtain higher beam intensities. Modifications of the devices for that purpose such as bending magnet, solenoid magnet, and their power supplies have been completed, while re-fabrication of the vanes of FCRFQ linac is under way. Fabrication of the new vanes is to be completed in the Summer of 1997. With this upgrade we can expect the

beam intensity much higher than the present one: e.g., by a factor of about 2 for Ar^{11+} ions.

References

- 1) T. Nakagawa et al.: RIKEN Accel. Prog. Rep. **30**, 188 (1997).
- 2) O. Kamigaito et al.: RIKEN Accel. Prog. Rep. **30**, 189 (1997).
- 3) O. Kamigaito et al.: RIKEN Accel. Prog. Rep. **30**, 191 (1997).

Development of RIKEN 18 GHz ECRIS

T. Nakagawa, J. Ärje,* Y. Miyazawa, M. Hemmi, T. Chiba, N. Inabe, M. Kase,
T. Kageyama, O. Kamigaito, A. Goto, and Y. Yano

After the successful production of highly charged ions from gas using RIKEN 18 GHz ECRIS, we tried to produce the metallic ions using the so-called "MIVOC (Metal Ion by Volatile Compounds) method"^{1,2)} in collaboration with Jyväskylä University.

Organic metallic compounds are in a high vapor pressure (i.e., 10^{-3} mbar) as the material transforms into its gaseous state at room temperature. As reported in Ref. 2, the main drawback of the MIVOC method is the contamination of the plasma chamber by carbon. In order to minimize this drawback, the plasma chamber wall was covered with a thin aluminum tube (of the thickness 1 mm) which can be easily changed upon contamination of its inner wall. Furthermore, it emits several secondary electrons by an electron impact, which helps to increase the density of plasma.³⁾ The compound chamber is attached to the gas feeding line with a regulation valve to control its floating rate. Figure 1 shows the beam intensities of highly charged Fe, Ni and Ru ions produced respec-

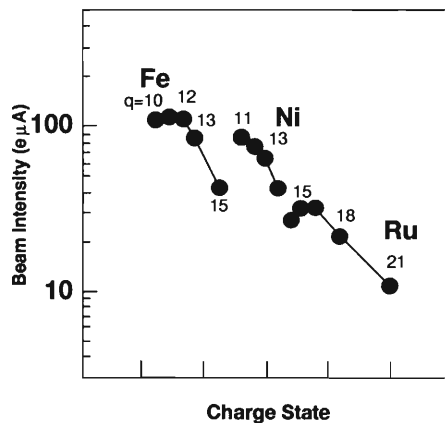


Fig. 1. Charge state distributions of Ni, Fe, and Ru ions.

tively from $\text{Fe}(\text{C}_5\text{H}_5)_2$, $\text{Ni}(\text{C}_5\text{H}_5)_2$ and $\text{Ru}(\text{C}_5\text{H}_5)_2$ at the extraction voltage (V_{ext}) of 10 kV. The typical gas pressures of the plasma chamber and extraction stage were 1.5×10^{-6} and 5×10^{-7} Torrs, respectively. The RF power was in the range of 300 ~ 500 W. The typical beam intensity of Fe^{13+} , Ni^{13+} , and Ru^{16+} were 80, 60, and 30 eμA, respectively. Because the Ru has the very high melting point of ~ 2450 °C, it is quite difficult to achieve such an intense beam of highly charged Ru ions by other methods.

In order to produce highly charged Ta ions, we inserted a Ta-rod (of 2 mm diameter) directly to the plasma. Figure 2 shows the best results of Ta ions at the extraction voltage of 14 kV. The beam intensity of Ta^{20+} was 32 eμA.

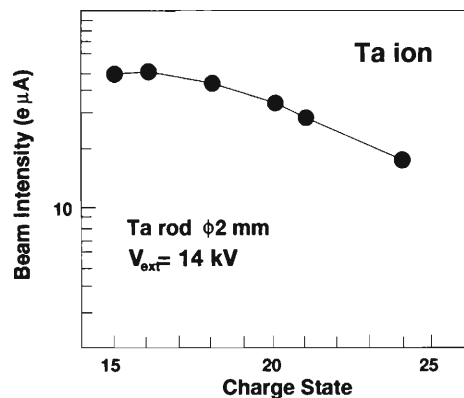


Fig. 2. Charge state distributions of Ta ions.

References

- 1) H. Koivisto et al.: Nucl. Instrum. Methods Phys. Res. B **94**, 291 (1994).
- 2) H. Waldmann et al.: Nucl. Instrum. Methods Phys. Res. B **98**, 532 (1995).
- 3) T. Nakagawa et al.: Jpn. J. Appl. Phys. **35**, 4077 (1996).

* Accelerator Laboratory, University of Jyväskylä, Finland

Performance Tests of a Variable-Frequency RFQ Linac for RILAC

O. Kamigaito, A. Goto, Y. Miyazawa, T. Chiba, M. Hemmi, M. Kase, S. Kohara, Y. Batygin, and Y. Yano

Performance tests of the variable-frequency RFQ were successfully carried out and the commissioning run has started in the RILAC beam line. The RFQ, based on a folded-coaxial resonator with a movable shorting plate, accelerates ions with mass-to-charge ratios of 6 to 26 up to 450 keV per charge in the cw mode.¹⁾ In the present paper we describe the results obtained from the performance tests as well as the improvements made during in this year.

In the initial stage of the high power tests carried out in the last year (1995), we encountered a problem on the ceramic pillars. They broke by the heat due to the dielectric loss around the metal screws fixing the pillars to the conductor tube, when the intervane voltage was above 25–30 kV.²⁾

This problem was solved by adopting a new structure for the pillars as illustrated in Fig. 1. This pillar consists of Al_2O_3 and is welded its top and bottom with copper-tungsten alloy. This kind of welding is possible because both materials have the similar coefficients of the linear thermal expansion. After this improvement, the RFQ is stably operating in the whole range of the acceleration voltage acceptable by the RILAC. The vacuum stays in a range of $1 - 3 \times 10^{-7}$ Torr at the pump head. No significant temperature-rise has been detected from the RFQ resonator during the operation.

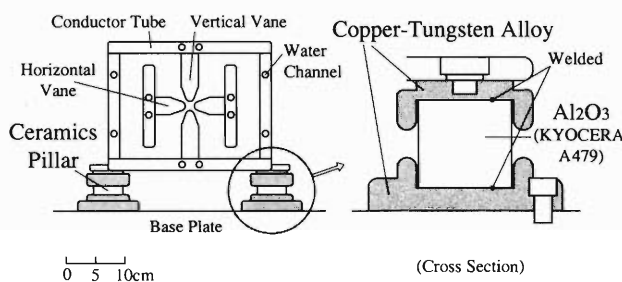


Fig. 1. Schematic drawing of the improved ceramic pillar.

Acceleration tests were performed using the ion beams transported from the 18-GHz ECRIS.³⁾ Figure 2 shows the schematic drawing of the beam line.⁴⁾ The extracted beam from the ion source is focused by an Einzel lens and is bent by a bending magnet. The bending magnet also has a focusing function by the slant pole edges. The beam is focused again by a solenoid before entering the RFQ.

There are two diagnostic chambers in the beam line. One chamber is located between the bending magnet

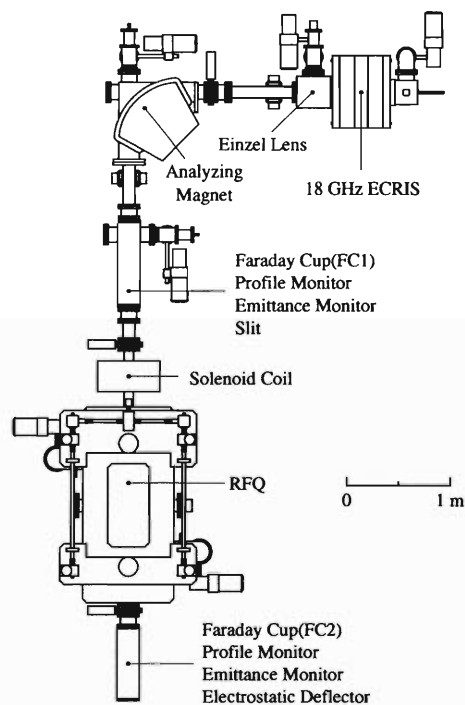


Fig. 2. Schematic drawing of the beam line for the acceleration tests.

and the solenoid, which contains a Faraday cup, two profile-monitors, and two slits. The other chamber is placed just after the RFQ, inside of which is equipped with a profile-monitor, a Faraday cup, two slits, and an electrostatic deflector with a scanning wire probe.

The so far accelerated ions are $\text{O}^{3,4,5+}$, Ne^{4+} , $\text{Ar}^{2,3,6,8,9,11+}$, Kr^{9+} , Xe^{12+} , $\text{Ta}^{7,16,17+}$ at the frequencies of 17.7, 19.5, 26.1, 29.5, 32.8, 34.4, 36.8 and 39.2 MHz applying the intervane voltage in the range of 17–35 kV. They are indicated by closed circles in Fig. 3. The maximum transmission efficiency, defined by the ratio of the beam current in the two Faraday cups (FC1 and FC2 in Fig. 2), was 88% with the beam intensity of 120 μA .

The emittances of the input and output beams were measured by the profile monitors, along with the slits. The input beam emittance from the ion source was 150–300 π mm·mrad, which decreases as the extraction voltage of the ion source and/or the charge states of ions increase. An example of the measured results is shown in Fig. 4. On the other hand, the output beam emittance is almost independent of the acceleration condition; in agreement with the PARMTEQ

simulation.

The energy distribution of the RFQ output beam was measured by the electrostatic deflector (40 mm in gap and 200 mm in length), along with the scanning wire probe placed downstream of the RFQ. The beam

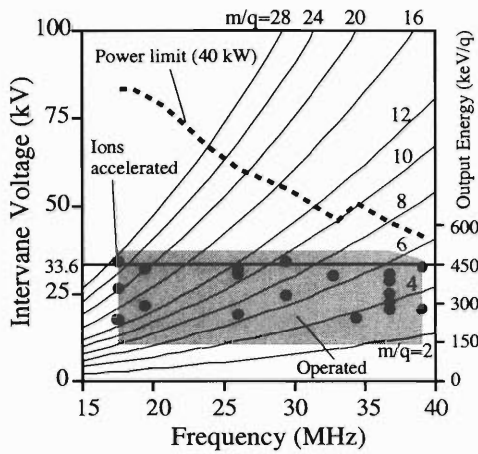


Fig. 3. Specification of the RFQ linac. The abscissa and the ordinate represent the resonant frequency and the intervane voltage, respectively. The output energy, proportional to the intervane voltage, is also indicated. The hatched area shows the region where the RFQ has ever been operated in the cw mode. The accelerated ions are indicated by closed circles. The solid curves represent the acceleration condition of ions, each of which is indicated by the m/q -value. The dashed curve shows the maximum attainable voltage with the present power source (40 kW), which is estimated by the measured shunt impedance of the resonator.

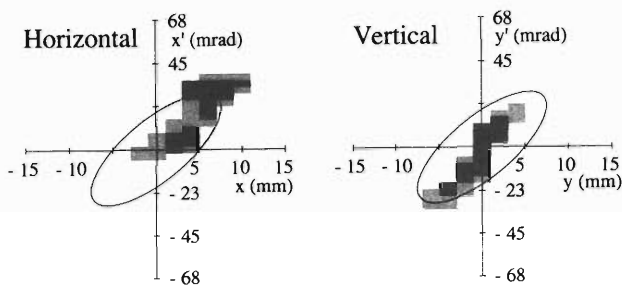


Fig. 4. Emittance of the input beam of Ar^{8+} extracted from the ECRIS at 8.5 kV. The measurement was done at 1400 mm upstream of the RFQ. The transmission efficiency was 87%. The ellipse indicates the emittance assumed in the vane design (145π mm-mrad).

energy was deduced from the beam position measured by the probe and the voltage applied to the deflector. As shown in Fig. 5, the output energy decreases as the intervane voltage is reduced, which is well reproduced by the simulation. The energy spread of the output beam was also measured by the same method. The result is 2–3% at FWHM and is consistent with the PARMTEQ simulation.

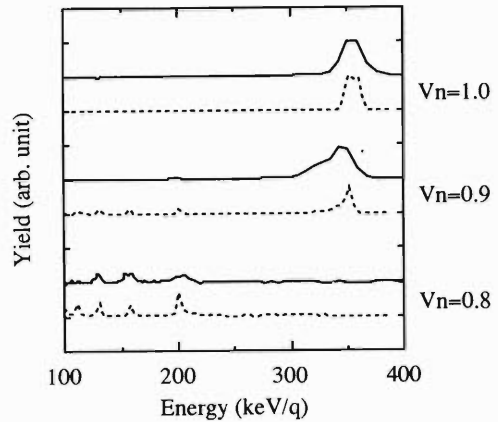


Fig. 5. Measured energy distribution (solid curves) and the PARMTEQ simulation (dashed curves). This measurement was done at the frequency of 17.64 MHz using Ar^{2+} beam. The corresponding output energy is 350 keV/q. The numbers represented by V_n indicate the ratios of the intervane voltage to the standard value of 26.1 kV.

The new injector system was installed in the RILAC beam line in August-1996 and the commissioning run has started. Preliminary results show that the transmission efficiency from the ion source to the end of the RILAC is 51%. Further improvements are expected for the transmission efficiency.

We are planning to raise the extraction voltage of the ion source to 20 kV in the near future. New vanes for the upgraded beams are under fabrication.

References

- 1) O. Kamigaito et al.: Jpn. J. Appl. Phys. **33**, L537 (1994) and O. Kamigaito et al.: Jpn. J. Appl. Phys. **34**, 5799 (1995).
- 2) O. Kamigaito et al.: RIKEN Accel. Prog. Rep. **29**, 221 (1996).
- 3) T. Nakagawa et al.: RIKEN Accel. Prog. Rep. **30**, 188 (1997).
- 4) N. Inabe et al.: RIKEN Accel. Prog. Rep. **28**, 166 (1995).

Beam Matching Section in the New Injector for RILAC

O. Kamigaito, A. Goto, Y. Miyazawa, T. Chiba, M. Hemmi,
M. Kase, S. Kohara, and Y. Yano

The beam matching section between the RFQ linac and the RILAC was designed and constructed. Figure 1 shows the schematic layout of the matching section. The transverse matching is achieved by two quadrupole doublets, while the longitudinal one is done by a rebuncher of the fundamental frequency. A dipole magnet is introduced for the injection of the beam from the Cockcroft-Walton injector. All the components have been working properly since their installations in the RILAC beam line in August 1996.

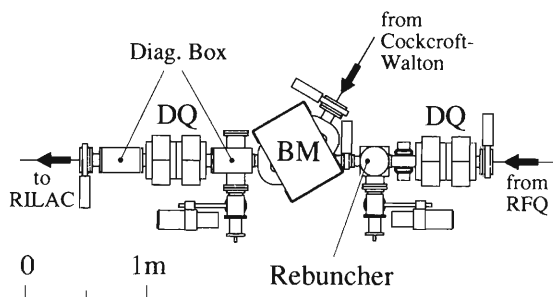


Fig. 1. Schematic layout of the beam matching section in the new injector for the RILAC. DQ and BM denote the quadrupole doublets and the bending magnet, respectively.

We optimized the transverse beam matching by use of the TRANSPORT code. The emittance of the output beam from the RFQ was calculated to be 22π mm·mrad with the PARMTEQ program. The acceptance of the RILAC was assumed to be 120π mm·mrad, taking the result in Ref. 1 into account. This value was also checked by the simulation code LINOR.²⁾ The optimized result is shown in Fig. 2, where the Twiss parameters of the emittance ellipses at the entrance of

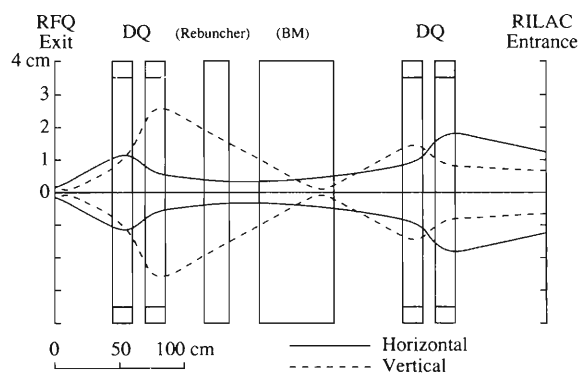


Fig. 2. Transverse beam optics optimized with the TRANSPORT code.

the RILAC are the same as those of the acceptance ellipses.

The calculation of the magnetic field in the quadrupole magnets was made by use of the POISSON program. The four quadrupole magnets have the same specification listed in Table 1. The maximum field gradient of 1.6 kG/cm was found large enough for the beam with the largest m/q value.

The dipole magnet is of the H type whose parameters were optimized with the POISSON code. Slight saturation of the magnetic field is observed in the highest field region. The main parameters are also listed in Table 1.

Table 1. Main parameters of the magnets.

Quadrupole	
Effective length	150 mm
Real length	115 mm
Bore radius	35 mm
Max. current	9152 AT/pole
Max. field gradient	1.6 kG/cm
Dipole	
Orbit radius	400 mm
Bending angle	60°
Edge angle	0°
Gap	60 mm
Pole width	170 mm
Max. current	36000 AT/pole
Max. magnetic field	13.5 kG

The longitudinal-matching condition was optimized with a transfer matrix method so that the output beam from the RFQ is focused at the entrance of the RILAC. According to the simulation using the PARMTEQ, the phase and the momentum spread at the end of the RFQ channel are 38 degree and $\pm 2\%$, respectively. The total effective voltage of 16 kV in the rebuncher is sufficient to realize this condition when it is placed in the downstream of the RFQ by 1.2 m.

The rebuncher resonator, having four gaps of 8 mm, is a coaxial resonator of a quarter-wavelength with a movable shorting plate, as shown in Fig. 3. All the geometrical parameters were optimized by use of the MAFIA code. The capacitance between the tall drift tubes as well as the large tuners make the coaxial line short. The bore diameter of the drift tube has to be kept 40 mm because the vertical beam size is that value at the entrance of the rebuncher, as shown in Fig. 2. In order to increase the transit time factor through these large holes, a thin mesh plate made of copper, whose

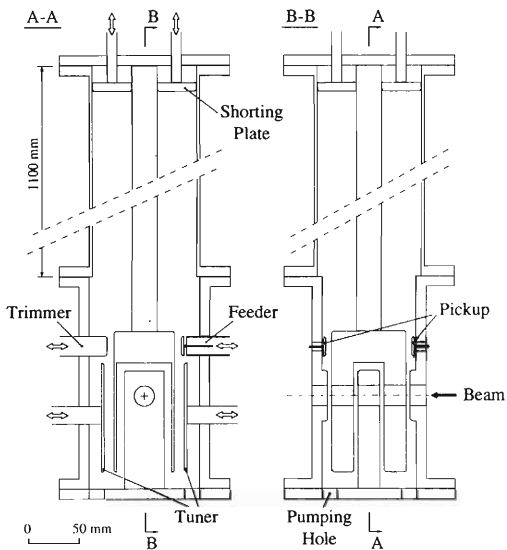


Fig. 3. Schematic drawing of the rebuncher resonator.

transmission efficiency is 95%, was put at every end of the drift tubes. A wide-band amplifier having the output power of 1 kW is used for the operation. The resonator is evacuated with a turbo molecular pump of 350 l/s.

Figure 4 shows the measured resonant frequency of the rebuncher resonator along with the calculated ones. The measured values are in good agreement with the MAFIA calculations. On the other hand, the measured Q-values are around 2500, being about one half of the calculated ones. One of the possible reasons for this deterioration is that the electric contacts are not perfect, particularly around the shorting plate where sliding contacts are used.

Two diagnostic boxes are installed in the matching section. One is located just after the rebuncher and the other is in front of the RILAC. They are equipped with two Faraday cups, two phase probes, two slits, and three profile monitors. The former one is evacuated with a turbo molecular pump of 350 l/s.

All the components have been assembled in the RILAC beam line and have worked properly. The vacuum stays in the range of $2-4 \times 10^{-7}$ Torr during the oper-

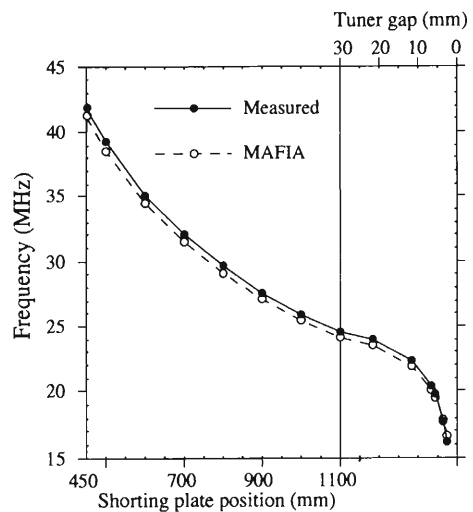


Fig. 4. Resonant frequency of the rebuncher resonator. The solid and the dashed lines represent the measured and calculated ones, respectively. Above 24 MHz, the resonant frequency is changed with the shorting plate, while the gap between the tuner and the drift tube is kept constant (30 mm). Below 24 MHz, it is changed with the tuners, keeping the position of the shorting plate to be the highest value of 1100 mm.

ation. The transmission efficiency including the RFQ and the matching section was 40–50% in the first stage of the test.

In a high beam-current operation, one of the mesh plate of the rebuncher has melted due to the high beam power. Therefore, we have removed all of them, and the transmission efficiency has increased to 70%. The gap voltage is still high enough for the matching condition even at the maximum output energy. Measurements of the effect of the mesh plate on the longitudinal emittance are in preparation.

References

- 1) M. Tonuma et al.: Rep. Inst. Phys. Chem. Res. (in Japanese) **51**, 53 (1975).
- 2) A. Goto et al.: Proc. Computing in Accelerator Design and Operation, Europhys. Conf., Berlin, W. Germany, Sept. (1983).

Maximum Beam Current in a Low-Energy Transport Line

Y. Batygin, A. Goto, and Y. Yano

A new RIKEN low energy beam transport line in between 18 GHz ECR ion source and RFQ linac¹⁾ consists of an einzel lens, a bending magnet and a solenoid coil (see Fig. 1). Parameters of the structure are listed in Table 1. Intensity of the transported beam in the beamline considered is limited by the einzel lens aperture, dipole gap, and solenoid aperture which have the same value of R_{\max} (: max beam radius) = 3.5 cm. In this paper we estimate the maximum value of current of the beam, that can be transported without particle losses.

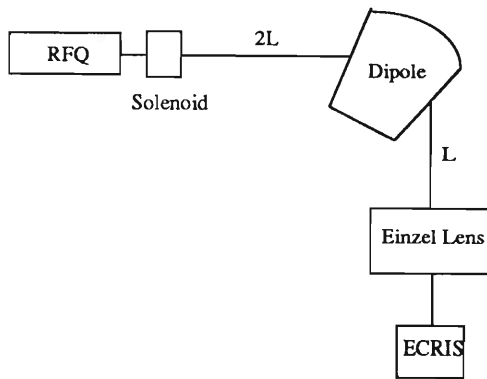


Fig. 1. Layout of extraction beamline of 18 GHz ECR ion source.

Table 1. Parameters of beam transport line.

Maximum ion magnetic rigidity	76 kG cm
Extraction voltage	8 ~ 10 kV
Einzel lens voltage	10 kV
Maximum magnetic field in dipole	1.6 kG
Maximum magnetic field in solenoid	6.3 kG

Evolution of the beam radius R in the drift space between focusing elements is described by Kapchinsky-Vladimirsky (KV) equation²⁾ for beam of circular cross-section:

$$\frac{d^2 R}{dz^2} - \frac{E^2}{R^3} - \frac{P^2}{R} = 0, \quad (1)$$

where E is the non-normalized beam emittance, $P = \sqrt{2I/(I_0\beta^3\gamma^3)}$ the space charge parameter, β the particle velocity, γ the Lorentz factor, I the beam current, and $I_0 = 4\pi\epsilon_0 mc^3/q$ the characteristic current. Equation (1) has a first integral:

$$\left(\frac{dR}{dz}\right)^2 = \left(\frac{dR}{dz}\right)_o^2 + \left(\frac{E}{R_o}\right)^2 \left(1 - \frac{R_o^2}{R^2}\right) + P^2 \ln\left(\frac{R}{R_o}\right). \quad (2)$$

Equation (1) has an approximate solution for $(dR/dz)_o = 0$:

$$\frac{R}{R_o} = 1 + 0.5z^2 \left(\frac{E^2}{R_o^4} + \frac{P^2}{R_o^2}\right). \quad (3)$$

From Eq. (3) it is easy to distinguish the threshold of different transport regimes, depending on which term in Eq. (3) is essential for beam spread. Space charge dominated beam transport results if the following condition is valid:

$$\frac{P R_{\min}}{E} > 1. \quad (4)$$

On the contrary, if the above combination of parameters is less than unit, emittance dominated beam drift is fulfilled:

$$\frac{P R_{\min}}{E} < 1. \quad (5)$$

From symmetry point of view, it is clear that beam should have a minimum size R_o (waist) in the middle point $z = L = 110$ cm between dipole and solenoid. Suppose the value of P is fixed, the differentiation $\partial E^2/\partial R_o = 0$ gives the following expression of optimal relationship between R_o and R_{\max} :

$$R_o = \frac{3}{8}R_{\max} \left[1 + \sqrt{1 - \left(\frac{4P}{3} \frac{L}{R_{\max}}\right)^2} \right]. \quad (6)$$

Substitution of Eq. (6) into Eq. (3) gives the maximum beam emittance A under a fixed space charge parameter for the beam:

$$A = E_{\max} = \frac{\sqrt{2}}{L} \sqrt{R_o^3 R_{\max} - R_o^4 - 0.5(L R_o P)^2}. \quad (7)$$

In Fig. 2 a dependence of the maximum beam emittance against the space charge parameter is presented.

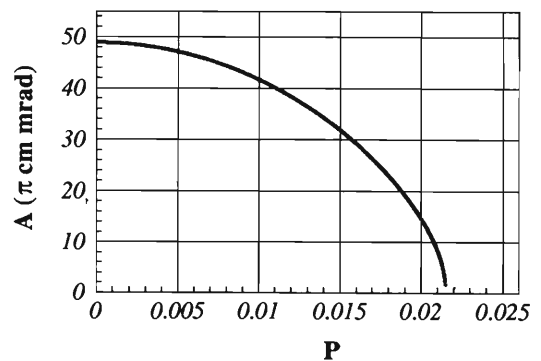


Fig. 2. The maximum beam emittance A as a function of the space charge parameter of beam $P = \sqrt{2I/(I_0\beta^3\gamma^3)}$.

As seen, the value of acceptance of the channel is 50π cm mrad. From Eqs. (6) and (7) it follows that the maximum value of space charge parameter is

$$P_{\max} = 0.0215. \quad (8)$$

Combining the expressions not only for parameter P but also for beam velocity β as a function of extraction voltage U_{ext} like

$$\beta = \sqrt{\frac{2U_{\text{ext}}}{(A/Z)(m_p c^2/e)}}, \quad (9)$$

the maximum beam current transported in the channel is found to be

$$I_{\max} = \sqrt{2} P_{\max}^2 \left(4\pi\epsilon_0 \frac{m_p c^3}{e} \right) \sqrt{\frac{Z}{A}} \left(\frac{e U_{\text{ext}}}{m_p c^2} \right)^{3/2}, \quad (10)$$

Table 2. Maximum transported beam current, I_{\max} .

Ion	U_{ext} [kV]	I_{\max} [μ kA]
Ar_{40}^{+8}	8.5	247
Ar_{40}^{+8}	10	318
Ar_{40}^{+5}	10	251

where $m_p c^2/e = 938.3$ MV is a proton rest energy. In Table 2 the values of maximum beam current for several ions are presented.

References

- 1) N. Inabe et al.: RIKEN Accel. Prog. Rep. **28**, 166 (1995).
- 2) I. M. Kapchinsky: Theory of resonance linear accelerators, Harwood, Chur, 1985.

Progress of RIKEN RI Beam Factory Project

Y. Yano, A. Goto, and T. Katayama

The project of "RI-Beam Factory", or "RIB-factory" for short, was formally approved by the Government in December, 1996.

An up-to-date layout of the RIB-factory is shown in Fig. 1. The K2500-MeV superconducting ring cyclotron (SRC) in the former design has been split into two stages: a four-sector SRC (SRC-4) for the first stage and a six-sector SRC (SRC-6) for the second one. This two-stage scheme has been adopted in order to make the simultaneous utilization of SRC-4 beams possible in the both existing experimental facility and

years; and the third phase to construct BSR for three new facility, and to relieve the difficulties in fabricating the SRC: such as huge cold masses, huge electromagnetic forces exerted on it, etc. Further details on the general features of SRC's are given in Ref. 1, and the design studies of their main components appear in the respective papers in this progress report. Construction of a full-scale model sector magnet of SRC-6 without a yoke has been undertaken. With this model magnet, which is scheduled to be completed late in 1997, we will verify the mechanical design of magnet and the cryogenic design of the main and trim coils.²⁾

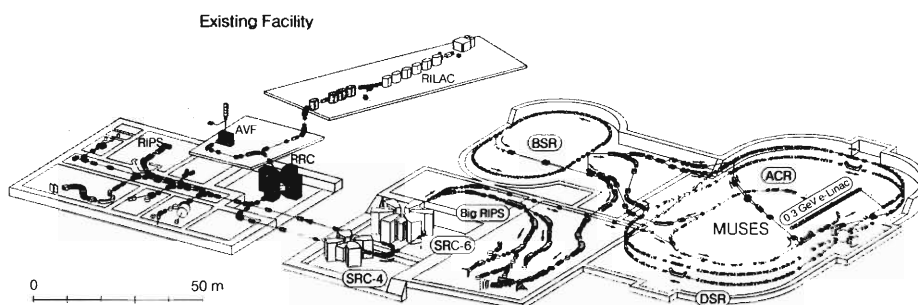


Fig. 1. Layout of the designed RIKEN RI Beam Factory.

The multi-use experimental storage rings (MUSES) will be accommodated in a one-story building, although in the former design it was in a two-story one. In the design work of MUSES, the circumferences of the both booster synchrotron ring (BSR) and double storage rings (DSR) have been elongated to reserve a more space for installation of the injection system. Namely, circumference of BSR has become 168 m instead of 135 m, and that of DSR 264 m instead of 258 m. Intersecting angle of the two rings of DSR at the colliding point has also been changed to be 10 mrad (or 0.57 degrees) instead of 10 degrees. Design studies of their main components and of the accumulator cooler ring (ACR) are given in separate papers in this progress report.

Construction of the RIB-factory is now scheduled in three phases. The first phase is to construct SRC-4, SRC-6, Big RIPS, and related experimental facilities for five years after one-year of the investigation and fundamental design of building; the second phase to construct ACR, DSR, and an electron linac for four

years. The first beam from the SRC-6 is scheduled for the year 2002.

In parallel to the above design work, a new injector system for the existing heavy-ion linac (RILAC), which had been essential to upgrade the beam intensity for the factory, was installed on site, and its commissioning started in October, 1996.³⁾ Beam acceleration tests showed the beam intensity and beam transmission efficiency much better than ever obtained. An $^{36}\text{Ar}^{5+}$ ion beam whose intensity of $1 \text{ p}\mu\text{A}$ was successfully extracted from the RRC for the first time, which is the maximum intensity required for the factory of our interest.

References

- 1) A. Goto et al.: RIKEN Accel. Prog. Rep. **30**, 186 (1996).
- 2) T. Kubo et al.: RIKEN Accel. Prog. Rep. **30**, 201 (1996).
- 3) A. Goto et al.: RIKEN Accel. Prog. Rep. **30**, 196 (1996).

The Superconducting Ring Cyclotrons for RIKEN RI Beam Factory

A. Goto, T. Kubo, H. Okuno, T. Kawaguchi, T. Mitsumoto, T. Tominaka, S. Fujishima, J.-W. Kim, K. Ikegami, N. Sakamaoto, S. Yokouchi, T. Morikawa, Y. Tanaka, and Y. Yano

In a previous design,¹⁾ a very large single SRC (Superconducting Ring Cyclotron) had been studied as a post-accelerator of RRC. After a further study, we have recently modified the design in such a way that SRC is split into two stages: a 4-sector SRC (SRC-4) for the first stage and a 6-sector SRC (SRC-6; $K = 2500$ MeV) for the second one. This two-stage scheme has two big advantages. Firstly, the simultaneous utilization of SRC-4 beams is possible in both the existing experimental facility and the new facility, when a part of the beams is charge-stripped and is transferred back to the existing facility. For an example, a 127 MeV/nucleon $^{16}\text{O}^{7+}$ beam from SRC-4, while the main part of which is injected into SRC-6, a part of which is charge-stripped to O^{8+} and delivered to the existing facility (where the magnetic rigidity of the O^{8+} beam can be accepted). Secondly, the difficulty of fabrication due to huge length of the cold mass and huge electromagnetic force on it is drastically eased compared to the single-stage scheme.

The maximum beam energy of SRC-6 is set to be 400 MeV/nucleon for light heavy ions, which should be achieved at 38 MHz, the maximum rf frequency stably operated in the injector heavy-ion linac (RILAC). This means that the velocity of RRC output beam has to be amplified by a factor of 2.26 by the two SRC's. Harmonic numbers of SRC-4 and SRC-6 are chosen to be 7 and 6, respectively, while that of the existing K540-MeV ring cyclotron (RRC) is 9, considering the maximum magnetic field strengths and the injection and extraction radii. The mean injection radius of SRC-4 is then taken to be 7/9 times the mean extraction radius of RRC, and the velocity gain factor of SRC-4 to be 1.50. (For 400 MeV/nucleon light heavy ions, their beam energy from SRC-4 becomes 127 MeV/nucleon, which is almost same as the maximum beam energy of RRC.) From the above conditions, the mean injection and extraction radii of SRC-4 are 2.77 m and 4.15 m, respectively, and those of SRC-6 are 3.56 m and 5.36 m, respectively. The sector angles of SRC-4 and SRC-6 are 51° and 25° , respectively. The radio-frequency of SRC-4 and SRC-6 ranges from 18 MHz to 38 MHz, which is the same as that of RILAC and RRC. The maximum magnetic fields required for SRC-4 and SRC-6 are to be 1.9 T and 4.2 T, respectively. This cascade of SRC's boosts energies of heavy ion beams up to: e.g., 400 MeV/nucleon for light heavy ions like carbon, 300 MeV/nucleon for krypton ions, and over 100 MeV/nucleon for uranium ions.

Geometries and characteristics of SRC-4 and SRC-

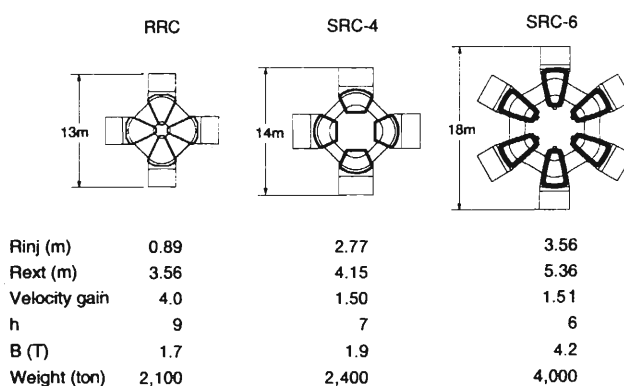


Fig. 1. Comparisons of the geometries and characteristics of RRC, SRC-4, and SRC-6.

6 thus designed are shown in Fig. 1 along with those of RRC. The structure and size of SRC-4 are similar to those of RRC. A warm-pole method is adopted for SRC-4, while a cold-pole method is adopted for SRC-6.¹⁾ At present, our effort is concentrated on the design of SRC-6: optimization of the geometry of the sector magnet by the calculation of tunes,²⁾ optimization of trim coil configuration,³⁾ fixing of the specifications of the main and trim coils,⁴⁾ structural design to support the main coil vessel and the whole cold mass,⁴⁾ design of the injection system,⁵⁻⁷⁾ etc.

We have started to construct a full-scale model sector magnet of SRC-6 without a yoke to verify particularly the mechanical design of magnet and the cryogenic design of the main and trim coils.⁸⁾ We have already placed orders with companies for the superconducting wires of the main and trim coils, and for the fabrication of the main coil vessel and cold pole. Test of the model magnet is scheduled to start in late 1997.

References

- 1) T. Mitsumoto et al.: Proc. 14th Int. Conf. on Cyclotrons and their Applications, Cape Town, p. 237 (1995).
- 2) T. Mitsumoto et al.: RIKEN Accel. Prog. Rep. **30**, 197 (1997).
- 3) J.-W. Kim et al.: RIKEN Accel. Prog. Rep. **30**, 209 (1997).
- 4) T. Kawaguchi et al.: RIKEN Accel. Prog. Rep. **30**, 199 (1997).
- 5) H. Okuno et al.: RIKEN Accel. Prog. Rep. **30**, 203 (1997).
- 6) T. Tominaka et al.: RIKEN Accel. Prog. Rep. **30**, 205 (1997).
- 7) S. Fujishima et al.: RIKEN Accel. Prog. Rep. **30**, 207 (1997).
- 8) T. Kubo et al.: RIKEN Accel. Prog. Rep. **30**, 201 (1997).

Design Study of Sector Magnets for RIKEN Superconducting Ring Cyclotron (I)

T. Mitsumoto, A. Goto, T. Kawaguchi, J.-W. Kim, Y. Tanaka, T. Kubo, H. Okuno, T. Tominaka, S. Fujishima, and Y. Yano

An “RI beam factory” has been proposed as the next facility-expansion project of the RIKEN Accelerator Research Facility (RARF).¹⁾ The “RI beam factory” aims at production and acceleration of radioactive isotope beams covering the whole mass region. It requires the energy of ion beam to be higher than 100 MeV/nucleon. To accomplish this requirement, the following two superconducting ring cyclotrons were adopted as post-accelerators of the existing RIKEN Ring Cyclotron (RRC): a 4-sector superconducting ring cyclotron (SRC-4) for the first stage and a 6-sector superconducting ring cyclotron (SRC-6) for the second stage.²⁾ The sector magnet of the SRC-6 has to be flexible enough to generate isochronous fields in a wide range of energies and for various q/A values. In this report we describe the feature of the sector magnet together with the field calculation and orbit analysis.

The maximum acceleration energy of the SRC-6 was determined by experimental requirements. The SRC-6 is expected to boost the energy of ion beam up to 400 MeV/nucleon for light heavy ions like carbon ions and 150 MeV/nucleon for very heavy ions like uranium ions. Beam current is expected to be more than 100 μA for light heavy ions and about 0.2 μA for 150 MeV/nucleon uranium ions.

To accomplish this requirement, the total velocity gain factor for the two new cyclotrons becomes 2.26. The velocity gain factors of the SRC-4 and SRC-6 are therefore selected to be 1.50 and 1.506, respectively. Main parameters of the SRC-6 are listed in Table 1.

Table 1. Main parameters of the SRC-6.

Number of sectors	6	
Harmonics	6	
Average radius:	injection	3.56 m
	extraction	5.36 m
Number of cavities	3	
RF frequency	18-38 MHz	

Size of the superconducting main coil is 284 mm (width) \times 310 mm (height). The maximum excitation current is 6 MA for one sector magnet. The superconducting main coil is installed inside the stainless steel Helium vessel which is fixed to the cold pole.

Superconducting trim coils are placed on the inner surface of the cold pole. The coils are not wound

along beam orbits but just straight in the beam region. These coils are controlled by three independent currents. Each coil is put in the same layer whose thickness is 2 cm. Configuration will be optimized by detailed analysis. Using three sets of superconducting trim coils, it is possible to adjust various distributions of isochronous fields within ± 0.01 T. Further fine adjustment will be done with the trim coils of room temperature.

Figure 1 shows typical magnetic field strengths along the center line of the sector magnet for typical ions. Maximum magnetic field in the accelerating region is 4.3 tesla.

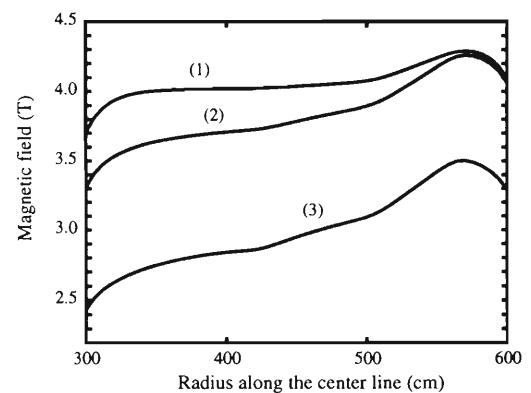


Fig. 1. Magnetic field strengths along the center line of the sector magnet for (1) $^{238}\text{U}^{58+}$ 150 MeV/nucleon, (2) $^{84}\text{Kr}^{30+}$ 300 MeV/nucleon and (3) $^{12}\text{C}^{6+}$ 400 MeV/nucleon.

Magnetic fields and related characteristics are calculated by a three-dimensional code TOSCA.³⁾ Equilibrium orbits and betatron tunes were calculated by the computer program that had been originally developed for the RRC. Results of the field distributions by TOSCA were used in the orbit calculations.

In the case of high energy acceleration, vertical tune ν_z goes down toward 1.0 as the energy increases. Preliminary estimation of $\nu_z=1$ resonance was simulated by the accelerating beam calculation. Figure 2 shows an example of the calculation for $^{12}\text{C}^{6+}$ 400 MeV/nucleon in the case that the tune values cross $\nu_z=1$ resonance. In this calculation, magnetic field has first order harmonics which come from the fact that one sector magnet and another sector magnet of opposite side are vertically displaced 1 mm and -1 mm, respectively. Amplitude of vertical oscillation increases fatally when the beam crosses the resonance.

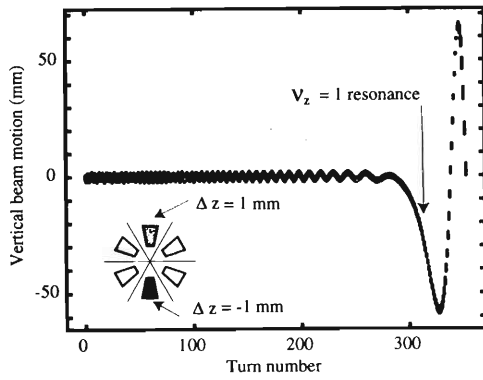


Fig. 2. Influence of $\nu_z=1$ resonance. The magnetic field has first order harmonics which come from the fact one sector magnet and another sector magnet of opposite side are vertically displaced 1 mm and -1 mm, respectively.

The sector shape was selected so that vertical tune values never cross $\nu_z = 1.0$. Smaller sector angle causes larger vertical focusing force. From the viewpoint of minimizing the maximum field, a large sector angle is preferable. Therefore, edge of the pole has a straight line from the injection side to the middle of the sector with the wide angle of 25 deg. Then the pole shape has a curvature in order to increase vertical tune ν_z at the extraction side.

Figure 3 shows tune values of three different pole

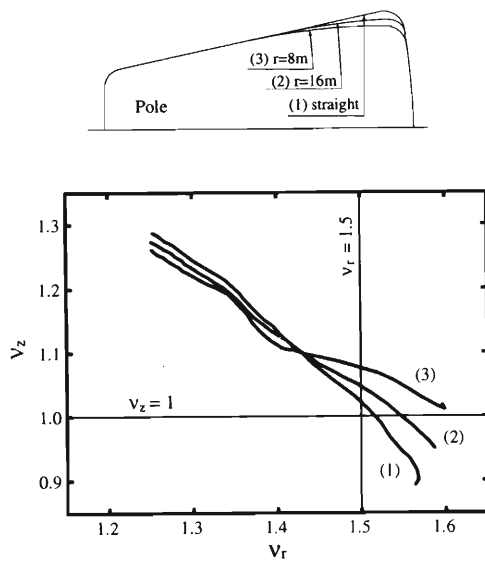


Fig. 3. Tune values of three different pole shapes for $^{12}\text{C}^{6+}$ 400 MeV/nucleon are shown in the case of (1) straight line, (2) 16 meters radius and (3) 8 meters radius.

shapes for $^{12}\text{C}^{6+}$ 400 MeV/nucleon. The radius of curvature of 8.0 m increases ν_z value by 0.12 to 1.01 at the extraction radius compared with the straight pole. Figure 4 shows typical tune values calculated for the sector magnet thus far designed. Figure 5 shows region of ions (grey area) which can be obtained from the SRC-6.

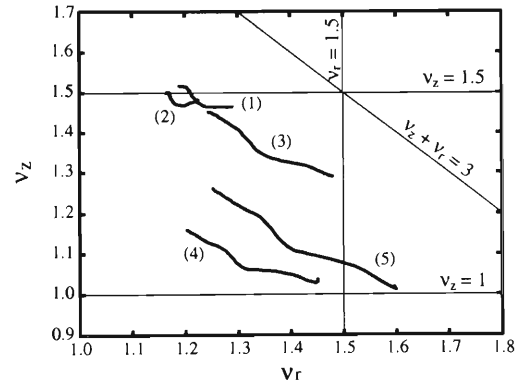


Fig. 4. Tune values for typical ions for (1) $^{238}\text{U}^{58+}$ 150 MeV/nucleon, (2) $^{238}\text{U}^{49+}$ 100 MeV/nucleon, (3) $^{84}\text{Kr}^{30+}$ 300 MeV/nucleon, (4) $^{12}\text{C}^{6+}$ 300 MeV/nucleon and (5) $^{12}\text{C}^{6+}$ 400 MeV/nucleon.

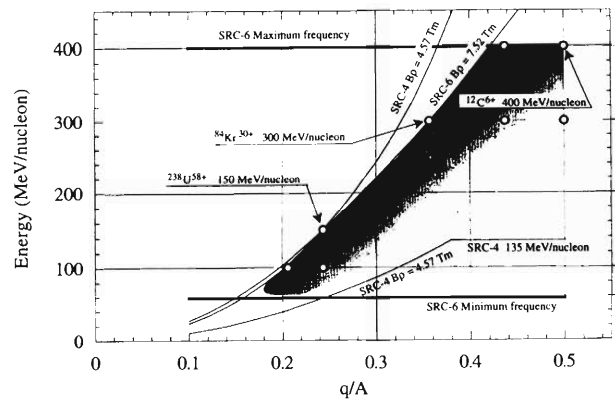


Fig. 5. Performance of the SRC-6. Grey area shows the region of the beam obtained. Typical ions are shown by white circles.

References

- 1) Y. Yano et al.: 14th Int. Conf. on Cyclotrons and Their Applications, Cape Town, South Africa, Oct. p. 590 (1995).
- 2) A. Goto et al.: RIKEN Accel. Prog. Rep. **30**, 196 (1997).
- 3) Vector Fields Limited, Oxford, England.

Design Study of Sector Magnets for RIKEN Superconducting Ring Cyclotron (II)

T. Kawaguchi, T. Kubo, T. Mitsunoto, T. Tominaka, S. Fujishima, H. Okuno, Y. Tanaka, J.-W. Kim, K. Ikegami, N. Sakamoto, S. Yokouchi, T. Morikawa, A. Goto, and Y. Yano

The RIKEN Superconducting Ring Cyclotrons, SRC-4 and SRC-6, are one of the main accelerators for the "RIKEN RI-Beam Factory".¹⁾ Here, the design study of the sector magnets for the SRC-6 is described.

Figure 1 and Table 1 show a cross sectional view and basic parameters of the sector magnet for the SRC-

6, respectively. Main components of the magnetic elements are superconducting and normal-conducting coils, poles, and a yoke. We use two kinds of superconducting coils; a pair of main coils and a group of trim coils. A group of normal-conducting trim coils is also arranged in the upper and lower side of the

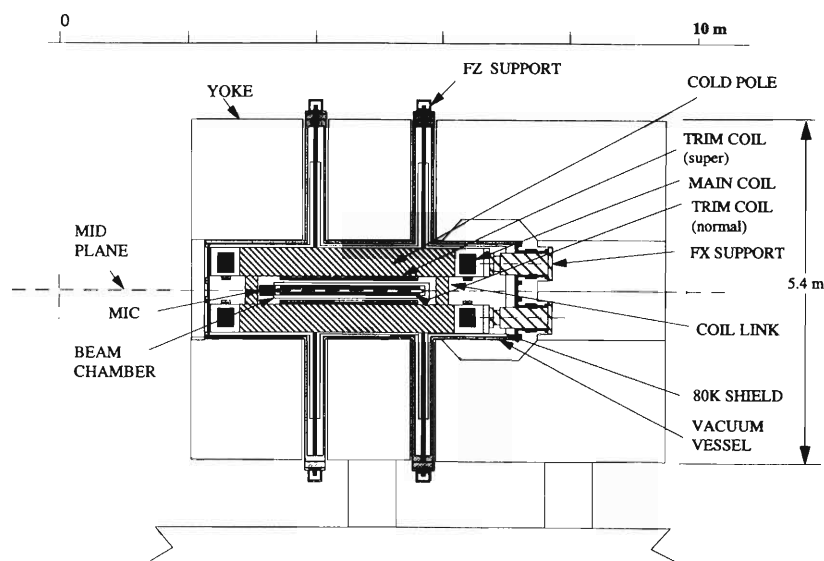


Fig. 1. Section view of the sector magnet.

Table 1. Parameters of the sector magnet.

Average radii of beam injection	3.56 m,
extraction	5.36 m.
Sector angle of main coil	25 degree
Maximum magnetic fields	
in beam orbital area	4.5 T,
in main coil	5.5 T,
in trim coil	5.0 T.
Main coil ampere turns per magnet	6.0 MA
Coil cooling method	LHe bath cooling
Magnetic stored energy for 6 magnets	450 MJ
(75 % in air, 17 % in cold poles, 8 % in yokes)	
Maximum operation Currents	
for main Coil	5000 A,
for trim Coil	500 A.
Iron weight of 6 magnets	
cold poles	216 tons,
yokes	3630 tons.

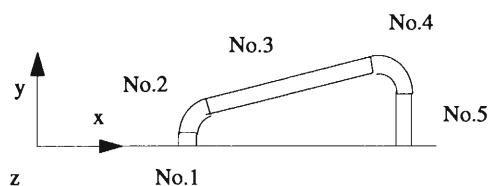
beam chamber. A special feature is the cold-pole arrangement. This arrangement gives a mechanical sup-

port against the huge magnetic force of the main coils, and gives the reductions of ampere-turns and of magnetic forces, compared with a warm-pole arrangement. A vertical magnetic force (F_z) is supported with two coil links which are attached the upper and lower cold poles. We have been investigating two ways of supporting a magnetic shifting force (F_x) in the radial direction. One way is to arrange a pair of cold rings which connect the cold masses (coils and cold poles) of the six sector magnets in 4.5 K region. A problem of the cold ring support system is the central space for the cyclotron. This space is limited for arranging the beam injection elements. Another way is to use large size thermal insulated supports made of high strength material like as titanium alloy, in between the cold mass and the yoke using the outer space of the sector magnet. The problems of the thermal insulating support system are its large heat leak, and its mechanical deflection which causes a position shift of the magnetic field. After optimization for decreasing the shifting force F_x , we have almost decided to use the thermal insulation support system as shown in Fig. 1.

Table 2 shows the calculated magnetic forces of the main coil and of the cold pole with an ampere turns of 6 MA per magnet (or per two coils). The vertical force F_z of 1154 tons will make a bending deflection of 2 mm in the normal direction to the cold pole of 465 mm thickness. The shifting force F_x of 104 tons will make the coil position change by 1 mm in the radial direction. This force F_x is generated by the arrangement of six sector coils and the asymmetry configuration of the coils and irons.

Table 2. Magnetic forces in a main coil and a cold pole.

	unit: ton		
For half coil	F_x	F_y	F_z
No. 1 element	-87	0	-9
No. 2	-166	132	-25
No. 3	-185	940	-254
No. 4	160	205	-84
No. 5	310	21	-115
Sum.	32	1298	-487
For a cold pole	-12	0	-180
For half cold mass	52	0	-1154
(one main coil and one cold pole)			
For a magnet	104	0	0
(one cold mass)			



The main superconducting coil has triangle shape with two long straight sections of about 3.5 m long.

The magnetic forces on the main coil are supported by the coil vessel and the cold pole. We apply a cryogenic stabilizing method for the main coil and trim coil to prevent coil quench. The average current density of them are 34 A/mm² and 41 A/mm², respectively. We were considering two materials for the stabilizer of the superconducting wire. One was pure copper having rough surface, and another was pure aluminum having flat surface. We have decided to use pure aluminum stabilizer considering the electrical and mechanical properties, the thermal contraction from room temperature to 4.5 K, and the price. Main reason of this choice was the price.

Two refrigerators having a capacity of 500 W each at 4.5 K will be used for cooling of the six sector magnets plus the beam injection/extraction magnets. The cold mass weight of the six sector magnets is 360 tons, and it will take one and a half months for cooling the cold mass from room temperature to 4.5 K. We expect the superconducting ring cyclotron to operate more than 6000 hours a year. The cold mass should be kept in low temperature as long as possible. When one refrigerator breaks down, the magnets can be kept at 5 to 6 K with another refrigerator. We will have one or two days of power off a year for the power system maintenance, and at that time a recovery compressor with an emergency power source will recover the evaporated helium gas to the buffer tank. We will have no liquid nitrogen in this cryogenic system for simplicity of the cooling system.

Currently we are constructing a real-size model sector magnet²⁾ to verify our design.

References

- 1) A. Goto et al.: RIKEN Accel. Prog. Rep. **30**, 196 (1997).
- 2) T. Kubo et al.: RIKEN Accel. Prog. Rep. **30**, 201 (1997).

Design of a Model Sector Magnet for RIKEN Superconducting Ring Cyclotron

T. Kubo, T. Kawaguchi, T. Mitsumoto, T. Tominaka, S. Fujishima, H. Okuno, J.-W. Kim, Y. Tanaka, K. Ikegami, N. Sakamoto, S. Yokouchi, T. Morikawa, A. Goto, and Y. Yano

In the RI-beam factory project, it is planned to build two superconducting ring cyclotrons (SRC) as post accelerators of RIKEN Ring Cyclotron.¹⁾ The SRC, previously designed as a single-stage device, has been determined to split into two stages. The first and second SRCs have been named SRC-4 and SRC-6, respectively. The details on the split are described in Ref. 1. Here we report on the design of a model superconducting sector magnet for the SRC-6.

As reported elsewhere within this progress report,^{2,3)} the SRC-6 consists of six superconducting sector magnets with a sector angle of 25 degrees. Its mean injection and extraction radii are decided to be 3.56 m and 5.36 m, respectively, and the maximum magnetic field of sector magnets is designed to be 4.3 T. These parameters are the same as those of the single-stage SRC except for the mean injection radius that was 2.37 m rather than 3.56 m of new design.

In the last progress report,⁴⁾ we reported a design of a full-scale model magnet for the single-stage SRC. New design of a model magnet for the SRC-6 is essentially the same as that old design, except the size reduced due to the split. Figure 1 shows a schematic drawing of the model sector magnet. Length of the model along the center line of sector has reduced in

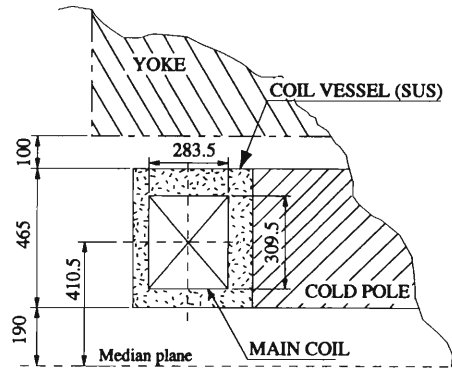


Fig. 2. Some details of the main coil and cold pole.

accordance with the increase of mean injection radius. The same cold pole method is adopted as before to support the huge electromagnetic force due to the large magnetic field and coil current.³⁾ Figure 2 shows some details of the main coil and cold pole. As seen from Figs. 1 and 2, the pole pieces are separated from the iron yoke and are cooled down together with the main coils in the cryostat. Two coil vessels that accommodate the main coils are attached to the side of the upper and lower pole pieces that are linked each other by pole links.

The pole gap is designed to be 380 mm, considering sizes of the trim coils and of the magnets for injection and extraction to be installed in the gap space. The cold-mass weight is estimated to be about 50 tons. The coil vessels are made of stainless steel. One of the important issues in the design is how to fix the coil vessel to the side of pole piece. At present we have not yet finalized it. The detailed design study is in progress, considering the stresses due to the thermal contraction and electromagnetic force.

A cryogenically-stabilized superconductor was designed based on Maddock's criterion, and is used for the main coil in order to prevent it from quenching. The main coil has been designed to be stable up to a current of 6000 A when the applied magnetic field is 6 T and the cooling efficiency is assumed to be 50%. The conductor has a rectangular shape, consisting of a Rutherford-type NbTi cable located at the center of conductor and a stabilizer housing. The conductor's cross-sectional area is 8 mm × 15 mm. The Rutherford-type cable is composed of ten NbTi superconducting wires of 1.25 mm diameter and 1.05 Cu/SC ratio. The diameter and twisting pitch of the filaments contained in each wire are 27 μm and 18 mm, respec-

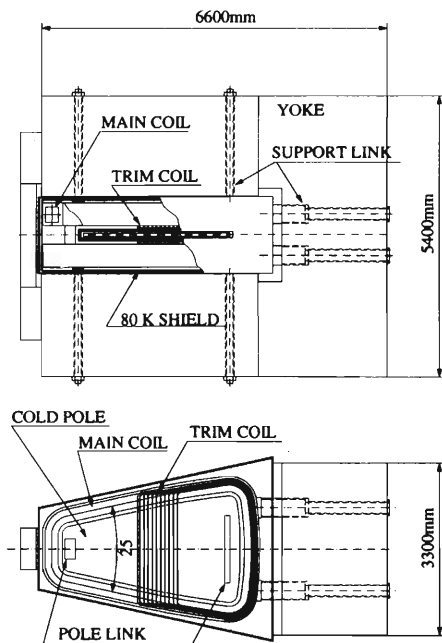


Fig. 1. Schematic drawing of the model sector magnet: a side view (upper figure); a top view (lower figure).

tively. Critical currents of the wire at 4.3 K is greater than 14500 A at 5 T, 11500 A at 6 T, and 8500 A at 7 T. The Rutherford-type cable has a rectangular cross-section of 2.35 mm \times 6.35 mm and has a twisting pitch of 55 mm. The stabilizer material has been chosen to be pure aluminum with a residual resistivity ratio greater than 500.³⁾ The condition of the stabilizer surface is flat. The Al:Cu:SC ratio of the conductor is 17 : 1.05 : 1. Fabrication of the conductor has been ordered from a conductor manufacturer.

Cross-sectional area of the main coil is 283.5 mm \times 309.5 mm, as shown in Fig. 2. The number of turns is 600 for each coil. The main coil is wound by the solenoid winding method in such a way that it has 30 layers in the horizontal direction and 20 turns in the vertical direction. The horizontal and vertical cooling gaps are taken to be 0.5 mm and 1.5 mm, respectively. These gap-widths are large enough to achieve the designed heat flux. The spacers of FRP (Fiber Reinforced Plastic) are placed in the gaps in such a way that 50% of conductor surface is exposed to the

liquid helium. We plan to excite the main coil with various currents lower than 5000 A, because deterioration of cooling and/or larger heating than expected may happen in some parts of the coil. The current density at 5000 A is estimated to be about 34.2 A/mm². The total ampere-turn is 6 MA at 5000 A, which is large enough to generate the designed field strength of the sector magnet.

Partial fabrications of the model magnet have been placed an order with manufacturers. The detailed design is going on in collaboration with the manufacturers.

References

- 1) A. Goto et al.: RIKEN Accel. Prog. Rep. **30**, 196 (1997).
- 2) T. Mitsumoto et al.: RIKEN Accel. Prog. Rep. **30**, 197 (1997).
- 3) T. Kawaguchi et al.: RIKEN Accel. Prog. Rep. **30**, 199 (1997).
- 4) T. Kubo et al.: RIKEN Accel. Prog. Rep. **29**, 236 (1996).

Design Study of Injection System for RIKEN Superconducting Ring Cyclotron (I)

H. Okuno, T. Tominaka, S. Fujishima, T. Kubo, T. Kawaguchi, T. Mitsumoto,
J.-W. Kim, K. Ikegami, N. Sakamoto, S. Yokouchi, T. Morikawa,
Y. Tanaka, A. Goto, and Y. Yano

In the RI beam factory project,¹⁾ two Superconducting Ring Cyclotrons (SRC-4 and SRC-6)²⁾ are designed to boost the energy of the ion beams available from the existing RIKEN Ring Cyclotron (RRC). Consequently, the output energies designed to the SRC-6 are 400 MeV/nucleon for light ions such as carbon and are 150 MeV/nucleon for heavy ions such as uranium. The injection energies (E_{inj}), required to obtain the designed output energies (E_{ext}), for three kinds of ion beams, are shown in Table 1. In present report, we describe the recent status of design study of the injection system for SRC-6.

Table 1. Energies of the injected and extracted beams at the full-power operation of SRC-6.

	Charge	E_{inj} (MeV/nucleon)	E_{ext} (MeV/nucleon)
^{16}O	8+	127.0	400
^{84}Kr	30+	102.5	300
^{238}U	59+	57.9	150

Figure 1 shows examples of the trajectories of injected beams in SRC-6. The beam is injected through

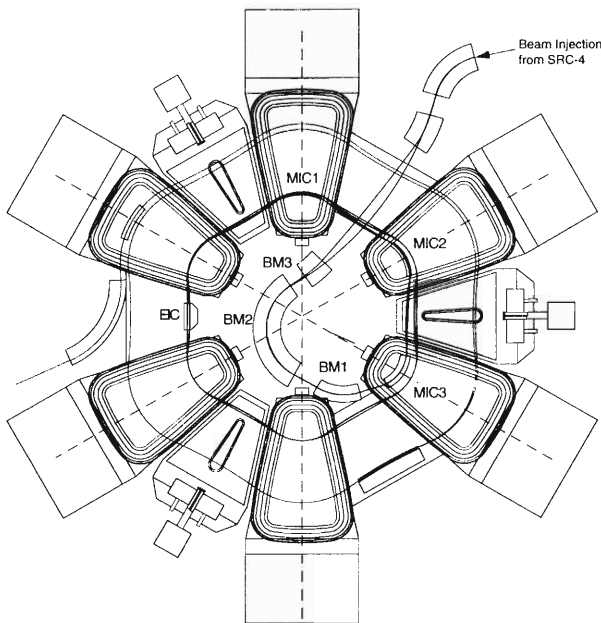


Fig. 1. A schematic layout of injection elements for the SRC-6, and possible trajectories for the injected beam.

one of the magnetic valleys into the central region of SRC-6, which is then radially guided to the first equilibrium orbit. The transport system consists of three bending magnets (BM1, BM2, BM3), three magnetic inflection channels (MIC1, MIC2, MIC3), and an electrostatic inflection channel (EIC). The MICs are inserted in the gap between the pair of poles of the sector magnets to increase the bending power of sector field locally. The EIC is placed in the position where the trajectory of injected beams matches finally with the first equilibrium orbit. The radial-injection method as shown in Fig. 1 is the most straightforward one adopted in many ring cyclotrons. However, to apply the same method on the SRC-6 is more difficult than to do on the normal conducting ring cyclotron, because a strong negative fringe field exists in the valley region and so the beam trajectory strongly depends on the acceleration condition for the case of SRC-6.

In the original layout of the injection system shown in the last progress report,³⁾ the injected beam crossed the EIC as for the case of normal conducting ring cyclotrons. Usually, the injected beam goes through a small hole in the EIC. In the SRC-6 case, however, the size of a hole is required to be more than 10 cm in diameter not to disturb the electric field in the EIC. We adopted a new layout where the injected beam dose not cross the EIC, because we could not find a simple mechanical structure for the EIC with small holes.

In order to accept the changes in the beam trajectory, the elements should be movable or have a large bore. We adopted the latter method, except for the EIC which is required to move 25 cm maximum in the radial direction, because the former method makes the mechanical structure of elements and the beam tuning complicated. It is important to make the change

Table 2. Conditions of the injection elements and changes (Δx) in the trajectories resulted from the numerical analysis of injection orbits.

	Radius [cm]	Angle [deg]	B or E (max.) [T] or [kV/cm]	Δx [cm]
EIC	—	—	100	12.0
MIC1	110.0	42.5	0.19	1.1
MIC2	110.0	47.5	0.22	1.2
MIC3	94.0	53.0	0.95	1.0
BM1	154.0	40.0	3.5	2.5
BM2	162.0	124.0	3.3	3.7
BM3	498.0	7.0	-1.89	10.2

of the beam trajectories inside the elements as small as possible. In the numerical analysis of the injection orbits,⁴⁾ we concentrated our effort to minimize them (Δx). Obtained results from such an analysis are shown in Table 2, together with their conditions. Further optimizations for the number and position of the injection elements are in progress.

The three bending magnets and the third inflection channel (MIC3) are required to be superconducting magnets in order to produce the required magnetic fields. The strong fringe fields mentioned above make these bending magnets difficult to be constructed, because we can not use the iron yoke for magnetic shielding. The total flux of the stray field is large enough to saturate the iron in the central region. Thus, we adopted the active shield type magnets for the BMs although more magnetic motive force is needed than the case of iron shield type. The BM1 has the smallest available space. In Table 3 the specifications of BM1 are listed. The BM1 has a space limit of ± 20 cm in the radial direction. Magnetic field analyses⁵⁾ show that superconducting coils can produce the required field with the current less than 50% of the critical current, and can be installed in the limited radial space. In the coil end region within the space of 10 cm needs to contain coil supports and cryostat walls. The design for the coil end region is in progress.

Table 3. The main specifications of BM1.

Item	Value
Type	Iron free active shield
Maximum field	3.5 [T]
Homogeneity	1×10^{-3} [/cm ²]
Beam Bore	40 (Horizontal) \times 20 (Vertical) mm ²
Radius	1540 mm
Angle	40 deg
Fringe Field	Less than 100 G at the first equilibrium orbit
Space limit in the radial direction	± 20 cm
Space for the coil end region	10 cm

References

- 1) Y. Yano et al.: RIKEN Accel. Prog. Rep. **30**, 195 (1997).
- 2) T. Mitsumoto et al.: RIKEN Accel. Prog. Rep. **30**, 197 (1997).
- 3) H. Okuno et al.: RIKEN Accel. Prog. Rep. **29**, 61 (1996).
- 4) S. Fujishima et al.: RIKEN Accel. Prog. Rep. **30**, 207 (1997).
- 5) T. Tominaka et al.: RIKEN Accel. Prog. Rep. **30**, 205 (1997).

Design Study of Injection System for RIKEN Superconducting Ring Cyclotron (II)

T. Tominaka, H. Okuno, S. Fujishima, T. Kubo, T. Kawaguchi, T. Mitsumoto, Y. Tanaka, S. Yokouchi,
J.-W. Kim, K. Ikegami, N. Sakamoto, T. Morikawa, A. Goto, and Y. Yano

The injection elements for a superconducting ring cyclotron (SRC) are designed.¹⁻³⁾ The injection system for the 6-sector SRC (SRC-6) consists of four bending magnets (BM1, BM2, BM3, BM4), three magnetic inflection channels (MIC1, MIC2, MIC3), and an electrostatic inflection channel (EIC).^{4,5)} In this present report, the design study of a bending magnet (BM1) is described. Major parameters of BM1 are shown in Table 1.

Table 1. Major parameters of BM1.

Bending field	3.6 T
Bore size	40 (H) × 20 (V) mm ²
Homogeneity (excluding quadrupole)	1×10^{-3}
Bending radius	1.54 m
Effective magnetic angle (length)	40° (1.08 m)
Stray field	<100 G at 0.5 m

A stray field up to 0.6 T is anticipated in the area of the BM1 due to the saturation of iron yoke of the main SRC's sector magnet, depending on the accelerating ions. Then, if the BM1 have its iron yoke, the iron yoke saturates due to the stray field. Such a saturation of the iron yoke was confirmed by the field calculation, with 3D electromagnetic calculation code of TOSCA, for the complete configuration of 6-sector magnets. As a result, the iron yoke of BM1 is ineffective to shield the field of bending magnet, though it is required to reduce the magnetic disturbance into the level of 100 G over the acceleration region. Therefore, an active-shield type magnet which is equipped with shield coils is adopted for the BM1 of SRC-6.

A schematic view of the designed BM1, which consists of three main coils and two shield coils, is shown in Fig. 1. It is assumed that both coils are fabricated from the superconducting wire having the cross section of $2 \times 4 \text{ mm}^2$ which permits the operating current of 1.8 kA. Distribution of the BM1's dipole field against bending along the x axis (horizontally transversal direction for the beam axis) is shown in Fig. 2. It is seen that the shield coil reduces the interior field of main coils by about 20%, but can compensate the exterior field of main coils. The dipole field in the midplane is shown in Fig. 3. The quadrupole field is produced due to the curved structure of BM1. The 2D multipole contents calculated from the field distribution along the circle of $r = 20 \text{ mm}$ and along the x axis are shown in Table 2. Both contents are slightly different

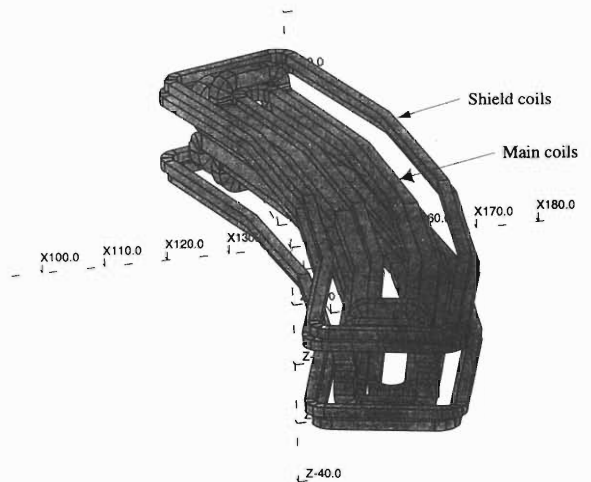


Fig. 1. Schematic view of the bending magnet (BM1).

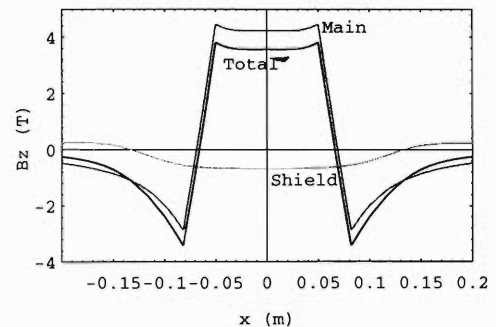


Fig. 2. Field distribution along the x axis (2D calculation).

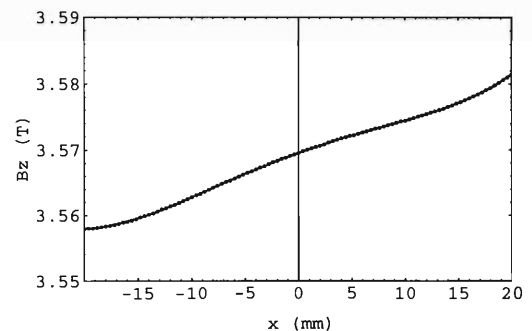


Fig. 3. Field distribution in the midplane (3D calculation).

each other due to the curved structure. The effective length of the dipole field along the beam axis shown in Fig. 4 is about 1.08 m.

Table 2. Contents of multipole components of BM1, with the reference radius of $r = 20$ mm.

n (Bref)	Pole	circle ($r = 20$ mm)	x axis
		3.5695	3.5695
1	dipole	1.	1.
2	quadrupole	0.00326	0.00327
3	sextupole	-0.00135	-0.00141
4	octupole	0.0000323	0.000065
5	decapole	0.00126	0.00161
6	dodecapole	$5.82 \cdot 10^{-6}$	0.00031

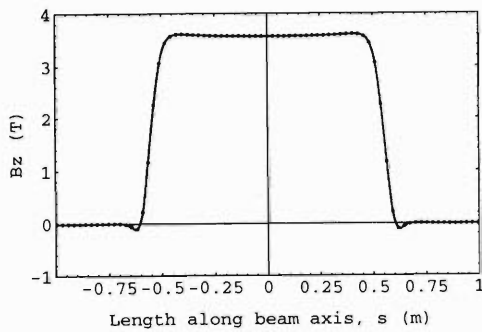


Fig. 4. Field distribution along the beam axis (3D calculation).

For the case with vertical bias field of -0.6 T, the distribution of field vectors is drawn, together with the cross sections of coils in Fig. 5. The inversely vertical bias field $-B_{\text{bias}}$ increases the total field between the main coils and the shield coils, and changes the location of the maximum field and changes the magnetic forces acting on each coil. The contour plot of $|B|$ is shown in Fig. 6. The white region corresponds to the max strength value of $|B|$, while the black region corresponds to the minimum $|B|$. The maximum field of coils is 4.2 T. The magnetic forces exerting on coils

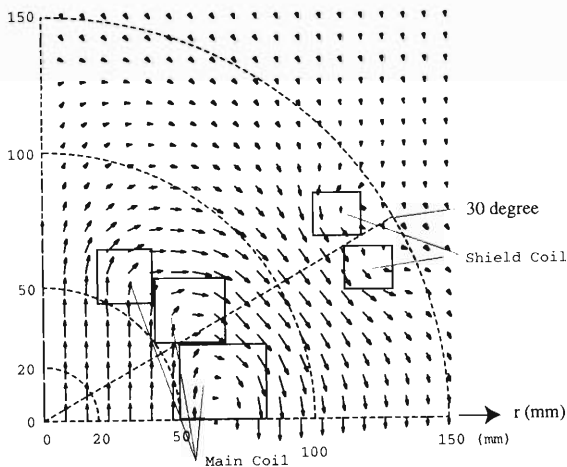


Fig. 5. Distribution of field vectors with vertical bias field of -0.6 T (2D calculation).

are shown in Fig. 7. Supporting structure for the magnetic forces should be optimized. The mechanical and cryogenic design are currently under study. Since the installation space for the bending magnet (BM1) is so limited, a compromise between the compactness for the whole structure and the easiness for the coil fabrication must be made.

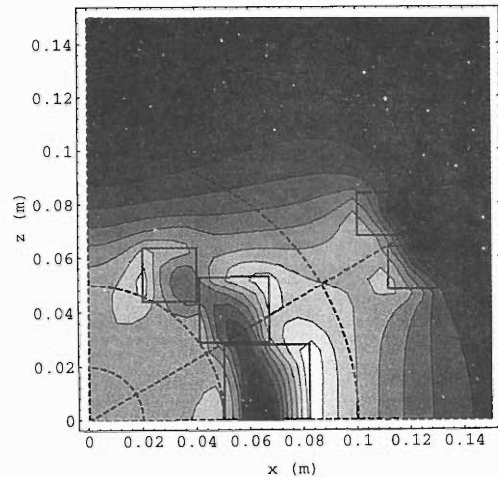


Fig. 6. Contour plot of $|B|$ with the vertical bias field (2D calculation).

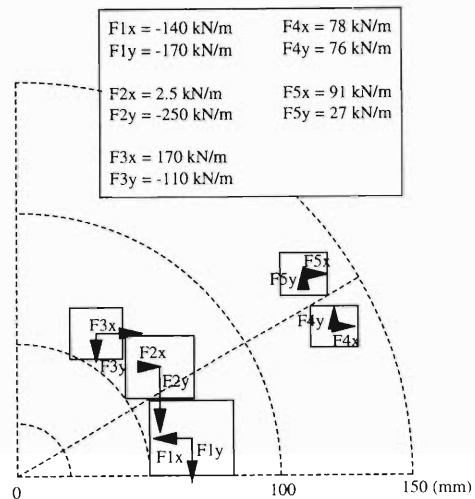


Fig. 7. Magnetic forces exerting on coils under the vertical bias field (2D calculation).

References

- 1) A. Goto et al.: RIKEN Accel. Prog. Rep. **30**, 196 (1997).
- 2) T. Mitsumoto et al.: RIKEN Accel. Prog. Rep. **30**, 197 (1997).
- 3) T. Kawaguchi et al.: RIKEN Accel. Prog. Rep. **30**, 199 (1997).
- 4) H. Okuno et al.: RIKEN Accel. Prog. Rep. **30**, 203 (1997).
- 5) S. Fujishima et al.: RIKEN Accel. Prog. Rep. **30**, 207 (1997).

Design Study of Injection System for RIKEN Superconducting Ring Cyclotron (III): Analysis of the injected beam trajectories

S. Fujishima, H. Okuno, T. Tominaka, T. Kubo, T. Kawaguchi, T. Mitsumoto, J.-W. Kim, K. Ikegami, N. Sakamoto, S. Yokouchi, T. Morikawa, Y. Tanaka, A. Goto, and Y. Yano

For the RI beam factory project, a design of the Superconducting Ring Cyclotron-6 (SRC-6) is in progress.¹⁾ We report current status of analysis of the injected beam trajectories.

To determine the layout of the injection elements, we are analyzing the injected beam trajectories by numerical calculation. For the numerical calculation, we use a code "INJECT" originally developed by Goto et al.²⁾ to design the presently existing RIKEN Ring Cyclotron. To calculate the injected beam trajectories, a Lorentz equation is solved with Runge-Kutta-Gill method. In the code "INJECT" an independent variable is the time normalized by the beam velocity. The beam trajectories are traced back from the injection points on the first equilibrium orbits against time. The magnetic field of the sector magnets is calculated with a 3D-code "TOSCA" by Mitsumoto.

Figures 1, 2, and 3 show examples of the calculation of the injected beam trajectories in the SRC-6.

The beams from a pre-accelerator are guided to the central region of the SRC-6 and then injected into the first equilibrium orbits. The injection system consists of two or three bending magnets (BM), three magnetic inflection channels (MIC), and an electric inflection channel (EIC).^{3,4)}

The SRC-6 has strong fringing field of the sector magnets, and the fringing field strongly depend on the condition of acceleration. Thus, the trajectories of various beams differ very much each other. This makes the design of the injection system difficult. For an example, at the injection points on the first equilibrium orbits in the valley, the maximum change in the radius

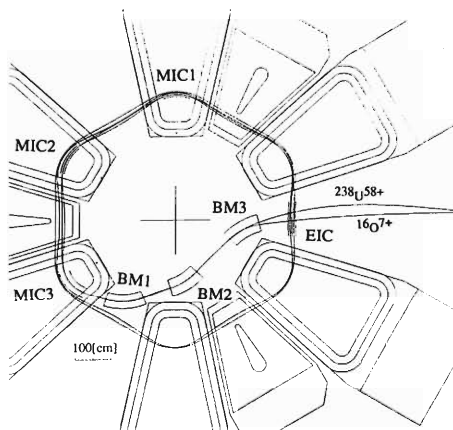


Fig. 1. Schematic layout of the injection elements and typical trajectories of the injected beams for Example 1.

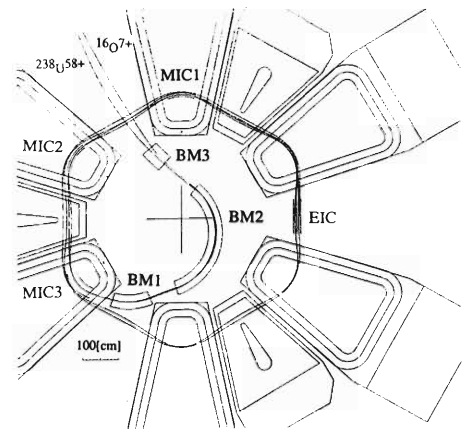


Fig. 2. Schematic layout of the injection elements and typical trajectories of the injected beams for Example 2.

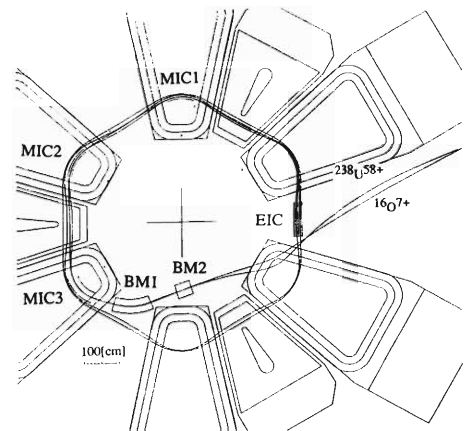


Fig. 3. Schematic layout of the injection elements and typical trajectories of the injected beams for Example 3.

of the orbits is about 12 cm. But the realizable gap width of the EIC is 1 or 2 cm at most. Thus, the EIC must be movable in the direction with radial range of 12 cm.

We have not yet determined the final layout of the injection elements. We merely introduce here three examples of the layout. Figures 1, 2, and 3 correspond to Example 1, 2, and 3, respectively. Figures 1, 2, and 3 schematically show the different layouts of the injection elements, and show typical trajectories of the injected beams. Table 1 shows their energies and magnetic rigidities. Tables 2, 3, and 4 show characteristics of the injection elements used for Example 1, 2, and 3, respectively. The characteristics of EIC, MIC1, MIC2,

Table 1. Energies and magnetic rigidities of typical beams.

	Energy [MeV/nucleon]		B ρ [Tm] injection
	injection	extraction	
$^{16}\text{O}^{7+}$	74.2	200	2.89
$^{238}\text{U}^{58+}$	58.0	150	4.57

Table 2. Characteristics of the injection elements for Example 1.

	Radius [cm]	Angle [deg]	Length [cm]	B or E (max.) [T] or [kV/cm]
EIC			(100)	100
MIC1	110.0	42.5		0.19
MIC2	110.0	47.5		0.22
MIC3	94.0	53.0		0.95
BM1	154.0	40.0		3.5
BM2	171.0	30.0	(90)	3.3
BM3	180.0	30.0		-1.89

MIC3, and BM1 are common in all three Examples.

In the case of Example 1, the beams guided from a pre-accelerator cross the EIC, and the distance between the crossing points of both beams is about 25 cm. Therefore, the EIC must be divided into two pieces. The difference of the trajectories in the BM3 is about 8 cm, thus the BM3 must have a large bore of more than 8 cm.

In the case of Example 2, the beams don't cross the EIC, and the magnetic field required for the BM3 is smaller than that of Example 1. But, the length of the BM2 is four times longer.

Table 3. Characteristics of the injection elements for Example 2.

	Radius [cm]	Angle [deg]	Length [cm]	B (max.) [T]
BM2	162.0	124.0	(351)	3.23
BM3	498.0	7.0	(61)	-1.14

Table 4. Characteristics of the injection elements for Example 3.

	Radius [cm]	Angle [deg]	Length [cm]	B (max.) [T]
BM2	1500.0	1.7	(45)	0.78

In the case of Example 3, the beams don't cross the EIC. And the BM3 is not necessary. The difference of the trajectories at the BM2 is only 1.3 cm and the magnetic field for the BM2 is only 0.8 T. Moreover, the length of the BM2 is shorter than those of other two examples. However, since the beams pass through the tip of a sector magnet, the space for the sector coil link is restricted.

References

- 1) A. Goto et al.: RIKEN Accel. Prog. Rep. **30**, 196 (1997).
- 2) A. Goto: Rep. Inst. Phys. Chem. Res. (in Japanese) **57**, 203 (1981).
- 3) H. Okuno et al.: RIKEN Accel. Prog. Rep. **30**, 203 (1997).
- 4) T. Tominaka et al.: RIKEN Accel. Prog. Rep. **30**, 205 (1997).

Optimization of Trim Coils in a Superconducting Ring Cyclotron

J.-W. Kim, S. Fujishima, A. Goto, K. Ikegami, T. Kawaguchi, T. Kubo, T. Mitsumoto,
T. Morikawa, T. Ohkawa, H. Okuno, N. Sakamoto, S. Yokouchi, Y. Tanaka,
T. Tominaka, I. Watanabe, and Y. Yano

In designing a superconducting ring cyclotron (SRC) as a variable energy and multi-ion accelerator, it is one of the main works to optimize a magnetic field trimming system for the field isochronization. Most of the ring and compact superconducting cyclotrons in operation uses resistive (normal) trim coils for their field trimming. On the other hand, it is not practical for a SRC to use resistive trim coils alone. Problems are that the pole piece of superconducting sector magnet, either cold or warm,¹⁾ is distant from the resistive trim coil, and is saturated. Therefore, the field correction by normal trim coils must rely on the magnetomotive force without much contribution from iron parts. The SRC-6 which is a booster cyclotron in the proposed RIKEN RI beam factory employs both superconducting and normal trim coils.²⁾ A major correction is made by the superconducting trim coils, and the remnant error field is corrected by the normal trim coils, because the power loss in the superconducting coils is independent of its total ampere-turns.

The isochronous and sector magnetic fields are shown in Fig. 1 for two test particles. The radial field profile by the sector magnet matches with that of the isochronous field of low q/A ions like $^{238}\text{U}^{58+}$, and the high q/A ions like $^{16}\text{O}^{7+}$ need a maximum correction field from trim coils. The optimization of both trim coils is now under way in terms of the number of independent coils, coil positions, and so on.

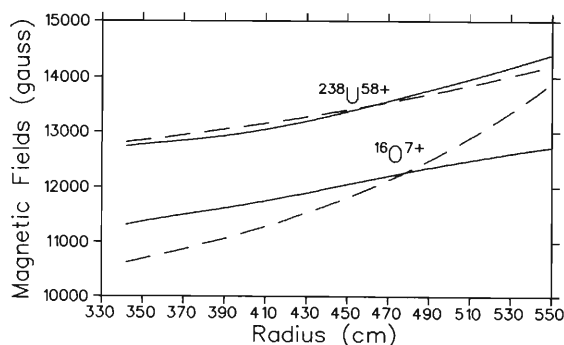


Fig. 1. Isochronous and sector magnetic fields for two test particles shown by dashed and solid lines, respectively. The magnetic field is the azimuthal average of the field at a given radius.

The criterion of optimization is not well defined as two different kinds of trim coils are involved. The condition of minimum power dissipation which is often adopted for the resistive trim coil optimization is not equally applicable to the superconducting trim coil.

In the SRC-6, high- T_c current leads will be used for its superconducting trim coils to reduce the heat conduction to liquid helium. (Furukawa electric company will supply the superconducting wire with operation current of 500 A.) The heat leak through the high- T_c current leads for the current of 500 A is about 0.2 W at 4.3 K which roughly corresponds to 2 kW at 300 K. The normal trim coil operating at 500 A, on the other hand, dissipates 3–4 kW. Two kinds of trim coils look comparable in aspect of power loss. However, in this calculation it is assumed that the normal trim coil has only one turn on each sector, whereas the power loss of the superconducting trim coils is independent of the number of turns. The field distributions of the trim coils are shown in Fig. 2. The field profile of the normal trim coil is not so optimal as a correction coil, considering the cancelation effect on adjacent coils. Therefore, it may be advantageous to use a large number of superconducting trim coils, but its usable number is limited by available space for the outlets of the current leads.

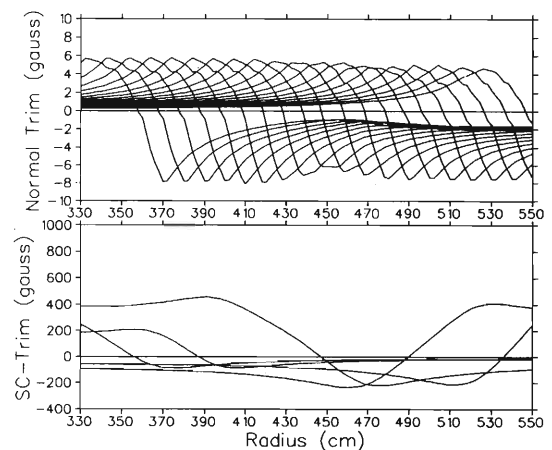


Fig. 2. Upper Graph: field distributions of twenty normal trim coils at 500 A, and Lower Graph: field distributions of five superconducting trim coils when the sector field at the center is 3.5 tesla.

First, we tried to make an isochronized field for $^{16}\text{O}^{7+}$ in the energy range of 55–400 MeV/u. The program used in this calculation utilizes a least square fitting subroutine, which is the same as used for the design of previous RIKEN cyclotrons.³⁾ As a function of the superconducting trim coil number, the leftover error fields after fitting were examined. For the cases of three to five superconducting trim coils, the error fields are shown in Fig. 3. With use of 5 sets of superconducting trim coils, the error field reduced within ± 10

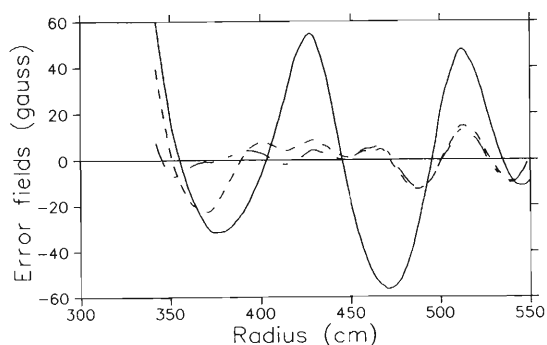


Fig. 3. The error fields remained after fitting with superconducting trim coils. The solid line shows the case fitted by three superconducting trim coils, the dashed line by four coils, and the dot-dashed line by five coils.

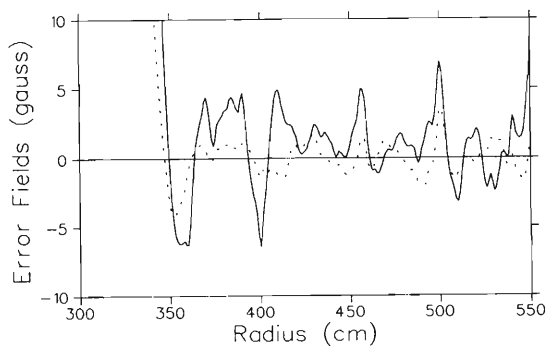


Fig. 4. The error fields leftover after fitting with twenty normal trim coils against those shown in Fig. 3. The solid line shows the final error field after four superconducting trim coils are used, and the dotted line shows that after five coils are used.

gauss, or $\pm 1\%$ of the isochronous field. The case of 6 trim coils was also calculated, but it didn't improve the fitting so much, although further investigation may be necessary on the locations of trim coils.

Twenty sets of resistive coils were then tested with uniform spacing of 10 cm at radii between 365 cm and 555 cm, and fitting was carried out. Figure 4 shows the leftover error fields after fitting with twenty normal trim coils for the two cases of four and five superconducting trim coils. The field error is less than $\pm 0.05\%$ for the case of the five superconducting trim coils, which meets our criterion of field isochronism. For the case of four superconducting trim coils it is surely feasible to use additional resistive trim coils and reduce the error fields, but it may be less attractive be-

cause of the higher electric power loss.

A combination of the normal and superconducting trim coils that satisfies our requirement has been found. Further optimization for different test ions in a full operating energy range is in progress.

References

- 1) T. Kawaguchi et al.: RIKEN Accel. Progr. Rep. **29**, 232 (1996).
- 2) T. Mitsumoto et al.: RIKEN Accel. Progr. Rep. **29**, 230 (1996).
- 3) H. Takebe et al.: RIKEN Accel. Progr. Rep. **15**, 173 (1981).

Design Study of the Accumulator Cooler Ring for MUSES

K. Ohtomo, Y. J. Yuan, J. Xia, and T. Katayama

In the proposed RI beam factory project, Accumulator Cooler Ring (ACR) will be used for the accumulation and cooling of the radioactive isotope (RI) beams which are produced by the beam from a Superconducting Ring Cyclotron (SRC) and pass through a fragment separator. The momentum spreads of these RI beams will be significantly reduced by the electron cooling and stochastic cooling devices in the ACR. Devices for multi-turn injection and RF stacking are also needed in order to build up the beam current. Lattice of the ACR shall be designed by taking the following requirements of devices into account:

- 1) Electron cooler requires a long straight free space (nearly 8.0 m) free from dispersion.
- 2) Stochastic cooling devices require a few pairs of dispersion-free space for a pickup and a kicker, and the phase advance of the betatron oscillation should be nearly $k\pi/4$ between them.¹⁾
- 3) Multi-turn injection requires the sections where the phase advance of the betatron oscillation is nearly π , to arrange kickers and septum magnets.
- 4) RF stacking requires a dispersion in the multi-turn injection section and a space for tunable RF cavity.
- 5) Accumulation of high current beams requires a large acceptance in the horizontal plane ($=125\pi$.mm.mrad) and a large momentum spread ($\Delta p/p \sim \pm 2\%$).

Optimized design of the lattice is shown in Table 1 and Figs. 1 and 2.

Table 1. Lattice parameters of ACR.

Circumference	$C = 168.4836$ m
Average Radius	$\bar{R} = 26.815$ m
Max. Magnetic Rigidity	$B\rho = 7.244$ T.m
Max. Beam Energy	$E = 500$ MeV/u ($Z/A=1/2$)
Momentum Compaction	$\alpha = 0.0402042$
Transition Gamma	$\gamma = 4.987$
Betatron Tune Values	$Q_x/Q_y = 4.555/3.540$
Natural Chromaticity	$Q'_x/Q'_y = -5.058/-6.571$
Max. β -Amplitude	$\beta_x/\beta_y = 18.33$ m/24.53 m
Max. Dispersion	$D_x/D_y = 4.518$ m/0.0 m

The ACR lattice consists of two arc sections and two long straight sections, as shown in Fig. 1 and is described as follows.

$$ACR = CELL-STRC-2CELL-STRC-CELL,$$

where STRC denotes the long straight section and CELL the half of the arc section. A CELL is symmetric and decomposed into two half elements, HCELL.

$$CELL = (HCELL, -HCELL)$$

A HCELL is described as follows:

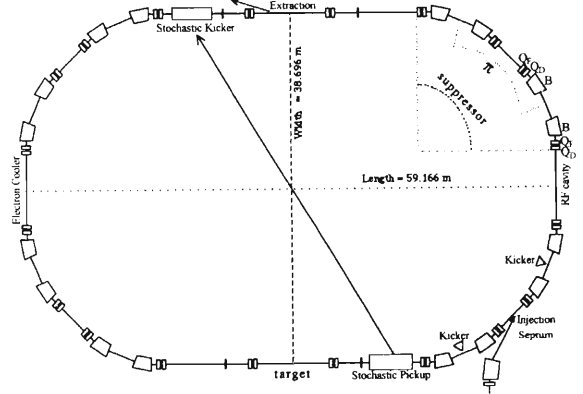


Fig. 1. The layout of ACR.

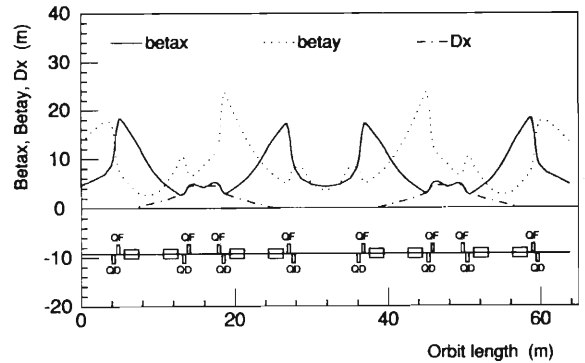


Fig. 2. Distributions of β and D_x in arc section.

$$HCELL = \frac{L_r}{Q_D-Q_F-B} \frac{L_k}{B-Q_D-Q_F} \frac{L_i}{-},$$

where Q_F and Q_D are the focusing and defocusing quadrupoles, B bending magnets, and L long drift space. Each CELL functions as a dispersion suppressor and makes the free dispersion space at L_r , where RF cavities or electron coolers are located. An injection kicker and septums occupy one CELL.

The two long straight sections are given as follows:

$$STRC = -Q_C-Q_D-Q_F \frac{L_e}{-} Q_F-Q_D-Q_C-$$

where Q_C is a quadrupole for chromaticity correction. L_e is a long drift space of 8.0 m for beam extraction devices or for an internal target.

Next, we evaluated the efficiency of RF stacking with the cooling devices. This process was simulated for typical nuclear beam of $^{132}\text{Sn}^{50+}$, using the parameters listed in Table 2.

The repetitive RF stacking procedure consists of the following steps. Firstly, an RF bucket of the capture voltage is prepared. After 1/4 period of synchrotron oscillation the RF voltage is sharply reduced

Table 2. Parameters of RF stacking.

Typical beams	$^{132}\text{Sn}^{50+}$
Kinetic energy	210 MeV/u
Harmonic number	30
RF frequency of injected beam	29.1 MHz
Momentum spread of injected beam	$\pm 0.5\%$
Phase spread of injected beams	$\pm 10^\circ$
Capture voltage	600 kV
Accelerating voltage	10 kV
Stacking period	30 ms
Transverse emittance	$5 \pi \cdot \text{mm} \cdot \text{mrad}$
Momentum difference at injection	-1%
Momentum difference at stack-top	2.7%

to the accelerating voltage and the beam is kept in the bucket. Then the RF voltage, frequency, and synchronous phase are adiabatically changed and the beam is moved to the top of the stacking orbit. Finally, the RF voltage is switched off and the beam is released on the stacking orbit. During the whole procedure the electron cooling and stochastic cooling are applied at the stacking-top.

The following differential equations describe the physical method of the RF stacking with electron cooling and stochastic cooling:

$$\frac{d\Delta p}{dt} = \frac{eV_{\text{RF}}}{2\pi R_s} (\sin \Phi - \sin \Phi_s) - k \frac{\Delta p}{(\theta^2 + \Delta p_{\text{rel}}^2)^{3/2}} \left(2L_{FH} + \frac{3\theta^2}{(\theta^2 + \Delta p_{\text{rel}}^2)} L_{MH} \right)$$

+ Stochastic cooling term

$$\frac{d\Phi}{dt} = -\frac{1}{2\pi} \cdot \frac{h\eta\omega_s}{R_s P_s} \frac{\Delta p}{2\pi R_s}$$

$$\frac{d\theta}{dt} = -k \frac{\theta}{(\theta^2 + \Delta p_{\text{rel}}^2)^{3/2}} \left(2L_{FH} + \frac{\theta^2 - 2\Delta p_{\text{rel}}^2}{(\theta^2 + \Delta p_{\text{rel}}^2)} L_{MH} \right)$$

Here, the stochastic cooling term was derived according to Ref. 2. L_{FH} and L_{MH} are constants, $\Delta p(t)$ is the momentum difference, $\Phi(t)$ is the phase of the particle, $\theta(t) = (\varepsilon_{x,y}/\beta_{x,y})^{1/2}$, $\Delta p_{\text{rel}}(t) = \Delta p(t)/(\gamma p_s)$, and $k = 2\pi r_e r_n j_e Z^2 / e\beta^4 \gamma^5 A$. These formula related to electron cooling were derived from Ref. 3.

The typical parameters of electron cooling and stochastic cooling are listed in Tables 3 and 4, respectively.

Table 3. Parameter of electron cooling.

Ratio of cooler length to circumference	2.1%
Electron current density	0.5 A/cm ²
Diameter of electron flow	5 cm

Table 4. Parameter of stochastic cooling.

Number of particles	10^7
Kicker efficiency	50%
Total temperature	400 K
Midband / width frequency	0.75 GHz / 0.5 GHz
Z_P / Z_C	25 Ω / 50 Ω
Number of pickups	10
Output power	10 kW

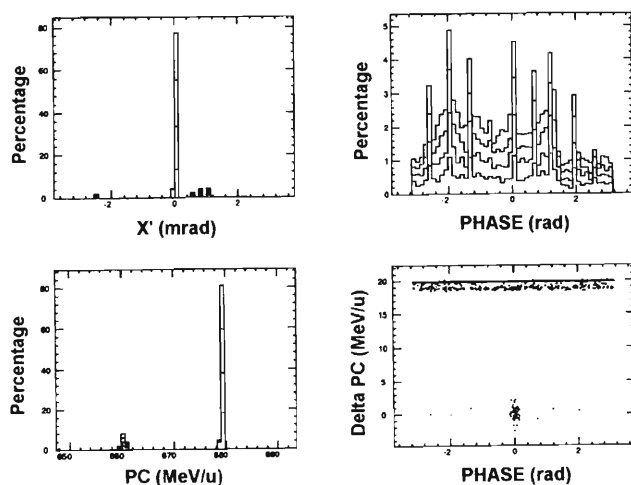


Fig. 3. Simulation of RF stacking for $^{132}\text{Sn}^{50+}$ with electron cooling and stochastic cooling: Graph at lower right shows the stacked beam on phase space. Histogram at lower left represents the distribution in momentum space, where a large peak at the right is stacked beams, while the left small peak is split one.

tively. The simulated results are shown in Fig. 3.

The simulation results show that the stacking efficiency is 80% and that $\Delta p/p$ reaches $\pm 0.03\%$. The efficiency are saturated when more than 100 periods of RF stacking are done because the acceptance is filled with the beams.

It should be noticed that the sharp decreasing pattern of the RF voltage is assumed in this simulation in order to compress the momentum spread of the injected beam when the beam captured. It is, however, difficult to realize this property in the proposed RF cavity which has a high voltage of 600 kV. Another and more realistic way to achieve a small momentum spread is to install debuncher cavities in the injection beam line for the reduction of the spread prior to the capture.

We have presented the ACR lattice design which fulfills the demand of the beam accumulation with RF stacking, stochastic cooling, and electron cooling, as well as the experimental equipments. It has many free space sections left for various devices. The RF stacking simulation results turn to be reasonable but is supposing a high-efficiency debuncher in the beam line. The designs of a pre-debuncher system and of the frequency-modulable RF devices for the RF stacking are in progress.

References

- 1) P. Krejcik et al.: Proc. Eur. Part. Accel. Conf., p. 788 (1988).
- 2) D. A. Goldenberg et al.: LBL-24979 (1988).
- 3) I. N. Meshkov: Phys. Part. Nucl. **25**, 631 (1994).

Design Study of Electron Cooling for ACR in MUSES

Y. Rao, K. Ohtomo, I. Watanabe, and T. Katayama

The Accumulator Cooler Ring (ACR) is one component of the Multi-Use Experimental Storage rings (MUSES) proposed for RIKEN RI beam factory.¹⁾ The use of electron cooling is planned for compression of the phase space volume of multturn-injected and RF-stacked ion beams at the top of stack, which helps increase the intensity of accumulated beam.

Heavy ion beams injected into ACR have energies from 150 to 500 MeV/u. Corresponding electron beam energies range from 82 to 274 keV. Therefore, voltage for the electron gun cathode is required to be adjustable within a range of 70–300 kV.

Larger electron current might be required to achieve a fast cooling during injection of hot ion beams. However, cooler operation with larger current may cause the loss of stored highly charged ions due to the radiative electron capture process in the cooling section. By compromise, a maximum electron current of 4.0 A is chosen.

The multturn-injected ion beam which has a maximum emittance of 120π mm·mrad horizontally and has a beta function of $\beta_h = 5$ m in the cooling section should be totally immersed in the electron beam. Therefore, the electron beam diameter in cooling section is determined as 50 mm.

Since ACR has a circumference of 168.48 m, the length of cooling section 3.6 m corresponds the relative cooler length $\eta_{ec} = 0.021$.

Because the electron beam with a low transverse temperature is preferable for faster cooling, our ACR electron cooler will utilize a magnetically expanded electron beam.²⁾ Normally, a solenoid field strength of 0.5–1.2 kG is required for maintaining the magnetized cooling regime. If we plan for an adiabatic expansion of the magnetic field by a factor of 10, the corresponding

gun solenoid field becomes 0.5–1.2 Tesla.

This expansion scheme will lower the electron beam transverse temperature by a factor of 10, because the transverse energy of electron divided by the strength of the longitudinal magnetic field is an adiabatic invariant under the changes of field strength. The ‘area’ of the electron beam cross section times the magnetic field strength is also an adiabatic invariant. Therefore, in order to keep the electron beam diameter 50 mm in the cooling solenoid, a flat cathode must be made with a diameter of 16 mm.

The electron gun consists of a flat cathode, a Pierce electrode, an anode, and an acceleration column, being somewhat similar to that of TARN-II.³⁾ Fig. 1 shows an example of the calculated electron trajectories.

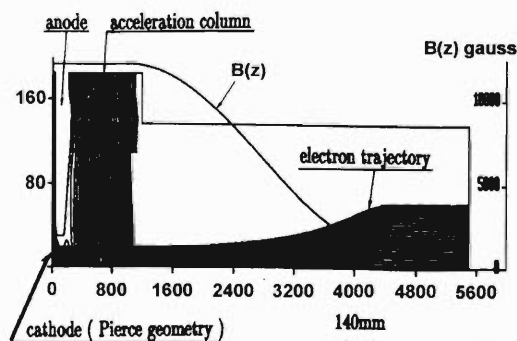


Fig. 1. Computer generated plot of electron trajectories in electron gun. Expanded electron beam trailed by $B(z)$ is observable.

Main parameters of the ACR electron cooling system are summarized in Table 1.

Table 1. Parameters of ACR electron cooling system.

Energy range of the cooled ions	150–500 MeV/u
Energy range of electrons	70–300 keV
Maximum electron current	4.0 A
Gun design	Pierce geometry + adiabatic focusing electrodes
Cathode diameter	16 mm
Electron beam diameter at cooling section	50 mm
Maximum solenoid field at acceleration section	1.2 T
Maximum solenoid field at cooling section	1.2 kG
Length of cooling section	3.6 m
B_{\perp}/B_{\parallel} in cooling section	$< 1.0 \times 10^{-4}$
Bending angle of toroids	90°
Collector efficiency	$>99.98\%$
Voltage stability of HVPS	$\pm 1.0 \times 10^{-5}$

By using this system, one can expect the cooling time of the order of 10 s, depending on different ions and their energies.

In the practical application of electron cooling at ACR, the cooling time and its dependence on some parameters must be known. The simulation was done in order to investigate the bunched beam emittance and relative momentum spread as a function of time, by using the analytical formulae of cooling force by I. N. Meshkov,⁴⁾ taking into account the betatron and synchrotron oscillations of particles and the influence of electron beam space charge in the cooling section.

The time evolution of transverse emittances (ϵ_h, ϵ_v) and longitudinal momentum spread ($\Delta p/p$) resulted from the simulation are shown in Fig. 2 for a beam of 210 MeV/u $^{132}\text{Sn}^{50+}$ with initial horizontal and vertical emittance of 120 and 5 $\pi\text{mm}\cdot\text{mrad}$, respectively, and with initial momentum spread of $\pm 2.5 \times 10^{-4}$.

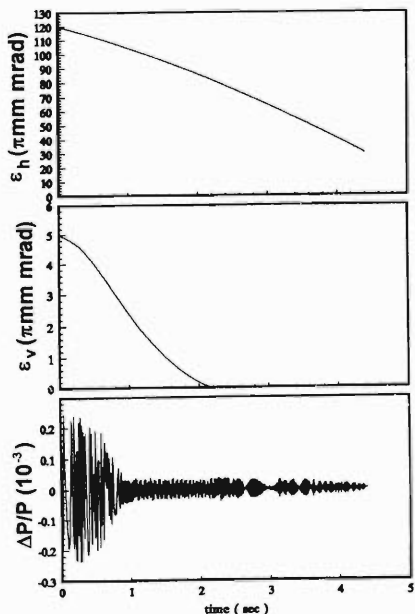


Fig. 2. Time evolutions of beam emittance and momentum spread.

In order to investigate the space charge effect due to electron beam, the above simulation was repeated by changing the neutralization factor f_n . Figure 3 shows the results of the longitudinal cooling for $f_n = 90\%$, 50%, and 0%, where the other parameters are kept the same and no dispersion was assumed in cooling section. It can be seen from the figure that the longitudinal cooling becomes much faster by neutralizing the space charge of electron beam.

Also, the transverse temperature kT_t of electron beam is one of the critical factors that influence the cooling speed. As a result of the simulation in Fig. 4, the destination cooling time i.e., the time duration needed to cool the ion beam from the initial horizontal emittance to a specified values of 30 $\pi\text{mm}\cdot\text{mrad}$,

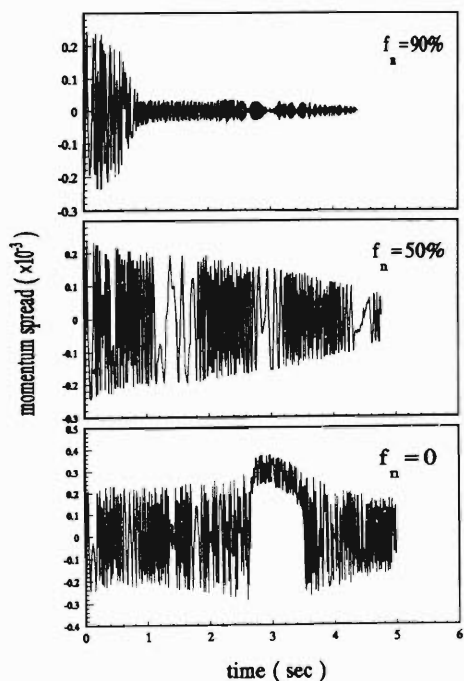


Fig. 3. Simulated longitudinal cooling effects for three different neutralization factors of electron beam space charge.

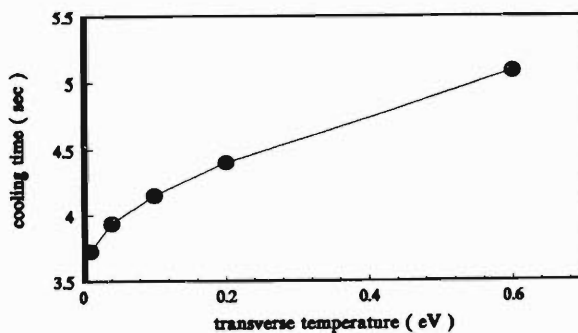


Fig. 4. The transverse cooling time as a function of the electron beam transverse temperature, when $f_n = 90\%$, $D_h = 0$ m.

changes from 3.73 to 5.08 seconds with the increase of kT_t from 0.01 to 0.6 eV. Therefore, an electron beam with low transverse temperature is expected to speed up the cooling process.

In conclusion, neutralizing the space charge of electron beam with a very low transverse temperature is preferable to finish cooling faster.

References

- 1) Y. Yano et al.: RIKEN Accel. Prog. Rep. **30**, 195 (1997).
- 2) D. Habs et al.: Workshop on beam cooling and related topics, Montreux, CERN 94-03, p. 188 (1994).
- 3) T. Tanabe et al.: Nucl. Instrum. Methods Phys. Res. A **307**, 7 (1991).
- 4) I. N. Meshkov: Phys. Part. Nucl. **25**, 631 (1994).

Design of the Booster Synchrotron for MUSES

T. Ohkawa and T. Katayama

The Booster Synchrotron Ring (BSR), a part of Multi-Use experimental Storage Rings (MUSES), functions exclusively for the acceleration of ion and electron beams. The maximum accelerating energy is, for example, to be 3 GeV for proton; 1.45 GeV/nucleon for light ions of $q/A = 1/2$; and 800 MeV/nucleon for heavy ions of $q/A = 1/3$. In this paper some results of lattice study of the BSR are presented.

The lattice structure was designed to be as compact as possible. Basically FODO structure was used, and we adopted a racetrack type to accommodate two long straight sections. The two long straight sections are used for fast and slow extractions of ion and electron beams, and each of them contains four long drift space where RF cavities and kicker magnets are inserted.

In this design, the total length of the structure was fixed to be 168.484 m which is 5 times the SRC extraction radius, and the maximum magnetic rigidity was determined to be 14.6 Tm corresponding to the energy of 800 MeV/nucleon for heavy ions with $q/A = 1/3$. Transition γ was chosen to be higher than 4.77, a value being still satisfactorily high for beam stability.

As shown in Fig. 1, the BSR consists of two arc sections and two long straight sections. Each arc section is a mirror symmetrical system, and there are two bending cells in it. Each bending cell is a dispersion suppressor, and consists of four FODO cells because this number of cells is pre-determined to raise γt sufficiently large. The two long straight sections are also mirror symmetry. The dispersion in the straight sections is zero. The length of a dipole magnet is 1.911 m, which is determined by the circumference specification. The maximum magnetic field of a dipole is then 1.5 T,

which is determined by required maximum rigidity of particles 14.6 Tm.

The lattice is specified for eight families of quadrupoles: QF1, QD1, QF4 and QD4 in the arcs, and QF2, QD2, QF3 and QD3 in the long straight sections. The structure of one FODO cell and short straight section(str2) in the arc are given as follows:

$$\begin{aligned} \text{cel} &= \text{QF1} \xrightarrow{d_1} \text{B} \xrightarrow{d_1} \text{QD1} \xrightarrow{d_1} \text{B} \xrightarrow{d_1}, \\ \text{cel2} &= \text{QF1} \xrightarrow{d_2} \text{B} \xrightarrow{d_2} \text{QD1} \xrightarrow{d_2} \text{B} \xrightarrow{d_2}, \end{aligned}$$

and

$$\text{str2} = \text{QF4} \xrightarrow{d_3} \text{QD4} \xrightarrow{d_s} \text{QD4} \xrightarrow{d_3} \text{QF4},$$

so the lattice of each arc section (60.365 m) is

$$\text{arc} = (\text{cel}, \text{cel2}, \text{cel2}, \text{cel}, \text{str2}, -\text{cel}, -\text{cel2}, -\text{cel2}, -\text{cel}).$$

In this structure, d_1 (0.5 m) and d_2 (0.511 m) between dipoles and quadrupoles are the drift spaces in which the sextupole magnets for chromaticity correction and the correction magnets for COD correction are installed. The lattice of each straight section (23.876 m) is

$$\begin{aligned} \text{str1} &= \xrightarrow{d_s} \text{QF2} \xrightarrow{d_3} \text{QD2} \xrightarrow{d_s} \text{QD3} \xrightarrow{d_3} \text{QF3} \\ &\quad \xrightarrow{d_3} \text{QD3} \xrightarrow{d_s} \text{QD2} \xrightarrow{d_3} \text{QF2} \xrightarrow{d_s}, \end{aligned}$$

where d_s is a free space of 4.819 m long in which RF cavities, injection kickers, and/or other devices are installed. Then, the whole lattice of the BSR is described as follows:

$$\text{BSR} = (\text{arc}, \text{str1}, \text{arc}, \text{str1}).$$

Parameters of the lattice are summarized in Table 1. The β and dispersion functions are shown in Fig. 2. Transition γ is 4.786 and the peak dispersion is 3.206 m. The peak β functions are 13.360 m in horizontal direction and 19.508 m in vertical direction. These calculations were performed using the MAD program.

Table 1. Lattice parameters of BSR.

Circumference	$C = 168.4836$ m
Average radius	$R = 26.815$ m
Max. magnetic rigidity	$B\rho = 14.6$ Tm
Momentum compaction	$\alpha = 0.0437$
Transition gamma	$\gamma_t = 4.786$
Betatron tune values	$Q_x/Q_y = 6.380/4.910$
Natural chromaticity	$Q'_x/Q'_y = -7.355/-7.004$
Max. β amplitude	$\beta_x/\beta_y = 13.360 \text{ m}/19.508 \text{ m}$
Max. dispersion	$D_x/D_y = 3.206 \text{ m}/0.0 \text{ m}$

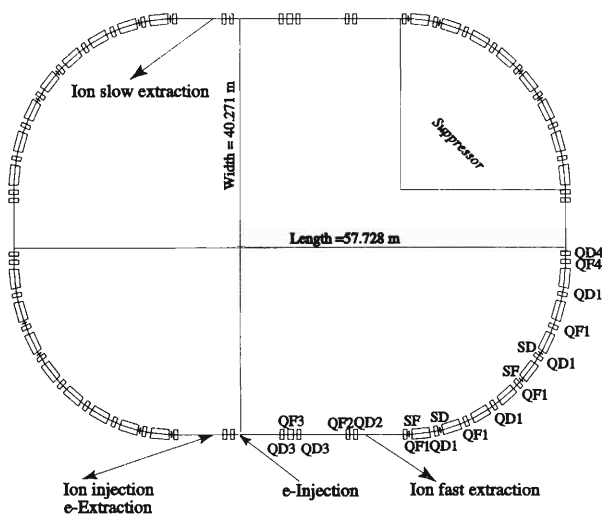


Fig. 1. Layout of the BSR.

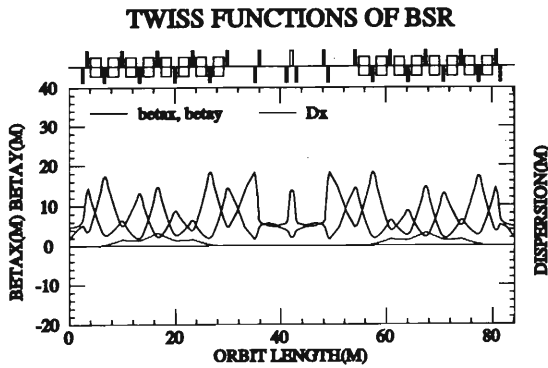


Fig. 2. Beta and dispersion functions along the lattice.

The dynamic aperture was seriously reduced when chromaticity was corrected. The reason for this is that strong-field sextupoles are necessary to use because of the low average value of dispersion in the ring aimed at high γt . In this lattice, natural chromaticity values are -7.355 (horizontal) and -7.004 (vertical), and they are corrected by two families of sextupoles (focusing SF and defocusing SD). Same family's sextupoles in one bending cell are located π apart in phase in order not to excite the third order resonance. The normalized field strengths of sextupoles required to correct chromaticity are relatively large: 7.642 m^{-3} for the SF and -11.998 m^{-3} for the SD. Multi-particle tracking was performed in this lattice to study the motion stability of particles with a large beam emittance. Results of the multi-particle tracking for the perfect lattice with chromaticity correction are shown in Fig. 3. At the initial state, 100 particles were distributed within an emittance of $\varepsilon_x = 125\pi \text{ mm.mrad}$ and $\varepsilon_y = 5\pi \text{ mm.mrad}$, which are the designed maximum value for the beam from ACR (Accumulator Cooler Ring). After 1000 turns, the motion of parti-

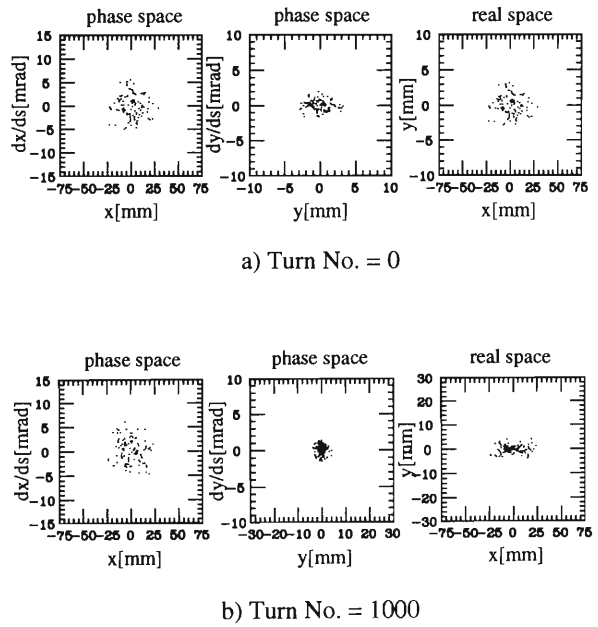


Fig. 3. Results of multi-particle tracking at a) Turn No. = 0 and b) Turn No. = 1000. The number of particles is 100.

cles was stable without any particle loss. In this study the dynamic aperture was determined by multi-particle tracking for a perfect machine with zero chromaticity over 1000 turns. The above tracking results show that the dynamic aperture of BSR is larger than $\varepsilon_x = 125\pi \text{ mm.mrad}$ and $\varepsilon_y = 5\pi \text{ mm.mrad}$. Further tracking has to be performed to obtain information about the main sources of dynamic aperture reduction and to estimate the level of multipole content tolerable in the dipoles.

We have designed the lattice of the BSR satisfying the fundamental requirements. Optimization of the lattice for the BSR is under way.

Design of the Double Storage Rings for MUSES

N. Inabe and T. Katayama

A design of the Double Storage Rings (DSR), which was reported in the last progress report,¹⁾ has been developed. The DSR is composed of two rings which are to be constructed vertically each other. One shown in Fig. 1(a) is mainly used to store electron beams (electron ring). When a merging or colliding experiment between ions is performed, ion beams are stored in the electron ring. Another ring in Fig. 1(b) is to store ion beams only (ion ring). The both rings have maximum rigidities of 14.6 Tm that corresponds to energy of 1 GeV/u with $A/Z = 3$ and circumference of 260.123 m which is 47/6 times of circumference of Super-conducting Ring Cyclotron.

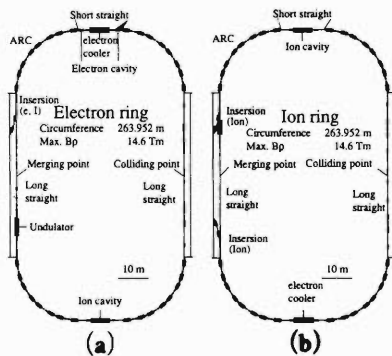


Fig. 1. Schematic drawing of two rings in the DSR. Electron ring are shown in (a) and ion ring, in (b).

The electron ring is consisting with 4 parts of arc, a short straight section, and two long straight sections. The arc is composed of 8 dipole magnets and 24 quadrupole magnets. To store the electron beams with small emittance ($\sim 10\pi$ nm*rad; small emittance mode), the arc has 4 unit cells with lattice of Double Bend Achromat (DBA). For electron beams with large emittance ($\sim 1\pi$ mm*rad; large emittance mode) the lattice is so designed that the DBA system is not adopted but that the center of the arc is a symmetry point of β and dispersion functions. The lattice for the ion beams (ion mode) is similar to that for the large emittance mode. The short straight section has cavities for the ion and electron beams, and has an electron cooler. The cavities are used to keep longitudinal emittance constant. The cavity for electron is used also to compensate energy of synchrotron radiation of light. The electron cooler is used to reduce emittance growth of ion beams originated from beam-beam effect during collisions. One of the long straight section is used for such merging experiments and for collision between X-rays and RI's. In this section, an undulator is located to produce X-ray. Insertion port is also located in this section. The electron and ion beams go

round counter-clockwise direction from the insertion point. The other long straight section is used for collision experiments between electron and RI beams. The details of construction for the merging and collision will be described later.

The ion ring is almost same as the electron ring. The main difference is in the construction of the colliding section. Other differences are a lack of devices needed for the electron beams such as the cavity for electron beam and undulator and two insertions. Because the ion beam only is stored in this ring, it is operated with the ion mode.

The β and dispersion functions at each section are calculated for several modes. The functions of the unit cell for the small emittance mode are shown in Fig. 2(a) and those of the arc for the large emittance mode are in Fig. 2(b). Figure 2(c) shows the ion mode. All dispersion function is 0 outside of the arc.

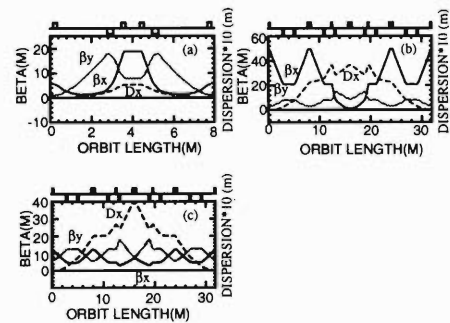


Fig. 2. β and dispersion functions in the arc. The small emittance mode is shown in (a), large emittance mode in (b), and the ion mode in (c).

The β functions of the ion mode for the short straight section are shown in Fig. 3. In this mode the β functions are required to be small and parallel for a highly efficient electron cooling. The designed β functions are ~ 6 m. For the other modes, the β functions are designed so as to connect their values between two arcs.

A side view of the merging section is shown in Fig. 4.

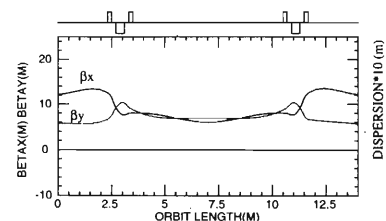


Fig. 3. β functions of the ion mode in the short straight section.

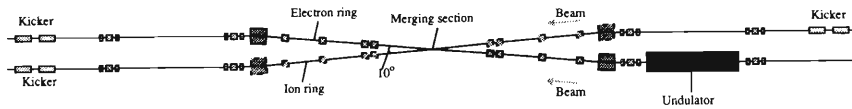


Fig. 4. Side view of the merging section.

The construction of two rings are same. In the figure the arrows show directions of ion beams. Merging angle is determined to be 10° from requirement of experiments. Beta and dispersion functions are shown in Fig. 5. Values of β at the merging point are 0.6 m for both vertical and horizontal directions. Dispersion is

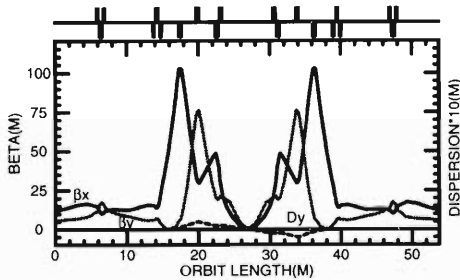


Fig. 5. β and dispersion functions in the merging section.

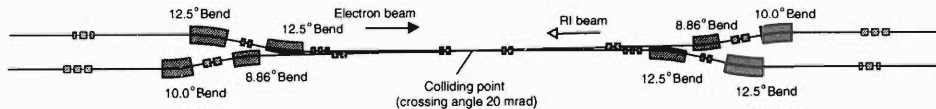


Fig. 6. Side view of the colliding section.

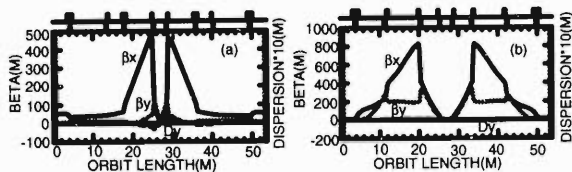


Fig. 7. β and dispersion functions in the colliding section. (a) is for the electron ring and (b), for the ion one.

0 m at the merging point.

A side view of the colliding section is shown in Fig. 6. In the figure, black arrows show electron beams of the large emittance mode while white ones show ion beams. The ion ring crosses to the electron ring with 20 mrad. The values of β at the colliding point are 0.02 m for electron beams in both directions and 0.1 m for ion beams. The small crossing angle and β values are required to obtain a large luminosity. Such small β 's can be achieved by locating two quadrupole doublets near the colliding point. The both beams pass through the quadrupole doublets when the colliding experiments are performed. For the other experiments such magnets are not used. The β and dispersion functions for electron beams are shown in Fig. 7(a) and those for ion beams in Fig. 7(b). The large maximum values of β are due to the small values of β at the colliding section. Dispersion functions are 0 at the colliding

point.

Ring parameters are summarized in Table 1 for several modes. In the table, electron 1 represents the large emittance mode and electron 2 does the small emittance mode. Parameters of ion beams are separately shown as ion 1 for ions colliding with electron, ion 2 for ions colliding with X-ray, ion 3 for ions stored in the ion ring for merging, and ion 4 for ions stored in the electron ring for merging. In particular, betatron tunes

Table 1. Ring parameters for several modes.

	electron 1	electron 2	ion 1	ion 2	ion 3	ion 4
Betatron tune(Q_x/Q_y)	5.080/8.751	16.802/9.186	5.532/6.394	5.755/5.788	5.711/5.691	5.791/5.426
Chromaticity(Q_x'/Q_y')	-75.5/-31.6	-43.9/-33.4	-50.0/-31.4	-8.70/-10.0	-11.3/-11.8	-11.0/-11.5
Momentum Compaction	0.0407	0.000118	0.0378	0.0377	0.0377	0.0372
Transition gamma	4.954	02.15	5.147	5.151	5.151	5.187
Max. betatron amplitude						
β_x .max, β_y .max (m)	487/113	55.0/66.7	828/336	57.1/51.9	102/76.4	102/76.4
Max. Dispersion						
D_x .max, D_y .max (m)	3.66/3.05	0.537/1.20	3.98/0.778	3.98/0.835	3.98/0.778	3.98/0.835
Beta at crossing point						
Merging(β_x, β_y , m)	9.76/1.02	1.11/22.8	1.08/0.888	1.08/0.888	0.6/0.6	0.6/0.6
Colliding(β_x, β_y , m)	0.02/0.02	3.76/10.0	0.1/0.1	13.5/1.75	13.5/1.75	6.59/6.68

and chromaticities are large for the small emittance mode, large emittance mode, and for ions to be used for collision. The largeness for the small emittance mode is due to the DBA system of the arc and that for the large emittance mode and ion for collision is due to lattice structure of the colliding section.

Dynamic apertures for several modes are studied currently.

References

- 1) N. Inabe and T. Katayama: RIKEN Accel. Prog. Rep. **29**, 248 (1996).

Expected Luminosity at MUSES[†]

K. Yoshida and T. Katayama

Luminosity of e-RI collision is evaluated for the current design of the Multi-Use Experimental Storage ring (MUSES). Luminosity L of the collision of two beams with Gaussian distributions in space is calculated by

$$L = n_1 n_2 c N_c E(\beta_1, \beta_2, \psi) \frac{1}{(2\pi)^3} \int \frac{dx dy dz dt}{\sigma_{x_1} \sigma_{y_1} \sigma_{z_1} \sigma_{x_2} \sigma_{y_2} \sigma_{z_2}} \times \exp \left[-\frac{1}{2} \left(\frac{x_1^2}{\sigma_{x_1}^2} + \frac{x_2^2}{\sigma_{x_2}^2} + \frac{y_1^2}{\sigma_{y_1}^2} + \frac{y_2^2}{\sigma_{y_2}^2} + \frac{(z_1 - c\beta_1 t)^2}{\sigma_{z_1}^2} + \frac{(z_2 - c\beta_2 t)^2}{\sigma_{z_2}^2} \right) \right]. \quad (1)$$

Here n_i ($i = 1, 2$) is the number of particles in one beam bunch in the Double Storage Ring (DSR), β_1 the ratio of beam velocity to the speed of light c , N_c the number of collisions per unit time, $\sigma_{x_1}, \sigma_{y_1}, \sigma_{z_1}$ the sizes of beam bunch in x, y, and z direction, and ψ the collision angle. Subscripts $i = 1, 2$ represents the electron and Radioactive Isotope (RI) beams, respectively. In Eq. (1) $E(\beta_1, \beta_2, \psi)$ is called kinematical factor and given as

$$E(\beta_1, \beta_2, \psi) = \sqrt{\beta_1^2 + \beta_2^2 + 2\beta_1\beta_2 \cos \psi - \beta_1^2\beta_2^2 \sin^2 \psi}. \quad (2)$$

As seen in Eq. (1), L depends on the number of particle in a beam bunch and on beam sizes. Therefore, we need to evaluate these to obtain the luminosity.

Production rates of RI beams are estimated with the code INTENSITY2.¹⁾ In the code, the physical feature of the fragmentation process is treated in an empirical way. The primary beam and the thickness of the Be production target are optimized so as to obtain the maximum production rate. In the calculation, the intensity of the primary beam is assumed to be 100 particle μ A. Figure 1 shows the result of the calculation with assumption of the acceptance of an RI-beam

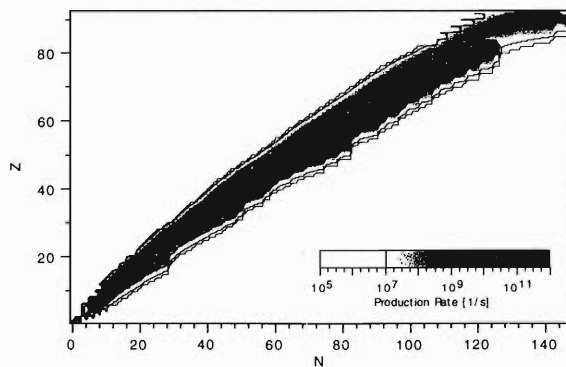


Fig. 1. Production rate of RI beams.

separator named Big-RIPS to be 10 mrad in angle and 1% in momentum.

RI beams separated by the Big-RIPS will then be stored and accumulated in the Accumulator-Cooler Ring (ACR). In the ACR, the momentum cooling will be continuously applied to the stacked beam during the RF stacking process. Both electron cooling and stochastic cooling were studied for the momentum cooling of particles. As a result, it was found that the stochastic cooling is always much faster than the electron cooling for the present case. The electron cooler with 3 m length and current density of 0.5 A/cm² gives the cooling times of 380 s for ⁶He and 0.42 s for ²³²U, whereas the stochastic cooling by a 10 kW feed back amplifier with a band width of 2 GHz gives 0.20 s and 5.0 ms, respectively. This is due to the following properties of the RI beam; the intensity is rather weak and the momentum- and emittance-spread are large. In Fig. 2, the cooling time achievable by the stochastic cooling is shown for various nuclei.

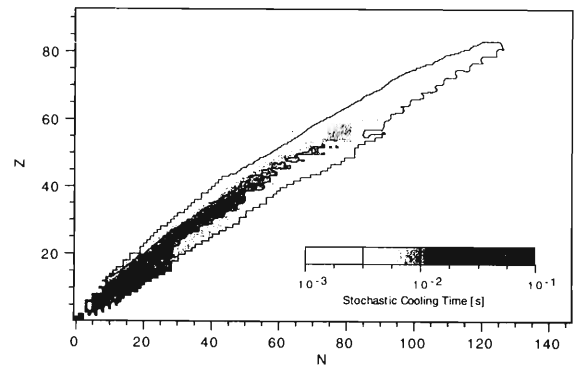


Fig. 2. Stochastic cooling time with a feedback amplifier of 10 kW and of 2 GHz in band width.

Accumulation of the RI beam is performed by using the RF stacking technique. The beam of unstable nuclei is injected into the ACR by means of a multi-turn injection with the time interval equal to the cooling time. The supply rate is

$$R_s = \frac{R_p \varepsilon_{inj}}{\tau_{cool}}, \quad (3)$$

where R_p is the production rate, ε_{inj} the efficiency of injection and τ_{cool} cooling time. The ε_{inj} is given as

$$\varepsilon_{inj} = N_{mult} \frac{h_{SRC} L_{ACR}}{f_{SRC} L_{SRC}}, \quad (4)$$

where N_{mult} is the number of multi-turn injection, h_{SRC}, f_{SRC} the harmonics number and RF frequency of the SRC, and L_{ACR}, L_{SRC} the circumference of ACR and that of the extraction orbit of SRC.

[†] Condensed from Proc. of 5th EPAC, Barcelona, June 1996.

The beams accumulated in the ACR is decaying with its own life time, τ . The maximum number of the nuclei stored in the ACR is determined by the balance of the supply rate and the decay rate,

$$N_{stl} = R_s \tau = R_p \varepsilon_{inj} \frac{\tau}{\tau_{cool}}. \quad (5)$$

The space charge limit of the ACR is also considered in the estimation of N_{stl} of Eq. (5). However, the space charge limit is only important for nuclei with the high production rate such as for stable nuclei and their neighbors.

The accumulated RI beam will be fast extracted from the ACR and be injected into the Booster Synchrotron Ring (BSR). In the BSR, the beams will be accelerated to the energy required for the experiment within 1 sec, and then be injected into the one ring of DSR to collide with the electrons stored in another ring of DSR. Since the RI beam is bunched by 46 pulses in the DSR, the maximum number of nuclei in a bunch is obtained by dividing the maximum stored nuclei in the ACR by 46. Result is shown in Fig. 3.

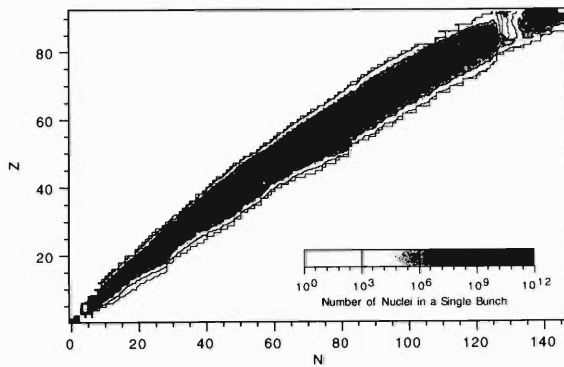


Fig. 3. The number of nuclei contained in a single bunch at DSR.

Electrons are accelerate up to 300 MeV in the electron linac and then injected to the BSR. The BSR boost electron energy up to 2.5 GeV and supply electrons to the one of the two rings of the DSR. Expected beam current in the DSR is approximately 500 mA. In order to make a synchronous collision of electrons and nuclei, the number of electron bunches will be varied from 30 to 45 according to the beam energy of nuclei which is in the ring from 300 MeV/u to 3.5 GeV/u. The number of electrons in a single bunch is then 9×10^{10} and 6×10^{10} , respectively.

Beam sizes of the electron and RI beams at the collision point also affect the Luminosity. Transverse beam sizes near the collision point are given by

$$\sigma_{x,y} = \sqrt{\varepsilon_{x,y} \beta_{x,y}^* \left(1 + \left(\frac{z}{\beta_{x,y}^*} \right)^2 \right)}, \quad (6)$$

where $\varepsilon_{x,y}$ is the beam emittance and $\beta_{x,y}^*$ is the beta-tron function at the collision center. The effect of the

beam size was studied by substituting Eq. (6) in to Eq. (1) and calculating the overlap integral in numerical way. Bunch lengths $\sigma_{z1,2}$ are determined by the RF voltage of DSR and are 50 cm for RI beam and 2 cm for electron beam. Fig. 4 shows the normalized luminosity as a function of $\beta_{x,y}^*$. As seen, the luminosity increases with decreasing the beta function. Since $\beta^* = 10$ cm is the technical limit for ions, the setting of $\beta^* = 2$ cm for electrons gives the maximum luminosity.

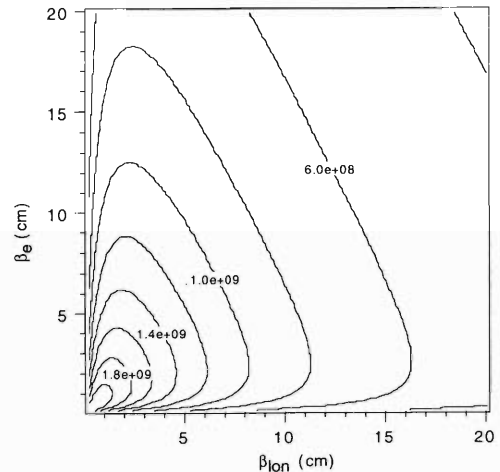


Fig. 4. Contour plot of the normalized luminosity as a function of the ion and electron betatron functions, β^* .

Luminosities at MUSES are now calculable by using Eq. (1). In Fig. 5, Luminosity of e-RI head-on collision is plotted for various nuclei in an N-Z plane. In the figure, plotted are only for the nuclei whose luminosity $L \geq 10^{27} \text{ cm}^2/\text{s}$, the numerical value corresponds to the minimum luminosity required to measure the charge distribution from the e-RI elastic scattering experiment. Those nuclei should have their life-times longer than about 1 min.

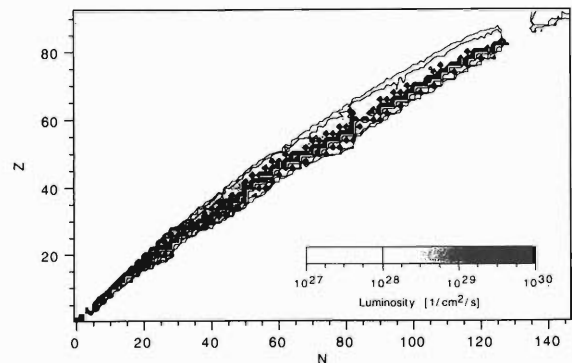


Fig. 5. Luminosity of e-RI collision for various nuclei.

References

- 1) J. A. Winger, B. M. Sherrill, and D. J. Morrissey: Nucl. Instrum. Methods Phys. Res. B **70**, 380 (1992).

One-Dimensional Compensation Scheme for Beam-Beam Effects

Y. Batygin and T. Katayama

From the study of the noise beam-beam phenomena,¹⁾ it follows that the linear beam-beam kick preserves the beam emittance even in the case of noise. Therefore, linearization of the kick is expected to be a way to improve particle stability. The trivial way assumes that the opposite beam is uniformly populated, or at least, its inner part is close to uniform. Another way suggests utilization of high order multipoles. Suppose, particles receive the Gaussian kick every turn:

$$\Delta p = -4\pi\xi x \frac{1 - \exp(-x^2/2\sigma^2)}{(x^2/2\sigma^2)}, \quad (1)$$

where $p = \beta (dx/dz)$, β is a β -function of a ring in the interaction point, ξ a linear part of beam-beam tune shift, and σ a standard deviation in size of a counteracted beam. If we apply the opposite kick:

$$\begin{aligned} \Delta p_{\text{opposite}} &= 4\pi\xi x \sum_{k=2}^{\infty} \frac{(-1)^{k-1}}{k!} \left(\frac{x^2}{2\sigma^2}\right)^{k-1} \\ &= 4\pi\xi x \left[-\frac{1}{2} \left(\frac{x^2}{2\sigma^2}\right) + \frac{1}{6} \left(\frac{x^2}{2\sigma^2}\right)^2 - \dots \right], \quad (2) \end{aligned}$$

then the total kick will be a linear function of coordinate (see Fig. 1). The opposite kick can be created by the high order multipole lenses located in the interaction point. After passing through the multipole of the order $n+1$ ($n = 3$ for octupole, $n = 5$ for duodecapole, etc.), the particle with rigidity $B\rho$ gets a kick:

$$\Delta p = \beta S_n x^n; \quad S_n = \left(\frac{B_o}{R_o^n}\right) \frac{d_n}{B\rho}, \quad (3)$$

where S_n is a multipole strength, d_n a multipole length, B_o a pole tip field, and R_o a pole radius. Octupole ($n = 3$) can be used for compensation of the first nonlinear term in beam-beam kick x^3 , then duodecapole ($n = 5$) can be used to compensate second nonlinear term in beam-beam kick x^5 , etc. Comparing the values of kicks obtained from beam-beam interaction and after crossing multipole lens, the values of the multipole strengths for compensation are

$$S_{2k-1} = \frac{4\pi\xi}{\beta} \frac{(-1)^{k-1}}{k! (2\sigma^2)^{k-1}}. \quad (4)$$

Let us note that in the presence of noise in beam-beam kick, the total kick is not a perfect linear function of coordinate, but also is a subject of noise. It is demonstrated in Fig. 1, where resulting kick for the noise in parameter σ is presented $\sigma^{(n)} = \sigma^{(o)} (1 \pm u_n)$. In Fig. 2 the results of beam-beam dynamics without and with nonlinear compensation are presented.

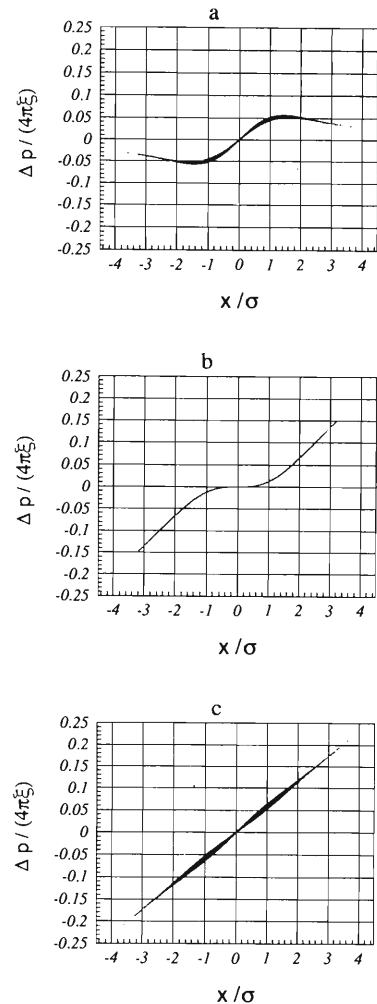


Fig. 1. (a) Beam-beam kick, (b) compensation kick, and (c) the resulting kick.

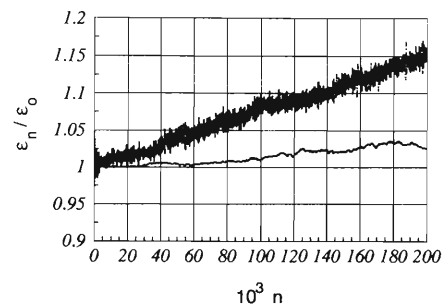


Fig. 2. Beam emittance growth in beam-beam interaction without compensation (upper trace) and with compensation (lower trace). Parameters of the interaction are as follow: $Q = 3.168$, $\xi = 0.005$, and noise in σ is 5%.

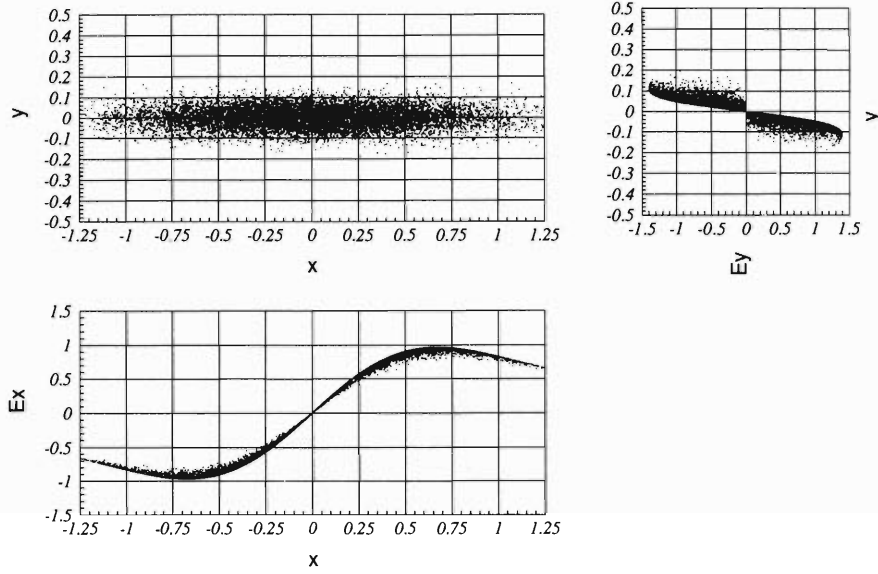


Fig. 3. Particle distribution and space charge forces (E_x and E_y) of a Gaussian beam when the semi-axis ratio $\sigma_x/\sigma_y = 10$.

Utilization of the suggested scheme can be complicated due to the realistic 2-dimensional particle distribution of the opposite beam, which is usually approximated by Gaussian function:

$$\rho(x, y) = \rho_0 \exp\left(-\frac{x^2}{2\sigma_x^2} - \frac{y^2}{2\sigma_y^2}\right). \quad (5)$$

Space charge potential of the beam with an elliptical cross section is given by the expression:²⁾

$$U(x, y) = U_0 \int_0^\infty \frac{\exp\left\{-\frac{x^2}{(2\sigma_x^2 + q)} - \frac{y^2}{(2\sigma_y^2 + q)}\right\}}{\sqrt{(2\sigma_x^2 + q)(2\sigma_y^2 + q)}} dq. \quad (6)$$

In the flat beam $\sigma_x \gg \sigma_y$, space charge forces in x-

direction are a weak function of y-position (see Fig. 3) and x - beam-beam kick is close to a single-valued function of x. The kick, obtained by the flat beam after passing through the multipole is also a single-valued function of coordinate. It allows to adjust the values of compensating multipoles according to Eq. (4). On the contrary, space charge forces in y - direction strongly depend on x-position, which results in a strong discrepancy of y-kicks. The value of compensating multipoles in y-direction cannot be adjusted for all the particles. Therefore, the suggested scheme requires further study to meet the realistic requirements.

References

- 1) Y. Batygin and T. Katayama: RIKEN Accel. Prog. Rep. **30**, 225 (1997).
- 2) B. Montague: CERN 68-38 (1968).

Hamiltonian Treatment of Nonlinear Beam-Beam Resonances

Y. Batygin and T. Katayama

Beam-beam instability is one of the main factors limiting achievable value of the collider luminosity. Beam-beam interaction excites nonlinear resonances, which are stable until different islands overlap each other¹⁾ or until the noise factor become dominant.²⁾ Stable particle motion in the phase space is governed by an invariant of motion. Hamiltonian for beam-beam interaction is usually treated as an unperturbed integrable system plus a small perturbation.³⁻⁵⁾ In present paper we derive the beam-beam Hamiltonian directly from mapping equations.

Let us consider linear matrix of particle motion in coordinates $(x, p = \beta dx/dz)$ with nonlinear beam-beam kick Δp_n between lattice arc with the betatron angle θ :

$$\begin{aligned} x_{n+1} &= x_n \cos \theta + p_n \sin \theta + \Delta p_n \sin \theta, \\ p_{n+1} &= -x_n \sin \theta + p_n \cos \theta + \Delta p_n \cos \theta. \end{aligned} \quad (1)$$

The beam-beam kick is usually approximated by Gaussian function:

$$\Delta p = -4\pi\xi x \frac{1 - \exp(-x^2/2\sigma^2)}{(x^2/2\sigma^2)}, \quad (2)$$

where ξ is the linear part of beam-beam tune shift and σ is a standard deviation in opposite beam size. Note that Jacobian of the transformation always equals unity:

$$\begin{aligned} J &= \begin{vmatrix} \frac{\partial x_{n+1}}{\partial x_n} & \frac{\partial x_{n+1}}{\partial p_n} \\ \frac{\partial p_{n+1}}{\partial x_n} & \frac{\partial p_{n+1}}{\partial p_n} \end{vmatrix} \\ &= \begin{vmatrix} \left(\cos \theta + \frac{\partial \Delta p_n}{\partial x_n} \sin \theta \right) (\sin \theta) \\ \left(-\sin \theta + \frac{\partial \Delta p_n}{\partial x_n} \cos \theta \right) (\cos \theta) \end{vmatrix} = 1. \end{aligned} \quad (3)$$

It indicates that this process obeys Liouville's theorem, i.e., phase space area occupied by the beam is conserved. We introduce action-angle variables:

$$\begin{aligned} x_n &= \sqrt{J_n} \cos \varphi_n, \\ p_n &= \sqrt{J_n} \sin \varphi_n. \end{aligned} \quad (4)$$

In mapping equations, the turn number n is equivalent to time t , therefore time-increment dt has to be substituted by turn-increment $dn = f_0 dt$, where f_0 is a revolution frequency. Hamiltonian equations of motions for new Hamiltonian $K = H/f_0$ are defined as follows:

$$\frac{dJ}{d(f_0 t)} = \frac{dJ}{dn} = J_{n+1} - J_n = -\frac{\partial K}{\partial \varphi}, \quad (5)$$

$$\frac{d\varphi}{d(f_0 t)} = \frac{d\varphi}{dn} = \varphi_{n+1} - \varphi_n = \frac{\partial K}{\partial J}. \quad (6)$$

Increment of action variable follows directly from the matrix equations:

$$J_{n+1} - J_n = 2p_n \Delta p_n + \Delta p_n^2 \approx 2p_n \Delta p_n. \quad (7)$$

Let us express the Gaussian beam-beam kick by power series of coordinate with coefficients δ_{2k-1} :

$$\Delta p = \sum_{k=1}^{\infty} \delta_{2k-1} J^{k-1/2} (\cos \varphi)^{2k-1}, \quad (8)$$

$$\delta_{2k-1} = 4\pi\xi \frac{(-1)^k}{k! (2\sigma^2)^{k-1}}. \quad (9)$$

The first Hamiltonian equation becomes as follows:

$$-\frac{\partial K}{\partial \varphi} = 2 \sin \varphi \sum_{k=1}^{\infty} \delta_{2k-1} J^k (\cos \varphi)^{2k-1}. \quad (10)$$

To obtain another Hamiltonian equation, let us utilize the second order difference equation,⁶⁾ which is equivalent to the mapping transformation of Eq. (1):

$$x_{n+1} - 2x_n \cos \theta + x_{n-1} = \Delta p_n \sin \theta. \quad (11)$$

If kick is absent or $\Delta p_n = 0$, solution to the Eq. (11) is trivial $x_n = a \cos n\theta$, i.e., angle advance per turn is equal to betatron tune $\varphi_{n+1} - \varphi_n = \theta$. In the presence of beam-beam kick the angle increment is corrected on a value of betatron tune shift as $\varphi_{n+1} - \varphi_n = \theta + \Delta\theta$. According to the method of harmonic balance, general solution to the nonlinear Eq. (11) can be expressed by Fourier series, $x_n = \sum_{k=0}^{\infty} a_k \cos kn\nu$.⁶⁾ To find the tune shift, one can use only the first term from series:

$$x_n = a \cos n\nu = \sqrt{J} \cos n(\theta + \Delta\theta). \quad (12)$$

Substituting the expected solution of Eq. (12) into the difference equation (11) and including expression for beam-beam kick (8) we have:

$$\begin{aligned} &2\sqrt{J} \cos n\nu (\cos \nu - \cos \theta) \\ &= \sin \theta \sum_{k=1}^{\infty} \delta_{2k-1} J^{k-1/2} (\cos n\nu)^{2k-1}. \end{aligned} \quad (13)$$

Using the power expression of trigonometric cosine function for $(\cos n\nu)^{2k-1}$ and taking into account Taylor expansion $\cos \nu = \cos \theta - \Delta\theta \sin \theta$, one can obtain the expected value of betatron tune shift:

$$\Delta\theta = - \left[\frac{\delta_1}{2} + \frac{3\delta_3}{8} J + \dots + \frac{\delta_{2k-1}}{2^{2k}} \frac{(2k)!}{(k!)^2} J^{k-1} \right]. \quad (14)$$

An important feature of the betatron tune shift is its amplitude dependence, which provides particle stability in phase space. Second Hamiltonian equation is

$$\frac{\partial K}{\partial J} = \theta + \Delta\theta + \chi(J, \varphi), \quad (15)$$

where the function $\chi(J, \varphi)$ describes higher order terms both in Fourier expansion of expected solution and in expansion of $(\cos n\nu)^{2k-1}$, which were neglected in usual calculations. Combining solutions of Eqs. (10) and (15), the Hamiltonian of beam-beam interaction is

$$\begin{aligned} K = & J\theta - \frac{\delta_1}{2}J - \frac{3\delta_3}{16}J^2 - \dots - \frac{\delta_{2k-1}}{2^{2k-1}} \frac{(2k-1)!}{(k!)^2} J^k + \dots \\ & + \delta_1 J (\cos \varphi)^2 + \frac{\delta_3 J^2}{2} (\cos \varphi)^4 + \dots \\ & + \frac{\delta_{2k-1} J^k}{k} (\cos \varphi)^{2k}. \end{aligned} \quad (16)$$

Particle motion, governed by the Hamiltonian (16), is stable due to amplitude dependence of the beam-beam tune shift. Typical phase space trajectories excited by beam-beam collisions are presented in Fig. 1. If betatron tune is close to a rational value $\theta/(2\pi) = m/n$ and if particle is inside the resonance, it's amplitude increases, which provides a detuning from resonance. Amplitude of particle decreases accordingly and particle again comes to resonance. This process repeats steadily and provides a stable particle motion.

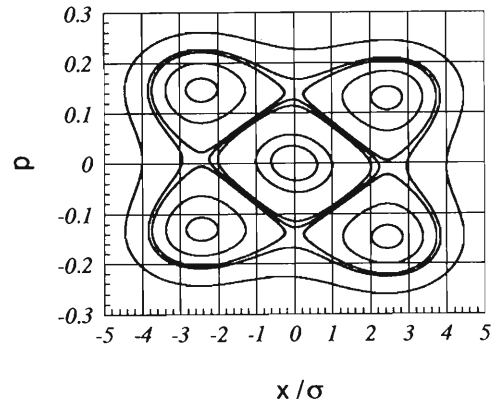


Fig. 1. The 4th order nonlinear resonance excited by the Gaussian kick, $\theta/2\pi = 3.26$.

References

- 1) B. Chirikov: Phys. Rep. **52**, 263 (1979).
- 2) Y. Batygin and T. Katayama: RIKEN Accel. Prog. Rep. **30**, 225 (1997).
- 3) L. R. Evans: CERN 84-15, p. 319 (1984).
- 4) A. G. Ruggiero and L. Smith: PEP Summer Study, 1973.
- 5) E. Keil: CERN 95-06, p. 539 (1995).
- 6) S. G. Peggs and R. M. Talman: Ann. Rev. Nucl. Sci. **36**, 287 (1986).

Beam-Beam Instability due to Noise in Opposing Beam Size

Y. Batygin and T. Katayama

One of the main problems in ion-ion circular colliders is a small value of achievable beam-beam tune shift $\xi = 0.005$. Physical reason for beam-beam limitation is usually attributed to the excitation of a set of nonlinear resonances due to a periodic nonlinear kick in linear system. If beam-beam interaction is too strong, resonant islands from different nonlinear resonances overlap each other, creating zones of unstable (stochastic) particle motion. Overlapping of nonlinear resonances is an universal mechanism of stochastic particle instability in nonlinear systems.¹⁾

Another mechanism of unstable particle motion is a diffusion, created by a noise.²⁻⁵⁾ This noise can exist, for example, due to mismatch of the beam with the channel. In this paper we study the noise which appears in an incoherent beam-beam interaction. As it is shown below, such a noise can induce beam-beam instability in much more simple conditions than the overlapping of nonlinear resonances. Due to the diffusion character, noisy beam-beam instability does not have a threshold character and can exist under any value of beam-beam tune shift.

Let us consider a 1-dimensional model, which combines linear matrix of particle motion in coordinates $(x, p = \beta dx/dz)$ with nonlinear beam-beam kick Δp_n between lattice arc with betatron angle $\theta = 2\pi Q$:

$$\begin{pmatrix} x_{n+1} \\ p_{n+1} \end{pmatrix} = \begin{pmatrix} \cos \theta & \sin \theta \\ -\sin \theta & \cos \theta \end{pmatrix} \begin{pmatrix} x_n \\ p_n + \Delta p_n \end{pmatrix}. \quad (1)$$

Beam-beam kick Δp is expressed by a Gaussian function of coordinate x , beam-beam tune shift ξ , and size of the opposite beam σ :

$$\Delta p = -4\pi\xi \times \frac{1 - \exp(-x^2/2\sigma^2)}{(x^2/2\sigma^2)}. \quad (2)$$

Nonlinear kick (2) induces a set of nonlinear resonances, which are stable, until islands do not overlap each other. In Fig. 1 an example of stable beam-beam interaction in the vicinity of the 6th order resonance is presented. In simulations, one beam was presented as a collection of 3000 particles. Simulations were done for the value of beam-beam tune shift $\xi = 0.005$ and betatron tune $Q = 3.168$, close to the 6th order resonance value 3.16666 (or $6Q = 19$). From the simulations it is clear that both the envelope and emittance are stable.

Another picture is observed if the parameter σ of beam-beam kick (2) is a subject of noise. In the calculations, presented in Fig. 2, parameters of the process were chosen to be the same as those in Fig. 1, but standard deviation σ was changed from turn to turn according to the expression:

$$\sigma^{(n)} = \sigma^{(0)} (1 \pm 0.025 u_n), \quad (3)$$

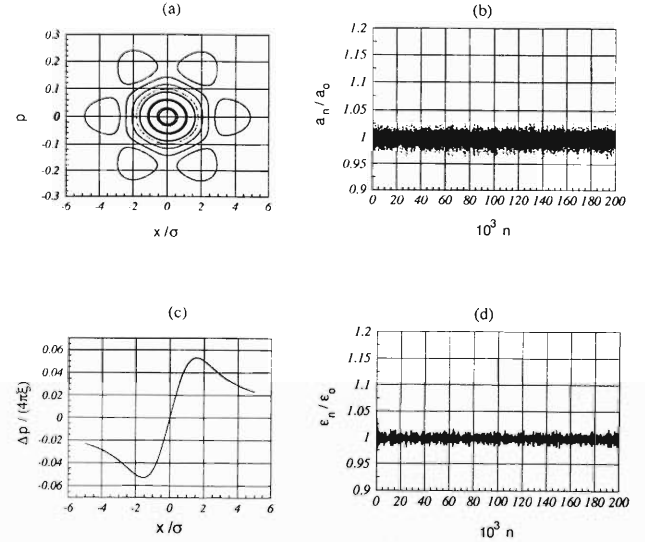


Fig. 1. Stable particle motion in the vicinity of the 6th order nonlinear resonance with the values of beam-beam tune shift $\xi = 0.005$ and betatron tune $Q = 3.168$: (a) phase space trajectories; (b) beam envelope; (c) beam-beam kick; (d) rms beam emittance.

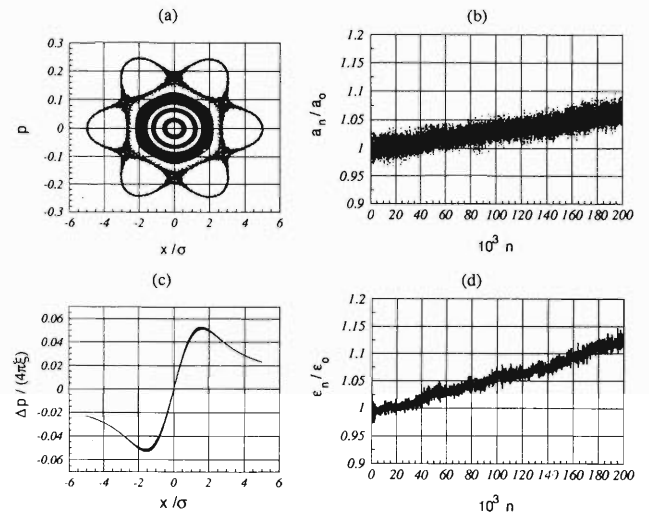


Fig. 2. Beam-beam instability under 5% noise in the parameter σ during particle interaction with $\xi = 0.005$ and $Q = 3.168$: (a) phase space trajectories; (b) beam envelope instability; (c) beam-beam kick; (d) beam emittance growth.

where u_n is a random noise function within the interval $(0,1)$. It corresponds to the noise in the size of the opposite beam, which can exist due to small beam mismatch with the channel. As shown in Fig. 2, this noise destroys the stability. In contrast with Fig. 1, phase

space trajectories of particles are not closed and both the beam envelope and beam emittance expand with time. Therefore, a weak noise in the opposite beam size creates instability.

Important feature of noise regime is that this kind of instability can exist apart from the excitation of nonlinear resonances. Noise beam-beam instability appears if two conditions are met:

- beam-beam kick is a nonlinear function of coordinate;
- parameter of beam-beam kick (beam standard deviation σ) is a subject of noise.

Let us provide analytical estimations of emittance growth under noise beam-beam interaction. Transfer matrix after n turns with arbitrary momentum kick at every turn, Δp_i , is given by the expression:⁶⁾

$$\begin{aligned} x_n &= a \cos(n\theta + \Psi) + \sum_{i=0}^{n-1} \Delta p_i \sin(n-i)\theta, \\ p_n &= -a \sin(n\theta + \Psi) + \sum_{i=0}^{n-1} \Delta p_i \cos(n-i)\theta, \end{aligned} \quad (4)$$

where Ψ is the initial phase of oscillations. Random beam-beam kick (Δp_i) can be expressed as a function of unperturbed trajectory. It gives an approximate treatment of the problem, valid for small values of perturbation. Suppose that perturbation is a linear function of coordinate:

$$\Delta p_i = \delta_i x_i. \quad (5)$$

We study evolution of the root-mean-square (rms) beam emittance $\varepsilon_n = 4\sqrt{\langle x_n^2 \rangle \langle p_n^2 \rangle - \langle x_n p_n \rangle^2}$, where brackets mean averaging on initial phases of particles. Calculation of beam emittance growth gives:

$$\begin{aligned} \frac{\varepsilon_n^2}{16} &= \left[\frac{a^2}{2} + \frac{a^2}{4} \sum_{i=0}^{n-1} \delta_i^2 \right]^2 \\ &- \left[\frac{a^2}{2} \sum_{i=0}^{n-1} \delta_i \sin(2n\theta - 2i\theta) \right. \\ &\quad \left. - \frac{a^2}{4} \sum_{i=0}^{n-1} \delta_i^2 \cos(2n\theta - 2i\theta) \right]^2 \\ &- \left[\frac{a^2}{2} \sum_{i=0}^{n-1} \delta_i \cos(2n\theta - 2i\theta) \right. \\ &\quad \left. + \frac{a^2}{4} \sum_{i=0}^{n-1} \delta_i^2 \sin(2n\theta - 2i\theta) \right]^2. \end{aligned} \quad (6)$$

Analysis of the expression (6) shows that terms proportional to δ , δ^2 , δ^3 are vanished. Rms beam emittance is conserved until high order of perturbation,

$$\frac{\varepsilon_n^2}{\varepsilon_0^2} = 1 + \zeta(\delta^4). \quad (7)$$

Above derivations are approximate due to suggestion that linear beam-beam kick is proportional to the unperturbed trajectory. Conservation of beam emittance is explained by the fact that in case of linear kick a beam of particles experiences sequence of linear transformation, each of them conserves beam emittance.

Let us consider now the case when kick is a nonlinear function of unperturbed trajectory:

$$\Delta p_i = 4 \delta_i x_i^3. \quad (8)$$

Calculation of rms beam emittance gives:

$$\begin{aligned} \frac{\varepsilon_n^2}{16} &= \left[\frac{a^2}{2} + \frac{5}{2} a^6 \sum_{i=0}^{n-1} \delta_i^2 \right]^2 \\ &- \left[\frac{3a^4}{2} \sum_{i=0}^{n-1} \delta_i \sin(2n\theta - 2i\theta) \right. \\ &\quad \left. - \frac{5a^6}{2} \sum_{i=0}^{n-1} \delta_i^2 \cos(2n\theta - 2i\theta) \right]^2 \\ &- \left[\frac{3a^4}{2} \sum_{i=0}^{n-1} \delta_i \cos(2n\theta - 2i\theta) \right. \\ &\quad \left. + \frac{5a^6}{2} \sum_{i=0}^{n-1} \delta_i^2 \sin(2n\theta - 2i\theta) \right]^2. \end{aligned} \quad (9)$$

In contrast with linear beam-beam kick the terms proportional to δ^2 in expression (9) do not vanish. Effective beam emittance growth is then as follows:

$$\frac{\varepsilon_n^2}{\varepsilon_0^2} = 1 + \delta^2 a^4 n + \zeta(\delta^4). \quad (10)$$

In the case of nonlinear kick, the beam emittance growth does not vanish in the first positive term δ^2 , which indicates that nonlinearity is an essential point for expansion of emittance growth under noise conditions.

Performed study shows importance of noise factor in beam-beam interaction, which can be one of the reason of small value of experimentally achievable beam-beam tune shift in existing colliders.

References

- 1) B. Chirikov: Phys. Rep. **52**, 263 (1979).
- 2) K. Cornelis: Proc. 3rd Workshop on LEP Performance, edited by J. Poole, CERN SL/93-19 (1993).
- 3) J. K. Koga and T. Tajima: Phys. Rev. Lett. **72**, 2025 (1994).
- 4) T. Sen and J. A. Ellison: Phys. Rev. Lett. **77**, 1051 (1996).
- 5) Y. Batygin and T. Katayama: Proc. EPAC96, p. 1173 (1996).
- 6) V. Lebedev et al.: Part. Accel. **44**, 147 (1994).

Beam Emittance Growth in Storage Ring due to the Ground Noise

Y. Batygin

Vibration of the ground is a serious concern for stability of beam dynamics in a storage ring. In Table 1 the typical amplitudes of cultural noise measured in different accelerator facilities are presented. Ground noise has its spectrum between 0.001–100 Hz with typical declined spectrum function with respect to the frequencies. The amplitude of ground noise is in the range 0.01–10 microns.

Table 1. Ground noise in accelerator facilities.

Accelerator	Amplitude	Noise frequency	Ref.
CERN	0.1 μm	>10 Hz	1)
HERA	0.1–2 μm	0.01–0.1 Hz	2)
SSC	0.015 μm	3 Hz	3)

Two aspects of the problem are essential to be investigated. The first is a motion of the equilibrium orbit caused by a few Hz noise. One of the results of this noise is that two colliding beams miss each other in the interaction point. This effect can be controlled by a feedback⁴⁾ to provide beam centering. If the beams are off centered, the modulation signal of feedback system is created to center the beam.

The second case is a few hundred Hz noise, which is serious for large colliders (SSC, HERA, LHC). Due to the average velocity of ground signal, $V_{\text{ground}} = 3\text{--}6$ km/sec, the noise kicks become uncorrelated for noise frequency $f_{\text{noise}} = 100$ Hz at the distance

$$\lambda = \frac{V_{\text{ground}}}{f_{\text{noise}}} = 30\text{--}60 \text{ m.} \quad (1)$$

This is a typical distance between two neighboring quadrupole magnets in a large ring. This kind of uncorrelation quickly transforms to the beam emittance growth.⁵⁾ According to estimations in Ref. 5, the most dangerous is a noise with frequency $f_{\text{noise}} = f_o \Delta\nu$, where f_o is a revolution frequency and $\Delta\nu$ is a spread of the betatron frequencies in a ring. For small rings with diameter around 100 m, noise in this spectrum looks not dangerous. Therefore, only the first case with a few Hz noise can be a subject of precaution.

Let us estimate the particle stability in a ring due to the ground noise. Matrix of particle motion in coordinates $(x, p \equiv \beta dx/dz)$ after N turns, assuming that particle trajectory receives random kick Δx_n once per revolution, is given by:

$$x_{N+1} = A \cos(N\theta + \Psi_o) + \sum_{i=0}^{N-1} \Delta x_i \cos(N-i)\theta,$$

$$p_{N+1} = -A \sin(N\theta + \Psi_o) - \sum_{i=0}^{N-1} \Delta x_i \sin(N-i)\theta, \quad (2)$$

where amplitude A and phase Ψ_o are defined by the initial conditions only. Averaged square of the single particle trajectory is:

$$\langle x_{N+1}^2 \rangle = \frac{1}{2\pi} \int_{-\pi}^{\pi} x_{N+1}^2 d\Psi_o. \quad (3)$$

In calculations we used an assumption that kicks are not correlated. Therefore

$$\begin{aligned} & \Delta x_k \cos(N-k)\theta \sum_{m=0}^{N-1} \Delta x_m \cos(N-m)\theta \\ &= \begin{cases} 0, & k \neq m \\ (\Delta x)^2 \cos^2(N-k)\theta, & k = m \end{cases}. \end{aligned} \quad (4)$$

After N turns the rms value of beam size is

$$\langle x_N^2 \rangle = \frac{A^2}{2} \left[1 + \left(\frac{\Delta x}{A} \right)^2 N \right]. \quad (5)$$

Using the relationship between beam size and beam emittance

$$\varepsilon = \frac{x_{\text{max}}^2}{\beta}, \quad (6)$$

the phase space area available for a beam under the noise fluctuation is

$$\frac{\varepsilon}{\varepsilon_o} = 1 + \left(\frac{\Delta x}{A} \right)^2 N. \quad (7)$$

Equation (7) is a general expression for emittance growth due to noise in linear oscillator system. In Eq. (7), Δx is the amplitude of an arbitrary noise. Ground noise has a frequency much smaller than revolution frequency. Therefore, instead of N in Eq. (7), we have to use $N (f_{\text{noise}}/f_o)$, which indicates that one ground kick appears every (f_o/f_{noise}) turns:

$$\frac{\varepsilon}{\varepsilon_o} = 1 + \left(\frac{\Delta x}{A} \right)^2 N \frac{f_{\text{noise}}}{f_o}. \quad (8)$$

For estimation, let us take the following parameters, typical for MUSES ring:

Revolution frequency, f_o	10 ⁶ Hz
Noise frequency, f_{noise}	10 Hz
Number of turns for 24 hours of ring operation, N	8.6 · 10 ¹⁰

In order to prevent the doubling of beam emittance, the distortion of beam orbit should be smaller than:

$$\frac{\Delta x}{A} < \sqrt{\frac{1}{N} \frac{f_o}{f_{\text{noise}}}} = \sqrt{\frac{1}{8.6 \cdot 10^{10}} \frac{10^6}{10}} = 10^{-3}. \quad (9)$$

In the colliding point the beam size is $A = 0.6$ mm. Therefore, the amplitude of ground noise should not be larger than

$$\Delta x < 10^{-3} A = 0.6 \text{ micron}. \quad (10)$$

Performed estimations shows that long term beam sta-

bility requirements impose strong restrictions on amplitudes of the ground noise (less than 1 micron).

References

- 1) Juravlev et al.: Proc. EPAC94, p. 2573 (1994).
- 2) V. Shiltsev et al.: DESY HERA 95-06 (1995).
- 3) K. Y. Ng et al.: Proc. PAC93, p. 1645 (1993).
- 4) H. Jostlein: Fermilab TM-1253 (1984).
- 5) V. Lebedev et al.: Part. Accel. **44**, 147 (1994).

Simulation of Beam Bunching by Electron Cooling for DSR in MUSES

M. Takanaka and T. Katayama

Collision experiments are planned with ion-ion or ion-electron beams in Double Storage Rings (DSR). Coasting or nearly-coasting ion beams are supplied from the cooler storage ring (ACR) or the booster synchrotron (BSR). The luminosity of the beams can become high by bunching them. The longitudinal space charge force is dominant over the longitudinal forces induced through the coupling impedances between beams and the vacuum chamber in the energy region 100 MeV/u to 1.5 GeV/u of the ring. As the currently-designed ion storage ring runs below the transition energy, the space charge force makes the bunch long. On the other hand, electron cooling force can make the bunch short under an RF-voltage application. The previous simulation of the beam bunching showed effectiveness of the cooling in the bunching, but whether the bunching process is stable or not was left to be answered.¹⁾ The question will be answered here, and the longitudinal phase space distribution near the equilibrium state will be shown together with the transverse one.

The tools of the bunching are RF voltage application and electron cooling. The former is just for rotating ions in the longitudinal phase space. The latter is for pushing ions towards the synchronous energy level where the velocity of ions is equal to that of the electron beam. As a result, ions gradually get together at the center of the RF separatrix. It would be possible to realize a very small bunching factor if there were no force but the two forces. However, the main longitudinal beam-self-induced force or the space charge force pushes ions outward from the bunch center. Roughly speaking, the bunch length settles at the equilibrium among the three forces. The bunching is possible without an increase of the momentum spread by applying both RF voltage and electron cooling, although bunching just with an RF voltage application always increases the momentum spread.

The bunching procedure is as follows. If the beam is not in the equilibrium state, or the cooling force is stronger than the space charge force, the momentum spread decreases. On the other hand, the increase of the RF voltage makes the RF bucket height large, which is followed by the increase of the momentum spread and by the decrease of the bunch length. One tunes the RF voltage as a control parameter under the constant electron current in the electron cooler, so that the momentum spread of the ion beam is kept around a given spread. The space charge force begins to compete with the cooling force as the bunch length decreases. One can easily get the equilibrium

by increasing the voltage, while paying attention not to load over-voltage.

The simulation has been carried out with 10^4 particles, using Runge-Kutta method. The following forces acting on ions have been taken into account: 1) the RF force, 2) the longitudinal electron cooling force and the transverse one,²⁾ 3) the transverse linear force coming from the ring lattice, and 4) the longitudinal space charge force. The space charge force has been evaluated each one-twentieth revolution by Fourier series expanding a bunch of beam line density up to 100th series and by using the gradient.

Hereby presented are the results for a 150 MeV/u U_{238}^{92+} beam with the $6 \times$ rms relative-momentum spread 10^{-3} and 4.5×10^6 ions per bunch or the full-bunched beam current 3.3 mA. One does not prefer the spread smaller than 10^{-3} , because the smaller the spread is the lower the beam-current threshold of the microwave instability becomes. The bunching process is seen to be stable, as seen in Fig. 1. The fluctuation of the relative-momentum spread is within $\pm 2 \times 10^{-5}$. The longitudinal equilibrium state seems to be realized at the end of the simulation, although the transverse emittance still decreases. The distributions in the longitudinal phase space and the horizontal one at the end are shown in Figs. 2 and 3, respectively. The longitudinal bunch structure is seen not to be Gaussian, nor to be centrally parabolic.³⁾ The momentum distribution is characterized by both a non-cooled broad background and a well-cooled high peak. The transverse distribution is like a starfish, whose shape is dependent on the beta-

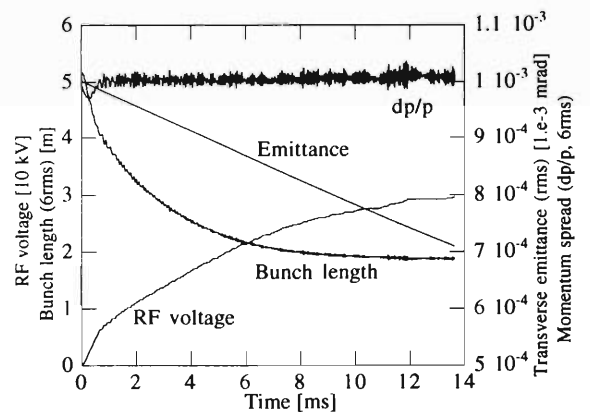


Fig. 1. Beam bunching of a 150 MeV/u U_{238}^{92+} beam of 4.5×10^6 ions per bunch. During the bunching, RF voltage is increased so that the momentum spread is kept constant.

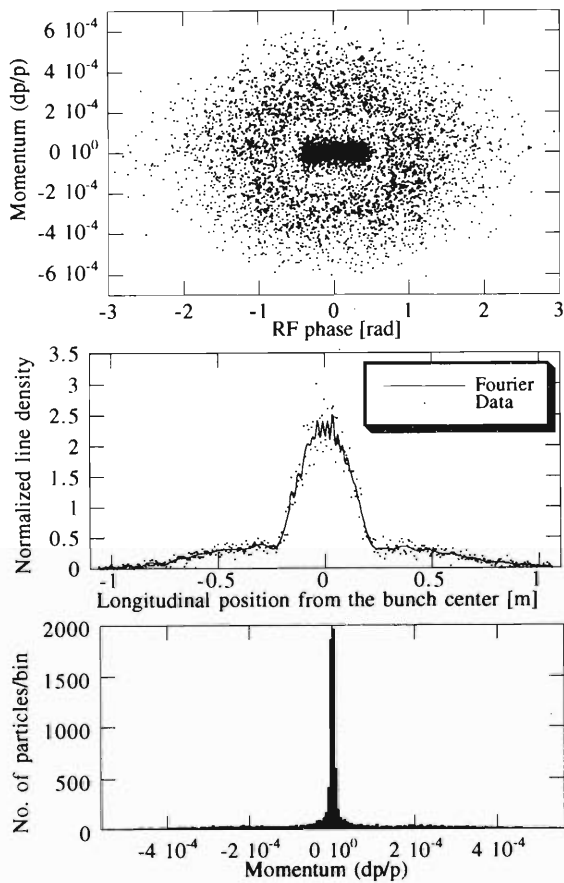


Fig. 2. Longitudinal phase space distribution, bunch structure, and momentum profile at the end of the simulation.

tron tune. The horizontal tune is just 7.4. The dense distribution at the center and the starfish are expected

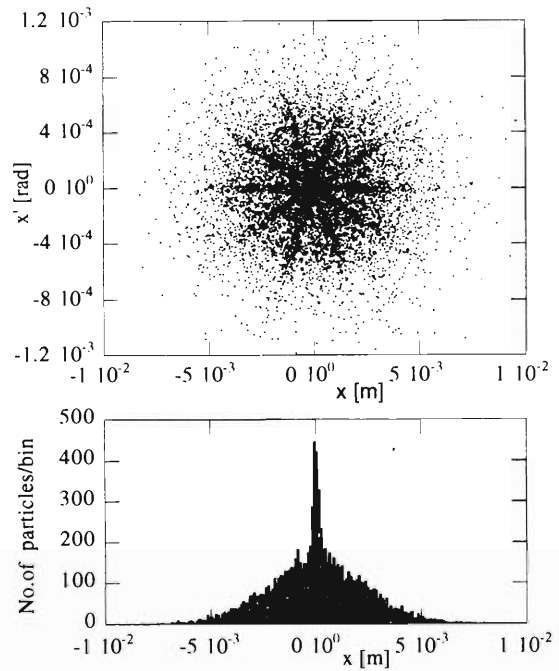


Fig. 3. Horizontal phase space distribution and position profile at the cooling section and at the end of the simulation.

to appear less clearly when the transverse space charge effects are taken into account.

References

- 1) M. Takanaka and T. Katayama: Proc. of EPAC'96, p. 1991 (1996).
- 2) I. N. Meshkov: Phys. Part. Nucl. **25**, 631 (1994).
- 3) S. S. Nagaitsev et al.: CERN 94-03, p. 405 (1994).

An RF System for the Electron Beam at DSR

M. Wakasugi and T. Katayama

An RF system for the electron beam at the DSR, which is a part of the MUSES project in the RI-Beam Factory (RIBF) program,¹⁾ is designed. It consists of four RF cavities with higher-order mode (HOM) dumper, a klystron, an RF transport system, a control system, and a cooling system. This RF system is needed to compensate the energy loss of the electron beam due to synchrotron radiation, and essential in order to store the beam for a long time inside the DSR.

The energy of the electron beam in DSR is $E_e = 0.3\text{--}2.5$ GeV. The energy loss of the electron beam is $U = 9\text{--}372$ keV/turn due to the bending magnet. The energy loss due to the undulator is about 25 keV/turn at $E_e = 2.5$ GeV.²⁾ The total energy loss is therefore $U = 400$ keV/turn approximately at the maximum beam energy of 2.5 GeV.

To ensure a long life for the stored electron beam, a large RF bucket should be prepared. Figure 1 shows the calculated Toushek lifetime versus the peak acceleration voltage V in the RF cavity. If the beam loading into the DSR is scheduled twice a day, the peak acceleration voltage should be at least 2-MV. This is also understandable in Fig. 2, which shows the relation between the energy acceptance of the RF bucket (dE/E) and the over voltage factor (V/U). The acceptance is saturated at around $V/U = 5$. This means that the RF voltage of 2.0 MV is enough from the energy acceptance point of view.

The RF cavity with the fundamental frequency of about 500 MHz is well established as an RF cavity for electron beam, and is chosen for our system. It is partly because the circumference of the DSR is 263.952 m³⁾ and the harmonics is 440, then the fundamental resonance frequency should become 499.745 MHz. Figure 3 shows a single cell cavity designed here at

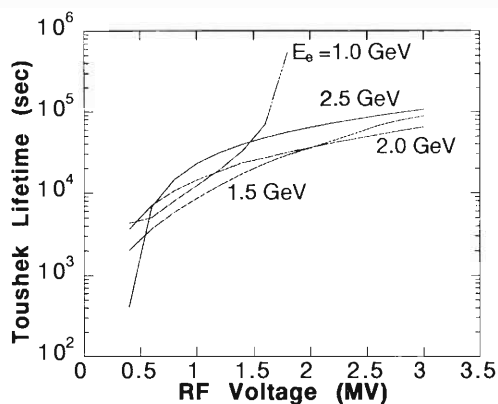


Fig. 1. Toushek lifetime of the electron beam in the DSR.

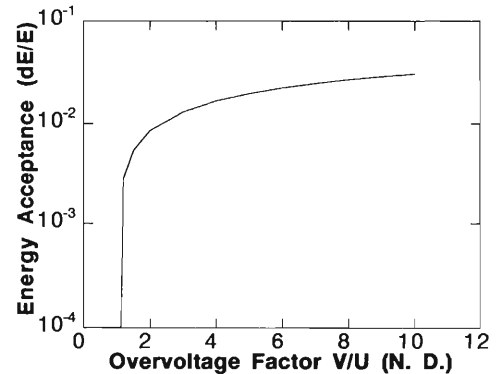


Fig. 2. Relation between the energy acceptance and the overvoltage factor.

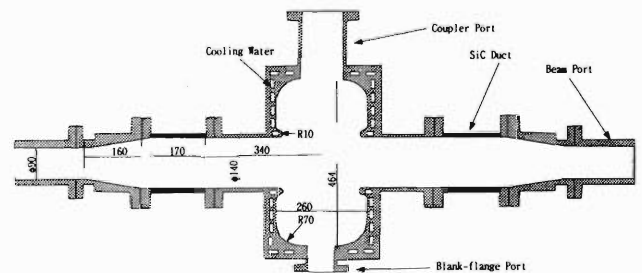


Fig. 3. Designed single cell cavity.

RIKEN. The main parameters relating to the RF cavity are listed in Table 1. The cavity has a coupler port, two tuner ports, a monitor port, beam ports, and cooling water lines. The size of the beam port is relatively large ($\phi 140$ mm), so that the HOM excited in the cavity can immediately escape through the beam ports. At the both sides of the cavity, a couple of the ceramic tubes made of SiC will be inserted to absorb the HOM. It has been confirmed that this tube can dump the HOM by $-20 \sim -30$ dB.

Four of the single cell cavities are inserted in the short straight sections at one ring of the double ring of the DSR.³⁾ The maximum acceleration voltage is 0.5 MV/cavity. In this case, the wall loss power is expected to be 35 kW/cavity, and one cavity has to feed the power of approximately 50 kW to the electron beam because the averaged beam current is 0.5 A at $E_e = 2.5$ GeV. The total input power is required to be about 340 kW.

The RF power is provided by two klystrons; each klystron has the output power of 180 kW. Since the power gain is expected to be about 44 dB, the input RF power to excite the klystron should be about 7–8

Table 1. Parameters relating to the RF system for the 2.5 GeV electron beam in the DSR.

Circumference	263.952 m
Revolution frequency	1.136 MHz
Harmonic number	440
Beam energy	0.3–2.5 GeV
Beam current	0.5 A
Momentum compaction factor	0.001
Natural energy spread	6.8×10^{-4}
Bunch length	0.5 cm
Radiation loss in bending magnets	372 keV
Radiation loss in insertion device	25 keV
Radio frequency	499.745 MHz
Synchrotron frequency	11.1 kHz
Number of cavity	4
Q value of the cavity	44000
Shunt impedance per cavity	7.68 M Ω
Peak voltage	2.0 MV
Over voltage factor	5.038
Wall loss per cavity	35 kW
Number of klystron	2
Klystron power	180 kW
Total klystron power	338.5 kW

W. Assuming the efficiency of the klystron of 55%, the electric power source of about 400 kW will be needed for the RF system of each klystron.

A block diagram of the RF system is shown in Fig. 4. The RF signal is divided into the two klystrons through the phase and power control systems. The RF power from each klystron is transported by the waveguides into two cavities through a 180-kW circulator, a magic-T, and phase controllers. The layout of the RF transport system is shown in Fig. 5. The klystron gallery will be located close to the short straight section of the DSR.

The water cooling system is necessary to cool the RF system; the water flow required here is estimated as follows: 140 l/min for a cavity, 410 l/min for a klystron, 170 l/min for a circulator, and 330 l/min for the other electronics. In total water flow of 2380 l/min is required.

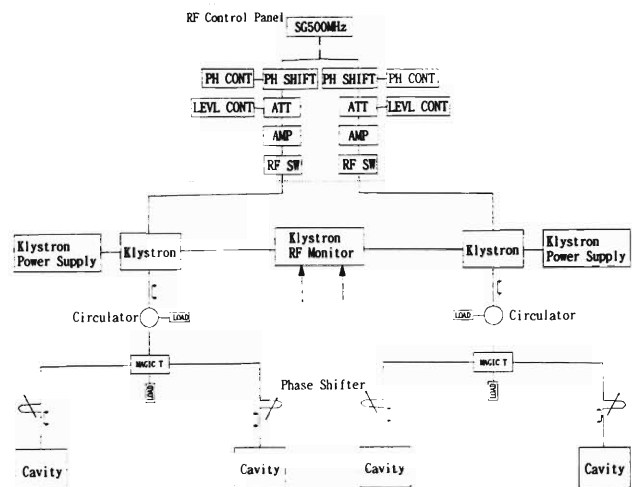


Fig. 4. Block diagram of the RF system.

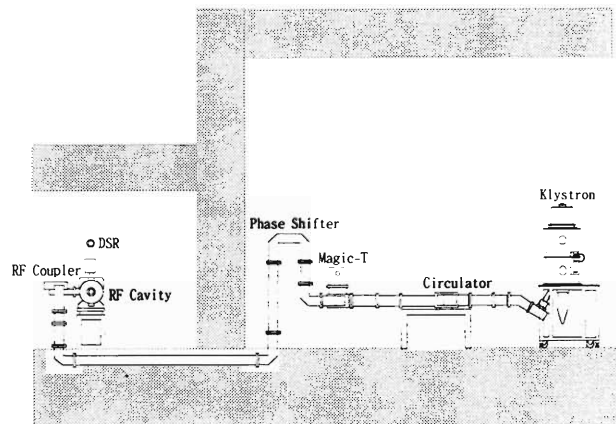


Fig. 5. Layout of the RF transport system.

References

- 1) Y. Yano et al.: RIKEN Accel. Prog. Rep. **29**, 226 (1996).
- 2) M. Wakasugi et al.: RIKEN Accel. Prog. Rep. **29**, 257 (1996).
- 3) N. Inabe et al.: RIKEN Accel. Prog. Rep. **30**, 217 (1997).

An Undulator for Elliptically Polarized X-ray Beam Line at DSR

M. Wakasugi, N. Inabe, and T. Katayama

An X-ray beam line is planned to be constructed at the merging section of the DSR. The beam line consists of an undulator and an X-ray transport line including an X-ray spectrometer. The undulator is a source of high brilliance X ray and an X-ray spectrometer is employed to improve the X-ray energy resolution.

A linear undulator has been conceptually designed in the previous last report.¹⁾ Another type of undulator, which is the elliptical undulator, is considered to achieve a higher photon flux and to obtain completely polarized photons. In this progress report, a comparison between the elliptical undulator and the linear one is reported. Conceptual design of the X-ray spectrometer and the performance calculation are also presented.

The value of the beta function has been changed from 5 m to 2 m at the undulator section in the DSR,²⁾ because the size of the X ray at the source should be as small as possible. Then, the quality of the X ray from the undulator has also changed. The parameters of the linear undulator are the same with the previous one.¹⁾ The elliptical undulator was considered, because the photon flux of it is expected to be larger than that of the linear undulator. The controllability of the polarization is also an advantage of the elliptical undulator. The higher-order harmonic radiation from the elliptical undulator can be expected much weaker than that from the linear one. The parameters of the elliptical undulator is listed in Table 1.

Table 1. Parameters of the elliptical undulator.

Length	6 m
Number of periods	200
K_x/K_y	0.3–2.0
Gap width	1.1–2.9 cm
Magnetic field	1.3 T at pole tip

Figure 1 shows the comparison of the calculated photon flux density (photons/sec mrad² 0.1%b.w.) between the two types of undulators, where the electron beam energy 1.0 GeV, the electron beam emittance $\varepsilon_x/\varepsilon_y = 1.37/4.08$ nrad and the current 500 mA were assumed. In this calculation, the parameters K_x and K_y , which are the bending factors in horizontal and vertical directions, respectively, are both unity, and the K value for the linear undulator is also unity. As seen in the figure, the photon flux from the elliptical undulator is about twice larger than that from the linear one. The ratio of the strength of the third-order harmonic radiation to that of the first-order harmonic radiation was calculated as a function of the electron

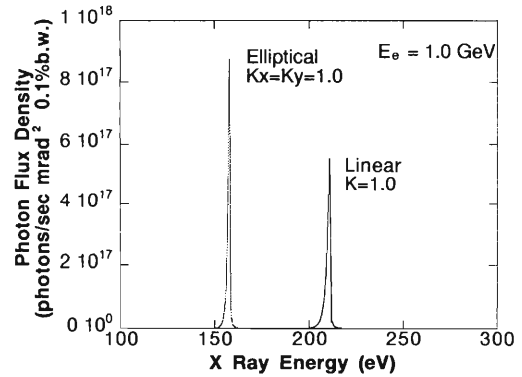


Fig. 1. X-ray flux from the elliptical undulator ($K_x = K_y = 1.0$) and the linear undulator ($K = 1.0$) at the electron beam energy of $E_e = 1.0$ GeV.

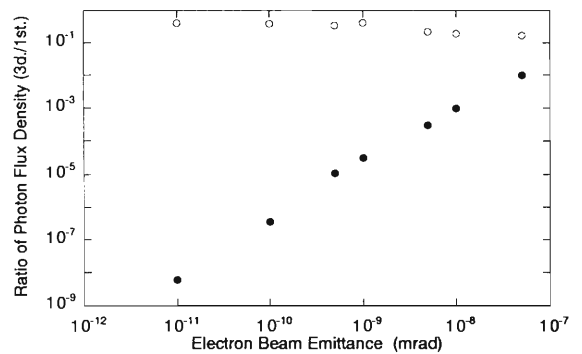


Fig. 2. Relative intensity of the third harmonic radiation from the elliptical (solid circles) and the linear (open circles) undulators.

beam emittance (Fig. 2). The ratio for the linear undulator is independent of the electron beam emittance and is nearly constant. It, however, strongly depends on the emittance for the case of the elliptical undulator. The ratio for the elliptical undulator is three-order smaller than that for the linear one at $E_e = 1.0$ GeV. This is important to avoid the radiation damage of the X-ray beam line due to higher energy X ray.

The polarization is required to be fully controllable. Figure 3 shows the relation between the X-ray energy and the polarization obtainable with the elliptical undulator. The energy and the polarization can be changed independently by tuning the K_x and K_y values. Shaded area shows the X ray produced with K_x and K_y values of 0.3–2.0 at the electron beam energy of 1.0 GeV. The maximum K value was determined from the minimum gap width of 1.1 cm. The shaded area can be moved by changing the electron beam energy from 0.3 to 2.5 GeV, which is the designed value for

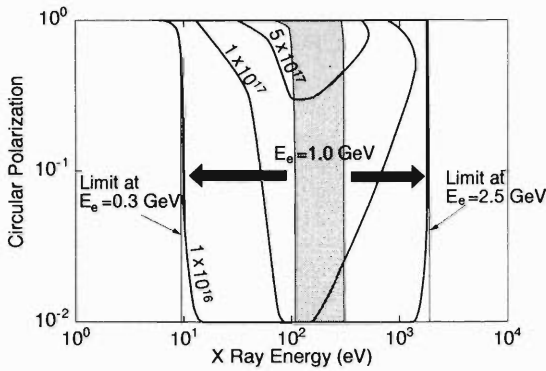


Fig. 3. Relation between the energy and the polarization of the X-ray from the elliptical undulator. The photon flux densities are shown by contour lines.

the DSR. Therefore, the elliptical undulator designed here can provide the X ray having any polarization in the energy range of 10–1800 eV. Higher photon flux density is obtainable with the circular polarization of close to unity.

The X ray extracted from the undulator is injected into the X-ray beam line that consists of an X-ray spectrometer and an X-ray mirror system. Figure 4 shows the layout of the X-ray beam line, which is inserted in between the vertically bending magnets near the merging section of the DSR. A pre-mirror M0 is used to make a horizontal focusing for injection into the X-ray spectrometer. The X-ray spectrometer has a movable mirror MM, a spherical grating G, and an entrance and exit slits. After the spectrometer, two mirrors M1 and M2 are used to re-inject the X-ray beam into the

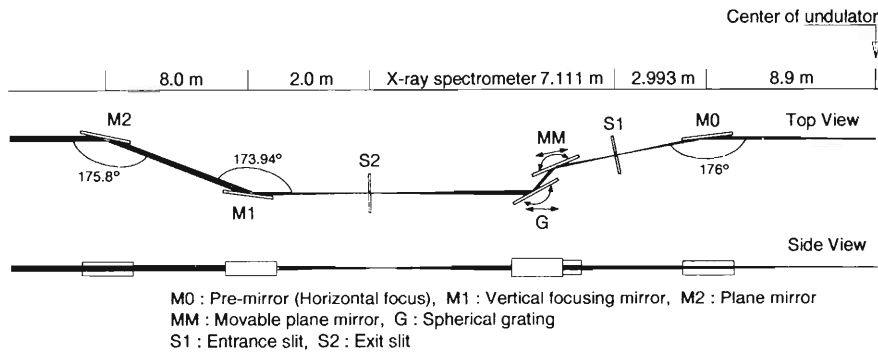


Fig. 4. Layout of the X-ray beam line inserted in between the vertically bending magnets at the merging section of the DSR.

other ring of the DSR, in which the RI beam is stored. The total length from the M0 to the M2 is about 21 m including the X-ray spectrometer of about 7.1-m length.

In principal, the X-ray spectrometer is designed to be of the Rowland circle type. Since the mirror MM and the grating G are movable, the entrance and exit beam axes are fixed even when the wavelength is changed. The positions of S1', G, and S2 are kept on the Rowland circle as shown in Fig. 5. Since the incident angle of the X ray on the grating has to be changed by changing the wavelength, the center of the Rowland circle is shifted. In our calculation, the energy resolution of the X-ray spectrometer is about $\Delta E_x/E_x = 7600$ at the wavelength of 40 nm, where the grating has 800 grooves/mm and the radius of curvature is 57.3 m. The requirement on the energy resolution is $\Delta E_x/E_x = 10000$. We are now optimizing the spectrometer and trying to make various ray-trace

calculations.

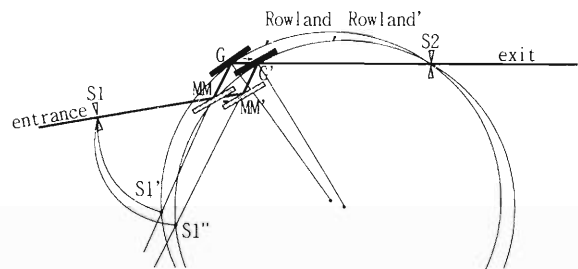


Fig. 5. Conceptual design of the X-ray spectrometer.

References

- 1) M. Wakasugi et al.: RIKEN Accel. Prog. Rep. **29**, 257 (1996).
- 2) N. Inabe et al.: RIKEN Accel. Prog. Rep. **30**, 217 (1997).

Calculations of Radiation Shield for RIKEN RI Beam Factory

N. Nakanishi, Y. Uwamino, S. Yamaji, H. Okuno, S. Fujita, and S. Nakajima

In the new project of RIKEN RI beam factory, all kinds of ions from protons to U's, and electrons are to be accelerated. Two successive superconducting ring cyclotrons (SRC) are designed to boost the energy of ion beams from the existing ring cyclotron up to 400 MeV/nucleon for light-heavy ions like Ar ions and 150 MeV/nucleon for very-heavy ions like U ions. Secondary beams produced by these primary heavy ions from the SRC are cooled and accelerated up to 1.45 GeV/nucleon by an accumulator-cooler ring (ACR) and by a booster synchrotron ring (BSR), respectively. On the other hand, electrons are accelerated by a 300 MeV injector linac followed by a 2.5 GeV BSR.

We have calculated the dose rate in the shielding material for radiations caused by 400 MeV/nucleon and 1.5 GeV/nucleon heavy ion beams, and 300 MeV and 2.5 GeV electron beams.

For radiations induced by high-energy heavy ions, the neutron transport code ANISN¹⁾ and nuclear data DLC-87/HILO²⁾ were adopted. Neutron spectra were obtained for the reactions of carbon beams incident on thick carbon and copper targets by calculations based on the quantum molecular dynamics.³⁾ These elements are typical materials used in accelerators and beam-focusing systems. Since the C + C reaction produces more high-energy neutrons than the C + Cu reaction does, we employed neutron spectra of the former reaction for both energies. Actually the shielding of the radiations produced by 400 MeV/nucleon ion-beams is more serious in spite of the lower energy relative to that of the 1.45 GeV/nucleon ion beams in the beam intensity point of view. The intensity of 400 MeV/nucleon ion beams is expected to be 2-orders higher than that of 1.45 GeV/nucleon ion beams. We have to use two-layer shields consisting of iron and concrete in order to reduce the total thickness of shielding materials. The thickness dependence of the product of dose rates and the distance between a radiation source and an observing point are shown in Fig. 1(a) for a radiation source by a 400 MeV/nucleon Ar + C reaction, where an additional iron wall of 2 m thickness is placed between a radiation source and the concrete shield. Here, the neutron spectra by a Ar + C reaction were scaled from those of a C + C reaction by multiplying the mass-ratio of Ar to C nuclei, 40/12.

We used empirical formula for the shielding of radiations by electron beams. It is known that gamma rays, neutrons, muons, and the gas bremsstrahlung contribute to the total dose rate. The gas bremsstrahlung is caused by the interaction of electron beams with residual gases in beam ducts, and raises intensity of

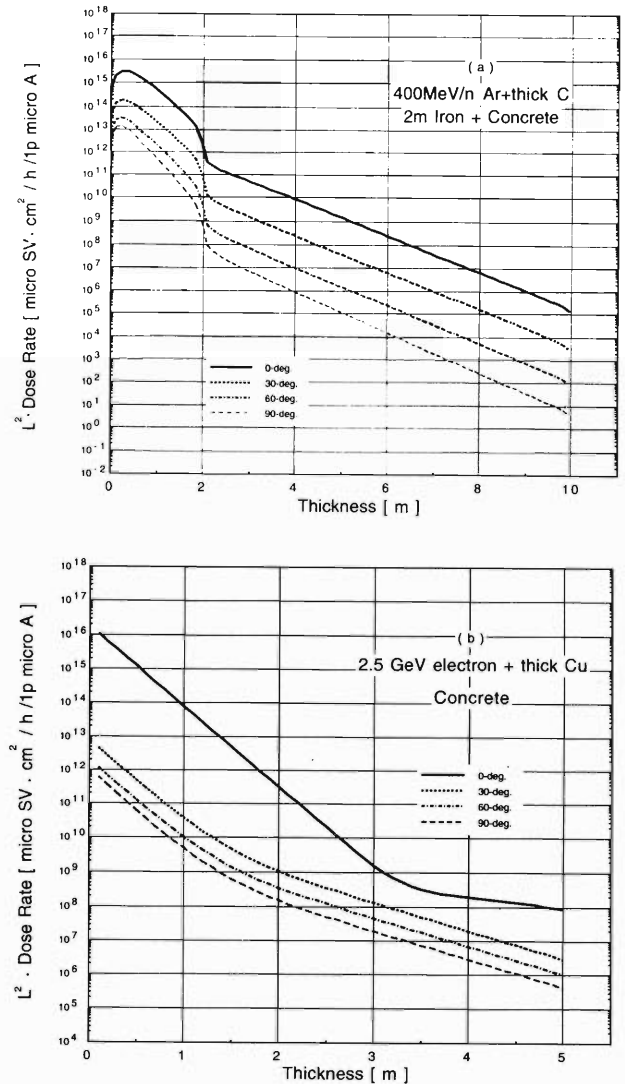


Fig. 1. Attenuation of the product of dose rate and distance L as a function of the thickness of specified shielding materials for radiations induced by (a) 400 MeV/nucleon heavy ion and (b) 2.5 GeV electron beams. The L denotes the distance between a radiation source and an observing point in units of cm.

electron beams effectively. For dose rates due to neutrons and gamma rays, the Swanson expressions⁴⁾ were used in the 0 deg. direction, and the Jenkins ones⁵⁾ in the directions between 30 and 130 degrees. The Swanson⁴⁾ and Rindi⁶⁾ expressions were used for the contributions by muons and the gas bremsstrahlung, respectively. Typical examples shown in Fig. 1(b) are the attenuation behavior in the concrete shield of the

dose rate by 2.5 GeV electrons on a Cu target. For the direction of 0 deg., the dose rates by gamma rays and muons are predominant. Since gamma rays attenuate steeply with the thickness of the concrete shield, the dose rate by muons is conspicuous in the region of the concrete of more than 3 m thickness. For the directions of more than 30 degrees, the contribution by gamma rays and neutrons is predominant in dose rates i.e., the dose rate by gamma rays is remarkable in the region of less than 1.5 m, and that by the neutrons in the outer region.

Further calculations will have to be made precisely against the actual structure of accelerators and/or beam lines from now on.

References

- 1) K. Koyama et al.: JAERI-M 6954 (1977).
- 2) DLC-87, RSIC, ORNL (1981).
- 3) J. Aichelin et al.: Phys. Rev. C **37**, 2451 (1988).
- 4) W. P. Swanson: Technical Report Series No. 188 (1979).
- 5) T. M. Jenkins: Nucl. Instrum. Methods **159**, 265 (1979).
- 6) A. Rindi: Health Phys. **42**, 187 (1982).

VI. RADIATION MONITORING

Leakage Radiation Measurements in the Ring Cyclotron Facility

S. Fujita, N. Nakanishi, H. Ohishi,* H. Uehara,* Y. Uwamino, and T. T. Inamura

Dose rates due to leakage radiation have been measured at various points around the beam distribution corridor. The results of similar measurements have been reported annually since 1995.^{1,2)}

In this year (1996), the measurements of leakage radiation were carried out with 113-MeV proton beams. The beam intensities were between 100 and 200 pμA. The beams were stopped at an iron target in the beam distribution corridor. Leakage radiation of neutrons from the corridor was measured with four neutron dose rate meters, TPS-451S's (Aloka). The beam current at

Table 1. Dose rates of neutron leakage radiation from a target placed in the beam distribution corridor. [For positions, see Fig. 1-(a),(b),(c)]. The unit of energy is MeV/nucleon. The unit of dose rate is (μSv/h)/(pμA).

Measured date	Jan 28, '96	Jun 27, '96
Accelerated particle	Proton	Proton
Energy	113	113
Position	Dose rate	Dose rate
1F a	3.70E-02	2.17E-02
1F c	2.66E-02	1.53E-02
1F b	2.26E-02	2.00E-02
E5 a	1.60E+01	1.04E+01
E5 c	1.14E+01	5.37E+00
E5 b	4.24E+01	1.61E+01
E4 a	4.26E+00	3.51E+00
E4 c	2.80E+00	1.77E+00
E4 b	8.57E-01	5.06E-01
B2 a	1.06E+01	8.38E+00
B2 c	7.57E+00	5.83E+00
B2 b	4.31E+00	3.74E+00
Out R	5.41E+00	5.33E+00
Out C	6.48E+00	6.18E+00
Out L	5.18E+00	4.89E+00
W R	2.20E-01	2.03E-01
W C	2.89E-01	2.54E-01
W L	1.99E-01	2.09E-01
G R	1.40E-01	1.51E-01
G C	1.59E-01	1.44E-01
G L	1.21E-01	1.24E-01

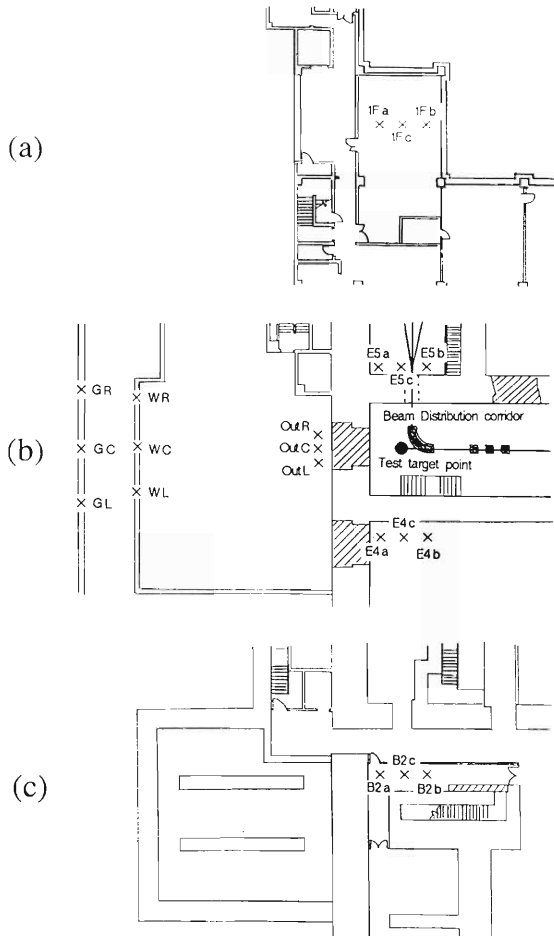


Fig. 1. Partial layout of the RIKEN Ring Cyclotron facility where the leakage radiation measurement was made. (a) Part of the 1st floor; (b) Part of the 1st basement floor; (c) Part of the 2nd basement floor. The target point is denoted by a closed circle. Leakage-radiation-dose measuring points are denoted by ×.

the target was read with a current integrator (ORTEC 439) and recorded with a personal computer. Figure 1-(a), (b), and (c) show the target point and the positions where the measurements were done. The positions of E5c and E4c are just right and left from the target point, respectively. Leakage of neutrons was detected also at the several points outside the building. The position denoted by OutC is right behind the target point. Results are summarized in Table 1. The data of dose rates were normalized with respect to the beam intensity of 1 pμA.

The behavior of leakage neutrons around the beam distribution corridor for several kinds of beams had been measured in series of measurements. For examples, Figs. 2 and 3 show the neutron dose rates at E4a, E4c, and E4b, and the attenuation curves of neutron dose rates measured along the points denoted in Fig. 1(b), respectively.

On the other hands, the automatic monitoring of leakage radiation using a computer (MX-3000) was also done continuously during this year. From the accumulated data of leakage neutrons, the radiation level in the controlled area was found to have been much less

* Faculty of Science and Technology, Chuo University

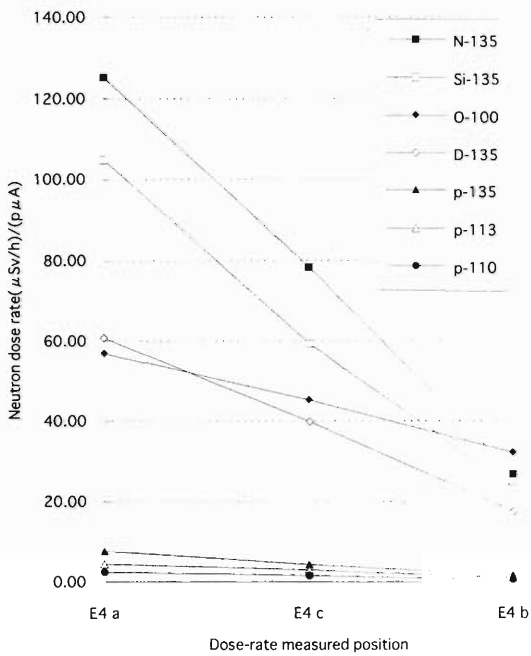


Fig. 2. Neutron dose rates at E4a, E4c and E4b [See, Fig. 1(b)]. The distances between E4c and E4a, and between E4c and E4b are 2 m, respectively.

than the safety limit (0.3 mSv/week). Leakage of neutrons has been recorded with a monitor in the ground-floor computer room just above a bending magnet that guides the beams from Ring Cyclotron vault to the distribution corridor. This radiation level is, however, much less than the safety limit (1 mSv/year) required at the boundary of the accelerator facility. No leakage of γ rays and neutrons was detected with environmental monitors outside the building during this reporting period.

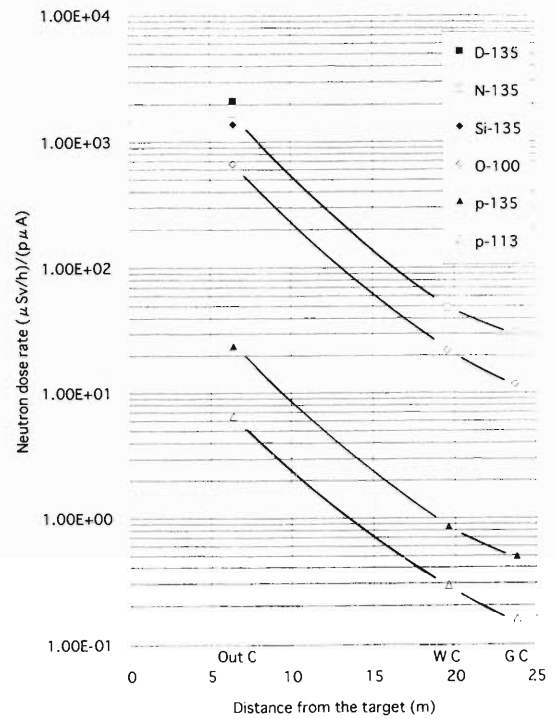


Fig. 3. Attenuation curves of neutron dose rates at OutC, WC, and GC [See, Fig. 1(b)]. The distances at OutC, WC, and GC are 6.4, 19.6, and 23.8 m from the target point, respectively.

References

- 1) S. Fujita, N. Nakanishi, S. Nakajima, M. Watanabe, H. Ohishi, K. Tanaka, Y. Uwamino, and T. T. Inamura: RIKEN Accel. Prog. Rep. **28**, 183 (1995).
- 2) S. Fujita, N. Nakanishi, S. Nakajima, M. Watanabe, H. Ohishi, Y. Uwamino, and T. T. Inamura: RIKEN Accel. Prog. Rep. **29**, 259 (1996).

Dose Rates due to Residual Activities in the Ring Cyclotron Facility

S. Fujita, H. Ohishi,* H. Uehara,* N. Nakanishi, Y. Uwamino, and T. T. Inamura

Dose rates due to residual radioactivities have routinely been measured at various points in the RIKEN Ring Cyclotron (RRC) Facility every summer, and at those along the beam lines after every experiment. The results of measurements have been reported annually since 1986.

Figure 1 shows the variation of the dose rates at the deflectors of the RRC and AVF in the last ten years. It is clearly seen that the dose rates have been about ten thousand $\mu\text{Sv/h}$ since 1990, while they were lower by two orders of magnitude until 1989. This is due to the increase in the maximum energy of the beam from the RRC, which has changed from 75 MeV/nucleon to 135 MeV/nucleon.

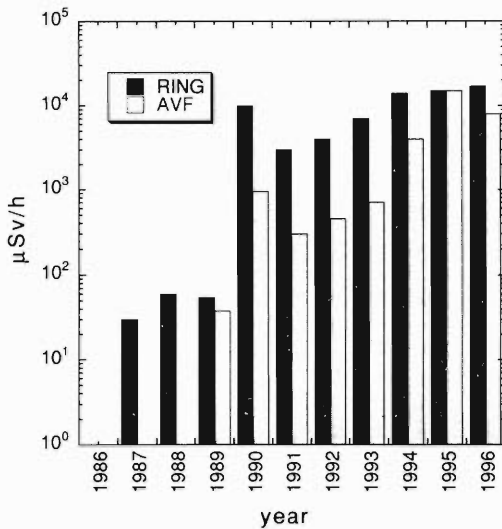


Fig. 1. Variation of the dose rates at the deflectors of the RIKEN Ring Cyclotron and AVF injector cyclotron.

In the period from Oct. 1, 1995 to Sep. 30, 1996, dose rates were measured along the beam lines. The points a-z in Fig. 2 denote the places where the dose rates exceeded 50 $\mu\text{Sv/h}$. Table 1 summarizes the observed dose rates together with the dates on which the measurements were performed. The maximum dose rate

was found to be 5000 $\mu\text{Sv/h}$ at the target chamber, denoted by the point V in Fig. 2.

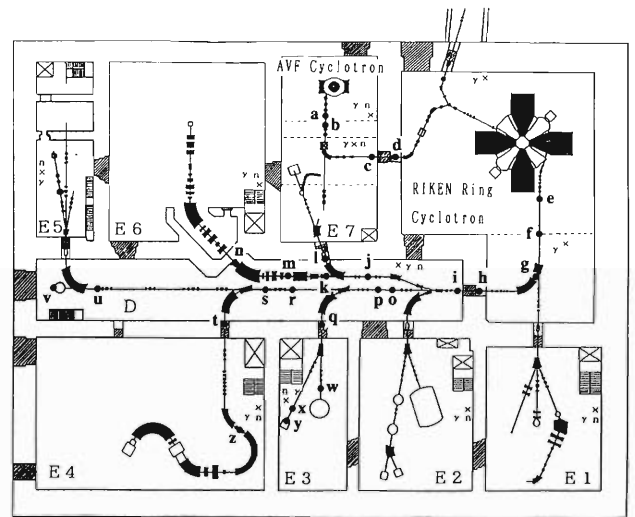
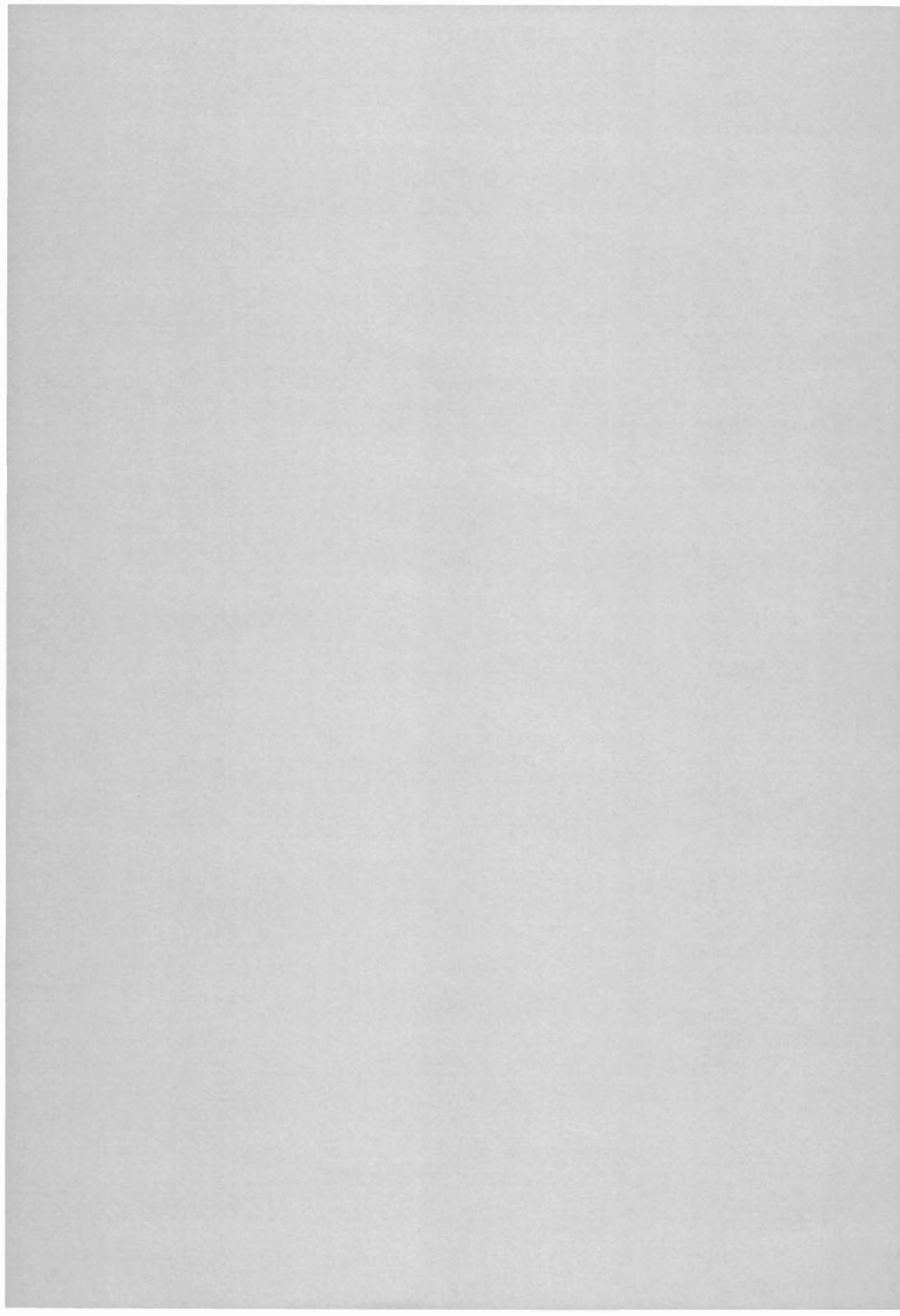


Fig. 2. Layout of the RIKEN Ring Cyclotron Facility in 1996. The positions where the residual activities were measured along the beam lines are denoted by a-z.

Table 1. Summary of the dose rates measured along the beam lines with ionization-chamber survey meters. The points a-z correspond to the positions shown in Fig. 2.

Detection point	Measured dose rate ($\mu\text{Sv/h}$)	Date	Detection point	Measured dose rate ($\mu\text{Sv/h}$)	Date
a	160	Nov 13, '95	n	1000	Nov 24, '95
b	60	Apr 25, '96	o	95	Oct 13, '95
c	50	Nov 8, '95	p	62	Oct 13, '95
d	60	Jun 6, '96	q	110	Aug 13, '96
e	270	Nov 13, '95	r	54	Oct 13, '95
f	220	Nov 13, '95	s	110	Dec 20, '95
g	350	Nov 13, '95	t	50	Jul 2, '96
h	60	Apr 25, '96	u	110	Nov 13, '95
i	300	Jul 2, '96	v	5000	Nov 13, '95
j	180	Aug 13, '96	w	220	Nov 27, '95
k	120	Aug 13, '96	x	3000	Mar 8, '96
l	120	Nov 24, '95	y	3000	Mar 8, '96
m	550	Mar 6, '96	z	50	Jan 31, '96

* Faculty of Science and Technology, Chuo University



VII. LIST OF PUBLICATIONS

1. Accelerator development and accelerator physics
 - A. Goto, Y. Miyazawa, M. Hemmi, O. Kamigaito, T. Nakagawa, M. Kase, T. Chiba, N. Inabe, S. Kohara, T. Kageyama, Y. Batygin, E. Ikezawa, and Y. Yano: "Construction of a new pre-injector system for the RILAC", Proc. 14th Int. Conf. on Cyclotrons and Their Applications, 1995-10, Cape Town, South Africa, pp. 202-205 (1995).
 - T. Mitsumoto, T. Kawaguchi, T. Kubo, H. Okuno, T. Tominaka, Y. Tanaka, S. Fujishima, K. Ikegami, A. Goto, and Y. Yano: "Design study of sector magnets of Superconducting Ring Cyclotron for the RIKEN RI Beam Factory", Proc. 14th Int. Conf. on Cyclotrons and Their Applications, 1995-10, Cape Town, South Africa, pp. 237-240 (1995).
 - M. Kase, N. Inabe, I. Yokoyama, M. Hemmi, A. Goto, and Y. Yano: "Applications of MCP phase monitor to operation of RIKEN heavy ion accelerators", Proc. 14th Int. Conf. on Cyclotrons and their Applications, 1995-10, Cape Town, South Africa, pp. 291-294 (1995).
 - Y. Yano, A. Goto, Y. Miyazawa, M. Hemmi, T. Chiba, T. Kageyama, K. Ikegami, M. Takanaka, T. Kawaguchi, S. Kohara, M. Kase, T. Tominaka, Y. Batygin, T. Kubo, T. Nakagawa, Y. Tanaka, E. Ikezawa, M. Wakasugi, T. Mitsumoto, N. Inabe, O. Kamigaito, H. Okuno, S. Fujishima, A. Ohtomo, and T. Ohkawa: "RIKEN RI Beam Factory project", (invited paper), Proc. 14th Int. Conf. on Cyclotrons and their Applications, 1995-10, Cape Town, South Africa, pp. 590-597 (1995).
 - Y. Batygin: "On space charge dominated beam transport without emittance growth", AIP Conf. Proc. 377, edited by S. Y. Lee, Woodbury, New York, pp. 290-306 (1996).
 - T. Nakagawa, Y. Miyazawa, M. Hemmi, T. Chiba, N. Inabe, M. Kase, T. Kageyama, O. Kamigaito, A. Goto, and Y. Yano: "Improvement of RIKEN 18 GHz electron cyclotron resonance ion source using aluminum tube", Jpn. J. Appl. Phys. **35**, 4077-4078 (1996).
 - T. Nakagawa, Y. Miyazawa, M. Hemmi, T. Chiba, N. Inabe, M. Kase, T. Kageyama, O. Kamigaito, A. Goto, and Y. Yano: "Determination of ion confinement time in RIKEN 18 GHz electron cyclotron resonance ion source (ECRIS) under pulsed mode operation", Jpn. J. Appl. Phys. **35**, L1124-L1126 (1996).
 - Y. Batygin: "Conservation of space-charge-dominated beam emittance in a strong nonlinear focusing field", Phys. Rev. E **53**, 5358-5365 (1996).
 - Y. Batygin: "Adiabatic matching of nonuniform intense charged - particle beam into the focusing channel", Phys. Rev. E **54**, 5673-5680 (1996).
 - N. Shimakura, S. Suzuki, Y. Murakami, and J. P. Gu: "Electron capture and target excitation in collisions of B^{q+} and Be^{q+} ions with H and He atoms at energies below 10 keV/u", Phys. Scr. T **62**, 39-42 (1996).
 - Y. Yano and A. Goto: "Progress of RIKEN RI Beam Factory project", Proc. 5th Eur. Part. Accel. Conf. (EPAC '96), pp. 536-538 (1996).
 - T. Katayama, S. Watanabe, Y. Batygin, N. Inabe, K. Ohtomo, T. Ohkawa, M. Takanaka, M. Wakasugi, Y. Yana, K. Yoshida, J. Xia, Y. Rao, and Y. Tuan: "MUSES project at RI Beam Factory", Proc. 5th Eur. Part. Accel. Conf. (EPAC '96), pp. 563-565 (1996).
 - M. Wakasugi, N. Inabe, and T. Katayama: "Undulator and photon spectrum at DSR", Proc. 5th Eur. Part. Accel. Conf. (EPAC '96), pp. 611-613 (1996).
 - O. Kamigaito, A. Goto, Y. Miyazawa, T. Chiba, M. Hemmi, S. Kohara, M. Kase, Y. Batygin, and Y. Yano: "Development of a variable-frequency RFQ linac for the RILAC", Proc. 5th Eur. Part. Accel. Conf. (EPAC '96), pp. 786-788 (1996).
 - K. Yoshida and T. Katayama: "Expected luminosity at MUSES", Proc. 5th Eur. Part. Accel. Conf. (EPAC '96), pp. 870-872 (1996).
 - N. Inabe and T. Katayama: "Design of double storage ring at MUSES", Proc. 5th Eur. Part. Accel. Conf. (EPAC '96), pp. 926-928 (1996).
 - T. Ohkawa and T. Katayama: "Design of booster synchrotron for MUSES", Proc. 5th Eur. Part. Accel. Conf. (EPAC '96), pp. 929-931 (1996).
 - J. W. Xia and T. Katayama: "Lattice for accumulator cooler ring for MUSES", Proc. 5th Eur. Part. Accel. Conf. (EPAC '96), pp. 932-934 (1996).
 - Y. N. Rao and T. Katayama: "Intrabeam scattering of heavy ion in DSR", Proc. 5th Eur. Part. Accel. Conf. (EPAC '96), pp. 1024-1026 (1996).
 - M. Takanaka and T. Katayama: "Beam current limitation due to single-beam collective effects in the ion storage ring of RIKEN RI-beam factory project", Proc. 5th Eur. Part. Accel. Conf. (EPAC '96), pp. 1138-1140 (1996).
 - Y. Batygin and T. Katayama: "Beam-beam interaction of electrons and ions at RIKEN RI beam factory", Proc. 5th Eur. Part. Accel. Conf. (EPAC '96), pp. 1170-1172 (1996).
 - Y. Batygin and T. Katayama: "Merging beam-beam collisions at RIKEN RI Beam Factory", Proc. 5th Eur. Part. Accel. Conf. (EPAC '96), pp. 1173-1175 (1996).
 - Y. N. Rao, K. Ohtomo, and T. Katayama: "Electron cooler at ACR", Proc. 5th Eur. Part. Accel. Conf. (EPAC '96), pp. 1182-1184 (1996).
 - Y. J. Yuan, K. Ohtomo, and T. Katayama: "Simulation of RF stacking combined with cooling effects", Proc. 5th Eur. Part. Accel. Conf. (EPAC '96), pp. 1338-1340 (1996).

- T. Nakagawa, J. Arje, Y. Miyazawa, M. Hemmi, M. Kase, T. Kageyama, O. Kamigaito, T. Chiba, N. Inabe, A. Goto, and Y. Yano: "Development of RIKEN 18 GHz ECRIS", Proc. 5th Eur. Part. Accel. Conf. (EPAC '96), pp. 1478–1480 (1996).
- M. Takanaka and T. Katayama: "Design of beam bunching system for the ion storage ring of RIKEN RI-beam factory project", Proc. 5th Eur. Part. Accel. Conf. (EPAC '96), pp. 1991–1993 (1996).
- T. Kubo, T. Kawaguchi, T. Mitsumoto, H. Okuno, T. Tominaka, J.-W. Kim, S. Fujishima, K. Ikegami, Y. Tanaka, A. Goto, and Y. Yano: "Design of model sector magnet for the RIKEN Superconducting Ring Cyclotron", Proc. 5th Eur. Part. Accel. Conf. (EPAC '96), pp. 2279–2280 (1996).
- T. Mitsumoto, A. Goto, T. Kawaguchi, J.-W. Kim, Y. Tanaka, T. Kubo, H. Okuno, T. Tominaka, W. Fujishima, and Y. Yano: "Design study of sector magnet for the RIKEN Superconducting Ring Cyclotron (I)", Proc. 5th Eur. Part. Accel. Conf. (EPAC '96), pp. 2302–2304 (1996).
- T. Kawaguchi, T. Kubo, T. Mitsumoto, T. Tominaka, S. Fujishima, H. Okuno, Y. Tanaka, J.-W. Kim, K. Ikegami, A. Goto, and Y. Yano: "Design study of sector magnet for the RIKEN Superconducting Ring Cyclotron (II)", Proc. 5th Eur. Part. Accel. Conf. (EPAC '96), pp. 2305–2307 (1996).
- S. Watanabe, T. Katayama, N. Inabe, T. Ohkawa, and M. Takanaka: "Study of a magnet power supply for a MUSES booster synchrotron", Proc. 5th Eur. Part. Accel. Conf. (EPAC '96), pp. 2340–2342 (1996).
- H. Okuno, T. Tominaka, T. Kubo, J.-W. Kim, T. Mitsumoto, T. Kawaguchi, Y. Tanaka, S. Fujishima, K. Ikegami, A. Goto, and Y. Yano: "Design study of the injection system of the RIKEN superconducting Ring Cyclotron", Proc. 5th Eur. Part. Accel. Conf. (EPAC '96), pp. 2397–2399 (1996).
- Y. Batygin, A. Goto, and Y. Yano: "Hollow beam profile in the extraction system of ECR ion source", Proc. Part. Accel. Conf. (PAC95), 1995-5, Dallas, U.S.A., pp. 1001–1003 (1996).
- Y. Batygin: "Invariability of intense beam emittance in nonlinear focusing channel", Proc. Part. Accel. Conf. (PAC95), 1995-5, Dallas, U.S.A., pp. 3251–3253 (1996).
- D. L. Bruhwiler and Y. K. Batygin: "Beam transport for uniform irradiation: Nonlinear space charge forces and the effect of boundary conditions", Proc. Part. Accel. Conf. (PAC95), 1995-5, Dallas, U.S.A., pp. 3254–3256 (1996).
- ## 2. Nuclear physics and nuclear instrumentation
- A. Ryowa, N. Hasebe, M. Kobayashi, K. Kondo, Y. Mishima, K. Nagata, T. Kohno, J. Kikuchi, and T. Doke: "Global distributions of trapped particle fluxes observed by OHZORA satellite during 1984–1987", Bulletin of General Education Faculty of Ehime Univ., p. 28 (1995).
- Y. Mizoi, T. Miyachi, Y. Matsuyama, T. Fukuda, H. Kobinata, Y. Watanabe, Y. Watanabe, A. Yoshida, H. Sakurai, and K. Kimura: "Construction of the New MUSIC detector system", INS Ann. Rep. pp. 38–39 (1995).
- N. Hasebe, K. Kondoh, M. Kobayashi, Y. Mishima, T. Doke, J. Kikuchi, T. Hayashi, K. Itsumi, T. Takashima, T. Yanagimachi, H. Murakami, A. Nakamoto, K. Nagata, T. Kashiwagi, K. Munakata, C. Kato, T. Kohno, Y. Muraki, T. Koi, K. Maetzawa, S. Yanagita, T. Terasawa, A. Nishida, K. Fujiki, J. Medina, J. Sequeiros, and B. Wilken: "Corotating ion events associated with cosmic ray modulation", J. Geomagn. Geoelectr. **47**, 1333–1338 (1995).
- Y. Koike and K. Tanaka: " Q^2 evolution of the nucleon's chiral-odd twist-three structure function: $h_L(x, Q^2)$ ", Phys. Rev. D **51**, 6125–6138 (1995).
- A. A. Gusev, T. Kohno, I. M. Martin, G. I. Pugacheva, A. Turtelli, A. Tyka, and K. Kudela: "Injection and fast radial diffusion of energetic electrons into the inner magnetosphere", Planet. Space Sci. **43**, 1131–1134 (1995).
- S. Shimoura: "Spectroscopy of neutron-rich nuclei via direct reactions using secondary nuclear beams at several tens of MeV per nucleon", Proc. Int. Conf. on Exotic Nuclei and Atomic Masses, edited by M. de Saint Simon and O. Sorlin, Editions Frontiers, France, pp. 217–225 (1995).
- H. Kurasawa and T. Suzuki: "A sum rule constraint on the soft dipole mode", Prog. Theor. Phys. **94**, 931–936 (1995).
- K. Oyamatsu: "Symmetry energy at subnuclear densities", Genshikaku Kenkyu **41**, 39–43 (1996).
- H. Kurasawa and T. Suzuki: "Electron scattering in relativistic and non-relativistic model", Genshikaku Kenkyu **41**, 103–110 (1996).
- G. I. Pugacheva, A. A. Gusev, I. M. Martin, W. N. Spjeldvik, and T. Kohno: "The temporal evolution of 3–9 MeV/nucleon He flux trapped in the magnetosphere", Geophys. Res. Lett. **23**, 2793–2796 (1996).
- K. Matsuta, M. Fukuda, M. Tanigaki, T. Minamisono, Y. Nojiri, H. Akai, T. Izumikawa, M. Nakazato, M. Mihara, T. Yamaguchi, A. Harada, M. Sasaki, T. Miyake, T. Ohnishi, K. Minamisono, T. Fukao, K. Sato, Y. Matsumoto, T. Ohtsubo, S. Fukuda, K. Yoshida, A. Ozawa, S. Momota, T. Kobayashi, I. Tanihata, J. R. Alonso, G. F. Krebs, and T. J. M. Symons: "Hyperfine interaction of ^{13}O and ^{23}Mg implanted in Pt", Hyperfine Interact. **97/98**, 501–508 (1996).
- H. Izumi, K. Asahi, H. Ueno, H. Okuno, H. Sato, K. Nagata, Y. Hori, M. Adachi, M. Aoi, A. Yoshida, G. Liu, N. Fukunishi, and M. Ishihara: "Measurement of electric quadrupole moments of neutron-rich nuclei ^{14}B and ^{15}B ", Hyperfine Interact. **97/98**, 509–517 (1996).
- K. Matsuta, T. Minamisono, M. Tanigaki, M. Fukuda,

- Y. Nojiri, M. Mihara, T. Onishi, T. Yamaguchi, A. Harada, M. Sasaki, T. Miyake, K. Minamisono, T. Fukao, K. Sato, Y. Matsumoto, T. Ohtsubo, S. Fukuda, S. Momota, K. Yoshida, A. Ozawa, T. Kobayashi, I. Tanihata, J. R. Alonso, G. F. Krebs, and T. J. M. Symons: “Magnetic moments of proton drip-line nuclei ^{13}O and ^9C ”, *Hyperfine Interact.* **97/98**, 519–526 (1996).
- T. Matsuzaki, K. Ishida, S. Nakamura, I. Watanabe, N. Kawamura, M. Tanase, K. Kurosawa, M. Koto, M. Hashimoto, K. Nagamine: “Muon catalyzed fusion experiment at RIKEN-RAL Muon Facility”, *JAERI-Conf 96-014* pp. 121–128 (1996).
- H. Kurasawa and T. Suzuki: “Does a soft dipole mode exist?”, *JHP-Suppl.* **20**, 21–25 (1996).
- H. Miyatake, M. Sasaki, H. Ueno, T. Shimoda, N. Aoi, T. Shirakura, K. Asahi, H. Izumi, H. Ogawa, G. Liu, and A. Yoshida: “Delayed neutron spectroscopy with using spin-polarized neutron-rich nuclei beam”, *JHP-Suppl.* **20**, 48–50 (1996).
- K. Sumiyoshi, K. Oyamatsu, and H. Toki: “Neutron stars and unstable nuclei in relativistic many-body framework”, *JHP-Suppl.* **20**, 279 (1996).
- A. A. Gusev, T. Kohno, W. N. Spijeldvik, I. M. Martin, G. I. Pugacheva, and A. Tutelli, Jr.: “Dynamics of low-altitude energetic proton fluxes beneath the main terrestrial radiation belts”, *J. Geophys. Res.* **101**, 19659–19663 (1996).
- N. Iwasa, T. Motobayashi, Y. Ando, M. Kurokawa, H. Murakami, J. Ruan, S. Shimoura, S. Shirato, N. Inabe, T. Kubo, Y. Watanabe, M. Gai, R. H. France III, K. I. Hahn, Z. Zhao, T. Nakamura, T. Teranishi, Y. Futami, K. Furutaka, Th. Delbar, and M. Ishihara: “Study of the $^7\text{Be}(p,\gamma)^8\text{B}$ reaction with Coulomb dissociation method”, *J. Phys. Soc. Jpn.* **65**, 1256–1263 (1996).
- H. Miyatake, T. Shimoda, M. Sasaki, T. Shirakura, N. Aoi, K. Asahi, H. Ueno, H. Izumi, H. Ogawa, A. Yoshida, and G. Liu: “Delayed neutron spectroscopy with using spin polarized RI Beam”, *KURRI-KR-3*, pp. 60–64 (1996).
- K. Kitao and M. Oshima: “Nuclear data sheets update for $A=127$ ”, *Nuclear Data Sheets* **77**, 1–298 (1996).
- Y. Tendow: “Nuclear data sheets for $A=129$ ”, *Nuclear Data Sheets* **77**, 631–770 (1996).
- H. Okada, T. Doke, K. Hasuike, J. Kikuchi, K. Masuda, M. Shinoda, T. Takahashi, and K. Terasawa: “Time stability of liquid xenon photoionization detectors”, *Nucl. Instrum. Methods Phys. Res. A* **374**, 188–192 (1996).
- M. Takada, T. Shibata, Y. Uwamino, and T. Nakamura: “A performance study on a phoswich detector consisting of an inner NE213 scintillator and an outer $\text{CaF}_2(\text{Eu})$ crystal wall”, *Nucl. Instrum. Methods Phys. Res. A* **379**, 293–306 (1996).
- T. Horibata and N. Onishi: “Self-consistent three-dimensional cranking calculation based on HFB”, *Nucl. Phys. A* **596**, 251–284 (1996).
- H. Kurasawa and T. Suzuki: “The mean energy, strength and width of the double giant dipole states”, *Nucl. Phys. A* **597**, 374–386 (1996).
- H. Hofmann, F. A. Ivanyuk, and S. Yamaji: “On the nature of nuclear dissipation, as a hallmark for collective dynamics at finite excitation”, *Nucl. Phys. A* **598**, 187–234 (1996).
- L. Chulkov, G. Kraus, O. Bochkarev, P. Egelhof, H. Geissel, M. Golovkov, H. Irnich, Z. Janas, H. Keller, T. Kobayashi, G. Münzenberg, F. Nickel, A. Ogloblin, A. Ozawa, S. Patra, A. Piechaczek, E. Roeckl, W. Schwab, K. Sümmerer, T. Suzuki, I. Tanihata, and K. Yoshida: “Interaction cross sections and matter radii of $A = 20$ isobars”, *Nucl. Phys. A* **603**, 219–237 (1996).
- Y. Futami, K. Yuasa-Nakagawa, T. Nakagawa, S. M. Lee, K. Furutaka, K. Matsuda, K. Yoshida, S. C. Jeong, H. Fujiwara, T. Mizota, Y. Honjo, S. Tomita, B. Heusch, K. Ieki, J. Kasagi, W. Q. Shen, and T. Matsuse: “Decay mechanism of a highly excited nucleus produced in the reaction $^{84}\text{Kr}+^{27}\text{Al}$ at 10.6 MeV/nucleon”, *Nucl. Phys. A* **607**, 85–104 (1996).
- A. Ozawa, I. Tanihata, T. Kobayashi, Y. Sugahara, O. Yamakawa, K. Omata, K. Sugimoto, D. Olson, W. Christie, and H. Wieman: “Interaction cross sections and radii of light nuclei”, *Nucl. Phys. A* **608**, 63–76 (1996).
- I. Tanihata and Y. Awaya: “RI Beam Facilities for 21-century”, (in Japanese), *Parity* **11**, 39–41 (1996).
- H. Izumi, K. Asahi, H. Ueno, H. Okuno, H. Sato, K. Nagata, Y. Hori, M. Adachi, N. Aoi, A. Yoshida, G. Liu, N. Fukunishi, and M. Ishihara: “Electric quadrupole moments of neutron-rich nuclei ^{14}B and ^{15}B ”, *Phys. Lett. B* **366**, 51–55 (1996).
- P. Strasser, K. Ishida, S. Sakamoto, K. Shimomura, N. Kawamura, E. Torikai, M. Iwasaki, and K. Nagamine: “Muon catalyzed fusion experiments on muonic deuterium atom deceleration in thin solid deuterium films”, *Phys. Lett. B* **368**, 32–38 (1996).
- R. L. Jaffe and N. Saito: “QCD selection rules in polarized hadron collisions”, *Phys. Lett. B* **382**, 165–172 (1996).
- T. Kikuchi, T. Motobayashi, N. Iwasa, Y. Ando, M. Kurokawa, S. Moriya, H. Murakami, T. Nishio, J. Ruan, S. Shimoura, S. Shirato, T. Uchibori, Y. Yanagisawa, T. Kubo, H. Sakurai, T. Teranishi, Y. Watanabe, M. Ishihara, M. Hirai, T. Nakamura, S. Kubono, M. Gai, R. H. France III, K. I. Hahn, Th. Delbar, P. Lipnik, and C. Michotte: “Experimental determination of the E2 component in the Coulomb dissociation of ^8B ”, *Phys. Lett. B* **391**, 261–266 (1996).
- N. Dinh Dang: “On the width of giant dipole resonance in hot nuclei”, *Phys. Rep.* **264**, 123–135 (1996).
- K. Sugawara-Tanabe, A. Arima, and N. Yoshida: “Magnetic dipole transitions in superdeformed nuclei”, *Phys. Rev. C* **53**, 195–200 (1996).
- G. Rainmann, A. Ozawa, R. N. Boyd, F. R. Chloupek,

- M. Fujimaki, K. Kimura, T. Kobayashi, J. J. Kolata, S. Kubono, I. Tanihata, Y. Watanabe, and K. Yoshida: "Levels in ^{17}C above the $^{16}\text{C}+\text{neutron}$ threshold", *Phys. Rev. C* **53**, 453–458 (1996).
- K. Yuasa-Nakagawa, J. Kasagi, T. Nakagawa, K. Yoshida, Y. Futami, S. M. Lee, K. Furutaka, K. Matsuda, and W. Q. Shen: "Binary decay fragment cross sections and pre-scission charge multiplicity in $^{84}\text{Kr}+^{27}\text{Al}$ at 10.6 MeV/nucleon", *Phys. Rev. C* **53**, 997–1000 (1996).
- F. Käppeler, K. A. Toukan, M. Schumann, and A. Mengoni: "Neutron capture cross sections of the cerium isotopes for the s- and p-process studies", *Phys. Rev. C* **53**, 1397–1408 (1996).
- H. Ueno, K. Asahi, H. Izumi, K. Nagata, H. Ogawa, A. Yoshimi, H. Ogawa, H. Sato, K. Adachi, Y. Hori, K. Mochinaga, H. Okuno, N. Aoi, M. Ishihara, A. Yoshida, G. Liu, T. Kubo, N. Fukunishi, T. Shimoda, H. Miyatake, M. Sasaki, T. Shirakura, N. Takahashi, S. Mitsuoka, and W.-D. Schmidt-Ott: "Magnetic moments of ^{17}N and ^{17}B ", *Phys. Rev. C* **53**, 2142–2151 (1996).
- A. A. Korshennikov, E. Yu. Nikolskii, T. Kobayashi, A. Ozawa, S. Fukuda, E. A. Kuzmin, S. Momota, B. G. Novatskii, A. A. Ogloblin, V. Pribora, I. Tanihata, and K. Yoshida: "Spectroscopy of the halo nucleus ^{11}Li by an experimental study of $^{11}\text{Li}+\text{p}$ collisions", *Phys. Rev. C* **53**, R537–R540 (1996).
- Y. Suzuki, K. Arai, Y. Ogawa, and K. Varga: "Occupation probability of harmonic-oscillator quanta for microscopic cluster-model wave functions", *Phys. Rev. C* **54**, 2073–2080 (1996).
- T. Nozawa, M. Hashimoto, K. Oyamatsu, and Y. Eriguchi: "Structure of rotating neutron stars with meson condensates", *Phys. Rev. D* **53**, 1845–1852 (1996).
- M. Wakamatsu: "Can the SU(3) chiral quark soliton model describe the nucleon properties better than the SU(2) model?", *Phys. Rev. D* **54**, 2161–2167 (1996).
- I. I. Balitsky, V. M. Braun, Y. Koike, and K. Tanaka: "The Q^2 evolution of chiral-odd twist-3 distributions $h_L(x, Q^2)$ and $e(x, Q^2)$ in the large- N_c QCD", *Phys. Rev. Lett.* **77**, 3078–3081 (1996).
- K. Matsuta, M. Tanigaki, M. Fukuda, T. Minamisono, Y. Nojiri, M. Mihara, T. Onishi, T. Yamaguchi, A. Harada, M. Sasaki, T. Miyake, K. Minamisono, T. Fukao, K. Sato, Y. Matsumoto, T. Ohtsubo, S. Fukuda, S. Momota, K. Yoshida, A. Ozawa, T. Kobayashi, I. Tanihata, J. R. Alonso, G. F. Krebs, and T. J. M. Symons: "Magnetic moments of proton drip-line nuclei", *Proc. Int. Conf. on Exotic Nuclei and Atomic Masses*, edited by M. de Saint Simon and O. Sorlin, Editions Frontiers, Gif-sur-Yvette Cedex, pp. 43–52 (1996).
- M. Tanigaki, K. Matsuta, M. Fukuda, T. Minamisono, Y. Nojiri, M. Mihara, K. Minamisono, T. Fukao, K. Sato, Y. Matsumoto, T. Ohtsubo, S. Fukuda, S. Momota, K. Yoshida, A. Ozawa, T. Kobayashi, I. Tanihata, J. R. Alonso, G. F. Krebs, and T. J. M. Symons: "Quadrupole moment of proton dripline nucleus $^{13}\text{O}(I^\pi = 3/2^-, T_{1/2} = 8.6 \text{ ms})$ ", *Proc. 10th Int. Conf. on Hyperfine Interactions*, edited by M. Rots, A. Vantomme, J. Dekoster, R. Coussement, and G. Langouche, J. C. Baltzer AG, Basel, pp. 549–552 (1996).
- T. Nakamura et al.: "Instrumentation and dosimetry at accelerator facilities", *Proc. 9th Int. Congr. on Radiation Protection*, Vol. 1, 1996–4, Vienna, Austria, pp. 123–130 (1996).
- A. A. Gusev, T. Kohno, I. M. Martin, G. I. Pugacheva, A. Turtelli, Jr., and A. J. Tylka: "Injection and fast radial diffusion of energetic electrons into the inner magnetosphere", *Proc. 24th Int. Cosmic Ray Conf.*, Vol. 4, 1995–9, Rome, Italy, pp. 981–984 (1996).
- A. Turtelli, T. Kohno, U. B. Jayanthi, J. H. Adams Jr., I. M. Martin, T. Villera, A. Neri, A. A. Gusev, G. I. Pugacheva, H. Kato, K. Nagata, A. J. Tylka, and P. R. Boberg: "Anomalous and solar cosmic ray observations with the first Brazilian Scientific Microsatellite", *Proc. 24th Int. Cosmic Ray Conf.*, Vol. 4, 1995–9, Rome, Italy, pp. 1275–1278 (1996).
- N. Dinh Dang and F. Sakata: "Damping of hot giant dipole resonance as a linear irreversible process", *Proc. 2nd Japan-Italy Joint Symp. on Perspectives in Heavy Ion Physics*, edited by M. Ishihara, T. Fukuda, and C. Signorini, World Scientific, Singapore, pp. 257–268 (1996).
- Y. Koike and K. Tanaka: "Perturbative QCD study of the chiral-odd twist-3 structure function: $h_L(x, Q^2)$ ", *Proc. RIKEN Symp. on Spin Structure of the Nucleon*, edited by T.-A. Shibata, S. Ohta, and N. Saito, World Scientific, Singapore, pp. 83–86 (1996).
- Y. Nishino and K. Tanaka: "Strange matrix elements of the proton and instantons in QCD", *Proc. RIKEN Symp. on Spin Structure of the Nucleon*, edited by T.-A. Shibata, S. Ohta, and N. Saito, World Scientific, Singapore, pp. 87–91 (1996).
- H. Kurasawa and T. Suzuki: "Double giant dipole states", *Proc. RIKEN Symp. on Structure of Medium Nuclei*, pp. 141–150 (1996).
- T. Nakamura et al.: "Activation cross-section measurements using quasi-monoenergetic neutron field from 20 to 150 MeV", *Proc. 2nd Specialists' Meet. on Shielding Aspects of Accelerators, Target and Irradiation Facilities*, Nuclear Energy Agency, OECD, pp. 215–220 (1996).
- S. Yamaji: "The temperature dependent of the friction in the fission", *Proc. Specialists' Res. Meet. on Frontier in Nuclear Fission Research Basic Science and Technology*, Res. Reactor Inst., Kyoto Univ., pp. 53–62 (1996).
- M. Takada, T. Nakamura, T. Shibata, and N. Nakao: "Development of a phoswich counter to detect neutrons and charged particles for space application",

- Proc. 1996 Topical Meet. of Radiation Protection and Shielding, Vol. 1, 1996-4, No. Falmouth, U.S.A., pp. 51–58 (1996).
- N. Nakanishi, S. Fujita, M. Watanabe, and S. Nakajima: “Neutron activation cross sections for ^{12}C , ^{27}Al , ^{56}Fe , ^{59}Co , ^{58}Ni , and ^{197}Au for energies up to 110 MeV”, Proc. 1996 Topical Meet. Radiation Protection and Shielding, Vol. 1, 1996-4, No. Falmouth, U.S.A., pp. 258–265 (1996).
- Y. S. Mochizuki, K. Oyamatsu, and T. Izuyama: “A microscopic model for physical origin of neutron star glitches”, Proc. Workshop on Astrophysics with Line X- and γ -Rays (IV), pp. 144–149 (1996).
- M. Wakamatsu: “Tracing the origin of the g_A problem in the skyrme model”, Prog. Theor. Phys. **95**, pp. 143–173 (1996).
- M. Wakamatsu: “Magnetic moments of octet and decuplet baryons in the $SU(3)$ chiral quark soliton model”, Prog. Theor. Phys. **95**, pp. 767–778 (1996).
- Y. S. Mochizuki, K. Oyamatsu, Y. Izuyama, and I. Tanihata: “Screened Coulomb potential for exotic nuclear deformation in neutron star crusts”, RIKEN Rev., No. 14, pp. 39–40 (1996).
- ### 3. Atomic and solid-state physics
- M. Kimura, I. Shimamura, and M. Inokuti: “Double and single ionization of He and H_2 by slow protons and antiprotons”, Atomic and Molecular Physics, edited by I. Alvarez, C. Cisneros, and T. J. Morgan, World Scientific, Singapore, pp. 243–246 (1995).
- Z. L. Peng and Y. Itoh: “Study of ionic transport in polymer electrolyte using positron lifetime distribution method”, Appl. Phys. A **63**, 267–270 (1996).
- Y. Itoh, H. Murakami, and A. Kinoshita: “Positron/positronium annihilation in low dimensional silicon materials”, Appl. Surf. Sci. **102**, 423–426 (1996).
- M. Kimura, A. B. Sannigrahi, J. P. Gu. G. Hirsch, R. J. Buenker, and I. Shimamura: “Charge transfer rate in collisions of H^+ ions with Si atoms”, Astrophys. J. **473**, 1114–1117 (1996).
- J. Z. Tang and I. Shimamura: “Hyperspherical close-coupling approach to single and double photoionization of two-electron systems”, Atomic and Molecular Photoionization, edited by A. Yagishita and T. Sasaki, Universal Academy Press, Tokyo, pp. 223–232 (1996).
- J. Z. Tang, M. Kimura, and I. Shimamura: “Absorption and emission spectra of alkaline-earth atoms in liquid helium: A theoretical study”, Chem. Phys. Lett. **256**, 327–333 (1996).
- M. Takami: “Spectroscopic study of atoms and molecules in liquid helium”, Comments At. Mol. Phys. **32**, 219–231 (1996).
- I. Watanabe, S. Nakajima, K. Nagase, T. Matsuzaki, K. Ishida, and K. Nagamine: “ μ^+ SR study on magnetic state of $\text{TlBa}_2\text{Y}_{1-x}\text{Ca}_x\text{Cu}_2\text{O}_y$ ”, Czechoslovak J. Phys. **46**, 2673–2674 (1996).
- K. Matsuta, M. Fukuda, M. Tanigaki, T. Minamisono, Y. Nojiri, H. Akai, T. Izumikawa, M. Nakazato, M. Mihara, T. Yamaguchi, A. Harada, M. Sasaki, T. Miyake, T. Onishi, K. Minamisono, T. Fukao, K. Sato, Y. Matsumoto, M. Ohtsubo, S. Fukuda, K. Yoshida, A. Ozawa, S. Momota, T. Kobayashi, I. Tanihata, J. R. Alonso, G. F. Krebs, and T. J. M. Symons: “Hyperfine interaction of ^{13}O and ^{23}Mg implanted in Pt”, Hyperfine Interact. **97/98**, 501–508 (1996).
- T. Briere, R. Kadono, A. Matsushita, and K. Nagamine: “Theoretical investigation of the structure and associated hyperfine properties of hydrogenic impurities in alkali halides”, Hyperfine Interact. C **1**, 17–20 (1996).
- R. Kadono, R. M. Macrae, A. Matsushita, K. Nishiyama, and K. Nagamine: “Bistability of muonium centers in crystalline Si and Ge probed by photo-induced μSR ”, Hyperfine Interact. C **1**, 195–198 (1996).
- Y. Awaya: “Nuclear power and atomic physics”, (in Japanese), J. At. Energy Soc. Jpn. **38**, 337 (1996).
- J. Z. Tang and I. Shimamura: “Differential cross sections for photoionization of He”, J. Electron. Spectrosc. Relat. Phenom. **79**, 259–261 (1996).
- Y. Kobayashi, Y. Yoshida, J. Nakamura, K. Yukihiro, K. Hayakawa, C. Yamamoto, A. Yoshida, N. Aoi, Y. Watanabe, N. Inabe, M. Kase, A. Goto, Y. Yano, M. Ishihara, and F. Ambe: “Mössbauer spectroscopy using a ^{57}Mn beam from the RIPS of RIKEN Ring Cyclotron”, JHP-Suppl. **20**, 369–371 (1996).
- M. F. V. Lundsgaard, N. Toshima, and C. D. Lin: “Dependence of electron loss cross section on the alignment and orientation of elliptic Rydberg states”, J. Phys. B **29**, 1045–1062 (1996).
- B. D. DePaola, Y. Kanai, P. Richard, Y. Awaya, H. Schöne, J. M. Sanders, J. P. Giese, and T. J. M. Zouros: “Stark beats from highly charged rydberg ions created in high-energy beam-foil collisions”, J. Phys. B: At. Mol. Opt. Phys. **29**, 1247–1262 (1996).
- N. Nakamura, Y. Awaya, F. J. Currell, T. Kambara, Y. Kanai, S. Kitazawa, M. Koide, S. Ohtani, U. I. Safronova, H. Suzuki, T. Takayanagi, and K. Wakiya: “Electron spectra from doublet and quartet states of $\text{N}^{4+}(1s3l3l')$ produced by 60 keV $\text{N}^{6+} + \text{H}_2, \text{O}_2$ collisions”, J. Phys. B: At. Mol. Opt. Phys. **29**, 1995–2006 (1996).
- X. Zhao, Y. Itoh, Y. Aoyagi, T. Sugano, K. Hirata, Y. Kobayashi, T. Ohdaira, R. Suzuki, and T. Mikado: “Positron/positronium annihilation in nanocrystalline silicon”, J. Radioanal. Nucl. Chem. **211**, 31–38 (1986).
- Y. Itoh, Z. L. Peng, A. Goto, N. Nakanishi, M. Kase, K. H. Lee, and Y. Ito: “Production of short-lived positron sources for spin-polarized positron beams using a 35 MeV α -beam”, Nucl. Instrum. Methods Phys. Res. A **383**, 272–276 (1996).
- H. Kageyama, K. Kawatsura, R. Takahashi, T. Awata,

- T. Nakae, S. Arai, T. Kambara, M. Oura, T. Papp, Y. Kanai, Y. Awaya, H. Takeshita, Y. Aoki, S. Yamamoto, P. Goppelt-Langer, H. Naramoto, Y. Horino, Y. Mokuno, and K. Fujii: "L X-ray spectra of Fe and Cu by 0.75 MeV/u H, He, Si and Ar ion impacts", Nucl. Instrum. Methods Phys. Res. B **107**, 47–50 (1996).
- I. Tanihata and Y. Awaya: "RI Beam Facilities for 21-century", (in Japanese), Parity **11**, 39–41 (1996).
- K. Kowari: "Electron degradation and thermalization in H₂ gas", Phys. Rev. A **53**, 853–866 (1996).
- M. Kimura, S. Suzuki, N. Shimakura, J. P. Gu, G. Hirsch, R. J. Buenker, and I. Shimamura: "Charge transfer in collisions of B²⁺ (²S, ²P) and B³⁺ (¹S) ions with He atoms below 200 keV", Phys. Rev. A **54**, 3029–3035 (1996).
- R. Kadono, R. F. Kiefl, W. A. MacFarlane, and S. R. Dunsiger: "Diffusion and localization of muonium in Na-doped KCl", Phys. Rev. B **53**, 3177–3182 (1996).
- R. Kadono, H. Okajima, A. Yamashita, K. Ishii, T. Yokoo, J. Akimitsu, N. Kobayashi, Z. Hiroi, M. Takano, and K. Nagamine: "Long-range magnetic ordering in the spin ladder compound LaCuO_{2.5} probed by muon-spin-relaxation", Phys. Rev. B **54**, R9628–R9630 (1996).
- J. L. Persson, Q. Hui, Z. J. Jakubek, M. Nakamura, and M. Takami: "Formation of AgHe₂ exciplex in liquid helium", Phys. Rev. Lett. **76**, 1501–1504 (1996).
- K. Ando, Y. Zou, T. Kambara, Y. Nakai, Y. Kanai, M. Oura, Y. Awaya, and T. Tonuma: "Lifetime measurements of some 2p⁵3p and 2p⁵3d levels in Ne-like CrXV and FeXVII", Phys. Scr. **53**, 33–36 (1996).
- N. Shimakura, S. Suzuki, Y. Murakami, J. P. Gu, G. Hirsch, R. J. Buenker, M. Kimura, and I. Shimamura: "Electron capture and target excitation in collisions of B^{q+} and Be^{q+} ions with H and He atoms at energies below 20 keV/u", Phys. Scr. T **62**, 39–42 (1996).
- Y. D. Wang, N. Toshima, and C. D. Lin: "One- and Two-electron processes in collisions of He with 10–5000 keV/amu Be^{q+} (q = 2–4) and B^{q+} (q = 2–5) ions", Phys. Scr. T **62**, 63–68 (1996).
- Z. L. Peng, Y. Itoh, S. Q. Li, and S. J. Wang: "Positron irradiation effects during positron annihilation lifetime measurement", Phys. Status Solidi A **155**, 299–303 (1996).
- K. H. Lee, Y. Itoh, I. Kanazawa, N. Ohshima, T. Nakajyo, and Y. Ito: "Practical usage of a W moderator for slow positron beam production", Phys. Status Solidi A **157**, 93–98 (1996).
- Y. C. Wu, Y. Itoh, and Y. Ito: "Positron annihilation studies on the interaction between hydrogen and defects in nickel", Phys. Status Solidi B **193**, 307–310 (1996).
- S. F. C. O'Rourke, I. Shimamura, and D. S. F. Crothers: "CDW-EIS calculations for recoil ion emission in proton-helium collisions", Proc. R. Soc. London A **452**, 175–184 (1996).
4. Radiochemistry, radiation chemistry, and radiation biology
- S. Y. Chen, S. Ambe, N. Takematsu, and F. Ambe: "Multitracer study on removal mechanisms of metal elements from seawater", Anal. Sci. **12**, 1–6 (1996).
- S. Ambe, M. Iwamoto, H. Maeda, and F. Ambe: "Separation of a multitracer from an Au target irradiated with high-energy heavy ions by means of a supported liquid membrane", Anal. Sci. **12**, 219–224 (1996).
- R. Amano, S. Oishi, S. Enomoto, and F. Ambe: "Biodistribution of trace elements in normal, Al-overloaded and Cd-overloaded mice: An application of the radioactive multitracer technique", Ann. Clin. Lab. Sci. **26**, 531–541 (1996).
- M. Yanaga, S. Enomoto, R. Hirunuma, R. Furuta, K. Endo, A. Tanaka, S. Ambe, M. Tozawa, and F. Ambe: "Multitracer study on uptake and excretion of trace elements in rats", Appl. Radiat. Isot. **47**, 235–240 (1996).
- Y. Kobayashi, T. Okada, Y. Noro, H. Kitazawa, and F. Ambe: "Giant magnetic hyperfine field of Ni²⁺ ions in spinel chromites", Conf. Proc. ICAME-95, edited by I. Ortalli, SIF, Bologna, Vol. 50, pp. 283–286 (1996).
- S. Ambe, T. Okada, and F. Ambe: "Emission Mössbauer studies of ⁵⁷Co²⁺ and ¹¹⁹Sb⁵⁺ adsorbed on γ -Fe₂O₃ and NiFe₂O₄ surfaces", Il Nuovo Cimento D **18**, 313–317 (1996).
- K. Nakagawa, M. Otoda, A. Kimura, D. Nurdawati, K. Tanaka, K. Kimura, and A. Ejiri: "A cluster model to explain the ionization potential and energy positions of photo-current structures of anthracene doped in supercritical xenon as a function of xenon density", J. Electron Spectrosc. Relat. Phenom. **78**, 415–418 (1996).
- K. Kimura: "Decay of core exciton and STE formed at high density in BaF₂ and CsCl single crystals", J. Electron Spectrosc. Relat. Phenom. **79**, 43–46 (1996).
- Y. Yoshida, Y. Kobayashi, K. Hayakawa, K. Yukihiro, H. Häßlein, S. Nasu, J. Nakamura, E. Yagi, Y. Hsia, and F. Ambe: "In-beam mössbauer study of ⁵⁷Fe in solid Ar and Xe", JHP-Suppl. **20**, 359–362 (1996).
- Y. Takahashi, Y. Minai, T. Ozaki, S. Ambe, M. Iwamoto, H. Maeda, F. Ambe, and T. Tominaga: "Multitracer study on the effect of humate formation on the adsorption behavior of metal ions on kaolinite and silica gel", J. Radioanal. Nucl. Chem. **205**, 255–260 (1996).
- S. Ambe, M. Iwamoto, H. Maeda, and F. Ambe: "Multitracer study on adsorption of metal ions on α -Fe₂O₃", J. Radioanal. Nucl. Chem. **205**, 283–289 (1996).
- S. Enomoto, M. Yanaga, R. Hirunuma, K. Endo, S. Ambe, and F. Ambe: "Multitracer study on distribution of carrier-free radioactive isotopes in organs of rats", J. Radioanal. Nucl. Chem. **205**, 291–298 (1996).

- (1996).
- T. Shinonaga, S. Ambe, S. Enomoto, H. Maeda, M. Iwamoto, T. Watanabe, and I. Yamaguchi: "Multitracer study on the behavior of various elements in atmosphere plant-system", *J. Radioanal. Nucl. Chem. Lett.* **212**, 163-172 (1996).
- A. Yokoyama, K. Takesako, T. Saito, H. Baba, Y. Ohkubo, A. Shinohara, and M. Furukawa: "Limiting behavior of target fragmentation in the reaction of lanthanide nuclei induced by heavy projectiles", *J. Radioanal. Nucl. Chem. Lett.* **212**, 451-459 (1996).
- R. Amano, S. Enomoto, M. Nobuta, M. Sakamoto, R. Tsujioka, and F. Ambe: "Bone uptake of vanadium in mice: Simultaneous tracing of V, Se, Sr, Y, Zr, Ru, and Rh using a radioactive multitracer", *J. Trace Elem. Med. Biol.* **10**, 145-148 (1996).
- K. Kimura: "LET-, ionic species-, and temperature-dependence on Auger-free and self-trapped exciton luminescence of ion-irradiated BaF₂ and CsCl single crystals", *Nucl. Instrum. Methods Phys. Res. B* **116**, 57-60 (1996).
- S. Ambe, T. Shinonaga, T. Watanabe, and I. Yamaguchi: "Multitracer study on absorption of radionuclides in atmosphere-plant system", *Proc. Int. Workshop on Improvement of Environmental Transfer Models and Parameters*, edited by M. J. Frissel, R. M. Brown, and S. Uchida, Tokyo, pp. 267-273 (1996).
- K. Matsumoto, T. Watanabe, S. Ambe, and I. Yamaguchi: "Transcuticular translocation of radionuclides on plant leaf surfaces", *Proc. Nuclear Cross-Over Res. Int. Workshop*, Tokyo, pp. 274-280 (1996).
- K. Kimura: "Time and depth resolved measurement of ion tracks in condensed matter", *Proc. 10th Workshop on Radiation Detectors and their uses*, edited by M. Miyajima and S. Sasaki, KEK, Tsukuba, p. 84 (1996).
- T. Abe and S. Yoshida: "Effect of heavy-ion beam on the specific stages of fertilization cycle of plants", *Radiation & Industries* **71**, 63-66 (1996).
- S. Ambe: "Preparation of multitracers", *RIKEN Rev. No. 13*, pp. 3-4 (1996).
- S. Ambe, M. Iwamoto, H. Maeda, and F. Ambe: "Multitracer study on adsorption of metal ions on α -Fe₂O₃", *RIKEN Rev. No. 13*, pp. 9-10 (1996).
- H. Yasuda, S. Ambe, and S. Uchida: "Multitracer study on sorption of platinum group metals onto agricultural soils", *RIKEN Rev. No. 13*, pp. 13-14 (1996).
- S. Y. Chen, S. Ambe, N. Takematsu, and F. Ambe: "Multitracer study on removal mechanisms of metal elements from seawater", *RIKEN Rev. No. 13*, pp. 15-16 (1996).
- S. Ambe, Y. Ohkubo, Y. Kobayashi, M. Iwamoto, H. Maeda, and F. Ambe: "Multitracer study on transport of metal ions in rice and soybean plants", *RIKEN Rev. No. 13*, pp. 17-18 (1996).
- T. Shinonaga, S. Ambe, T. Watanabe, and I. Yamaguchi: "Multitracer study on behavior of various elements in atmosphere-plant system", *RIKEN Rev. No. 13*, pp. 19-20 (1996).
- R. Hirunuma, K. Endo, M. Yanaga, S. Enomoto, B. Liu, S. Ambe, and F. Ambe: "Studies on distribution of radioisotopes in rats using the multitracer technique", *RIKEN Rev. No. 13*, pp. 21-22 (1996).
- M. Yanaga, R. Hirunuma, K. Endo, S. Enomoto, B. Lui, S. Ambe, and F. Ambe: "Uptake and excretion of various elements in rats", *RIKEN Rev. No. 13*, pp. 23-24 (1996).
- R. Amano, S. Oishi, S. Enomoto, and F. Ambe: "Bone accumulation of vanadium: Simultaneous tracing of V, Se, Sr, Y, Zr, Ru, and Rh in mice", *RIKEN Rev. No. 13*, pp. 25-26 (1996).
- S. Enomoto, M. Yanaga, R. Hirunuma, K. Endo, S. Ambe, and F. Ambe: "Metabolic and biochemical studies of trace elements in zinc-deficient rats: Biochemical properties of platinum-group elements", *RIKEN Rev. No. 13*, pp. 27-28 (1996).
- R. Amano, S. Oishi, S. Enomoto, and F. Ambe: "Comparative uptake behavior of trace elements in normal, Al-overloaded and Cd-overloaded mice", *RIKEN Rev. No. 13*, pp. 29-30 (1996).
- S. Enomoto, B. Lui, R. Amano, S. Ambe, and F. Ambe: "Metabolic and pathological studies on rare-earth elements in non-insulin dependent diabetes mellitus model mice", *RIKEN Rev. No. 13*, pp. 31-32 (1996).
- S. Oishi, R. Amano, A. Ando, S. Enomoto, and F. Ambe: "Comparative study on biodistribution of multitracers in LEC and wistar rats", *RIKEN Rev. No. 13*, pp. 33-34 (1996).
- B. Lui, S. Enomoto, S. Ambe, R. G. Weginwar, and F. Ambe: "Study of labeling immunoglobulin G with a multitracer", *RIKEN Rev. No. 13*, pp. 35-36 (1996).

5. Material analysis

- N. Arai, N. Takai, W. Sakamoto, K. Yoshida, and K. Maeda: "Fish otoliths analysis by PIXE: Application to stock determination", *Int. J. PIXE* **5**, 153-157 (1995).
- Y. Ikeda, N. Arai, W. Sakamoto, T. Murayama, K. Maeda, and K. Yoshida: "Preliminary report on the PIXE analysis of the squid statoliths", *Int. J. PIXE* **5**, 159-162 (1995).
- H. Hamanaka, A. Itoh, Y. Kurosawa, K. Hasegawa, and K. Maeda: "Influence of sample charging on satellite spectra of characteristic X-rays from insulating materials", *Proc. 14th Symp. on Materials Science and Engineering Research Center of Ion Beam Technology*, Hosei University, edited by T. Inada, pp. 129-134 (1995).
- N. Arai, W. Sakamoto, and K. Maeda: "Correlation between ambient seawater temperature and strontium-calcium concentration ratios in otoliths of

- red sea bream *Pagrus major*”, *Fisheries Sci.* **62**, 652–653 (1996).
- X. Zhao, Y. Itoh, Y. Aoyagi, T. Sugano, K. Hirata, Y. Kobayashi, T. Ohdaira, R. Suzuki, and T. Mikado: “Positron/positronium annihilation in nanocrystalline silicon thin films”, *J. Radioanal. Nucl. Chem. Article* **211**, 31–38 (1996).
- H. Hamanaka, K. Hasegawa, and K. Maeda: “Study of sample charging effects on satellite spectra of Ca $K\alpha$ by means of high-resolution PIXE”, *Nucl. Instrum. Methods Phys. Res. B* **109/110**, 203–205 (1996).
- J. Kawai, K. Maeda, N. Sakauchi, and I. Konishi: “Strong X-ray emission due to electrification”, *Nucl. Instrum. Methods Phys. Res. B* **109/110**, 206–208 (1996).
- N. Arai, W. Sakamoto, and K. Maeda: “An attempt to analyze fish otoliths by in-air PIXE”, *Nucl. Instrum. Methods Phys. Res. B* **109/110**, 341–344 (1996).
- K. Maeda and H. Hamanaka: “Influence of sample charging on satellite spectra during particle induced X-ray emission analysis”, *Spectrochim. Acta B* **51**, 343–348 (1996).

VIII. LIST OF PREPRINTS

1996

RIKEN-AF-NP

- 218 A. Ono and H. Horinouchi: “Antisymmetrized molecular dynamics of wave packets with stochastic incorporation of Vlasov equation”
- 219 I. Tanihata: “Recent studies with radioactive beams at RIKEN”
- 220 D. Hirata, K. Sumiyoshi, B. V. Carlson, H. Toki, and I. Tanihata: “Triaxial deformation of unstable nuclei in the relativistic mean field theory”
- 221 K. Arai, Y. Ogawa, Y. Suzuki, and K. Varga: “Structure of the mirror nuclei ${}^9\text{Be}$ and ${}^9\text{B}$ in a microscopic cluster model”
- 222 N. Sakamoto: “A study of the d-p elastic scattering at $E_d = 270$ MeV”
- 223 R. L. Jaffe and N. Saito: “QCD selection rules in polarized hadron collisions”
- 224 S. Yamaji, F. A. Ivanyuk, and H. Hofmann: “Variation of transport coefficients for average fission dynamics with temperature and shape”
- 225 M. Honma, T. Mizusaki, and T. Otsuka: “Nuclear shell model by the quantum Monte Carlo diagonalization method”
- 226 N. Saito: “Spin physics with PHENIX detector system at RHIC”
- 227 M. M. Obuti, T. Kobayashi, D. Hirata, Y. Ogawa, A. Ozawa, K. Sugimoto, I. Tanihata, D. Olson, W. Christie, and H. Wieman: “Interaction cross section and radius of the ${}^8\text{B}$ nucleus”
- 228 A. Ozawa, I. Tanihata, T. Kobayashi, Y. Sugahara, O. Yamakawa, K. Omata, K. Sugimoto, D. Olson, W. Christie, and H. Wieman: “Interaction cross-section and radii of light nuclei”
- 229 I. Tanihata: “RI Beam Factory project”
- 230 F. A. Ivanyuk, H. Hofmann, V. V. Pashkevich, and S. Yamaji: “Collective motion at finite excitations in terms of Cassini ovaloids”
- 231 D. Hirata, K. Sumiyoshi, I. Tanihata, Y. Sugahara, T. Tachibana, and H. Toki: “A systematic study of even-even nuclei up to the drip lines within the relativistic mean field framework”
- 232 A. A. Korshennikov, E. A. Kuzmin, E. Yu. Nikolskii, C. A. Bertulani, O. V. Bochkarev, S. Fukuda, T. Kobayashi, S. Momota, B. G. Novatskii, A. A. Ogloblin, A. Ozawa, V. Privora, I. Tanihata, and K. Yoshida: “Elastic and inelastic scattering of exotic nuclei”
- 233 A. A. Korshennikov, E. Yu. Nikolskii, C. A. Bertulani, S. Fukuda, T. Kobayashi, E. A. Kuzmin, S. Momota, B. G. Novatskii, A. A. Ogloblin, A. Ozawa, V. Pribora, I. Tanihata, and K. Yoshida: “Scattering of radioactive nuclei ${}^6\text{He}$ and ${}^3\text{H}$ by proton. Effects of neutron skin and halo in ${}^6\text{He}$, ${}^8\text{He}$, and ${}^{11}\text{Li}$ ”
- 234 S. Kim and S. Ohta: “Quenched KS light hadron mass at $\beta = 6.5$ on a $64 \times 48 \times 3$ lattice”
- 235 A. U. Luccio: “Field map generated matrices for spin tracking”
- 236 A. Ozawa, M. Fujimaki, S. Fukuda, G. Kalnins, S. Momota, T. Suzuki, I. Tanihata, and H. Yamazaki: “Production of a low energy ${}^{12}\text{B}$ beam and observation of its nuclear polarization”

- 237 M. Petrascu, I. Tanihata, T. Kobayashi, A. Isbasescu, H. Petrascu, A. Korshennikov, E. Nikolski, S. Fukuda, H. Kumagai, S. Momota, A. Ozawa, K. Yoshida, C. Bordeanu, I. Lazar, I. Mihai, G. Vaman, and M. Giurgiu: “Neutron pre-emission at the fusion of ^{11}Li halo nuclei with Si target”
- 238 A. Ozawa, M. Fujimaki, S. Hukuda, S. Ito, T. Kobayashi, S. Momota, T. Suzuki, I. Tanihata, and K. Yoshida: “Measurement of the beta-decay branching ratio of ^{17}Ne into the first excited state of ^{17}F ”
- 239 N. D. Dang, A. Arima, T. Suzuki, and S. Yamaji: “Spreading of Gamow-Teller resonance in ^{90}Nb and ^{208}Bi ”
- 240 N. Aoi, K. Yoneda, H. Miyatake, H. Ogawa, Y. Yamamoto, E. Ideguchi, T. Kishida, T. Nakamura, M. Notani, H. Sakurai, T. Teranishi, H. Wu, S. S. Yamamoto, Y. Watanabe, A. Yoshida, and M. Ishihara: “ β -delayed neutron decay of drip line nuclei ^{11}Li and ^{14}Be ”
- 241 N. Aoi, K. Yoneda, H. Miyatake, H. Ogawa, Y. Yamamoto, E. Ideguchi, T. Kishida, T. Nakamura, M. Notani, H. Sakurai, T. Teranishi, H. Wu, S. S. Yamamoto, Y. Watanabe, A. Yoshida, and M. Ishihara: “ β -spectroscopy of ^{11}Li and ^{14}Be : With a β -n- γ ”
- 242 H. Sakurai, N. Aoi, A. Goto, M. Hirai, N. Inabe, M. Ishihara, H. Kobinata, T. Kubo, H. Kumagai, T. Nakagawa, T. Nakamura, M. Notani, Y. Watanabe, Y. Watanabe, and A. Yoshida: “Production and identification of new neutron-rich nuclei, ^{31}Ne and ^{37}Mg , in the reaction $80\text{ A MeV }^{50}\text{Ti} + ^{181}\text{Ta}$ ”
- 243 I. Tanihata: “Planned storage ring facilities in Japan and China”
- 244 M. Wakasugi, M. Hies, N. Inabe, T. Katayama, T. Kubo, H. Okuno, S. Ozawa, I. Tanihata, Y. Watanabe, Y. Yano, and A. Yoshida: “Collinear laser spectroscopy of high-energy Li-like ^{11}B beam”
- 245 H. Sakurai, N. Aoi, D. Beaumel, N. Fukuda, M. Hirai, E. Ideguchi, M. Ishihara, H. Iwasaki, T. Kishida, T. Kubo, H. Kumagai, S. M. Lukyanov, T. Nakamura, M. Notani, Yu. Ts. Oganessian, Yu. E. Penionzhkevich, T. Teranishi, Y. Watanabe, Y. Watanabe, K. Yoneda, and A. Yoshida: “Search for new neutron-rich with a $70\text{ A MeV }^{48}\text{Ca}$ beam”
- 246 A. Yoshida, C. Signorini, T. Fukuda, Y. Watanabe, N. Aoi, M. Hirai, M. Ishihara, H. Kobinata, Y. Mizoi, L. Mueller, Y. Nagashima, J. Nakano, T. Nomura, Y. H. Pu, and F. Scarlassara: “Fusion and breakup at the barrier with ^{11}Be ”
- 247 N. D. Dang, A. Arima, T. Suzuki, and S. Yamaji: “Description of Gamow-Teller resonance in heavy nuclei: Examples with ^{90}Nb and ^{208}Bi ”
- 248 T. Nakamura, T. Motobayashi, Y. Ando, A. Mengoni, T. Nishio, H. Sakurai, S. Shimoura, T. Teranishi, Y. Yanagisawa, and M. Ishihara: “Coulomb excitation of ^{11}Be ”

IX. PAPERS PRESENTED AT MEETINGS

1. Accelerator development and accelerator physics
 - Y. Yano, T. Katayama, and RARF Accelerator Group: "RIKEN RI Beam Factory projector", Tamura Symp. on Accelerator Physics, Austin, U.S.A., Nov. (1995).
 - A. Goto: "On the RI Beam Factory project at RIKEN", 1st Beam Phys. Meet., Uji, Mar. (1996).
 - Y. Batygin, A. Goto, and Y. Yano: "Nonlinear beam dynamics effects in heavy ion transport line", 5th Eur. Part. Accel. Conf. (EPAC '96), Barcelona, Spain, June (1996).
 - Y. Batygin, A. Goto, and Y. Yano: "Suppression of space charge induced beam emittance growth in transport line," 5th Eur. Part. Accel. Conf. (EPAC '96), Barcelona, Spain, June (1996).
 - Y. Batygin, A. Goto, O. Kamigaito, and Y. Yano: "Beam transmission efficiency study at RIKEN RFQ linac", 5th Eur. Part. Accel. Conf. (EPAC '96), Barcelona, Spain, June (1996).
 - Y. Batygin and T. Katayama: "Merging beam-beam collisions at RIKEN RI Beam Factory", 5th Eur. Part. Accel. Conf. (EPAC '96), Barcelona, Spain, June (1996).
 - Y. Batygin and T. Katayama: "Beam-beam interaction of electrons and ions at RIKEN RI Beam Factory", 5th Eur. Part. Accel. Conf. (EPAC '96), Barcelona, Spain, June (1996).
 - A. Goto, Y. Yano, and T. Katayama: "RIKEN RI Beam Factory project," 5th Eur. Part. Accel. Conf. (EPAC '96), Barcelona, Spain, June (1996).
 - O. Kamigaito, A. Goto, Y. Miyazawa, T. Chiba, M. Hemmi, S. Kohara, M. Kase, Y. Batygin, and Y. Yano: "Development of a variable-frequency RFQ linac for the RILAC," 5th Eur. Part. Accel. Conf. (EPAC '96), Barcelona, Spain, June (1996).
 - T. Mitsumoto, A. Goto, T. Kawaguchi, J. W. Kim, Y. Tanaka, T. Kubo, H. Okuno, T. Tominaka, S. Fujishima, and Y. Yano: "Design study of sector magnet for the RIKEN Superconducting Ring Cyclotron (I)", 5th Eur. Part. Accel. Conf. (EPAC '96), Barcelona, Spain, June (1996).
 - T. Nakagawa, J. Arje, Y. Miyazawa, M. Hemmi, M. Kase, T. Kageyama, O. Kamigaito, T. Chiba, N. Inabe, A. Goto, and Y. Yano: "Development of RIKEN 18 GHz ECRIS", 5th Eur. Part. Accel. Conf. (EPAC '96), Barcelona, Spain, June (1996).
 - M. Okamura, T. Kawaguchi, T. Tominaka, and T. Katayama: "Three dimensional field analysis of helical snake magnets for RHIC", 5th Eur. Part. Accel. Conf. (EPAC '96), Barcelona, Spain, June (1996).
 - H. Okuno, T. Tominaka, T. Kubo, J.-W. Kim, T. Mitsumoto, T. Kawaguchi, Y. Tanaka, S. Fujishima, K. Ikegami, A. Goto, and Y. Yano: "Design study of the injection system of the RIKEN Superconducting Ring Cyclotron", 5th Eur. Part. Accel. Conf. (EPAC '96), Barcelona, Spain, June (1996).
 - Y. N. Rao and T. Katayama: "Intrabeam scattering of heavy ion in DSR", 5th Eur. Part. Accel. Conf. (EPAC '96), Barcelona, Spain, June (1996).
 - Y. N. Rao, K. Ohtomo, and T. Katayama: "Electron cooling at ACR", 5th Eur. Part. Accel. Conf. (EPAC '96), Barcelona, Spain, June (1996).
 - K. Yoshida and T. Katayama: "Expected luminosity at MUSES", 5th Eur. Part. Accel. Conf. (EPAC '96), Barcelona, Spain, June (1996).
 - Y. J. Yuan, K. Ohtomo, and T. Katayama: "Simulation of rf stacking combined with cooling effects", 5th Eur. Part. Accel. Conf. (EPAC '96), Barcelona, Spain, June (1996).
 - J. W. Xia and T. Katayama: "Lattice for accumulator cooler ring for MUSES", 5th Eur. Part. Accel. Conf. (EPAC '96), Barcelona, Spain, June (1996).
 - O. Kamigaito, A. Goto, Y. Miyazawa, T. Chiba, M. Hemmi, S. Kohara, M. Kase, Y. Batygin, and Y. Yano: "Development of a folded-coaxial RFQ linac for the RILAC", 18th Int. Linac Conf. (LINAC96), Geneva, Switzerland, Aug. (1996).
 - A. Goto, Y. Miyazawa, M. Hemmi, O. Kamigaito, T. Nakagawa, M. Kase, T. Chiba, N. Inabe, S. Kohara, T. Kageyama, Y. Batygin, and Y. Yano: "New pre-injector system of the RILAC for the RIKEN RI Beam Factory project", 6th China-Japan Joint Symp. on Accelerator for Nuclear Science and Their Applications, Chengtu, China, Oct. (1996).
 - A. Goto, Y. Yano, and T. Katayama: "RIKEN RI Beam Factory project", 6th China-Japan Joint Symp. on Accelerator for Nuclear Science and Their Applications, Chengtu, China, Oct. (1996).
 - M. Kase, A. Goto, T. Kageyama, I. Yokoyama, M. Nagase, S. Kohara, T. Nakagawa, N. Inabe, K. Ikegami, O. Kamigaito, J. Fujita, and Y. Yano: "Status report on RIKEN Ring Cyclotron", 6th China-Japan Joint Symp. on Accelerator for Nuclear Science and Their Applications, Chengtu, China, Oct. (1996).
 - J. W. Kim, S. Fujishima, A. Goto, T. Kawaguchi, T. Kubo, T. Mitsumoto, H. Okuno, T. Tominaka, and Y. Yano: "Design study of sector magnet for the RIKEN Superconducting Ring Cyclotron", Fall Meet. Korean Phys. Soc., Seoul, Korea, Oct. (1996).
 - Y. Batygin, A. Goto, and Y. Yano: "Nonlinear matcher for prevention of emittance growth in space charge dominated beams", 14th Int. Conf. on Application of Accelerators in Research and Industry, Univ. North Texas, Denton, U.S.A. Nov. (1996).
2. Nuclear physics and nuclear instrumentation
 - Y. S. Mochizuki: "Glitch problems: Superfluidity and nuclei inside neutron stars", Seminar at Dept. As-

- tronomy, Univ. Tokyo, Tokyo, Nov. (1995).
- Y. S. Mochizuki, K. Oyamatsu, and T. Izuyama: "Glitch problems: Superfluidity and nuclei inside neutron stars", Workshop on Astrophysics with Line X- and γ -Rays (IV), Sagami-hara, Nov.–Dec. (1995).
- N. Saito: "Spin physics with PHENIX detector system at RHIC", Adriatico Res. Conf. on Trends in Collider Spin Physics, Trieste, Italy, Dec. (1995).
- N. Saito: "Spin physics with PHENIX detector system at RHIC", RIKEN Symp. on Spin Structure of the Nucleon, Wako, Dec. (1995).
- T. Kohno: "Experimental facility available at current and future RIKEN", Workshop on high and ultra-high energy neutrino astrophysics, Irkutsk, Russia, Dec. (1995).
- T. Kishida: "Production of high spin isomer beam", Grant-in-Aid Symp. on Science of Short-lived Nuclear Beam, Tanashi, Jan. (1996).
- T. Motobayashi, N. Iwasa, T. Kikuchi, Y. Ando, M. Kurokawa, S. Moriya, H. Murakami, T. Nishio, J. Ruan (Gen), S. Shimoura, S. Shirato, T. Uchibori, Y. Yanagisawa, N. Inabe, M. Ishihara, T. Kubo, Y. Watanabe, M. Hirai, T. Nakamura, H. Sakurai, T. Teranishi, S. Kubono, M. Gai, R. H. France III, K. I. Hahn, Z. Zhao, Y. Futami, K. Furutaka, Th. Delbar, C. Michotte, and P. Lipnik: "Coulomb excitation measurement for ${}^7\text{Be}(p,\gamma){}^8\text{B}$ and missing-solar-neutrino problem", Int. Symp. on Origin of Matter and Evolution of Galaxies in the Universe, Atami, Jan. (1996).
- S. Yamaji: "The temperature dependence of the friction in the fission", Specialists' Meet. on Frontier in Nuclear Fission Research Basic Science and Technology, Kumatori, Jan. (1996).
- H. Miyatake, T. Shimoda, M. Sasaki, T. Shirakura, N. Aoi, K. Asahi, H. Ueno, H. Izumi, H. Ogawa, A. Yoshida, and G. Liu: "Delayed neutron spectroscopy with using spin polarized RI Beam", Specialists' Res. Meet. on Scientific and Engineering Researches of Unstable Nuclei and on Their Nuclear Methodology, Res. Reactor Inst., Kyoto Univ., Kyoto, Jan. (1996).
- H. Miyatake, M. Sasaki, H. Ueno, T. Shimoda, N. Aoi, T. Shirakura, K. Asahi, H. Izumi, H. Ogawa, G. Liu, and A. Yoshida: "Delayed neutron spectroscopy with using spin-polarized neutron-rich nuclei beam", Symp. on Science with Radioactive Nuclear Beams, INS, Tokyo, Jan. (1996).
- Y. Gono: "Recent development of gamma detector for nuclear spectroscopy and multi-detectors", 15th RCNP Osaka Int. Symp. on Nuclear Physics Frontiers with Electro-Weak Probes, Osaka, Mar. (1996).
- T. Motobayashi: "Coulomb breakup of ${}^8\text{B}$ and S -factor", 15th RCNP Osaka Int. Symp. on Nuclear Physics Frontiers with Electro-Weak Probes, Osaka, Mar. (1996).
- T. Kishida: "Summary", RIKEN Symp. on γ -ray spectroscopy and exotic nuclear beams, Wako, Mar. (1996).
- E. Kim, T. Nakamura, A. Konno, M. Imamura, T. Shibata, S. Shibata, N. Nakao, Y. Uwamino, N. Nakanishi, and S. Tanaka: "Measurements of neutron spallation cross sections", 1996 Spring Meet. At. Energy Soc. Jpn., Suita, Mar. (1996).
- T. Matsuzaki, K. Ishida, S. Nakamura, I. Watanabe, N. Kawamura, M. Tanase, K. Kurosawa, M. Koto, M. Hashimoto, and K. Nagamine: "Muon catalyzed fusion experiment at RIKEN-RAL Muon Facility", 1st Workshop of Neutron Science Research Program, Tokai, Mar. (1996).
- K. Asahi: "Physics and applications of stopped radioactive nuclei", 51st Ann. Meet. Phys. Soc. Jpn., Kanazawa, Mar.–Apr. (1996).
- T. Horibata, M. Oi, and N. Onishi: "Two-dimensional GCM calculation of TAR states", 51st Ann. Meet. Phys. Soc. Jpn., Kanazawa, Mar.–Apr. (1996).
- T. Kishida: "Study by using the merging beam facility", 51st Ann. Meet. Phys. Soc. Jpn., Kanazawa, Mar.–Apr. (1996).
- T. Kohno et al.: "International collaboration program of cosmic ray observation on board the first Brazilian scientific micro satellite", 51st Ann. Meet. Phys. Soc. Jpn., Kanazawa, Mar.–Apr. (1996).
- M. Kurokawa, T. Motobayashi, H. Murakami, Y. Iwata, T. Uchibori, T. Nomura, J. C. Jeong, Y. Tagaya, M. Wada, N. Ikeda, S. Kubono, I. Katayama, K. Morita, Y. H. Pu, A. Yoshida, Y. Nagai, H. Kudo, K. Sueki, H. Nakahara, T. Shinozuka, M. Fujioka, H. Miyatake, Y. Fujita, T. Shimoda, and K. Tanikawa: "Alpha decay of the evaporation residues produced by the ${}^{40}\text{Ar}+{}^{232}\text{Th}$ reaction", 51st Ann. Meet. Phys. Soc. Jpn., Kanazawa, Mar.–Apr. (1996).
- A. Mengoni: "Neutron capture reactions and the structure of light nuclei", 51st Ann. Meet. Phys. Soc. Jpn., Kanazawa, Mar.–Apr. (1996).
- M. Mihara, M. Fukuda, T. Fukao, M. Tanigaki, T. Onishi, K. Matsuta, Y. Nojiri, T. Minamisono, T. Ohtsubo, M. Ishihata, T. Nakamura, S. Fukuda, S. Ito, T. Kobayashi, S. Momota, A. Ozawa, T. Suzuki, I. Tanihata, and K. Yoshida: "Reaction cross section of ${}^8\text{B}$ ", 51st Ann. Meet. Phys. Soc. Jpn., Kanazawa, Mar.–Apr. (1996).
- Y. Mizoi, T. Fukuda, Y. Matsuyama, J. Nakano, T. Miyachi, H. Kobinata, Y. Watanabe, Y. Watanabe, A. Yoshida, H. Sakurai, and K. Kimura: "Development and research of the new MUSIC detector", 51st Ann. Meet. Phys. Soc. Jpn., Kanazawa, Mar.–Apr. (1996).
- Y. S. Mochizuki, T. Izuyama, and K. Oyamatsu: "Nuclear fusion induced by superfluid vortices in the neutron star crusts", 51st Ann. Meet. Phys. Soc. Jpn., Kanazawa, Mar.–Apr. (1996).
- T. Motobayashi, T. Kikuchi, N. Iwasa, Y. Ando, M. Kurokawa, S. Moriya, H. Murakami, T. Nishio, J. Ruan (Gen), S. Shirato, S. Shimoura, T. Uchibori, Y. Yanagisawa, T. Kubo, H. Sakurai, T. Teranishi,

- Y. Watanabe, M. Ishihara, M. Hirai, T. Nakamura, S. Kubono, M. Gai, R. France III, K. I. Hahn, Th. Delbar, P. Lipnik, and C. Michotte: "Coulomb dissociation of ^8B (2)", 51st Ann. Meet. Phys. Soc. Jpn., Kanazawa, Mar.-Apr. (1996).
- T. Motobayashi: "Nuclear astrophysics at the RI Beam Factory", 51st Ann. Meet. Phys. Soc. Jpn., Kanazawa, Mar.-Apr. (1996).
- N. Nishimori, K. Sagara, T. Fujita, F. Wakamatsu, H. Akiyoshi, T. Bussaki, K. Tsuruta, H. Nakamura, K. Maeda, and T. Nakashima: "Comparison between A_y of n-d and p-d scatterings at 12 MeV", 51st Ann. Meet. Phys. Soc. Jpn., Kanazawa, Mar.-Apr. (1996).
- M. Oi, N. Onishi, and T. Horibata: "Angular momentum projection of the tilted axis rotating states", 51st Ann. Meet. Phys. Soc. Jpn., Kanazawa, Mar.-Apr. (1996).
- K. Oyamatsu and Y. S. Mochizuki: "The equation of state of nuclear matter and the moment of inertia of the neutron star crust", 51st Ann. Meet. Phys. Soc. Jpn., Kanazawa, Mar.-Apr. (1996).
- A. Ozawa, S. Ito, T. Kobayashi, T. Suzuki, I. Tanihata, S. Fukuda, M. Fujimaki, S. Momota, K. Yoshida, G. Münzenberg, and G. Kraus: "Measurement of β -decay branching ratio of ^{17}F into the first excited state of ^{17}O ", 51st Ann. Meet. Phys. Soc. Jpn., Kanazawa, Mar.-Apr. (1996).
- Y. H. Pu, K. Morita, M. G. Hies, O. K. Lee, A. Yoshida, T. Nomura, Y. Tagaya, T. Uchibori, T. Motobayashi, Y. Minemura, T. Ariga, K. Sueki, and A. Shin: "Synthesis of new isotope ^{196}Rn by heavy-ion reactions", 51st Ann. Meet. Phys. Soc. Jpn., Kanazawa, Mar.-Apr. (1996).
- T. Uesaka, T. Wakui, M. Wakasugi, and Y. Yano: "Development of polarized ^3He target at RIKEN (II)", 51st Ann. Meet. Phys. Soc. Jpn., Kanazawa, Mar.-Apr. (1996).
- M. Wakasugi: "Measurement of nuclear charge radii and electromagnetic moments at MUSES", 51st Ann. Meet. Phys. Soc. Jpn., Kanazawa, Mar.-Apr. (1996).
- Y. Yanagisawa, T. Motobayashi, S. Shimoura, K. Ieki, Y. Ando, H. Murakami, Y. Iwata, T. Kikuchi, T. Nishio, S. Moriya, T. Nakamura, T. Teranishi, N. Aoi, M. Notani, H. Ishihara, and J. Péter: "Coulomb excitation of ^{56}Ni ", 51st Ann. Meet. Phys. Soc. Jpn., Kanazawa, Mar.-Apr. (1996).
- K. Yoneda, N. Aoi, H. Miyatake, H. Ogawa, Y. Yamamoto, E. Ideguchi, T. Kishida, T. Nakamura, M. Notani, H. Sakurai, T. Teranishi, S. S. Yamamoto, Y. Watanabe, A. Yoshida, and M. Ishihara: "Beta decay of ^{11}Li ", 51st Ann. Meet. Phys. Soc. Jpn., Kanazawa, Mar.-Apr. (1996).
- A. Yunoki, T. Katoh, H. Okada, K. Terasawa, N. Fukuda, T. Kozu, J. Kikuchi, T. Doke, K. Masuda, E. Shibamura, I. Tanihata, and M. Kase: "Development of a LAr ionization chamber with excellent energy resolution for heavy ion energy measurement", 51st Ann. Meet. Phys. Soc. Jpn., Kanazawa, Mar.-Apr. (1996).
- A. Mengoni, T. Otsuka, T. Nakamura, and M. Ishihara: "Exotic properties of light nuclei and their neutron capture cross sections", Int. Seminar on Interaction of Neutrons with Nuclei, Dubna, Russia, Apr. (1996).
- A. Mengoni: "Photon production and absorption in light nuclei", 2nd Res. Co-ordination Meet. on Measurement, Calculation and Evaluation of Proton Production Data, IAEA, Vienna, Austria, May (1996).
- Y. S. Mochizuki: "Glitch problems: Superfluidity and nuclei inside neutron stars", Seminar at Coll. Art Sci., Univ. Tokyo, Tokyo, May (1996).
- A. Mengoni, T. Otsuka, T. Nakamura, and M. Ishihara: "Exotic structure of light nuclei and their neutron capture reaction rates", Int. Conf. Nuclei in the Cosmos, Notre Dame, U.S.A., June (1996).
- N. Aoi, K. Yoneda, H. Miyatake, H. Ogawa, Y. Yamamoto, E. Ideguchi, T. Kishida, T. Nakamura, M. Notani, H. Sakurai, T. Teranishi, H. Wu, S. S. Yamamoto, Y. Watanabe, A. Yoshida, and M. Ishihara: " β -spectroscopy of ^{11}Li and ^{14}Be ", 4th Int. Conf. on Radioactive Nuclear Beams (RNB-4), Omiya, June (1996).
- Y. S. Mochizuki, K. Oyamatsu, and T. Izuyama: "A microscopic model for the origin of neutron star glitches", 4th Int. Conf. on Radioactive Nuclear Beams (RNB-4), Omiya, June (1996).
- T. Motobayashi, T. Kikuchi, N. Iwasa, Y. Ando, M. Kurokawa, S. Moriya, H. Murakami, T. Nishino, J. Ruan (Gen), S. Shirato, S. Shimoura, T. Uchibori, Y. Yanagisawa, T. Kubo, H. Sakurai, T. Teranishi, Y. Watanabe, M. Ishihara, M. Hirai, T. Nakamura, S. Kubono, M. Gai, R. France III, K. I. Hahn, Th. Delbar, P. Lipnik, and C. Michotte: "New measurement of ^8B Coulomb dissociation and E2 component", 4th Int. Conf. on Radioactive Nuclear Beams (RNB-4), Omiya, June (1996).
- K. Oyamatsu and Y. S. Mochizuki: "Symmetry energy at subnuclear densities and nuclei in neutron star crusts", 4th Int. Conf. on Radioactive Nuclear Beams (RNB-4), Omiya, June (1996).
- H. Sakurai et al.: "Search for new neutron-rich nuclei with a 70 A MeV ^{48}Ca beam", 4th Int. Conf. on Radioactive Nuclear Beams (RNB-4), Omiya, June (1996).
- S. Shimoura, T. Teranishi, Y. Ando, M. Hirai, N. Iwasa, T. Kikuchi, S. Moriya, T. Motobayashi, T. Murakami, T. Nakamura, T. Nishino, H. Sakurai, T. Uchibori, Y. Watanabe, Y. Yanagisawa, and M. Ishihara: "Charge exchange reaction of the neutron-halo nucleus ^{11}Li ", 4th Int. Conf. on Radioactive Nuclear Beams (RNB-4), Omiya, June (1996).
- T. Suzuki: "Nuclear radii of Na and Mg isotopes". 4th Int. Conf. on Radioactive Nuclear Beams (RNB-4), Omiya, June (1996).
- Y. S. Mochizuki: "Glitch problems: Superfluidity and

- nuclei inside neutron stars”, Seminar at Adv. Res. Center for Sci. Eng., Waseda Univ., Tokyo, June (1996).
- T. Motobayashi: “Measurement of the E2-component in the Coulomb dissociation of ^8B ”, 4th Int. Symp. on Nuclear Astrophysics (NIC96), Notre Dame, U.S.A., June (1996).
- Y. Gono, T. Morikawa, T. Kishida, E. Ideguchi, T. Murakami, S. Mitarai, A. Odahara, M. Kidera, M. Shibata, H. Tsuchida, H. Watanabe, M. Oshima, H. Kusakari, M. Sugawara, H. Y. Wu, and M. Ishihara: “High-spin isomer beams at RIKEN”, Int. Workshop on Isomeric Beams: Why and How? GANIL, Caen, France, June (1996).
- T. Kishida, Y. Gono, E. Ideguchi, T. Morikawa, M. Kidera, M. Shibata, H. Tsuchida, K. Miyazaki, H. Watanabe, H.-Y. Wu, A. Tanokura, S. S. Yamamoto, A. Yoshida, S. Mitarai, A. Odahara, T. Murakami, M. Oshima, H. Kusakari, M. Sugawara, M. Kubo, T. Murata, M. Shimura, H. Kumagai, and M. Ishihara: “High spin isomer beam line at RIKEN”, Conf. on Nuclear Structure at the Limits, Argonne, U.S.A., July (1996).
- N. Aoi, K. Yoneda, H. Miyatake, H. Ogawa, Y. Yamamoto, E. Ideguchi, T. Kishida, T. Nakamura, M. Notani, H. Sakurai, T. Teranishi, H. Wu, S. S. Yamamoto, Y. Watanabe, A. Yoshida, and M. Ishihara: “ β -delayed neutron decay of drip line nuclei ^{11}Li and ^{14}Be ”, Int. Conf. on Nuclear Structure around the Turn of the Century, Crete, Greece, July (1996).
- K. Tanaka and K. Sugawara-Tanabe: “Origin of the $\Delta I=2$ staggering in superdeformed states”, Int. Conf. on Nuclear Structure around the Turn of the Century, Crete, Greece, July (1996).
- K. Sugawara-Tanabe: “Magnetic dipole transitions in superdeformed shape nuclei”, Int. Conf. on Nuclear Structure around the Turn of the Century, Crete, Greece, July (1996).
- Y. S. Mochizuki: “Glitch problems: Superfluidity and nuclei inside neutron stars”, Seminar at Cosmic Radiation Lab., RIKEN, Wako, July (1996).
- T. Kohn: “Radiation measurements with Japanese spacecraft”, Seminar at Univ. Alabama Huntsville, Huntsville, U.S.A., July (1996).
- A. Mengoni, T. Otsuka, T. Nakamura, and M. Ishihara: “Halo structure of ^{11}Be from its Coulomb dissociation”, Gull Lake Conf. on Nuclear Physics near the Drip Lines, Gull Lake, U.S.A., Aug. (1996).
- T. Suzuki: “Matter radii of Na and Mg isotopes”, Talk Presented in Physics of Unstable Nuclear Beams, São Paulo, Brazil, Aug. (1996).
- E. Kim, T. Nakamura, M. Imamura, T. Shibata, S. Shibata, N. Nakao, Y. Uwamino, S. Tanaka, and Y. Nakane: “Measurements of neutron spallation cross sections (2)”, 1996 Fall Meet. At. Energy Soc. Jpn., Sendai, Sept. (1996).
- K. Yuasa-Nakagawa, T. Nakagawa, K. Yoshida, K. Furutaka, K. Matsuda, Y. Futami, X. Liu, Y. Aoki, S. M. Lee, J. Kasagi, D. X. Jiang, T. Suomijarvi, W. Q. Shen, T. Wada, S. Yamaji, and Y. Abe: “Dynamical effect and angular momentum dependence of fission phenomena in medium mass nuclei”, 3rd Int. Conf. on Dynamical Aspects of Nuclear Fission, Casta-Papiernicka, Slovak Republic, Sept. (1996).
- M. Wakasugi, M. Hies, N. Inabe, T. Katayama, T. Kubo, H. Okuno, S. Ozawa, I. Tanihata, Y. Watanabe, Y. Yano, and A. Yoshida: “Collinear laser spectroscopy of high-energy Li-like ^{11}B beam”, 8th Int. Conf. on the Physics of Highly Charged Ions (HCI-96), Omiya, Sept. (1996).
- M. Wakamatsu: “BARYON structure based on the SU(3) chiral quark soliton model”, 13th Int. Seminar on High Energy Physics Problem, Dubna, Russia, Sept. (1996).
- I. I. Balitsky, V. M. Braun, Y. Koike, and K. Tanaka: “ Q^2 evolution of chiral-odd twist-3 distributions $h_L(x, Q^2)$ and $e(x, Q^2)$ in the large- N_c limit”, 12th Int. Symp. on High-Energy Spin Physics, Amsterdam, The Netherlands, Sept. (1996).
- H. En’yo: “Spin physics at RHIC”, 12th Int. Symp. on High-Energy Spin Physics, Amsterdam, The Netherlands, Sept. (1996).
- N. Hayashi, Y. Goto, and N. Saito: “Possible measurements of the gluon polarization in the nucleon with the PHENIX detector system”, 12th Int. Symp. on High-Energy Spin Physics, Amsterdam, The Netherlands, Sept. (1996).
- M. Hirai, S. Kumano, and M. Miyama: “Numerical solution of NLO Q^2 evolutions equations for spin-dependent structure functions”, 12th Int. Symp. on High-Energy Spin Physics, Amsterdam, The Netherlands, Sept. (1996).
- Y. Koike and N. Nishiyama: “ Q^2 -evolution of chiral-odd twist-3 structure function and fragmentation function: $e(x, Q^2)$ and $\hat{e}(z, Q^2)$ ”, 12th Int. Symp. on High-Energy Spin Physics, Amsterdam, The Netherlands, Sept. (1996).
- N. Saito: “Measurements of anti-quark polarizations with PHENIX detector system at RHIC”, 12th Int. Symp. on High-Energy Spin Physics, Amsterdam, The Netherlands, Sept. (1996).
- T. Yamanishi and T. Morii: “Test of Δg in spin correlations between target protons and produced Λ^+c at the COMPASS experiments”, 12th Int. Symp. on High-Energy Spin Physics, Amsterdam, The Netherlands, Sept. (1996).
- A. Arima, N. Dinh Dang, T. Suzuki, and S. Yamaji: “Study of Gamow-Teller resonance in ^{208}Pb taking $1p1h$ - $2p2h$ configuration mixing and ground-state correlations beyond RPA into account”, Int. Symp. on Non-Nucleonic Degrees of Freedom Detected in Nucleus, Osaka, Sept. (1996).
- A. Ozawa, M. Fujimaki, S. Fukuda, G. Kalnins, S. Momota, T. Suzuki, I. Tanihata, and H. Yamazaki: “Production of a low energy ^{12}B beam and observa-

- tion of its nuclear polarization”, Int. Symp. on Non-nucleonic Degree of Freedom Detected in Nucleus, Osaka, Sept. (1996).
- H. Kurasawa and T. Suzuki: “Nuclear response to electromagnetic field”, Int. Symp. on Non-nucleonic Degrees of Freedom Detected in Nucleus, Osaka, Sept. (1996).
- M. Hirai, S. Kumano, and M. Miyama: “Numerical solution for Q^2 -evolution equations”, RHIC-SPIN Meet., Marseille, France, Sept. (1996).
- S. Kumano: “Light antiquark flavor asymmetry $\bar{u}-\bar{d}$ ”, RHIC-SPIN Meet., Marseille, France, Sept. (1996).
- T. Kohno: “Scientific programs on Japanese experiment module”, Round Table of Int. Sch. Space Science, L’Aquila, Italy, Sept. (1996).
- Y. Goto: “PHENIX studies on direct photons”, RSC Ann. Meet., Marseille, France, Sept. (1996).
- N. Hayashi: “Gluon spin via charmonium production at PHENIX”, RSC Ann. Meet., Marseille, France, Sept. (1996).
- N. Saito: “Physics probes W and Z: PHENIX studies”, RSC Ann. Meet., Marseille, France, Sept. (1996).
- N. Saito: “New theoretical ideas A_{TT}/A_{LL} ”, RSC Ann. Meet., Marseille, France, Sept. (1996).
- Y. Gono, T. Morikawa, T. Kishida, E. Ideguchi, T. Murakami, S. Mitarai, A. Odahara, M. Kidera, M. Shibata, H. Tsuchida, H. Watanabe, M. Oshima, H. Kusakari, M. Sugawara, H. Y. Wu, and M. Ishihara: “A germanium counter telescope for studies of high-spin states with HSIB”, 7th Franco-Japonais Colloq. on Frontier and Perspective of Nuclear Science, Dogashima, Sept.–Oct. (1996).
- N. Saito: “RHIC spin project”, Circum-Pan-Pacific Workshop on High Energy Spin Physics, Kobe, Oct. (1996).
- H. Okamura, T. Uesaka, T. Wakasa, Y. Satou, T. Ohnishi, T. Nonaka, H. Sakai, S. Ishida, N. Sakamoto, T. Ichihara, T. Niizeki, and H. Ohnuma: “ $^{90}\text{Zr}(\vec{d}, \vec{d}')^{90}\text{Y}$ reaction at 270 MeV”, 1996 Fall Meet. APS Division of Nuclear Physics, Cambridge, U.S.A., Oct. (1996).
- Y. Satou: “Measurement of the $^{12}\text{C}(\vec{d}, \vec{d}')$ reaction at $E_d = 270$ MeV”, 1996 Fall Meet. APS Division of Nuclear Physics, Cambridge, U.S.A., Oct. (1996).
- Y. S. Mochizuki: “Vortex pinning to nuclei in neutron star crusts”, Fall Meet. Astron. Soc. Jpn., Mizusawa, Oct. (1996).
- T. Ariga, M. G. Hies, M. Wakasugi, K. Morita, Y. Pu, W. G. Jin, T. Murayama, T. Ishizuka, H. Katsuragawa, and T. Inamura: “Development of an on-line laser ion source using resonance ionization at RIKEN GARIS/IGISOL”, 1996 Fall Meet. Phys. Soc. Jpn., Saga, Oct. (1996).
- M. Fukuda, M. Mihara, T. Fukao, M. Tanigaki, T. Onishi, K. Matsuta, Y. Nojiri, T. Minamisono, T. Ohtsubo, S. Fukuda, S. Ito, T. Kobayashi, S. Momota, A. Ozawa, T. Suzuki, I. Tanihata, K. Yoshida, M. Ishihara, and T. Nakamura: “Reaction cross sections for ^8B and its density distribution”, 1996 Fall Meet. Phys. Soc. Jpn., Saga, Oct. (1996).
- T. Horibata, M. Oi, and N. Onishi: “Two-dimensional GCM calculation of TAR states II”, 1996 Fall Meet. Phys. Soc. Jpn., Saga, Oct. (1996).
- E. Ideguchi, Y. Gono, S. Mitarai, T. Morikawa, A. Odahara, M. Kidera, M. Shibata, H. Tsuchida, T. Kishida, M. Oshima, Y. Hatsukawa, S. Hamada, H. Iimura, T. Ishii, and M. Ishihara: “High-spin states in ^{146}Eu ”, 1996 Fall Meet. Phys. Soc. Jpn., Saga, Oct. (1996).
- T. Matsuzaki, K. Ishida, S. N. Nakamura, I. Watanabe, K. Nagamine, N. Kawamura, M. Iwasaki, M. Tanase, M. Kato, K. Kurosawa, G. H. Eaton, P. Wright, R. Hall, D. Haynes, W. A. Morris, G. Thomas, and H. J. Jones: “Muon catalyzed fusion experiment in D-T mixture at RIKEN-RAL Muon Facility (1): Experimental facility”, 1996 Fall Meet. Phys. Soc. Jpn., Saga, Oct. (1996).
- K. Ishida, T. Matsuzaki, S. N. Nakamura, K. Nagamine, N. Kawamura, S. Sakamoto, M. Tanase, M. Kato, K. Kurosawa, and G. H. Eaton: “Muon catalyzed fusion experiment in D-T mixture at RIKEN-RAL Muon Facility (2): X-ray measurement of α -sticking probability”, 1996 Fall Meet. Phys. Soc. Jpn., Saga, Oct. (1996).
- N. Kawamura, T. Matsuzaki, K. Ishida, S. N. Nakamura, K. Nagamine, S. Sakamoto, M. Tanase, M. Kato, K. Kurosawa, K. Kudo, and G. H. Eaton: “Muon catalyzed fusion experiment in D-T mixture at RIKEN-RAL Muon Facility (3): Fusion neutron measurement”, 1996 Fall Meet. Phys. Soc. Jpn., Saga, Oct. (1996).
- T. Kubota and M. Wakamatsu: “ISOSPIN asymmetry of $q\bar{q}$ sea in the nucleon based on the chiral quark soliton model”, 1996 Fall Meet. Phys. Soc. Jpn., Saga, Oct. (1996).
- T. Matsuzaki, K. Nagamine, K. Ishida, S. Nakamura, I. Watanabe, N. Kawamura, M. Iwasaki, M. Tanase, K. Kurosawa, M. Kato, M. Hashimoto, G. H. Eaton, P. Wright, R. Hall, D. Haynes, W. A. Moriis, G. Thomas, and H. J. Jones: “Experimental apparatus for advanced DT muon catalyzed fusion research at RIKEN-RAL Muon Facility”, 1996 Fall Meet. Phys. Soc. Jpn., Saga, Oct. (1996).
- M. Mihara, M. Fukuda, T. Fukao, M. Tanigaki, T. Onishi, K. Matsuta, Y. Nojiri, T. Minamisono, T. Ohtsubo, M. Ishihata, T. Nakamura, S. Fukuda, S. Ito, T. Kobayashi, S. Momota, A. Ozawa, T. Suzuki, I. Tanihata, K. Yoshida, and Y. Ogawa: “Momentum distribution of ^7Be produced in ^8B fragmentation”, 1996 Fall Meet. Phys. Soc. Jpn., Saga, Oct. (1996).
- Y. S. Mochizuki, T. Izuyama, and I. Tanihata: “A model for nuclear fusion induced by superfluid vortices in neutron star crusts”, 1996 Fall Meet. Phys. Soc. Jpn., Saga, Oct. (1996).
- M. Notani et al.: “Search for new neutron-rich nuclei

- with a 70 A MeV ^{48}Ca beam”, 1996 Fall Meet. Phys. Soc. Jpn., Saga, Oct. (1996).
- M. Oi, N. Onishi, N. Tajima, and T. Horibata: “Riemann surface for the Euler angle space of overlap kernel of TAR state”, 1996 Fall Meet. Phys. Soc. Jpn., Saga, Oct. (1996).
- T. Onishi, K. Matsuta, M. Fukuda, M. Mihara, M. Sasaki, T. Yamaguchi, T. Miyake, K. Sato, K. Minamisono, Y. Nojiri, T. Minamisono, T. Otsubo, A. Ozawa, S. Fukuda, S. Momota, K. Yoshida, T. Suzuki, T. Kobayashi, I. Tanihata, G. F. Krebs, J. R. Alonso, and T. J. M. Symons: “Electric quadrupole moment of ^{23}Mg ”, 1996 Fall Meet. Phys. Soc. Jpn., Saga, Oct. (1996).
- K. Oyamatsu: “From masses and radii of unstable nuclei to the neutron star structure”, 1996 Fall Meet. Phys. Soc. Jpn., Saga, Oct. (1996).
- S. Ozawa, T. Ariga, M. G. Hies, N. Inabe, T. Katayama, T. Kubo, H. Okuno, I. Tanihata, M. Wakasugi, Y. Watanabe, Y. Yano, and A. Yoshida: “Collinear laser spectroscopy of $^{11}\text{B}^{2+}$ ”, 1996 Fall Meet. Phys. Soc. Jpn., Saga, Oct. (1996).
- H. Sato, M. Tsuda, A. Yoshimi, K. Sakai, M. Adachi, K. Asahi, H. Izumi, H. Ogawa, N. Kurokawa, H. Okuno, T. Kubo, S. Fukuda, A. Yoshida, M. Ishihara, K. Yoneda, and M. Notani: “Polarization of short-lived nuclei by means of polarized ^{129}Xe solid stopper”, 1996 Fall Meet. Phys. Soc. Jpn., Saga, Oct. (1996).
- Y. Suzuki, K. Arai, Y. Ogawa, and K. Varga: “Occupation probability of harmonic-oscillator quanta for microscopic cluster-model wave functions”, 1996 Fall Meet. Phys. Soc. Jpn., Saga, Oct. (1996).
- M. Tsuda, H. Sato, A. Yoshimi, K. Sakai, M. Adachi, and K. Asahi: “Polarization of ^{129}Xe by means of diode-laser optical pumping”, 1996 Fall Meet. Phys. Soc. Jpn., Saga, Oct. (1996).
- M. Wakamatsu: “EXTENDED Nambu-Jona-Lasinio model and hidden local symmetry of low energy QCD”, 1996 Fall Meet. Phys. Soc. Jpn., Saga, Oct. (1996).
- A. Yunoki, T. Katoh, Y. Piau, K. Ozaki, H. Okada, K. Terasawa, J. Kikuchi, T. Doke, K. Masuda, E. Shibamura, I. Tanihata, M. Kase, and M. Niimura: “Development of a LAr ionization chamber with excellent energy resolution for heavy ion energy measurement II”, 1996 Fall Meet. Phys. Soc. Jpn., Saga, Oct. (1996).
- K. Asahi: “Test of time-reversal violation with polarized ^{129}Xe ”, 1996 Fall Meet. Phys. Soc. Jpn., Yamaguchi, Oct. (1996).
- T. Kohno: “Summary of scientific satellite OHZORA”, Int. Standard Org. 5th ISO/TC20/SC14/WG4 Meet., Pasadena, U.S.A., Oct. (1996).
- A. Mengoni, T. Otsuka, T. Nakamura, and M. Ishihara: “Neutron capture and neutron halos”, Int. Symp. on Capture γ -Ray Spectroscopy and Related Topics, Budapest, Hungary, Oct. (1996).
- T. Nakagawa, K. Yuasa-Nakagawa, K. Yoshida, K. Furutaka, K. Matsuda, Y. Futami, X. Liu, Y. Aoki, S. M. Lee, J. Kasagi, D. X. Jiang, T. Suomijarvi, W. Q. Shen, T. Wada, S. Yamaji, and Y. Abe: “Angular momentum dependence of pre-scission time and mass distribution for medium mass nuclei”, Int. Symp. on Large-scale Collective Motion of Atomic Nuclei, Brolo, Italy, Oct. (1996).
- K. Oyamatsu: “Nuclei in nuclear reactors and stars”, Specialists’ Meet. on Frontier in Nuclear Fission Research, Basic Science and Technology, Res. Reactor Inst., Kyoto University, Kyoto, Oct. (1996).
- T. Kohno: “Other scientific proposal for JEM”, Symp. on Space Station Experiment JEM-EC for Cosmic Nuclei, Tokyo, Oct. (1996).

3. Atomic and solid-state physics

- L. Engström, R. Hutton, S. Huldt, I. Kink, I. Martinson, B. Nyström, K. Ando, Y. Awaya, P. Bengtsson, T. Kambara, Y. Kanai, T. M. Kojima, and Y. Nakai: “The lifetime of the $3s3p\ ^3P_1$ level of high Z Mg-like ions”, Ann. Meet. Swedish Phys. Soc., Uppsala, Sweden, Nov. (1995).
- K. Kimura: “Time- and depth-resolved measurements of ion tracks in condensed matter”, Symp. on Radiation Detectors and Their Uses, Tsukuba, Jan. (1996).
- Y. Kobayashi, Y. Yoshida, J. Nakamura, K. Yukihiro, K. Hayakawa, S. Nasu, E. Yagi, Y. Watanabe, A. Yoshida, N. Aoi, M. Ishihara, N. Inabe, M. Kase, A. Goto, Y. Yano, and F. Ambe: “Mössbauer spectroscopy using a ^{57}Mn beam from the RIPS of RIKEN Ring Cyclotron”, Symp. on Science with Radioactive Nuclear Beams, Tanashi, Jan. (1996).
- Y. Yoshida, Y. Kobayashi, K. Hayakawa, K. Yukihiro, K. Häflein, S. Nasu, J. Nakamura, E. Yagi, Y. Hsia, and F. Ambe: “In-beam Mössbauer Study of ^{57}Fe in Solid Ar and Xe”, Symp. on Science with Radioactive Nuclear Beams, Tanashi, Jan. (1996).
- A. Igarashi: “Muon-transfer reaction between hydrogenic atoms in excited states $t + d\mu (n = 2) \rightarrow t\mu (n = 2) + d$ ”, 4th RIKEN Symp. on the Theory of Atomic and Molecular Processes, Wako, Jan. (1996).
- M. Kimura: “What would cross sections for heavy-particle collisions behave below MeV regime?”, 4th RIKEN Symp. on the Theory of Atomic and Molecular Processes, Wako, Jan. (1996).
- J. Z. Tang: “Dynamics of atoms in liquid helium”, 4th RIKEN Symp. on the Theory of Atomic and Molecular Processes, Wako, Jan. (1996).
- P. Bengtsson: “Spectroscopy of heavy-highly-charged ions using beam-foil method”, RIKEN Symp. on Studies on Condensed Matter Physics, Atomic Physics, Nuclear Chemistry, and Biology and Medicine Using RIKEN Accelerators, Wako, Feb. (1996).

- T. Kambara: "Comments on RIKEN accelerator future projects from non-nuclear physics fields", RIKEN Symp. on Studies on Condensed Matter Physics, Atomic Physics, Nuclear Chemistry, and Biology and Medicine Using RIKEN Accelerators, Wako, Feb. (1996).
- Y. Kanai: "Experimental study of ion-atom collisions by using low energy ions from ECRIS", RIKEN Symp. on Studies on Condensed Matter Physics, Atomic Physics, Nuclear Chemistry, and Biology and Medicine Using RIKEN Accelerators, Wako, Feb. (1996).
- M. Matsuda and T. Kambara: "Heavy-ion irradiation effects of high-temperature superconductors", RIKEN Symp. on Studies on Condensed Matter Physics, Atomic Physics, Nuclear Chemistry, and Biology and Medicine Using RIKEN Accelerators, Wako, Feb. (1996).
- Y. Kobayashi, Y. Yoshida, J. Nakamura, K. Yukihiro, K. Hayakawa, S. Nasu, E. Yagi, Y. Watanabe, A. Yoshida, N. Aoi, M. Ishihara, N. Inabe, M. Kase, A. Goto, Y. Yano, R. Sielemann, H. Häßlein, A. Feinauer, and F. Ambe: "In-beam Mössbauer spectroscopy in RIKEN accelerator research facility", RIKEN Symp. on Studies on Condensed Matter Physics, Atomic Physics, Nuclear Chemistry, and Biology Using RIKEN Ring Cyclotron, Wako, Feb. (1996).
- Y. Awaya and Y. Kanai: "Impact parameter dependence of double-electron capture processes in low-energy highly-charge ion collisions", Symp. on the Physics of Highly-Charged Ions, Niigata, Mar. (1996).
- I. Watanabe, K. Kumagai, S. Nakajima, K. Nagase, T. Matsuzaki, S. N. Nakamura, and K. Nagamine: " μ^+ SR study on the magnetic properties of Tl- and La-systems high-TC superconductor", Workshop on the Neutron Science Projects, JAERI, Mar. (1996).
- P. Bengtsson, K. Ando, T. Kambara, Y. Kanai, T. M. Kojima, Y. Nakai, Y. Awaya, L. Engström, R. Hutton, I. Kink, I. Martinson, and B. Nyström: "Intercombination lines in highly charged ions", 51st Ann. Meet. Phys. Soc. Jpn., Kanazawa, Mar.-Apr. (1996).
- R. Hutton, L. Engström, S. Huldt, B. Nyström, I. Martinson, K. Ando, P. Bengtsson, T. Kambara, T. M. Kojima, Y. Nakai, and Y. Awaya: "Observation of a systematic deviation between experimental and theoretical lifetimes for the $3s3p\ ^3P_1$ level of high Z Mg-like ions", 51st Ann. Meet. Phys. Soc. Jpn., Kanazawa, Mar.-Apr. (1996).
- A. Igarashi: "Theoretical study of positron scattering by atoms", 51st Ann. Meet. Phys. Soc. Jpn., Kanazawa, Mar.-Apr. (1996).
- Y. Kanai, Y. Nakai, K. Soejima, T. M. Kojima, T. Kambara, and Y. Awaya: "Present status of the RIKEN 14.5 GHz ECRIS", 51st Ann. Meet. Phys. Soc. Jpn., Kanazawa, Mar.-Apr. (1996).
- S. Kaneko, H. Sawada, H. Sakata, N. Nishida, T. Mochiku, K. Kadowaki, T. Kambara, and Y. Awaya: "Investigations of boundary effects in high-Tc superconductors using LT-STs", 51st Ann. Meet. Phys. Soc. Jpn., Kanazawa, Mar.-Apr. (1996).
- K. Kimura, T. Morita, Y. Yoshioka, W. Sekiguchi, M. Iimura, and W. Hon: "Bragg curve of near-liquid rare gasses", 51st Ann. Meet. Phys. Soc. Jpn., Kanazawa, Mar.-Apr. (1996).
- T. M. Kojima, M. Bannister, X.-Q. Guo, and G. Dunn: "Electron-impact dissociation of DCO^+ into CO^+ fragment", 51st Ann. Meet. Phys. Soc. Jpn., Kanazawa, Mar.-Apr. (1996).
- J. Nakamura, I. Watanabe, K. Asai, H. Anbe, and K. Nagamine: " $\text{Fe}_{1.15}\text{Sb}$ studied by μ^+ SR", 51st Ann. Meet. Phys. Soc. Jpn., Kanazawa, Mar.-Apr. (1996).
- T. Okada, Y. Noro, Y. Kobayashi, H. Kitazawa, J. Nakamura, and F. Ambe: "Relation between the hyperfine magnetic field of ^{61}Ni and crystal distortion II", 51st Ann. Meet. Phys. Soc. Jpn., Kanazawa, Mar.-Apr. (1996).
- H. Takeuchi, H. Sato, J. Z. Tang, M. Kimura, and I. Shimamura: "Potential-energy curves of the alkali-He and alkaline-earth-He systems", 51st Ann. Meet. Phys. Soc. Jpn., Kanazawa, Mar.-Apr. (1996).
- Y. Tamagawa, M. Kagawa, D. Chiba, R. Yamamoto, K. Wakiya, T. Takayanagi, Y. Kanai, and Y. Awaya: "Study of multiply excited highly charged ions formed by collisions with neutral atoms using toroidal electron energy analyzer", 51st Ann. Meet. Phys. Soc. Jpn., Kanazawa, Mar.-Apr. (1996).
- J. Z. Tang, M. Kimura, and I. Shimamura: "Dynamics of alkali atoms in liquid helium", 51st Ann. Meet. Phys. Soc. Jpn., Kanazawa, Mar.-Apr. (1996).
- G. Tataru, M. Matsuda, K. Katsumata, T. Kambara, Y. Awaya, T. Mitamura, M. Terasawa, Y. Endoh, K. Yamada, and S. Hosoya: "Heavy-ion irradiation effect on mixed state of $\text{La}_{1.85}\text{Sr}_{0.15}\text{CuO}_4$ single crystal", 51st Ann. Meet. Phys. Soc. Jpn., Kanazawa, Mar.-Apr. (1996).
- K. Uematsu, H. Sato, M. Kimura, and I. Shimamura: "Computations of doubly excited electronic states of the H_2 molecules", 51st Ann. Meet. Phys. Soc. Jpn., Kanazawa, Mar.-Apr. (1996).
- N. Watanabe, T. Kambara, Y. Nakai, T. M. Kojima, and Y. Awaya: "Recoil ion momentum spectroscopy in 6 MeV B^{4+} -He collisions", 51st Ann. Meet. Phys. Soc. Jpn., Kanazawa, Mar.-Apr. (1996).
- I. Watanabe, S. Nakajima, K. Nagase, T. Matsuzaki, S. N. Nakamura, and K. Nagamine: " μ SR on $\text{TlBa}_2\text{Y}_{1-x}\text{Ca}_x\text{Cu}_2\text{O}_y$ in the magnetically ordered phase", 51st Ann. Meet. Phys. Soc. Jpn., Kanazawa, Mar.-Apr. (1996).
- I. Watanabe, S. Nakajima, K. Nagase, T. Matsuzaki, S. N. Nakamura, and K. Nagamine: " μ SR on related materials to high-TC superconductors (2)", 51st Ann. Meet. Phys. Soc. Jpn., Kanazawa, Mar.-Apr. (1996).

- E. Yagi and S. Koike: "State of hydrogen in Nb-Mo alloys", 51st Ann. Meet. Phys. Soc. Jpn., Kanazawa, Mar.-Apr. (1996).
- A. Yamashita, H. Okajima, K. Ishii, J. Akimitsu, R. Kadono, N. Kobayashi, Z. Hiroi, M. Takano, and K. Nagamine: " μ SR on $\text{LaCuO}_{2.5}$ ", 51st Ann. Meet. Phys. Soc. Jpn., Kanazawa, Mar.-Apr. (1996).
- J. Akimitsu, H. Okajima, A. Yamashita, K. Ishii, T. Yokoo, R. Kadono, N. Kobayashi, Z. Hiroi, M. Takano, and K. Nagamine: "Appearance of long range magnetic ordering in the spin ladder compound $\text{LaCuO}_{2.5}$ ", 7th Int. Conf. on Muon Spin Rotation/Relaxation/Resonance, Nikko, Apr. (1996).
- T. Briere, T. P. Das, R. Kadono, A. Matsushita, and K. Nagamine: "Structure and associated hyperfine properties of hydrogenic centers in potassium bromide", 7th Int. Conf. on Muon Spin Rotation/Relaxation/Resonance, Nikko, Apr. (1996).
- R. Kadono, R. M. Macrae, K. Nishiyama, and K. Nagamine: "Muonium centers in crystalline Ge under illumination", 7th Int. Conf. on Muon Spin Rotation/Relaxation/Resonance, Nikko, Apr. (1996).
- R. Kadono, R. M. Macrae, and K. Nagamine: "Muonium centers in heavily n-doped Si under illumination: Evidence for Mu-hole interaction", 7th Int. Conf. on Muon Spin Rotation/Relaxation/Resonance, Nikko, Apr. (1996).
- R. Kadono, I. Watanabe, and K. Nagamine: "Quantum diffusion of positive muon in pure tantalum", 7th Int. Conf. on Muon Spin Rotation/Relaxation/Resonance, Nikko, Apr. (1996).
- R. M. Macrae, R. Kadono, F. L. Pratt, K. Tanigaki, K. Nishiyama, and K. Nagamine: "Longitudinal field repolarization studies of reorientational dynamics in the fullerenes C_{60} and C_{70} ", 7th Int. Conf. on Muon Spin Rotation/Relaxation/Resonance, Nikko, Apr. (1996).
- M. Matsuda, K. Katsumata, I. Watanabe, and K. Nagamine: " μ SR measurements of BaNiO_3 ", 7th Int. Conf. on Muon Spin Rotation/Relaxation/Resonance, Nikko, Apr. (1996).
- I. Watanabe, S. Nakajima, K. Nagase, T. Matsuzaki, S. N. Nakamura, and K. Nagamine: "Observation of magnetic ordered state in $\text{TlBa}_2\text{Y}_{1-x}\text{Ca}_x\text{Cu}_2\text{O}_y$ by μ^+ SR", 7th Int. Conf. on Muon Spin Rotation/Relaxation/Resonance, Nikko, Apr. (1996).
- Y. Kobayashi, Y. Yoshida, K. Hayakawa, K. Yukihiro, S. Nasu, J. Nakamura, E. Yagi, and F. Ambe: "In-beam Mössbauer spectroscopy in materials science with RI Beam at RIKEN", 4th Int. Conf. on Radioactive Nuclear Beams (RNB-4), Omiya, June (1996).
- Y. Itoh, Z.-L. Peng, Y. Itoh, A. Goto, N. Nakanishi, and M. Kase: "Slow positron production using RIKEN AVF Cyclotron III", 33rd Ann. Meet. on Radioisotopes in the Physical Sciences and Industries, Tokyo, July (1996).
- K. Kimura: "Fast dynamics of core and self-trapped excitons formed at high density in iontracks in BaF_2 and CsCl single crystal", Gordon Res. Conf. on Radiation Chemistry, Newport, U.S.A., July (1996).
- Q. Hui, J. L. Persson, Z. J. Jakubek, M.-P. Coquard, M. Nakamura, and M. Takami: "Formation and dynamics of Ag- He_2 exciplex in liquid helium", 20th Int. Quantum Electronics Conf., Sydney, Australia, July (1996).
- Y. Kasai, N. Yonekura, Q. Hui, M. Nakamura, G. Rouillé, and M. Takami: "Laser spectroscopy of molecules in superfluid helium", 20th Int. Quantum Electronics Conf., Sydney, Australia, July (1996).
- Z. J. Jakubek, Q. Hui, and M. Takami: "Spectroscopy of silver in cold helium gas ($T \approx 4-25$ K)", 20th Int. Quantum Electronics Conf., Satellite Meet., Cairns, Australia, July (1996).
- M. Kimura and I. Shimamura: "Multiple ionization of He and Ne by slow protons and antiprotons", ITAMP Workshop on Exotic Atoms, Harvard, U.S.A., July (1996).
- I. Shimamura: "Introduction: Atomic processes associated with antiprotonic atoms", ITAMP Workshop on Exotic Atoms, Harvard, U.S.A., July (1996).
- I. Watanabe, S. Nakajima, K. Nagase, T. Matsuzaki, S. N. Nakamura, and K. Nagamine: " μ^+ SR study on magnetic ordered state of $\text{TlBa}_2\text{Y}_{1-x}\text{Ca}_x\text{Cu}_2\text{O}_y$ ", 21st Int. Conf. on Low Temperature Physics (LT21), Prague, Czech Republic, Aug. (1996).
- I. Watanabe, S. Nakajima, K. Nagase, T. Matsuzaki, S. N. Nakamura, and K. Nagamine: " μ^+ SR study on superconducting and magnetic ordered states of $\text{TlBa}_2\text{Y}_{1-x}\text{Ca}_x\text{Cu}_2\text{O}_y$ ", Int. Conf. on Physics and Chemistry of Molecular and Oxide Superconductors (MOS'96), Karlsruhe, Germany, Aug. (1996).
- E. Yagi and S. Koike: "Site occupancy change of hydrogen in Nb on alloying with undersized Mo atoms", Int. Symp. on Metal-Hydrogen Systems, Fundamentals and Applications, Les Diablerets, Switzerland, Aug. (1996).
- T. Kambara, A. Igarashi, N. Watanabe, Y. Nakai, T. M. Kojima, and Y. Awaya: "Recoil ion momentum analyses for 0.5-1 MeV/u B - He collisions", 21st Meet. Soc. for Atomic Collision Research, Tokyo, Aug. (1996).
- H. Tsuchida, H. Suzuki, M. Miyabe, M. Imai, A. Itoh, N. Imanishi, Y. Nakai, T. Kambara, and Y. Awaya: "Fragmentation processes of C_{60} by fast charged particles", 21st Meet. Soc. for Atomic Collision Research, Tokyo, Aug. (1996).
- K. Kimura: "Dynamical studies on exciton reactions formed at high-density in some insulator crystals by ion irradiation", 8th Int. Conf. on Phys. of Highly Charged Ions (HCI-96), Omiya, Sept. (1996).
- N. Toshima: "Couple-channel study of collision processes involving highly-charged ions", 8th Int. Conf. on the Physics of Highly Charged Ions (HCI-96), Omiya, Sept. (1996).
- P. Bengtsson, K. Ando, T. Kambara, Y. Awaya, and R.

- Hutton: "Intercombination lines in highly charged ions Al-like and Si-like ions", 8th Int. Conf. on the Physics of Highly Charged Ions (HCI-96), Omiya, Sept. (1996).
- M. Imai, M. Sataka, Y. Yamazaki, K. Komaki, K. Kawatsura, and Y. Kanai: "Electron spectra from highly excited Si ions", 8th Int. Conf. on the Physics of Highly Charged Ions (HCI-96), Omiya, Sept. (1996).
- K. Ishii, T. Nishida, Y. Kimura, M. Fujiwara, T. Nakano, S. Kawae, K. Ando, and T. Kambara: "Beam-foil spectra of highly charged Neon ions in visible region", 8th Int. Conf. on the Physics of Highly Charged Ions (HCI-96), Omiya, Sept. (1996).
- K. Ishii, T. Nishida, Y. Kimura, M. Fujiwara, T. Nakano, S. Kawae, K. Ando, and Y. Awaya: "Beam-foil spectra of highly charged Argon ion in visible region", 8th Int. Conf. on the Physics of Highly Charged Ions (HCI-96), Omiya, Sept. (1996).
- T. Kambara: "Recoil-ion momentum spectroscopy of fast collisions with HCI", 8th Int. Conf. on the Physics of Highly Charged Ions (HCI-96), Omiya, Sept. (1996).
- K. Kawatsura, M. Sataka, M. Imai, K. Komaki, Y. Yamazaki, K. Kuroki, Y. Kanai, and N. Stolterfoht: "Charge state dependence of very low projectile autoionizing transitions from 2 MeV/u S + He collisions", 8th Int. Conf. on the Physics of Highly Charged Ions (HCI-96), Omiya, Sept. (1996).
- M. Kimura, A. B. Sannigrahi, J. P. Gu, G. Hirsch, R. J. Buenker, and I. Shimamura: "Charge transfer in collisions of H⁺ ions with Si atoms below keV energies", 8th Int. Conf. on the Physics of Highly Charged Ions (HCI-96), Omiya, Sept. (1996).
- M. Kimura, S. Suzuki, N. Shimakura, J. P. Gu, G. Hirsch, R. J. Buenker, and I. Shimamura: "Charge transfer in collisions of B²⁺(²S,²P) and B³⁺(¹S) ions with He atoms below 200 keV", 8th Int. Conf. on the Physics of Highly Charged Ions (HCI-96), Omiya, Sept. (1996).
- M. Matsuda, G. Tatara, K. Katsumata, T. Kambara, Y. Awaya, T. Mitamura, M. Terasawa, K. Yamada, Y. Endoh, and S. Hosoya: "Heavy-ion irradiation effects on the single crystal La_{1.85}Sr_{0.15}CuO₄", 8th Int. Conf. on the Physics of Highly Charged Ions (HCI-96), Omiya, Sept. (1996).
- T. Mitamura, M. Terasawa, X. Fan, T. Kohara, K. Ueda, T. Kambara, Y. Awaya, M. Matsuda, and G. Tatara: "Heavy-ion irradiation effects on the super-conducting material, La_{1.85}Sr_{0.15}CuO₄", 8th Int. Conf. on the Physics of Highly Charged Ions (HCI-96), Omiya, Sept. (1996).
- Y. Nakai, A. Itoh, T. Kambara, Y. Bitoh, and Y. Awaya: "Mass correlation of fragment ions in fast C⁵⁺-C₆₀ collision", 8th Int. Conf. on the Physics of Highly Charged Ions (HCI-96), Omiya, Sept. (1996).
- M. Sataka, M. Imai, K. Komaki, Y. Yamazaki, K. Kawatsura, Y. Kanai, H. Tawara, D. R. Schultz, and C. O. Reinhold: "Binary peak electrons observed at 0 degree for 0.5-1.0 MeV/u Ag^{q+} and Au^{q+} ions in collision with a He target", 8th Int. Conf. on the Physics of Highly Charged Ions (HCI-96), Omiya, Sept. (1996).
- Y. Tamagawa, D. Chiba, T. Takayanagi, K. Wakiya, Y. Kanai, T. Kambara, and Y. Awaya: "Toroidal spectrometer for measurement of emitted electron spectra arising from collisions between highly charged ions and neutral atoms", 8th Int. Conf. on the Physics of Highly Charged Ions (HCI-96), Omiya, Sept. (1996).
- J. Akimitsu: "Magnetic ordering in spin ladder compounds", RIKEN Symp. on Muon Science '96, Wako, Sept. (1996).
- K. Ishii, T. Nishida, Y. Kimura, M. Fujiwara, S. Kawae, T. Nakano, K. Ando, and T. Kambara: "Rydberg transitions of highly charged Neon ion in beam-foil collision", 1996 Fall Meet. Phys. Soc. Jpn., Yamaguchi, Oct. (1996).
- K. Kimura, T. Kohama, D. Kawakami, and W. Hon: "Excitation-density and temperature enhanced decay of self-trapped excitons in ion irradiated BaF₂ crystal", 1996 Fall Meet. Phys. Soc. Jpn., Yamaguchi, Oct. (1996).
- K. Kimura: "Depth-differential excimer dynamics along ion tracks of rare gases", Symp. on Phys. of collision of cluster system, 1996 Fall Meet. Phys. Soc. Jpn., Yamaguchi, Oct. (1996).
- M. Kimura, I. Shimamura, J. P. Gu, G. Hirsch, and R. J. Buenker: "Electron capture in H⁺ + C, N, O, Si collisions", 1996 Fall Meet. Phys. Soc. Jpn., Yamaguchi, Oct. (1996).
- A. Koyama, A. Yoneda, K. Ogiwara, and M. Uda: "TEMPERATURE dependence of Al-LVV auger electron spectra I", 1996 Fall Meet. Phys. Soc. Jpn., Yamaguchi, Oct. (1996).
- Y. Nakai: "Fragmentation of C₆₀ by fast ion impact-coincidence measurement with the charge change of projectiles", 1996 Fall Meet. Phys. Soc. Jpn., Yamaguchi, Oct. (1996).
- T. Okada, H. Kitazawa, J. Nakamura, Y. Kobayashi, and F. Ambe: "⁵⁷Fe Mössbauer effect of CuGeO₃", 1996 Fall Meet. Phys. Soc. Jpn., Yamaguchi, Oct. (1996).
- Y. Tamagawa, D. Chiba, T. Takayanagi, K. Wakiya, Y. Kanai, T. Kambara, and Y. Awaya: "Measurements of angular distribution for emitted electron energy analyzer", 1996 Fall Meet. Phys. Soc. Jpn., Yamaguchi, Oct. (1996).
- J. Z. Tang, I. Shimamura, M. Kimura, H. Takeuchi, and H. Sato: "Spectroscopy of alkaline atoms in liquid-He", 1996 Fall Meet. Phys. Soc. Jpn., Yamaguchi, Oct. (1996).
- N. Toshima: "Theory of relativistic ion-atom collisions", 1996 Fall Meet. Phys. Soc. Jpn., Yamaguchi, Oct. (1996).
- T. Wakui, K. Hasegawa, S. Haga, T. Takagi, H.

- Uematsu, W. G. Jin, T. Minowa, H. Katsuragawa, and M. Wakasugi: "Atomic beam diode-laser spectroscopy", 1996 Fall Meet. Phys. Soc. Jpn., Yamaguchi, Oct. (1996).
- X. Fan, M. Terasawa, T. Mitamura, T. Kohara, K. Ueda, H. Tsubakino, T. Kambara, M. Matsumoto, G. Tatara, and Y. Awaya: "Magnetic properties of $\text{La}_{1.85}\text{Sr}_{0.15}\text{CuO}_4$ irradiated by swift heavy-ions", 1996 Fall Meet. Phys. Soc. Jpn., Yamaguchi, Oct. (1996).
- I. Watanabe, S. Nakajima, K. Nagase, T. Matsuzaki, S. N. Nakamura, F. L. Pratt, and K. Nagamine: " μSR on $\text{TlBa}_2\text{Y}_{1-x}\text{Ca}_x\text{Cu}_2\text{O}_y$ in the magnetic and superconducting phase", 1996 Fall Meet. Phys. Soc. Jpn., Yamaguchi, Oct. (1996).
- Z. J. Jakubek, Q. Hui, and M. Takami: "Ag-He interaction in superfluid helium and cold helium gas", 12th Interdisciplinary Laser Sci. Conf., Rochester, U.S.A., Oct. (1996).
- Q. Hui, J. L. Persson, Z. J. Jakubek, M. Nakamura, and M. Takami: "Formation of AgHe_2 exciplex in liquid helium", Int. Symp. on Atomic and Molecular Physics III, Pohang, Korea, Oct. (1996).
- Y. Kasai, Q. Hui, M. Nakamura, and M. Takami: "Detection of macromolecules in superfluid helium by laser induced dispersed fluorescence", Int. Symp. on Atomic and Molecular Physics III, Pohang, Korea, Oct. (1996).
- A. Igarashi: "Scattering of a photon and a positron by atoms", 5th RIKEN Symp. on the Theory of Atomic and Molecular Processes, Yamaguchi, Oct. (1996).
- I. Shimamura: "Theory of electron scattering", 5th RIKEN Symp. on the Theory of Atomic and Molecular Processes, Yamaguchi, Oct. (1996).
- Y. Kobayashi, Y. Yoshida, K. Yukihira, K. Hayakawa, J. Nakamura, E. Yagi, S. Nasu, and F. Ambe: "In-beam Mössbauer spectroscopy in materials science with the RIKEN accelerators", 40th Symp. on Radiochemistry, Wako, Oct. (1996).
- J. Nakamura, T. Okada, Y. Noro, Y. Kobayashi, H. Kitazawa, and F. Ambe: "Correlation between huge hyperfine magnetic field and quadrupole splitting at Jahn-Teller Ni^{2+} ion in $\text{Cu}_{1-x}\text{Ni}_x\text{Cr}_2\text{O}_4$ ", 40th Symp. on Radiochemistry, Wako, Oct. (1996).
- T. Okada, H. Kitazawa, J. Nakamura, Y. Kobayashi, and F. Ambe: " ^{57}Fe Mössbauer spectroscopy of $\text{Cu}_{1-x}\text{Fe}_x\text{GeO}_3$ ", 40th Symp. on Radiochemistry, Wako, Oct. (1996).
- Y. Awaya: "X-rays emitted by heavy ions passing through the target foils", 13th RIKEN Symp. on Atomic Physics Using Accelerators, Wako, Nov. (1996).
- M. Matsuda, T. Kambara, and G. Tatara: "Material irradiation by the Ring Cyclotron", 13th RIKEN Symp. on Atomic Physics Using Accelerators, Wako, Nov. (1996).
- Y. Nakai: "Fragmentation of C_{60} molecule by heavy ion impact", 13th RIKEN Symp. on Atomic Physics Using Accelerators, Wako, Nov. (1996).
- A. Igarashi: "Positron scattering with atoms", Meet. of the Recent Progress in Positron Spectroscopy, Tokyo, Dec. (1996).
- #### 4. Radiochemistry, radiation chemistry, and radiation biology
- S. Ambe, T. Okada, and F. Ambe: "Emission Mössbauer studies of $^{57}\text{Co}^{2+}$ and $^{119}\text{Sb}^{5+}$ adsorbed on $\gamma\text{-Fe}_2\text{O}_3$ and NiFe_2O_4 surfaces", Int. Conf. on the Applications of the Mössbauer Effect, Rimini, Italy, Sept. (1995).
- Y. Takahashi, Y. Minai, T. Ozaki, S. Ambe, M. Iwamoto, H. Maeda, F. Ambe, and T. Tominaga: "Multitracer study on influence of metal-humate complexation on adsorption of trace elements on clay minerals, silica gel, and hematite", Int. Chem. Congr. Pacific Basin Soc. (Pacifichem '95), Honolulu, U.S.A., Dec. (1995).
- S. Yoshida, T. Abe, S. Kumata, and T. Torashima: "Effect of heavy-ion beam on the specific stages of fertilization cycle of plants", 6th Radiation Process Symp., Tokyo, Jan. (1996).
- S. Ambe, T. Shinonaga, T. Watanabe, and I. Yamaguchi: "Multitracer study on absorption of radionuclides in atmosphere-plant system", Int. Workshop on Improvement of Environmental Transfer Models and Parameters, Tokyo, Feb. (1996).
- K. Matsumoto, T. Watanabe, S. Ambe, and I. Yamaguchi: "Absorption and translocation of radionuclides on plant leaf surfaces", 34th Ann. Meet. At. Energy Soc. Jpn., Osaka, Mar. (1996).
- R. Hirunuma, K. Oda, K. Endo, M. Yanaga, S. Enomoto, S. Ambe, and F. Ambe: "The effects of vitamin D on the uptake of trace elements in rats", 116th Ann. Meet. Pharm. Soc. Jpn., Kanazawa, Mar. (1996).
- N. Ito, H. Narita, Y. Saito, K. Kimura, T. Yaita, S. Tachimori, S. Ambe, and F. Ambe: "Substituent effect of N, N-dialkyl aliphatic amides on their extraction of noble metals", 70th Spring Meet. Chem. Soc. Jpn., Tokyo, Mar. (1996).
- S. Enomoto, B. Liu, R. G. Weginwar, S. Ambe, and F. Ambe: "Distribution and pathological studies of rare-earth elements in diabetes mellitus mice", 9th Int. Symp. on Trace Elements in Man and Animals, Banff, Canada, May (1996).
- S. Enomoto, B. Liu, R. G. Weginwar, S. Ambe, and F. Ambe: "Multitracer study on the uptake of inorganic ions by tumor", 9th Int. Symp. on Trace Elements in Man and Animals, Banff, Canada, May (1996).
- S. Enomoto, R. G. Weginwar, B. Liu, S. Ambe, and F. Ambe: "Biodistribution of gold complexes in mice", 9th Int. Symp. on Trace Elements in Man and Animals, Banff, Canada, May (1996).
- R. Hirunuma, K. Endo, S. Enomoto, S. Ambe, and F. Ambe: "The effects of vitamin D on behavior

- of various trace elements in rat”, 8th Symp. on Roles of Metals in Biological Reactions, Biology and Medicine, Hiroshima, May (1996).
- T. Ozaki, S. Enomoto, Y. Minai, S. Ambe, F. Ambe, and T. Tominaga: “STUDY on the accumulation and roles of rare earth element in ferns by multitracer technique and neutron activation analysis”, 8th Symp. on Roles of Metals in Biological Reactions, Biology and Medicine, Hiroshima, May (1996).
- N. Sotogaku, R. Hirunuma, K. Endo, S. Enomoto, S. Ambe, and F. Ambe: “Influence of pH on the metal-binding of various serum-protein investigated by means of multitracer technique”, 8th Symp. on Roles of Metals in Biological Reactions, Biology and Medicine, Hiroshima, May (1996).
- A. Higashi, T. Kanai, H. Tomura, Y. Futami, N. Matsufuji, A. Itano, H. Karashima, and Y. Hishikawa: “Rotatable proton gantry by using wobbler method”, 13th Ann. Meet. Jpn. Assoc. Med. Phys., Suita, July (1996).
- K. Eguchi-Kasai, M. Murakami, H. Itsukaichi, K. Fukutsu, T. Kanai, K. Sato, and F. Yatagai: “DNA repair and cell killing by charged particles”, 31st Sci. Ass. of COSPAR, Birmingham, U.K., July (1996).
- A. Higashi, T. Kanai, H. Tomura, Y. Futami, and N. Matsufuji: “Test experiment by using 160 and 210 MeV proton at RIKEN”, 1st Workshop on Charged Particle Therapy System, Chiba, July (1996).
- M. Suzuki, Y. Kase, T. Kanai, K. Ando, M. Watanabe, and F. Yatagai: “LET dependence of chromatin breakage induced by heavy-ion”, 10th Ann. Meet. Biological Sciences in Space, Kyoto, Sept. (1996).
- R. Hirunuma, K. Endo, S. Enomoto, S. Ambe, and F. Ambe: “Application of the multitracer technique: Effect of vitamin D on distribution of various elements in rats”, 4th Int. Conf. on Nuclear and Radiochemistry, St. Malo, France, Sept. (1996).
- Y. Takahashi, Y. Minai, S. Ambe, H. Maeda, F. Ambe, and T. Tominaga: “Multitracer study on stability constants of humates with various metal ions”, 4th Int. Conf. on Nuclear and Radiochemistry, St Malo, France, Sept. (1996).
- T. Ozaki, S. Enomoto, Y. Minai, S. Ambe, F. Ambe, and T. Tominaga: “STUDY on the trace elements in ferns”, 60th Ann. Meet. Botanic. Soc. Jpn., Fukuoka, Oct. (1996).
- C. H. Bae, T. Abe, and S. Yoshida: “Characteristics of salt-tolerant plants induced by heavy-ion beams irradiation”, 31st Ann. Meet. Soc. Chem. Reg. Plants, Kyoto, Oct. (1996).
- Y. Einaga, O. Sato, T. Iyoda, Y. Kobayashi, F. Ambe, K. Hashimoto, and A. Fujishima: “Mössbauer study on photo-induced and cation driven electron transfer in a cobalt-iron cyanide”, 40th Symp. on Radiochemistry, Wako, Oct. (1996).
- R. Hirunuma, Y. Okamoto, N. Sotogaku, K. Endo, S. Enomoto, S. Ambe, and F. Ambe: “Comparison of behavior of trace elements between vitamin D-overloaded and deficient rats using the multitracer technique”, 40th Symp. on Radiochemistry, Wako, Oct. (1996).
- N. Ito, Y. Okamoto, N. Kimura, H. Narita, T. Yaita, S. Tachimori, S. Ambe, and F. Ambe: “Multitracer study on the extraction of noble metals with N, N-dialkyl aliphatic amides”, 40th Symp. on Radiochemistry, Wako, Oct. (1996).
- T. Ozaki, S. Enomoto, Y. Minai, S. Ambe, F. Ambe, and Y. Makide: “STUDY on the absorption of trace elements into plants by multitracer technique”, 40th Symp. on Radiochemistry, Wako, Oct. (1996).
- K. Mukai, A. Yokohama, S. Morimoto, T. Saito, H. Baba, Y. Ohkubo, A. Shinohara, T. Muroyama, M. Furukawa, and S. Kojima: “Momentum Transfer in the Reaction Systems of $^{14}\text{N} + ^{165}\text{Ho}$ and $^{40}\text{Ar} + ^{141}\text{Pr}$ at Intermediate Energies”, 40th Symp. on Radiochemistry, Wako, Oct. (1996).
- A. Shinohara, T. Muroyama, A. Yokoyama, S. Morimoto, T. Saito, Y. Ohkubo, S. Shibata, S. Kojima, F. Ambe, H. Baba, and M. Furukawa: “Linear Momentum Transfer in the Heavy-Ion Reaction of Copper at Intermediate and High Energies”, 40th Symp. on Radiochemistry, Wako, Oct. (1996).
- N. Sotogaku, R. Hirunuma, K. Endo, S. Enomoto, S. Ambe, and F. Ambe: “The bio-trace element-binding of various serum-protein investigated by means of multitracer technique”, 40th Symp. on Radiochemistry, Wako, Oct. (1996).
- Y. Takahashi, Y. Minai, S. Ambe, F. Ambe, and Y. Makide: “Multitracer study on the interaction of various metal ions with humic acid and polycarboxylic acids”, 40th Symp. on Radiochemistry, Wako, Oct. (1996).
- A. Higashi, T. Kanai, H. Tomura, Y. Futami, and N. Matsufuji: “Experimental results by using 160 and 210 MeV proton beam at RIKEN”, 3rd Workshop on Charged Particle Therapy System, Chiba, Oct. (1996).
- F. Yatagai, Y. Kagawa, M. Hirano, N. Inabe, K. Eguchi-Kasai, Y. Furusawa, M. Suzuki, M. Watanabe, T. Kato, and F. Hanaoka: “Analysis of mutations in the human HPRT gene induced by heavy-ion irradiation”, 25th Ann. Meet. Jpn. Environmental Mutagenesis Soc., Tokyo, Nov. (1996).
- S. Koike, K. Anndou, C. Yujan, T. Ariga, N. Hori, M. Iizuka, T. Kanai, and F. Yatagai: “Skin shrinkage caused by neon-20 and carbon-12”, 39th Ann. Meet. Jpn. Rad. Res. Soc., Osaka, Nov. (1996).
- H. Sasaki, F. Yatagai, Y. Furusawa, T. Kanai, F. Hanaoka, W.-G. Zhu, and P. Meinati: “LET dependence of interphase cell-death induction by accelerated heavy-ions”, 39th Ann. Meet. Jpn. Rad. Res. Soc., Osaka, Nov. (1996).
- S. Tsubouchi, K. Fukutsu, H. Itsukaichi, K. Eguchi-Kasai, Y. Furusawa, M. Murakami, T. Kanai, S. Koike, K. Ando, A. Kawano, S. Matsushita, H. Oohara, F. Yatagai, and E. Kano: “Dose response re-

lations in acute cell death of pancreatic islets after irradiation of golden hamster with X-ray, 70 MeV proton and 290 MeV carbon beams”, 39th Ann. Meet. Jpn. Rad. Res. Soc., Osaka, Nov. (1996).

F. Yatagai, T. Shimazu, Y. Kagawa, M. Hirano, N. Inabe, K. Eguchi-Kasai, Y. Furusawa, M. Suzuki, M. Watanabe, T. Kato, and F. Hanaoka: “Analysis of mutations in the human HPRT gene induced by heavy-ion irradiation II”, 39th Ann. Meet. Jpn. Rad. Res. Soc., Osaka, Nov. (1996).

5. Material analysis

Y. Itoh, H. Murakami, and A. Kinoshita: “Positron/positronium annihilation in low dimensional silicon materials”, Int. Symp. on Si Heterostructures: From Physics to Devices, Crete, Greece, Sept. (1995).

H. Hamanaka, A. Itoh, Y. Kurosawa, K. Hasegawa, and K. Maeda: “PIXE spectra of charged-up samples”, 14th Symp. on Materials Science and Engineering Research Center of Ion Beam Technology, Hosei University, Koganei, Dec. (1995).

W. Hong, S. Hayakawa, K. Maeda, S. Fukuda, M. Yanokura, M. Maeda, K. Kimura, Y. Gohshi, and I. Tanihata: “Development of mass-analyzing method of high resolution, TOF-ERDA using ion beam”, 1996 Fall Meet. Appl. Phys. Soc. Jpn., Urawa, Mar. (1996).

W. Hong, S. Hayakawa, K. Maeda, S. Fukuda, M. Yanokura, M. Aratani, K. Kimura, Y. Gohshi, and

I. Tanihata: “STUDY on high mass resolution ion beam analysis by TOF-ERDA”, 43rd Spring Meet. Jpn. Soc. Appl. Phys. Relat. Soc., Asaka, Mar. (1996).

F. L. Pratt, S. J. Blundell, P. A. Pattenden, W. Hayes, K. H. Chow, A. P. Monkham, T. Ishiguro, K. Ishida, and K. Nagamine: “Spin dynamics in conducting polymers studied by msr”, 7th Int. Conf. on Muon Spin Rotation/Relaxation/Resonance, Nikko, Apr. (1996).

X. Zhao, Y. Itoh, Y. Aoyagi, T. Sugano, K. Hirata, Y. Kobayashi, T. Ohdaira, R. Suzuki, and T. Mikado: “Positron/positronium annihilation in nanocrystalline silicon thin films”, 5th Int. Workshop on Positron and Positronium Chemistry (PPC-5), Lillafüred, Hungary, June (1996).

Y. Itoh, Z. L. Peng, K. H. Lee, A. Goto, N. Nakanishi, M. Kase, and Y. Itoh: “Slow positron beam production by irradiation of p^+ , d^+ , and He^{++} on various targets”, 7th Int. Workshop of Slow Position Beam Study (SLOPOS-7), Unterageri, Switzerland, June (1996).

K. Maeda, H. Hamanaka, and K. Hasegawa: “High resolution PIXE using crystal spectrometers combined with position sensitive detector”, 2nd Int. Symp. on Bio-PIXE, Beijing, China, Aug. (1996).

K. Maeda, H. Hamanaka, and K. Hasegawa: “In-air high-resolution PIXE system”, 14th PIXE Symp., Uji, Oct. (1996).

X. LIST OF SYMPOSIA

(Jan.–Dec. 1996)

- 1) Symp. on Theory of Atomic and Molecular Processes IV
10–11 Jan., Wako, RIKEN, Atomic Physics Lab.
- 2) Symp. on γ -Ray Spectroscopy and Exotic Beams
28 Feb., Wako, RIKEN, Radiation Lab.
- 3) Symp. on Bio-Trace Elements '96
25 Mar., Wako, RIKEN, Nuclear Chemistry Lab.
- 4) 4th Int. Conf. on Radioactive Nuclear Beams
4–7 June, Omiya, RIKEN, Linear Accelerator Lab., Radiation Lab., and Cyclotron Lab.
- 5) Symp. on Nuclear Physics at RI Beam Factory
17 June, Wako, RIKEN, Linear Accelerator Lab.
- 6) Symp. on Theory of Atomic and Molecular Processes V
4–5 Oct., Yamaguchi, RIKEN, Atomic Physics Lab.
- 7) 40th Symp. on Radiochemistry
22–24 Oct., Wako, RIKEN, Nuclear Chemistry Lab.
- 8) Symp. on Development of Positron Application by Using Accelerators
20 Nov., Wako, RIKEN, Cyclotron Lab. and Nuclear Chemistry Lab.
- 9) 13th Symp. on Atomic Physics Using Accelerators
27 Nov., Wako, RIKEN, Atomic Physics Lab.
- 10) Symp. on Nuclear Physics of the 21st Century Opened up by γ -Ray Spectroscopy
25–26 Dec., Wako, RIKEN, Radiation Lab.

XI. LIST OF SEMINARS

(Jan.–Dec. 1996)

Radiation Lab., Cyclotron Lab., and
Linear Accelerator Lab.

- 1) V. Kapin, Kyoto Univ. (Kyoto), 1 Jan.
“Study of RFQ accelerating structures base on multi-conductor transmission line resonators”
- 2) J. Ärje, Univ. Jyväskylä (Finland), 23 Jan.
“Developments and studies at the 18 GHz ECRIS”
- 3) T. Shigetani, Tokyo Metrop. Univ. (Tokyo), 25 Jan.
“Structure functions of hadrons in the QCD effective theory”
- 4) S. H. Lee, Yonsei Univ. (Korea), 5 Feb.
“Instantons and chiral symmetry restoration in QCD with N_f flavors”
- 5) K. Takahashi, Max-Plank-Inst. Tech. Univ. Munich (Germany), 7 Feb.
“Nucleosynthesis of heavy elements and nucleocosmochronology”
- 6) N. Bhattacharya, VECC, Calcutta (India), 14 Feb.
“The superconducting cyclotron project at Calcutta”
- 7) M. Fukuda, JAERI, Takasaki (Gunma), 16 Feb.
“High intensity proton acceleration at the PSI cyclotron facility and simulation of beams using transfer matrices”
- 8) H. Ui, Hiroshima Univ. (Hiroshima), 19 Feb.
“A novel application of spontaneously broken local gauge theory to molecular dynamics: Are corioli and centrifugal force *Fictitious force*?”
- 9) P. von Brentano, Univ. Koeln (Germany), 26 Feb.
“Experiments on multiphonon states in Gamma soft nuclei”
- 10) W.-D. Schmidt-Ott, Univ. Göttingen (Germany), 27 Feb.
“Alignment and polarization measurements for projectile fragmentation at the GSI Energy”
- 11) Colloquium for master’s thesis based on work at Ring Cyclotron in 1995, 13 Mar.
- 12) H. E. Conzett, LBL, Univ. California (U.S.A.), 15 Mar.
“The vanishing analyzing power in ep elastic scattering: Symmetries and dynamics”
- 13) V. W. Hughes, Yale Univ. (U.S.A.), 18 Mar.
“Nucleon spin structure”
- 14) D. Diakonov, St. Petersburg Nuclear Physics Institute (Russia), 25 Mar.
“Baryon number violation at high energies/temperatures/densities in the electroweak theory”
- 15) S. Biri, ATOMIKI, Debrecen (Hungary), 27 Mar.
“(1) Status of the hungarian ECRIS program; (2) Computer simulation of ECRIS magnetic traps”
- 16) D. Bibet, GANIL (France), 27 Mar.
“Status of acceleration facility and the SPIRAL project at GANIL”
- 17) A. Krasznahorkay, Inst. Nucl. Res. Hungarian Acad. Sci. (Hungary), 25 Apr.
“Experimental study of exotic nuclear shapes”
- 18) A. A. Grib, St. Petersburg Univ. Economics and Finance (Russia), 26 Apr.
“Particle creation in the early universe”
- 19) F. Ye, IMP, Lanzhou (China), 15 May
“Operation and improvement of HIRFL”
- 20) P. Bozek, Kyoto Univ. (Kyoto), 28 May
“Observation of the Mott momentum in heavy ion collisions”
- 21) D. Ghose, VECC, Calcutta (India), 30 May
“Helium extraction from thermal spring gases”
- 22) W. von Oertzen, Hahn Meitner Inst. (Germany), 12 June
“Dimers and chain states based on the $\alpha + \alpha$ potential and two-center states in ${}^9\text{Be}$, ${}^{10}\text{Be}$ ”
- 23) I. J. Thompson, Univ. Surrey (U.K.), 20 June
“Few-body structure of halo nuclei”
- 24) H. Shimizu, RIKEN (Saitama), 28 June
“Development of superconducting-tunnel-junction particle detector”
- 25) J. Schubert, MSU, Michigan (U.S.A.), 1 July
“A design of an 8 Tesla superconducting cyclotron”

- 26) E. Hiyama, Kyushu Univ. (Fukuoka), 16 July
“Structure of neutron-rich and proton-rich hyper-nuclei”
- 27) B. Vaishali, VECC, Calcutta (India), 17 July
“Design of ECR ion source for RIB Facility at Calcutta”
- 28) I. J. Thompson, Univ. Surrey (U.K.), 18 July
“Few-body physics for experimentalists”
- 29) A. Luccio, BNL/RIKEN (U.S.A./Saitama), 19 July
“Spin tracking in RHIC”
- 30) S. Hirezaki, Nara Women’s Univ. (Nara), 23 July
“Deeply bound pionic atoms”
- 31) A. van der Woude, KVI (The Netherlands), 29 July
“The isoscalar monopole resonance in cold and hot nuclei”
- 32) T. Kuehl, GSI (Germany), 1 Aug.
“Atomic physics goes full circle”
- 33) H. Sagawa, Univ. Aizu (Fukushima), 5 Aug.
“Single-particle and collective properties of drip line nuclei”
- 34) L. Yixiao, Inst. Modern Phys., Chinese Academy of Science (China), 7 Aug.
“Nuclear physics research in IMP: Studies of hot nuclei and nuclei far from stability”
- 35) W. Yifang, Inst. Modern Physics, Chinese Academy of Sciences (China), 19 Aug.
“Status and upgrade of HIRFL”
- 36) A. Bonasera, INFN, Catania (Italy), 19 Aug.
“Critical chaos”
- 37) A. Ono, Tohoku Univ. (Sendai), 9 Sept.
“Antisymmetrized molecular-dynamics with Vlasov equation and multifragmentation in heavy ion collisions”
- 38) F. Caspers, CERN, Geneva (Switzerland), 18 Sept.
“Recent progress of stochastic cooling”
- 39) S. Kuyucak, Australian Natl. Univ. (Australia), 30 Sept.
“Description of deformed and superdeformed nuclei in the interacting Boson Model”
- 40) A. N. Skrinsky, BINP, Novosibirsk (Russia), 9 Oct.
“Accelerator development at Novosibirsk: Status and prospects”
- 41) M. Kumada, NIRS, Inage (Chiba), 11 Oct.
“Propose of a cyclotron which has quick responses”
- 42) Y. S. Chen, China Inst. Atomic Energy (China), 28 Oct.
“Identical bands and quantized alignment in superdeformed nuclei”
- 43) W. Pelzer, HMI, (Germany), 6 Nov.
“Status of the ISL (Ionen Strahl Lab.) project”
- 44) W. Pelzer, HMI, (Germany), 11 Nov.
“Some design aspects of the ISL accelerators”
- 45) Y. Oganessian, Joint Inst. Nuclear Research (Dubna), 12 Dec.
“Recent study at JINR”
- 46) S. Ben-Hao, China Inst. Atomic Energy (China), 13 Dec.
“(1) Strange antibaryon production data and the reduction of strange quark production in sulphur-nucleus collisions at CERN Energy;
(2) Liquid-gas phase transition and decay mode transformations shown in the decay of projectile remnant in Au + Au reaction at GSI Energy”
- 47) Z. Ma, China Inst. At. Energy/RCNP (China/Osaka), 18 Dec.
“Study of unstable nuclei in relativistic and non-relativistic approaches”
- 48) Z. Ren, Nanjing Univ. (China), 19 Dec.
“Mean-field study on nuclei far from stability”
- 49) Z. Sun, China Institute of Atomic Energy (China), 19 Dec.
“What can we learn from the dimuon measurement for the spin structure of the nucleon with PHENIX?”
- 50) A. Chakrabarti, VECC, Calcutta (India), 25 Dec.
“Design of a 4-rod RFQ linac for VECC-RIB”;
“Reaching the proton drip-line & beyond with low energy proton-rich radioactive ion beam”

Atomic Physics Lab.

- 1) M.-T. Huang, Kansas State Univ. (U.S.A.), 9 Jan.
“Charge capture from Rydberg targets: Comparing experiment with theory”

- 2) A. Warczak, Univ. Cracow (Poland), 25 Jan.
“Radiative electron capture in fast HCl-atom collisions”
- 3) J. Burgdörfer, Univ. Tennessee (U.S.A.), 8 Feb.
“On the relation between double ionization by photons and charged particles”
- 4) J. Eichler, Hahn-Meitner-Institut (Germany), 15 Feb.
“Electron-positron pair production in relativistic collisions between heavy ions”
- 5) J. H. McGuire, Tulane Univ. (U.S.A.), 16 Feb.
“An overview of the dynamics of electron correlations”
- 6) I. L. Baigman, Lebedev Physical Institute (Russia), 16 Feb.
“Semiclassical approach to transitions between Rydberg states induced by collisions with charged particles”
- 7) T. Åberg, Helsinki Univ. Technol. (Finland), 24 Apr.
“Double photoionization and related phenomena in the inner-shell XUV region”
- 8) J. Horacek, Charles Univ., Prague (Czech Republic), 26 Dec.
“Vibrational excitation and dissociative attachment in electron collisions with HBr, DBr, and HI”

Nuclear Chemistry Lab.

- 1) C. Chai, Inst. High Energy Phys. (China), 13 Dec.
“Study of characterization and chemical species of inorganic components in environmental and biological systems by nuclear analysis”

Seminars on Physics at the RI Beam Factory

- 1) Y. Suzuki, Niigata Univ. (Niigata), 29 Jan.
“Shell structure of unstable nuclei in a multi-cluster theory”
- 2) T. Suzuki, RIKEN (Saitama), 26 Feb.
“Nuclear radii of Na and Mg isotopes studied via the interaction cross sections”
- 3) Y. Kanada-En'yo, Kyoto Univ. (Kyoto), 18 Mar.
“Structure of light unstable nuclei studied with AMD”
- 4) T. Otsuka, Univ. Tokyo (Tokyo), 13 May
“New regime of nuclear structure explored by the quantum Monte Carlo Shell Model”
- 5) R. F. Casten, Yale Univ. (U.S.A.), 26 Nov.
“Measurement of key signatures of nuclear structure with radioactive beams by low energy Coulomb excitation”
- 6) K. Takahashi, Max-Planck-Inst. Astrophysics (Germany), 2 Dec.
“Possible RIB and storage ring experiments on heavy nuclei of astrophysical interest- and optimistic view of a theorist”

XII. LIST OF PERSONNEL

RIKEN Accelerator Research Facility

ISHIHARA Masayasu 石原正泰 (Facility Director)
AWAYA Yohko 粟屋容子 (Vice Facility Director)
YANO Yasushige 矢野安重 (Vice Facility Director)

Linac Division

CHIBA Toshiya 千葉利哉
IKEZAWA Eiji 池沢英二
KOHARA Shigeo 小原重夫

HEMMI Masatake 逸見政武
KASE Masayuki 加瀬昌之
MIYAZAWA Yoshitoshi 宮沢佳敏^{*1}

Ring Cyclotron Division

FUJITA Jiro 藤田二郎
IKEGAMI Kumio 池上九三男
KAGEYAMA Tadashi 影山正
KASE Masayuki 加瀬昌之
KUBO Toshiyuki 久保敏幸
NAKAGAWA Takahide 中川孝秀
OKUNO Hiroki 奥野広樹
YOKOYAMA Ichiro 横山一郎

GOTO Akira 後藤彰^{*1}
INABE Naohito 稲辺尚人
KAMIGAITO Osamu 上垣外修一
KOHARA Shigeo 小原重夫
NAGASE Makoto 長瀬誠
OGIWARA Kiyoshi 荻原清
SAKAMOTO Naruhiko 坂本成彦

Experimental Support Division

ICHIHARA Takashi 市原卓
KANAI Yasuyuki 金井保之
KUMAGAI Hidekazu 熊谷秀和
MORITA Kosuke 森田浩介
WATANABE Yasushi 渡邊康

KAMBARA Tadashi 神原正^{*1}
KOBAYASHI Toshio 小林俊雄
MATSUZAKI Teiichiro 松崎禎一郎
OKUBO Yoshitaka 大久保嘉高
YATAGAI Fumio 谷田貝文夫

Radioisotope Facilities Division

AMBE Fumitoshi 安部文敏^{*1}
KOBAYASHI Yoshio 小林義男

IWAMOTO Masako 岩本正子

Radiation Protection Group

FUJITA Shin 藤田新
NAKANISHI Noriyoshi 中西紀喜^{*1}

NAKAJIMA Shunji 中島諄二
UWAMINO Yoshitomo 上蓑義朋

Secretariat

NAKAMURA Toshiko 中村とし子
YOSHIDA Tohru 吉田徹^{*2}

NUMATA Shigeo 沼田茂男

Steering Committee

AMBE Fumitoshi 安部文敏
AWAYA Yohko 粟屋容子
HANAOKA Fumio 花岡文雄
INOUE Yorinao 井上頼直
KAMBARA Tadashi 神原正
KOBAYASHI Toshio 小林俊雄
MATSUOKA Masaru 松岡勝
MIYAZAWA Yoshitoshi 宮沢佳敏
TAKAMI Michio 高見道生
YAGI Eiichi 八木栄一
YATAGAI Fumio 谷田貝文夫
YOSHIDA Tohru 吉田徹

AONO Masakazu 青野正和
GOTO Akira 後藤彰
INAMURA Takashi T. 稲村卓
ISHIHARA Masayasu 石原正泰
KATSUMATA Koichi 勝又紘一
KUMAGAI Noritaka 熊谷教孝
MATSUZAKI Teiichiro 松崎禎一郎
NAGAMINE Kanetada 永嶺謙忠
TANIHATA Isao 谷畑勇夫^{*3}
YANO Yasushige 矢野安重
YOSHIDA Shigeo 吉田茂男

^{*1} Group Leader, ^{*2} Manager, ^{*3} Chairperson

Scientific and Engineering Personnel

Cosmic Radiation Laboratory

KATO Hiroshi 加藤 博

KOHNO Tsuyoshi 河野 毅

(Visitors)

HASEBE Nobuyuki 長谷部信行 (Fac. Gen. Educ., Ehime Univ.)

KASHIWAGI Toshisuke 柏木利介 (Fac. Eng., Kanagawa Univ.)

KATO Chihiro 加藤千尋 (Fac. Sci., Shinshu Univ.)

MUNAKATA Kazuoki 宗像一起 (Fac. Sci., Shinshu Univ.)

MURAKAMI Hiroyuki 村上浩之 (Fac. Sci., Rikkyo Univ.)

NAGATA Katsuaki 永田勝明 (Fac. Eng., Tamagawa Univ.)

NAKAMOTO Atsushi 中本 淳 (Fac. Sci., Rikkyo Univ.)

YAMAGIWA Iwao 山際 巖 (Grad. Sch. Sci. Eng., Saitama Univ.)

YANAGIMACHI Tomoki 柳町朋樹 (Fac. Sci., Rikkyo Univ.)

(Students)

ITO Tomoyuki 伊藤朋行 (Fac. Sci. Eng., Waseda Univ.)

ITSUMI Norifumi 逸見憲史 (Fac. Sci. Eng., Waseda Univ.)

SHINO Tomoaki 篠 智彰 (Fac. Sci. Eng., Waseda Univ.)

TAKASHIMA Takeshi 高島 健 (Fac. Sci. Eng., Waseda Univ.)

Cyclotron Laboratory

ARIGA Takehiro 有賀健博

FUJITA Shin 藤田 新

IKEGAMI Kumio 池上九三男

ISHIDA Satoru 石田 悟

KAGEYAMA Tadashi 影山 正

KASE Masayuki 加瀬昌之

KOHARA Shigeo 小原重夫

KUROKAWA Meiko 黒川明子

NAGASE Makoto 長瀬 誠

NAKAGAWA Takahide 中川孝秀

NAKANISHI Noriyoshi 中西紀喜

OKUNO Hiroki 奥野広樹

PU Yuehu 蒲 越虎

SHIMOSAKA Takuya 下坂琢哉

TAGAYA Yu 多加谷 祐

WAKASUGI Masanori 若杉昌徳

YANO Yasushige 矢野安重^{*3}

FUJITA Jiro 藤田二郎

GOTO Akira 後藤 彰^{*1}

INABE Naohito 稲辺尚人

JIN Wei-Guo 金 衛国

KAMIGAITO Osamu 上垣外修一

KATAYAMA Takeshi 片山武司^{*2}

KUBO Toshiyuki 久保敏幸

MORITA Kosuke 森田浩介

NAKAGAWA Keiko 中川惠子

NAKAJIMA Shunji 中島諄二

OGIWARA Kiyoshi 荻原 清

OTSUKA Takaharu 大塚孝治^{*2}

SAKAMOTO Naruhiko 坂本成彦

SUZUKI Toshio 鈴木敏男^{*2}

UESAKA Tomohiro 上坂友洋

YAMAJI Shuhei 山路修平^{*1}

YOKAYAMA Ichiro 横山一郎

^{*1} Senior Scientist, ^{*2} Senior Visiting Scientist, ^{*3} Chief Scientist

(Visitors)

ABE Yasuhisa 阿部恭久 (Yukawa Inst. Theor. Phys., Kyoto Univ.)

AKUTSU Takao 阿久津亮夫 (NASDA)

AOKI Shiro 青木司郎 (NASDA)

ARAI Eiichi 新井栄一 (Res. Lab. Nucl. React., Tokyo Inst. Technol.)

ARAKAWA Kazuo 荒川和夫 (JAERI, Takasaki Rad. Chem. Res. Estab.)

ARJE Juha (Jyvaskyla Univ., Finland)

BABA Shinji 馬場信次 (NASDA)

CHAKRABARTI Alok (Var. Energy Cyclotron Cen., India)

DATÉ Schin 伊達 伸 (JASRI)

DEAN David (Oak Ridge Natl. Lab., U.S.A.)

EJIRI Hiroyasu 江尻宏泰 (Fac. Sci., Osaka Univ.)

EN'YO Hideto 延与秀人 (Fac. Sci., Kyoto Univ.)

FUJIOKA Manabu 藤岡 学 (Cyclotron Radioisot. Cen., Tohoku Univ.)
 FUJISAWA Takashi 藤沢高志 (Denki Kogyo Co. Ltd.)
 FUJISHIMA Shiro 藤島史郎 (I.H.I.)
 FUJITA Yoshitaka 藤田佳孝 (Fac. Sci., Osaka Univ.)
 FUJIWARA Mamoru 藤原 守 (RCNP, Osaka Univ.)
 FUKUDA Mitsuhiro 福田光宏 (JAERI, Takasaki Rad. Chem. Res. Estab.)
 FUKUMOTO Sadayoshi 福本貞義 (KEK)
 FURUNO Kohei 古野興平 (Tandem Accel. Cen., Univ. Tsukuba)
 FURUSE Kaoru 古瀬 馨 (NASDA)
 FUTAMI Yasuyuki 二見康之 (N.I.R.S.)
 GOKA Tateo 五家建夫 (NASDA)
 HADA Takashi 羽田尚志 (NASDA)
 HAMA Hiroyuki 浜 広幸 (I.M.S.)
 HAMAMOTO Ikuko 浜本育子 (Lund Inst. Technol., Lund Univ., Sweden)
 HARADA Toru 原田 融 (Sapporo Gakuin Univ.)
 HASHIMOTO Miwa 橋本美和 (NASDA)
 HASHIMOTO Osamu 橋本 治 (Inst. Nucl. Study, Univ. Tokyo)
 HATANAKA Kichiji 畑中吉治 (RCNP, Osaka Univ.)
 HATSUKAWA Yuichi 初川雄一 (JAERI, Tokai Res. Estab.)
 HATTORI Toshiyuki 服部俊幸 (Res. Lab. Nucl. React., Tokyo Inst. Technol.)
 HAYANO Ryugo 早野龍五 (Fac. Sci., Univ. Tokyo)
 HEIGUCHI Kazuhiko 平口和彦 (Sch. Medicine, Niigata Univ.)
 HIES Markus G. (Dept. Phys., Mainz Univ., Germany)
 HIRAO Yasuo 平尾泰男 (N.I.R.S.)
 HIROSE Takayuki 広瀬孝幸 (NASDA)
 HONMA Michio 本間道雄 (Aizu Univ.)
 HONMA Toshihiro 本間寿広 (Cyclotron Radioisot. Cen., Tohoku Univ.)
 HORIBATA Takatoshi 堀端孝俊 (Fac. Eng., Aomori Univ.)
 HORIGUCHI Takayoshi 堀口隆良 (Fac. Sci., Hiroshima Univ.)
 HORIUCHI Hisashi 堀内 昶 (Fac. Sci., Kyoto Univ.)
 HOSONO Kazuhiko 細野和彦 (RCNP, Osaka Univ.)
 IGARASHI Toshio 五十嵐敏雄 (NASDA)
 IKEDA Akitsu 池田秋津 (Shizuoka Inst. Sci. & Tech.)
 IKEDA Kiyomi 池田清美 (Fac. Sci., Niigata Univ.)
 IKEDA Nobuo 池田伸夫 (Inst. Nucl. Study, Univ. Tokyo)
 IKEZOE Hiroshi 池添 博 (JAERI, Tokai Res. Estab.)
 IMAI Kenichi 今井憲一 (Fac. Sci., Kyoto Univ.)
 IMAMURA Mineo 今村峯雄 (Inst. Nucl. Study, Univ. Tokyo)
 INOUE Makoto 井上 信 (Inst. Chem. Res., Kyoto Univ.)
 ISHIZUKA Takeo 石塚武男 (Fac. Sci., Saitama Univ.)
 ITO Yasuo 伊藤泰男 (Atomic Energy Res. Cen., Univ. Tokyo)
 IWAMOTO Akira 岩本 昭 (JAERI, Tokai Res. Estab.)
 IWASHITA Yoshihisa 岩下芳久 (Inst. Chem. Res., Kyoto Univ.)
 IZUMOTO Toshiaki 泉本利章 (Coll. Sci., Rikkyo Univ.)
 JEONG S. C. (Inst. Nucl. Study, Univ. Tokyo)
 JIN Weigou 金 衛国 (Fac. Sci., Toho Univ.)
 JYAN Donshin 江 棟興 (Peking Univ., China)
 KAMIMURA Masayasu 上村正康 (Fac. Sci., Kyushu Univ.)
 KAMMURI Tetsuo 冠 哲夫 (Fac. Sci., Osaka Univ.)
 KANAZAWA Mitsutaka 金沢光隆 (N.I.R.S.)
 KATAYAMA Ichiro 片山一郎 (Inst. Nucl. Study, Univ. Tokyo)
 KATO Kiyoshi 加藤幾芳 (Fac. Sci., Hokkaido Univ.)
 KATO Shohei 加藤昌平 (Fac. Sci., Osaka Univ.)
 KATORI Kenji 鹿取謙二 (Fac. Sci., Osaka Univ.)
 KATSURAGAWA Hidetsugu 桂川秀嗣 (Fac. Sci., Toho Univ.)
 KAWAGUCHI Takeo 川口武男 (Mitsubishi Electric Co., Ltd.)
 KAWAI Mitsuji 河合光路 (Fac. Sci., Kyushu Univ.)
 KITAGAWA Hisashi 北川 尚 (Inst. Phys., Univ. Tsukuba)

KOHAMA Akihisa 小濱洋央 (Fac. Sci., Univ. Tokyo)
 KONDO Michiya 近藤道也 (RCNP, Osaka Univ.)
 KOSAKO Toshiso 小佐古敏莊 (Atomic Energy Res. Cen., Univ. Tokyo)
 KOTAJIMA Kyuya 古田島久哉 (Fac. Eng., Tohoku Univ.)
 KUBOYAMA Satoshi 久保山智司 (NASDA)
 KUDO Hisaaki 工藤久昭 (Fac. Sci., Niigata Univ.)
 KUMATA Masayuki 熊田雅之 (N.I.R.S.)
 KUSANO Junichi 草野淳一 (Yuuai Corp.)
 LEE Kong Ok 李康玉 (Rika Women's Coll., Korea)
 LEE Sang Mu 李相茂 (Inst. Phys., Univ. Tsukuba)
 LI Hongling 李洪玲 (RCAST, Univ. Tokyo)
 LI Peng Zi (Wuhan Univ., China)
 MAEDA Kazuhide 前田和秀 (Fac. Sci., Kyushu Univ.)
 MARUMORI Toshio 丸森寿夫 (Fac. Sci. Tech., Sci. Univ. Tokyo)
 MATSUDA Sumio 松田純夫 (NASDA)
 MATSUI Yoshiko 松井芳子 (Fac. Tech., Univ. Tokyo Agri. Tech.)
 MATSUKI Seishi 松木征史 (Inst. Chem. Res., Kyoto Univ.)
 MATSUMOTO Akihiro 松本暁洋 (NASDA)
 MATSUSE Takehiro 松瀬丈浩 (Dept. Phys., Shinshu Univ.)
 MATSUYANAGI Kenichi 松柳研一 (Fac. Sci., Kyoto Univ.)
 MATSUZAKI Kazuhiro 松崎一浩 (NASDA)
 MIDORIKAWA Shoichi 緑川章一 (Fac. Eng., Aomori Univ.)
 MINAMISONO Tadanori 南園忠則 (Fac. Sci., Osaka Univ.)
 MITSUMOTO Toshinori 蜜本俊典 (Sumitomo Heavy Industries, Ltd.)
 MIURA Iwao 三浦岩 (RCNP, Osaka Univ.)
 MIYATAKE Hiroari 宮武宇也 (Fac. Sci., Osaka Univ.)
 MIZOTA Takeshi 溝田武志 (FEL Res. Inst. Inc.)
 MIZUNO Yoshiyuki 水野義之 (RCNP, Osaka Univ.)
 MIZUSAKI Takahiro 水崎高浩 (Fac. Sci., Univ. Tokyo)
 MORI Yoshiharu 森義治 (Inst. Nucl. Study, Univ. Tokyo)
 MUKHOPADHTAY M. (Variable Energy Cyclotron Cen., India)
 MURAKAMI Hideoki 村上英興 (Tokyo Gakugei Univ.)
 MURAKAMI Tetsuya 村上哲也 (Fac. Sci., Kyoto Univ.)
 MURAYAMA Toshiyuki 村山利幸 (Univ. Tokyo, Mercantile Marine)
 MUROYA Shin 室谷心 (Sch. Sci. & Eng., Waseda Univ.)
 MUTO Kazuo 武藤一雄 (Fac. Sci., Tokyo Inst. Technol.)
 NAGAI Yasuki 永井泰樹 (Fac. Sci., Tokyo Inst. Technol.)
 NAGAI Yuki 永井由紀 (NASDA)
 NAITO Ichiro 内藤一郎 (NASDA)
 NAKADA Hitoshi 中田仁 (Coll. Art & Sci., Chiba Univ.)
 NAKAHARA Hiromichi 中原弘道 (Fac. Sci., Tokyo Metrop. Univ.)
 NAKAI Kozi 中井浩二 (KEK)
 NAKAMURA Hiroyuki 中村裕之 (Fac. Sci., Kyushu Univ.)
 NAKAMURA Ichiro 中村市郎 (Fac. Sci., Saitama Univ.)
 NAKAMURA Masao 中村正夫 (NASDA)
 NAKAMURA Takashi 中村尚司 (Cyclotron Radioisot. Cen., Tohoku Univ.)
 NAKAO Noriaki 中尾徳晶 (Inst. Nucl. Study, Univ. Tokyo)
 NGUYEN DINH Dang (Inst. Nucl. Sci. Tech., Vietnam)
 NIIMURA Masanobu 新村正信 (Sch. Sci. & Eng., Waseda Univ.)
 NODA Akira 野田章 (Inst. Chem. Res., Kyoto Univ.)
 NODA Kouji 野田耕司 (N.I.R.S.)
 NOMURA Toru 野村亨 (Inst. Nucl. Study, Univ. Tokyo)
 NOZAKI Tadashi 野崎正 (Kagami Memorial Lab. Materials & Sci., Waseda Univ.)
 OGAWA Kengo 小川健吾 (Fac. Educat., Chiba Univ.)
 OHIRA Hideharu 大平秀春 (NASDA)
 OHKAWA Tomohiro 大川智宏 (Mitsubishi Heavy Industries, Ltd.)
 OHTOMO Kiyotaka 大友清隆 (Sumitomo Heavy Industries, Ltd.)
 OHTSUKI Tsutomu 大槻勤 (Lab. Nucl. Sci., Tohoku Univ.)

OHYA Jiro 大矢次郎 (NASDA)
 OKAMURA Hiroyuki 岡村弘之 (Fac. Sci., Univ. Tokyo)
 OKUMURA Susumu 奥村進 (JAERI, Takasaki Rad. Chem. Res. Estab.)
 ONISHI Naoki 大西直毅 (Coll. Art. Sci., Univ. Tokyo)
 ONO Akira 小野章 (Fac. Sci., Tohoku Univ.)
 ORMAN Erich (Tennessee Univ., U.S.A.)
 OSUGA Toshiaki 大須賀敏明 (Coll. Art & Sci., Chiba Univ.)
 OTA Kiyoshi 太田清 (Fac. Sci., Saitama Univ.)
 QUAN Zhuo-Shu 全卓樹 (Coll. Eng., Hosei Univ.)
 SAGARA Kenshi 相良建至 (Fac. Sci., Kyushu Univ.)
 SAITO Motozo 齊藤始三 (Former Staff of RIKEN)
 SAKAI Hideyuki 酒井英行 (Fac. Sci., Univ. Tokyo)
 SAKATA Fumihiko 坂田文彦 (Inst. Nucl. Study, Univ. Tokyo)
 SATO Ken-ichi 佐藤憲一 (Dept. Phys., Tohoku Coll. Pharm.)
 SATO Kenji 佐藤健次 (RCNP, Osaka Univ.)
 SATO Yukio 佐藤幸夫 (N.I.R.S.)
 SEBE Takashi 瀬部孝 (Coll. Eng., Hosei Univ.)
 SEKINE Toshiaki 関根俊明 (JAERI, Tokai Res. Estab.)
 SHIBATA Tokushi 柴田徳思 (Inst. Nucl. Study, Univ. Tokyo)
 SHIKAZONO Naoya 鹿園直哉 (JAERI, Tokai Res. Estab.)
 SHIMIZU Akira 清水昭 (RCNP, Osaka Univ.)
 SHIMOMURA Kouichiro 下村浩一郎 (Meson Sci. Lab., KEK Brunch, Univ. Tokyo)
 SHIN Kazuo 秦和夫 (Fac. Eng., Kyoto Univ.)
 SHINDO Hiroyuki 新藤浩之 (NASDA)
 SHINOZUKA Tsutomu 篠塚勉 (Cyclotron Radioisot. Cen., Tohoku Univ.)
 SHIRAI Toshiyuki 白井敏之 (Yukawa Inst. Theor. Phys., Kyoto Univ.)
 SHUGYO Shin-ichi 修行新一 (NASDA)
 SUEKI Keisuke 末木啓介 (Fac. Sci., Tokyo Metrop. Univ.)
 SUGAI Isao 菅井勲 (Inst. Nucl. Study, Univ. Tokyo)
 SUGIMOTO Kenji 杉本憲治 (NASDA)
 SUGIYAMA Hiroki 杉山大樹 (NASDA)
 SUMIYOSHI Hiroyuki 住吉広行 (Matsusho-Gakuen Junior Coll.)
 SUZUKI Toshio 鈴木俊夫 (Coll. Sci. Tech., Nihon Univ.)
 TAGISHI Yoshihiro 田岸義宏 (Tandem Accel. Cen., Univ. Tsukuba)
 TAJIMA Naoki 田嶋直樹 (Coll. Art Sci., Univ. Tokyo)
 TAKADA Masashi 高田真志 (N.I.R.S.)
 TAKEMASA Tadashi 武政尹士 (Kyoto Univ. Education)
 TAKEUCHI Suehiro 竹内末広 (JAERI, Tokai Res. Estab.)
 TAKIGAWA Noboru 滝川昇 (Fac. Sci., Tohoku Univ.)
 TAMAGAKI Ryoza 玉垣良三 (Fac. Sci., Kyoto Univ.)
 TAMURA Takashi 田村高志 (NASDA)
 TANABE Kazuko 田辺和子 (Otsuna Women's Coll.)
 TANABE Kousai 田辺孝哉 (Fac. Sci., Saitama Univ.)
 TANAKA Jinichi 田中仁市 (Inst. Nucl. Study, Univ. Tokyo)
 TANAKA Kazuhiro 田中和廣 (Medical Dept., Jyuntendo Univ.)
 TANAKA Yasushi 田中保志 (Kyokuto Boeki Kaisha, Ltd.)
 TANIKAWA Masashi 谷川勝至 (Fac. Sci., Univ. Tokyo)
 TOHYAMA Mitsuru 遠山満 (Kyorin Univ.)
 TOMIMASU Takio 富増多喜夫 (FEL Res. Inst. Inc.)
 TOMINAKA Toshiharu 富中利治 (Hitachi, Ltd.)
 TOMITANI Takehiro 富谷武浩 (N.I.R.S.)
 TOMIZAWA Masahito 富澤正人 (Inst. Nucl. Study, Univ. Tokyo)
 TOMODA Toshiaki 友田敏章 (Fac. Eng., Aomori Univ.)
 TORIYAMA Tamotsu 鳥山保 (Dept. Phys., Musashi Inst. Technol.)
 TSUBAKI Noriyuki 椿則幸 (NASDA)
 TSUKINO Akihisa 月野晃久 (NASDA)
 UTSUNOMIYA Hiroaki 宇都宮弘章 (Fac. Sci., Konan Univ.)
 VITTURI Andrea (Univ. Padova, Italy)

WADA Michiharu 和田道治 (Inst. Nucl. Study, Univ. Tokyo)
 WADA Ryoichi 和田良一 (Texas A & M Univ., U.S.A.)
 WADA Takahiro 和田隆宏 (Fac. Sci., Konan Univ.)
 WAKAI Masamichi 若井正道 (Fac. Sci., Osaka Univ.)
 WAKUTA Yoshihisa 和久田義久 (Fac. Eng., Kyushu Univ.)
 WATANABE Ikuo 渡辺郁男 (Toshiba Corp.)
 WATANABE Shin-ichi 渡辺伸一 (Inst. Nucl. Study, Univ. Tokyo)
 WEI Baowen 魏宝文 (Inst. Modern Phys., Acad. Sinica, China)
 WONG Ji Chen (Inst. Modern Phys., Acad. Sinica, China)
 XIA Jiawen 夏佳文 (Inst. Modern Phys., Acad. Sinica, China)
 YABANA Kazuo 矢花一浩 (Fac. Sci., Niigata Univ.)
 YAMADA Taiichi 山田泰一 (Coll. Eng., Kanto Gakuin Univ.)
 YAMANOUCI Mikio 山内幹雄 (Inst. Phys., Univ. Tsukuba)
 YAMAZAKI Hirohito 山崎寛仁 (Lab. Nucl. Sci., Tohoku Univ.)
 YAMAZAKI Takashi 山崎魏 (RCNP, Osaka Univ.)
 YE Feng 叶峰 (Inst. Modern Phys., Acad. Sinica, China)
 YOKOUCHI Shigeru 横内茂 (Osaka Vacuum Ltd.)
 YONEMARU Mitsunori 米丸充規 (NASDA)
 YOSHIDA Nobuaki 吉田宣章 (Fac. Sci., Univ. Tokyo)
 YOSHIDA Shiro 吉田思郎 (Dept. Phys., Ishinomaki Senshu Univ.)
 YOSHINAGA Naotaka 吉永尚孝 (Fac. Sci., Saitama Univ.)
 YOSHIOKA Yasuhiro 吉岡康弘 (NASDA)
 YOSHIZAWA Yasukazu 吉沢康和 (Fac. Eng., Kyushu Univ.)
 ZHAN Li (Inst. Modern Phys., Acad. Sinica, China)
 ZHAO Jin Hua (Inst. Modern Phys., Acad. Sinica, China)

(Students)

AKABORI Taisuke 赤堀泰祐 (Dept. Phys., Musashi Inst. Technol.)
 AKIYOSHI Hiromichi 秋吉啓充 (Fac. Sci., Kyushu Univ.)
 AOKI Yuka 青木由香 (Lab. Nucl. Sci., Tohoku Univ.)
 BUSAKI Toru 佛崎透 (Fac. Sci., Kyushu Univ.)
 FUJITA Takeshi 藤田建 (Fac. Sci., Kyushu Univ.)
 HASHIMOTO Satoshi 橋本賢 (Fac. Sci., Univ. Tokyo)
 HIRAKAWA Tetuya 平川哲也 (Fac. Sci., Saitama Univ.)
 KIM Eunn Joo (Fac. Sci., Tohoku Univ.)
 KOBAYASHI Kentarou 小林健太郎 (Coll. Sci. Tech., Nihon Univ.)
 KURATOMI Kouichi 倉富弘一 (Dept. Phys., Musashi Inst. Technol.)
 KURITA Tetsuro 栗田哲郎 (Inst. Sci., Univ. Tsukuba)
 KUROSAWA Tadahiro 黒澤忠弘 (Fac. Eng., Tohoku Univ.)
 LIU Xin (Inst. Phys., Univ. Tsukuba)
 MATSUI Shinjiro 松井信二郎 (Fac. Sci., Saitama Univ.)
 MIURA Takashi 三浦崇 (Inst. Phys., Univ. Tsukuba)
 MOGI Yoshihiko 茂木喜彦 (Coll. Sci., Chuo Univ.)
 NAKAO Makoto 中尾誠 (Cyclotron Radioisot. Cen., Tohoku Univ.)
 OHSHIMA Nagayasu 大島永康 (KEK)
 OHTSUKA Takahiro 大塚崇広 (Dept. Phys., Musashi Inst. Technol.)
 OI Makito 大井万紀人 (Coll. Art. Sci., Univ. Tokyo)
 ONO Shinji 小野慎二 (Fac. Eng., Kyoto Univ.)
 OZAWA Shuichi 小澤修一 (Coll. Sci., Rikkyo Univ.)
 SASAHARA Takafumi 笹原孝文 (Coll. Sci., Chuo Univ.)
 SASAKI Haruka 佐々木玄 (Inst. Phys., Univ. Tsukuba)
 SASAKI Michiya 佐々木道也 (Fac. Eng., Tohoku Univ.)
 SATO Takehiko 佐藤武彦 (Fac. Sci., Tohoku Univ.)
 SONE Hayato 曾根逸人 (Fac. Sci. Tech., Sci. Univ. Tokyo)
 TANIGUCHI Shingo 谷口真吾 (Cyclotron Radioisot. Cen., Tohoku Univ.)
 TOMITA Shigeo 富田成夫 (Inst. Phys., Univ. Tsukuba)
 TSURUTA Kaoru 鶴田薫 (Fac. Sci., Kyushu Univ.)
 UCHIYAMA Yoshiko 内山佳子 (Fac. Sci., Univ. Tokyo)

WAKAMATSU Fumihiko 若松文彦 (Fac. Sci., Kyushu Univ.)
 WAKUI Takashi 湧井崇志 (Fac. Sci., Toho Univ.)
 YAMAMOTO Shiro 山本史郎 (Tokyo Gakugei Univ.)
 YODA Tetsuhiko 依田哲彦 (Lab. Nucl. Sci., Tohoku Univ.)
 YUKI Hideyuki 結城秀行 (Fac. Sci., Tohoku Univ.)

Linear Accelerator Laboratory

CHIBA Toshiya 千葉利哉	FUJIMAKI Masaki 藤巻正樹
FUKUDA Shigekazu 福田茂一 ^{*1}	HEMMI Masatake 逸見政武
IKEZAWA Eiji 池沢英二	ITO Sachiko 伊藤祥子 ^{*1}
KASE Masayuki 加瀬昌之	KOBAYASHI Toshio 小林俊雄 ^{*2}
KORSHENINNIKOV Alexei	KUMAGAI Hidekazu 熊谷秀和
MIYAZAWA Yoshitoshi 宮沢佳数	MOCHIZUKI Yuko S. 望月優子 ^{*1}
MOMOTA Sadao 百田佐多生 ^{*1}	OGAWA Yoko 小川洋子 ^{*1}
OZAWA Akira 小沢顕	SUGAHARA Yuichi 菅原雄一 ^{*3}
SUZUKI Takeshi 鈴木健	TANIHATA Isao 谷畑勇夫 ^{*4}
TONUMA Masao 戸沼正雄	YANOKURA Minoru 矢野倉実
YOSHIDA Koichi 吉田光一	

^{*1} Special Postdoctoral Researcher, ^{*2} Senior Scientist, ^{*3} Postdoctoral Researcher,
^{*4} Chief Scientist

(Visitors)

ADACHI Shizuko 安達静子 (ICFD)
 ARATANI Michi 荒谷美智 (Inst. Environmental Sci.)
 BOLBOT Michael (Notre Dame Univ., U.S.A.)
 BOYD Richard (Ohio Univ., U.S.A.)
 BROCKMANN Roff (Inst. Phys., Univ. Mainz, Germany)
 DAVID Dean J (CALTEC, U.S.A.)
 DEMYANOVA Alla S. (Kurchatov Inst. Atomic Energy, Russia)
 FUJIWARA Mamoru 藤原守 (RCNP, Osaka Univ.)
 GOLOVKOV Mkhel S (Kurchatov Inst., Russia)
 GONCHAROV Sergei A (Kurchatov Inst., Russia)
 HIRENZAKI Satoru 比連崎悟 (Fac. Sci., Nara Women's Univ.)
 HORIUCHI Hisashi 堀内昶 (Fac. Sci., Kyoto Univ.)
 IWAMOTO Akira 岩本昭 (JAERI, Tokai Res. Estab.)
 IZUYAMA Takeo 伊豆山健夫 (Fac. Sci., Toho Univ.)
 KATORI Kenji 鹿取謙二 (Fac. Sci., Osaka Univ.)
 KIKUCHI Jun 菊地順 (Sci. Eng. Res. Lab., Waseda Univ.)
 KIMURA Kikuo 木村喜久雄 (Fac. Eng., Nagasaki Inst Appl. Sci.)
 KOLATA James (Notre Dame Univ., U.S.A.)
 MARUYAMA Tomoyuki 丸山智之 (Fac. Sci., Kyoto Univ.)
 MATSUTA Kensaku 松多健策 (Fac. Sci., Osaka Univ.)
 MATSUYAMA Yoshitaka 松山芳孝 (Inst. Nucl. Study, Univ. Tokyo)
 MATUOKA Nobuyuki 松岡伸行 (Res. Cen. Nucl. Phys., Osaka Univ.)
 MITTING M. (GANIL, France)
 MIYAKE Yasuo 三明康郎 (Fac. Sci., Univ. Tsukuba)
 MIYAMURA Osamu 宮村修 (Fac. Sci., Hiroshima Univ.)
 MOCHIZUKI Keiko 望月圭子 (Fac. Sci., Osaka Univ.)
 MORIMOTO Koji 森本幸司 (JST)
 MURAOKA Mitsuo 村岡光男 (Fac. Eng., Aomori Univ.)
 NOJIRI Yoichi 野尻洋一 (Fac. Sci., Osaka Univ.)
 OGAWA Kengo 小川健吾 (Coll. Arts. Sci., Chiba Univ.)
 OGLOBLIN Alexei A. (Kurchatov. Inst., Russia)
 OHNISHI Akira 大西明 (Fac. Sci., Hokkaido Univ.)
 OHTSUBO Takashi 大坪隆 (Fac. Sci., Niigata Univ.)
 OJIMA Minoru 小嶋稔 (Fac. Sci., Osaka Univ.)

OMATA Kazuo 小俣和夫 (Inst. Nucl. Study, Univ. Tokyo)
 ORYU Shinsho 尾立晋祥 (Fac. Sci. and Tech., Science Univ. Tokyo)
 OYAMATSU Kazuhiro 親松和浩 (Dept. Energy Eng. Sci., Nagoya Univ.)
 PETRASCU Horia (Inst. Phys. Nucl. Eng., Romania)
 PETRASCU Marius (Inst. Phys. Nucl. Eng., Romania)
 RAIMANN Gerhard (Ohio State Univ., U.S.A.)
 SAGAWA Hiroyuki 佐川弘幸 (Cen. Mathematical Sci., Aizu Univ.)
 SAKAI Hideyuki 酒井英行 (Fac. Sci., Univ. Tokyo)
 SATO Kazuhiro 佐藤和広 (Tokyo Fire Dept.)
 SEKI Ryoichi 関良一 (California Univ., U.S.A.)
 SHERRIL B. (Michigan State Univ., U.S.A.)
 SUDA Toshimi 須田利美 (Fac. Sci., Tohoku Univ.)
 SUGANUMA Hideo 菅沼秀夫 (RCNP, Osaka Univ.)
 SUGAWARA Masahiko 菅原昌彦 (Fundam. Sci., Chiba Inst. Technol.)
 SUZUKI Hideyuki 鈴木英之 (KEK)
 SUZUKI Tsuneo 鈴木恒雄 (Fac. Sci., Kanazawa Univ.)
 SUZUKI Yasuyuki 鈴木宣之 (Fac. Sci., Niigata Univ.)
 TACHIBANA Takahiro 橘孝博 (Senior High School of Waseda Univ.)
 TAKAHASHI Yutaka 高橋豊 (Fac. Sci., Osaka Univ.)
 TOKI Hiroshi 土岐博 (RCNP, Osaka Univ.)
 TORBJOEN Baeck (Phys. Dept. Frescat., Sweden)
 VARGA Kalman (Inst. Nucl. Res., Hungarian Acad. Sci., Hungary)
 WADA Takahiro 和田隆宏 (Fac. Sci., Konan Univ.)
 YAGI Hirosuke 八木浩輔 (Fac. Sci., Univ. Tsukuba)
 YORANN Alhassid (Yale Univ., U.S.A.)
 ZAHAR Mohamed (Dept. Phys., Notre Dame Univ., U.S.A.)

(Students)

BOKU Yudan 朴勇男 (Fac. Sci. Eng., Waseda Univ.)
 HIBINO Masaru 日比野優 (Fac. Sci. Eng., Waseda Univ.)
 HIYAMA Emiko 肥山詠美子 (Fac. Sci., Kyushu Univ.)
 HONG Wang 洪完 (Fac. Eng., Univ. Tokyo)
 IKEDA Takayuki 池田隆之 (Grad. Sch., Osaka Univ.)
 ISHIGA Kenichi 石賀健一 (Grad. Sch., Osaka Univ.)
 KANO Kenji 叶健治 (Fac. Sci., Univ. Tsukuba)
 KATO Toshiyuki 加藤俊幸 (Fac. Sci. Eng., Waseda Univ.)
 KIUCHI Hiroshi 木内宏 (Fac. Sci., Saitama Univ.)
 KONO Sachiko 甲野祥子 (Fac. Sci. Eng., Waseda Univ.)
 KOZU Tomotake 神津友武 (Fac. Sci. Eng., Waseda Univ.)
 MARUYAMA Yukiko 丸山由紀子 (Fac. Sci., Osaka Univ.)
 MATSUMOTO Akiko 松本晶子 (Fac. Sci. Eng., Waseda Univ.)
 MIKI Keitaro 三木敬太郎 (Fac. Sci., Konan Univ.)
 OZAKI Kiminori 尾崎公教 (Fac. Sci. Eng., Waseda Univ.)
 SAITO Masanori 齋藤正憲 (Fac. Sci., Osaka Univ.)
 SAKAGUCHI Takao 坂口貴男 (Fac. Sci. Eng., Waseda Univ.)
 SHIMOOKA Masaaki 下岡正明 (Fac. Sci., Kyoto Univ.)
 TAKAHASHI Kenichi 高橋賢一 (Grad. Sch., Waseda Univ.)
 TAKEHANA Naohiro 竹花直弘 (Fac. Sci. Eng., Waseda Univ.)
 TAKENAKA Sunao 竹中直 (Fac. Sci. Eng., Waseda Univ.)
 TANIHATA Chiharu 谷畑千春 (Fac. Sci., Waseda Univ.)
 TERUHI Shigeru 照日繁 (Fac. Sci. Eng., Waseda Univ.)
 YUNOKI Akira 柚木彰 (Grad. Sch., Waseda Univ.)
 WANG Haiming 王海鳴 (Fac. Sci., Univ. Tokyo)

Radiation Laboratory

BEAUMEL Didier* ¹	DEVI Yelamanchili Durga* ¹
GAI Moshe* ²	GOTO Yuji 後藤雄二
HAHN Kevin I.* ¹	HAYASHI Naoki 林直樹* ³
HIRAI Masaaki 平井正明	ICHIHARA Takashi 市原卓
IDEGUCHI Eiji 井手口栄治* ³	IMAI Kenichi 今井憲一* ⁴
ISHIHARA Masayasu 石原正泰* ⁵	KISHIDA Takashi 岸田隆
LUCCIO Alfredo* ¹	MENGONI Alberto* ¹
NOTANI Masahiro 野谷将広	OKAMURA Masahiro 岡村昌宏* ³
SAITO Naohito 齐藤直人	SAKURAI Hiroyoshi 櫻井博儀
SUN Zuxun* ²	TERANISHI Takashi 寺西高
WATANABE Yasushi 渡邊康	WATANABE Yutaka 渡辺裕
YOSHIDA Atsushi 吉田敦	

*¹ Visiting Researcher, *² Eminent Scientist, *³ Special Postdoctoral Researcher,
*⁴ Senior Visiting Scientist, *⁵ Chief Scientist

(Visitors)

ABE Yasuhisa 阿部恭久 (Yukawa Inst. Theor. Phys., Kyoto Univ.)
ADACHI Minoru 足立實 (Fac. Sci., Tokyo Inst. Technol.)
ANDO Yoshiaki 安藤嘉章 (Coll. Sci., Rikkyo Univ.)
ASAHI Koichiro 旭耕一郎 (Fac. Sci., Tokyo Inst. Technol.)
BECK F. A. (Groupe RSN, Strasbourg, France)
BROGLIA R. (Univ. Milano & INFN, Italy)
CASTEN Rick (Phys. Dept., Brookhaven Natl. Lab., U.S.A.)
CHAE Soo Joh 蔡洙 (Dept. Phys., Seoul Natl. Univ., Korea)
DON Yubin 董宇兵 (Inst. High Energy Phys.)
DOOI Makoto 堂井真 (Univ. Tsukuba)
EN'YO Hideto 延与秀人 (Fac. Sci., Kyoto Univ.)
FLOCARD Hubert (Div. Phys. Theorique, Inst. Phys., Orsay, France)
FUCHI Yoshihide 渕好秀 (Inst. Nucl. Study, Univ. Tokyo)
FUKUDA Mitsunori 福田光順 (Osaka Univ.)
FUKUDA Tomokazu 福田共和 (Inst. Nucl. Study, Univ. Tokyo)
FURUTAKA Kazuyoshi 古高和禎 (JAERI, Adv. Sci. Res. Cen.)
GONO Yasuyuki 郷農靖之 (Fac. Sci., Kyushu Univ.)
HAMAGAKI Hideki 浜垣秀樹 (Inst. Nucl. Study, Univ. Tokyo)
HAMAMOTO Ikuko 浜本育子 (Lund Inst. Technol., Lund Univ., Sweden)
HASEGAWA Takeo 長谷川武夫 (Fac. Eng., Miyazaki Univ.)
HATSUDA Tetsuo 初田哲男 (Univ. Tsukuba)
HONMA Saburo 本間三郎 (Inst. Nucl. Study, Univ. Tokyo)
HOSAKA Masahito 保坂将人 (Inst. Nucl. Study, Univ. Tokyo)
ICHIMURA Munetake 市村宗武 (Coll. Arts Sci., Univ. Tokyo)
IEKI Kazuo 家城和夫 (Coll. Sci., Rikkyo Univ.)
KAMAE Tsuneyoshi 釜江常好 (Fac. Sci., Univ. Tokyo)
KASAGI Jirota 笠木治郎太 (Lab. Nucl. Sci., Tohoku Univ.)
KATAYAMA Ichiro 片山一郎 (Inst. Nucl. Study, Univ. Tokyo)
KATO Seigo 加藤静吾 (Fac. Ed., Yamagata Univ.)
KATORI Kenji 鹿取謙二 (Fac. Sci., Osaka Univ.)
KAWASHIMA Hideo 川島英雄 (Inst. Nucl. Study, Univ. Tokyo)
KIM Jong Chan (Dept. Phys., Seoul Natl. Univ., Korea)
KITAO Kensuke 喜多尾憲助 (Data Eng. Inc.)
KODAIRA Jirou 小平治郎 (Fac. Sci., Hiroshima Univ.)
KOIKE Yuji 小池裕司 (Fac. Sci., Niigata Univ.)
KOSOWER David A. (Service de Physique Theorique Centre d'Etudes Saclay, France)
KUBONO Shigeru 久保野茂 (Inst. Nucl. Study, Univ. Tokyo)
KUMANO Shunzo 熊野俊三 (Fac. Sci. and Eng., Saga Univ.)
KUSAKARI Hideshige 草刈英榮 (Fac. Ed., Chiba Univ.)
LEE Sang Mu 李相茂 (Inst. Phys., Univ. Tsukuba)

LIU Guanhua 劉冠華 (Inst. Mod. Phys., Acad. Sinica, China)
 LOUKIANOV Serguei (JINR, Flerov Lab. Nucl. Reactions, Russia)
 LUO Yixiao (Inst. Mod. Phys., Acad. Sinica, China)
 MAEDA Kazushige 前田和茂 (Coll. Gen. Ed., Tohoku Univ.)
 MAO Yajun (China Inst. Atom. Energy, China)
 MATSUI Tetsuo 松井哲男 (Yukawa Inst. Theor. Phys., Kyoto Univ.)
 MATSUYANAGI Kenichi 松柳研一 (Fac. Sci., Kyoto Univ.)
 MIN Byung-Joo 閔丙珠 (Korea Atomic Energy Res. Inst., Korea)
 MITARAI Shiro 御手洗志郎 (Fac. Sci., Kyushu Univ.)
 MITSUOKA Shinichi 光岡真一 (JAERI, Adv. Sci. Res. Cen.)
 MIYACHI Takashi 宮地孝 (Inst. Nucl. Study, Univ. Tokyo)
 MIYATAKE Hiroari 宮武宇也 (Coll. Gen. Ed., Osaka Univ.)
 MORII Toshiyuki 森井俊行 (Kobe Univ.)
 MORIKAWA Tsuneyasu 森川恒安 (Fac. Sci., Kyushu Univ.)
 MORINOBU Shunpei 森信俊平 (Fac. Sci., Kyushu Univ.)
 MOTOBAYASHI Toru 本林透 (Coll. Sci., Rikkyo Univ.)
 MOTTELSON Ben R. (NORDITA, Copenhagen, Denmark)
 MUELLER Ludwig (Univ. Padova, Italy)
 MURAKAMI Takeshi 村上健 (Natl. Inst. Radiol. Sci.)
 NAGAI Yasuki 永井泰樹 (Fac. Sci., Tokyo Inst. Technol.)
 NAGAMIYA Shoji 永宮正治 (Columbia Univ., U.S.A.)
 NAGASHIMA Yasuo 長島泰夫 (Inst. Phys., Univ. Tsukuba)
 NAKAJIMA Mitsuo 中島充夫 (The Graduate School at Nagatsuta, Tokyo Inst. Technol.)
 NAKAMURA Shogo 中村正吾 (Fac. Ed., Yokohama Natl. Univ.)
 NAKAMURA Takashi 中村隆司 (Fac. Sci., Univ. Tokyo)
 NAKAYAMA Shintaro 中山信太郎 (Coll. Gen. Ed., Tokushima Univ.)
 NIIZEKI Takashi 新関隆 (Fac. Sci., Tokyo Inst. Technol.)
 NORO Tetsuo 野呂哲夫 (Res. Cen. Nucl. Phys., Osaka Univ.)
 ODAHARA Atsuko 小田原厚子 (Fac. Sci., Kyushu Univ.)
 OGAWA Masao 小川雅生 (The Graduate School at Nagatsuta, Tokyo Inst. Technol.)
 OKAMURA Hiroyuki 岡村弘之 (Fac. Sci., Univ. Tokyo)
 ONUMA Hajime 大沼甫 (Fac. Sci., Tokyo Inst. Technol.)
 ORIHARA Hikonojyo 織原彦之丞 (Cyclotron and Radioisotope Cen., Tohoku Univ.)
 OSHIMA Masumi 大島真澄 (JAERI, Adv. Sci. Res. Cen.)
 OTSUKA Takaharu 大塚孝治 (Fac. Sci., Univ. Tokyo)
 OYAIZU Michihiro 小柳津充広 (Inst. Nucl. Study, Univ. Tokyo)
 PENIONJKEVITCH Yuri (JINR, Flerov Lab. Nucl. Reactions, Russia)
 RUAN (GEN) Jian-Zhi 阮建治 (Coll. Sci., Rikkyo Univ.)
 SAGAWA Hiroyuki 佐川弘幸 (Cen. Mathematical Sci., Aizu Univ.)
 SAKAGUCHI Harutaka 坂口治隆 (Fac. Sci., Kyoto Univ.)
 SAKAI Kenji 酒井健二 (Fac. Sci., Tokyo Inst. Technol.)
 SAKAI Mitsuo 坂井光夫 (Inst. Nucl. Study, Univ. Tokyo)
 SAKURAGI Hiroyuki 櫻木弘之 (Fac. Sci., Osaka City Univ.)
 SATO Hikaru 佐藤皓 (Natl. Lab. High Energy Phys.)
 SATO Hiroshi 佐藤竝 (Seikei Univ.)
 SCHAEFER Markus (Physicalisches Inst., Univ. Goettingen, Germany)
 SCHMIDT-OTT Wolf-Dieter (II, Physicalisches Inst., Univ. Goettingen, Germany)
 SHIBATA Toshiaki 柴田利明 (Fac. Sci., Tokyo Inst. Technol.)
 SHIMIZU Hajime 清水肇 (Fac. Ed., Yamagata Univ.)
 SHIMIZU Yoshifumi 清水良文 (Fac. Sci., Kyushu Univ.)
 SHIMODA Tadashi 下田正 (Coll. Gen. Ed., Osaka Univ.)
 SHIMOURA Susumu 下浦享 (Coll. Sci., Rikkyo Univ.)
 SHIRATO Syoji 白土鈿二 (Coll. Sci., Rikkyo Univ.)
 SIGNORINI Cosimo (Phys. Dept., Inst. Nazionale di Fisica Nucl., Italy)
 SUGAWARA Masahiko 菅原昌彦 (Chiba Inst. Technol.)
 SUZUKI Masayo 鈴木昌世 (Jpn. Synchrotron Rad. Res. Inst.)
 SUZUKI Yasuyuki 鈴木宜之 (Fac. Sci., Niigata Univ.)
 TAKADA Eiichi 高田栄一 (Natl. Inst. Radiol. Sci.)

TAKAHASHI Noriaki 高橋憲明 (Coll. Gen. Ed., Osaka Univ.)
 TAKAHASHI Tadayuki 高橋忠幸 (Fac. Sci., Univ. Tokyo)
 TAKAKU Seisaku 高久清作 (Inst. Nucl. Study, Univ. Tokyo)
 TAKIGAWA Noboru 滝川昇 (Fac. Sci., Tohoku Univ.)
 TANAKA Masahiko 田中雅彦 (Inst. Nucl. Study, Univ. Tokyo)
 TANOKURA Atsushi 田野倉敦 (Fac. Sci. Technol., Sophia Univ.)
 TERAOKAWA Atsuki 寺川貴樹 (Cyclotron and Radioisotope Cen., Tohoku Univ.)
 THOMPSON Ian Joseph (Univ. Surrey, U.K.)
 TOKI Hiroshi 土岐博 (Res. Cen. Nucl. Phys., Osaka Univ.)
 TOYAMA Takeshi 外山毅 (Nat. Lab. High Energy Phys.)
 TOYOKAWA Hidenori 豊川秀訓 (Res. Cen. Nucl. Phys., Osaka Univ.)
 UENO Hideki 上野秀樹 (Fac. Sci., Osaka Univ.)
 UNO Masahiro 宇野正宏 (Ministry Ed., Sci. Culture)
 WAKAMATSU Masashi 若松正志 (Fac. Sci., Osaka Univ.)
 WANG Yifang (Inst. Mod. Phys., Acad. Sinica, China)
 WU Heyu 吳和宇 (Inst. Mod. Phys., Acad. Sinica, China)
 YAMAMOTO Sukeyasu 山本祐靖 (Fac. Sci. Technol., Sophia Univ.)
 YAMANISHI Teruya 山西輝也 (Res. Cen. Nucl. Phys., Osaka Univ.)
 YAZAKI Koichi 矢崎紘一 (Univ. Tokyo)
 YOSHINAGA Naotaka 吉永尚孝 (Coll. Liberal Arts, Saitama Univ.)
 YOSOI Masaru 與曾井優 (Fac. Sci., Kyoto Univ.)
 ZHOU Xiaohong (Inst. Mod. Phys., Acad. Sinica, China)

(Students)

AOI Nori 青井考 (Fac. Sci., Univ. Tokyo)
 FUJISAWA Eiji 藤澤栄二 (Fac. Sci., Tokyo Inst. Technol.)
 FUJITA Satoshi 藤田哲史 (Fac. Sci., Univ. Tokyo)
 FUJIWARA Hideki 藤原秀樹 (Coll. Sci., Rikkyo Univ.)
 FUKUDA Naoki 福田直樹 (Fac. Sci., Univ. Tokyo)
 FUKUSAKA Shouichi 福坂将一 (Fac. Sci., Univ. Tokyo)
 HARUYAMA Seigo 春山征吾 (Fac. Sci., Univ. Tokyo)
 HIGURASHI Yoshihide 日暮祥英 (Coll. Sci., Rikkyo Univ.)
 HISANAGA Isamu 久永勇 (Coll. Sci., Rikkyo Univ.)
 IINO Hayato 飯野勇人 (Coll. Sci., Rikkyo Univ.)
 IKEDA Takashi 池田貴 (Fac. Sci., Univ. Tokyo)
 ITO Kazuya 伊藤和也 (Cyclotron and Radioisotope Cen., Tohoku Univ.)
 IWASAKI Hironori 岩崎弘典 (Fac. Sci., Univ. Tokyo)
 IWATA Yoshiyuki 岩田佳之 (Coll. Sci., Rikkyo Univ.)
 IZUMI Hideaki 出水秀明 (Fac. Sci., Tokyo Inst. Technol.)
 KANG Sung Tae 姜成泰 (Coll. Sci., Rikkyo Univ.)
 KIDERA Masanori 木寺正憲 (Fac. Sci., Kyushu Univ.)
 KIJIMA Takeshi 鬼島丈 (Coll. Sci., Rikkyo Univ.)
 KOBAYASHI Syusaku 小林秀策 (Coll. Sci., Rikkyo Univ.)
 KUROKAWA Nobuo 黒河暢雄 (Fac. Sci., Tokyo Inst. Technol.)
 MATSUZAKI Keiichi 松崎恵一 (Fac. Sci., Univ. Tokyo)
 MINEMURA Toshiyuki 峯村俊行 (Coll. Sci., Rikkyo Univ.)
 MIYACHI Takahiko 宮地岳彦 (Inst. Nucl. Study, Univ. Tokyo)
 MIYAZAKI Kousuke 宮崎光介 (Fac. Sci., Kyushu Univ.)
 MIZOI Yutaka 溝井浩 (Inst. Nucl. Study, Univ. Tokyo)
 NAGATA Kazuhiro 永田和広 (Fac. Sci., Univ. Tokyo)
 NAKANO Joe 中野讓 (Inst. Nucl. Study, Univ. Tokyo)
 NISHIO Teiji 西尾禎治 (Coll. Sci., Rikkyo Univ.)
 NONAKA Takamasa 野中敬正 (Fac. Sci., Univ. Tokyo)
 NOZAKI Mari 野崎真利 (Coll. Sci., Rikkyo Univ.)
 OGAWA Hiroshi 小川博嗣 (Fac. Sci., Tokyo Inst. Technol.)
 OHMORI Takamasa 大森崇雅 (Coll. Sci., Rikkyo Univ.)
 ONODERA Atsushi 小野寺淳之 (Coll. Sci., Rikkyo Univ.)
 OONISHI Tetsuya 大西哲哉 (Fac. Sci., Univ. Tokyo)

OTSU Hideaki 大津秀暁 (Fac. Sci., Univ. Tokyo)
 OZAWA Yojiro 小沢洋二郎 (Coll. Sci., Rikkyo Univ.)
 SAITO Yoshitaka 齋藤芳隆 (Fac. Sci., Univ. Tokyo)
 SAKAMOTO Naoki 坂本直紀 (Coll. Sci., Rikkyo Univ.)
 SATO Hiromi 佐藤広海 (Fac. Sci., Tokyo Inst. Technol.)
 SATO Koji 佐藤構二 (Fac. Sci., Univ. Tokyo)
 SATO Yoshiteru 佐藤義輝 (Fac. Sci., Univ. Tokyo)
 SEKIGICHI Kimiko 関口仁子 (Fac. Sci., Univ. Tokyo)
 SEKINE Mizue 関根瑞恵 (Coll. Sci., Rikkyo Univ.)
 SHIBATA Masataka 柴田雅隆 (Fac. Sci., Kyushu Univ.)
 SHIRATO Yoshiyuki 白土良之 (Coll. Sci., Rikkyo Univ.)
 SHIZUMA Toshiyuki 静間俊行 (Fac. Sci., Kyushu Univ.)
 SUZUKI Ken 鈴木謙 (Fac. Sci., Tokyo Inst. Technol.)
 SUZUKI Masataka 鈴木正恭 (Coll. Sci., Rikkyo Univ.)
 SUZUKI Takayuki 鈴木孝幸 (Fac. Sci., Tokyo Inst. Technol.)
 TAKEUCHI Satoshi 武内聡 (Coll. Sci., Rikkyo Univ.)
 TANAKA Junichi 田中純一 (Fac. Sci., Univ. Tokyo)
 TANIMOTO Sayaka 谷本明佳 (Fac. Sci., Osaka Univ.)
 TSUDA Masaki 津田理樹 (Fac. Sci., Tokyo Inst. Technol.)
 TUCHIDA Hideo 土田英夫 (Fac. Sci., Kyushu Univ.)
 UCHIYAMA Yasuhito 内山靖仁 (Fac. Sci., Tokyo Inst. Technol.)
 UDA Makoto 宇田誠 (Coll. Sci., Rikkyo Univ.)
 WAKASA Tomotsugu 若狭智嗣 (Fac. Sci., Univ. Tokyo)
 WATANABE Hiroshi 渡邊寛 (Fac. Sci., Kyushu Univ.)
 YAKO Kentaro 矢向謙太郎 (Fac. Sci., Univ. Tokyo)
 YAMADA Kazunari 山田一成 (Coll. Sci., Rikkyo Univ.)
 YAMANO Tetsuya 山野哲也 (Coll. Sci., Rikkyo Univ.)
 YANAGISAWA Yoshiyuki 柳沢善行 (Coll. Sci., Rikkyo Univ.)
 YOKOYAMA Go 横山剛 (Fac. Sci., Univ. Tokyo)
 YONEDA Kenichiro 米田健一郎 (Fac. Sci., Univ. Tokyo)
 YONEYAMA Shigenobu 米山茂信 (Fac. Sci., Tokyo Inst. Technol.)
 YOSHIDA Toru 吉田亘 (Fac. Sci., Tokyo Inst. Technol.)
 YOSHIMI Akihiro 吉見彰洋 (Fac. Sci., Tokyo Inst. Technol.)

Atomic Physics Laboratory

ANDO Kozo 安藤剛三	AWAYA Yohko 粟屋容子 ^{*1}
IGARASHI Akinori 五十嵐明則	KAMBARA Tadashi 神原正 ^{*2}
KANAI Yasuyuki 金井保之	KITAJIMA Masashi 北島昌史
KOJIMA Takao M. 小島隆夫	LIN Chii-Dong 林啓東 ^{*3}
MARTINSON Indrec ^{*3}	NAKAI Yoichi 中井陽一
NISHIDA Masami 西田雅美	NYSTRÖM Bosse ^{*4}
OURA Masaki 大浦正樹	SCHMIDT-BÖCKING Horst ^{*3}
SHIMAMURA Isao 島村勲 ^{*2}	URAMOTO Seiiti 浦本聖一
WATANABE Naoki 渡部直樹	

^{*1} Chief Scientist, ^{*2} Senior Scientist, ^{*3} Eminent Scientist, ^{*4} Visiting Researcher

(Visitors)

ACHLER Matthias (Inst. Kernphysik, Univ. Frankfurt, Germany)
 AZUMA Toshiyuki 東俊行 (Coll. Arts Sci., Univ. Tokyo)
 CHIMI Yasuhiro 知見康弘 (JAERI, Tokai Res. Estab.)
 COCKE C. Lewis, Jr. (Kansas State Univ., U.S.A.)
 DEPAOLA Brett D. (Kansas State Univ., U.S.A.)
 ENGSTRÖM Lars (Lund Inst. Technol., Lund Univ., Sweden)
 FUJIMA Kazumi 藤間一美 (Fac. Eng., Yamanashi Univ.)
 FUKUDA Hiroshi 福田宏 (Sch. Administration and Informatics, Univ. Shizuoka)
 HARA Shunsuke 原俊介 (Dept. Gen. Educ., Tsukuba Coll. Technol.)

HARSTON Michael R. (Dept. Math., Univ. Nottingham, U.K.)
 HINO Ken-ichi 日野健一 (Dept. Appl. Phys. Chem., Univ. Electro-Commun.)
 HIRAYAMA Takato 平山孝人 (Dept. Phys., Gakushuin Univ.)
 HULDT Sven (Lund Inst. Technol., Lund Univ., Sweden)
 HUTTON Roger (Lund Inst. Technol., Lund Univ., Sweden)
 ICHIMURA Atsushi 市村 淳 (Inst. Space and Astr. Sci.)
 ISHII Keishi 石井慶之 (Dept. Eng. Sci., Kyoto Univ.)
 ISHIKAWA Norito 石川法人 (JAERI, Tokai Res. Estab.)
 ISOZUMI Yasuhito 五十棲泰人 (Inst. Chem. Res., Kyoto Univ.)
 ITO Shin 伊藤 真 (Radioisot. Res. Cen., Kyoto Univ.)
 ITOH Akio 伊藤秋男 (Fac. Eng., Kyoto Univ.)
 ITOH Yoh 伊藤 陽 (Fac. Sci., Josai Univ.)
 IWASE Akihiro 岩瀬彰宏 (JAERI, Tokai Res. Estab.)
 JÄGER Martin (Inst. Kernphysik, Univ. Frankfurt, Germany)
 KAWATSURA Kiyoshi 川面 澄 (Fac. Eng. Design, Kyoto Inst. Technol.)
 KIMURA Masahiro 木村正廣 (Fac. Sci., Osaka Univ.)
 KIMURA Mineo 季村峯生 (The School of Allied Health Sciences, Yamaguchi Univ.)
 KINK Ilmar (Lund Inst. Technol., Lund Univ., Sweden)
 KOBAYASHI Nobuo 小林信夫 (Dept. Phys., Tokyo Metropol. Univ.)
 KOHARA Takao 小原孝夫 (Fac. Sci., Himeji Inst. Technol.)
 KOIKE Fumihiko 小池文博 (Sch. Med., Kitasato Univ.)
 KOIZUMI Tetsuo 小泉哲夫 (Dept. Phys., Rikkyo Univ.)
 KOMAKI Ken-ichiro 小牧研一郎 (Coll. Arts Sci., Univ. Tokyo)
 KOROBV Vladimir I. (Joint Inst. Nucl. Res., Russia)
 KUROKI Kenro 黒木健郎 (Natl. Res. Inst. Police Sci.)
 KUROTA Naoshi 黒田直志 (JAERI, Tokai Res. Estab.)
 MATSUO Takashi 松尾 崇 (Dept. Pathol., Tokyo Med. Dent. Univ.)
 MATSUZAWA Michio 松澤通生 (Dept. Appl. Phys. Chem., Univ. Electro-Commun.)
 MERGEL Volker (Inst. für Kernphysik, Germany)
 MITAMURA Tohru 三田村 徹 (Fac. Eng., Himeji Inst. Technol.)
 MIZOGAWA Tatsumi 溝川辰巳 (Nagaoka Coll. Technol.)
 MOKLER Paul (GSI, Germany)
 MUKOYAMA Takeshi 向山 毅 (Inst. Chem. Res., Kyoto Univ.)
 NAKAMURA Masato 中村正人 (Coll. Sci. Technol., Nihon Univ.)
 NELMS Nick (Leicester Univ., U.K.)
 NISHIDA Nobuhiko 西田信彦 (Fac. Sci., Tokyo Inst. Technol.)
 OHTANI Shunsuke 大谷俊介 (Inst. Laser Sci., Univ. Electro-Commun.)
 OKAYASU Satoru 岡安 悟 (JAERI, Tokai Res. Estab.)
 OKUNO Kazuhiko 奥野和彦 (Dept. Phys., Tokyo Metropol. Univ.)
 SAKATA Hideaki 坂田英明 (Fac. Sci., Tokyo Inst. Technol.)
 SAKURAI Makoto 桜井 誠 (Fac. Sci., Kobe Univ.)
 SATO Hiroshi 佐藤浩史 (Fac. Sci., Ochanomizu Univ.)
 SATOH Kazuhiko 佐藤一彦 (Fac. Sci., Tokyo Inst. Technol.)
 SATOH Yukinori 佐藤幸紀 (Res. Inst. Sci. Meas., Tohoku Univ.)
 SEKIOKA Tsuguhisa 関岡嗣久 (Fac. Eng., Himeji Inst. Technol.)
 SHIBATA Hiromi 柴田裕実 (Res. Cen. Nucl. Sci., Univ. Tokyo)
 SHIMA Kunihiko 島 邦博 (Tandem Accel. Cen., Univ. Tsukuba)
 SHIMAKURA Noriyuki 島倉紀之 (Fac. Sci., Niigata Univ.)
 SUZUKI Isao 鈴木 功 (Electrotech. Lab.)
 TAKAYANAGI Toshinobu 高柳俊暢 (Dept. Phys., Sophia Univ.)
 TANG Jian-Zhi (Dept. Physics, Univ. Tennessee, U.S.A.)
 TAWARA Hiroyuki 俵 博之 (Natl. Inst. Fusion Sci.)
 TERASAWA Mititaka 寺澤倫孝 (Fac. Eng., Himeji Inst. Technol.)
 TOSHIMA Nobuyuki 戸嶋信幸 (Inst. Appl. Phys., Univ. Tsukuba)
 WAKIYA Kazuyoshi 脇谷一義 (Dept. Phys., Sophia Univ.)
 WATANABE Shinichi 渡辺信一 (Dept. Appl. Phys. Chem., Univ. Electro-Commun.)
 YAGISHITA Akira 柳下 明 (Natl. Lab. High Energy Physics)
 YAMAZAKI Yasunori 山崎泰規 (Coll. Arts Sci., Univ. Tokyo)

YODA Jun 依田 潤 (Natl. Res. Lab. Metrol.)
YOSHINO Masuhiro 吉野益弘 (Lab. Phys., Shibaura Inst. Technol.)
ZORAN Valriiu L. (Inst. At. Phys., Inst. Nucl. Eng., Rumania)
ZOU Yaming 邹 亚明 (Jiao Tong Univ., China)

(Students)

CHIBA Daisuke 千羽大介 (Dept. Phys., Sophia Univ.)
FAN Xiao Jun 樊 晓骏 (Fac. Eng. Himeji Inst. Technol.)
FUJINO Atsushi 藤野 敦 (Dept. Phys., Rikkyo Univ.)
FUJIWARA Masamichi 藤原正満 (Dept. Eng. Sci., Kyoto Univ.)
KANEKO Shinichi 金子真一 (Fac. Sci., Tokyo Inst. Technol.)
KAWAE Sotaro 川江宗太郎 (Dept. Phys., Sophia Univ.)
KIMURA Yasuyuki 木村恭之 (Dept. Eng. Sci., Kyoto Univ.)
NAKANO Tomohide 仲野友秀 (Dept. Eng. Sci., Kyoto Univ.)
OKUMA Ryuji 大熊隆次 (Dept. Phys., Rikkyo Univ.)
ONO Yasuhiro 小野泰弘 (Fac. Sci. Tokyo Inst. Technol.)
SAWADA Hirokazu 澤田浩和 (Fac. Sci., Tokyo Inst. Technol.)
SHIMIZU Masakuni 清水正邦 (Fac. Sci., Tokyo Inst. Technol.)
SUZUKI Hajime 鈴木 一 (Fac. Eng., Kyoto Univ.)
TAKEUCHI Hiroko 竹内浩子 (Dept. Phys., Ochanomizu Univ.)
TAMAGAWA Yoshihisa 玉川祥久 (Dept. Phys., Sophia Univ.)
TSUCHIDA Hidetsugu 土田秀次 (Fac. Eng., Kyoto Univ.)

Muon Science Laboratory

FUJITA Ayumi 藤田あゆみ* ¹	HIGEMOTO Wataru 髭本 亘* ¹
ISHIDA Katsuhiko 石田勝彦	KADONO Ryosuke 門野良典
KOYAMA Akio 小山昭雄	KRISHNAMURTHY Vemuru* ²
MATSUZAKI Teiichiro 松崎禎市郎* ³	NAGAMINE Kanetada 永嶺謙忠* ⁴
NAKAMURA Satoshi N. 中村 哲	WATANABE Isao 渡邊功雄
YAGI Eiichi 八木栄一* ³	

*¹ Special Postdoctoral Researcher, *² Visiting Researcher, *³ Senior Scientist,
*⁴ Chief Scientist

(Visitors)

AKIMITSU Jun 秋光 純 (Coll. Sci. Eng., Aoyama Gakuin Univ.)
ASAI Kichizo 浅井吉蔵 (Univ. Electro-Commun.)
BRIERE Tina Marie (Dept. Phys., State Univ. New York, Albany, U.S.A.)
DAS Prasad Tara (Dept. Phys., State Univ. New York, Albany, U.S.A.)
HASHIMOTO Masashi 橋本雅史 (JAERI, Tokai Res. Estab.)
KATO Mineo 加藤岑生 (JAERI, Tokai Res. Estab.)
KINO Yasushi 木野康志 (Fac. Sci., Tohoku Univ.)
KUROSAWA Kiyoyuki 黒沢清行 (JAERI, Tokai Res. Estab.)
MACRAE Roderick M. (JSPS Fellowship)
MATSUSHITA Akira 松下 明 (Contract Researcher)
NISHIDA Nobuhiko 西田信彦 (Fac. Sci., Tokyo Inst. Univ.)
NISHIYAMA Kusuo 西山樟生 (Fac. Sci., Univ. Tokyo)
PRATT Francis Laurence (Dept. Phys., Univ. Oxford, U.K.)
SHIMOMURA Koichiro 下村浩一郎 (Fac. Sci., Univ. Tokyo)
STRASSER Patrick (Nucl. Phys. Div., Inst. Nucl. Study, Univ. Tokyo)
TANASE Masakazu 棚瀬正和 (JAERI, Tokai Res. Estab.)
TORIKAI Eiko 鳥養映子 (Fac. Eng., Yamanashi Univ.)
YONEDA Akira 米田 晃 (Messege Co., Ltd.)

(Students)

DAWSON Wayne (Fac. Sci., Univ. Tokyo)
SASAHARA Takafumi 笹原孝文 (Fac. Sci. and Eng., Chuo Univ.)

Magnetic Materials Laboratory

KATSUMATA Koichi 勝又 紘一*¹
OKADA Takuya 岡田 卓也*²

MATSUDA Masaaki 松田 雅晶
TATARA Gen 多々良 源*³

*¹ Chief Scientist, *² Senior Scientist, *³ Visiting Researcher

Inorganic Chemical Physics Laboratory

AMBE Shizuko 安部 静子
MATSUO Yukari 松尾由賀利

MAEDA Kunuko 前田 邦子
TAKAMI Michio 高見 道生*

* Chief Scientist

(Visitors)

ARAI Nobuaki 荒井 修亮 (Dept. Fisheries, Kyoto Univ.)
ISHII Keizo 石井 慶造 (Cyclotron Radioisot. Cen., Tohoku Univ.)
KAWAI Jun 河合 潤 (Dept. Metallurgy, Kyoto Univ.)

Nuclear Chemistry Laboratory

AMBE Fumitoshi 安部 文敏*
ITOH Yoshiko 伊東 芳子
KOBAYASHI Yoshio 小林 義男
OHKUBO Yoshitaka 大久保嘉高

ENOMOTO Shuichi 榎本 秀一
IWAMOTO Masako 岩本 正子
MAEDA Haruka 前田はるか

* Chief Scientist

(Visitors)

AMANO Ryohei 天野 良平 (Fac. Med., Kanazawa Univ.)
ASAI Kichizo 浅井 吉蔵 (Univ. Electro-Commun.)
BABA Hiroshi 馬場 宏 (Fac. Sci., Osaka Univ.)
CHOU Ju (Changchun Inst. Appl. Chem., China)
ENDO Kazutoyo 遠藤 和豊 (Showa Coll. Pharm. Sci.)
FURUKAWA Michiaki 古川 路明 (Fac. Sci., Nagoya Univ.)
FURUSATO Naohisa 古里 直久 (Coll. Sci. Eng., Aoyama Gakuin Univ.)
HIRUNUMA Rieko 蛭沼利江子 (Showa Coll. Pharm. Sci.)
HSIA Yuanfu 夏 元復 (Dept. Phys., Nanjing Univ., China)
HULETT D. Lester (Oak Ridge Natl. Lab., U.S.A.)
ITO Nobuhiko 伊藤 伸彦 (Sch. Veter. Med. Animal Sci., Kitasato Univ.)
ITO Yasuo 伊藤 泰男 (Res. Cen. Nucl. Sci., Univ. Tokyo)
KANAZAWA Ikuzo 金沢 育三 (Fac. Educ., Tokyo Gakugei Univ.)
KATAYAMA Masayuki 片山 真之 (Fac. Agr., Univ. Osaka Pref.)
KIMURA Kan 木村 幹 (Coll. Sci. Eng., Aoyama Gakuin Univ.)
KOJIMA Sadao 小島 貞男 (Nucl. Med. Cen., Aichi Medical Univ.)
KOMURA Kazuhisa 小村 和久 (Fac. Sci., Kanazawa Univ.)
KUNUGIYAMA Iwao 櫛山 巖 (Sch. Veter. Med. Animal Sci., Kitasato Univ.)
LIU Bin 劉 斌 (Dept. Tech. Phys., Peking Univ., China)
MINAI Yoshitaka 薬袋 佳孝 (Fac. Sci., Univ. Tokyo)
MURAKAMI Hideoki 村上 英興 (Fac. Educ., Tokyo Gakugei Univ.)
NAKAMURA Jin 中村 仁 (Univ. Electro-Commun.)
NASU Saburo 那須 三郎 (Fac. Eng. Sci., Osaka Univ.)
OKAMOTO Yoichi 岡本 洋一 (Showa Coll. Pharm. Sci.)
OZAKI Takuo 尾崎 卓郎 (Fac. Sci., Univ. Tokyo)
PENG Zhilin 彭 治林 (Wuhan Univ., China)
SAITO Tadashi 斎藤 直 (Fac. Sci., Osaka Univ.)
SHIBATA Sadao 柴田 貞夫 (Natl. Inst. Radiol. Sci.)
SHIBATA Seiichi 柴田 誠一 (Inst. Nucl. Study, Univ. Tokyo)
SHINOHARA Atsushi 篠原 厚 (Fac. Sci., Nagoya Univ.)

TANAKA Akira 田中 彰 (Showa Coll. Pharm. Sci.)
WANG Haifang (Peking Univ., China)
WEGINWAR Rajiv G. (Chandrapur Coll. Engineer., India)
YANAGA Makoto 矢永 誠人 (Jikei Univ. Sch. Med.)
YASUDA Hiroshi 保田 浩志 (Natl. Inst. Radiol. Sci.)
YOKOTA Yuko 横田 裕子 (Coll. Sci. Eng., Aoyama Gakuin Univ.)
YOKOYAMA Akihiko 横山 明彦 (Fac. Sci., Osaka Univ.)
YOSHIDA Yutaka 吉田 豊 (Shizuoka Inst. Sci. Technol.)

(Students)

DAIRAKU Tomohisa 大樂 知久 (Fac. Sci., Nagoya Univ.)
ENDO Rieko 遠藤理枝子 (Fac. Sci., Tokyo Metrop. Univ.)
HANYU Takafumi 羽生 貴文 (Showa Coll. Pharm. Sci.)
HAYAKAWA Nobutaka 早川 信隆 (Showa Coll. Pharm. Sci.)
INOUE Takakazu 井上 貴和 (Fac. Sci., Osaka Univ.)
ITOH Masahiro 伊藤 昌宏 (Shizuoka Inst. Sci. Tech.)
ITOH Naoya 伊藤 直弥 (Coll. Sci. Eng., Aoyama Gakuin Univ.)
ITOU Mayu 伊藤 麻由 (Sch. Veter. Med. Animal Sci., Kitasato Univ.)
IWATSUKI Akira 岩月 晶 (Sch. Veter. Med. Animal Sci., Kitasato Univ.)
KASAHARA Ichiro 笠原 一朗 (Showa Coll. Pharm. Sci.)
KATAYAMA Osamu 片山 修 (Fac. Sci., Toho Univ.)
KAWASAKI Yuko 川崎 祐子 (Fac. Sci., Toho Univ.)
KAWASHIMA Yasuko 川島 康子 (Sch. Hygien. Sci., Kitasato Univ.)
MASUDA Yasuhisa 増田 泰久 (Shizuoka Inst. Sci. Tech.)
MORIMOTO Shinya 森本 真哉 (Fac. Sci., Osaka Univ.)
MUKAI Kazuhiko 向 和彦 (Fac. Sci., Osaka Univ.)
MURATA Chihiro 村田 千裕 (Fac. Sci., Nagoya Univ.)
MUROYAMA Toshiharu 室山 俊浩 (Fac. Sci., Nagoya Univ.)
NAKAGAWA Akihiro 中川 彰宏 (Shizuoka Inst. Sci. Technol.)
NAKAJO Terunobu 中條 晃伸 (Tokyo Gakugei Univ.)
NISHIZAWA Satoshi 西沢 諭 (Sch. Hygien. Sci., Kitasato Univ.)
ODA Hirotaka 小田 寛貴 (Fac. Sci., Nagoya Univ.)
ODA Kaori 小田 香織 (Showa Coll. Pharm. Sci.)
OIKAWA Shinji 及川 真司 (Fac. Sci., Kanazawa Univ.)
OSHIMA Nagayasu 大島 永康 (Tokyo Gakugei Univ.)
SASAKI Jin 佐々木 仁 (Tokyo Gakugei Univ.)
SAWADA Naoto 澤田 直人 (Shizuoka Inst. Sci. Technol.)
SEKIGUCHI Akiko 関口 明子 (Coll. Sci. Eng., Aoyama Gakuin Univ.)
SHIBUYA Eriko 渋谷 江利子 (Showa Coll. Pharm. Sci.)
SOGA Kyoko 曾我 恭子 (Fac. Sci., Nagoya Univ.)
SOTOGAKU Naoki 外角 直樹 (Showa Coll. Pharm. Sci.)
TAKAHASHI Yoshio 高橋 嘉夫 (Fac. Sci., Univ. Tokyo)
TANAKA Kenya 田中 研也 (Fac. Sci. Technol., Chuo Univ.)
YASHIKI Kazuhiro 屋鋪 一尋 (Fac. Sci., Toho Univ.)

Chemical Dynamics Laboratory

KIMURA Kazuie 木村 一字

USHIDA Kiminori 丑田 公規

(Visitor)

KAZAMA Shigeo 風間 重雄 (Dept. Phys., Chuo Univ.)

(Students)

HONG Wan 洪 完 (Dept. Chem., Univ. Tokyo)
KAWAKAMI Daisuke 河上大輔 (Dept. Phys., Chuo Univ.)
KOHAMA Takanori 小浜 考徳 (Dept. Phys., Chuo Univ.)

Cellular Physiology Laboratory

HANAOKA Fumio 花岡文雄*
YATAGAI Fumio 谷田貝文夫**

KITAYAMA Shigeru 北山 滋

* Chief Scientist, ** Senior Scientist

(Visitors)

ANDO Koichi 安藤興一 (Natl. Inst. Radiol. Sci.)
FUKUMURA Akifumi 福村明史 (Natl. Inst. Radiol. Sci.)
FURUSAWA Yoshiya 古澤佳也 (Natl. Inst. Radiol. Sci.)
HAMA Yoshimasa 浜 義昌 (Sci. Eng. Res. Lab., Waseda Univ.)
HASHIMOTO Shozo 橋本省三 (Fac. Med., Keio Univ.)
HOSHINO Kazuo 星野一雄 (Natl. Inst. Radiol. Sci.)
IIZUKA Masayuki 飯塚正之 (Natl. Inst. Radiol. Sci.)
ITO Hisao 伊東久夫 (Sch. Med., Chiba Univ.)
ITOH Hiroko 伊藤浩子 (Natl. Inst. Radiol. Sci.)
ITSUKAICHI Hiromi 五日市ひろみ (Natl. Inst. Radiol. Sci.)
KANAI Tatsuaki 金井達明 (Natl. Inst. Radiol. Sci.)
KASAI Kiyomi 笠井清美 (Natl. Inst. Radiol. Sci.)
KAWACHI Kiyomitsu 河内清光 (Natl. Inst. Radiol. Sci.)
KIKUCHI Masahiro 菊地正博 (JAERI, Takasaki Rad. Chem. Res. Estab.)
KIMOTO Masafumi 木元正史 (Natl. Inst. Radiol. Sci.)
KOBAYASHI Yasuhiko 小林泰彦 (JAERI, Takasaki Rad. Chem. Res. Estab.)
KOHNO Toshiyuki 河野俊之 (Natl. Inst. Radiol. Sci.)
KOIKE Sachiko 小池幸子 (Natl. Inst. Radiol. Sci.)
KOJIMA Eiichi 小島栄一 (Natl. Inst. Radiol. Sci.)
KOSAKA Toshifumi 小坂俊文 (Dept. Vet. Radiol., Nihon Univ.)
KUBOTA Nobuo 窪田宜夫 (Fac. Med., Yokohama City Univ.)
MATSUFUJI Naruhiro 松藤成弘 (Natl. Inst. Radiol. Sci.)
McINTYRE Cindy L. (Radiobiol. Unit, Med. Res. Counc., U.K.)
MINOHARA Shinichi 箕原伸一 (Natl. Inst. Radiol. Sci.)
MIYAHARA Nobuyuki 宮原信幸 (Natl. Inst. Radiol. Sci.)
MURAI SO Chidori 村磯知採 (Natl. Inst. Radiol. Sci.)
MURAKAMI Masahiro 村上正弘 (Natl. Inst. Radiol. Sci.)
NAKAI Hirokazu 中井弘和 (Dept. Agric., Shizuoka Univ.)
OHARA Hiroshi 大原 弘 (Dept. Gen. Cult., Okayama Univ.)
OKUMURA Toshiyuki 奥村敏之 (Fac. Med., Univ. Tsukuba)
SASAKI Hiroshi 佐々木 弘 (Fac. Med., Kyushu Univ.)
SHIKAZONO Naoya 鹿園直哉 (JAERI, Takasaki Rad. Chem. Res. Estab.)
SOGA Fuminori 曾我文宣 (Inst. Nucl. Study, Univ. Tokyo)
SUDO Michio 須藤美智雄 (Natl. Inst. Radiol. Sci.)
TAGUCHI Yasuko 田口泰子 (Natl. Inst. Radiol. Sci.)
TAKATUJI Toshihiro 高辻俊宏 (RI Cen., Nagasaki Univ.)
TANAKA Atsushi 田中 淳 (JAERI, Takasaki Rad. Chem. Res. Estab.)
TANAKA Kaoru 田中 薫 (Natl. Inst. Radiol. Sci.)
TATSUZAKI Hideo 立崎英夫 (Fac. Med., Univ. Tsukuba)
TOMURA Hiromi 外村浩美 (Natl. Inst. Radiol. Sci.)
TSUBOI Atsushi 坪井 篤 (Natl. Inst. Radiol. Sci.)
TSUBOUCHI Susumu 坪内 進 (Suzuka Med. Technol. Univ.)
WATANABE Hiroshi 渡辺 宏 (JAERI, Takasaki Rad. Chem. Res. Estab.)
WATANABE Masami 渡辺正己 (Fac. Pharm., Nagasaki Univ.)
YAMASHITA Shoji 山下昌次 (Natl. Saitama Hospital)

(Students)

FUJI Hiroshi 藤 浩 (Fac. Med., Univ. Tsukuba)
KAWASHIMA Mitsuhiko 河島光彦 (Fac. Med., Univ. Tsukuba)
TAKAHASHI Hideyuki 高橋英幸 (Fac. Med., Univ. Tsukuba)

Plant Functions Laboratory

ABE Tomoko 阿部知子
YOSHIDA Shigeo 吉田茂男*²

BAE Chang-Hyu 裴昌然*¹

*¹ Collaborative Scientist, *² Chief Scientist

Microbial Toxicology Laboratory

YAMAGUCHI Isamu 山口勇*

* Chief Scientist

(Member)

ARIE Tsutomu 有江力

(Visitors)

GOUTHO Satyanarayana

SHINONAGA Taeko 篠永妙子

WATANABE Tadakazu 渡部忠一 (Agro-Kanesho Co. Ltd.)

(Student)

MATSUMOTO Ken-ichi 松本健一 (Shimane Univ.)

Safety Center

HARASAWA Kaoru 原沢薫
MATSUZAWA Yasuhide 松沢安秀
NAKANISHI Noriyoshi 中西紀喜*
UWAMINO Yoshitomo 上叢義朋

KAGAYA Satoru 加賀屋悟
MIYAGAWA Makoto 宮川真言
SHINOHARA Shigemi 篠原茂己
YAMANAKA Akira 山仲暁

* Head

Surface Characterization Center

IWAKI Masaya 岩木正哉*

NAKAO Aiko 中尾愛子

* Head

Radioisotope Technology Division

NAKANO Kazushiro 中野和城

YATAGAI Fumio 谷田貝文夫*

* Head

(Visitors)

IJIRI Kenichi 井尻憲一 (Radioisot. Cen., Univ. Tokyo)

ISHIKAWA Masanobu 石川雅紀 (Univ. Tokyo Fisheries)

KAGAWA Yasuhiro 香川康浩 (Toray Res. Cen. Inc.)

KASE Youko 加瀬陽子 (Natl. Inst. Radiol. Sci.)

MAEZAWA Hiroshi 前澤博 (Fac. Med., Tokai Univ.)

OGURA Koichi 小倉紘一 (Coll. Ind. Technol., Nihon Univ.)

OHARA Hiroshi 大原弘 (Dept. Gen. Sci., Okayama Univ.)

SUZUKI Masao 鈴木雅雄 (Fac. Pharm., Nagasaki Univ.)

YATO Osamu 矢頭治 (Kagoshima Agr. Exp. Stn.)

(Students)

HAMANAKA Kenichi 浜中健一 (Fac. Sci. Eng., Waseda Univ.)

MATSUMOTO Hideya 松本英哉 (Fac. Sci. Eng., Waseda Univ.)

AUTHOR INDEX

- ABE Ryo 阿部 亮 3
 ABE Tomoko 阿部知子 127
 ADACHI Minoru 足立 實 61, 64
 AIHARA Toshimitsu 藍原利光 5
 AKAGI Hiroyasu 赤木宏安 3
 AKIMITSU Jun 秋光 純 98
 AKIYOSHI Hiromichi 秋吉哲充 40
 AKUTSU Takao 阿久津亮夫 102
 ALONSO Jose R. 62, 63
 AMANO Ryohei 天野良平 105, 106, 109
 AMBE Fumitoshi 安部文敏 88, 89, 91, 92, 93, 103,
 104, 105, 106, 107, 108,
 109, 110, 111, 112, 113,
 114, 115, 119, 120, 121,
 122, 123
 AMBE Shizuko 安部静子 107, 108, 109, 110, 111, 112,
 113, 114, 115, 116, 118, 119,
 120, 121, 122, 123
 ANDO Atsushi 安東 醇 106
 ANDO Kozo 安藤剛三 77, 78, 79, 80, 81, 82, 146
 ANDO Yoshiaki 安藤嘉章 51, 52
 AOI Nori 青井 考 48, 49, 50, 58, 59, 61, 88, 143
 ARAI Kouji 新井好司 11
 ARATANI Michi 荒谷美智 162
 ARIE Tsutomu 有江 力 117
 ARIGA Takehiro 有賀健博 41, 150
 ARIMA Akito 有馬朗人 13, 19
 ÄRJE Juha 188
 ASAHI Koichiro 旭 耕一郎 59, 61, 64
 AWAYA Yohko 粟屋容子 75, 76, 77, 79, 80, 81, 82,
 83, 99, 100, 101, 145, 146,
 168
 BABA Hiroshi 馬場 宏 124
 BAE Chang-Hyu 裴 昌然 127
 BALITSKY Ianko I. 28
 BATYGIN Yuri 186, 189, 193, 221, 223, 225, 227
 BEAUMEL Didier 48, 49, 50
 BENGTTSSON Peter 79, 80, 82
 BOCHKAREV Oleg 57
 BRAUN Vladimir M. 28
 BUENKER Robert J. 67, 68, 71
 CHIBA Daisuke 千羽大介 145
 CHIBA Toshiya 千葉利哉 5, 186, 188, 189, 191
 CHULKOV Leonid 57
 COQUARD Marie-Pierre 85
 DELBAR Therry 51
 DEPAOLA Brett D. 75
 DINH DANG Nguyen 廷燈 阮 19
 DOKE Tadayoshi 道家忠義 148
 DÖRNER Reinhard 75
 DUTTA C. M. 69
 EATON Gordon H. 37, 39
 EGUCHI-KASAI Kiyomi 江口(笠井)清美 131, 133
 ENDO Kazutoyo 遠藤和豊 108, 110, 111, 112, 113
 ENDOH Yasuo 遠藤康夫 99
 ENGSTRÖM Lars 79
 ENOMOTO Shuichi 榎本秀一 105, 106, 107, 108, 109,
 110, 111, 112, 113, 114,
 115
 EN'YO Hideto 延与秀人 33, 34, 36, 156
 FAN Xiao Jun 樊 曉駿 100
 FEINAUER Adolf 103
 FRANCE III Ralph H. 51
 FUJIMAKI Masaki 藤卷正樹 60, 65
 FUJISHIMA Shiro 藤島史朗 196, 197, 199, 201, 203,
 205, 207, 209
 FUJITA Jiro 藤田二郎 3, 167
 FUJITA Shin 藤田 新 235, 237, 239
 FUJITA Tatsuru 藤田 建 40
 FUJIWARA Masamichi 藤原正満 77, 78
 FUKAO Tetsuhiro 深尾哲宏 54, 55
 FUKUDA Mitsunori 福田光順 54, 55, 62, 63
 FUKUDA Naoki 福田直樹 48, 49, 50, 143
 FUKUDA Shigekazu 福田茂一 54, 55, 60, 62, 63, 64,
 65, 162
 FUKUDA Tomokazu 福田共和 143, 154
 FUKUMOTO Noriko 福本紀子 105
 FUKUNISHI Nobuhisa 福西暢尚 57, 61, 133
 FUKUSHIMA Kimichika 福島公親 100
 FURUKAWA Michiaki 古川路明 124
 FURUSAWA Yoshiya 古澤佳也 132, 133
 FUTAMI Yasuyuki 二見康之 128
 FUWA Toshihiro 不破敏博 90
 GAI Moshe 51
 GEISSEL Hans 57
 GOHSHI Yoichi 合志陽一 162
 GOLOVKOV Mikhail S. 57
 GONO Yasuyuki 郷農靖之 42, 43, 44, 136, 137
 GOTO Akira 後藤 彰 3, 88, 102, 125, 126, 167, 169,
 171, 186, 188, 189, 191, 193,
 195, 196, 197, 199, 201, 203,
 205, 207, 209
 GOTO Yuji 後藤雄二 33, 34, 35, 36, 156
 GOUTHU Satyanarayana 117

- GRUND Thomas 103
- GU Jian-Ping 67, 68
- HÄßLEIN Helmut 103, 104
- HAHN Kevin Inskik 51
- HAMADA Shingo 濱田真悟 42, 43
- HAMANAKA Hiromi 浜中廣見 159
- HANAOKA Fumio 花岡文雄 132, 133
- HARADA Akihiko 原田昭彦 63
- HARASAWA Kaoru 原沢 薫 164
- HASEBE Hiroo 長谷部裕雄 5
- HASEGAWA Ken-ichi 長谷川賢一 159
- HASHIMOTO Masashi 橋本雅史 151
- HASHIZUME Akira 橋爪 朗 165
- HATANAKA Kichiji 畑中吉治 33, 45, 176, 180, 182,
183
- HATSUDA Tetsuo 初田哲男 30
- HATSUKAWA Yuichi 初川雄一 42, 43
- HAYAKAWA Kazuo 早川一生 88, 104
- HAYAKAWA Nobutaka 早川信隆 108
- HAYAKAWA Shinjiro 早川慎二郎 162
- HAYASHI Naoki 林 直樹 33, 34, 35, 36, 156
- HEMMI Masatake 逸見政武 5, 186, 188, 189, 191
- HIES Markus G. 41, 149, 150
- HIGASHI Akio 東 明男 128
- HIRAI Masaaki 平井正明 48, 49, 50, 51, 52
- HIRAI Masanori 平井正紀 27, 35
- HIRANO Masahiko 平野昌彦 133
- HIRATA Daisy 57
- HIROI Zenji 広井善二 98
- HIROSE Takayuki 広瀬孝幸 102
- HIRSCH Gerhard 67, 68, 71
- HIRUNUMA Rieko 蛭沼利江子 110, 111, 112, 113
- HOFMANN Helmut 21
- HOMMA Takayuki 本間隆之 3
- HONG Wan 洪 完 129, 162
- HONMA Michio 本間道雄 18
- HORI Yoichi 堀 陽一 61
- HORIBATA Takatoshi 堀端孝俊 20
- HOSOYA Syoichi 細谷正一 99
- HUI Qin 惠 泰 85
- HULDT Sven 79, 146
- HUTTON Roger 79, 80, 81, 82, 146
- ICHIHARA Takashi 市原 卓 33, 34, 36, 45, 47, 155,
156
- ICHIKAWA Ryuji 市川龍二 3
- IDEUCHI Eiji 井出口栄治 42, 43, 44, 48, 49, 50, 58,
59, 136, 137
- IGARASHI Akinori 五十嵐明則 74, 76
- IIMURA Hideki 飯村秀紀 42, 43
- IKEDA Naoshi 池田 直 90
- IKEGAMI Kumio 池上九三男 3, 169, 196, 199, 201,
203, 205, 207, 209
- IKEZAWA Eiji 池沢英二 5, 186
- IMAI Kenichi 今井憲一 33, 34, 36, 156
- INABE Naohito 稲辺尚人 3, 88, 102, 133, 149, 188,
217, 233
- INADA Nobuya 稲田伸哉 163
- INAMURA Takashi T. 稲村 卓 150, 237, 239
- IRNICH Hartmut 57
- ISHIDA Katsuhiko 石田勝彦 37, 38, 39, 95, 151
- ISHIDA Satoru 石田 悟 45, 46, 47
- ISHIHARA Masayasu 石原正泰 17, 33, 34, 36, 42, 43,
44, 48, 49, 50, 51, 52,
54, 55, 58, 59, 61, 64,
88, 136, 137, 143, 154,
156, 176
- ISHII Keishi 石井慶之 77, 78, 80, 81
- ISHII Koji 石井康二 98
- ISHII Tetsuro 石井哲朗 42, 43
- ISHIZUKA Takeo 石塚武男 150
- ISSHIKI Hiroshi 一色 博 3
- ITO Hisao 伊東久夫 134
- ITO Naoya 伊藤直弥 119
- ITO Sachiko 伊藤祥子 54, 55, 60, 142
- ITO Yasuo 伊藤泰男 125, 126
- ITOH Kazuya 伊藤和也 46
- ITOH Yoshiko 伊東芳子 125, 126, 161
- ITSUKAICHI Hiromi 五日市ひろみ 131
- IVANYUK Fedor A. 21
- IWAMOTO Masako 岩本正子 120, 121
- IWASA Naohito 岩佐直仁 51, 52
- IWASAKI Hironori 岩崎弘典 48, 49, 50
- IWASAKI Masahiko 岩崎雅彦 152
- IZUMI Hideaki 出水秀明 59, 61, 64
- IZUMIKAWA Takuji 泉川卓司 63
- JÄGER Martin 75, 80
- JAKUBEK Zygmunt J. 85
- JANAS Zennon 57
- JIN Wei-Guo 金 衛国 84, 150
- KADONO Ryosuke 門野良典 97, 98
- KAGAWA Yasuhiro 香川康浩 133
- KAGAYA Satoru 加賀谷 悟 164
- KAGEYAMA Tadashi 影山 正 3, 167, 169, 186, 188
- KALNINS George 65
- KAMBARA Tadashi 神原 正 75, 76, 78, 79, 80, 81,
82, 83, 99, 100, 101,
145, 146, 164, 168
- KAMIGAITO Osamu 上垣外修一 3, 186, 188, 189, 191

- KANAI Tatsuki 金井達明 128, 130, 131, 132, 134
KANAI Yasuyuki 金井保之 75, 79, 83, 145, 168
KANEKO Shin-ichi 金子真一 101
KASE Masayuki 加瀬昌之 3, 88, 102, 126, 148, 167,
185, 186, 188, 189, 191
KATAYAMA Takeshi 片山武司 33, 149, 176, 178, 180,
182, 183, 195, 211,
213, 215, 217, 219,
221, 223, 225, 229,
231, 233
KATO Hiroshi 加藤 博 147
KATO Mineo 加藤岑生 37, 39, 151
KATO Takesi 加藤武司 133
KATO Toshiyuki 加藤俊幸 148
KATSUMATA Koichi 勝又紘一 99
KATSURAGAWA Hidetsugu 桂川秀嗣 84
KAWADA Tetsuya 川田哲也 134
KAWAE Sotaro 川江宗太郎 77, 78
KAWAGUCHI Takeo 川口武男 175, 178, 180, 182, 183,
196, 197, 199, 201,
203, 205, 207, 209
KAWAI Jun 河合 潤 163
KAWAKAMI Daisuke 河上大輔 129
KAWAMURA Naritoshi 河村成肇 37, 39
KELLER Horst 57
KIDERA Masanori 木寺正憲 42, 44
KIKUCHI Jun 菊池 順 148
KIKUCHI Tadashi 菊地 正 51, 52
KIM Jong-Won 金 鐘元 173, 175, 196, 197, 199, 201,
203, 205, 207, 209
KIMURA Kan 木村 幹 119
KIMURA Kazuie 木村一字 129, 162
KIMURA Mineo 季村峯生 67, 68, 69, 71, 73
KIMURA Yasuyuki 木村恭之 77, 78
KINK Ilmar 79, 81
KISHIDA Takashi 岸田 隆 42, 43, 44, 48, 49, 50, 58,
59, 136, 137
KITAGAWA Hisashi 北川 尚 12, 30, 31, 60
KITAJIMA Masashi 北島昌史 83
KITAO Kensuke 喜多尾憲助 165
KITAYAMA Shigeru 北山 滋 130
KITAZAWA Hideaki 北澤英明 89, 91
KOBAYASHI Naoya 小林齊也 98
KOBAYASHI Toshio 小林俊雄 53, 54, 55, 56, 57, 60,
62, 63, 142
KOBAYASHI Yoshio 小林義男 88, 89, 91, 92, 93, 103,
104
KOBINATA Hideo 小日向秀夫 154
KODAIRA Jiro 小平治郎 26
KOHAMA Takanori 小浜考徳 129
KOHARA Shigeo 小原重夫 3, 5, 186, 189, 191
KOHARA Takao 小原孝夫 100
KOHN Kay 近 桂一郎 90
KOHNO Tsuyoshi 河野 毅 102, 147
KOIKE Shigetoshi 小池茂年 94
KOIKE Yuji 小池裕司 28, 29
KOJIMA Sadao 小島貞男 124
KOJIMA Takao M. 小島隆夫 75, 76, 79, 81, 168
KORSHENINNIKOV Alexei 53
KOYAMA Akio 小山昭雄 86, 87
KRAUS Gerald 57, 60
KREBS Gary F. 62, 63
KUBO Atsushi 久保敦司 134
KUBO Madoka 久保 円 44
KUBO Toshiyuki 久保敏幸 48, 49, 50, 51, 59, 61, 64,
149, 173, 175, 196, 197,
199, 201, 203, 205, 207,
209
KUBONO Shigeru 久保野 茂 51
KUDO Katsuhisa 工藤勝久 37
KUMADA Masayuki 熊田雅之 185
KUMAGAI Hidekazu 熊谷秀和 44, 48, 49, 50
KUMANO Shunzo 熊野俊三 27, 35
KURASAWA Haruki 倉沢治樹 22
KUROKAWA Meiko 黒川明子 41, 51, 135
KUROKAWA Nobuo 黒河暢雄 64
KUROSAWA Kiyoyuki 黒沢清行 37, 39, 151
KUSAKARI Hideshige 草刈英榮 44
LI Yuan 71
LIPNIK Peter 51
LIU Bin 劉 斌 109
LIU Guanhua 劉 冠華 61
LUCCIO Alfredo 33, 176
LUKYANOV Sergei M. 48, 49, 50
MACRAE Roderick M. 97
MAEDA Haruka 前田はるか 120, 121
MAEDA Kazuhide 前田和秀 40
MAEDA Kuniko 前田邦子 159, 162, 163
MAIE Takeshi 真家武士 3
MAKIDE Yoshihiro 巻出義紘 115
MAO Yajun 冒 亜軍 33, 34, 36
MARTINSON Indrek 79, 80, 81, 146
MASAIKE Akira 政池 明 33, 34, 156
MASUDA Kimiaki 増田公明 148
MATSUDA Masaaki 松田雅昌 99, 100
MATSUDA Sumio 松田純夫 102
MATSUFUJI Naruhiro 松藤成弘 128
MATSUMOTO Ken-ichi 松本健一 116

- MATSUTA Kensaku 松多健策 54, 55, 56, 62, 63
- MATSUYAMA Yoshitaka 松山芳孝 143
- MATSUZAKI Teiichiro 松崎禎市郎 37, 39, 151
- MENNONI Alberto 17
- MERGEL Volker 75
- MICHOTTE Carrine 51
- MIHARA Mototsugu 三原基嗣 54, 55, 62, 63
- MIKI Keitaro 三木敬太郎 142
- MINAI Yoshitaka 葉袋佳孝 114, 115, 121
- MINAMISONO Kei 南園 啓 62
- MINAMISONO Tadanori 南園忠則 54, 55, 62, 63
- MINEMURA Toshiyuki 峯村俊行 41
- MINOWA Tatsuya 箕輪達哉 84
- MITAMURA Tohru 三田村 徹 99, 100
- MITARAI Shiro 御手洗志郎 42, 43, 44
- MITSUMOTO Toshinori 密本俊典 196, 197, 199, 201, 203, 205, 207, 209
- MITSUOKA Shinichi 光岡真一 59, 61
- MIYACHI Takahiko 宮地岳彦 143, 154
- MIYAKE Mami 三宅麻美 43
- MIYAKE Toru 三宅 徹 62, 63
- MIYAMA Masanori 深山正紀 27, 35
- MIYATAKE Hiroari 宮武宇也 58, 59, 61, 143
- MIYAZAKI Kousuke 宮崎光介 44
- MIYAZAWA Yoshitoshi 宮沢佳敏 5, 186, 188, 189, 191
- MIZOI Yutaka 溝井 浩 59, 143, 154
- MIZUSAKI Takahiro 水崎高浩 18
- MOCHINAGA Kensuke 持永建介 61
- MOCHIZUKI Yuko S. 望月優子 24
- MOMOTA Sadao 百田佐多生 54, 55, 60, 62, 63, 65
- MORI Shigehisa 森 茂久 126
- MORII Toshiyuki 森井俊行 32, 35
- MORIKAWA Tetsuya 森川鐵也 196, 199, 201, 203, 205, 207, 209
- MORIKAWA Tsuneyasu 森川恒安 42, 43, 44, 137
- MORIMOTO Shinya 森本真哉 124
- MORITA Kosuke 森田浩介 41, 135, 150
- MORIYA Shingo 守屋真吾 51, 52
- MOTOBAYASHI Tohru 本林 透 41, 51, 52, 135
- MUKAI Kazuhiko 向 和彦 124
- MÜNZENBERG Gottfried 57, 60
- MURAKAMI Hiroyuki 村上浩之 51, 52
- MURAKAMI Masahiro 村上正弘 131
- MURAKAMI Takeshi 村上 健 44
- MURATA Tomoki 村田知樹 44
- MURAYAMA Toshiyuki 村山利幸 150
- MUROYAMA Toshiharu 室山俊浩 124
- NAGAI Yuki 永井由紀 102
- NAGAMINE Kanetada 永嶺謙忠 37, 38, 39, 95, 96, 97, 98, 151
- NAGASE Makoto 長瀬 誠 3
- NAGATA Katsuaki 永田勝明 147
- NAGATA Kazuhiko 長田和彦 61
- NAKADA Yoko 中田陽子 33, 34, 36
- NAKAGAWA Takahide 中川孝秀 3, 167, 171, 186, 188
- NAKAI Yoichi 中井陽一 75, 76, 79, 81, 83, 168
- NAKAJIMA Satoru 中島 理 96
- NAKAJIMA Shunji 中島諄二 235
- NAKAMURA Hiroyuki 中村裕之 40
- NAKAMURA Jin 中村 仁 88, 89, 90, 91, 92, 93, 103, 104
- NAKAMURA Masao 中村正夫 102
- NAKAMURA Masato 中村仁音 85
- NAKAMURA Satoshi N. 中村 哲 37, 39, 151, 152
- NAKAMURA Takashi 中村隆司 17, 48, 49, 50, 51, 52, 53, 54, 55, 58, 141
- NAKANISHI Noriyoshi 中西紀喜 125, 126, 141, 235, 237, 239
- NAKANO Tomohide 中野友英 77, 78
- NAKAO Noriaki 中尾徳晶 141
- NAKASHIMA Takao 中島孝夫 40
- NAKAYAMA Toshitake 中山俊威 134
- NAKAZATO Masahisa 中里真久 63
- NARITA Hirokazu 成田弘一 119
- NASU Saburo 那須三郎 104
- NEUMAIER Sigurt 57
- NICKEL Frank 57
- NIIMURA Masanobu 新村正信 148, 169, 171
- NIIZEKI Takashi 新関 隆 45, 47
- NIKOLSKI Evgenii Yu 53
- NISHIDA Nobuhiko 西田信彦 101
- NISHIDA Tetsuo 西田哲朗 77, 78
- NISHIMORI Nobuyuki 西森信行 40
- NISHIO Teiji 西尾禎二 51, 52
- NISHIYAMA Kusuo 西山樟雄 96, 97
- NISHIYAMA Naoki 西山直樹 29
- NOJIRI Yoichi 野尻洋一 54, 55, 62, 63
- NOMURA Toru 野村 亨 41, 135
- NONAKA Takamasa 野中敬正 45, 46, 47
- NORDLANDER Peter 69
- NORO Yoshihiko 野呂良彦 89, 92, 93
- NOTANI Masahiro 野谷将広 48, 49, 50, 58, 59, 64, 143, 154
- NOZAKI Tadashi 野崎 正 125
- NUMATA Shigeo 沼田茂男 186
- NYSTRÖM Bo 79, 80, 81
- ODAHARA Atsuko 小田原厚子 42, 44
- OGANESSIAN Yuri Ts. 48, 49, 50

- OGAWA Hiroshi 小川博嗣 58, 59, 61, 64
 OGAWA Yoko 小川洋子 11, 55
 OGIWARA Kiyoshi 荻原 清 7, 86, 87, 159
 OHBAYASI Yoshide 大林由英 10
 OHIRA Hideharu 大平秀春 102
 OHIRA Seiko 大平聖子 96
 OHISHI Hidenori 大石英典 237, 239
 OHISHI Kazuki 大石一城 98
 OHKAWA Tomohiro 大川智宏 209, 215
 OHKI Tomonori 大木智則 5
 OHKUBO Yoshitaka 大久保嘉高 124
 OHNUMA Hajime 大沼 甫 45, 47
 OHTOMO Kiyotaka 大友清隆 211, 213
 OHTSUBO Takashi 大坪 隆 54, 55, 62, 63
 OI Makito 大井万紀人 20
 OISHI Shigeo 大石茂雄 105, 106
 OKADA Takuya 岡田卓也 89, 90, 91, 92, 93
 OKAMURA Hiroyuki 岡村弘之 45, 46, 47
 OKAMURA Masahiro 岡村昌宏 33, 178, 180, 182, 183
 OKUNO Hiroki 奥野広樹 61, 64, 149, 196, 197, 199,
 201, 203, 205, 207, 209, 235
 OLSON Douglas 56
 ONISHI Naoki 大西直毅 20
 ONISHI Takashi 大西 崇 54, 55, 62, 63
 ONO Yasuhiro 小野泰弘 101
 OONISHI Tetsuya 大西哲哉 45, 46, 47, 139
 OSHIMA Masumi 大島真澄 42, 43, 44
 OTSU Hideaki 大津秀暁 45, 46
 OTSUKA Takaharu 大塚孝治 9, 17, 18
 OYAMATSU Kazuhiro 親松和浩 23
 OZAKI Takuo 尾崎卓郎 114, 115, 121
 OZAWA Akira 小沢 顕 53, 54, 55, 56, 57, 59, 60, 62,
 63, 65, 142
 OZAWA Shuichi 小澤修一 149
 PENIONZHKEVICH Yuri E. 48, 49, 50
 PERSSON John L. 85
 PIAO Yongnan 148
 PIECHACZECK Andreas 57
 PRATT Francis L. 95
 PRESNYAKOV Leonid P. 72
 PU Yuehu 蒲 越虎 41, 135, 150
 RAO Yinong 饶 亦農 213
 RÖCKL Ernst 57
 RUAN Jian-Zhi 阮 健治 51
 SAGARA Kenshi 相良建至 40
 SAGAWA Hiroyuki 佐川弘幸 12
 SAITO Naohito 齋藤直人 33, 34, 35, 36, 156, 176
 SAITO Tadashi 齋藤 直 124
 SAITO Yuko 齋藤裕子 119
 SAKAI Hideyuki 酒井英行 45, 46, 47, 139
 SAKAI Kenji 酒井健二 64
 SAKAMOTO Naruhiko 坂本成彦 45, 46, 47, 196, 199,
 201, 203, 205, 207,
 209
 SAKAMOTO Shinichi 坂元眞一 37, 38, 39
 SAKATA Hideaki 坂田英明 101
 SAKEMI Yasuhiro 酒見泰寛 31, 33, 34
 SAKURAI Hiroyoshi 櫻井博儀 48, 49, 50, 51, 52, 58,
 143
 SANNIGRAHI A. B. 68
 SASAKI Hiroshi 佐々木 弘 132
 SASAKI Makoto 佐々木 誠 62, 63
 SASAKI Mitsuru 佐々木 充 61
 SATO Hikaru 佐藤 皓 33, 183
 SATO Hiromi 佐藤広海 61, 64
 SATO Hiroshi 佐藤 竝 15, 16
 SATO Kazunori 佐藤和則 62
 SATO Koki 佐藤弘毅 131
 SATOH Kazuhiko 佐藤一彦 101
 SATOU Yoshiteru 佐藤義輝 45, 46, 47
 SCHMIDT-BÖCKING Horst W. 75
 SCHMIDT-OTT W.-D. 61
 SCHWAB Wolfgang 57
 SEEGER Alfred 103
 SETO Sayuri 瀬戸小百合 105
 SHIBAMURA Eido 柴村英道 148
 SHIBATA Masataka 柴田雅隆 42, 43, 44, 136
 SHIBATA Michihiro 柴田理尋 43
 SHIBATA Tokushi 柴田德思 141
 SHIBATA Toshi-aki 柴田利明 33, 34, 35, 156
 SHIGEMATSU Naoyuki 茂松直之 134
 SHIKAZONO Naoya 鹿園直哉 130
 SHIMAMURA Isao 島村 勲 67, 68, 73
 SHIMAZU Tsuneo 島津恒夫 133
 SHIMODA Tadashi 下田 正 59, 61
 SHIMOSAKA Takuya 下坂琢哉 126
 SHIMOURA Susumu 下浦 享 51, 52
 SHIMURA Masakatsu 志村正勝 44
 SHINOHARA Atsushi 篠原 厚 124
 SHINOHARA Shigemi 篠原茂己 164
 SHINONAGA Taeko 篠永妙子 118
 SHIRAKURA Tetsuya 白倉徹也 61
 SHIRATO Shoji 白土鈿二 51
 SHUGYO Shinichi 修行新一 102
 SOTOGAKU Naoki 外角直樹 110, 112, 113
 SUEKI Keisuke 末木啓介 41
 SUELEMANN Raiser 103
 SUGAWARA Masahiko 菅原昌彦 44

- SUGAWARA-TANABE Kazuko 田辺和子 13, 14 196, 197, 199, 201,
SUGIMOTO Kenji 杉本憲治 102 203, 205, 207, 209
- SÜMMERER Klaus 57
- SUN Zuxun 孫祖訓 33
- SUZUKI Masao 鈴木雅雄 133
- SUZUKI Takeshi 鈴木健 54, 55, 57, 60, 62, 63, 65
- SUZUKI Toshio 鈴木俊夫 9, 19, 22
- SUZUKI Yasuyuki 鈴木宜之 10, 11
- SYMONS T. James M. 62, 63
- TACHIMORI Shoichi 館盛勝一 119
- TAGAYA Yu 多加谷祐 41, 135
- TAJIMA Naoki 田嶋直樹 12
- TAKADA Eiichi 高田栄一 142
- TAKADA Masashi 高田真志 141
- TAKADA Tadanori 高田忠徳 106
- TAKAFUJI Rie 高藤里江 106
- TAKAHASHI Katsuhiko 高橋克彦 3
- TAKAHASHI Noriaki 高橋憲明 61
- TAKAHASHI Yoshio 高橋嘉夫 121
- TAKAMI Michio 高見道生 85
- TAKANAKA Masao 高仲政雄 229
- TAKANO Mikio 高野幹夫 98
- TAKAYANAGI Toshinobu 高柳俊暢 145
- TAKEDA Naoto 武田直人 37
- TAKEMATSU Noburu 竹松伸 122, 123
- TAKEZAWA Nobuhisa 竹澤伸久 100
- TAMAGAWA Yoshihisa 玉川祥久 145
- TANABE Kazuko see SUGAWARA-TANABE K.
- TANABE Kosai 田辺孝哉 14
- TANAKA Atsushi 田中淳 130
- TANAKA Kazuhiro 田中和廣 28
- TANAKA Yasushi 田中保志 196, 197, 199, 201, 203,
205, 207, 209
- TANASE Masakazu 棚瀬正和 37, 39, 151
- TANG Jian-Zhi 唐建志 73
- TANIGAKI Minoru 谷垣実 54, 55, 63
- TANIGUCHI Shingo 谷口真吾 141
- TANIHATA Isao 谷畑勇夫 53, 54, 55, 56, 57, 60, 62,
63, 65, 148, 149, 162
- TANIMOTO Sayaka 谷本明佳 59
- TANO Shigemitsu 田野茂光 130
- TANOKURA Atsushi 田野倉敦 44
- TATARA Gen 多々良源 99, 100
- TAWARA Hiroyuki 俵博之 72
- TENDOW Yoshihiko 天道芳彦 165
- TERANISHI Takashi 寺西高 48, 49, 50, 51, 52, 58
- TERASAWA Mititaka 寺澤倫孝 99, 100
- TOMINAGA Takeshi 富永健 114, 121
- TOMINAKA Toshiharu 富中利治 178, 180, 182, 183,
- TOMURA Hiromi 外村浩美 128
- TOSHIMA Nobuyuki 戸嶋信幸 70
- TOYA Kazuhito 戸矢和仁 134
- TSUCHIDA Hideo 土田英夫 42, 43, 44, 137
- TSUDA Masaki 津田理樹 64
- TSUKIORI Noritoshi 月居憲俊 3
- UCHIBORI Takeshi 内堀武司 41, 51, 52
- UDA Masayuki 宇田応之 86, 87
- UEDA Koh-ichi 上田光一 100
- UEHARA Hideki 上原秀樹 237, 239
- UEMATSU Haruko 植松晴子 84
- UENO Hideki 上野秀樹 59, 61
- UESAKA Tomohiro 上坂友洋 45, 46, 47, 139
- USKOV Dmitry B. 72
- URAI Teruo 浦井輝夫 7
- UWAMINO Yoshitomo 上養義朋 141, 164, 235, 237,
239
- VARGA Kálmán 10, 11
- WAKAMATSU Fumihiko 若松文彦 40
- WAKAMATSU Masashi 若松正志 25
- WAKASA Tomotsugu 若狭智嗣 45, 46, 47
- WAKASUGI Masanori 若杉昌徳 84, 139, 149, 150, 231,
233
- WAKIYA Kazuyoshi 脇谷一義 145
- WAKUI Takashi 涌井崇志 46, 84, 139
- WANG Haifang 王海芳 122, 123
- WATANABE Hiroshi 渡辺宏 43, 44, 130
- WATANABE Ikuo 渡辺郁男 209, 213
- WATANABE Isao 渡邊功雄 96, 151
- WATANABE Masami 渡辺正己 133
- WATANABE Naoki 渡部直樹 76
- WATANABE Tadakazu 渡部忠一 116
- WATANABE Yasushi 渡邊康 33, 34, 36, 48, 49, 50,
51, 52, 58, 88, 143,
149, 154, 155, 156
- WATANABE Yutaka 渡辺裕 48, 49, 50, 143, 154
- WEGINWAR Rajiv G. 107
- WIEMAN Howard 56
- WU Heyu 吳和宇 33, 44, 58, 176
- XIA Jiawen 夏佳文 211
- YAGI Eiichi 八木栄一 7, 94, 103, 104
- YAITA Tsuyoshi 矢板毅 119
- YAMADA Kazuyoshi 山田和芳 99
- YAMADA Nobuyoshi 山田修義 90
- YAMAGUCHI Isamu 山口勇 116, 117, 118
- YAMAGUCHI Takayuki 山口貴之 62, 63
- YAMAJI Shuhei 山路修平 19, 21, 235

- YAMAMOTO Sukeyasu Steve 山本祐靖 44, 58
 YAMAMOTO Yoshifumi 山本佳史 58, 59
 YAMANISHI Teruya 山西輝也 32, 35
 YAMASHITA Atsushi 山下敦司 98
 YAMASHITA Shoji 山下昌次 134
 YAMAUCHI Hiromoto 山内啓資 5
 YAMAZAKI Hiroki 山崎展樹 65
 YANAGISAWA Yoshiyuki 柳澤善行 51, 52
 YANO Yasushige 矢野安重 3, 88, 102, 139, 149, 167,
 169, 171, 186, 188, 189,
 191, 193, 195, 196, 197,
 199, 201, 203, 205, 207,
 209
 YANOKURA Minoru 矢野倉 実 162
 YATAGAI Fumio 谷田貝文夫 128, 131, 132, 133
 YIDA-SAKATE A. T. 134
 YOKOTA Yukihiko 横田幸彦 130
 YOKOUCHI Shigeru 横内 茂 196, 199, 201, 203,
 205, 207, 209
 YOKOYAMA Akihiko 横山明彦 124
 YOKOYAMA Go 横山 剛 45, 46
 YOKOYAMA Ichiro 横山一郎 3
 YONEDA Akira 米田 晃 86, 87
 YONEDA Ken-ichiro 米田健一郎 48, 49, 50, 58, 49,
 64, 143
 YOSHIDA Atsushi 吉田 敦 41, 44, 48, 49, 50, 58, 61,
 64, 88, 143, 149,
 154, 155, 165
 YOSHIDA Hyogo 吉田兵吾 125
 YOSHIDA Koichi 吉田光一 53, 54, 55, 56, 57, 60, 62,
 63, 142, 219
 YOSHIDA Shigeo 吉田茂男 127
 YOSHIDA Yutaka 吉田 豊 88, 103, 104
 YOSHIMI Akihiro 吉見彰洋 61, 64
 YOSOI Masaru 與曾井 優 33, 34
 YUAN Youjin 原 有進 211
 YUKIHIRA Ken-ichi 行平憲一 88, 104
 YUNOKI Akira 柚木 彰 148
 ZHAO Xinwei 趙 新馬 161
 ZHOU Xiaohong 周 小紅 42, 43
 ZI-LIN Peng 治林 彭 125
 ZOU Yaming 邹 亚明 79, 146

RIKEN Accelerator Progress Report Vol. 30

理化学研究所加速器年次報告 第30巻 (1997)

印刷 平成9年(1997)3月21日
発行 平成9年(1997)3月31日

発行者 理化学研究所
代表者 有馬朗人
〒351-01 埼玉県和光市広沢2番1号
電話 (048) 462-1111

編集者 理化学研究所加速器研究施設
運営委員会

印刷所 株式会社ユニバーサル・アカデミー・プレス
〒113 東京都文京区本郷6丁目16番2号BR本郷5ビル

定価5,000円
(消費税別)

理化学研究所

埼玉県 和光市 広沢